An improved description of the Z-boson mass lineshape, and a first joint analysis of electroweak parameters and parton distribution functions with the ATLAS experiment at the LHC

Juan Salvador Tafoya Vargas

université
PARIS-SACLAY

An improved description of the Z-boson mass lineshape, and a first joint analysis of electroweak parameters and parton distribution functions with the ATLAS experiment at the LHC

Une description améliorée de la forme de distribution de masse du boson Z, et une première analyse simultanée des paramètres électrofaibles et des fonctions de distribution des partons avec l'expérience ATLAS au LHC

École doctorale n°576 Particules hadrons énergie et noyau : instrumentation, imagerie, cosmos et simulation (PHENIICS)
Spécialité de doctorat: Physique des particules
Graduate School : Physique. Référent : Faculté des sciences d'Orsay

Thèse préparée dans l'unité de recherche **IJCLab (Université Paris-Saclay, CNRS)**, sous la direction de **Zhiqing ZHANG**, directeur de recherche, et la co-direction de **Louis FAYARD**, directeur de recherche émérite.

Thèse soutenue à Paris-Saclay, le 13 octobre 2023, par

Juan Salvador TAFOYA VARGAS

Composition du jury

Membres du jury avec voix délibérative

Maarten BOONEKAMP Directeur de recherche, Université Paris-Saclay	Président
Katerina LIPKA Professeure, DESY et University of Wuppertal	Rapporteure & Examinatrice
Guillaume UNAL Directeur de recherche, CERN	Rapporteur & Examinateur
Claire GWENLAN Professeure, University of Oxford	Examinatrice
Jean-Philippe LANSBERG Directeur de recherche, Université Paris-Saclay	Examinateur

THESE DE DOCTORAT
NNT : 2023UPASP121

université PARIS-SACLAY

ÉCOLE DOCTORALE
Particules, hadrons, énergie et noyau : instrumentation, imagerie, cosmos et simulation (PHENIICS)

Titre: Une description améliorée de la forme de distribution de masse du boson Z, et une première analyse simultanée des paramètres électrofaibles et des fonctions de distribution des partons avec l'expérience ATLAS au LHC

Mots clés: ATLAS, Fonctions de Distribution de Partons, Paramètres électrofaibles, Statistique, Calorimètre, Étalonnage

Résumé: Le travail rapporté dans cette thèse est présenté en deux parties. La première est centrée sur l'étude d'une technique d'étalonnage nouvellement proposée, tandis que la seconde décrit les résultats des premiers ajustements combinés m_W+PDF effectués dans ATLAS.

Le calorimètre électromagnétique à argon liquide est étalonné en examinant la distribution en masse du boson Z dans le canal diélectrons. En utilisant les échantillons d'événements correspondant aux mesures de 2018, une nouvelle technique d'étalonnage Monte Carlo a été mise en œuvre avec l'objectif d'absorber le désaccord restant entre les formes de masse des données mesurées et leur simulation. La méthode consiste en une correction de la résolution en énergie électron par électron, paramétrée en fonction de la pseudorapidité de l'électron et du moment transverse. L'ajustement final a permis d'améliorer l'accord entre les données et le MC, en faisant passer le χ^2 de 2323 à 122 pour 100 degrés de liberté. La même technique d'étalonnage a été répétée par la suite avec des passes spéciales à faible empilement à $13\ \mathrm{TeV}$, pour étudier son impact sur la mesure de la masse du boson W.

Dans le cadre des études de minimisation mises en œuvre pour l'étalonnage, une nouvelle méthode statistique a été proposée afin de traiter les discontinuités dans une courbe χ^2 multidimensionnelle produite par la comparaison entre les histogrammes de deux échantillons. La méthode est basée sur la paramétrisation de l'histogramme pertinent via une forme fonctionnelle continue, qui est utilisée pour estimer un χ^2 par rapport à l'autre histogramme. Cette méthode permet de mettre en œuvre l'ajustement des 40 paramètres utilisés pour définir la correction de la résolution.

L'étude combinée m_W et PDF vise principalement à déterminer la corrélation entre les deux mesures. L'étude porte sur les sections efficaces des bosons W mesurées par les données à faible empilement en fonction du moment transverse du lepton (p_{T}^{ℓ}), utilisé pour sonder la dépendance de p_{T}^{ℓ} en fonction de m_W ; pour les besoins de cette étude, des pseudo-données à $m_W^{\mathrm{nom}} 80.4\ \mathrm{GeV}$ ont été utilisées à à la place des mesures réelles. La contrainte de la partie PDF a été mise en œuvre comme une extension de l'ajustement ATLASpdf21, qui utilise uniquement les données ATLAS (en plus des sections efficaces DIS de HERA). Les études combinées ont révélé une influence importante des PDF sur la valeur ajustée de m_W, conduisant à des décalages de m_W^{fit} (par rapport à m_W^{nom}) qui dépendent de la forme des pseudo-données. Les ajustements combinés finaux de m_W+PDF sur les pseudodonnées (qui incluent toutes les sources systématiques pertinentes) ont montré un décalage de $\Delta m_W = (-7 \pm 23)\ \mathrm{MeV}$ avec une corrélation globale de $\rho_{m_W} \approx 0.39$.

université PARIS-SACLAY

ÉCOLE DOCTORALE
Particules, hadrons, énergie et noyau : instrumentation, imagerie, cosmos et simulation (PHENIICS)

Title: An improved description of the Z-boson mass lineshape, and a first joint analysis of electroweak parameters and parton distribution functions with the ATLAS experiment at the LHC
Keywords: ATLAS, Parton Distribution Functions, Electroweak parameters, Statistics, Calorimeter, Calibration

Abstract: The work reported in this thesis is presented in two parts. The first is focused on the study of a newly proposed calibration technique, while the second describes the results of the first combined m_W+PDF fits performed in ATLAS.

The Liquid Argon electromagnetic calorimeter is calibrated by looking at the mass lineshape of the Z-boson in the di-electron channel. Using the event samples corresponding to 2018 measurements, a newly proposed Monte Carlo calibration technique was implemented with the objective of absorbing the remaining disagreement between the mass lineshapes of the measured data and its simulation. The method consists of an electron-by-electron energy resolution correction, parametrised as functions of electron pseudorapidity and transverse momentum. The final fit improved the data-to-MC agreement, improving the χ^2 from 2323 to 122 for 100 degrees of freedom. The same calibration technique was later repeated with special low pile-up runs at $13\ \mathrm{TeV}$, studying its impact in the measurement of the mass of the W-boson.

As part of the minimisation studies implemented for the calibration, a new statistical method was proposed in order to treat discontinuities in a multidimensional χ^2 curve produced by the histogrammed comparison between two samples. The method is based on the parametrisation of the relevant histogram via a continuous functional form, which is used to estimate a χ^2 against the other histogram. This method allows to implement the fit of the 40 parameters used to define the resolution correction.

The combined m_W and PDF study aims primarily to determine the correlation between both measurements. The study revolves around the low pile-up inclusive W-boson cross sections as a function of lepton transverse momentum (p_{T}^{ℓ}), used to probe the dependency of p_{T}^{ℓ} as a function of m_W; for the purpose of this study, pseudodata at $m_W^{\mathrm{nom}} = 80.4\ \mathrm{GeV}$ was used instead of real unfolded measurements. The constraining of the PDF part was implemented as an extension of the ATLASpdf21 fit, which only uses ATLAS data (on top of HERA DIS cross sections). Combined studies revealed an important influence of the PDF on the fitted value of m_W, leading to shifts of m_W^{fit} (with respect to m_W^{nom}) that depend on the shape of the pseudodata. The final combined m_W+PDF fits on pseudodata (which includes all the relevant sources of systematic) retrieved a shift of $\Delta m_W = (-7 \pm 23)\ \mathrm{MeV}$ with a global correlation of $\rho_{m_W} \approx 0.39$.

Acknowledgements

This thesis marks the culmination of years of dedicated work. A compendium of such magnitude would have not been possible without a wealth of contributions from different individuals that copiously influenced this pilgrimage.

Foremost, I want to thank Guillaume and Katerina for their invaluable role as thesis reviewers, providing comprehensive feedback that greatly enriched this document. Similarly, I extend my thanks to Claire and Jean-Phillipe for being part of my jury, and to Maarten for his dual role as a juror and jury president. The pre- and post-defense discussions have profoundly influenced the content of this thesis and expanded my understanding of its implications.

I am indebted to my supervisors, Louis and Zhiqing, for their unwavering guidance and ceaseless encouragement to work autonomously; the invaluable experience I gathered through the PhD would have been hardly reproducible otherwise. I want to particularly thank Louis for the continuous discussions on academic and cultural matters, as well as for all the help he incessantly provided. It has been a pleasure to work with you over the last years.

Thorough acknowledgment goes to Fra for the guidance and enormous patience offered while struggling with the implementation of PDF fits; getting familiarised with several aspects of these fits would have been nightmarishly difficult and inefficient otherwise. Similarly, I want to thank Hua-Sheng for the many discussions and troubleshooting concerning the theoretical side of cross-section predictions. In the same lines, I consider prudent acknowledging the ATLAS PDF forum, e/γ group and statistics group for the many discussions and their consequential effect over various parts of the work reported in this thesis.

I want to show my appreciation to the IJCLab LHCb group for the honorary adoption and to the IJCLab ATLAS members that I got to meet (whose names shall not be listed in fear of accidentally leaving somebody out) for the motley discussions and happenstances.

I extend my unwavering thanks to my various climbing mates, and particularly those that played a role in keeping me alive, for the far-from-boring unorthodox (sometimes spontaneous and haphazard) adventures that we could coordinate in between thesis works, which complemented my academic life in a non-trivial manner.

Very importantly, I extend my deepest gratitude towards my colleagues and friends with whom I have shared the joyful experiences that unequivocally come entangled with a PhD. Particularly, and alphabetically, I am grateful to have shared such exuberant and manifold times with Andrii, Lera, Polina, Vidya and Yuya. Your company since the days of the Master, and especially towards the end of the PhD, has been invaluable and unforgettable; thank you.

Finally, and supremely, I thank my family. Mami, Papi, Jesusito (y escribo sin algún orden en particular, porque simplemente no me sería posible): les estoy enormemente agradecido por su continuo apoyo incondicional, la constante motivación que me brindan y la infinita paciencia que tienen conmigo. Ustedes han sido parte fundamental de todo lo que he logrado hasta ahora y de lo que está por venir, y por todo eso (y mucho más) les estoy inmensurablemente agradecido. Aunque no tengo las palabras para capturar plenamente mi gratitud, les aseguro que cada paso que doy lo hago teniéndolos presentes. Los amo.

Strategy is beyond the techniques.
Technique is beyond the tools.

Contents

Résumé détaillé en français

L'étude du Modèle Standard est essentielle pour améliorer notre compréhension de la physique fondamentale qui régit notre univers. La conception et les performances des détecteurs ATLAS et CMS tirent parti des énergies record atteintes dans les collisions proton-proton au grand collisionneur de hadrons (LHC), ce qui en fait des pièces maîtresses pour démêler les mécanismes fondamentaux prédits par le Modèle Standard.

La précision de la mesure et de la reconstruction des collisions du LHC dépend fortement de la caractérisation correcte de chacun des sous-systèmes du détecteur ATLAS, ce qui nécessite leur amélioration continue via d'études de performance et d'étalonnage. Ceci est particulièrement intéressant pour le calorimètre électromagnétique à argon liquide, car la plupart des études reposent sur la mesure et la reconstruction de haute qualité des électrons et des photons, comme dans le cas des désintégrations des Z et des bosons de Higgs en diélectrons et diphotons.

Les études axées sur les secteurs électrofaible et fort permettent de tester des propriétés spécifiques du Modèle Standard. En raison de la complexité des deux secteurs, on considère généralement qu'ils ne sont pas corrélés l'un à l'autre, ce qui permet de supposer que les résultats donnés par l'un d'entre eux permettent d'étudier l'autre. Cette approche permet d'étudier les propriétés du Modèle Standard avec une grande précision, mais elle néglige la corrélation possible que les deux secteurs pourraient avoir dans une mesure spécifique, ce qui pourrait conduire à une mauvaise estimation de leurs incertitudes.

Cette thèse est organisé comme suit:

Le chapitre 1 présente le Modèle Standard en passant en revue les particules qui en font partie. Il est suivi d'une description théorique résumée des mécanismes d'interaction pertinents, et un accent particulier est mis sur le traitement utilisé pour étudier la structure cinématique interne du proton en fonction de ses fonctions de distribution des partons (PDF).

Le chapitre 2 présente la base du formalisme statistique utilisé pour les études de physique des hautes énergies, en mettant l'accent sur les techniques appliquées dans l'analyse décrite plus tard. Ce chapitre fournit également une description du logiciel de minimisation `MINUIT`, qui est utilisé pour tous les ajustements de paramètres effectués dans les chapitres d'analyse.

Le chapitre 3 présente une vue d'ensemble des propriétés expérimentales du LHC et du

détecteur ATLAS, couvrant leur état actuel et les améliorations prévues. La description porte à la fois sur les sous-détecteurs et sur la reconstruction des événements.

Le chapitre 4 couvre l'aspect informatique des simulations de mesures expérimentales, en passant par la description théorique de la physique utilisée, par une simulation du détecteur et en finissant par sa comparaison avec les données réelles.

Le chapitre 5 décrit la première partie du travail effectué dans le cadre de ce programme doctoral, qui a consisté à mettre en œuvre une nouvelle méthode d'étalonnage sur des échantillons Monte Carlo pour le calorimètre électromagnétique à argon liquide d'ATLAS afin d'améliorer l'accord entre les données et les modélisations Monte Carlo de $Z \to ee$ à la dernière étape de la procédure d'étalonnage standard. L'étalonnage est mis en perspective avec son impact sur la détermination de la masse du boson W. De plus, ce chapitre décrit une nouvelle méthode statistique capable de traiter les discontinuités de χ^2.

Le chapitre 6 présente la deuxième partie de l'analyse, qui vise à un ajustement simultané des secteurs électrofaible et QCD pour l'étude de leur corrélation. Il décrit les bases des mesures de sections efficaces et des études de PDF du proton, suivies par des études de sensibilité spécifiques et termine par l'ajustement combiné axé sur la masse du boson W.

Le Modèle Standard, les variables électrofaibles et les PDF des protons

Le Modèle Standard de la physique des particules est une théorie quantique des champs qui décrit toutes les particules fondamentales connues et leurs interactions. Il se compose de trois secteurs interdépendants, qui fournissent chacun des éléments constitutifs de notre univers. Il s'agit du secteur électrofaible (responsable de la description des processus électromagnétiques et nucléaires faibles) et du secteur fort (décrit par la chromodynamique quantique).

Les éléments de base du modèle électrofaible sont construits à partir d'une théorie mathématique de Yang-Mills associée à un groupe de symétrie locale, qui définit les couplages entre les composantes gauches et droites des leptons (et des quarks), par l'échange des photons, et des bosons W et Z. La caractérisation correcte de ces bosons est fondamentale pour la description de la plupart des processus physiques, car ils sont impliqués dans de nombreux diagrammes d'ordre principal. Parmi ces médiateurs, la mesure du boson W s'est avérée être l'une des plus difficiles en raison de ses modes de désintégration, qui conduisent à des paires lepton-neutrino (appelé canal semileptonique, et affecté par l'incapacité de mesurer expérimentalement le neutrino), ou à des paires quark-antiquark (appelé canal hadronique, avec les quarks résultant dans des jets). Le travail présenté ici se concentre sur les désintégrations semileptoniques, qui bénéficient de la mesure précise du lepton, tandis que les propriétés du neutrino sont approximées comme l'"énergie manquante" reconstruite à partir des autres mesures cinématiques.

Le secteur fort, à l'instar de son homologue électrofaible, est également décrit par une théorie de Yang-Mills. Ce secteur engendre la quantité conservée appelée nombre quantique de couleur, qui permet la médiation des interactions par l'échange de bosons de jauge colorés que nous appelons gluons. Enfin, ce secteur est responsable du confinement des quarks, qui permet l'existence d'états liés stables tels que les protons et les neutrons. Alors que le Modèle Standard prédit ces états confinés, il n'existe aucune prédiction théorique de la dynamique de leur contenu (composé de quarks et de gluons, et décrit par leur PDF). Au lieu de cela, il faut les contraindre par des prescriptions approximatives utilisant des données réelles. Il s'agit là du point essentiel des études de chromodynamique quantique, qui se propage vers les mesures électrofaibles par le biais de contributions importantes dans les incertitudes finales.

La mesure précise des propriétés de chaque secteur est fondamentale pour la compréhension et la validation du Modèle Standard, ainsi que pour déterminer si un phénomène spécifique pourrait être une manifestation d'une nouvelle physique. Il est donc intéressant de chercher en permanence à améliorer les mesures afin d'atteindre la plus grande précision possible, et de les refaire lorsque les progrès théoriques et informatiques permettent d'élaborer des modèles plus sophistiqués et plus précis.

Étalonnage du calorimètre électromagnétique

Toutes les études en physique des particules sont étroitement liées aux performances des détecteurs utilisés pour mesurer les produits des collisions des particules. Le traitement correct des signaux électroniques et leur traduction en quantités physiques sont fondamentaux dans toute étude de précision, et c'est pourquoi des efforts importants sont déployés pour améliorer l'étalonnage complet d'un détecteur.

Dans l'expérience ATLAS, le calorimètre électromagnétique à argon liquide est chargé de la mesure précise et de la reconstruction des photons et des électrons produits par les collisions du LHC, ainsi que de la mesure partielle de l'énergie des jets et de l'aide à l'identification des particules. Cela en fait un élément précieux dans la reconstruction de toute collision de particules, et un instrument fondamental dans l'étude du Modèle Standard. À ce titre, une chaîne d'étalonnage complexe a été mise en place afin de prendre en compte dans les simulations toutes les caractéristiques possibles du détecteur réel. À la fin de la chaîne d'étalonnage, l'amélioration de l'accord entre les mesures et les simulations permet de générer des mesures qui sont souvent limitées par la modélisation de la physique réelle.

En examinant le dernier accord entre les données et la simulation de la masse invariante du boson Z, plusieurs divergences peuvent être extraites malgré les efforts continus pour améliorer l'étalonnage sur la base d'arguments physiques. Cherchant à comprendre les implications de ce désaccord persistant, cette thèse explore une nouvelle méthode de calibration proposée, basée sur des corrections de résolution en énergie des électrons de la

simulation.

La mise en œuvre finale de la nouvelle méthode d'étalonnage a permis d'obtenir un accord presque parfait entre les données et la simulation, qui reste stable à travers le calorimètre [1]. L'implication de cette méthode d'étalonnage a ensuite été étudiée par quelques étudiants en stage, qui ont vérifié si le même étalonnage peut être extrapolé à des échantillons de données à faible empilement.

Un bon étalonnage du calorimètre électromagnétique est particulièrement important pour la détection des bosons W qui se désintègrent par les canaux électron-neutrino. Par conséquent, l'impact de la nouvelle méthode d'étalonnage sur la mesure de m_W a été étudié par les étudiants en stage, cherchant à comprendre le décalage attendu par rapport aux échantillons étalonnés de façon nominale.

Nouvelle méthode statistique pour l'estimation des paramètres de χ^2

La méthode de calibration mentionnée ci-dessus a pour objectif principal d'améliorer l'accord entre les données et les distributions simulées de la masse invariante $Z \to ee$. Cela implique que les paramètres sont déterminés en minimisant la différence de forme entre ces 2 distributions, ce qui a été fait via un χ^2 obtenu par une comparaison d'histogrammes.

Comme le χ^2 est estimé entre un histogramme de référence fixe (données) et un histogramme changeant (simulation calibrée), la minimisation a conduit à un problème statistique couramment rencontré (mais généralement contourné), se traduisant par des discontinuités du χ^2 sur l'ensemble de l'intervalle testé, ce qui conduit à un minimum mal défini. Comme aucun traitement clair n'était disponible pour les besoins de cette étude, j'ai proposé une nouvelle méthode statistique capable de traiter les discontinuités, permettant de revenir à une courbe de χ^2 lisse avec un minimum bien défini. Cette méthode fait l'objet d'une note, qui a été acceptée par le groupe statistique d'ATLAS et publiée comme ATLAS PubNote [2].

Mesures de m_W et ajustements de la PDF

Les études de précision dans le secteur électrofaible et les PDF sont réalisées en supposant que ces deux secteurs sont décorrélés, ce qui permet de supposer l'un d'entre eux pour étudier l'autre. Cela s'explique en partie par la complexité inhérente à l'étude de chaque secteur, qui aboutirait sinon à de grosses difficultés du point de vue humain et informatique.

Les dernières mesures de la masse du boson W au LHC bénéficient d'échantillons statistiques plus importants et de contributions systématiques bien étudiées provenant du détecteur. Cependant, l'incertitude totale reçoit une contribution majeure propagée à

partir des PDF. Comme la mesure de m_W suppose une décorrélation totale des PDF, on peut s'attendre à une mauvaise estimation de son effet sur l'incertitude totale, conduisant à une valeur supérieure (ou inférieure) à la valeur réelle.

Afin de mieux comprendre la corrélation entre m_W et les PDF, une nouvelle approche de leur ajustement est discutée dans cette thèse, cherchant à contraindre simultanément ces deux quantités. L'étude se concentre en particulier sur l'extension d'une étude existante des PDF (à savoir, l'ajustement ATLASpdf21) en ajoutant des données ATLAS supplémentaires, sous la forme de sections efficaces différentielles de bosons W inclusifs à faible empilement en fonction de p_{T}^{ℓ}, utilisées pour la mesure de m_W.

L'étude présentée ici est réalisée avec des pseudodonnées représentatives des sections efficaces mesurées à faible empilement, effectuées par étapes afin de mieux comprendre l'impact des différentes sources d'incertitude systématique sur la mesure finale. La corrélation globale entre la valeur m_W ajustée et la PDF est montrée, ainsi que le décalage de la masse ajustée par rapport à celle injectée par les pseudodonnées.

Contribution de l'auteur

Les contributions spécifiques de l'auteur à la collaboration ATLAS et aux sous-groupes d'analyse dédiés sont les suivantes :

Etude et mise en œuvre d'une nouvelle technique d'étalonnage proposée (par l'USTC) pour le calorimètre électromagnétique. Elle consiste en une correction de la résolution d'énergie électron par électron appliquée à l'échantillon de Monte Carlo, optimisée à l'aide d'une paramétrisation non linéaire dont les paramètres ont été déterminés à l'aide d'un cadre de minimisation entièrement conçu par l'auteur autour de `MINUIT`. De plus, sous la supervision de l'auteur, la même technique d'étalonnage a été appliquée par des étudiants en stage sur des séries d'empilement particulièrement faibles, ce qui a été suivi par une étude de son impact sur la mesure de la précision de la masse du boson W.

Comme résultat secondaire du travail d'étalonnage, l'auteur a proposé une méthode pour corriger les discontinuités de χ^2, un problème qui est généralement contourné en utilisant des techniques approximatives. Cette méthode a été acceptée par le groupe de statistiques d'ATLAS et rendue publique sous la forme d'une ATLAS PubNote.

Enfin, l'auteur a mené des études sur les ajustements combinés m_W+PDF, qui n'étaient pas étudiés par la collaboration ATLAS auparavant. Il s'agit notamment d'études de sensibilité des sections efficaces aux variations de m_W, de la mise en œuvre de la méthode d'ajustement combiné dans le cadre d'ajustement PDF `xFitter`, d'études de closure et de biais, et d'ajustements exploratoires effectués sur des pseudo-données. L'objectif final est de déterminer la corrélation entre m_W et les PDF, tout en étudiant son effet sur la valeur mesurée de la masse du boson W. Ces ajustements ont été effectués sur une réplique de pseudodonnées utilisés pour mesurer une section efficace inclusive de W en fonction de p_{T}^{ℓ}, ce qui a permis d'étudier l'influence de chaque systématique sur la valeur ajustée de m_W et sa corrélation avec le reste des paramètres des PDF.

Introduction

The study of the Standard Model is cardinal to improve our understanding of the fundamental physics that governs our universe. The design and performance of the ATLAS and CMS detectors take advantage of the record energies attainable in proton-proton collisions at the Large Hadron Collider, which makes them key pieces for unravelling the root mechanisms predicted by the Standard Model.

Precise measurement and reconstruction of LHC collisions rely heavily on the proper characterisation of each of the subsystems of the ATLAS detector, which calls for their continuous improvement via performance and calibration studies. This is of special interest for the Liquid Argon electromagnetic calorimeter, as most studies rely on the high-quality measurement and reconstruction of electrons and photons, such as the case of diphoton Higgs-boson decays and neutral di-electron decays of Drell-Yan events.

Studies focused on the electroweak and strong sectors are fundamental to test specific properties of the Standard Model. Due to the complexity of both sectors, these are typically approximated to be uncorrelated from each other, often leading to assume the results given by one of them in order to study the other. Such an approach is used to study Standard Model properties with high precision, but it neglects the possible correlation that both sectors could have into a specific measurement, potentially leading to misestimation of their uncertainties.

The structure of this thesis is as follows:

Chapter 1 provides an introduction to the Standard Model, going through the particles that integrate it. It is followed by a summarised theoretical description of the relevant interaction mechanisms, and particular focus is put towards the mathematical treatment used to study the internal kinematic structure of the proton according to its parton distribution functions.

Chapter 2 shows the basis of the statistical formalism used for high-energy physics studies, emphasising techniques relevant to the analysis described thereupon. This Chapter also provides a description of the minimisation framework `MINUIT`, which is used as the base of all the parameter fits implemented in the analysis chapters.

Chapter 3 shows a general overview of the experimental properties of the LHC and the ATLAS detector, covering their current state and planned upgrades. The description encompasses both hardware characteristics and the event reconstruction process.

Chapter 4 covers the computational side of the simulations of experimental measurements, going through the theoretical prescription of the relevant physics, passing through a simulation of the detector, and finalising by its comparison to real data.

Chapter 5 describes the first part of the work done for this doctoral program, which consisted of the implementation of a new calibration method on Monte Carlo samples for the Liquid Argon electromagnetic calorimeter of ATLAS in order to improve the agreement between the data and Monte Carlo $Z \to ee$ mass lineshape at the last stage of the standard calibration procedure. The calibration is put in perspective of its impact on the determination of the mass of the W-boson. Moreover, this Chapter describes a novel statistical method capable of treating χ^2 discontinuities.

Chapter 6 reports the second part of the analysis, which aims for a simultaneous fit of the electroweak and QCD sectors for the study of their correlation. It describes the basics of cross-section measurements and proton PDF studies, followed by dedicated sensitivity studies and finalised by a first combined fit aimed towards a measurement of the mass of the W-boson.

Contribution of the author

The specific contributions of the author towards the ATLAS collaboration and dedicated analysis subgroups are:

Study and implementation of the conceptual idea for a new calibration technique proposed for the electromagnetic calorimeter. It consists of an electron-by-electron energy resolution correction applied on the Monte Carlo sample, optimised using a non-linear parametrisation whose parameters were determined using a minimisation framework designed entirely by the author around `MINUIT`. Moreover, under the supervision of the author, the same calibration technique was applied by internship students on special low pile-up runs, which was followed by a study of its impact on the W-boson mass precision measurement.

As a secondary outcome of the calibration work, the author has proposed a method to correct χ^2 discontinuities, a problem that typically is worked around using approximate techniques. This method has been accepted by the ATLAS statistics group and released to the public as an ATLAS PubNote.

Finally, the author carried out studies for combined m_W+PDF fits, which were not studied by the ATLAS collaboration before. This includes dedicated cross-section sensitivity studies to changes of m_W, implementation of the combined fit method in the PDF fitting framework `xFitter`, closure and bias studies, and exploratory fits performed on pseudodata. The final target is to determine the correlation between m_W and the PDF while inspecting its effect on the measured value of the W-boson mass. These fits were performed on a pseudodata replica of the ongoing effort to measure an inclusive W cross section as a function of p_{T}^{ℓ}, which allowed to study of the influence of each systematic on the fitted value of m_W and its correlation with the rest of the PDF parameters.

1 Theoretical foundations

1.1 The Standard Model in brief

The Standard Model (SM) of particle physics is a quantum field theory that describes all known fundamental particles and their interactions. It is typically described using group theory representations that are bound by the local gauge symmetry given by

$$G = SU(3)_C \times SU(2)_L \times U(1)_Y, \tag{1.1}$$

where $SU(2)_L \times U(1)_Y$ govern the electroweak sector (that is, electromagnetic (em) and nuclear weak processes, often conjointly referred to as EW), while $SU(3)_C$ shapes the strong sector. All interactions between particles are mediated by gauge bosons that are specific to each sector, which define the characteristics of each process and constrain all possible processes. The strong sector is mediated by massless gluons (G^a_μ, where a takes values from 1 to 8). Electroweak interactions are mediated by the gauge bosons (W^i_μ, B_μ), which spawn three massive vector bosons ($W^\pm, Z^0$) and a massless vector boson (γ, the photon) after the spontaneous symmetry breaking of $SU(2)_L \times U(1)_Y \to U(1)_{\text{em}}$.

Noether's theorem [3] states that every differentiable (and thus, continuous) symmetry of a physical system has a corresponding conserved quantity. Following from the local gauge symmetry G of the SM, each of the operators in Eq. (1.1) spawn a set of quantum numbers that are conserved:

- $U(1)_Y$ leaves invariant the weak hypercharge Y;
- $SU(2)_L$ conserves the weak isospin multiplet I;
- $SU(3)_C$ gives defines colour multiplet C;

allowing the electric charge Q to be define via

$$Q = T_3 + \frac{1}{2}Y,$$

where T_3 is the third component of the corresponding weak isospin I.

The total Lagrangian describing the physics that governs the SM can be written as the sum of the specific contributions from each sector, allowing their characteristics to

be studied separately. For the purpose of the studies developed in this thesis, one may represent said Lagrangian as

$$\mathcal{L}_{\text{SM}} = \mathcal{L}_{\text{EW}} + \mathcal{L}_{\text{QCD}} + \mathcal{L}_{\text{Higgs}} + \mathcal{L}_{\text{Yukawa}}. \tag{1.2}$$

While the details are beyond the scope of this manuscript, one can show that the action of the various gauge transformations encompassed by symmetry group G on each of the components of the $\mathcal{L}_{\text{SM}}$ define the kinematics of the SM and its conservation rules. Requiring invariance under such symmetries spawns the operators that describe the fermions and bosons (including those described above), which are identified by the aforementioned quantum numbers. Following the notation defined above, a typical representation of the SM particles is given as $(C, I)_Y$, where C corresponds to a singlet for leptons and the Higgs boson and triplet for quarks, and I represents a doublet for left-handed chirality fermions and Higgs and singlet for right-handed fermions. Consequently, each particle can be represented as

$$\begin{aligned}
\text{Leptons} : l_{iL} &= \begin{pmatrix} \nu_i \\ e_i \end{pmatrix}_L : (1,2)_{Y=-1}, \quad e_{iR} : (1,1)_{Y=-2} \\
\text{Quarks} : q_{iL} &= \begin{pmatrix} u_i \\ d_i \end{pmatrix}_L : (3,2)_{Y=1/3}, \quad u_{iR} : (3,1)_{Y=4/3}, \quad d_{iR} : (3,1)_{Y=-2/3} \\
\text{Higgs} : \Phi &= \begin{pmatrix} \phi^+ \\ \phi^0 \end{pmatrix} : (1,2)_{Y=1}
\end{aligned}$$

noting the absence of right-handed neutrinos (which is forbidden under the current formalism). In more practical terms, these representations correspond to the 3 families of leptons (e, μ, τ) and neutrinos $(\nu_e, \nu_\mu, \nu_\tau)$, along 3 generations of u- (u, c, t) and d-type (d, s, b) quarks. A schematic representation of all the particles (and their corresponding antiparticles) predicted by the SM is provided in Fig. 1.1, which also depicts their classification in generations, mass, charge and spin.

The following paragraphs are intended to briefly overview the theoretical prescription used to describe the SM. Further details may be found in dedicated theoretical [5, 6, 7] or historical [8] sources.

Let us quickly examine each term that contributes to the SM Lagrangian from a group theory point of view. For the sake of compactness and clarity, let us write the operators involved in the SM using the reduced tensorial notation under Minkowski's metric (η). That is, using

$$\eta_{\mu\nu} = \begin{pmatrix} 1 & 0 & 0 & 0 \\ 0 & -1 & 0 & 0 \\ 0 & 0 & -1 & 0 \\ 0 & 0 & 0 & -1 \end{pmatrix}, \tag{1.3}$$

we define the product of two tensors A^μ and B^ν in the reduced form as

$$A \otimes B = A_\mu B^\mu = \eta_{\mu\nu} A^\nu B^\mu = \sum_\mu \sum_\nu (\eta_{\mu\nu} A^\nu B^\mu) = A^0 B^0 - A^1 B^1 - A^2 B^2 - A^3 B^3 \tag{1.4}$$

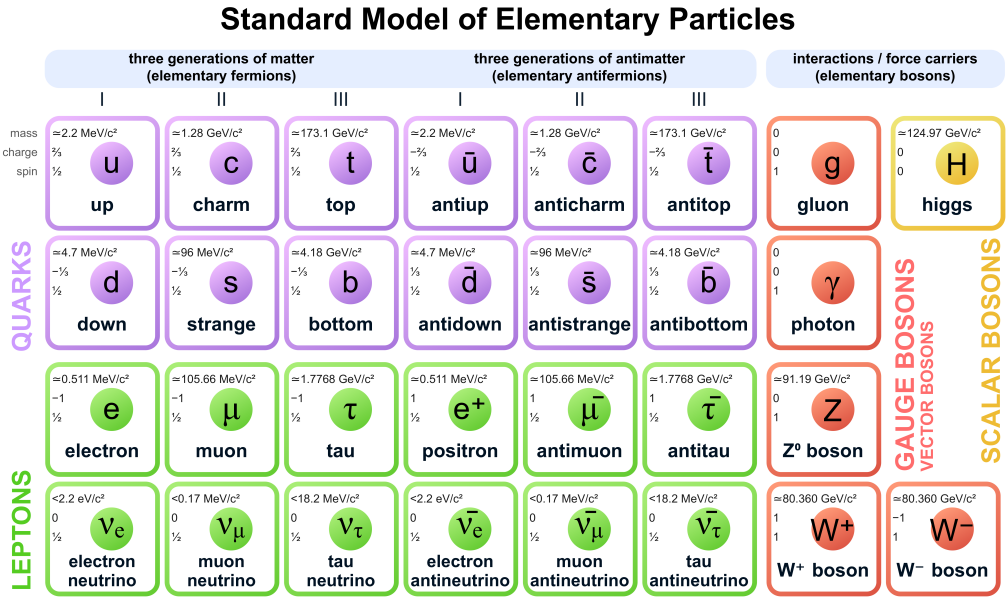

Figure 1.1: Fermions and bosons predicted by the Standard Model [4]. The mass, charge and spin of each particle are also shown.

such that Greek indices (μ, ν) run from 0 to 3.

The operators describing the electroweak sector are defined under a Yang-Mills theory [9], defined by the symmetry group $SU(2)_L \times U(1)_Y$. The basic blocks of the electroweak kinematics are built around the field strength intensities of the $U(1)$ gauge boson (called $B_{\mu\nu}$) and that of $SU(2)$ (denoted $W^i_{\mu\nu}$); and the couplings between left-handed (Ψ_L) and right-handed (Ψ_R) components of leptons (and quarks). Overall, the contribution of the electroweak sector to the SM Lagrangian takes the form of

$$\mathcal{L}_{\text{EW}} = -\frac{1}{4} W^i_{\mu\nu} W_i^{\mu\nu} - \frac{1}{4} B_{\mu\nu} B^{\mu\nu} + \bar{\Psi}_L i\gamma^\mu D_\mu \Psi_L + \bar{\Psi}_R i\gamma^\mu D_\mu \Psi_R, \tag{1.5}$$

where

$$\begin{aligned} W^i_{\mu\nu} &= \partial_\mu W^i_\nu - \partial_\nu W^i_\mu + g\epsilon^{ijk} W^j_\mu W^k_\nu, \quad B_{\mu\nu} = \partial_\mu B_\nu - \partial_\nu B_\mu, \\ D_\mu \Psi_L &= \left(\partial_\mu + ig\frac{\sigma_i}{2} W^i_\mu + ig'\frac{Y}{2} B_\mu\right) \Psi_L, \quad D_\mu \Psi_R = \left(\partial_\mu + ig'\frac{Y}{2} B_\mu\right) \Psi_R. \end{aligned} \tag{1.6}$$

Here, σ_i are the Pauli matrices, γ^μ correspond to the Dirac matrices, and D_μ represents the gauge covariant derivative. Moreover, ϵ^{ijk} are the structure constants of the $SU(2)$ representation. The values g and g' play the role of simple coupling constants for the $SU(2)$ and $U(1)$ groups, respectively. N.B. following from the second line of Eq. (1.6) (and as briefly alluded to a few paragraphs ago), Ψ_L couples to the fields W^i_μ and B_μ (i.e. $SU(2) \times U(1)$), while Ψ_R interacts only with $W^i_\mu \in SU(2)$.

Similarly to the electroweak sector, the strong sector is also described by a Yang-Mills theory defined by the $SU(3)_C$ symmetry group. Since such symmetry spawns the colour quantum number [10], the theory describing the strong interaction is typically called Quantum Chromodynamics (QCD). It is in charge of describing gluon physics via the strength tensor $G^a_{\mu\nu}$ (where a takes values from 1 and 8) and the corresponding gauge covariant derivative D_μ. Thus, the QCD contribution to the SM Lagrangian takes the shape of

$$\mathcal{L}_{\text{QCD}} = -\frac{1}{4} G^a_{\mu\nu} G^{\mu\nu}_a + \bar{q}\gamma^\mu D_\mu q, \tag{1.7}$$

with

$$G^a_{\mu\nu} = \partial_\mu G^a_\nu - \partial_\nu G^a_\mu + g_s f^{abc} G^b_\mu G^c_\nu, \quad D_\mu q = \left(\partial_\mu + i g_s \frac{\lambda_a}{2} G^a_\mu\right) q. \tag{1.8}$$

Here, q represents the quark Dirac field (both for left-handed and right-handed particles, and for all the 6 flavours), the term $-\frac{1}{4} G^a_{\mu\nu} G^{\mu\nu}_a$ describes the kinematics of gluons, and their action as propagator between pairs of quarks gets defined by $\bar{q}\gamma^\mu D_\mu q$. The term f^{abc} corresponds to the structure constants of the representation of the $SU(3)$ group, whose generators λ_a typically follow the Gell-Mann representation [10].

The quantity g_s in Eq. (1.8) corresponds to the strong coupling constant, whose value depends on the kinematics of the system: at high energy (equivalent short distance), g_s vanishes according to the "asymptotic freedom" of QCD. This phenomenon prevents the creation of infinite gluons as quarks stride apart from each other, limiting the range on which strong interactions can occur. In the lower energy side (known as the infrared limit), the "quark confinement" phenomenon prevents quarks from becoming isolated from the rest of the partons, which would result in free coloured fermions. Consequently, while individual quarks confined within a hadron have colour, free particles must be colourless.

Unlike the electroweak and strong prescriptions, the Higgs sector is described by a scalar field (labelled as Higgs field and represented by Φ), defined as an $SU(2)$ complex doublet. This doublet can be written in terms of a charged (ϕ^+) and neutral (ϕ^0) complex component as

$$\Phi = \begin{pmatrix} \phi^+ \\ \phi^0 \end{pmatrix},$$

leading to the Lagrangian

$$\mathcal{L}_{\text{Higgs}} = |D_\mu \Phi|^2 - V(\Phi), \tag{1.9}$$

with

$$\begin{aligned} D_\mu \Phi &= \left(\partial_m uu + i g \frac{\sigma_i}{2} W^i_\mu + i g' \frac{Y_L}{2} B_\mu\right) \Phi \\ V(\Phi) &= \mu^2 \Phi^\dagger \Phi + \lambda (\Phi^\dagger \Phi)^2. \end{aligned} \tag{1.10}$$

While it is not relevant to the studies shown in the following chapters, one should notice that the spontaneous symmetry breaking of the Higgs potential (along with the capability

of $V(\Phi)$ to take positive and negative values) and its subsequent rewriting as a scalar field h becomes into the process responsible for the mass generation of particles, which receives the name of the Higgs mechanism. In the case of the mass generation of fermions, the Higgs field acts through a Yukawa term which looks as

$$\mathcal{L}_{\text{Yukawa}} = -y^u_{ij}\bar{q}_{iL}u_{jR}\tilde{\Phi} - y^d_{ij}\bar{q}_{iL}d_{jR}\Phi - y^e_{ij}\bar{l}_{iL}e_{jR}\Phi + h.c. \tag{1.11}$$

where the Yukawa coupling matrices for u-type, d-type and leptons (excluding neutrinos) are denoted by $y^{u,d,e}_{ij}$; $\tilde{\Phi}$ is the charge-conjugate of the Higgs field such that

$$\tilde{\Phi} = i\sigma_2\Phi^* = \begin{pmatrix} \bar{\Phi}^0 \\ -\bar{\Phi}^+ \end{pmatrix};$$

and $h.c.$ accounts for the "hermitian conjugate" of the operators on the left.

1.2 The matrix element and process cross sections

The Lagrangians and corresponding operators defined in Section 1.1 allow for specific particle processes to be mathematically described, as long as these are allowed by the symmetry group. Such description relies on the matrix representation of a propagator (typically a gauge boson) acting between two quantum states, which estimates the transition probability between states. For an initial $|\psi_{\text{initial}}\rangle$ and final $|\psi_{\text{final}}\rangle$ state mediated by an operator A, the matrix element gets defined by

$$\mathcal{M} = \langle\psi_{\text{final}}|A|\psi_{\text{initial}}\rangle, \tag{1.12}$$

such that

$$|\mathcal{M}|^2 = \mathcal{M}^\dagger\mathcal{M} \tag{1.13}$$

computes the transition probability. As this probability is dependent on the phase space of the final particles, there is an equivalence (up to a constant) between $|\mathcal{M}|^2$ and the cross section σ of such process, i.e.

$$\sigma \propto |\mathcal{M}|^2. \tag{1.14}$$

By choosing a specific final state observable (such as an angular or kinematic property) and integrating along the phase space of all the others, one can determine the corresponding differential cross-section distribution. For an observable X out of a set $\{p^\mu\}$ with N variables, this may look as

$$\frac{\mathrm{d}\sigma}{\mathrm{d}X} \propto \underbrace{\int_{\Omega_{p^1\neq X}} \cdots \int_{\Omega_{p^N\neq X}}}_{N-1} \left(\prod_{\mu \mid p^\mu \neq X} \mathrm{d}p^\mu \right) |\mathcal{M}|^2. \tag{1.15}$$

Following the previous equations, cross sections are a direct manifestation of the theoretical properties used to describe the SM. Consequently, the measurement of cross sections

for specific processes and their comparison with their predictions gives invaluable information regarding the reliability of theoretical building blocks, allowing the value of some of the constants in $\mathcal{L}_{\text{SM}}$ to be determined and detailed features of particle kinematics to be studied.

It is worth mentioning that, while the detailed description of a process is completely defined by its matrix element, it is often useful to appeal to the use of visual aids such as Feynman diagrams [11, 12]. By defining a set of graphical rules that encodes the mathematically complex operators that represent propagators (bosons) and fermions in space-time, Feynman diagrams are used to build a schematic drawing that is physically equivalent to a given matrix element. A basic example of such a diagram is shown in Fig. 1.2, which depicts a case of electron-positron scattering.

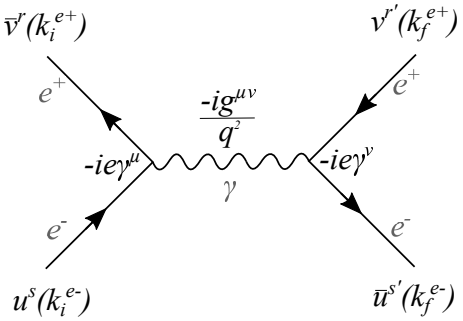

Figure 1.2: Feynman diagram corresponding to electron-positron scattering, mediated by a photon. Relevant quantities are shown, which include the initial and final momentum and spin states of the leptons, as well as the interaction couplings and the propagator operator.

1.3 Electroweak sector generals

While interactions in the electroweak sector are defined by $\mathcal{L}_{\text{EW}}$, the corresponding kinematics rely on knowledge of constants, which may account for properties such as particle masses or coupling strengths. Since such constants are predicted by the SM, it is often possible to extract direct measurements using high-precision methods from dedicated experiments. Such is the case of the mass of the Z- and W-bosons, which where discovered in 1983 at CERN using $p\bar{p}$ collisions [13, 14, 15, 16]. Consequently, the studies in charge of extracting such parameters are typically referred to as "precision measurements". Overall, this allows determining many of the particle properties summarised in Fig. 1.1.

In a nutshell, interactions in the electroweak sector are governed by either of 3 mediators:

- photons (γ), which are massless and charge-neutral;

- Z-boson, which is massive ($m_Z = 91.188 \pm 0.0021$ GeV, with width $\Gamma_Z = 2.485 \pm 0.0023$ GeV [17]) and charge-neutral;
- W-boson, which is also massive ($m_W = 80.379 \pm 0.012$ GeV and $\Gamma_W = 2.085 \pm 0.042$ GeV [17]) and carries integer charge (± 1).

Coupling between charged particles (such as quarks and leptons) can be mediated by γ and Z-bosons. The strength of the coupling between γ and charged particles is scale-dependent with a value given by the fine structure constant α, where

$$\alpha = \alpha(Q^2 = 0) \approx 1/137 \quad \text{and} \quad \alpha(Q^2 = m_W^2) \approx 1/128,$$

while the coupling of the Z-boson is given by the weak coupling constants (see g and g' in Eq. (1.6)). Both propagators conserve the total charge Q and leptonic number of the initial particles. While these bosons share similarities, Z-boson propagators are more likely to spawn at higher interaction energies, where the centre-of-mass energy is comparable to m_Z.

Conversely, W-bosons can couple either to lepton-neutrino pairs or quark-quark pairs. W-bosons, which can be either positively or negatively charged (W^+ and W^-, respectively), along with Z-bosons, are the only propagators in the SM that can couple to neutrinos. All couplings conserve the total charge Q and the leptonic number but can change the leptonic flavour of the system. Similarly to the Z-boson, the strength of the coupling with leptons (which conserves the leptonic generation number, e.g. $W^- \to e^- \bar{\nu}_e$) is given by the weak coupling constants g and g'. In the case of quark-quark pairs, cross-generation interactions are allowed, although with different probabilities: $W^- \to \bar{u}d$ and $W^- \to \bar{u}s$ processes will occur in different proportions. This gets quantified by a 3×3 unitary complex matrix known as the Cabibbo–Kobayashi–Maskawa (CKM) matrix [18, 19], which gathers the coupling strength of each quark combination. One of the most common ways to write is

$$V_{\text{CKM}} = V_L^u V_L^{d\dagger} = \begin{pmatrix} V_{ud} & V_{us} & V_{ub} \\ V_{cd} & V_{cs} & V_{cb} \\ V_{td} & V_{ts} & V_{tb} \end{pmatrix}, \tag{1.16}$$

where the magnitude of each component, according to the PDG [17], is given by

$$\begin{pmatrix} |V_{ud}| & |V_{us}| & |V_{ub}| \\ |V_{cd}| & |V_{cs}| & |V_{cb}| \\ |V_{td}| & |V_{ts}| & |V_{tb}| \end{pmatrix} = \begin{pmatrix} 0.97370 & 0.2245 & 3.82 \times 10^{-3} \\ 0.221 & 0.987 & 41.0 \times 10^{-3} \\ 8.0 \times 10^{-3} & 38.8 \times 10^{-3} & 1.013 \end{pmatrix}. \tag{1.17}$$

1.4 W-boson mass

The importance of a good measurement of the mass of the W-boson is clearly motivated by its relationship with other properties of the SM. The prediction from the electroweak fit, including Z-pole data and the measured masses of the top quark and of the Higgs boson, gives a W-boson mass of 80.356 ± 0.006 GeV [17]. This uncertainty sets the scale for the desired precision of any measurement. The following paragraphs briefly summarise the main measurements of m_W determined by various collaborations.

The first precise measurement of m_W was done by the UA2′ collaboration [20], which constrained a value of $80.350 \pm 0.33(\text{stat.}) \pm 0.17(\text{syst.})$ GeV via proton-antiproton collisions at a center-of-mass energy of 630 GeV.

A combination of all pre-2022 CDF and D0 results using proton-antiproton collisions at $\sqrt{s} = 1.96$ TeV yields a Tevatron average of 80.387 ± 0.016 GeV [21].

The combination of the four LEP experiments, which corresponds to 3 fb^{-1} collected at centre-of-mass energies between 130 GeV and 209 GeV, results in a LEP average W-boson mass of m_W of 80.376 ± 0.033 GeV [22].

There are two published W-boson measurements at the LHC using proton-proton collisions, released by ATLAS [23] (80.370 ± 0.019 GeV, determined with 4.6 fb^{-1} of data collected at $\sqrt{s} = 7$ TeV) and by LHCb [24] (80.354 ± 0.032 GeV, 1.7 fb^{-1} of data at $\sqrt{s} = 13$ TeV).

One should note that the ATLAS 2011 data [23] has been re-analysed with an advanced fitting technique based on a profile likelihood approach [25]. This updated measurement yields a preliminary value of 80.360 ± 0.016 GeV.

In April 2022, the CDF collaboration published a measurement of the W-boson mass, which was based on their full Run II dataset of 8.8 fb^{-1}. The collaboration measured a mass with a reduced uncertainty, with a value of 80.4335 ± 0.0094 GeV [26]. This new high-precision result is in significant tension from the other measurements [27], as shown in Fig. 1.3.

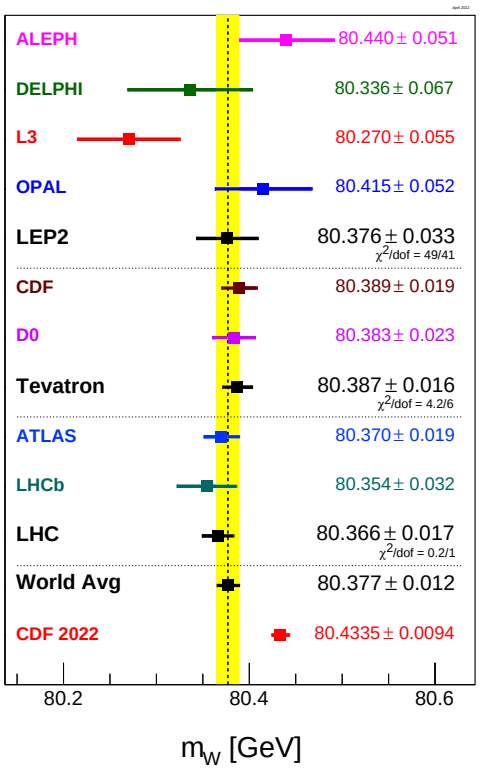

Figure 1.3: Measurements of the W-boson mass as determined by various experiments [17].

1.5 Quantum chromodynamics generals

The sector defined by strong interactions via $\mathcal{L}_{\text{QCD}}$ (Eq. (1.7)) is mediated by the gluon, which is responsible for the quark confinement phenomenon that impedes the existence of free quarks and confines them within composite particles called "hadrons". As briefly discussed above, the $SU(3)$ group is responsible for the colour quantum number [10], which takes 3 possible states (namely, red r, green g or blue b; and the corresponding anticolours $\bar{r}$, $\bar{g}$ and $\bar{b}$ for antiparticles). While each of the quarks is massive and carries a single colour, gluons are massless nil-charged particles that carry colour-anticolour combinations. Such combinations define a base of generators, which are typically defined under the Gell-Mann representation, leading to the definition of a colour singlet

$$(r\bar{r} + g\bar{g} + b\bar{b})/\sqrt{3}, \tag{1.18}$$

which is associated with stable composite strong particles (i.e. hadrons), and an octet of linearly independent states given by

$$\begin{aligned} &(r\bar{b} + b\bar{r})/\sqrt{2}, && -i(r\bar{b} - b\bar{r})/\sqrt{2}, \\ &(r\bar{g} + g\bar{r})/\sqrt{2}, && -i(r\bar{g} - g\bar{r})/\sqrt{2}, \\ &(b\bar{g} + g\bar{b})/\sqrt{2}, && -i(g\bar{g} - g\bar{b})/\sqrt{2}, \\ &(r\bar{r} - b\bar{b})/\sqrt{2}, && (r\bar{r} + b\bar{b} - 2g\bar{g})/\sqrt{6}; \end{aligned} \tag{1.19}$$

which in Eq. (1.8) are accounted for via the λ_a generators.

While the octet allows for interaction between gluons and coloured particles (i.e. quarks or other gluons), particles in the singlet state (which are colourless) can only interact with other singlets. This means that entire protons ($p = uud$) cannot interact via gluon exchange with other free coloured particles, but can do so with e.g. other protons (although not at leading order) or leptons.

1.6 Structure functions

In the context of hadronic interactions, it is of interest to understand the dynamics of the quarks and gluons (conjointly called "partons") confined within the hadron, as their precise description is fundamental to model the interaction mechanisms and measure properties of the QCD sector. The following paragraphs will discuss the particular case of the proton.

A general model of the internal content of the proton is based on the definition of a sea of infinitely abundant gluons and transitory pairs of quarks of all flavours, which exist along u-valence and d-valence quarks. Consequently, despite its complex internal structure, the proton can be represented from a macroscopical point of view by its valence quark structure uud, which defines conditions that any proton content model must fulfil.

1.6.1 Elastic and inelastic lepton-hadron scattering

Elastic electron-muon scattering

Following the standard theoretical treatment [28], let us start the study by looking at the $e^-\mu^-$ elastic scattering process at centre-of-mass energy $s \gg M = m_\mu$ [28, 29]. For a transfer of momentum given by $q^\mu = k_i^\mu - k_f^\mu$ at tree level, the matrix element is given by

$$\begin{aligned} |\overline{\mathcal{M}_{fi}}|^2 &= \frac{e^4}{q^4} L^{e^-}_{\mu\nu} L^{\mu\nu}_{\mu^-} \\ &= \frac{8e^4}{q^4} 2M^2 E_i E_f \left(\cos^2(\theta/2) - \frac{q^2}{2M^2} \sin^2(\theta/2) \right), \end{aligned} \tag{1.20}$$

where

$$q^2 = -2k_i \cdot k_f = -4E_i E_f \sin^2(\theta/2).$$

This leads to a differential cross section defined by

$$\frac{\mathrm{d}\sigma^{e^-\mu^-}}{\mathrm{d}\Omega} = \frac{\alpha^2}{4E_i^2 \sin^2(\theta/2)} \frac{E_i}{E_f} \left(\cos^2(\theta/2) - \frac{q^2}{2M^2} \sin^2(\theta/2) \right), \tag{1.21}$$

which may be rewritten as

$$\frac{\mathrm{d}\sigma^{e^-\mu^-}}{\mathrm{d}y} = \frac{e^2 e'^2}{8\pi Q^4} [1 + (1-y)^2)] s \quad \overset{e' = e}{=} \quad \frac{2\pi\alpha^2}{Q^4} [1 + (1-y)^2)] s. \tag{1.22}$$

Electron-quark and electron-hadron scattering

The formalism described in the previous Section can be extended to describe electron-quark scattering of the sort $lh \to l'X$ by including additional considerations. The first of these being that the charge e' of the quark takes values of $\frac{2}{3}e$ or $-\frac{1}{3}e$, which gets generalised as $e' = e_i e$. The second is related to the description of the kinematics of the quark as part of the hadron.

Let us consider a scattering process such as the one depicted Fig. 1.4 (which focuses on $e^- p^+ \to e^{-\prime} X$ scattering), where a quark q contained in the hadron (in this case, a proton with 4-momentum p^μ) interacts with a lepton (e^- with initial and final 4-momenta given by $k^\mu_{i,f}$) via the exchange of a virtual vector boson V^* (γ, Z or $W^\pm$) with 4-momentum

$$q^\mu = k_f^\mu - k_i^\mu,$$

and a centre-of-mass energy squared defined by

$$s = (p + k_i)^2.$$

Auxiliary variables are built, such as the negative of the squared invariant mass of the boson

$$Q^2 = -q^2,$$

the energy transferred to the nucleon by the scattering electron

$$\nu = \frac{p \cdot q}{M},$$

the fraction of the longitudinal momentum of the proton with which the electron is interacting (known as the Bjorken-x scaling variable [30] in this system)

$$x = -\frac{q^2}{2p \cdot q} = \frac{Q^2}{2M\nu} \qquad 0 \leq x \leq 1$$

(which implies that the quark momentum and centre-of-mass energy of the quark-lepton system are given by xp and xs), and the related variable

$$y = \frac{p \cdot q}{p \cdot k_i} \qquad\qquad 0 \leq y \leq 1.$$

Considering a relativistic interaction, the current notation allows to write

$$Q^2 = s\ x\ y,$$

and to define the invariant mass of the final hadronic state as

$$W^2 = M_X^2 = (q + p)^2.$$

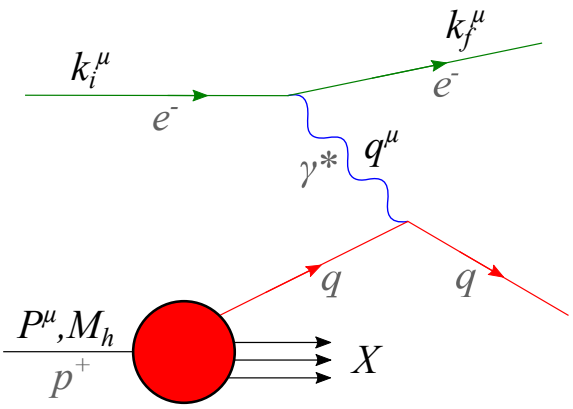

Figure 1.4: Schematic representation of $e^- p^+ \rightarrow e^{+\prime} X$ scattering, where a quark q within the proton (4-momentum P^μ and mass $M_h = m_p = 938.27$ GeV [17]) is exchanging a virtual photon γ^* (4-momentum q^μ, which can be replaced by a $W^\pm$ or Z) with the external electron (whose initial and final 4-momentum are $k^\mu_{i,f}$). Note that the 4-momentum transferred to the nucleon is given by $q^\mu = k^\mu_f - k^\mu_i$.

By extension of the $e^-\mu^-$ case, the electron-quark scattering cross section can be written as

$$\frac{\mathrm{d}\sigma^{lh}}{\mathrm{d}y} = \frac{2\pi\alpha^2}{Q^4}[1 + (1 - y)^2)]\ x\ s\ e_i^2. \tag{1.23}$$

A quark i does not carry a specific fraction x of the total momentum p. Instead, x takes values according to the probability density given by a distribution function $q_i(x)$ (often, it is also written as $f_i(x)$). Subsequently, one may define the corresponding momentum distribution, or density, $xq_i(x)$, which henceforward shall be known as the "parton distribution function", or PDF, of quark i. Using the above notation, the electron-quark scattering model can be extended to describe electron-hadron incoherent scattering double differential cross section by summing over all the possible types of quark at a specific value of x via

$$\frac{\mathrm{d}^2\sigma^{lh}}{\mathrm{d}x\mathrm{d}y} = \frac{2\pi\alpha^2}{Q^4}[1+(1-y)^2)]\ s\sum_i e_i^2\ x\ q_i(x), \tag{1.24}$$

or

$$\frac{\mathrm{d}^2\sigma^{lh}}{\mathrm{d}x\mathrm{d}Q^2} = \frac{2\pi\alpha^2}{xQ^4}[1+(1-y)^2)]\sum_i e_i^2\ x\ q_i(x). \tag{1.25}$$

Inelastic electron-hadron scattering

In order to see the effects of the internal structure of the proton, let us generalise the tensorial description of the electron-hadron scattering. By extension to the treatment of the $e^-\mu^-$ case, the matrix element of $lh \to l'X$ can be defined in an analogous way by means of the substitution $L^{\mu\nu}_{\mu^-} \to W_p^{\mu\nu}$ (N.B. this follows the notation given in [28], and it must not be confused with the term $W_i^{\mu\nu}$ defined in Eq. (1.6)). This leads to the matrix element

$$|\overline{\mathcal{M}_{fi}}|^2 \sim L^{e^-}_{\mu\nu}W_p^{\mu\nu}, \tag{1.26}$$

such that

$$W_p^{\mu\nu} = -W_1 g^{\mu\nu} + \frac{W_2}{M_h^2}p^\mu p^\nu + \frac{W_4}{M_h^2}q^\mu q^\nu + \frac{W_5}{M_h^2}(p^\mu q^\nu + q^\mu p^\nu) \tag{1.27}$$

where the functions $W_i, i \in \{1,..,5\}$ depend on the internal structure of the proton. By imposing current conservation via $q_\mu W^{\mu\nu} = q_\nu W^{\mu\nu} = 0$, these functions can be written as

$$\begin{aligned} W_5 &= -\frac{p\cdot q}{q^2}W_2, \\ W_4 &= \left(\frac{p\cdot q}{q^2}\right)^2 W_2 + \frac{M_h^2}{q^2}W_1; \end{aligned} \tag{1.28}$$

leading to the tensor

$$W_p^{\mu\nu} = W_1\left(-g^{\mu\nu} + \frac{q^\mu q^\nu}{q^2}\right) + \frac{W_2}{M_h^2}\left(p^\mu - \frac{p\cdot q}{q^2}q^\mu\right)\left(p^\nu - \frac{p\cdot q}{q^2}q^\nu\right). \tag{1.29}$$

Under this notation, the functions W_1 and W_2 account for the internal structure of the proton, which depends on Q^2, ν, x and y. Eventually, this leads to the charged lepton-hadron (labelled lh) differential cross section described by

$$\frac{\mathrm{d}^2\sigma^{lh}}{\mathrm{d}x\mathrm{d}y} = \frac{4\pi\alpha^2 s}{Q^4}\left[x\ y^2\ F_1^{lh}(x,y) + (1-y)\ F_2^{lh}(x,y)\right], \tag{1.30}$$

where the functions $F_1 = W_1$ and $F_2 = \nu W_2/M_h^2$ are known as the "structure functions" of the proton. Additionally, by defining the longitudinal structure function as

$$F_L = F_2 - 2xF_1 = F_2 - F_T \tag{1.31}$$

(where $F_T = 2xF_1$ denotes the transverse structure function), the cross section can be expressed as

$$\frac{\mathrm{d}^2\sigma^{lh}}{\mathrm{d}x\mathrm{d}Q^2} = \frac{2\pi\alpha^2}{xQ^4}\left[Y_+F_2^{lh}(x,y) - y^2F_L^{lh}(x,y)\right], \tag{1.32}$$

for $Y_+ = 1 + (1-y)^2$. N.B. by comparing Eqs. (1.25) and (1.32), one can identify that

$$F_2^{lh}(x,Q^2) = \sum_i e_i^2\ x\ q_i(x), \tag{1.33}$$

where one can identify that the parton model predicts Bjorken scaling, implying that F_2 depends only on x. Moreover, let us remember that F_1 and F_2 are related to the unpolarised quark distributions, so contributions from longitudinally polarised quarks would cancel out in the computation of F_L. Thus, as the parton model is based on scattered spin-$\frac{1}{2}$ quarks, it also predicts

$$F_L^{lh}(x,Q^2) = 0, \tag{1.34}$$

which leads to the Callan-Gross equality

$$2xF_1^{lh} = F_2^{lh}. \tag{1.35}$$

For the sake of completeness, let us recall the invariant mass of the final hadronic system and rewrite it such that

$$\begin{aligned} W^2 = M_X^2 = (q+p)^2 &= M_h^2 + 2p\cdot q + q^2 = M_h^2 + \frac{Q^2}{x} - Q^2 \\ &= M_h^2 + \frac{Q^2}{x}(1-x). \end{aligned} \tag{1.36}$$

In the elastic scattering scenario, this expression yields $M_X^2 = M_h^2 \iff x = 1$, while the inelastic case ($x \in [0,1]$) yields

$$M_X \geq M_h + m_\pi > M_h. \tag{1.37}$$

Moreover, one should notice that energetic enough $e^{\pm}p$ interactions lead to a large transfer of momentum onto the proton, resulting in

$$Q^2 \gg M_h^2 \approx 1\ \mathrm{GeV}^2, \tag{1.38}$$

which allows the quark content of the hadron to be probed deeply. Consequently, such scattering processes are known as Deep Inelastic Scattering (DIS). Such processes have been measured and studied with high precision at the Hadron-Elektron-Ringanlage (HERA [31]) particle accelerator by the H1 and ZEUS collaborations [32], and modern PDF studies rely heavily on this data.

1.6.2 Functional form of the PDF

Regardless of the theoretical description of DIS processes provided by Eq. (1.32), one must notice that the term F_2 is defined around the sum of PDFs (Eq. (1.33)), which is not inherently predicted by QCD. Hence, while physical constraints based on general kinematics can be defined to each of the $q_i(x)$, the exact shape of the distribution of x for each parton is not derived from physical principles. Such ambiguity motivates building ad-hoc parametrisations of the $q_i(x)$ distributions whose exact behaviour must be determined by comparing sensitive data measurements with the corresponding theoretical predictions. This measurement process was initially done using DIS data (such as that measured by HERA [32]), and most recent studies also include proton-proton measurements.

As the parton content of a given hadron is not equal for any of its partons, it becomes useful to distinguish between the quark and antiquark sea contributions, as well as to separate their contribution to the valence value. This is defined by

$$xq(x) = xq_v(x) + xq_{\text{sea}}(x), \qquad x\bar{q}(x) = x\bar{q}_{\text{sea}}(x), \tag{1.39}$$

where it is assumed that

$$xq_{\text{sea}}(x) = x\bar{q}_{\text{sea}}(x). \tag{1.40}$$

These relationships allow to choose which parton distributions to parametrise, which usually results in a mixture of sea and valence (anti)quarks that fulfil some sort of cross-relationship (e.g. $u_v = u - \bar{u}$) around the u-, d- and s-quarks (this last one gets denoted by S); the most common sets are $\{u_v, d_v, S, g, \bar{d} - \bar{u}\}$ and $\{u, \bar{u}, d, \bar{d}, g\}$.

In the case of the proton, the functional forms of $q_i(x)$ are delineated via physically-motivated arguments such as its splitting functions (see Section 1.6.3), which represent nothing more than probabilities. This leads to a set of constraints that each component of a PDF must follow:

- By definition, $q_i(x) > 0 \ \forall x \in [0, 1]$
- The PDF must vanish at $x = 0$ (otherwise, a parton would carry no momentum with respect to the proton) and at $x = 1$ (preventing a single parton from carrying the entirety of the momentum of the proton);
- Satisfy the number sum rules for each of the partons:

$$\int_0^1 \mathrm{d}x \ u_v(x) = 2, \qquad \int_0^1 \mathrm{d}x \ d_v(x) = 1; \tag{1.41}$$

- Satisfy the momentum sum rule:

$$\text{for } \Sigma^{\text{tot.}}(x) = u(x) + \bar{u}(x) + d(x) + \bar{d}(x) + s(x) + \bar{s}(x) + c(x) + \bar{c}(x) + g(x), \tag{1.42}$$

one can impose that all the partons carry the entirety of the momentum of the proton via

$$\int_0^1 \mathrm{d}x \ x\Sigma^{\text{tot.}}(x) = 1; \tag{1.43}$$

The specific choice of the parametrisation of $q_i(x)$ is given, in part, by the collaboration carrying a given PDF study. One of the most common parametrisations, and the one relevant for the studies shown in Chapter 6, is that given by the HERA collaboration, known as "HERAPDF style". It is defined by the polynomial functional form

$$xq_i(x) = A_i x^{B_i}(1-x)^{C_i}(1+D_i x+E_i x^2) \underbrace{-A'_g x^{B'_g}(1-x)^{C'_g}}_{\text{term used exclusively for the gluon}}, \tag{1.44}$$

where the normalisation values A_i get defined by the sum rules, the term x^{B_i} and $(1-x)^{C_i}$ account for the first constraint ($x \neq 0, 1$) and describe the behaviour of the PDF at low and high x (respectively), and the additional term $(1+D_i x+E_i x^2)$ is intended to include specific behavioural features at intermediate x values. In addition, the gluon PDF is provided of a negative term (which depends on the primed constants A'_g, B'_g, C'_g), intended to account for the limited constraining power of the available measurements and to provide a flexible parametrisation that can describe a wide range of experimental measurements, allowing the parametrisation to accommodate potential uncertainties and statistical fluctuations in the data. The procedure with which the parameters A_i, B_i, etc. are determined is described in detail in Section 6.3.

1.6.3 Evolution equations

Further developments on top of the previously described theoretical treatment have allowed obtaining a QCD-improved parton model, permitting generalising the prediction defined in Section 1.6 to any energy scale. From a physical point of view, this allows taking into account gluon radiative corrections, such as gluon infrared singularities that get absorbed by renormalisation and induce a Q^2 dependency. Such generalisation was independently derived by Dokshitzer, Gribov, Lipatov, Altarelli and Parisi, giving birth to what is now known as the DGLAP evolution equations [28, 33, 34, 35].

In a nutshell, these equations take the form

$$\begin{aligned}\frac{\partial}{\partial \ln(Q^2)}\begin{pmatrix} q_i(x,Q^2) \\ g(x,Q^2)\end{pmatrix} = &\frac{\alpha_s(Q^2)}{2\pi}\sum_j \int_x^1 \frac{\mathrm{d}\xi}{\xi} \\ &\begin{pmatrix} P_{q_i q_j}(\frac{x}{\xi},\alpha_s(Q^2)) & P_{q_i g}(\frac{x}{\xi},\alpha_s(Q^2)) \\ P_{g q_j}(\frac{x}{\xi},\alpha_s(Q^2)) & P_{gg}(\frac{x}{\xi},\alpha_s(Q^2))\end{pmatrix}\begin{pmatrix} q_j(\xi,Q^2) \\ g(\xi,Q^2)\end{pmatrix},\end{aligned} \tag{1.45}$$

where $P_{ij}(\frac{x}{\xi},\alpha_s(Q^2))$ are the splitting functions that describe the probability of a parton i to split into a different one j due to hadronisation. By defining $z = \frac{x}{\xi}$, the splitting

functions may be expanded as a power series in $\alpha_s(Q^2)$ as

$$\begin{aligned} P_{q_i q_j}(z,\alpha_s) &= \delta_{ij} P_{qq}^{(0)}(z) + \frac{\alpha_s}{2\pi} P_{qq}^{(1)}(z) + \cdots , \\ P_{qg}(z,\alpha_s) &= P_{qg}^{(0)}(z) + \frac{\alpha_s}{2\pi} P_{qg}^{(1)}(z) + \cdots , \\ P_{gq}(z,\alpha_s) &= P_{gq}^{(0)}(z) + \frac{\alpha_s}{2\pi} P_{gq}^{(1)}(z) + \cdots , \\ P_{gg}(z,\alpha_s) &= P_{gg}^{(0)}(z) + \frac{\alpha_s}{2\pi} P_{gg}^{(1)}(z) + \cdots . \end{aligned} \tag{1.46}$$

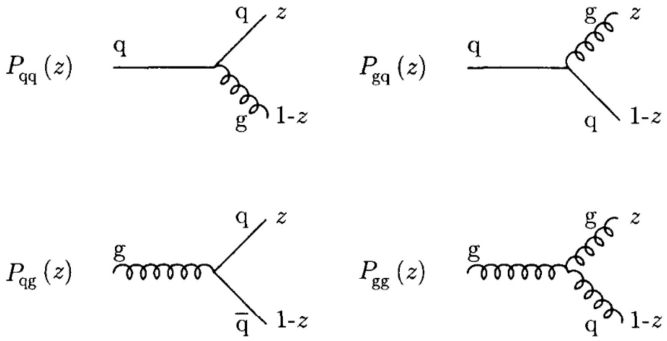

Figure 1.5: The DGLAP splitting functions.

Figure 1.5 summarises graphically the DGLAP splitting functions, which also illustrates that $P_{gq}(z) = P_{qq}(1-z)$. The leading order expressions for these terms take the form of

$$\begin{aligned} P_{gq}(z) &= \frac{4}{3}\left[\frac{1+(1-z)^2}{z}\right] \\ P_{qq}(z) &= \frac{4}{3}\left[\frac{1+z^2}{(1-z)_+} + \frac{3}{2}\delta(1-z)\right] \\ P_{gg}(z) &= 6\left[\frac{1-z}{z} + \frac{z}{(1-z)_+} + z(1-z)\right] + \frac{33-2\eta_f}{6}\delta(1-z), \end{aligned} \tag{1.47}$$

where the terms containing $\delta(1-z)$ are in charge of regularising the $1/(1-z)$ singularities when $z \to 1$, a limit that is associated with the emission of soft gluons.

The development of the DGLAP equations allowed more complex phenomena to be described precisely, which translates as a better understanding of the theory behind high energy scattering processes while retaining universality such that the equations are applicable to any parton in various hadronic systems. In modern QCD studies, it is the DGLAP equations which make possible the determination of high-precision PDFs, enabling high-order perturbative predictions.

1.6.4 The factorisation theorem and hadron-hadron collisions

An important implication of the DGLAP equations is the possibility to decouple (namely, to factorise[1]) hadronic cross sections as the convolution of individual hard scattering cross sections (denoted by $\hat{\sigma}$) and a non-perturbative parton density. This property, known as the factorisation theorem, allows the theoretical estimation of the cross section to be simplified by writing it as a function of well-known processes that are fully independent of the parton distribution functions.

One of the main impacts of the factorisation theorem is in the prediction of hadron-hadron cross sections, as it simplifies what would otherwise be an extremely challenging theoretical task. By considering that the cross section of a given $pp \to X$ process will be defined by all the possible combinations of interaction between partons (one from each proton, labelled 1 and 2), the factorisation theorem allows to write the global proton-proton cross section as

$$\sigma_{pp\to X} = \sum_{i,j} \int \mathrm{d}x_1 \mathrm{d}x_2 \underbrace{f_i^p(x_1, Q^2)}_{PDF} \underbrace{f_j^p(x_2, Q^2)}_{PDF} \times \hat{\sigma}_{ij}(x_1 x_2 s, \alpha_s(Q^2)), \tag{1.48}$$

where $\hat{\sigma}_{ij}(x_1 x_2 s, \alpha_s(Q^2))$ accounts for the hard scattering cross section contribution of each i-j parton-parton combination. One should note that the factorisation theorem does not explicitly account for QCD perturbative order, and the only way this information can be propagated to the final cross-section $\sigma_{pp\to X}$ is via the hard scattering terms. This means that the perturbative precision of a prediction $\sigma_{pp\to X}$ is given almost entirely by the precision of the $\hat{\sigma}_{ij}$ terms and by the order of the DGLAP evolution equations.

1.6.5 Overview of existent PDF sets

There are a few research groups worldwide whose sole task is determining proton PDFs. The obvious differences between the approaches each group takes are the choice of datasets used to constrain the PDF, the exact parametrisation of the PDF, and the methodology used to constrain the PDF parameters. Moreover, these characteristics get amplified by the order of the theory used to generate the relevant cross-section predictions and by the treatment of the heavy quark mass threshold, thus becoming the leading differentiating characteristic between PDF studies. A fully fitted PDF comprises a group of predictions, referred to as a "PDF set", which (typically) contains a central "member" and many linearly independent replicas that account for the uncertainty on the fit. The following paragraphs briefly show a few of the most popularly used PDFs, as well as the parametrisation used in each study following the notation of the original references.

---

[1] Subsequent mentions of "factorisation" are done in the context of collinear factorisation. Thus, a perturbative description as a function of α_s is possible for the relevant process (therefore allowing for a description using Feynman diagrams)

HERAPDF 2.0 [36] is a fit performed by the H1 and ZEUS collaborations using all of the $e^{\pm}p$ DIS data collected with HERA accelerator from years 1992 to 2000 and from 2002 to 2007 (known as phase I and II). PDFs get parametrised using the definition given in Eq. (1.44), and the parameters were fitted using a χ^2 minimisation (see Chapter 2) using the framework HERAFitter [37] (now generalised and re-branded as xFitter [38]). Ultimately, it provides a PDF description obtained using NNLO DGLAP evolution equations, which makes it an NNLO-level PDF.

The ABMP16 [39] PDF (named after the initials of the members of the authors) is based on extensive studies around a mathematical transformation of a PDF which allows the exchange of the dependency on x by integers n. This transformation receives the name of "Mellin moments", and at the n-th order it gets defined as

$$\tilde{q}(n, Q^2) = \int_0^1 \mathrm{d}x \; x^{-n} q(x, Q^2). \tag{1.49}$$

Mellin moments are of general interest in any PDF fit, as these allow to simplify various mathematical aspects of the computation of theoretical predictions with a high level of precision. All the NNLO Mellin moments derived by the ABMP authors are used in other PDF studies, making it a ubiquitous reference of almost any fit.

The CT18NNLO [40] PDF, determined by the CTEQ-TEA collaboration, uses a parametrisation given by

$$x f_i(x, Q_0) = a_0 \; x^{a_1 - 1} \; (1 - x)^{a_2} \; P_i(f(x); a_3, a_4, ..),$$

where $P_i(f(x); a_3, a_4, ..)$ is the sum of Bernstein polynomials dependent on some functional form of x (such as $f(x) = \sqrt{x}$), which allows to account for different features in the distribution of x of each parton. The parameters a_i are fitted to a large selection of Tevatron and LHC data on top of the HERA I and II DIS data, leading to a PDF capable of precisely describing a large selection of physics processes.

The MSHT20NNLO [41] PDF (also named after the initials of the members of the collaboration) shares some similarities with CT18NNLO, as it is fitted using a large selection of data that includes measurements from LHC, HERA, Tevatron and fixed target collisions. The PDF is parametrised as an explicit polynomial base modified by Chebyshev polynomials $T_i^{\mathrm{Ch}}(y(x))$, so that

$$x f_i(x, Q_0^2) = A x^{\delta} (1 - x)^{\eta} \left(1 + \sum_{i=1}^{n} a_i T_i^{\mathrm{Ch}}(y(x)) \right),$$

where $y = 1 - 2x^k$ for $k = 0.5$, and the sum runs up to the index $n = 6$. While it is beyond the scope of the work presented further ahead, it is worth mentioning that the same group has performed a PDF study at approximate NNNLO (aN^{3}LO) level under the name MSHT20aN^{3}LO [42], which relies on approximations to the N^{3}LO structure

functions and DGLAP evolution of the PDF; such study establishes a remarkable effort towards higher precision PDF fits.

The NNPDF3.1NNLO [43], determined by the NNPDF collaboration, takes a very different approach from the others mentioned above. Instead of relying on an explicit functional parametrisation of the PDF, their study is based on the extraction of partonic information via unbiased neural networks used to construct Monte Carlo representations (see Chapter 2) of the PDFs. This means that the shape of $xf_i(x, Q_0^2)$ is not predefined, which may lead to effects different from those seen in PDFs whose functional form is indicated a priori. Specifically, the approach leads to a PDF set with no central member, where all the replicas are equally probable, implying that a central prediction gets defined as the average of the predictions given by all the members. The NNPDF3.1NNLO is fitted to data obtained via DIS, fixed-target Drell-Yan, Tevatron and LHC Run-1, which should give it a degree of generality comparable to that of the other PDFs mentioned above.

The last PDF that will be discussed, named ATLASpdf21 [44], is the most relevant for the studies carried out in Chapter 6. It corresponds to the latest attempt of the ATLAS collaboration to determine a high-precision PDF by fitting a comprehensive selection of ATLAS measurements added on top of the HERA I+II $e^{\pm}p$ DIS data, seeking to describe a large range of phenomena (see Section 6.3.4 for a description of the relevant data). The ATLASpdf21 set is fitted using the HERAPDF style parametrisation given in Eq. (1.44), and minimising a χ^2 using the xFitter [38] framework. The fit is available for "tolerance" values of 1 and 3, which is a feature related to the quality of the minimisation procedure, and are labelled _T1 and _T3.

As it may be clear to the reader, the reliability of a PDF to describe a specific phenomenon is determined by the data used during the fitting procedure and by the selected parametrisation. In other words, it is related to the level of generality of the PDF and to how well it extrapolates to processes (and energies) not seen during the fit. The PDF4LHC working group provides continuous PDF recommendations for their use with specific LHC studies [45], which is an invaluable reference for any kind of precision analysis.

2 Statistical concepts and methods

Particle physics relies heavily on analysing large datasets, accounting for discrete collections of millions of event measurements derived from particle collisions. Consequentially, such studies rely naturally on statistical data analysis methods based on frequentist approaches.

This chapter is intended to provide an overview of the statistical formalism relevant to the studies performed through this thesis work. General concepts are built around the treatment and notation used by G. Cowan [46], with further numerical techniques based on specialised references.

2.1 General formalism

Measurements are based on the comparison of theoretical prediction models with collected data. Such models will typically rely on a set of unknown parameters θ whose optimal value must be determined using a given data, seeking to find those which reliably describe the observations within a reasonable degree of fidelity. The procedure of estimating the value of a parameter is called "parameter fitting".

Let us consider a set of n independent measurements $\boldsymbol{x} = \{x_i\}$, which, under a given probability density function $f(x, \theta)$ (simply called p.d.f., which typically takes the form of Gaussian or Poisson distributions), are best described for the parameter truth value $\theta = \theta_0$. If the parameter is unknown, a test statistic

$$t_\theta(\boldsymbol{x}) = f(x_1, .., x_n) \tag{2.1}$$

is defined in order to measure the compatibility between the measured data and its theoretical modelling given some parameter θ. The construction of such a test is based on minimalist statistical requirements, seeking generalisation and simplicity.

2.1.1 Parameter estimation and statistical uncertainty

Since the value of θ_0 is unknown (and it may stay like that permanently), one can only estimate its value via the implementation of a statistical test called "estimator". The value of θ determined with such an estimator will be called $\hat{\theta}$. Following reference [46], a good estimator should be

- consistent: in the limit of large sample size n (also referred to as "asymptotic limit"), $\hat{\theta}$ should converge to θ_0.
- unbiased: for $E[x]$ the expectation value of x and bias b defined as

$$b = E[\hat{\theta}] - \theta_0, \tag{2.2}$$

  the estimator should be such that $b = 0$.
- efficient: the covariance of the estimator should converge asymptotically to the minimum Rao-Cramér-Frechet (RCF) bound (see Eq. (2.7)).
- robust: insensitive to the choice of p.d.f..

Classical statistics provides no unique method for constructing estimators, allowing for some freedom in its definition according to desirable properties, such as the size (or nihility) of the bias or different convergence speeds. A natural construction arises from the desire to maximise the probability of observing the data $\boldsymbol{x}$ given $f(x;\theta)$ for a specific θ value. As all the x_i measurements are fixed and independent among them, such conjoint probability can be quantified by

$$L(\theta) = \prod_{i=1}^{n} f(x_i;\theta), \tag{2.3}$$

where $L(\theta)$ receives the name of "likelihood function". Accordingly, by seeking to maximise the value of $L(\theta)$, this defines the "Maximum Likelihood Estimator" (MLE), which provides an estimation of θ_0 such that

$$\hat{\theta} = \arg\max_{\theta} L(\theta) \tag{2.4}$$

where

$$\left.\frac{\partial L(\theta)}{\partial \theta}\right|_{\hat{\theta}} = 0. \tag{2.5}$$

In practice, rather than maximising Eq. (2.3), it is more practical to minimise the related quantity defined as

$$-2\log L = -2\sum_{i=1}^{n} \log f(x_i;\theta), \tag{2.6}$$

which receives the name of "Negative Log. Likelihood" (NLL).

Following the RCF inequality [46], also called "information inequality", a lower bound for an estimator variance is given by

$$V[\hat{\theta}] \geq \left(1 + \frac{\partial b}{\partial \theta}\right)^2 \Big/ E\left[-\frac{\partial^2 \log L}{\partial \theta^2}\right]. \tag{2.7}$$

Generalising to a case with more than one parameter, i.e. $\boldsymbol{\theta} = \{\theta_1, ..., \theta_m\}$, we define the "Fisher information matrix" I_θ as

$$(I_{\boldsymbol{\theta}})_{ij} = E\left[-\frac{\partial^2 \log L(\boldsymbol{\theta})}{\partial \theta_i \partial \theta_j}\right], \tag{2.8}$$

where the matrix with elements

$$(H_{\log L}(\boldsymbol{\theta}))\, ij = \frac{\partial^2 \log L(\boldsymbol{\theta})}{\partial \theta_i \partial \theta_j} \tag{2.9}$$

receives the name of the Hessian matrix of $\log L$. For the following, it is useful to notice that, due to the central value theorem, one can write

$$E\left[-\frac{\partial^2 \log L(\boldsymbol{\theta})}{\partial \theta_i \partial \theta_j}\right] = -\left.\frac{\partial^2 \log L(\boldsymbol{\theta})}{\partial \theta_i \partial \theta_j}\right|_{\hat{\boldsymbol{\theta}}}.$$

If the estimator is unbiased ($b = 0$, such as the case of the MLE) and the data sample is sufficiently large, then the expectation value of Hessian matrix can be used through Eq. (2.7) to estimate the covariance matrix V_{ij} of the estimators $\hat{\theta}_k$ with

$$(\widehat{V^{-1}})_{ij} = (I_{\boldsymbol{\theta}})_{ij} = -\left.\frac{\partial^2 \log L(\boldsymbol{\theta})}{\partial \theta_i \partial \theta_j}\right|_{\hat{\boldsymbol{\theta}}}. \tag{2.10}$$

This powerful relationship is one of the preferred ways to estimate the covariance matrix when numerically fitting a set of parameters. A clear example of this is the program `MINUIT` [47] (see Section 2.2).

Reliable estimation of the covariance matrix is desired due to 2 things: estimation of parameter uncertainty and correlation between parameters. In a nutshell, for a given V_{ij} covariance matrix (or its estimator), we define the uncertainty σ_i of parameter i as

$$\sigma_i = \sqrt{V_{ii}}, \tag{2.11}$$

while the correlation C_{ij} between two parameters i and j is given by

$$C_{ij} = \frac{V_{ij}}{\sigma_i \sigma_j}, \tag{2.12}$$

which defines the "correlation matrix" C. Correlation values range from -1 to $+1$, accounting for the mutual parameter (in)dependency. In other words, assigns a number

to the impact that a change in the estimated parameter i would have on the value of parameter j.

Let us consider the correlation between a variable θ_i and any possible linear combination Y of all the other variables θ_j s.t. $i \neq j$, denoted by $\rho(\theta_i, Y)$. The "global correlation coefficient" [48, 49] of a parameter i is defined as the largest value of $\rho(\theta_i, Y)$, and accounts for the total amount of correlation between θ_i and the rest of the parameter ensemble. This quantity can be written as a function of the covariance matrix V (and its inverse V^{-1}) via

$$\rho_i^2 = 1 - [V_{ii} \cdot (V^{-1})_{ii}]^{-1}. \tag{2.13}$$

2.1.2 Binned scenarios

As the total number of data points n_{tot} grows, it becomes difficult to compute a likelihood as in Eq. (2.6). In such scenarios, it becomes attractive to use a histogram in order to classify the various data measurements. For an N-binned histogram, this means the construction of a new set of bin-wise measurements $\boldsymbol{n} = \{n_1, ..., n_N\}$, where n_k simply counts the number of events $x_a, x_b, ...$ which fall within the boundaries of the k-th bin (whose centre is located at x_k). In such case, by defining the expectation value of the bin contents as $\boldsymbol{\nu} = \{\nu_1, ..., \nu_N\}$, and following a motivation similar to Eq. (2.3), one can define a likelihood for the binned scenario where the joint probability function f follows Poisson probabilities as

$$f_{\text{joint}}(\boldsymbol{n}; \boldsymbol{\nu}) = \frac{n_{\text{tot}}!}{n_1!...n_N!} \left(\frac{\nu_1}{n_{\text{tot}}}\right)^{n_1} ... \left(\frac{\nu_N}{n_{\text{tot}}}\right)^{n_N}, \tag{2.14}$$

which is simply expressing the probability of bin i as the ratio ν_i/n_{tot}. By taking the logarithm of Eq. (2.14), it is possible to recover a log-likelihood function for the binned scenario:

$$\log L(\boldsymbol{\theta}) = \sum_{i=1}^{N} n_i \log \nu_i(\boldsymbol{\theta}) + K_{\text{constant}}. \tag{2.15}$$

If the measured values n_i can be regarded as a Gaussian random variable (with variance $\delta_i = \sqrt{n_i}$) centred around the true (predicted) value λ_i, then it becomes possible to define an N-dimensional Gaussian joint p.d.f. which looks as

$$g(n_1, ..., n_N; \lambda_1, ..., \lambda_N, \delta_1^2, ..., \delta_N^2) = \prod_{i=1}^{N} \frac{1}{\sqrt{2\pi\delta_i^2}} \exp\left(\frac{-(n_i - \lambda_i)^2}{2\delta_i^2}\right), \tag{2.16}$$

where $\lambda = \lambda(x; \boldsymbol{\theta})$. By taking the logarithm of Eq. (2.16), it becomes

$$\log L(\boldsymbol{\theta}) = -\frac{1}{2} \sum_{i=1}^{N} \frac{(n_i - \lambda(x; \boldsymbol{\theta}))^2}{\delta_i^2} \; + \; K_{\text{constant}}, \tag{2.17}$$

where K_{constant} does not depend on any of the parameters θ_i. As we are interested only in maximizing the log-likelihood, the term K_{constant} can be safely ignored. Furthermore, instead of maximising Eq. (2.17), it is much more convenient to minimise $-2\times$(Eq. (2.17)). Thus, this defines

$$\chi^2(\boldsymbol{\theta}) = \sum_{i=1}^{n} \frac{(n_i - \lambda_i(x_i, \boldsymbol{\theta}))^2}{\delta_i^2}, \tag{2.18}$$

which is known as the "Least Square Estimator" (LSE) or simply χ^2. Equation (2.18) can be interpreted as follows: at each bin, the relative difference between measure and prediction (for a given $\boldsymbol{\theta}$ and weighted by the statistical uncertainty σ_i) is estimated. By squaring it, both over- and under-estimations are treated the same, and their impact on the agreement of the prediction gets scaled. Such differences are accumulated to get a global histogram-prediction χ^2 value given some $\boldsymbol{\theta}$.

Analogue to the treatment applied to the MLE, the use of LSE along RCF inequality and the information matrix, an estimator of the covariance matrix in the LSE can be defined as

$$\widehat{(V^{-1})}_{ij} = 2\left(- \left. \frac{\partial^2 \log \chi^2(\boldsymbol{\theta})}{\partial\theta_i \partial\theta_j} \right|_{\hat{\boldsymbol{\theta}}} \right). \tag{2.19}$$

Both MLE and LSE are widely used techniques in high-energy physics statistical analysis, and the choice between one or the other gets reduced to situational requirements and some personal preference.

2.1.3 Correlated case scenarios

In everything that was discussed in the previous section, the data points $\boldsymbol{x}$ were treated as completely independent, and as a consequence, the histograms defined with them generate completely uncorrelated bins. In some particular cases, such as after going through convolution unfolding methods (see Section 6.2.1), a non-diagonal covariance matrix V_{bins} across bins may arise.

A non-diagonal bin-wise covariance matrix has an effect on the definition of the joint p.d.f., so if we go back to Eq. (2.16) and generalise it (for N bins), it will take the form

$$g(\boldsymbol{y}; \boldsymbol{\lambda}) = \frac{1}{\sqrt{(2\pi)^N |V_{\text{bin}}|}} \exp\left(\frac{1}{2} (\boldsymbol{y} - \boldsymbol{\lambda})^T \, V_{\text{bins}}^{-1} \, (\boldsymbol{y} - \boldsymbol{\lambda}) \right). \tag{2.20}$$

In the particular case of the LSE, correlated measurements will propagate as

$$\begin{aligned} \chi^2(\boldsymbol{\theta}) &= \sum_{i,j=1}^{n} (y_i - \lambda_i(x_i, \boldsymbol{\theta}))(V_{\text{bins}}^{-1})_{ij}(y_j - \lambda_j(x_j, \boldsymbol{\theta})) \\ &= (\boldsymbol{y} - \boldsymbol{\lambda})^T \, V_{\text{bins}}^{-1} \, (\boldsymbol{y} - \boldsymbol{\lambda}). \end{aligned} \tag{2.21}$$

2.2 MINUIT

The recurrent need for reliable parameter fitting and the increasing complexity of studies (both due to the size of the data sample and the non-analytically-approachable nature of a study) requires, more often than not, numerical approaches in order to find the minimum of an estimator such as a MLE (in its NLL form) or an LSE. Consequently, diverse generalised minimisation codes have been developed seeking to provide a stable yet easy-to-use tool capable of doing such a thing. One of the most common ones in particle physics is MINUIT [47] [49].

MINUIT [47] is a numerical minimisation software designed to find the minimum value of a general multi-parameter function and to perform a quick shape analysis around the minimum. It was conceived at CERN, primarily as a tool to aid in the minimisation of estimators such as NLL or χ^2.

Initially written in Fortran (and now translated to C++ under the name "MINUIT2"), MINUIT acts on a generic multi-parameter function FCN : $\mathbb{R}^N \to \mathbb{R}$ in a very generalised way: given a set of N free parameters $\boldsymbol{p} = \{p_1, .., p_N\}$, a MINUIT routine will propose a set of numerical values for $\boldsymbol{p}$, which are then evaluated in FCN, and a single numerical value gets retrieved. By performing multiple numerical variations of $\boldsymbol{p}$, MINUIT is capable of constructing numerical quantities representative of the shape of FCN, such gradients and Hessian matrices, which can then be used to approximate the position of the minimum or to estimate parameter errors. The exact procedure with which the values $\boldsymbol{p}$ are proposed is dependent on the exact MINUIT subroutine [49].

It is important to note that MINUIT holds no knowledge of physics; it will simply search for the minimum of a provided function. Hence, from a statistical perspective, the quality (consistency, bias, etc.) of the estimator passed to MINUIT (FCN) must be studied beforehand.

Configuration of MINUIT is relatively simple, as it just needs to be provided with a function and indicate the number of free parameters. Further configuration can be defined, such as parameter constraints (initial value, initial step value, limits), desired numerical precision, maximum number of iterations, change in the stringency of the convergence criteria, and more. While optional and study-dependent, providing such configuration can prove to be highly rewarding, as one can take into consideration qualitative and quantitative characteristics that would otherwise hinder the minimisation (such as the presence of multiple local minima), and sheds information on ways to restrain MINUIT so that it operates where FCN is best defined.

The next few paragraphs describe superficially three of such subroutines, which are the most relevant ones for the study contained in this thesis: MIGRAD, HESSE, Further detailed descriptions can be found in the technical description note [49].

2.2.1 MIGRAD

Based on a variable metric method proposed by Fletcher [50], the subroutine MIGRAD relies on knowledge of the first and second derivatives (gradient and Hessian matrix, respectively), which is used to approximate FCN as a parabolic curve and predict candidates of the position of the minimum.

In a nutshell, MIGRAD works in the following way

- At a given point $\boldsymbol{p}$, the gradient (∇FCN) is estimated numerically by performing variations Δp_i of all the parameters (one and several at a time) and evaluating FCN. Similarly, the covariance matrix V is estimated using the information of the second derivatives and Eq. (2.19).
- Once the gradient is known, and assuming that FCN behaves as a parabola, a Newton's step is taken to $\boldsymbol{p'} = \boldsymbol{p} - V * \nabla\text{FCN}$, which would correspond to the minimum if V were the true covariance matrix. As FCN will generally not be parabolic, $\boldsymbol{p'}$ is not guaranteed to be the position of the minimum, but it should point in the right direction.
- At each iteration, MINUIT computes an "Estimated vertical Distance to the Minimum" (EDM) with
$$\text{EDM} = (\nabla\text{FCN})^T * V * (\nabla\text{FCN}), \tag{2.22}$$
with which the convergence criterion is defined.
- The procedure is repeated at the new step $\boldsymbol{p'}$, where a new gradient and covariance matrix are estimated, and another step is taken.

The iterative procedure above repeats until the EDM value is below some threshold, representing a solution that is "close enough" to the minimum. A typical definition of such a threshold is
$$\text{EDM} < 0.1 * \text{UP} = 0.1 \tag{2.23}$$
where UP = 1 is the definition of the errors, and this can be modified to the most convenient value for each study. As a general rule, the convergence threshold is desired such that, given the uncertainty $\hat{\sigma}_i$ of any fitted parameter $\hat{p}_i$,
$$\text{EDM} \ll \text{FCN}(\hat{p}_i \pm \hat{\sigma}_i) - \text{FCN}(\hat{p}_i) = \text{UP} = 1. \tag{2.24}$$

Figure 2.1 shows a schematic representation of the quantities defined above and MINUIT's estimation of FCN.

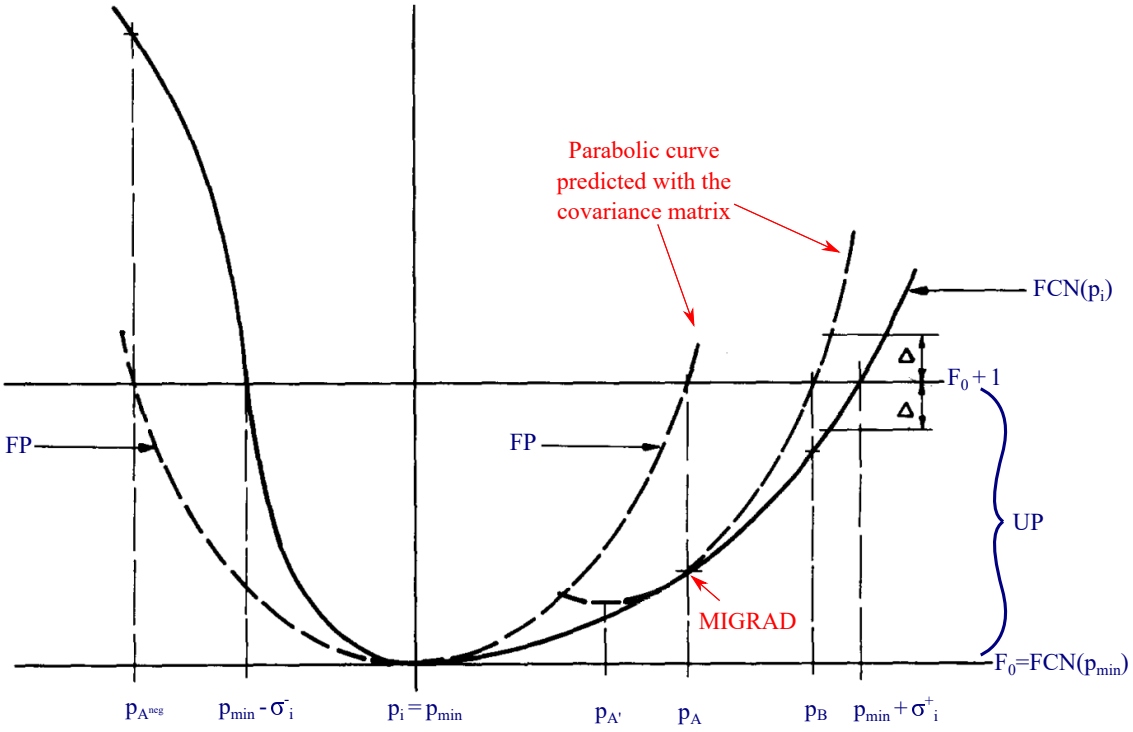

Figure 2.1: Notation and general numerical treatment used by `MINUIT` [49]. The symmetric dashed parabolas FP are predicted from the covariance matrix, while the solid line FCN corresponds to the real shape of the function around its minimum. Predicted curves (and by extension, its discrepancy against the real one) are shown at two different points: $p_i = p_{\min}$ (the absolute minimum of FCN) and $p_i = p_A$. The parabolic predictions show the general behaviour of `MIGRAD` (when moving towards $p_{\min}$) and `MINOS` (when moving away from it, towards $p_{\min} + \sigma_i^+$) at different points (p_A, p_B), while the vertical dashed lines show their comparison against references built around the analytical FCN curve.

2.2.2 HESSE

The `HESSE` subroutine is intended to provide a fast estimation of a covariance matrix, and by extension, of parameter uncertainties and their correlations. As the name suggests, this method relies fully on knowledge of the Hessian matrix via Eq. (2.19), which can provide a reliable error estimation at the minimum of FCN if the curve is approximately parabolic. The covariance matrix is estimated in the same fashion as what was described for the `MIGRAD` method.

One must bear in mind that, by construction, the parameter errors estimated via a Hessian matrix will be symmetric, which may not be the case in general. As such, and despite its celerity, `HESSE` estimated errors must be used with care.

2.2.3 MINOS

Similar to the HESSE method, MINOS is designed to probe parameter errors around the minimum of FCN. However, MINOS does so by numerically probing parameter values around $\boldsymbol{p_{\min}}$ (the minimum of FCN determined with MIGRAD). Consequently, MINOS is capable of determining asymmetric errors for each of the parameters, namely σ_i^- and σ_i^+ for parameter p_i, making it a much more powerful uncertainty estimator.

The numerical exploration done by MINOS is not random. Starting from the minimum $\boldsymbol{p_{\min}}$, it takes step-wise guesses (which takes values according to parabolic estimations based on the covariance matrix) aiming to find the points where $\mathrm{FCN}(\boldsymbol{p_{\min}} + \Delta p_i) - \mathrm{FCN}(\boldsymbol{p_{\min}}) = \mathrm{UP} = 1$. As almost certainly such estimations will not be correct, several iterations of such predicted steps are performed until reaching the $\Delta\mathrm{FCN} = 1$ criterion. In a way, it works similarly to MIGRAD, but in reverse.

Looking at the concrete example of Fig. 2.1, the estimation around $p_{\min}$ would lead to check p_A. After evaluating FCN here and finding a small vertical change, another parabolic guess is done, leading to p_B. This is iteratively repeated until reaching the correct value $p_{\min} + \sigma_i^+$, whose validity is based on a convergence threshold similar to the MIGRAD case.

Figure 2.1 exemplifies errors estimated with HESSE and MINOS in the general case of a non-symmetric FCN functor. While HESSE would estimate a symmetric error with size $p_A - p_{\min} = p_{\min} - p_{A^{\mathrm{neg}}}$, MINOS exactly accounts for the particular shape of FCN, being able to correctly determine a larger error on the positive side, and smaller one on the negative one.

While the numerically estimated asymmetric errors provided by MINOS are much more reliable than the analytically approximated symmetric ones given by HESSE, one must note that it is also a far more time-consuming technique. The numerical evaluation of asymmetrical variations around the minimum requires an increased number of iterations, which scale quickly with the number of free parameters. Ergo, it may be best to reserve this technique for the most advanced stages of an analysis, as a large computing time during the initial part of a study could prove wasteful in exchange for precise error determination. This, however, is something that must be decided on a case-by-case basis.

2.2.4 General considerations

As it may be clear by now, the MINUIT subroutines described above rely heavily on accurate estimation of first and second derivatives. Such a task is trivial if the functor FCN is analytically continuous as a function of the parameters p_i, such as when fitting a function a p.d.f. to a histogram where only statistical uncertainty comes into play. However, many sophisticated studies (such as those affected by systematical uncertainties) induce small discontinuities on FCN, which blight the numerically computed derivatives if the steps Δp_i are tiny (compared to the real uncertainty). In practical terms, this implies a few

things:

- `MIGRAD` and `MINOS` may take longer to converge, as the Newton's steps towards the minimum may be over- (or under-) estimated;
- While `MIGRAD` generally manages to find an improvement in the value of FCN (that is, a smaller value than the initial one), it is not trivial to predict whether the estimated values are the optimal ones;
- The estimated EDM may not be as precise, which means that a converging fit could get wrongly labelled as a "failed" attempt;
- Errors computed with the `HESSE` are not guaranteed to be reliable.

Some of the effects of non-continuous FCN can be smoothed by an appropriate choice of `MINUIT` configuration, such as by using different relative precision values.

Generally speaking, rather than taking the result of `MINUIT` as an absolute truth and blindly trusting it, it is worth carefully inspecting the chain of output and using this to decide whether it has found the desired result. As it was said before, `MINUIT` is just in charge of running the minimisation routines, and it does not know any of the underlying physics.

2.3 Resampling techniques

Propagation of uncertainties is a task of major importance when performing precision studies, as this shows the final contribution of the uncertainties generated at each step of the data collection and treatment process onto the total uncertainty of a final measurement. Analytical propagation is desired, as this is the most straightforward and time-efficient approach, but it works primarily for simpler cases with symmetric errors and where linear approximations are valid. A generalised method for the propagation of uncertainties relies on resampling techniques [51].

2.3.1 Toys

Let us consider a histogram with bin contents $\boldsymbol{n} = \{n_1, ..., n_N\}$, where each bin has its own uncertainty σ_i, which is used to perform some measurement M_{nominal}. A "toy" replica [52] $\boldsymbol{t_\alpha}$ of the histogram $\boldsymbol{n}$ is nothing but a random fluctuation of each of the bin content given by its statistical uncertainty, given a random generator seed α. In the large statistics limit, such fluctuation can be done with a Gaussian p.d.f. centred at n_i and with standard deviation σ_i (see Fig.2.2 for a practical example). For each toy replica α, the same analysis process can be applied, yielding a measurement M_α (which is, in general, different from M_{nominal}). The Central Limit Theorem [46] assures two things:

- for a given bin i, the average of all $(\boldsymbol{t_\alpha})_i$ values are equal to n_i and have variance σ_i,
- and the average value of all the measurements M_α will be M_{nominal}.

Conversely, the variance σ_{toys} of the M_α values correspond exactly the propagated uncertainty on M_{nominal}.

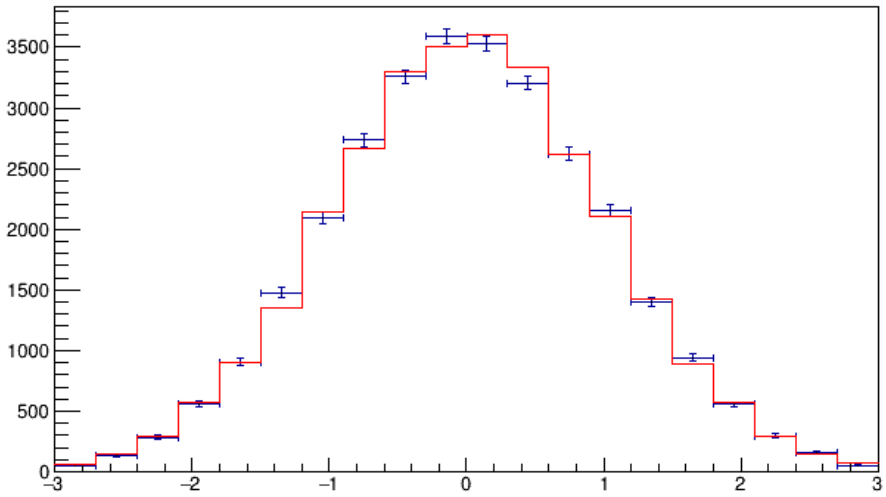

Figure 2.2: Example of a nominal histogram (in blue, also showing the bin uncertainty bands), and a toy replica (red) obtained by fluctuating the bin content with a Gaussian p.d.f.

The precision of the toy-estimated error depends on the number of replicas used, which should at least be above a few hundred but can easily reach several thousands.

2.3.2 Bootstrap

The "bootstrap" method [53] can be seen as a generalisation of the toy replica method. Let us consider a sample of raw individual measurements $\boldsymbol{x} = \{x_1, ..., x_n\}$, which will be used to perform a measurement M_{nominal}. A bootstrap replica $\boldsymbol{b_\alpha}$ of the sample $\boldsymbol{x}$ given a random seed α is defined by building a certain number of copies of each individual measurement x_i according to an integer Poisson p.d.f. normalised to 1. This means that many events will be accounted for 0 times, others just once, a few will be repeated twice, even fewer thrice, etc. The objective of this is to replicate the stochastic nature of individual measurements. A particular bootstrap replica may look as

$$\boldsymbol{b_\alpha} = \{x_1, x_3, x_3, x_4, x_6, x_6, x_6, x_6, x_8, ..\},$$

and will contain an average of n events. The same measurement performed on the nominal sample can be repeated with multiple bootstrap replicas $\boldsymbol{b_\alpha}$, yielding a corresponding M_α. Another consequence of the Central Limit Theory [46] is that the mean of all the M_α is equal to M_{nominal}, and its variance $\sigma_{\text{bootstrap}}$ corresponds to the uncertainty on M_{nominal}.

2.4 Closure and bias tests

With increasing study complexity and the need for novel techniques designed to make a certain analysis possible, it becomes difficult to gauge the properties of an estimator, especially important ones such as whether it is unbiased or consistent.

As lots of high-energy physics studies rely on the comparison between measured data and simulated samples, a common practice is to build a so-called "pseudodata" set (also referred to as an "Asimov" dataset) using simulations where, by definition, the true value of every single parameter is known. As such, preliminary studies using statistically independent pseudodata and simulations can be performed, which can also test whether the chosen estimator and general methodology are capable of unwaveringly measuring some observable M. If the injected value of the observable M_{injected} with which the pseudodata was created is compatible with the measured $M^{\text{measured}}_{\text{pseudodata}}$ within the estimated statistical uncertainty $\sigma_{\text{pseudodata}}$, then it is said that the method and estimator give "closure". In other words, we say that there is closure if

$$M_{\text{injected}} \in [M^{\text{measured}}_{\text{pseudodata}} - \sigma_{\text{pseudodata}}, M^{\text{measured}}_{\text{pseudodata}} + \sigma_{\text{pseudodata}}],$$

which can be expressed in terms of the bias as

$$|b| = |M_{\text{injected}} - M^{\text{measured}}_{\text{pseudodata}}| < \sigma_{\text{pseudodata}}.$$

If there is no closure, then either the methodology or the choice of estimator is inducing a "bias" which must be understood and accounted for in any final measurement.

The exact treatment of a closure and bias test is not trivial and must be designed in a case-by-case manner. One must be sure to test for closure in many scenarios, as different biases could be induced as a function of the amount (and quality) of the data.

3 Experimental demeanour

3.1 Large Hadron Collider

The Large Hadron Collider (LHC) is a circular 2-way particle accelerator located at the European Organisation for Nuclear Research (CERN). It spans across the border between France and Switzerland to account for a total circumference of 27 kilometres. It consists of a series of superconducting magnets that are capable of bending protons and heavy ions to very high energies and colliding them with each other at four specific points along the ring, where large detectors are installed and prepared to record the results of the collisions.

The LHC is the largest and most powerful particle accelerator in the world, capable of accelerating particles to nearly the speed of light and creating conditions similar to those that existed in the universe shortly after the Big Bang. Quantitatively speaking, it is capable of accelerating protons up to an energy of 6.8 TeV, accounting for a centre-of-mass collision energy of 13.6 TeV. Its primary goal is to study the fundamental properties of matter and the forces that govern the behaviour of subatomic particles, as well as to search for new particles and test predictions derived from the Standard Model of particle physics and its possible extensions. The LHC is known mainly for being key to the discovery of the Higgs boson in 2012, a particle that had been long predicted by theoretical models but never before measured, and continues to push the boundaries of our understanding of the universe.

As the nature of the work described in this thesis is based on proton-proton collisions at the LHC, the focus of the subsequent descriptions will be focused towards these.

3.1.1 The CERN accelerator complex and the LHC

As with any machine, the LHC is not a do-it-all device capable of implementing every single stage of the acceleration process on its own. Namely, it is not capable on its own of generating protons and accelerating them from an almost still state to nearly the speed of light. Instead, before even reaching the LHC ring for its final acceleration, every proton must go through a series of systems to successively increase its energy (Fig. 3.1).

In a nutshell, the acceleration process for the Run-1 and Run-2 periods is as follows:

1. The whole process starts with simple hydrogen gas, whose atoms get exposed to a strong electric field in order to strip them of their electrons.

2. By using the Radio Frequency Quadrupole (QRF), protons are gathered together to form proton bunches bunch, and a certain speed is obtained.

3. These protons are guided to the LINAC 2 linear accelerator (in the case of lead ions, LINAC 3 is used instead), which increases their kinetic energy up to 50 MeV.

4. Protons are then fed to the Proton Synchrotron Booster, where they reach energies of 1.4 GeV,

5. and then get passed to the Proton Synchrotron (PS) to be further accelerated to energies of 26 GeV.

6. Thereupon, the proton beams are driven to the Super Proton Synchrotron (SPS), where these will accumulate into longer bunch trains (each bunch containing about 115 billion protons) and receive an acceleration up to 450 GeV.

7. Up to 2,808 proton bunches are then distributed in both directions of the main LHC ring, where a final acceleration to the desired centre-of-mass energy will be performed right before initiating collisions at either of the 4 pre-determined interaction points, which will take place every 25 nanoseconds (equivalent to a bunch collision rate of 40 MHz).

Acceleration, confinement and general control of the proton beam are only possible thanks to an array of specifically designed superconducting magnets, classified mainly into 3 different families:

- Dipole magnets are used to bend the beam by providing a constant-and-parallel magnetic field orthogonal to the direction of the accelerator ring. As the energy of the beam increases, higher dipole magnetic fields are required in order to bend the beam enough so that it stays within the accelerator, and as such, this is the main limitator regarding the maximum possible energy one can reach with a circular accelerator. LHC uses about 1,232 dipoles, capable of generating magnetic fields from 0.54 to 8.3 Tesla, which sets a maximum acceleration energy of about 7 TeV (which will be obtained from Run-4 onwards).

- Quadrupole magnets are equivalent to magnetic lenses. These work as a way of focusing the beam and controlling its cross section, and play a vital role in the beam lifetime, as these are used to limit beam losses (which can happen when e.g. stray protons hit the walls of the accelerator). There are 392 quadrupoles along the LHC ring, of which the stronger quadrupole magnets are located near the intersection points in order to aggrandise the chances of interaction at the region where the two beams interweave.

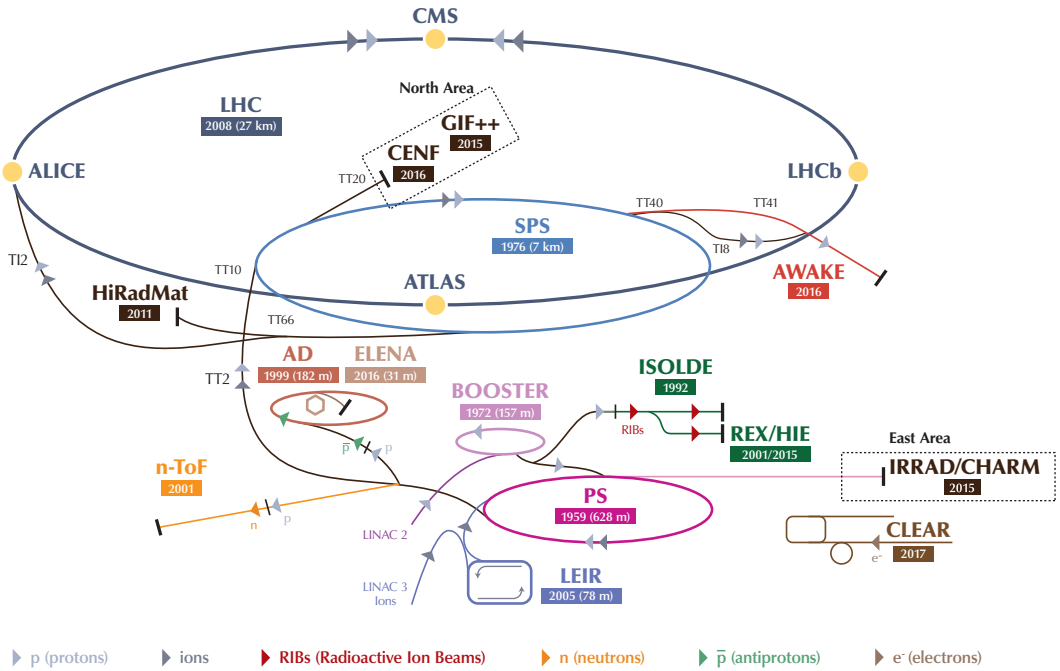

LHC - Large Hadron Collider // SPS - Super Proton Synchrotron // PS - Proton Synchrotron // AD - Antiproton Decelerator // CLEAR - CERN Linear Electron Accelerator for Research // AWAKE - Advanced WAKefield Experiment // ISOLDE - Isotope Separator OnLine // REX/HIE - Radioactive EXperiment/High Intensity and Energy ISOLDE // LEIR - Low Energy Ion Ring // LINAC - LINear ACcelerator // n-ToF - Neutrons Time Of Flight // HiRadMat - High-Radiation to Materials // CHARM - Cern High energy AcceleRator Mixed field facility // IRRAD - proton IRRADiation facility // GIF++ - Gamma Irradiation Facility // CENF - CErn Neutrino platForm

Figure 3.1: Schematic representation of the CERN Accelerator Complex [54] for Run-2.

- Nonlinear correctors (sextupoles, octupoles, etc) magnets come into play in a more subtle way, as their primary role is to implement phase, chromaticity and orbit corrections on the beam. In other words, these magnets allow for obtaining beam uniformity.

3.1.2 Hadron collisions at the LHC

By design, the LHC has 8 possible interaction points distributed uniformly around the accelerator (Fig. 3.2). Out of the 8 interaction points, 4 of them are home to the main experiments, located about 100 metres below ground, responsible for the detection of collisions given different technical designs and with interests in specific aspects of physics.

Points 1 and 5 harbours, respectively, the ATLAS (A Toroidal LHC Apparatus) and CMS (Compact Muon Solenoid) experiments, both symmetric general-purpose detectors designed to search for new and known particles, such as the Higgs boson and the top quark, as well as to study the properties of the known particles in more detail, and to look for phenomena beyond the standard model. These detectors offer wide angular coverage for the detection of particles, with their highest efficiency being around the central

region. While both experiments share similarities in their conceptual purpose, their technical design differs vastly. The reason behind this apparent redundancy is to provide multiple measurements of the same phenomena despite the use of different techniques, which ultimately should provide compatible results if everything is done correctly.

Point 2 is home to ALICE (A Large Ion Collider Experiment), a dedicated heavy-ion detector that is designed to study the properties of the quark-gluon plasma (QGP), a state of matter that existed in the early universe in which partons are deconfined for a very brief period of time before hadronisation.

Finally, Point 8 shelters LHCb (Large Hadron Collider beauty experiment), a detector that is designed to study the properties of particles containing the b-quark. It is primarily focused on studying the differences between matter and antimatter, as well as the study of rare decays of particles containing the b-quark. Different from the previously described experiments, LHCb is an asymmetric single-arm spectrometer, with coverage only around the forward region given that two b-hadrons production is predominantly highly boosted.

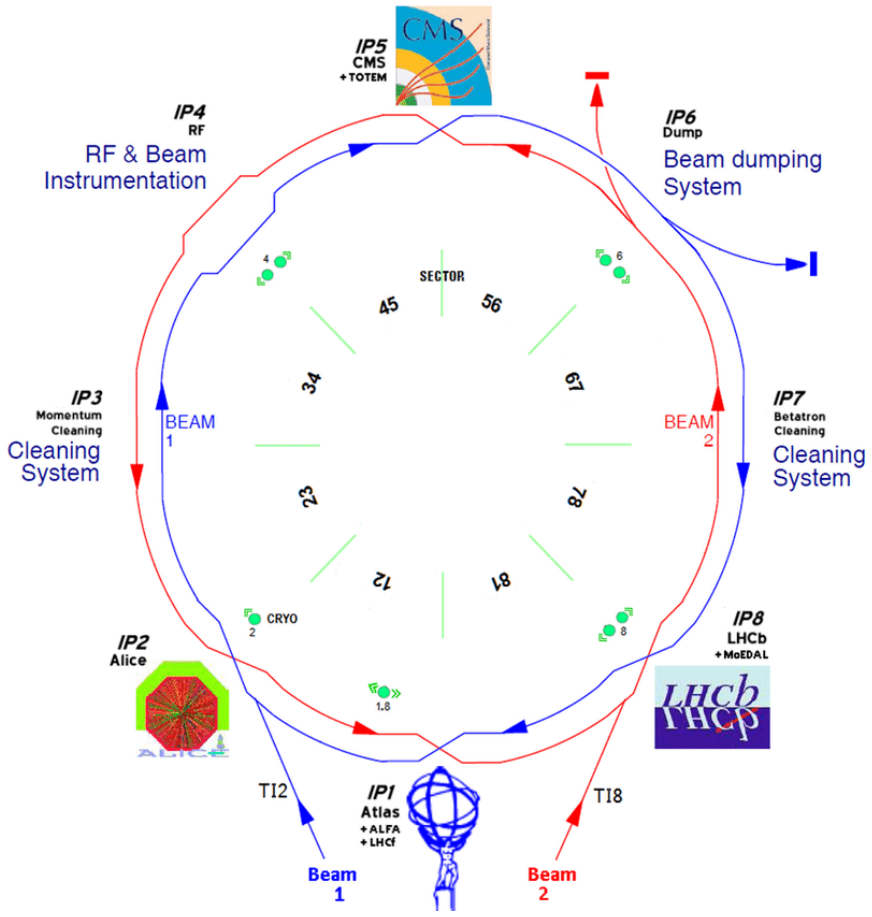

Figure 3.2: Schematic layout of the LHC, its 8 interaction points and the 4 main experiments.

The schematic shown in Fig. 3.19 provides general details of the evolution in run conditions of the LHC, starting from Run-1 and showing the foreseen conditions for the High-Luminosity LHC (HL-LHC) stage (further details are given in Section 3.4). Run-1 accounted for a total integrated luminosity of 30 fb^{-1}, collected at a centre of mass energy ($\sqrt{s}$) of 7 and 8 TeV from 2010 to 2012. This was followed by Run-2, which yielded a total luminosity of 156 fb^{-1} at $\sqrt{s} = 13$ TeV from 2015 to 2018. Run-3 (which started collecting data in the summer of 2022) is operating at $\sqrt{s} = 13.6$ TeV, foreseeing a total integrated luminosity of 450 fb^{-1} by the end of the data taking period in 2025. Run-4 onwards are aimed at an increase of instantaneous luminosity in order to considerably speed up the data-taking rate, eventually leading to a total luminosity of 300 to 4000 fb^{-1}, allowing to improve the sensitivity of rare processes and to perform more accurate physics measurements.

3.1.3 Luminosity and pile-up

As with any physical measurement, it is not enough to measure phenomena a single time at very specific laboratory conditions (such as centre-of-mass energy or bunch crossing angles), but rather, one must achieve repeatability and collect a statistically representative size of measurements before comparing with any model. In particle physics, the number (or rather, the rate) of events produced via proton collisions is quantified via a quantity called Luminosity (L), which in its most basic form looks like

$$L = \frac{1}{\sigma}\frac{\mathrm{d}N}{\mathrm{d}t}, \tag{3.1}$$

where σ is the total cross section for a given proton-proton interaction, and $\mathrm{d}N/\mathrm{d}t$ accounts for their interaction rate. It is worth noticing the peculiar units of the Luminosity, that is

$$\frac{\text{events}}{\text{distance}^2 \times \text{time}}[=]\frac{1}{m^2 s},$$

which is equivalent to a particle interaction rate normalised by the cross section.

As we are interested specifically in proton-proton collisions, it is much more useful to re-write Eq. (3.1) in terms of parameters representative of each proton beam. Consequently, the luminosity can take the form

$$L = \frac{N_1 N_2 f N_b}{4\pi\sigma_x\sigma_y} S, \tag{3.2}$$

where N_1 and N_2 are the numbers of protons in each of the interacting bunches, f accounts for the revolution frequency of the bunches (around the accelerator), N_b accounts for the total number of bunches in a fill, σ_x and σ_y measure the transverse width of the beam at the collision point along the x and y directions, and S is a luminosity geometric reduction factor which accounts for the crossing angle of the beams (as this can translate to inefficient overlapping of the encountering bunches).

Given the values of σ in particle physics are extremely small, in order to escape the constant use of tiny (or huge) powers, it is much more convenient to use the quantity "barn" (b) defined as

$$1 \text{ b} = 10^{-28} \text{ m}^2 = 10^{-24} \text{ cm}^2.$$

Through 2018, the peak luminosity delivered to ATLAS was measured to be 21.0×10^{33} cm^{-2}s^{-1} = 21.0 nb^{-1}s^{-1}. Figure 3.3 shows the peak luminosity per fill delivered to ATLAS through the year 2018.

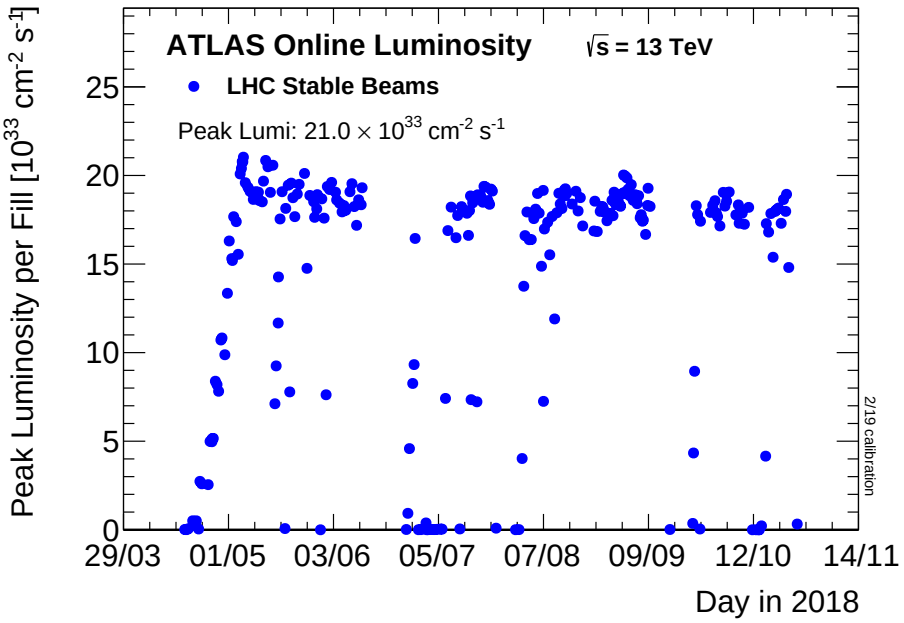

Figure 3.3: The peak instantaneous luminosity delivered to ATLAS during stable beams for *pp* collisions at 13 TeV centre-of-mass energy for each LHC fill as a function of time in 2018 [55].

Since we are interested in collecting a large enough number of measurements, it is necessary to look at the size of the statistical sample accumulated over some period of time. In consistency with the previous paragraphs, we use the integrated luminosity, simply defined as

$$L_{\text{int}} = \int L \, \mathrm{d}t, \tag{3.3}$$

which is nothing more than the total number of produced events normalised by the total cross section. Figure 3.4 shows the accumulative total integrated luminosity produced by LHC and recorded by ATLAS in the 2015-2018 period at 13 TeV centre-of-mass energy.

As it should be abundantly clear by now, we are interested in gathering as much data as possible. Not only that, but we would like to do so over a period of time as short as possible, which intuitively leads to attempting to increase the instantaneous luminosity by

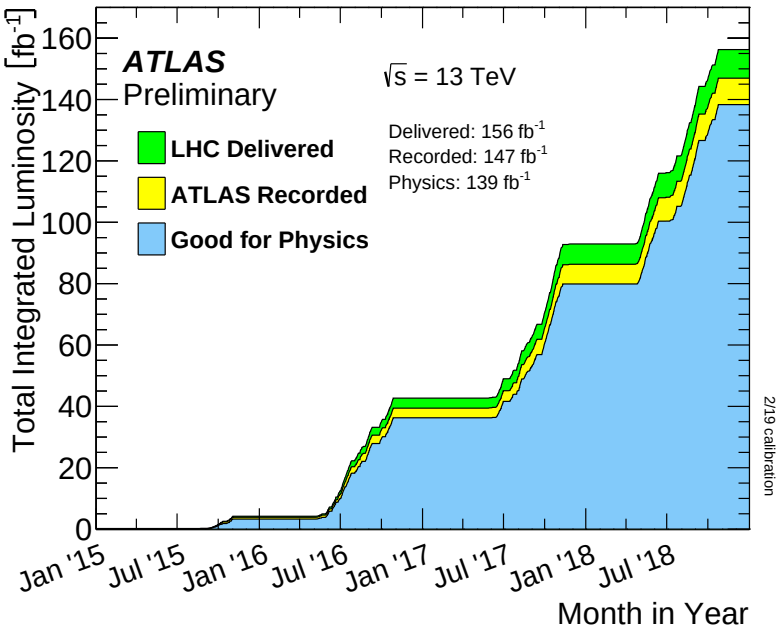

Figure 3.4: Cumulative luminosity versus time delivered to ATLAS (green), recorded by ATLAS (yellow), and certified to be good quality data (blue) during stable beams for pp collisions at 13 TeV centre-of-mass energy in 2015-2018 [55].

e.g. creating bunches with larger numbers of protons or optimising the geometric reduction factor (see Eq. (3.2)). However, one must realise that a single bunch crossing can (and, in general, will) produce more than a single proton-proton interaction, all of which will reach the detector at very similar times. Such effect, called "in-time pile-up" (often simply named as "pile-up" and denoted by μ), generates an additional challenge in the measurement and reconstruction of events, as the amalgamation of multiple simultaneously-occurring collisions and their overlapping measurement increases the difficulty of the association of signals to their specific collision progenitor, and also complicates full event reconstruction. Moreover, the detector is also sensitive to contributions from preceding and subsequent bunch crossings, which receives the name of "out-of-time pile-up". Figure 3.5 shows an event display of the ATLAS experiment (see Section 3.2 for more details on the detector), where 25 simultaneous collisions were produced and recorded. It is worth mentioning that the main limitations with the highest recordable pile-up values are related to hardware (and, by extension, to their software), and there are continuous efforts to overcome such limitations (see Section 3.4 for more details).

Given different physics motivations, one may be interested in different pile-up regions given the trade-off between luminosity (thus, the number of events recorded) and the quality of the measurements. Figure 3.6 shows the luminosity, recorded over different years, at specific mean pile-up ($\langle\mu\rangle$) values.

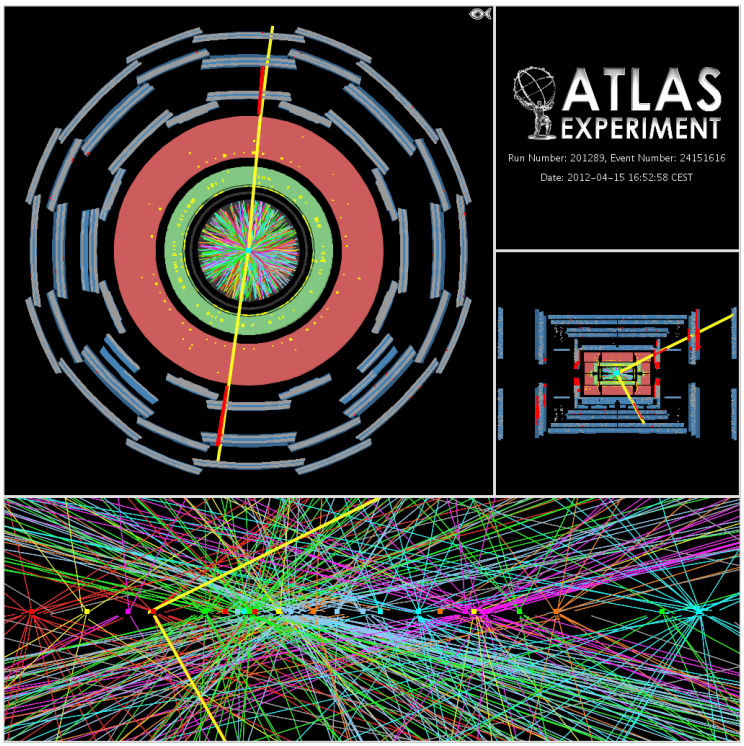

Figure 3.5: Example of the signal produced on the event display by a collision with pile-up = 25 [56].

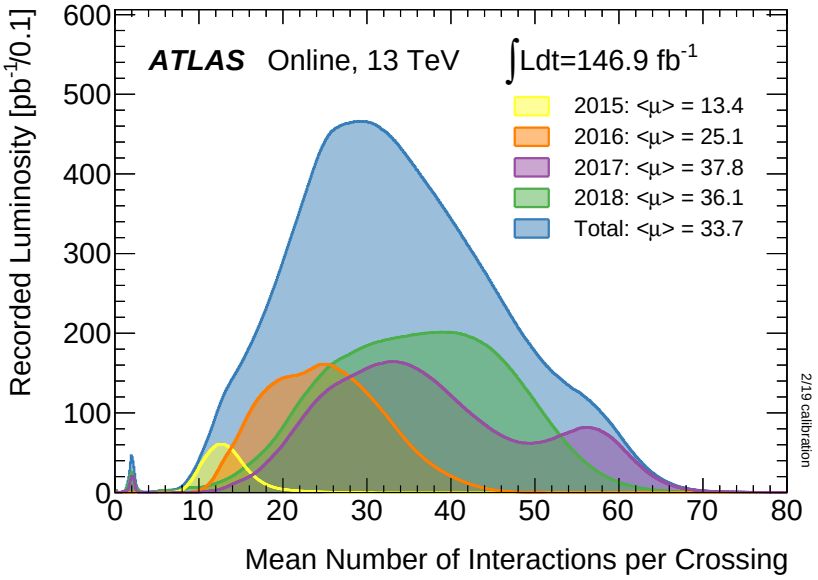

Figure 3.6: Luminosity-weighted distribution of the mean number of interactions (pile-up) per crossing for the 2015 – 2018 *pp* collision data at 13 TeV centre-of-mass energy [55].

3.2 The ATLAS experiment

Being one of the 4 main experiments at the LHC, the ATLAS experiment is a general-purpose particle detector installed at the Interaction Point (IP) 1 of the LHC, geographically located 100 meters underground in Meyrin, Switzerland. Its main purpose is to take advantage of the extremely high energies facilitated by the LHC in order to understand the fundamental structure of matter, test the Standard Model, probe QCD, perform precision electroweak measurements, allow for flavour physics studies, and provide a search window for possible new physics predicted by theoretical models.

The ATLAS detector itself is a cylindrical (and symmetric) detector, measuring 44 metres in length and 25 metres in diameter. The detector is perfectly aligned with the beamline in such a way that the proton beams run through the very middle of the detector, and collisions can occur only very close to its geometrical centre. It is divided into many sub-detectors, each playing a specific and fundamental role in the identification and detection of the different particles produced by proton-proton collisions. Figure 3.7 shows a schematic representation of the ATLAS detector, its size and the sub-detectors that comprise it.

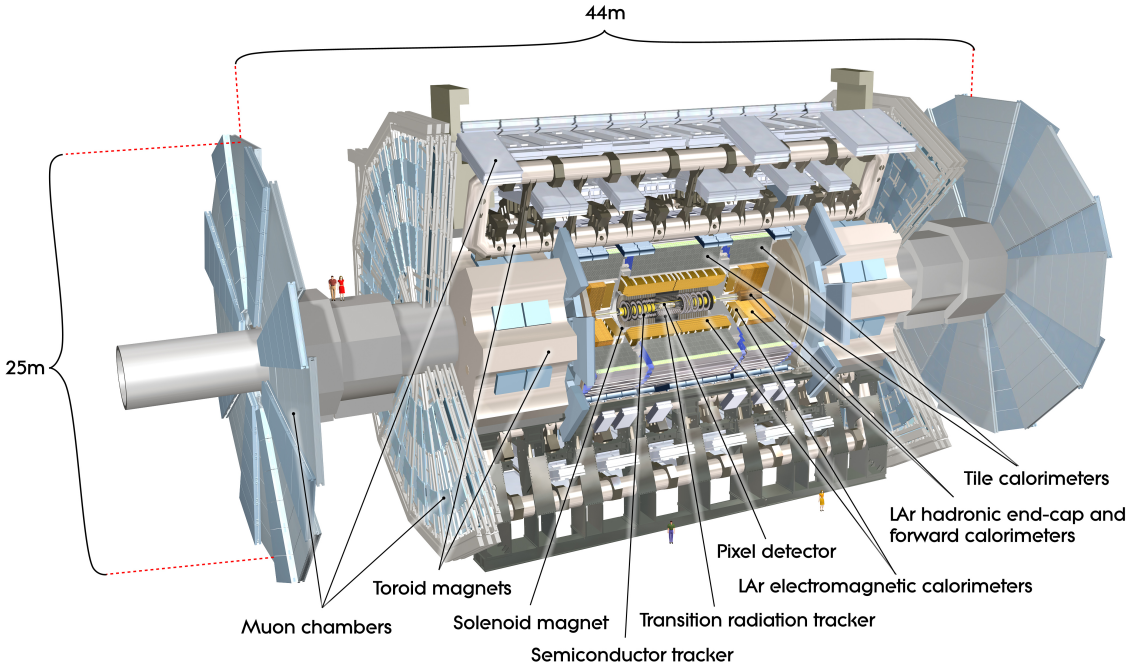

Figure 3.7: The ATLAS experiment and its various detectors [57].

The design of ATLAS and its sub-detectors is motivated by the experimental conditions at the LHC and by a series of requirements that must be fulfilled for the optimal collection

and analysis of hadronic collisions [58]:

- Detectors require fast, radiation-hard electronics and sensor elements;
- Due to the large particle fluxes and in order to gain spatial resolution, high detector granularity is needed;
- Large acceptance in pseudo-rapidity with almost full azimuthal angle coverage;
- Optimal charged-particle momentum resolution and reconstruction efficiency in the inner tracker are essential. For offline tagging of τ-leptons and b-jets, vertex detectors close to the interaction region are required to observe secondary vertices;
- Very good electromagnetic (EM) calorimetry for electron and photon identification and measurements;
- Full-coverage hadronic calorimetry for accurate jet and missing transverse energy measurements are important requirements, as these measurements form the basis of many of the studies mentioned above.
- Good muon identification and momentum resolution over a wide range of momenta and the ability to determine unambiguously the charge of high transverse momentum muons are fundamental requirements;
- Highly efficient triggering on low transverse-momentum objects with sufficient background rejection.

Consequently, ATLAS is divided into concentric layers of detectors. Each system is specialised in the detection of specific particles, and they are layered so that they affect minimally the pass of other non-target particles that will be detected in the outer layers. Naming from the inner-most region towards the outside, the ATLAS detector is comprised of the inner detector, electromagnetic calorimeter, hadronic calorimeter, and muon spectrometer, all of them sharing (and relying) on the magnet and trigger systems.

3.2.1 The detector reference frame

Before diving into each of the detectors that make up ATLAS, it is worth building a reference frame relative to the experimental setup. Let us begin by defining a Cartesian coordinate system such that the origin is located at the interaction point, the z-axis is perfectly aligned along the beam direction, the x-axis points directly towards the centre of the LHC ring, and the y-axis points directly towards the sky. Given the cylindrical construction of the detector and the importance of the interaction point IP, it is natural to move towards a coordinate system that relies on angular quantities. Thus, let us consider a point $\vec{p} = \{x, y, z\}$ located over the surface of the cylinder shown in Fig. 3.8. An azimuthal angle ϕ can be defined as $\tan\phi = y/x$, measured anti-clock-wise over the xy-plane, such that the x-axis corresponds to $\phi = 0$, and the y-axis is equivalent to $\phi = \pi/2$.

Moreover, let us define θ as the angle between $\vec{p}$ and its projection along the z-axis (that is, $\cos\theta = \dfrac{\{x,y,z\}\cdot\{0,0,|z|\}}{|\{x,y,z\}||\{0,0,z\}|} = \dfrac{|z|}{\sqrt{x^2+y^2+z^2}}$).

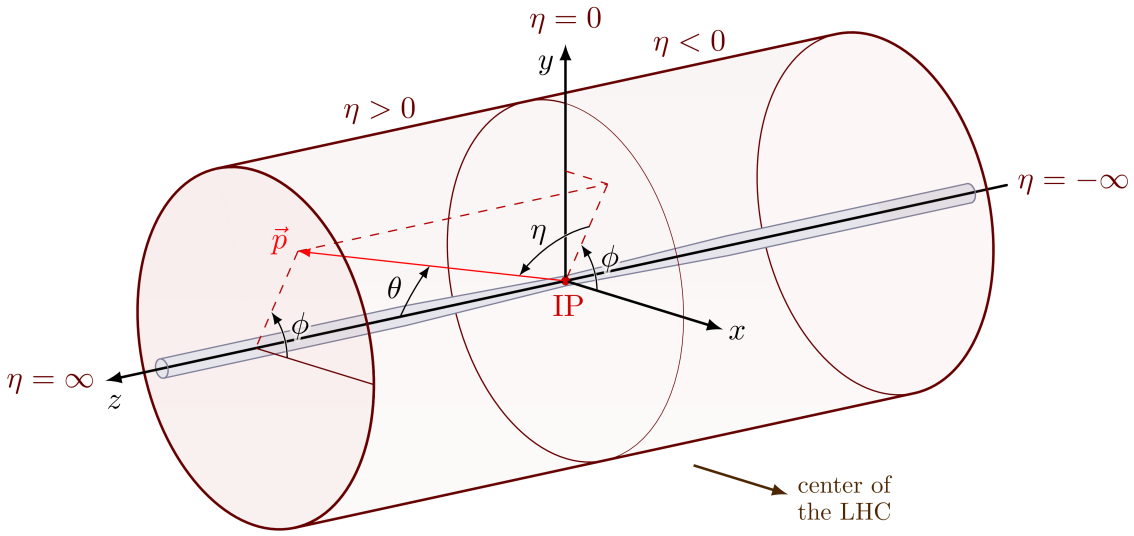

Figure 3.8: Experimental reference frame of the ATLAS experiment [59].

In a physics context, it is useful to study the angular direction of a particle in terms of its rapidity y (not to be confused with the y-axis coordinate used above), which is given by

$$y = \frac{1}{2}\ln\left(\frac{E+p_z}{E-p_z}\right), \tag{3.4}$$

where E is the energy of the particle, and p_z is the component of its momentum along the beam axis (also called "longitudinal momentum"). The rapidity is particularly interesting for 2-particle systems, as the amount $\Delta y = y_1 - y_2$ is Lorentz-invariant for boosts along the z-axis.

The pseudorapidity η offers an alternative way of expressing the angle between the beamline and the particle direction (θ) via

$$\eta = -\ln\left[\tan\frac{\theta}{2}\right]. \tag{3.5}$$

It is worth noticing that when a particle is moving along the beamline, η diverges. That is, $\eta \underset{\theta\to 0}{\longrightarrow} +\infty$ and $\eta \underset{\theta\to\pi}{\longrightarrow} -\infty$. On the other hand, when the particle moves orthogonally away from the beamline, we have $\eta \underset{\theta\to\pi/2}{\longrightarrow} 0$. In the mass-less limit, the pseudorapidity becomes equal to the rapidity, i.e.

$$y \underset{m\to 0}{\longrightarrow} \eta. \tag{3.6}$$

In general, particle 4-vectors are defined in this reference frame by using both angular quantities, their total energy, and their transverse momentum p_{T} (which is nothing more

than the projection of momentum on the xy-plane: $p_{\mathrm{T}} = \sqrt{p_x^2 + p_y^2}$). Consequently, a representation of a particle 4-vector may look as follows:

$$p_\mu = (E, \eta, \phi, p_{\mathrm{T}}).$$

Another advantage of such a reference frame is the simplicity of estimating angular quantities between particles. If we are interested in the angle ΔR between $\vec{p}_1$ and $\vec{p}_2$, it can be computed directly with $\Delta R = \sqrt{\Delta\eta^2 + \Delta\phi^2}$, which is (in the mass-less particle limit) Lorentz-invariant along the z-axis.

3.2.2 Inner detector

The Inner Detector (ID) [60] of the ATLAS experiment is designed to track the paths of charged particles produced at the interaction vertex. It is composed of three sub-detectors (Figs. 3.9 and 3.10): the Pixel Detector, the Semi-Conductor Tracker (SCT), and the Transition Radiation Tracker (TRT).

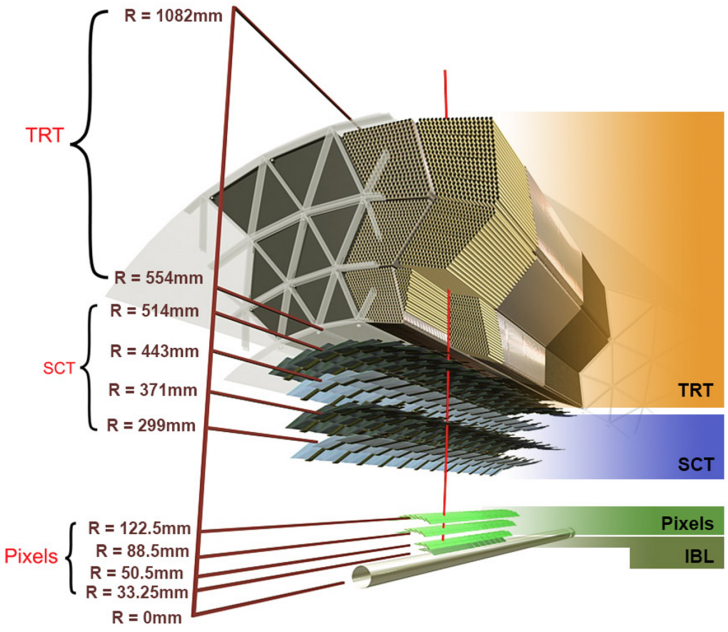

Figure 3.9: ATLAS Inner Detector and its subdetectors [61].

The Pixel Detector is the innermost sub-detector of the ID. During Run-1, it consisted of three layers of silicon pixel sensors. In 2014, before Run-2, the Insertable B-Layer (IBL) [63] was installed in such a way that the innermost layer is located only 3.3 cm from the beamline. It has the highest spatial resolution of any tracking detector, allowing it to precisely measure the positions of charged particles as they pass through.

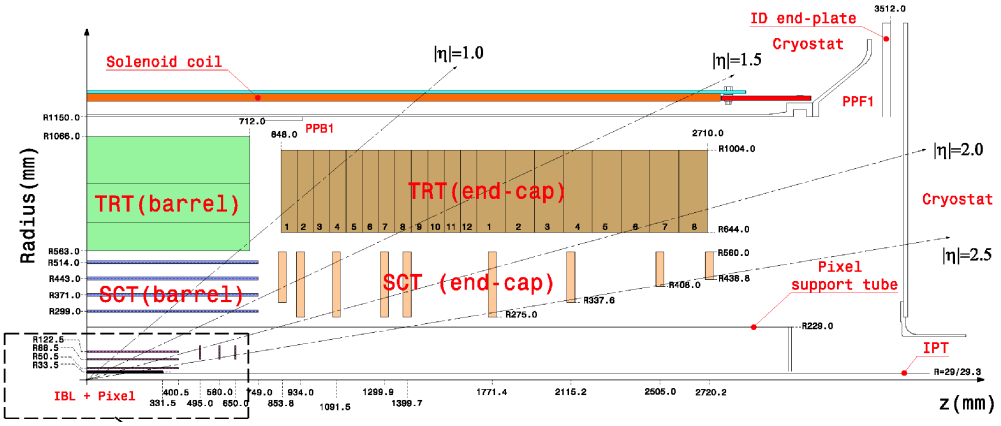

Figure 3.10: The layout of the ATLAS inner tracking detector, including the additional IBL detector layer [62].

Similar to the Pixel Detector, the SCT is also made up of silicon sensors, but they are arranged in the shape of long, narrow strips. The SCT is crucial for recreating the entire route of particles with lower momentum and offers an extra assessment of charged particle trajectories.

The TRT is the outermost sub-detector. It is composed of many straw tubes filled with an Argon- or Xenon-based gas mixture. The travel of charged particles through the tubes induces a net ionisation of the gas, producing an electrical signal per tube that can be used to track their trajectories. The TRT is used to measure the particle momentum and to distinguish between particles such as electrons, which produce X-ray transition radiation, and charged hadrons, which do not.

3.2.3 Liquid argon electromagnetic calorimeter

The Liquid Argon Electromagnetic Calorimeter (often referred to simply as LAr ECAL or EMCAL) [65] is a sampling calorimeter which consists of an accordion-shaped structure made of lead absorber plates interleaved with active layers filled with liquid argon that guarantees a full ϕ coverage. The design follows from an original idea by D. Fournier [66]. The purpose of the LAr ECAL is to measure the energy of electrons and photons produced as byproducts of the central collision, as well as to measure their impact point and angular direction.

When an electron or photon passes through the lead absorbers, it generates a shower of secondary particles that ionise the liquid argon in the active layers. Aided by a differential of electric potential between either side of an active layer, the ionisation charges are collected by electrodes. The current induced by the drift of the charges is then amplified and shaped, and the resulting electrical signal is digitised with an ADC converter, providing a measure that is proportional to the energy of the original electron or photon.

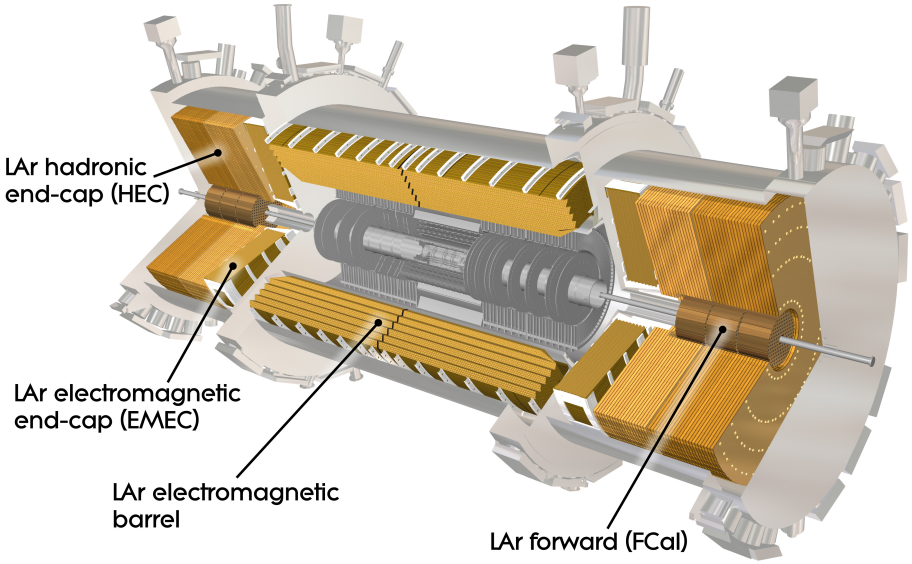

Figure 3.11: ATLAS electromagnetic and hadronic Liquid Argon detector [64].

Globally speaking, the LAr calorimeter has a thickness of 24 radiation lengths (X_0), allowing it to fully absorb and measure the primary electrons and photons produced at the interaction vertex. The LAr calorimeter is divided into three sectors: the barrel, the endcaps, and the presampler:

- The barrel is a cylindrical section, centred at the interaction vertex and aligned along the beamline, which offers uniform coverage along all azimuthal angles (ϕ) and extends along the central pseudo-rapidity (η) region of the ATLAS detector.
- The endcaps are flat lids located at both ends of the barrel, installed in a perpendicular manner with respect to the beamline. They cover the forward pseudo-rapidity regions while also offering uniform azimuthal coverage.
- The presampler is a thin layer of LAr placed in front of the barrel and the outer part of the endcap, which measures the energy lost by particles as they pass through the inner detector and other material before entering the calorimeter.

The barrel and endcap are each divided into three layers (Fig. 3.12), designed in such a manner to provide increasing angular granularity (measured as $\Delta\phi \times \Delta\eta$) and improve the energy resolution. The first layer (with a width of $\sim 5X_0$), closest to the interaction point, has the highest granularity, allowing to precisely measure the position and shape of the beginning of the EM showers. The second and third layers have successively lower

granularity and are designed to catch any energy that may have leaked out of the first layer, with the second layer also being in charge of collecting most of the energy of incoming electrons and photons.

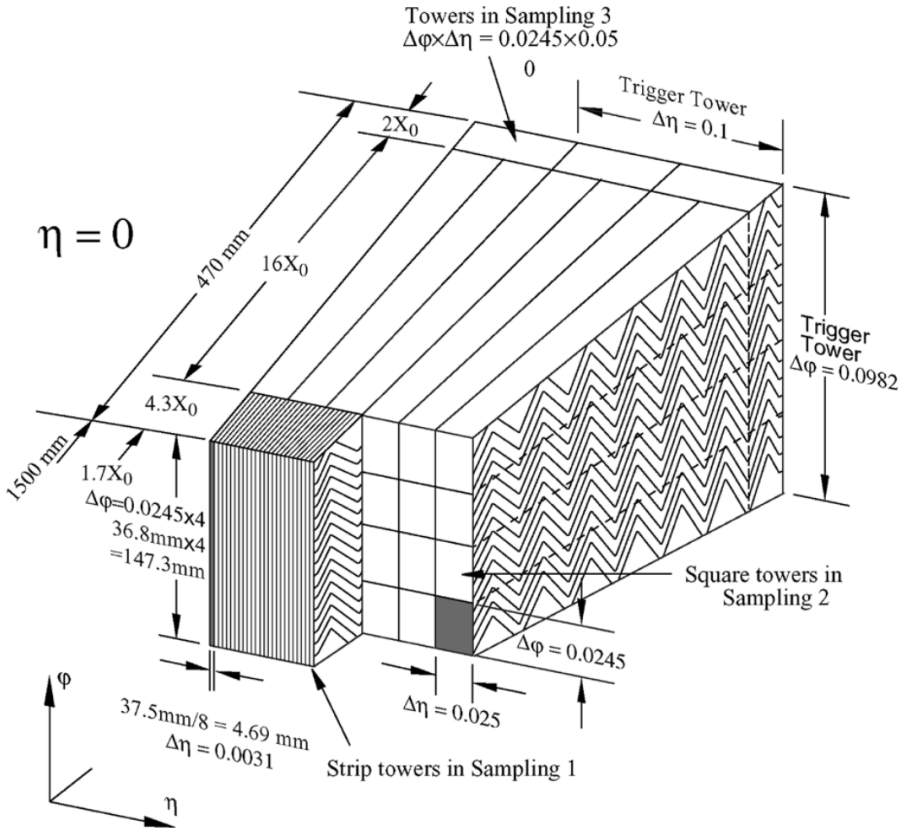

Figure 3.12: Segmentation and granularity of the electromagnetic barrel calorimeter [65].

The granularity of the LAr calorimeter is achieved by dividing each layer into a number of cells, with the angular size of each cell changing according to the layer to which they belong. Figure 3.12 exemplifies the angular granularity in a central tranche (around $\eta = 0$) of the barrel, where it is worth noticing the changing configurations and dimensions of the cells as a function of the sampling layer:

- Sampling 1: strip towers, $\Delta\phi \times \Delta\eta = 0.0982 \times 0.0031$;
- Sampling 2: square towers, $\Delta\phi \times \Delta\eta = 0.0245 \times 0.025$;
- Sampling 3: rectangular towers, $\Delta\phi \times \Delta\eta = 0.0245 \times 0.05$.

The combination of increasing lead density and variable cell size in the layers of the LAr calorimeter results in excellent energy resolution for electrons and photons produced in the LHC collisions. The energy resolution is typically better than $10\%/\sqrt{E(\text{GeV})}$

for electrons and photons with energies up to 1 TeV, and remains good even at higher energies [67].

Generally speaking, the electromagnetic calorimeter provides a resolution σ_E for particles with energy E that follows the standard behaviour given by

$$\frac{\sigma_E}{E} = \frac{a}{\sqrt{E}} \oplus \frac{b}{E} \oplus c, \tag{3.7}$$

where a is the stochastic term accounting for statistical fluctuations in the shower detection, b corresponds to the electronic and pile-up noise term, and c is a constant term that accounts for miscalibration effects and detector instabilities. In the case of EMCAL and for E in GeV, $a \approx 10\%$, $b \approx 0.3$, $c_{\text{barrel}} < 1\%$ and $c_{\text{endcap}} \approx 1 - 2\%$.

Overall, the high-precision energy measurements for electrons and photons provided by the LAr calorimeter make it a crucial part of precision measurements. It is primordial for the study of known particles such as the W, Z and Higgs bosons, as well as to perform searches for new physics.

3.2.4 Hadronic calorimeter

Working as a complement to its electromagnetic-dedicated counterpart, the hadronic calorimeter [68] is in charge of measuring the energy of hadrons, such as protons, neutrons, and mesons. It is also a sampling calorimeter that consists of alternating layers of dense absorber material and an active medium. When a hadron passes through the absorber material, it interacts with the nuclei in the material and produces a shower of secondary particles, which later deposit their energy in the active medium in the form of atomic or molecular excitation (depending on the choice of active material). Almost immediately after, the subsequent de-excitation generates photons that are later collected by photomultiplier tubes and converted into an electrical signal. The number of photons is proportional to the amount of energy transferred into the active medium, and the intensity of the electric signal is proportional to the photons collected, hence retrieving a measurement of such energy from each layer.

The HCAL is divided into three sub-detectors (Fig. 3.13): the Tile Calorimeter, the Hadronic Endcap Calorimeter (HEC), and the Forward Hadronic Calorimeter (FCAL). The Tile Calorimeter is located in the central region and uses steel as the absorber material and scintillating tiles as the active material. The HEC is located in the endcap region, closest to the beamline, and uses copper as the absorber material and liquid argon as the active material. The FCAL is located in the forward region, using copper or tungsten as the absorber material and liquid argon as the active material.

All put together, the HCAL is capable of measurements with a resolution of

$$\frac{\sigma_E}{E} = \frac{52\%}{\sqrt{E}} \oplus 5.7\% \tag{3.8}$$

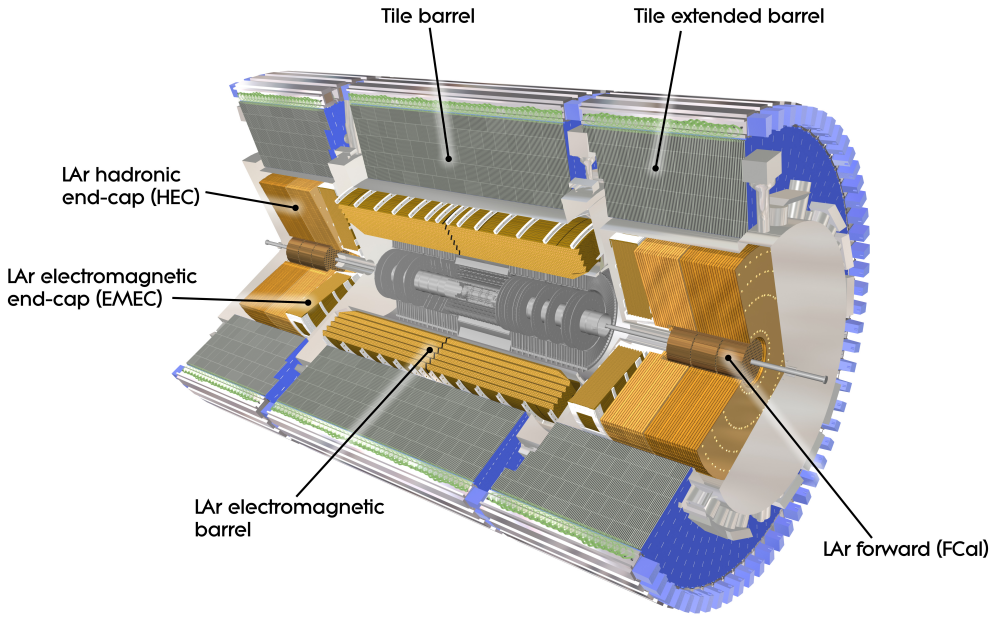

Figure 3.13: ATLAS hadronic and electromagnetic calorimeters [69].

for E in GeV.

The HCAL is primordial in the energy measurement of hadrons produced in the interaction vertex and for identifying the presence of jets, which are nothing but collimated collections of hadrons that result from the fragmentation and immediate hadronisation of quarks and gluons. Along with the electromagnetic calorimeter, the HCAL is also vital for the detection of new physics phenomena that may be produced in the LHC collisions, such as exotic particles or heavy resonances that decay into hadronic final states.

3.2.5 Muon spectrometer

Different from the previously mentioned particles, muons have a particularity that makes their full measurement challenging: they are minimally ionising particles. This means that, upon interaction with some material, muons will deposit very small amounts of energy as a form of ionisation, and more often than not, they will escape the material regardless of its composition. Such nature imposes a challenge, as one cannot rely on calorimeters to fully absorb them and measure their energy (as opposed to e.g. electrons, photons and hadrons).

While one must discard the possibility of fully absorbing and measuring the energy of muons created by LHC collisions, it is still possible to measure the momentum of the muon by taking advantage of its electric charge (which allows it to be bent by a magnetic

field) and its trace of (almost uniform) ionisation across the material in which it travels. Furthermore, one can take advantage of the aforementioned minimally ionising nature in order to implement a unique measuring system: since there is close to no disturbance on the muon while it travels across the other innermost detectors, the detector can be located in the outermost sector of the ATLAS experiment. Such are properties which, among others, led to the design of the Muon Spectrometer (MS) [70].

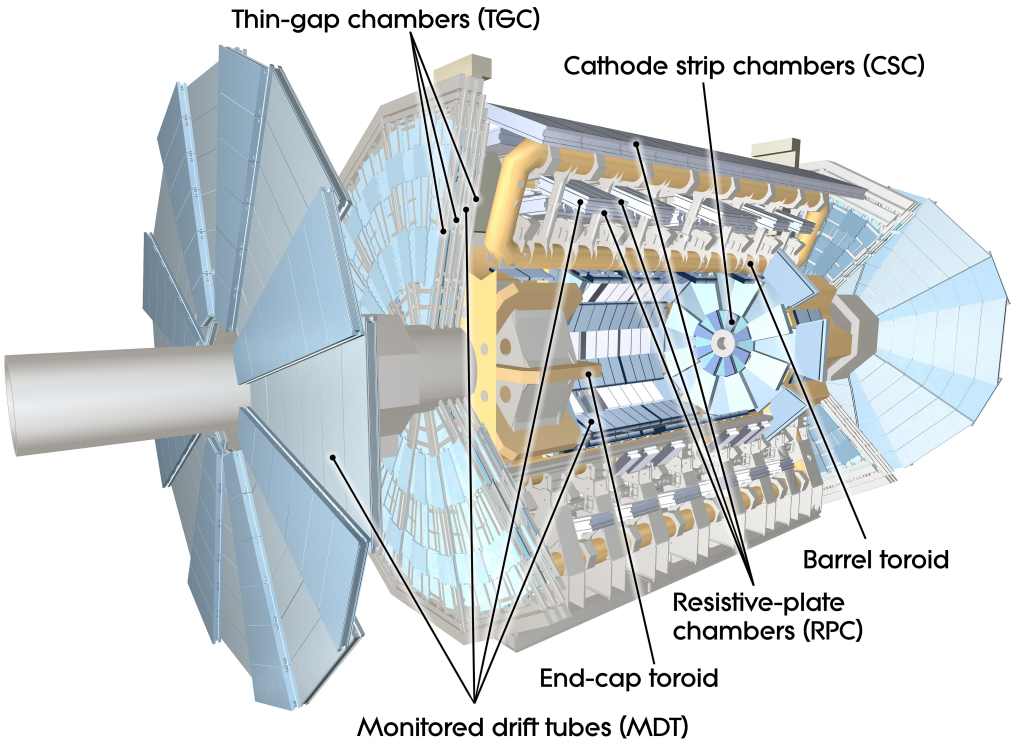

Figure 3.14: ATLAS Muon Spectrometer [71].

Globally speaking, the muon spectrometer is in charge of identifying and measuring the momentum of muons (although an equivalent measurement is also done by the inner tracker). It consists of a system of three large air-core toroidal magnets used to curve the trajectory of the muons generated at the interaction centre(see Section 3.2.6), which work in conjunction with several layers of tracking detectors that are used to measure the position of the muons as they pass through the magnetic field. These tracking detectors include the Monitored Drift Tubes (MDT), which are precision gas detectors, and the Cathode Strip Chambers (CSC), which are fast high-rate detectors used in the forward regions (Fig. 3.14). Muons passing through the tracking detectors ionise the gas, producing electrons that are collected by the detectors, providing a measurement of the muon's trajectory (and thus, of its momentum).

The MS also includes two types of gas detectors:

- The Resistive Plate Chambers (RPCs), which have a fast response time, with a time resolution of a few nanoseconds, and are used for fast triggering on muons.
- The Thin Gap Chambers (TGCs), which have a spatial resolution of a few millimeters and are used for track reconstruction and triggering.

As muons are a signature of many physics processes of interest, and their measurement is vital for the full kinematic reconstruction of any event, the MS is a fundamental component of the ATLAS experiment. Moreover, direct muon measurements are necessary for the study of specific processes, such as the decay of heavy particles like the Higgs, W- and Z-bosons, or the top quark.

One must bear in mind that LHC collisions are not the only source of muons, as there is always a background coming from atmospheric showers generated by cosmic particles. While dedicated techniques (which rely in great part on the triggering systems) are implemented in order to separate real physics signals generated by LHC collisions from the background, such external contributions should always be kept in mind.

3.2.6 Magnet system

As alluded to in the previous sections, the operation of the ATLAS experiment relies substantially on the Magnet System [72], which consists of a superconducting solenoid magnet and three large air-core toroidal magnets. The following paragraphs summarise some of the aforementioned characteristics of the system, which are worth concentrating on in a single space for the sake of compartimentability.

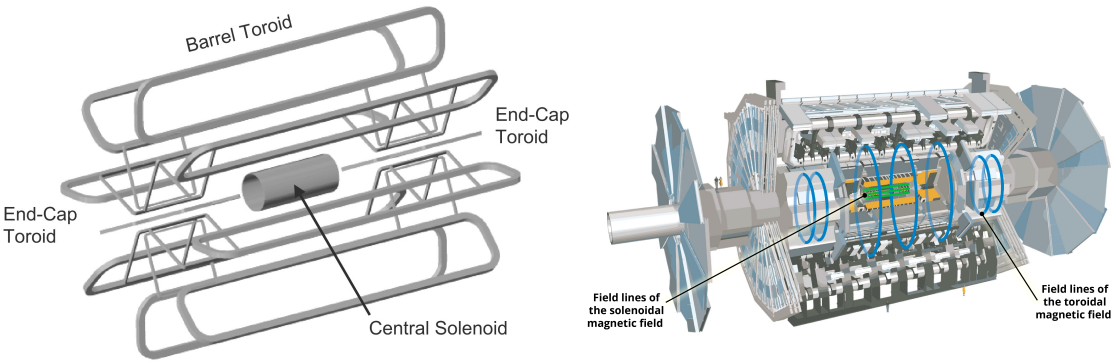

Figure 3.15: Spectrometer superconducting magnets of the ATLAS experiments, and their resulting magnetic field [73, 74].

The solenoid magnet (Fig. 3.15) is located between the inner detector and the EM calorimeter, housed inside the cryostat of the barrel of the EM LAr calorimeter, and generates a strong magnetic field of 2 Tesla that is used to curve the trajectories of charged particles produced in the collisions. The solenoid magnet is composed of a coil of superconducting wire, cooled to a temperature of 4.5 K using liquid helium, and has a length of 5.3 m and a diameter of 2.5 m.

The toroidal magnets are located outside the calorimeters and around the muon spectrometer. These generate a magnetic field that is used to measure the momentum of the muons produced in the collisions. The magnetic field is composed of a central barrel and two endcap magnets, which are divided into eight identical sectors. The barrel magnet has an inner diameter of 5.9 m, an outer diameter of 12.5 m, and a length of 25.3 m. The endcap magnets have a diameter of 10.8 m and a length of 22.5 m. The magnetic field in the barrel magnet is about 0.5 T, while the field in the endcap magnets is about 1.0 T.

3.2.7 Trigger system and data acquisition

The trigger system and data acquisition (DAQ [75]) system of the ATLAS experiment is responsible for triggering, selecting and storing the collision events that are of interest for physics analyses out of the millions of collisions that occur per second at the LHC. In other words, it works as a judge of the quality of each measured event and its potential to provide reliable information about the underlying physics. The actual detection and storage of physics-relevant data are fully dependent on the trigger system and data acquisition, as it is impossible to store every single signal sent off by the detectors at each collision, both due to limitations on storage and bandwidth.

The trigger system consists of two levels: the Level-1 (L1) trigger and the High-Level Trigger (HLT). The L1 trigger is implemented in hardware and uses a subset of detector information to reduce the data rate from the initial collision rate of 40 MHz to 100 kHz. The HLT is a software-based trigger that uses more sophisticated algorithms and a wider range of detector information to further reduce the data rate to around 1 kHz, which is then recorded for further analysis.

Subsequently, the data collected from each detector component is processed through a series of electronic modules to convert analogue signals into digital data, which are then sent to the DAQ system for processing. The DAQ is responsible for the collection, storage, and distribution of such digitised data, passed from the detector to the ATLAS computing centres for long-term storage and posterior analysis.

During stable beam collisions, the ATLAS experiment generates a huge amount of data, approximately 1 PB (petabyte) of raw data per second, which requires a high-performance computing infrastructure to store and process the data. The ATLAS data acquisition systems are located at Point 1, and a first-pass data processing is done at the CERN Tier0. Reprocessing and MC production are based on a distributed architecture, which involves a network of computing centres located around the world with a common software and data processing framework.

3.2.8 All the detectors, working together

While each of the previously described detectors is designed for probing specific characteristics of different particles, it is only when working together that we can begin to unravel what is actually happening at the vertex of the collision.

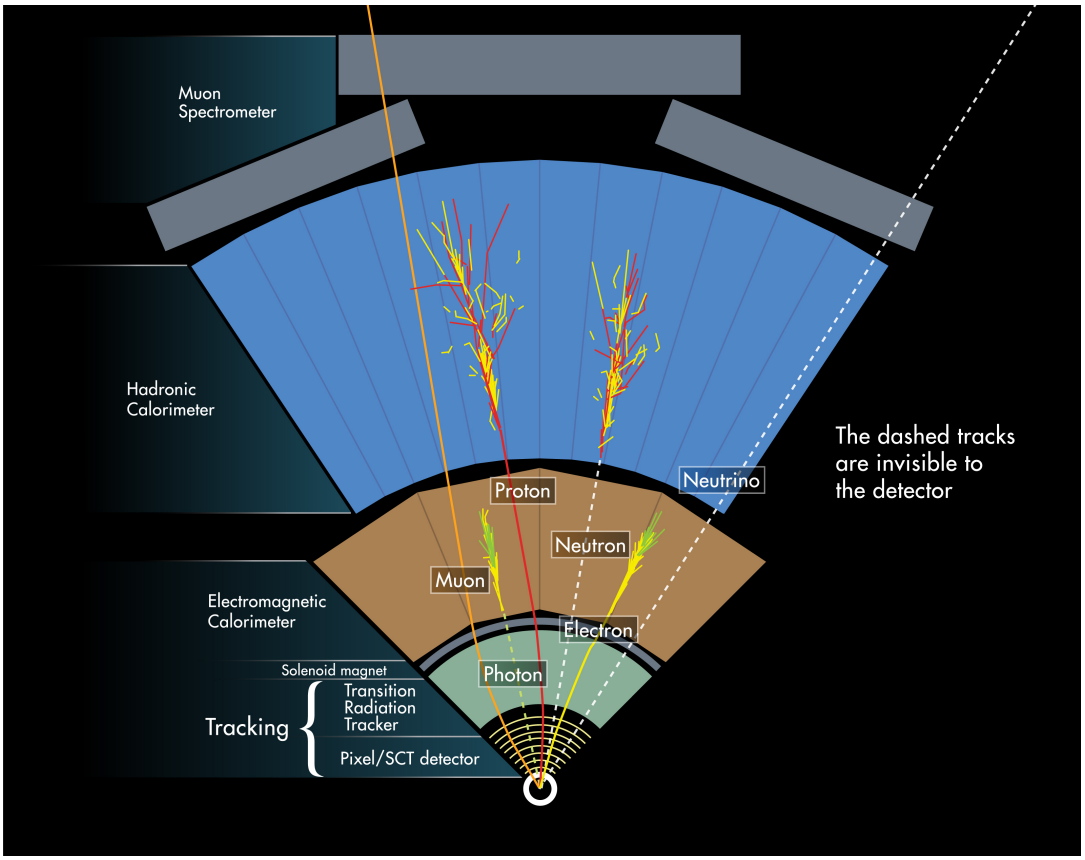

Figure 3.16: Paths and interaction of each kind of particle with the different detectors of the ATLAS experiment [76].

Figure 3.16 shows a schematic representation of a slice of a cross section (orthogonal to the beam-line) of the ATLAS experiment, showing its detectors and their interaction with different particles generated during an LHC collision. Solid lines represent a signal interacting in each detector, while a dashed line represents a track that is invisible in the corresponding detector. Briefly summarizing the trajectory of each particle:

- Electrons (yellow line) are charged, which implies that they can interact with the various tracking systems at the innermost part of the calorimeter. Their charge also allows their trajectory to be modified (in fact, curved) by the magnetic field generated by the solenoid magnet, which overall provides measurements of their direction and momentum. Afterwards, electrons get fully absorbed by the electromagnetic calorimeter (where they get showered in combinations of smaller energy electrons

and photons, also represented schematically in Fig. 3.16), providing a measurement of their energy. One must consider that electrons reaching the calorimeter have lost some energy due to their interaction with the matter of the inner detector, which leads to bremsstrahlung photon emission due to the interaction of the electron with the electric field of an atom.

- Photons (green line), however, have a neutral electric charge, so they are invisible to the tracking systems. At first order, photons will only be measured using the electromagnetic calorimeter. However, in the matter of the inner tracker, photon conversion into an e^+e^- pair can occur, which must be considered by the reconstruction algorithms.
- Muons (orange line), despite being similar to electrons, will interact minimally with each of the detectors traversed by these. This means that muons will induce a signal through all of the detectors (including the hadronic calorimeter), all the way until they cross the muon spectrometer and escape.
- Since protons (red line) are also charged particles, these will generate a signal while crossing through the tracking and electromagnetic calorimeter systems, but their energy will only be measured when fully absorbed by the hadronic calorimeter. As suggested by the schematic representation and according to the previous sections, protons are absorbed by showering them into photons and other hadrons inside of the corresponding calorimeter.
- Neutrons (white dashed line) are almost invisible to all of the inner layers of the calorimeter, and these will deposit a signal only on the hadronic calorimeter in a similar fashion to that of protons.
- Neutrinos (also white dashed line) will travel through all of the detectors without generating any kind of signal. Rather than detecting them via direct measurements, their transverse momentum is often estimated by measuring the amount of "missing transverse energy".

3.3 Object reconstruction and identification at ATLAS

Thanks to the multiple layers of detectors that integrate the ATLAS detector, it is possible to measure various properties of specific particles and to follow their development as they travel through the various subsystems. The probing offered by each sub-detector is such that, given an adequate analysis, it can ultimately allow for the reconstruction and classification of many of the physics objects generated at the collision point, such as the produced leptons and photons. The ATLAS experiment has established a series of dedicated reconstruction techniques which seek to efficiently recover physical particle properties from the signals induced on each of the subsystems. The next sections briefly describe the general methodology used for each kind of object.

3.3.1 Track and vertex reconstruction

As charged particles travel through the inner detector, traces of sequential signals are generated, which can eventually lead to particle track reconstruction [77]. Given the layered and highly granular nature of the ID, it is possible to generate 3D maps by collecting all the signals generated by a particle. By combining information (clusters of signals) from the pixel and SCT detectors (see Fig. 3.17 for a schematic representation), it becomes possible to generate first track seeds. From here, the actual definition and creation of tracks is mainly a combinatory problem, as one must be able to discern between the signals generated by completely independent particles. Thus, by the implementation of combinatorial Kalman filters, seeds are capable of generating track candidates (N.B. the same seeds may be compatible with multiple track candidates). Final track ambiguities are solved via quality scores (using information such as intrinsic resolution, track multiplicity, track-estimated momentum and quality of the track fit) and neural networks trained on merged clusters. Followed by the track ambiguity removal, the high-resolution track fits provide a final measurement for a given collection of signals.

As pp interactions occur with a spread (from the bunch size) of ~ 3.5 cm, the next task at hand is to look for the interaction vertex that proceeds the already defined and isolated tracks [77]. This is achieved by first generating vertex seed positions thanks to the recollection of the tracks which fulfil specific characteristics, and then by performing fits on all these seeds in order to determine the optimal vertex position compatible with the tracks. As pile-up opens the possibility of multiple vertices, the fits are done in an iterative manner such that all tracks are compared to a given vertex fit: if a track is highly incompatible with a given vertex, this is then weight-penalised and eventually removed from the fit (to be used in the determination of a different vertex). In the ATLAS experiment, one often defines a main vertex by choosing the one with the larger

$$\sum_{i \in \text{vertex}} p_{T,i}^2,$$

which receives the name of hard-scattered (HS) vertex. All the rest are simply called pile-up vertices.

3.3.2 Electrons and photons

While the electromagnetic calorimeter is responsible for the energy measurement of electrons and photons, it is only in conjunction with the inner detector that full and reliable reconstruction can be obtained. As the ID provides information on charged particles only, firstly, it allows discerning between electrons and photons by comparing ID and EMCAL signals. Moreover, the high granularity of the ID is fundamental to track the trajectory of electrons and to provide information on secondary interactions happening between the interaction point and the EMCAL. Such is the case of photons being converted into electron-positron pairs, additional photons created due to the interaction of electrons

with matter, or by bremsstrahlung losses. Figure 3.17 illustrates a simplified scenario following the trajectory (and induced detector signals) of an electron created (almost) at the interaction point.

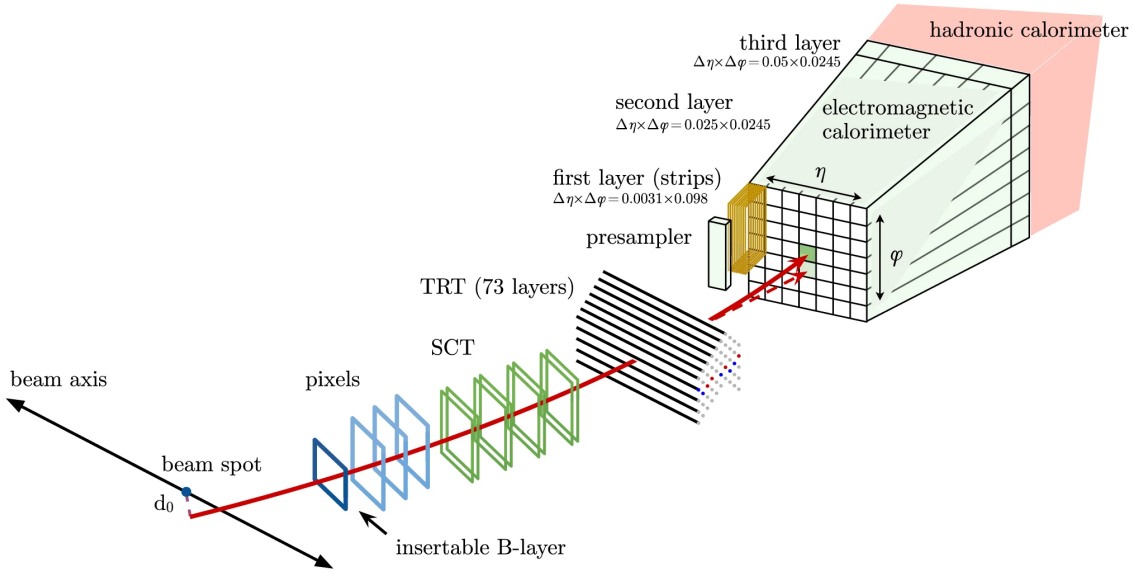

Figure 3.17: Schematic representation of the path described by an electron through the inner detector and electromagnetic calorimeter. The solid red curve represents the trajectory of the electron, while the dashed red curve (after the presampler) represents the path of a photon that can be created upon the interaction of the electron with the material of the tracker [78].

Given the fine granularity of the EMCAL and its operation design induces electromagnetic showers on the arriving electrons and photons, the signal produced by these will not be fully contained in a single EMCAL cell. On the contrary, a single electron will generate a raceme of signals, each accounting for a fraction of the original electron's energy. Hence, reconstruction starts by employing clustering algorithms on the EMCAL signals in order to isolate possible electron (or photon) candidates, which should be large enough to encompass as much of the electron signal as possible without collecting contributions induced on the EMCAL by other particles. Overall, general enough clusters optimised to reduce misidentification are desired.

The accumulation of ID signals across its many layers defines particle tracks, which provide information on the trajectory and energy losses that would otherwise not be identifiable by the EMCAL alone. For primary electrons, tracks must be generated at the main interaction vertex (complementary, a vertex located away from the interaction point will typically correspond to photon conversion). Final electron candidates are defined by matching EMCAL clusters to primary electron ID tracks.

In order to account for Bremsstrahlung emission, a special track finding and fitting

methodology is added, which affects the reconstructed electron track trajectory. One must also consider that collinearly emitted secondary particles may generate multiple ID tracks that may appear compatible with a single EMCAL cluster. If these tracks can be associated with a single primary electron, then the track closest to the cluster (that is, with the smallest ΔR distance) and with more than 3-pixel hits is used to define the electron candidate.

The definition of photons follows a complementary methodology to that used for electrons: if an EMCAL cluster cannot be matched to any track, it is classified as an unconverted (or primary) photon.

While the track definition is relatively straightforward, the construction of the EMCAL cluster is less trivial and, to some extent, case-dependent. As clusters are created in a general enough manner, a likelihood-based discriminant response is built around the expected and measured shape of electromagnetic showers within the EMCAL. Such discriminant allows for a selection of working points, which provide a trade-off between identification and reconstruction efficiency. These are labelled "tight", "medium" and "loose", with their identification efficiency being energy-dependent. For instance, for an electron with $E_{\mathrm{T}} = 40$ GeV, their efficiencies are respectively 80%, 88% and 93% [78]. The same working points (with the exception of "medium") are applied to photons.

During the early stages of LHC (namely, during Run-1 and Run-2), event reconstruction in the calorimeter systems was based on fixed sliding window algorithms independent of energy. Current reconstruction in the electromagnetic and hadronic calorimeter is achieved with an algorithm developed in 2017 [79], which is based on the definition of topologically connected cell clusters that receive the simple name of "topo-clusters".

Given the absolute energy of a calorimeter cell $E^{\mathrm{EM}}_{\mathrm{cell}}$ and the cell noise $\sigma^{\mathrm{EM}}_{\mathrm{noise,cell}}$ (which accounts both for electronic and pile-up noises), the definition and processing of topo-clusters begins with the cell energy significance

$$\zeta^{\mathrm{EM}}_{\mathrm{cell}} = \left| \frac{E^{\mathrm{EM}}_{\mathrm{cell}}}{\sigma^{\mathrm{EM}}_{\mathrm{noise,cell}}} \right| . \tag{3.9}$$

In a nutshell, topo-clusters are defined as follows:

1. Build a proto-cluster = collection of adjacent cells s.t. $\zeta^{\mathrm{EM}}_{\mathrm{cell}} \geq 4$;
2. Scan the neighbouring cells iteratively and add to the proto-cluster all of the cells with $\zeta^{\mathrm{EM}}_{\mathrm{cell}} \geq 2$;
3. Repeat the scan until every neighbouring $\zeta^{\mathrm{EM}}_{\mathrm{cell}} \geq 2$ has been gathered;
4. Combine nearby cells with $\zeta^{\mathrm{EM}}_{\mathrm{cell}} \geq 0$ into the cluster defined above.

It is worth noticing that the cells comprising a single topo-cluster can be a mixture of LAr and Tile calorimeter cells. In the particular case of electrons and photons, initial

clusters are defined using exclusively EM calorimeter cells. Here, an initial cut on the cluster energy for each cluster in the EM fraction f_{EM}, defined as

$$f_{\mathrm{EM}} = \frac{E_{\mathrm{L_1}} + E_{\mathrm{L_2}} + E_{\mathrm{L_3}} + w \cdot (E_{\mathrm{E_4}} + E_{\mathrm{PS}})}{E_{\mathrm{cluster}}}, \tag{3.10}$$

where $E_{\mathrm{L_i}}$ is the cluster energies in layer i, is applied, asking that f_{EM} is larger than this threshold. The parameter w is equal to 1 when $1.37 < |\eta| < 1.63$, and $w = 0$ elsewhere: this means that the term $(E_{\mathrm{E_4}} + E_{\mathrm{PS}})$ is only accounted for cluster in the barrel-endcap transition region, as the amount of energy deposited in the pre-sampler and E4 scintillators becomes non-negligible (for other regions of the calorimeter, this term is ignored in order to decrease noise). The threshold of the f_{EM} is estimated via simulations, seeking a rejection of 60% of pile-up clusters and is found to be equal to 0.5. Furthermore, only clusters with deposited energy larger than 400 MeV are considered to reject pile-up clusters or $\pi^0 \to \gamma\gamma$ signals.

Generally speaking, reconstruction is heavily dependent on the environmental settings of the run, especially on pile-up: by increasing the average pile-up of the run, so does the pile-up cell noise (and thus, its contribution alone yields a larger value of $\sigma^{\mathrm{EM}}_{\mathrm{noise,cell}}$, which then modifies the value of $\zeta^{\mathrm{EM}}_{\mathrm{cell}}$). Moreover, the energy threshold may be changed when collecting data in special runs, which manifests as a change in the total reconstructed energy and energy resolution shape. For instance, in the case of low pile-up runs where $\langle\mu\rangle = 2$, a lower energy threshold is used in order to take advantage of the low noise environment and allow for higher precision measurements, which translates into an overall larger total reconstructed energy. Overall, this means that one should not neglect the pile-up dependency of a specific measurement and that dedicated treatment may be needed in a case-by-case scenario.

3.3.3 Muons

Muons will travel through all the layers of the ATLAS detector. These will not be completely absorbed but will generate a series of tracks. Reconstruction of muons is based primarily on the matching of tracks generated in the inner detector and the corresponding signal in the muon spectrometer after taking into account muon energy losses.

3.3.4 Jet reconstruction and flavour tagging

Product of the hadronisation of quarks and gluons, jets are one of the trickiest physics events to reconstruct accurately. They consist of ensembles of relatively collinear charged and neutral hadrons, which tend to propagate in a cone-like fashion. Consequently, jets will deposit energy in extended angular regions of the tracker and calorimeters.

Jet reconstruction is based on the definition of EMCAL and HCAL topo-clusters, and in the estimation of the jet propagation via clustering algorithms such as anti-k_t [80, 81]. Given the angularly extensive signal produced by a single jet, its reconstruction relies

heavily on the radius parameter ΔR, which is often set to $\Delta R = 0.4$ (small jets) and $\Delta R = 1.0$ (large jets) seeking a trade-off between capturing all the jet development while also isolating it from other processes.

In a nutshell, the anti-k_t algorithm works by iteratively merging signals around the most energetic entity found within the jet. Such merging is performed in descending p_{T} order, including only the ones that satisfy

$$d_{ij} = \min\left(\frac{1}{k_{t,i}^2}, \frac{1}{k_{t,j}^2}\right)\frac{\Delta R_{ij}^2}{R} < d_{iB} = \frac{1}{k_{t,i}^2} \tag{3.11}$$

for $k_{t,i}$ and $k_{t,j}$ the transverse momentum of signals i and j, $\Delta R_{ij}^2 = (y_1 - y_2)^2 + (\phi_1 - \phi_2)^2$ the angular distance between them. By design, the anti-k_t algorithm works assuming conical jets, implying that the final jet signal on the detector will be circular. Many of the algorithms are also Infra-Red Collinear (IRC) safe so that reconstruction is independent of the particle multiplicity and of the initial soft radiation.

The input of the anti-k_t jet finding algorithm is pre-processed objects generated with the Particle Flow algorithm [82], which provides further constraining power in the jet reconstruction process by removing calorimeter energy deposits due to charged hadrons from the jet reconstruction and using instead momenta measurements from the tracker, all of this while retaining the calorimeter measurements of neutral-particle energies. The main advantage of the Particle Flow algorithm is to remove pile-up from charged particles, and it has proved to be particularly useful when there are low momenta tracks whose resolution is better than the calorimeter resolution. Similarly, for larger momenta tracks, the degrading resolution leads the Particle Flow jets towards the anti-k_t ones.

The exact choice of algorithm is motivated by seeking an improvement of the jet energy and angular resolutions, as well as to increase the reconstruction efficiency and stability with respect to pile-up. The choice of algorithm is especially important looking towards the future, as the large increase in pile-up during HL-LHC can easily lead to several overlapping jets generating intertwined signals.

Jet flavour tagging is performed by looking at specific kinematic properties of the jet as indicators of the progenitor hadron. Such can be the orientation of the jet, displaced vertices (related to long-lived particles, such as a boosted b-quark), or the total energy of the jet. In the central region ($|\eta| < 2.47$), in particular, jets may be tagged as light-flavour (u-, d-, s-quarks or gluon), c-jets or b-jets. All the previous being said, jet flavour tagging is typically performed using neural networks.

Tagging is particularly relevant for studies where decay channels finish up with individual partons, such as $H \to b\bar{b}$ or $gg \to t\bar{t}$, so there is a great interest in their proper reconstruction and tagging. These turn up to be of special importance for QCD studies, where probing of higher-order partonic interactions largely contribute to e.g. the differential cross section of a specific process.

3.3.5 Missing transverse energy

While the amalgamation of detectors is capable of directly measuring a large fraction of the particles produced at the interaction point, this is not true for particles that interact weakly with matter. Particles such as neutrinos must be measured using indirect methods by taking advantage of physical conservation rules, particularly by using momentum conservation before and after the proton collision.

As protons are moving in the longitudinal direction, each proton parton carries unknown amounts of initial longitudinal momentum, which disables the possibility of using this information. Nevertheless, the transversal momentum (that is, the fraction of the momentum perpendicular to the beamline) is, on average, nil. That means that the total transverse momentum of the produced particles after the collision must also be zero, and this is a value that one could recover if it were possible to measure every single product of the collision. Since some particles (such as neutrinos) will escape without leaving a signal behind, this will get reflected as a deficit in the total final transverse momentum that receives the name of "missing transverse energy" (as estimated using the calorimeters), or just $\vec{E}_{\mathrm{T}}^{\mathrm{miss}}$. In other words, momentum conservation gives the following expression:

$$\vec{0} = \sum_i \vec{E}_{\mathrm{T},i}^{\mathrm{measured}} + \vec{E}_{\mathrm{T}}^{\mathrm{miss}},$$

which leads to

$$\vec{E}_{\mathrm{T}}^{\mathrm{miss}} = -\sum_i \vec{E}_{\mathrm{T},i}^{\mathrm{measured}} = -\sum_{i\in\text{hard objects}} \vec{E}_{\mathrm{T},i} - \sum_{i\in\text{soft objects}} \vec{E}_{\mathrm{T},i}, \tag{3.12}$$

where "hard objects" includes all the final state particles that were measured and identified, and "soft objects" accounts for the rest of the signals which were measured but not associated with any physical particle yet still carry part of the total transverse momentum.

In the particular case of a single Drell-Yan-produced W-boson decaying as $W \to \ell\,\nu_\ell$, where a single neutrino expected (see Fig. 3.18), one can write

$$\vec{E}_{\mathrm{T}}^{\mathrm{miss}} = \vec{p}_{\mathrm{T}}^{\,\nu} = -(\vec{u}_{\mathrm{T}} + \vec{p}_{\mathrm{T}}^{\,\ell}), \tag{3.13}$$

where $\vec{u}_{\mathrm{T}} = \sum_i \vec{E}_{\mathrm{T},i}$ accounts for the total hadronic recoil, and $\vec{p}_{\mathrm{T}}^{\,\ell}$ is the amount of momentum measured on the lepton.

Generally speaking, the estimation of $\vec{E}_{\mathrm{T}}^{\mathrm{miss}}$ is a delicate task. Firstly, one must avoid double-counting particles, which is achieved by forcing some hierarchy in the order that the sums are done. Moreover, the resolution of $\vec{E}_{\mathrm{T}}^{\mathrm{miss}}$ is greatly affected by the presence of jets, whose reconstruction gets hindered in higher pile-up scenarios. Consequently, particular studies that rely heavily on measurements of $\vec{E}_{\mathrm{T}}^{\mathrm{miss}}$ will prefer specific setups, such as low pile-up runs.

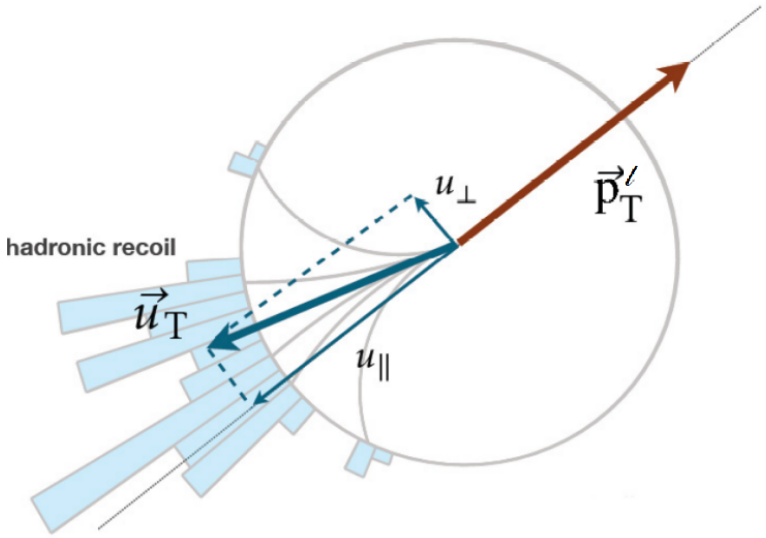

Figure 3.18: Hadronic recoil in a $W \to \ell\ \nu_\ell$ decay.

3.4 Plans of the LHC, high luminosity LHC and the upgrades of the ATLAS detector

In general terms, the operation of the LHC is based on alternating cycles of data-taking periods (Runs), during which physics-relevant beam collisions occur, and extended beam-less periods (Long Shutdowns, LS), during which maintenance and upgrade work is performed on the different experiments. As Fig. 3.19 schematically shows, we are currently about 1/4 into Run-3.

As higher precision measurements are performed using LHC data, there is an increasing interest towards the study of rare processes and searches for new physics, which require much larger amounts of data than currently available, leading naturally to a desired increase in luminosity. LHC is currently operating at 2 times the nominal luminosity (i.e., that for which the LHC was designed), which is the limit of what can be efficiently recorded using the existing setups. Consequently, the High Luminosity LHC (HL-LHC) project aims to ultimately increase the instantaneous luminosity by a factor of 5 to 7.5 times the nominal value, coming along a series of specific hardware and software upgrades for each experiment.

By definition, HL-LHC means a faster data collection rate, but it comes hand-in-hand with an increase in pile-up that requires specific systems to be prepared for efficient data-taking and processing. On-site preparation works have already started during LS2, which will be monitored through Run-3, followed by LS3 where the final detector upgrades will be installed right before a dramatic increase in luminosity during Run-4. Figure 3.19

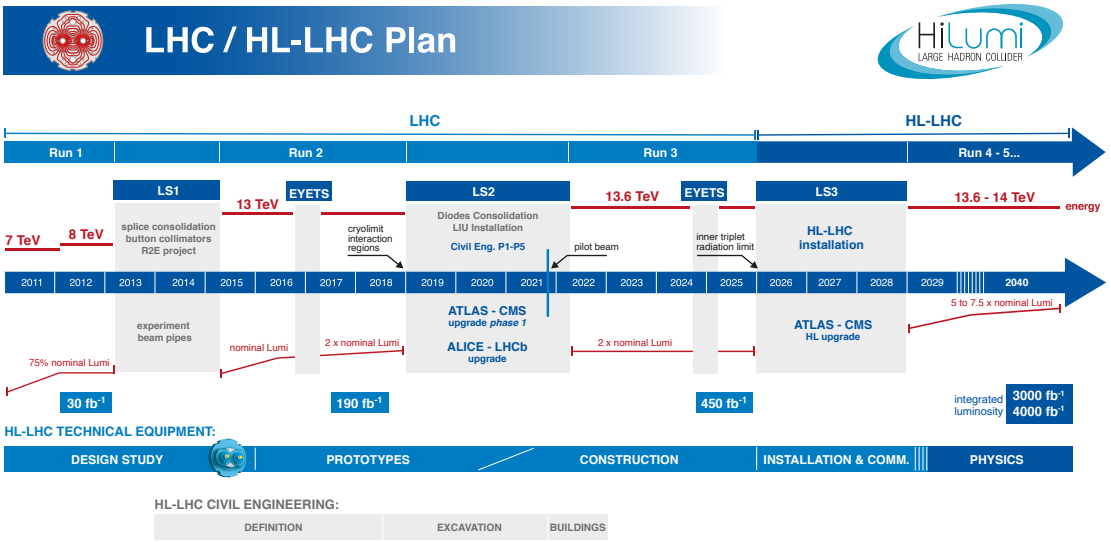

Figure 3.19: LHC / HL-LHC Plan, showing the physics-taking and shutdown schedules (as of March 2023) [83].

shows a schematic representation of the current schedule for the LHC and the planned preparation works towards the HL-LHC.

For the ATLAS experiment in particular, a series of upgrades and new detectors are to be installed during LS3 (and, in fact, work has already started in LS2). Below, there is a brief description of some of these upgrades.

3.4.1 ITk

In order to improve tracking performance and to obtain faster readout capabilities, the current inner detector will be completely replaced by a new all-silicon pixel Inner Tracker (ITk) detector, where the coverage in η will be extended from 2.5 (current) to 4.0. By construction, the finer granularity of ITk results in the level of precision required to track particles in a high pile-up environment adequately. The ITk will be composed of two subsystems: a Strip Detector [84] surrounding a Pixel Detector [85].

3.4.2 HGTD

The High Granularity Timing Detector (HGTD) [86] is designed to measure the timing of particles produced in LHC collisions with high precision in the forward region ($2.4 < |\eta| < 4.0$), which can provide important information about the origin of the particles and the physics of the collision. The detector is located in the forward region close to the beamline. HGTD consists of a series of silicon sensors arranged in layers, with each layer measuring the time of arrival of particles with increasing precision. The sensors are able to measure the time of arrival of particles with a precision of less than 30 picoseconds, which is much faster than other detectors currently installed. The increased timing precision is particularly interesting for pile-up jet rejection and time-wise vertex separation.

3.4.3 Calorimeter

The upgrades of the LAr calorimeter are split into two iterations, named Phase-I [87] and Phase-II [88], scheduled to take place during LS2 and LS3 respectively. Phase-I (already installed and undergoing validation) included the migration to a digital trigger, capable of providing a finer readout granularity and consequently giving an improved sensitivity to the shower development measurements (timing- and shape-wise) within the calorimeter. Together, Phase-I upgrades have the potential to allow for tighter selection and reconstruction criteria, which has a direct impact on background rejection and reduces the possible ambiguities generated by the increased pile-up. Phase-II is more closely related to the increased interaction rate. It results in an upgrade of the readout in order to allow for larger bandwidths and radiation hardening so as to withstand the increased levels of radiation produced by the rise in luminosity far beyond the initially foreseen values. This means a replacement of the low-voltage powering systems and an upgrade of the main read-out electronics.

3.4.4 Trigger

In order to catch up with the increased pile-up, several upgrades in the trigger and data acquisition system are foreseen during LS3. The new trigger [89] is based on hardware and includes a Level-0 trigger (L0) operating at 40 MHZ along an Event Filter (EF) that is based on 1 MHz CPU farms. L0 includes a global and central trigger (CTP) sub-system, as well as dedicated systems for the calorimeter (L0Calo) and muon (L0Muon) triggers, which assist in the reconstruction of events in these systems. Moreover, the global trigger sub-system is capable of combining inputs from L0Calo and L0Muon in order to build and apply kinematic-base selection. On the other hand, the main purpose of the EF is the refinement of the L0 selection (e.g. by applying off-line reconstruction techniques) that will ultimately optimise the final data storage.

4 Prediction and simulation of physical processes

Precise measurement and analysis of every single particle generated by LHC collisions is an extremely complicated task, both due to the underlying physics governing the interactions between protons at such high energies and due to the many detector and statistical effects which come into play when collecting data.

4.1 General motivation for the use of simulations

Let us consider the hypothetical case where no detector effects are present. In this scenario, and following from the foundations described in Chapter 1, full theoretical predictions of the physical processes responsible for the output of a given proton-proton collision via analytical functions are hindered by some limitations:

- Modelling is done in a perturbative manner, both in an electroweak (EW) and a quantum chromodynamics (QCD) basis. While it is desired to do so at the highest possible perturbative order (and, in fact, infinite order would provide full modelling), by increasing the order (and thus, by including intermediate processes and the contributions of multiple emissions of particles and radiation), the complexity of the computation increases exponentially.
- By stopping at a specific perturbative order, resummation techniques must be applied in order to recover the (estimated) higher-order contributions and to compensate for the numerical effects derived from approximations done along the modelling, such as the apparition of large logarithms arising from cross-section calculations.

All the previous calls for computational approaches, such as numerical integration, which in general disconnects any evident "fit" of an analytical theoretical model to the observed data.

In reality, the detector is not capable of perfectly measuring every single particle generated at the interaction point, if at all (see Section 3.3). Resolution and stochastic effects in the particle detection process degrade the otherwise perfect recovery of the properties of a particle, which is not predictable in an analytical manner. Such effects are varied:

- Some particles, such as neutrinos, cannot be directly measured.
- The resolution of the detector is not infinitesimally small: there is a finite granularity. This means that it is not possible to fully follow and measure a particle at absolutely any desired time or position, but rather measurements retrieve information in a discreet manner.
- Interaction of particles with the material is governed by stochastic effects, such as electronic noise, randomness of the response of the detector, and detector resolutions.

As a consequence, most high-energy physics studies rely on comparisons between collected data events and several simulations of analogous events using a given theoretical physics model. Provided a good enough understanding and calibration of the electronics, one can estimate physics parameters (e.g. the mass of the W-boson, called m_W) by comparing several samples of simulated events, tuned for specific values of m_W, against the equivalent measured samples. The following sections are dedicated to giving a cursory view of the generation of samples and simulation of detector effects.

4.2 Event generation

Sample simulation begins with the generation of individual events according to a theoretical prescription. For a given model (e.g. a function describing a differential cross section), one can generate events following such model by repeatedly and randomly sampling the model according to its probability distribution function. In the limit of an infinitely large generated sample, the distribution described by the accumulation of all events (e.g. by filling a specific variable into a histogram that is then normalised, although in reality, it concerns a multidimensional phase space) will be identical to the theoretical model. Such techniques receive the name of "Monte Carlo methods" [90], and the collection of generated events are typically called "Monte Carlo samples" or simply MC.

In essence, MC samples are generated to simulate physics. In the limit scenario where the detector is capable of perfectly measuring every single particle, given a good enough understanding of the underlying theoretical description, one could generate a MC sample that perfectly mimics the observations (up to statistical effects).

Given the huge amount of possible processes derived from an LHC collision, a given MC sample is not intended to fully describe every single sub-product of the main interaction (see Fig. 4.1 for a general example). Instead, MC samples are generated for specific processes, given a set of theoretical constraints (such as PDF, QCD and EW perturbative order, flavour treatment, parton shower, and hadronisation modelling). Such processes are chosen in such a way that equivalent data measurements can be (almost fully) isolated via selection rules. For instance, in the case of $pp \to Z^0 \to e^+e^-$ events, one can start

by asking for 2 electrons (often, "electron" is used as a generic word for electron and positron) with a common vertex, totalling an invariant mass within a window around 91 GeV, specific electron kinematics, and more. One should always remain sceptical of such selection rules, as very tight requirements can decrease the number of usable events by huge factors, and too loose ones would lead to the inclusion of background signals generated by other processes (in the case of $Z \to e^+e^-$ signal, dominant backgrounds are $Z \to \tau^+\tau^- \to e^+e^-(\mu^+\mu^-) + 4\nu$ or $t\bar{t} \to W^+bW^-\bar{b} \to e^+e^-\ \nu\bar{\nu}\ b\bar{b}$) but passing the selection process.

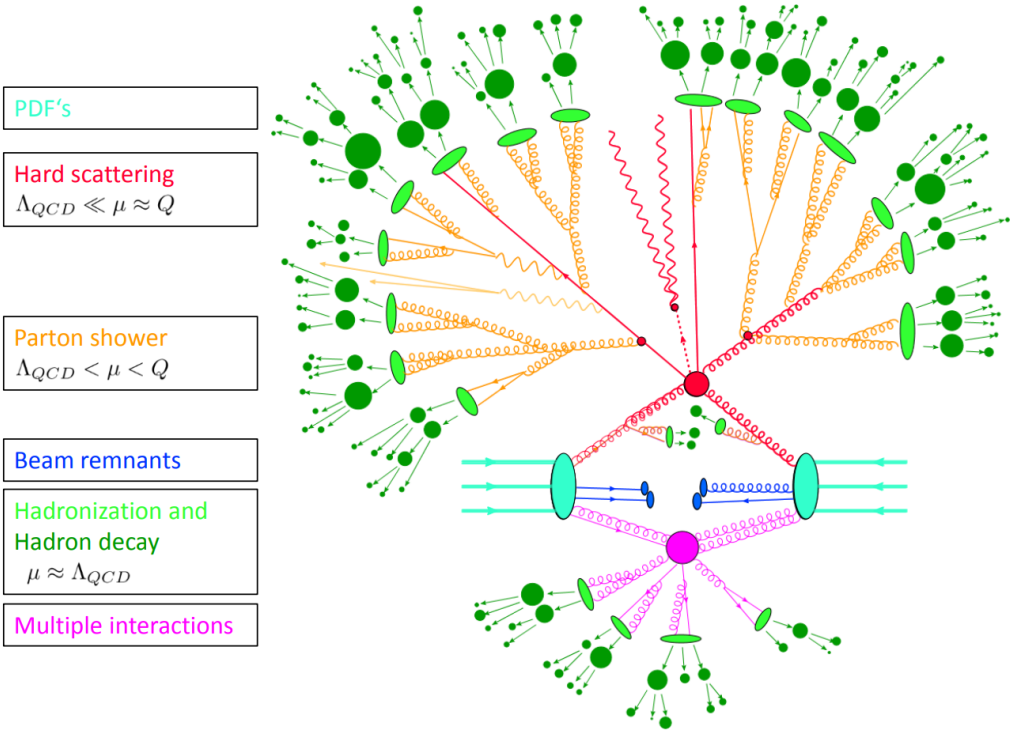

Figure 4.1: Schematic representation of the simulation of a proton-proton collision and the development of sub-products into a non-specified final state [91].

The full simulation of an event is not performed in a single push. Instead, the overall particle development is factorised into smaller steps, each accounting for different phenomena and allowing to implement punctual tweaking. Moreover, such factorisation allows for the development of specific computational frameworks dedicated to the simulation of specific processes, ultimately giving a modular workbench where the best tool for a specific study can be (with some limitations) transparently introduced or modified. Figure 4.1 shows the evolution of a particle simulation (for an unspecified, general final state) and the sub-division into intermediate physical states. The following sections provide a quick glance at each of the steps.

Since the MC sample can be generated as desired, one must choose the number of events that will compose it. In an ideal situation, it is desired to have an infinitely

large sample size so that statistical effects get fully mitigated. In practice, such a large sample size becomes detrimental due to computational limitations. A general rule of thumb is for MC samples to have $\sim$ 10 times as many events as the equivalent data counterpart, which translates as an increase of the total statistical uncertainty by a factor of about $1/\sqrt{10} \sim 0.3$ (compare to the asymptotic scenario) while allowing for relatively fast computational processing.

In order to account for the relative size of the MC sample with respect to data and to account for computational effects arising from the employed numerical methods, simulated events have an associated "weight", which works as a scaling factor for quick normalisation to data. In the case where the ratio of sample sizes ($n_{\text{MC}}/n_{\text{data}}$) is exactly 10, typical MC weight w_i for an event i will have a value around 0.1 (conversely, each data event has a weight of exactly 1.0). Generally speaking, the intrinsic weights of generated MC samples do not have to be exactly the same for each event, but rather these will be different as a consequence of the sampling in different regions of the phase-space and can even lead to negative weights. Moreover, weights allow performing post-generation adjustments of a given MC sample by applying small modifications through a process called "reweighting", which is used to improve the agreement between data and MC of poorly modelled quantities such as the transverse momentum of the Z-boson.

4.2.1 Parton Distribution Functions

Simulation starts with the description of the partonic content within each of the protons, which is given by their Parton Distribution Functions (PDFs). These are typically determined beforehand through dedicated studies, which are performed by few groups around the world by using different approaches and datasets, providing an ultimately fixed partonic description (at a specific QCD perturbative order) as a function of the fraction of momentum carried by each parton (denoted by x, which takes values between 0 and 1), the factorisation scale μ_F, and the energy scale of the interaction (often denoted by $\hat{s}$).

PDF sets are typically stored in LHAPDF [92] format, which is both a dedicated tool for evaluations of parton distribution functions and a library that collects previously fitted PDFs. The specific choice of PDF is often motivated by various particularities of the study, with broad recommendations, such as those provided by the PDF4LHC [45] group, being made available in a regular manner.

4.2.2 Hard scattering

Let us consider two partons, each coming from one of the protons, with given 4-momentum vectors. Their interaction receives the name of hard scattering ("hard" refers to the large momentum transfer), and this can be predicted via theoretical calculations. On its own, hard scattering processes are independent from the PDF, and these are described by their "hard scattering cross section". Hard processes are estimated using fixed-order perturbation theory by defining partonic cross-sections $\sigma_{a,b\to X}$ through computations in series, expanded around the strong coupling factor α_s, such as

$$\sigma_{a,b\to X} = \alpha_s^n[\underbrace{\sigma_0}_{\text{LO}} + \underbrace{\alpha_s\sigma_1}_{\text{NLO}} + \underbrace{\alpha_s^2\sigma_2}_{\text{NNLO}} + \underbrace{\alpha_s^3\sigma_3}_{\text{N}^3\text{LO}} + \mathcal{O}(\alpha_s^4)]. \tag{4.1}$$

By choosing a specific order, a generated sample will account only for a limited number of contributions, ignoring higher-order loop effects. Figure 4.2 represents the contributions at LO, NLO and NNLO on Eq. (4.1). Focusing on these diagrams, it is worth mentioning that NLO virtual contributions generated from the interference between the LO diagram and higher-order loop diagrams (such as the first one in the NNLO row) lead to divergence in the computation, which can be compensated by the tree level higher order NLO diagrams if the integration in phase space is properly done. This divergence compensation on its own may lead to non-physical features, such as spikes, which can be smoothed by resummation algorithms thanks to the correction of large logarithms. Consequently, higher-order predictions must undergo some form of parton showering via dedicated generators (see Section 4.2.3).

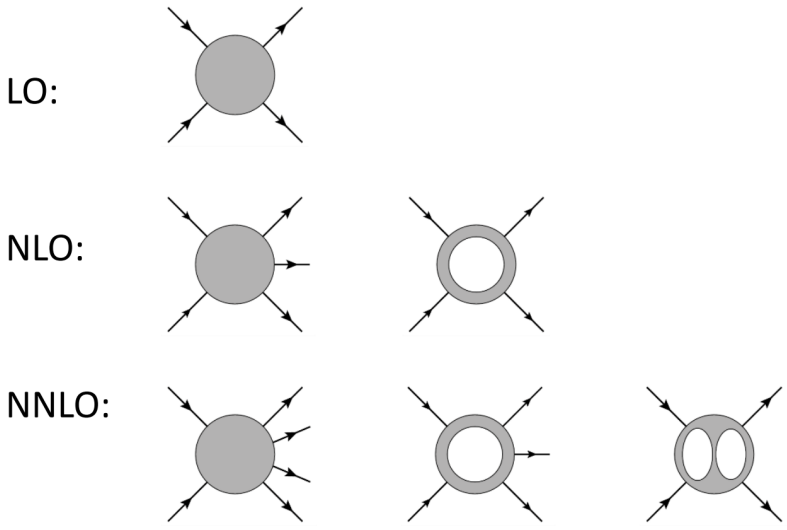

Figure 4.2: Schematic representation of fixed order contributions at different perturbative levels [91].

In an LHC collision, the momentum of any given parton does not take a specific value but rather follows a distribution described by the PDF: by knowing the total momentum

of the proton, the PDF estimates what is the probability that a particular parton carries a specific fraction of the total momentum. By convoluting the PDF of both protons with the hard scattering cross sections for the process of interest and summing over all the possible quark combinations, a fixed order prediction can be determined. Equation (1.48) depicts such estimation, as given by the factorisation theorem.

Among the various frameworks used to generate specific process predictions, one of the most popular ones is `POWHEG` [93], which can generate NLO calculations for interfacing with parton shower generators. `POWHEG` stands for "Positive Weight Hardest Emission Generator", which implies two things:

- computations start by generating the hardest radiation first, later followed by an algorithm which groups higher-order perturbative contributions;
- and most events are positively weighted (although a small fraction of them, about 1%, get negative weights).

Generally speaking, the popularity of `POWHEG` is due to the variety of processes available within the framework and because it is intended to be interfaced with shower generators avoiding order-matching ambiguities.

4.2.3 Parton Shower

Posterior parton shower can be performed via resummation techniques or with MC parton shower modelling. It is intended to include the effect of particle emission, such as Initial State and Final State Radiation (IRS and FSR, respectively) and gluon splitting, on top of the cross sections derived from the Fixed Order (F.O.) predictions, which rely on the matrix element of the process. Such a process compensates for an otherwise infinite number of parton shower emissions, leading to a divergent matrix element spectrum.

As a practical example, let us concentrate on the case of p_{T}^{W}, i.e. the transverse momentum of the W-boson at NLO (Fig. 4.3). At fixed order, the NLO prediction diverges when $p_{\mathrm{T}}^{W} \to 0$ (i.e. $p_{\mathrm{T}}^{W} << m_W$) due to the presence of soft and collinear emissions, which leads to ultraviolet divergence. Mathematically speaking, it gets affected by large logarithms of the type

$$\alpha_s^n \ln^m(m_W/p_{\mathrm{T}}^{W}). \tag{4.2}$$

After parton showering, resummation corrections take care of such problem by implementing a Next-to-Next-Leading-Logarithm (NNLL) correction, leading to finite cross-section terms (red curve in Fig. 4.3).

A variety of frameworks are used to implement MC-based parton showering, each being preferred for specific implementations and qualities of the study. Among the most common ones are `PYTHIA` [95], `HERWIG` [96] and `SHERPA` [97].

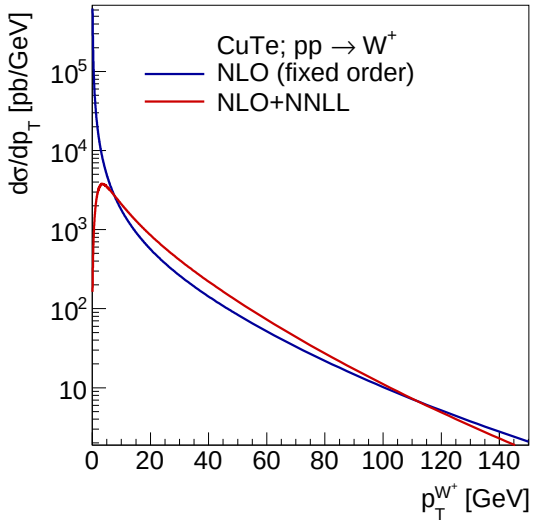

Figure 4.3: Theoretical prediction of the p_{T}^{W} differential cross section at NLO, as given by the fixed order prediction (blue) and after NNLL resummation corrections (red) [94]. N.B. the divergence of the blue curve towards $+\infty$ as $p_{\mathrm{T}}^{W} \to 0^{+}$ is compensated by real corrections with a spike to $-\infty$ at $p_{\mathrm{T}}^{W} = 0$ (said spike is not shown in the diagram above).

4.2.4 Beam remnants, multiple interactions, and hadronic processes

The generation and evolution of secondary particles that do not belong to the main process of interest cannot be computed directly due to the large number of degrees of freedom. Generally speaking, such predictions are estimated numerically via non-perturbative models that are tuned using $e^{+}e^{-}$ data (as these collisions are not PDF dependent), using frameworks such as `PYTHIA` [95]. A good understanding of these processes is vital for the full analysis of the collection of particles created after an LHC collision, which leads to better classification of signals over all the ATLAS detector, and for the indirect measurement of quantities such as the Missing Transverse Energy (MET). Hadronisation and hadron decay are of particular interest for jet studies, as these generate signals across multiple detectors over large angular sectors. As these are not of particular relevance to the studies contained in this thesis, no more details will be provided on their simulation.

4.2.5 Simulated event information

The full generation of an event yields a collection of particles, each defined by a series of parameters that characterise their physical properties. The information of a single event is stored in a computational object called "tuple", which organises the properties of each event in a table. A row within a tuple corresponds to each of the generated particles, and each column stores the relevant physical information (such as their 4-momentum, particle type [using the PDGid number, defined according to the numbering scheme provided by the Particle Data Group (PDG) [17]], particle charge, progenitor process [e.g. mother boson, Daliz decay, light meson], etc). The collection of all events that compose a sample receives the name of n-tuple.

In order to allow for compatibility between the many aforementioned frameworks, few standardised formats are used by the physics community. The LHE format [98] is one of the most common ones in the early stages of particle generation, as it simplifies interfacing e.g. `POWHEG` to `PYTHIA`. As later stages of the particle simulation add secondary particles and develop their evolution, additional particle entries may appear within the same event, leading to possible changes in format in order to facilitate their usage. These format changes may also group multiple secondary particles into single variables (such as collecting collinear photons around a main particle and adding them to its 4-momentum). Such changes lead to secondary formats, such as EVNT, xAOD [99] or DxAOD [100], which are preferred for specific uses within the ATLAS group, such as for calibration or measurement studies.

As the characteristics of simulated particles are fully known at each point of their development, these variables are often referred to as "truth". As one can choose at which point of the simulation to "measure" a truth value (e.g. a particle 4-momentum), a few definitions arise naturally in order to include or exclude certain steps of the development. The most typical ones include:

- Born: value right after particle generation, before any FSR is emitted.
- Bare: measured after FSR has been emitted, and includes exclusively the central particle.
- Dressed: similar to Bare, it is measured after FSR. However, the Dressed definition also collects all the collinear photons within a radius of the main particle, seeking to reduce the effects of Bremsstrahlung radiation in the later stages of particle development.

A schematic representation of the truth definitions is shown in Fig. 4.4, exemplified by $Z^0 \to e^+e^-$ decay as the central event.

The exact choice of a truth-level definition is heavily correlated with the kind of study performed, as it carries particle information before any detector effects are applied. This

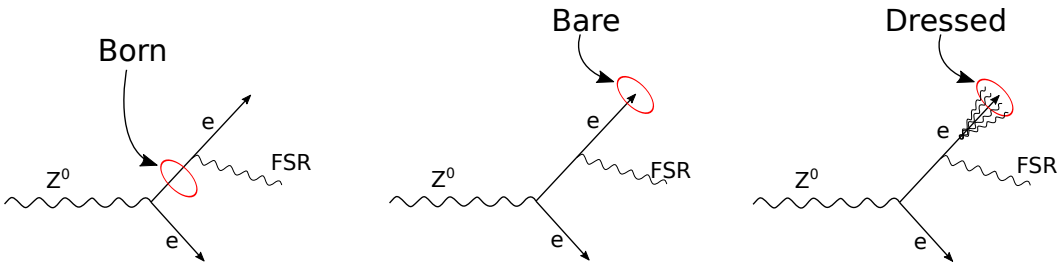

Figure 4.4: Definitions of "truth" level information, exemplified by a $Z^0 \to e^+e^-$ decay. Born: before FSR. Bare: after FSR, electron alone. Dressed: after FSR, electron + collinear photons

means that, if chosen correctly, a specific definition can be a valuable reference point when compared with real detector-degraded measurements. Section 5.3 provides a clear example of such choice, where the "Dressed" definition is used in order to perform calibration of electron resolution measurements.

4.3 Detector simulation

As all the systems integrating the ATLAS detector are specifically designed and assembled from scratch, there is an excellent understanding of the geometry and localised behaviour of the experimental setup. The modularity of each component and its prior in-depth characterisation factorise a global detector response into smaller step-wise measurements, thus converting from individual electrical signals to physical measurements with a high degree of precision.

Just as one can simulate physics models and generate MC samples in a purely computational manner, it is also possible to reproduce the response of the detector to each of these computationally created particles and to obtain a simulation of their predicted measurement. The platform `Geant4` [101] (which stands for GEometry ANd Tracking) is the tool by excellence used to simulate the interaction between particles and the detector, to such extent that every ATLAS measurement (as well as measurements recorded by all the other experiments) relies on it.

`Geant4` is used to build a virtual copy of the detector using relatively simple instructions, which are used to describe physical characteristics such as structural geometry, material description and detector response. The main characteristics which make `Geant4` attractive for the ATLAS experiment are:

- Capability of describing intricate geometrical characteristics (such as the accordion-shaped LAr calorimeter) and exact positioning of each detector, as well as defining material properties of each layer/sector of the sub-detectors.

- Ability to simulate the passage of particles through matter, whose interaction can lead to subsequent decays and eventual electromagnetic/hadronic showers within the detector. The tracking of each of those secondarily created particles is also provided by `Geant4`.
- Sequential simulation of the passage of one particle through many detectors: an electron reaching the LAr calorimeter would be affected by its passage through the inner tracker systems, thus modifying its final measurement.
- Simulation of the detector response to the interaction with each particle. Specific response behaviour is typically determined beforehand using the real experimental setup via characterisation runs, as well as by means of electronics studies and dedicated test beams.

Figure 4.5 shows an example of all of the above, depicting the complex particle shower generated on a single layer of the LAr calorimeter.

As the simulation of physical events passing through `Geant4` reproduces the measurements expected from real-life detectors, it is natural to apply the reconstruction algorithms (see Section 3.3) on top of these in order to recover the final measurement of particle characteristics (such as their identification and momentum measurement). Since the "truth" information of each particle is known, simulated measurements can be compared to the output of the reconstructed variables, which offers a way of testing and improving such algorithms. The final reconstructed value of a variable is simply called "reco", and it is analogous to the data values reconstructed in a real collision.

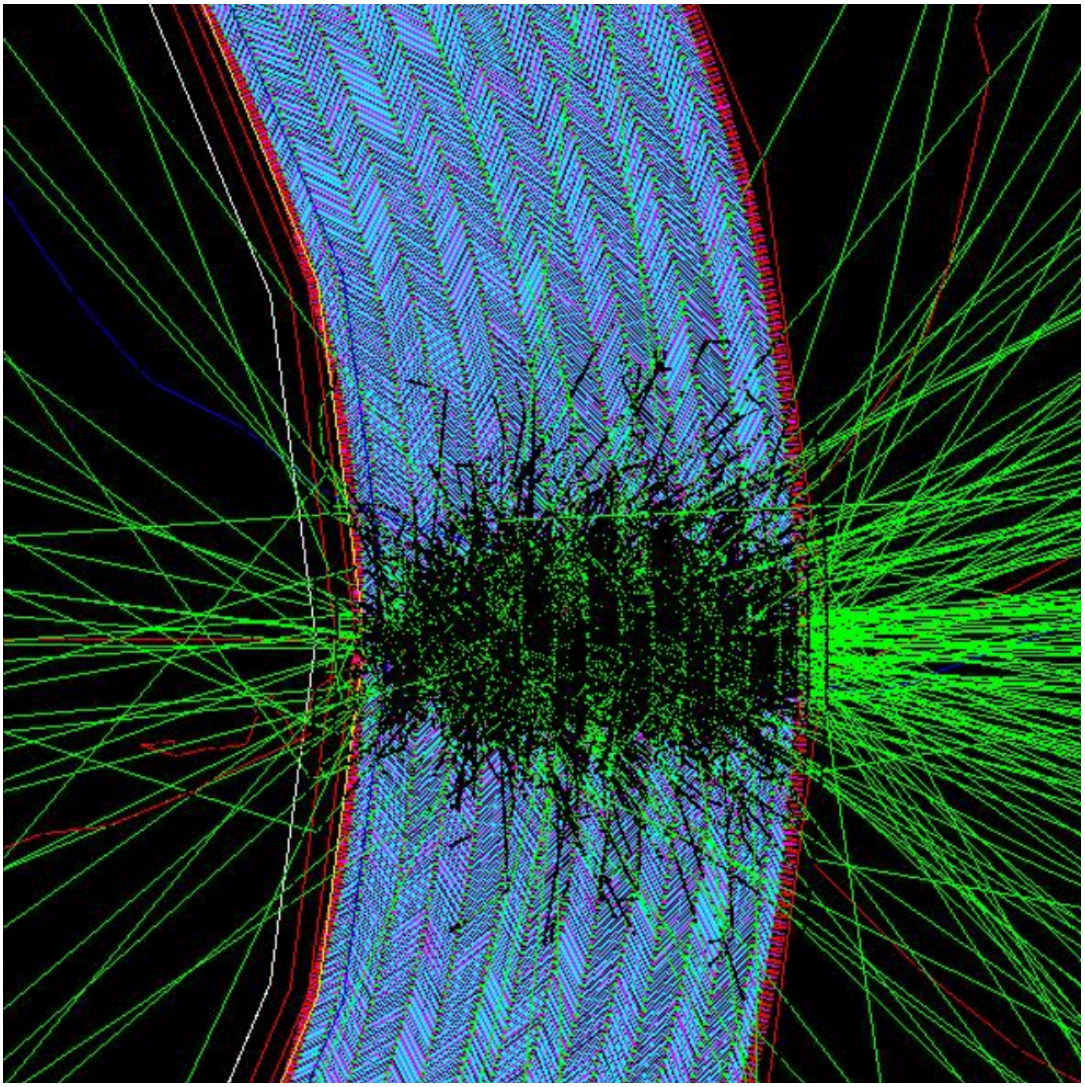

Figure 4.5: Example of `Geant4` simulation of the ATLAS EM calorimeter, depicting the proverbial accordion-shaped LAr sampling calorimeter and the shower development of an incident particle [102].

4.4 Compatibility between simulations and real measurements

While the theoretical modelling of particle processes and the simulation are done with as much precision as possible, small mismatches between theory and reality propagate as (occasionally not so) small disagreements between real measurements and the equivalent simulations. Such effects may be generated from specific sources such as improper description of the simulated detector (due to extremely intricate structural properties), approximations done during the characterisation studies, missing perturbative order contributions in the physical models, or changing properties of the materials (e.g. due to radiation ageing).

In ATLAS, specific treatments have been developed in order to minimise discrepancies between data and simulations. These are implemented via calibration techniques, which are defined via well-known and easy-to-reconstruct processes, and may be applied to either the data or MC samples. Typical examples of these calibration procedures are the use of energy scales (generally applied on data measurements, accounting for missing linearly proportional contributions on the energy reconstruction), resolution corrections on the reconstructed MC (due to possible mismodelling of the detector response) or reweighting of the MC sample to bring badly modelled quantities (such as p_{T}^{Z}) closer to the measured values. Chapter 5 explains in detail the calibration processes used for electrons and photons in the EM calorimeter, focusing later on a novel approach for MC electron energy resolution corrections.

5 Calibration of the LAr Electromagnetic Calorimeter

The Liquid Argon Electromagnetic Calorimeter (LAr EMCAL, or simply EMCAL) [65] is in charge of the precise measurement and reconstruction of photons and electrons produced by LHC collisions, as well as partially measuring jet energies and aid in particle identification.

The design of the EMCAL, born from an original idea by D. Fournier [66], derived into a sampling calorimeter which consists of alternating layers of lead (passive absorber) and liquid argon (active medium) installed in an accordion-like array (see Section 3.2.3 for general details). The particular design of the EMCAL is key to recovering energy measurements with an excellent resolution, although its complexity imposes unique challenges in the measurement and calibration process.

The following sections describe the general measuring process in the EMCAL, starting from the interaction of particles with the calorimeter and following the signal development to a digital measurement, followed by the calibration procedure defined for the LAr EMCAL. The current chapter concludes with the study and application of a novel resolution calibration technique (based on a conceptual idea proposed by the USTC group [103]), which was developed from scratch as part of the work done in this thesis, leading to the release of a detailed internal note [1] describing the calibration study (page 113) and an ATLAS PubNote [2] which proposes a technique to treat χ^2 discontinuities (page 167).

5.1 LAr EMCAL operation

Calorimetry in the ATLAS EMCAL exploits the well-understood electromagnetic interaction between the passive material of the detector (lead layers) and the arriving electrons and photons. Globally speaking, such interaction can happen in a few ways:

- Interaction with atomic electrons: Ionisation or excitation (photons are emitted upon recombination and de-excitation);
- Interaction with atomic nucleus: Compton scattering and bremsstrahlung (both of which emit additional photons), and in the specific case of incident photons,

interaction with a nucleus may lead to electron-pair production;

- Transition radiation
- Cherenkov radiation

The first two happen in a punctual manner (interaction with a specific atom), while the latter are collective effects.

Generally speaking, interaction with the material can (and will) develop into sequential interactions of the above-mentioned ones, leading to what is known as "particle showers". For the following, it is useful to notice that, in the range of energies that are interesting for us, the primary source of energy loss for electrons is due to bremsstrahlung radiation, while in the case of photons, it is due to pair production.

The exact phenomenology behind an electromagnetic shower is dependent on the distribution of the material and the arriving particle, which leads to different shower compositions, shapes and sizes. As the passage of an electron with matter leads to energy losses, a way to characterise the interaction is obtained via the "radiation length" X_0, defined as the longitudinal shower length needed for an electron to be reduced to $1/e$ (where $e = 2.718\ldots$) $\sim 37\%$. Consequently, one can measure the energy loss E as a function of the penetration length X with

$$\frac{\mathrm{d}E}{\mathrm{d}X} = -\frac{E}{X_0}. \tag{5.1}$$

Figure 5.1 offers a schematic representation of the development followed by an incident electron, which at each radiation length leads to the emission of multiple photons and electrons with smaller energies. In the case of photons, the mean free path is about $\frac{9}{7}X_0$, having a $1-1/e$ probability of converting into a pair of electrons and $1/e$ probability of not converting. The materials of the LAr EMCAL (lead and liquid argon) have respectively a value X_0 of 0.56 cm and 14.2 cm, providing enough overall stopping power to absorb electrons and photons fully.

As it has been mentioned, the LAr EMCAL is composed of alternating layers of lead and liquid argon. The lead layers receive the name of "passive" material, as its only purpose is to induce showers from the incoming particles. In the particular case of electromagnetic showers, these result in an ensemble of electrons and photons that carry a fraction of the initial total particle energy, making it of interest to measure all of them in order to reconstruct the energy of the incident particle. Such measurement can be done thanks to the liquid argon layer, which plays the role of "active" material.

As low-energy electrons and photons travel through the liquid argon medium, part of their energy gets transferred to the atomic electrons, inducing the ionisation of argon atoms (the ionisation potential in argon being equal to 15.8 eV), ultimately generating a number of electron-ion pairs that is proportional to the transferred energy. The slow electrons created by ionisation are then attracted across the 2 mm thick layer of liquid

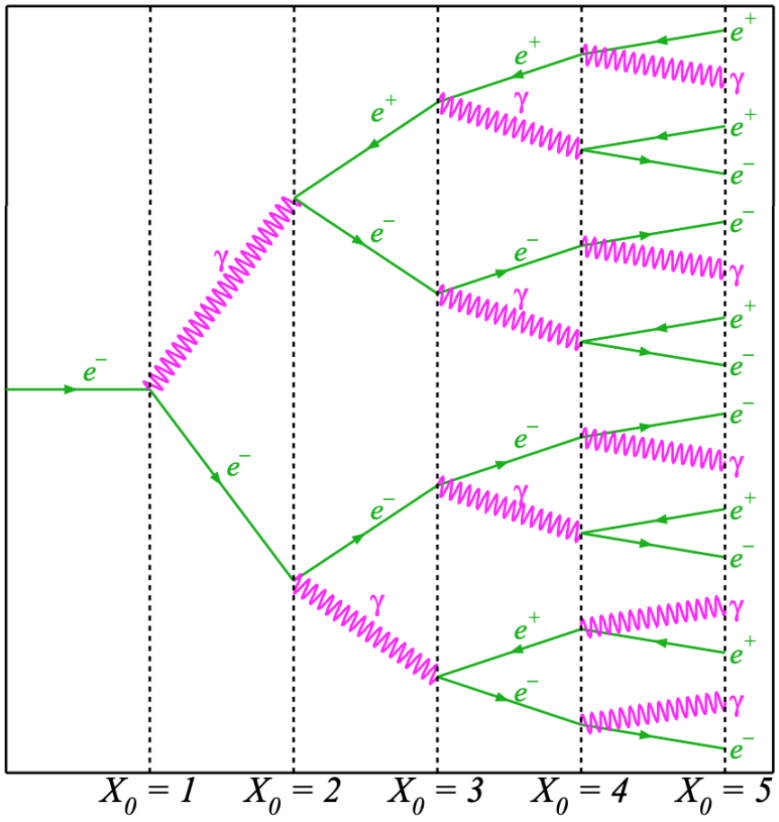

Figure 5.1: Schematic and very approximate representation of the development of the electromagnetic shower generated by an electron (moving from left to right) in a material with radiation length equal to X_0 [104].

argon towards a copper electrode, which lives along the middle plane of the liquid argon layer, and this is also responsible for their collection (see Fig. 5.2). In order to implement such collection, an electric field is generated between the walls separating the lead and argon layers (grounded) and the central copper electrode (positive potential) in such a way that the field lines are orthogonal to the electrodes (thus describing parallel field lines) all along the accordion (which is less true at each bending point due to charge inhomogeneities). The full collection of ionisation electrons by the copper electrode gives a measure of the number of electrons released in a specific layer, leading to a measurement of the transferred energy

Electrons (and photons) derived from a shower travel at relativistic speeds, so their passage through the liquid argon layer can be considered instantaneous. This implies that, for practical purposes, all the ionisation electrons are separated from their progenitor atoms all at once. Due to homogeneity within the liquid argon layer, one can assume that the electrons are generated (via ionisation) uniformly along all the layers. In addition, the ionised electrons have a small range and, before drifting, stay very close form their

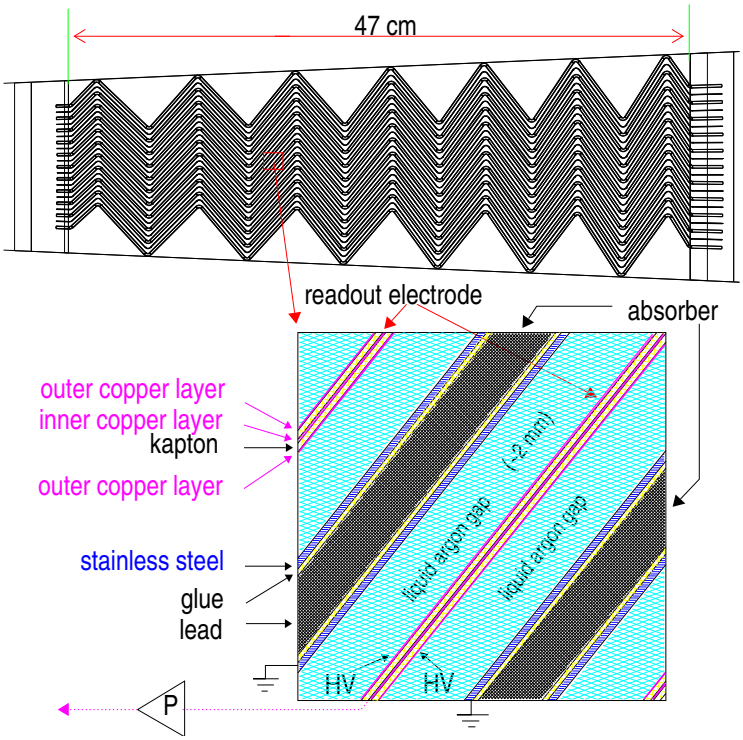

Figure 5.2: Accordion structure of the EMCAL barrel, showing details of the alternating layers of absorber (lead, displayed as black hatching) and active material (liquid argon, blue hatching), as well as showing the copper readout electrodes and the corresponding electric potentials [105].

progenitor.

Since the electric field $\vec{E}$ between the copper electrode and the lead layer is uniform, all ionisation electrons will drift towards the electrode with a constant rate given by the electric field $\vec{E}$ (see Fig. 5.3, left), travelling up to 2 mm before reaching it. As drifting electrons will reach the electrode at different times, the collection of all the ionisation electrons (generated by all of the electromagnetic shower sub-products) induces a current in the electrode that develops over time, leading to a triangular signal (see Fig. 5.3, right) that is proportional to the number of collected electrons. The signal is shaped (derived and integrated) so that the peak current is sensitive primarily to the initial current to reduce time pile-up effects. The digitisation of the shaping occurs every 25 nanoseconds via Analog-to-Digital Converter (ADC) converters, allowing its reconstruction via the combination of several (currently 4) samples through Optimal Filtering Coefficients (OFCs). The digitised pulse measurement is later translated into an energy measurement according to a model estimated during the detector characterisation stage [106, 107, 108].

Conversely, due to having the opposite charge, argon ions drift in the opposite direction with a much smaller drift velocity ($\mathcal{O}(10^{-3})$ of that of electrons), and one can safely neglect

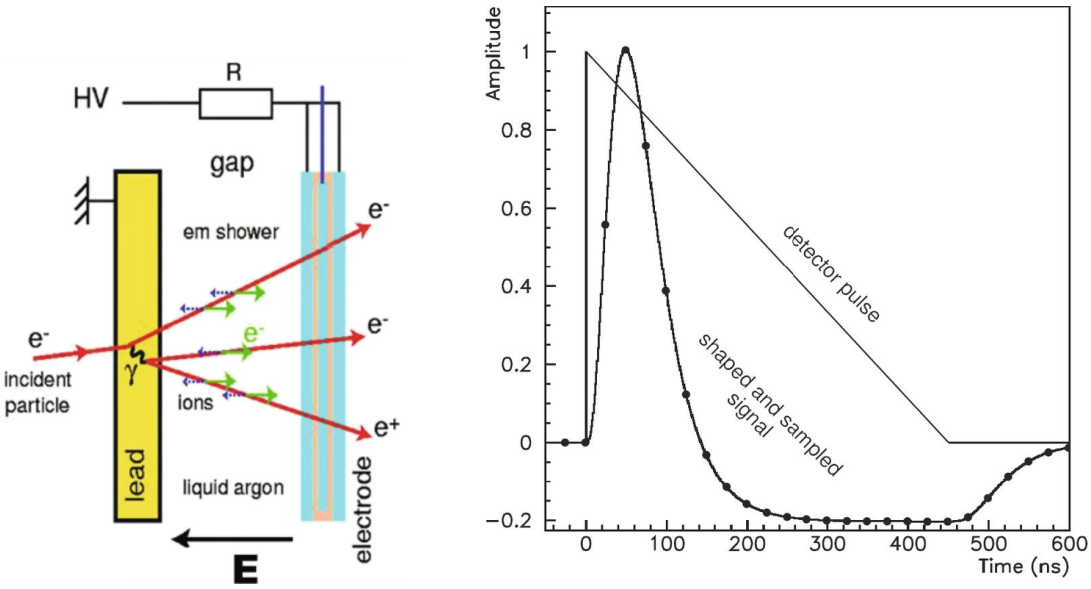

Figure 5.3: Left: Ionisation electron drift within a liquid argon layer. Right: Detector pulse shape generated by the collected ionisation electrons [109].

their signals. Upon reaching the grounded walls of the lead layer, ions will recombine by recovering a missing electron, and the resulting neutral atoms will later re-distribute themselves along the liquid argon layer due to thermostatic equilibrium.

The collection of signals across ensembles of cells via the topo-cluster formalism (Section 3.3.2) is used to recover a global measurement of the total energy deposited by an electron or photon into a specific layer of the LAr detector, as well as providing a rough measurement of its η and ϕ coordinates (Section 3.2.1).

5.2 Overview of the ATLAS electromagnetic calorimeter calibration

While the procedure described above can retrieve precise energy measurements of electrons and photons (henceforth referred to as e/γ), a handful of approximations are made along the way to optimise the reconstruction sequence. These approximations, along with the presence of locally inhomogeneous detector responses and systematic uncertainties propagated from measurements (and their handling), may lead to slight deviations from the "truth" energy of the interacting electron or photon. Moreover, the simulation of the geometry and response of the detector is also tarnished by imperfect modelling of every single aspect of the LAr EMCAL. Overall, all of the previous propagates as mismatches between the observed data and the simulated measurements, which call for additional calibration (on both sides) seeking to remove the remaining discrepancies, leading ultimately

to data and MC samples that are fully compatible across themselves.

In the context of this calibration, the MC samples were generated using the `POWHEG` event generator using the CT10 PDF, interfaced to `PYTHIA8` with the `AZNLO` tune for parton showering. The resulting `POWHEG+PYTHIA8` samples are subsequently interfaced to `PHOTOS++` to simulate the effect of final state QED radiation. A priori, this event generation chain accounts for all the physics phenomena relevant for Z production, leading to samples that differ from real measurements only due to calorimeter simulation effects.

The calibration of the ATLAS electromagnetic calorimeter is based on the sequential application of corrections on data and MC. Such corrections may be fixed (as in the case of uniformity corrections) or require parameter tuning before their application (as is needed for resolution corrections). Figure 5.4 depicts the various steps in the calibration chain. As a general rule, calibration techniques are tuned and validated using relatively simple events that can be fully reconstructed. In the case of the ATLAS EMCAL, tuning is done via $Z \to ee$ samples, while their validation is evaluated on $J/\Psi \to ee$ and $Z \to ee\gamma$ samples. The calibration was done in Run-1 [110] and in Run-2 [111] with the sliding window algorithm (see Section 3.3.2) and then slightly updated for Run-2 [112] with the use of topo-clusters.

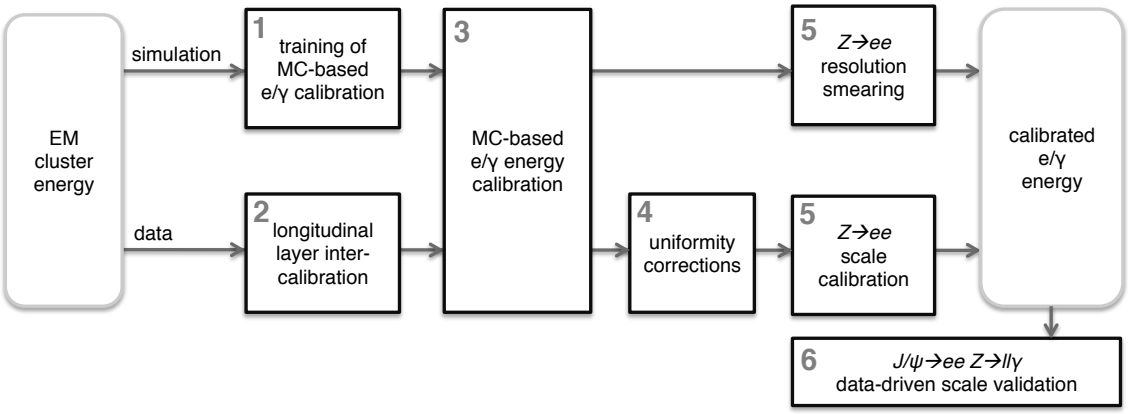

Figure 5.4: Calibration chain for electrons and photons in the ATLAS electromagnetic calorimeter [110].

Due to further developments, the latest calibration chain [113] has major improvements from what is shown in Fig. 5.4 [110]: it is now provided with additional calibration steps which seek to account for higher order effects, such as the implementation of photon leakage corrections, while the measured residual non-linearities of the electron energy scaled are used to constrain systematic uncertainties [112, 114]. However, as the study done for this thesis and described in Section 5.3 is implemented on the calibration chain of Fig. 5.4, the following descriptions will be done around this one.

5.2.1 Reconstruction of calorimeter pulses

The conversion between the current registered in a calorimeter cell and the deposited energy responsible for generating such a signal is performed with

$$E_{\text{cell}} = F_{\mu A \to \text{MeV}}\ F_{\text{DAC}\to\mu A}\ \frac{1}{\frac{M_{\text{phys}}}{M_{\text{cal}}}}\ G\ \sum^{\text{samples}}\ a_j(s_j - p), \tag{5.2}$$

where

- s_j are the measured digital samples (in ADC counts)
- p is the electronic pedestal (measured in specific calibration runs);
- G is the gain of the cell (expressed in ADC $\to$ DAC);
- $F_{\mu A\to\text{MeV}}$ is the conversion factor between the ionisation current and the total energy deposited in MeV (measured with test beams);
- $F_{\text{DAC}\to\mu A}$ converts between the digital signal sent to the calibration card and its analogical output current, leading samples s_j back to the original current (known from the calibration cards construction);
- the factor $\left(\frac{M_{\text{phys}}}{M_{\text{cal}}}\right)^{-1}$ corrects the gain to take into account that physics signal is triangular while the calibration signal is exponential (estimated from delayed calibration runs);
- and a_j are OFCs coefficients, which allow the shape of the measured signal to be determined (with respect to the expected shape of the signal).

Out of these constants,

- $F_{\mu A\to\text{MeV}}$ takes a single value in the presampler, two values in the barrel (for $\eta < 0.8$ and $\eta > 0.8$), and in the endcap it varies as a function of η (but not ϕ) due to gap variations and different high voltage regions;
- $F_{\text{DAC}\to\mu A}$ changes as a function of the layer but remains constant in large η regions;
- p, a_j, G and $\frac{M_{\text{phys}}}{M_{\text{cal}}}$ are specific to each cell.

The reconstructed values of E_{cell} are used to build the objects which define the beginning of the calibration chain.

5.2.2 MVA calibration

The first steps of the calibration are dedicated to recovering the energy losses generated outside of the EMCAL due to upstream material, leakage towards the outside of the cluster, longitudinal downstream leakage, and accidental exclusion of LAr cells during the topo-cluster definition. Such effects are taken into consideration through the use of multivariate analysis (MVA) techniques, which rely on Boosted Decision Trees (BDT) in order to perform the corresponding calibration from reconstructed to truth energy [115]. In a nutshell, multiple BDTs are trained to MC using single-particle no-pile-up samples in regions of particle $|\eta|$ and E_{T}, seeking to optimise specifically electrons, as well as converted and unconverted photons.

The MVA takes several inputs for the training, such as η region of the cluster, total energy deposited along the presampler and 3 LAr layers, and the ratio of energy measured by the 1st and 2nd layer (namely, E_1/E_2). Additional variables are included for converted photons, such as conversion radius and tracks.

5.2.3 Longitudinal layer inter-calibration

The total energy measurement requires a good relative calibration of the deposited energy in the different layers of the calorimeter in order to recover accurate measurements of the longitudinally developed shower. As the MVA calibration relies on the information on the shower development, it is of interest to keep a compatible layer response between data and MC, leading to calibration of the presampler and inter-layer calibration of layers 1 and 2. Ultimately, this calibration technique can reduce residual effects due to mismodelling of the upstream material, misalignment effects, cross-talk, and electronics miscalibration.

The presampler measures, primarily, signs of early shower development induced by the material of the inner detector, before reaching the lead layers. Its calibration relies on electrons generated from Z and W bosons (in Ref. [113], it relies on muons) and is quantified by the energy scale factor α_{PS}. It is defined in bins of η by

$$\alpha_{\mathrm{PS}} = \frac{E_0^{\mathrm{data}}}{E_0^{\mathrm{MC}}}, \tag{5.3}$$

where E_0 simply makes reference to the mean energy measured by the PS.

The relative response between layers 1 and 2 is adjusted via the inter-layer calibration factor $\alpha_{1/2}$. It is derived with $Z \to \mu\mu$ samples (in Ref. [113], it also uses $Z \to ee$ samples), via

$$\alpha_{1/2} = \frac{E_1^{\mathrm{data}}/E_2^{\mathrm{data}}}{E_1^{\mathrm{MC}}/E_2^{\mathrm{MC}}}. \tag{5.4}$$

Muons are used for the estimation of the factor $\alpha_{1/2}$ due to their minimally ionizing nature, which means that these are almost unaffected by the upstream material, giving localised information on the relative inter-layer responses.

5.2.4 Uniformity corrections

The signals collected by the readout electrodes are digitised via a 12 bits ADC, which is then amplified and shaped by the front-end using one of 3 linear electronic gains: High, Medium and Low Gain (HG, MG and LG, respectively), where the ratios of the three gains are 93/9/1. Overall, this leads to thousands of amplifiers, each with slightly different responses, which leads to a non-homogeneous response. This is corrected via a scale factor α_{G}, which is mapped over all the detector in $\eta \times \phi$ coordinates.

5.2.5 Resolution smearing and scale calibration

Also referred to as "in-situ calibration", this step is intended to calibrate all the residual energy response differences using the $Z \to ee$ invariant mass peak as reference. These corrections are applied to data and MC by means of an energy scale correction α and a resolution constant term c (respectively), which are tuned as a function of pseudo-rapidity η bins [114, 116, 117, 118].

Let us imagine a single detected particle with energy E^{data} and its corresponding simulation E^{MC}, which is measured at cluster pseudo-rapidity η. The small discrepancy between both of these energies can be quantified by the corresponding energy scale correction $\alpha(\eta)$ by means of

$$E^{\mathrm{data}} = E^{\mathrm{MC}}(1 + \alpha(\eta)), \tag{5.5}$$

where the term $(1+\alpha(\eta)$ corresponds to the energy scale factor. Assuming that the energy scale on the simulation is exactly 0, the correction $\alpha(\eta)$ acts on the data-measured energy values.

Considering now the discrepancy between the measured relative energy resolution and the corresponding prediction, the constant term c is applied as an additional random smear following a normal distribution $\mathcal{N}(0,1)$. This acts as

$$\left(\frac{\sigma(E)}{E}\right)^{\mathrm{data}} = \left(\frac{\sigma(E)}{E}\right)^{\mathrm{MC}} \oplus\ c(\eta), \tag{5.6}$$

which leads to

$$E^{\mathrm{data}} = E^{\mathrm{MC}}(1 + c(\eta) \times \mathcal{N}(0,1)). \tag{5.7}$$

The parameters $\alpha(\eta)$ and $c(\eta)$ are fitted by looking at the $Z \to ee$ invariant mass distribution. Let us remember that, for a pair of ultra-relativistic electrons with energies E_1 and E_2 propagating with an angle θ_{12} between them, their invariant dilepton mass is given by

$$m_{ee} = \sqrt{2E_1E_2(1 - \cos\theta_{12})}. \tag{5.8}$$

This means that the in-situ calibration propagates via

$$m_{ee}^{\mathrm{data}} = m_{ee}^{\mathrm{MC}}\sqrt{(1 + \alpha(\eta_1))(1 + \alpha(\eta_1))(1 + c(\eta) \times \mathcal{N}_1)(1 + c(\eta) \times \mathcal{N}_2)}. \tag{5.9}$$

The numerical values of $\alpha(\eta)$ and $c(\eta)$ are fitted by looking at templates of $Z \to ee$ invariant mass distributions (such as the one displayed in Fig. 5.6), where difference between the lineshape is minimised via χ^2 techniques [119]. Figure 5.5 shows an example of their fitted values as a function of η, following the results of a partial Run-2 study [111]. One should note that background sources (such as $Z \to \tau\tau$ and $t\bar{t}$) are not included, as their impact is negligible [120, 121, 122].

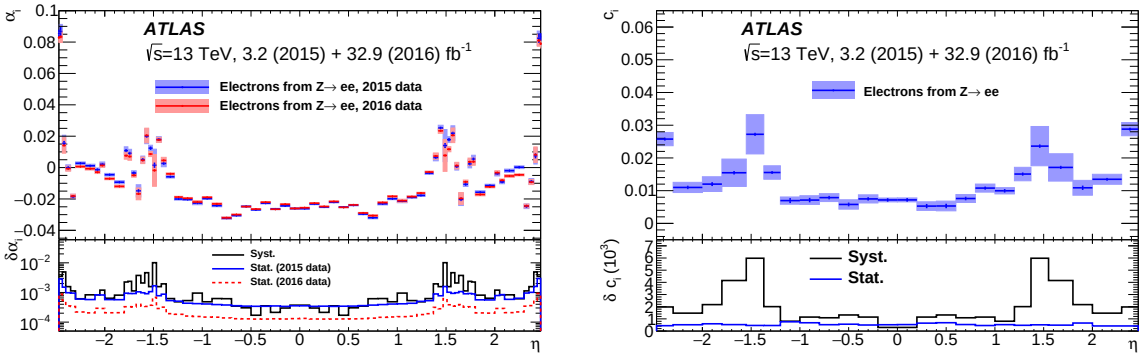

Figure 5.5: Fitted values of $\alpha(\eta)$ and $c(\eta)$ using 2015 and 2016 data [111].

Once their value has been fitted, the energy scales α are applied to data measurements (via $E^{\text{data}}/(1+\alpha)$), while the constant term c is left to act on MC alone.

5.2.6 Final data to simulation agreement

The final effect of the EMCAL calibration chain described above can be evaluated by looking at a dilepton mass lineshape such as the one shown in Fig. 5.6 where there is good data to MC agreement, especially around the mass peak. Nevertheless, there are several remaining discrepancies in the low and high mass tails of the lineshape, accounting for up to $\sim 5\%$ of disagreement between samples.

The starting point of the study described in the following sections is precisely at the last step of the official calibration chain. It seeks to account for the final lineshape discrepancies by exploring an alternative technique, which is based on detailed electron energy resolution corrections. Such an approach shows an advantage with respect to the current method, which involves the constant term c, because it is not restricted to the Gaussian assumption, and instead, it can control specific features of the MC resolution distributions. All the studies described through the rest of this chapter are derived from the work done for this thesis, which is also documented in an ATLAS technical note [1] and led to the release of an ATLAS PubNote [2]. Both of these notes can be found attached at the very end of this chapter, starting respectively at pages 113 and 167.

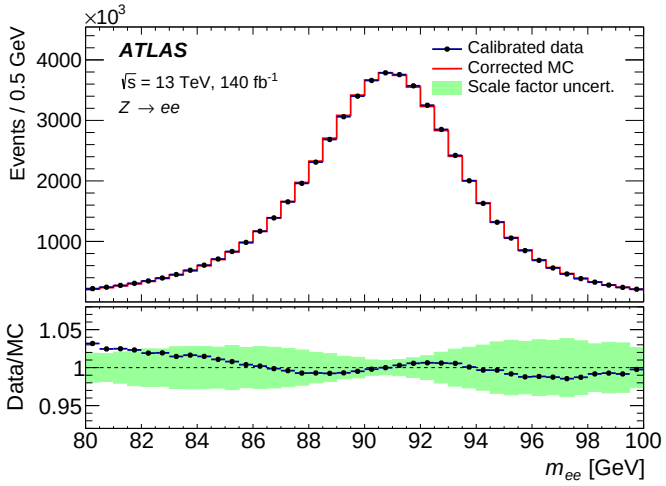

Figure 5.6: $Z \to ee$ invariant mass lineshape for data and MC after the calibration and resolution corrections described in Fig. 5.4. The ratio plot of data/MC distributions shows the remaining discrepancy between samples [123].

5.3 Energy resolution corrections, a.k.a. the Δ′ method

Aiming to further understand and try to account for the remaining discrepancy between the data and MC lineshapes of Fig. 5.6, alternative calibration techniques are being explored. While these new methods are not necessarily founded on specific physical phenomena, their motivation is rooted in exploring the extent of the contribution that a single source of miscalibration could have on the global agreement. The method described ahead was initially proposed by the USTC group [103], and it relies on scalings of the MC electron energy resolution (mainly via a polynomial function). Contrary to the technique described in Section 5.2.5, which works under the assumption that the MC resolution is "narrower" than that of data, the method described in this section is free of that notion. The USTC group motivated this method in order to make viable a $\sin^2\theta_{\mathrm{W}}$ measurement using 13 TeV ATLAS data [124] collected in the forward region, allowing to reduce the uncertainty [125] but requiring an improved calibration of the forward calorimeter. Eventually, this calibration technique was extended by the USTC group to the central calorimeters [126].

Let us consider a couple of samples, data and MC, corresponding to $Z \to ee$ events. For a given simulated electron, let us define the quantity

$$\Delta = E_{\mathrm{reco}} - E_{\mathrm{truth}}, \tag{5.10}$$

where E_{reco} corresponds to the calibrated reconstructed energy (i.e. the output value after the calibration chain), and E_{truth} is the truth level energy at Dressed level (i.e. after FSR, but including collinear photons, see Fig. 4.4). As the variable Δ measures the shift in the measured energy with respect to the true value, it works as a representation of the resolution for that particular measurement. Then, one can define a corrected resolution

Δ' as a scaling that depends on the initial value of Δ according to a set of parameters $\vec{p} = \{p_0, ..., p_{m-1}\}$ through a given functional form f, namely

$$\Delta' = f(\Delta; \vec{p}), \tag{5.11}$$

which gets reflected as a new electron energy

$$E'_{\text{reco}} = E_{\text{truth}} + \Delta'. \tag{5.12}$$

Let us momentarily consider a scenario where all electrons have the same E_{truth} value. By gathering all the values of Δ, one can build a Gaussian-like distribution which would correspond to the effect of the resolution on E_{truth}: the standard deviation of the distribution would be compatible with the value predicted by Eq. (3.7). As Δ' acts on Δ, the function $f(\Delta; \vec{p})$ is, in fact, acting on the resolution distribution as a shape modifier. That is, by wisely choosing the functional form of f, one can manipulate specific shape features of the distribution such as its width, tail asymmetry, skewness, etc.

Resolution corrections have a direct impact on the invariant dilepton mass of an electron-pair, which after corrections looks like

$$\begin{aligned} m'_{ee} &= \sqrt{2E'_{\text{reco},1}E'_{\text{reco},2}(1 - \cos\theta_{12})} \\ &= \sqrt{2(E_{\text{truth},1} + \Delta'_1)(E_{\text{truth},2} + \Delta'_2)(1 - \cos\theta_{12})}. \end{aligned} \tag{5.13}$$

By intelligently modifying the shape of the resolution distribution, one can aim to finely modify the MC dilepton mass distribution by targeting specific features that would lead to a better agreement against data. Looking at Fig. 5.6, one could focus on e.g. improving the MC tails (i.e. low and high-mass regions) by leaving the centre of the resolution distribution unchanged but give/take away far resolution tails with a function such as $f(\Delta) = \Delta + p\Delta^5$.

The complexity of the function $f(\Delta; \vec{p})$ can be chosen as desired in order to take into account very intricate resolution effects, bearing in mind that an increasing number m of free parameters p_i can lead to strong correlations among them and generate minimisation problems when simultaneously fitting their values. One may also optimise the effect of such resolution corrections by adding further dependencies in the functional form of f, such as explicit dependency on the electron pseudo-rapidity η or transverse energy E^{T} (leading to e.g. $\Delta' = f(\Delta, \eta, E^{\text{T}}; \vec{p})$), or by fitting the best parameters $\hat{\vec{p}}$ in bins of these quantities.

As the final goal of the Δ' technique is to mitigate the remaining dilepton mass disagreement of Fig. 5.6, a natural approach for the fit of the parameters $\vec{p}$ is by comparing the shape of the data mass distribution (which is a constant under the current approach) with the corresponding prediction after the application of the Δ' resolution corrections (which shall be called $\text{MC}'(\vec{p})$) using a χ^2 estimator. In other words, the best values of the parameters $\vec{p}$ (namely, $\hat{\vec{p}}$) will be those which minimise $\chi^2(\text{data}, \text{MC}'(\vec{p})) = \chi^2(\vec{p})$.

Once the optimal functional form f and corresponding parameters $\hat{\vec{p}}$ have been determined, a methodical study of the changes induced to the resolution distribution at different values of E_{truth} could assist in tracking down the origin of the disagreement (provided that it is indeed completely generated by mismodelling of the energy resolution), which can be performed via studies of the resolution behaviour predicted by Eq. (3.7), or exploring specific sub-optimal considerations implemented through the simulation process.

5.4 Minimisation methodology

The natural approach to compare the shape of the data and MC′ histograms via a χ^2 estimator would be through a modified version of Eq. (2.18) that includes the statistical uncertainty of both samples, which for an n bin histogram would read as

$$\chi^2(\vec{p}) = \sum_{i=1}^{n} \frac{(\text{data}_i - \text{MC}'(\vec{p})_i)^2}{[\delta(\text{data}_i)]^2 + [\delta(\text{MC}'(\vec{p})_i)]^2} \tag{5.14}$$

for a bin uncertainty δ in either of the histograms. Equation (5.14) will simply be referred to as "bin-to-bin" χ^2. Let us also remember the effect of the Δ' correction on the dilepton mass m'_{ee}, described by Eq. (5.13). By testing different parameters $\vec{p}$, the value m'_{ee} of a given electron-pair will change according to Δ'_1 and Δ'_2, which means that such dilepton masses can (and will) enter different bins in the corresponding histogram. By looking at a specific mass bin (which has some width), changes of $\vec{p}$ of different magnitudes mean that some events will remain in the same bin, while others will leave from its range and others will enter it. Such bin migration occurs in a discrete manner, which leads to a discontinuously changing $\text{MC}'(\vec{p})_i$ and $\delta(\text{MC}'(\vec{p})_i)$, and ultimately reflects as a discontinuous χ^2 curve [2]. Consequently, while Eq. (5.14) is good for comparing the general agreement between samples, it is not the optimal estimator for the fit of $\vec{p}$.

At the time of developing this study, there were no techniques that would make feasible the efficient and accurate minimisation of such a discontinuous curve. This led, as a byproduct of the Δ' study, to the development of a new technique capable of retrieving a continuous χ^2 curve that can be minimised by means of numerical methods such as `MINUIT`. Such a technique consists of the χ^2-like comparison of the data histogram and a fit of the MC′, which is used to smoothen the effect of MC′ bin content changes while providing minimal shape bias to the original MC′ histogram. This method was later accepted by the ATLAS Statistics Group and led to the publication of an ATLAS PubNote [2] on behalf of the collaboration. The note is provided at the end of this chapter, on page 167. A thorough description of the implementation of such a technique as an estimator for the fit of the parameters of Δ' is given in the corresponding ATLAS Internal Note [1].

5.5 Approach to the parameter optimisation

Following from the working point described in the previous sections, the ultimate target of the Δ' method is to improve the agreement between the data and MC dilepton mass lineshapes, which is evaluated via a χ^2 estimator between their histogrammed distributions. Below there is a summary describing specific details of the intended approach:

- The dilepton mass distributions are created at "reco" level using histograms in the $m_{ee} \in [80, 100]$ GeV range, which are made out of 100 equal-sized bins of width 0.2 GeV.

- We seek to evaluate the effect of the energy resolution corrections exclusively on the shape of the mass distribution. Consequently, the $\mathrm{MC}'(\vec{p})$ histogrammed distribution is actively normalised to data, such that

$$\text{integral(data)} = \text{integral}(\mathrm{MC}'(\vec{p})) \quad \forall \quad \vec{p} = \{p_0, .., p_{m-1}\} \in \mathbb{R}^m.$$

- Resolution corrections are expected to change discreetly for different sectors of the calorimeter as a function of the pseudo-rapidity η_{calo}, as both their material and responses change in a non-continuous manner. Uniformity around the azimuthal angle ϕ_{calo} is expected, as well as symmetry for positive and negative values of η_{calo}. Thus, several sets of parameters $\vec{p}_\eta$ are to be fitted, one for each η_{calo}-region of the calorimeter, following the standard calorimeter segmentation into 6 regions:

$\lvert\eta_{\text{calo}}\rvert$	0.00		0.60		1.00		1.37	1.55		1.82		2.47
region	-	1		2		3	4		5		6	-
name	barrel						crack	endcap				

Table 5.1: Pseudo-rapidity (η) binning of the electromagnetic calorimeter.

This is achieved by splitting the data and MC samples into smaller sub-samples, according to the electron pseudo-rapidity measured by the calorimeter η_{calo}. However, as a single $Z \to ee$ event contains a pair of electrons (which shall treated as indistinguishable and be labelled simply electron-1 and electron-2), the splitting of the samples generates a 2-dimensional grid of events, classified according to their $\eta_{\text{calo},1} \times \eta_{\text{calo},2}$ region. Ergo, this 2-D array is symmetric with respect to the diagonal regions, i.e. $(\text{region}-1, \text{region}-2) = (\text{region}-2, \text{region}-1)$.

- The classification of events into $\eta_{\text{calo},1} \times \eta_{\text{calo},2}$ regions leads to statistically independent sub-samples, as any given event cannot belong to 2 different regions. However, the minimisation of parameters $\vec{p}_{\eta_i}$ for region i can be obtained by independently minimizing $\vec{p}$ in regions i-j and i-k, which leads to correlation across fitted parameters $\hat{\vec{p}}_{\eta_i}$.

- In order to take into account changes in electron kinematics at different η values [1], explicit dependency on $E_{\mathrm{T}}^{\mathrm{truth}}$ will be introduced in the functional form f. N.B. $E^{\mathrm{T}} = E/\cosh\eta$ represents the transverse momentum of the electron as "measured" by the calorimeter. (The transverse momentum measured by the bending in the tracker receives the name p^{T}. Similarly, the pseudo-rapidity measured by the tracker, which is much more precise than the one measured by the calorimeter, is called η_{tracker}.)

- As the Δ' correction is not physical and regions of the calorimeter are separated by the binning along η_{calo}, one could, in principle, use different functional forms for each of the η-regions. This freedom allows specific features to be modified (and eventually corrected), which could prove valuable during the optimisation procedure.

The above-described prescription leads to a total of 6 $|\eta|$-regions, where the electron energy resolution corrections are applied as a function of their pseudo-rapidity via

$$\Delta' = f_{\eta}(\Delta, E_{\mathrm{T}}^{\mathrm{truth}}; \vec{p}_{\eta}). \tag{5.15}$$

As the data and MC samples are divided into statistically independent sub-samples (which, in turn, are sensitive to the Δ' correction applied to 2 η-regions), a region-specific χ^2 is defined, which for the η-region-i,j looks as

$$\chi^2_{i,j} = \chi^2_{i,j}(\vec{p}_{\eta_i}, \vec{p}_{\eta_j}) = \chi^2\left(\mathrm{data}_{i,j}, \mathrm{MC}'_{i,j}(\vec{p}_{\eta_i}, \vec{p}_{\eta_j})\right). \tag{5.16}$$

In order to account for the correlation across different-η parameter sets, a global χ^2 estimator is defined as the addition of the individual region-wise contributions, such that

$$\chi^2_{\mathrm{global}} = \chi^2_{\mathrm{global}}(\vec{p}_{\eta_1}, ..., \vec{p}_{\eta_6}) = \sum_i \sum_j \chi^2_{i,j}, \tag{5.17}$$

which can be minimised using the approach described in Section 5.4.

5.6 Summary of the study

The capabilities of resolution corrections on the electron energy were studied using data collected in 2018, which is composed of about 2.7×10^7 events, alongside its corresponding MC simulation, which consists of 1.1×10^8 events. Both of these samples have passed through the whole calibration procedure described in Fig. 5.4 (which was documented by L. Guo [119]), and thus the starting point of this study is at the "calibrated $e\gamma$ energy" box. Figure 5.7 shows the corresponding data and MC dilepton mass lineshapes (which thenceforward shall be called "nominal"), as well as the data/MC ratio. The corresponding bin-to-bin χ^2 between both curves (see Eq.(2.18)) is also shown in Fig. 5.7, which accounts for a total of 2014.31 while the number of bins is 100.

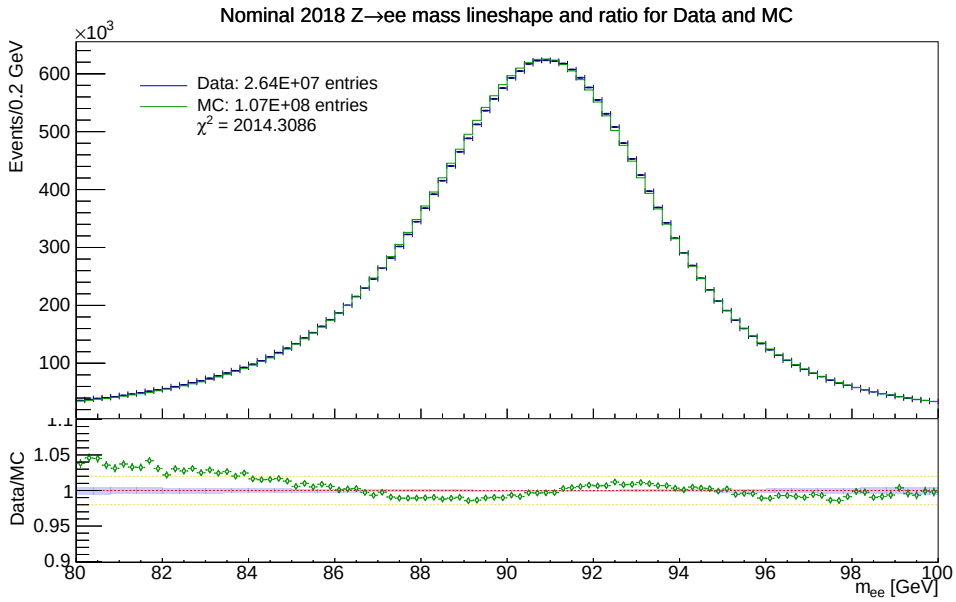

Figure 5.7: $Z \to ee$ invariant mass lineshape, including all the available samples after the energy scale correction described in Ref. [119]. The ratio plot shows the relative data bin uncertainty as a blue band around 1, while the yellow lines illustrate a discrepancy of $\pm 2\%$ with respect to the central value of data. The bin-to-bin χ^2 value between data and MC is shown, along with the size of each sample.

Following the results explained in detail in the corresponding internal note [1] (provided at the end of this chapter, starting from page 113), the best functional form of Δ' was found to be

$$\Delta' = \left[p_0 + p_3(E_{\mathrm{T}}^{\mathrm{truth}} - 45\ \mathrm{GeV})\right]\Delta + \left[p_1 + p_4(E_{\mathrm{T}}^{\mathrm{truth}} - 45\ \mathrm{GeV})\right]\Delta^2 + \begin{cases} \left[p_2 + p_5(E_{\mathrm{T}}^{\mathrm{truth}} - 45\ \mathrm{GeV})\right] & \text{if } |\eta| < 1.37 \\ \left[p_2 + p_5(E_{\mathrm{T}}^{\mathrm{truth}} - 45\ \mathrm{GeV}) + p_6(E_{\mathrm{T}}^{\mathrm{truth}} - 45\ \mathrm{GeV})^2 + p_7(E_{\mathrm{T}}^{\mathrm{truth}} - 45\ \mathrm{GeV})^3\right] & \text{if } |\eta| > 1.37 \end{cases} \tag{5.18}$$

which, after the simultaneous fit of the 6 sets of parameters $\vec{p}_\eta$, led to an improvement of the agreement between all of the data and MC samples by decreasing their χ^2 value from 2323.70 to 122.61. This suggests that, in the current context, mismodelling of the electron energy resolution could be responsible for the remaining disagreement seen between data and MC after the standard calibration chain. Figure 5.8 shows the data/MC ratio of the dilepton mass distributions before and after applying the Δ' calibration method, also depicting their bin-to-bin χ^2 values and the mean values of the mass distributions. The value of the fitted parameters $\hat{\vec{p}}_\eta$ is given in Fig. 5.9.

Specific implications of the fitted functional form of Δ', as well as its impact on the resolution distributions and breakdown of effects per η-region-i, j are detailed in the internal note [1], which is provided on page 113. The reading of the said note is strongly

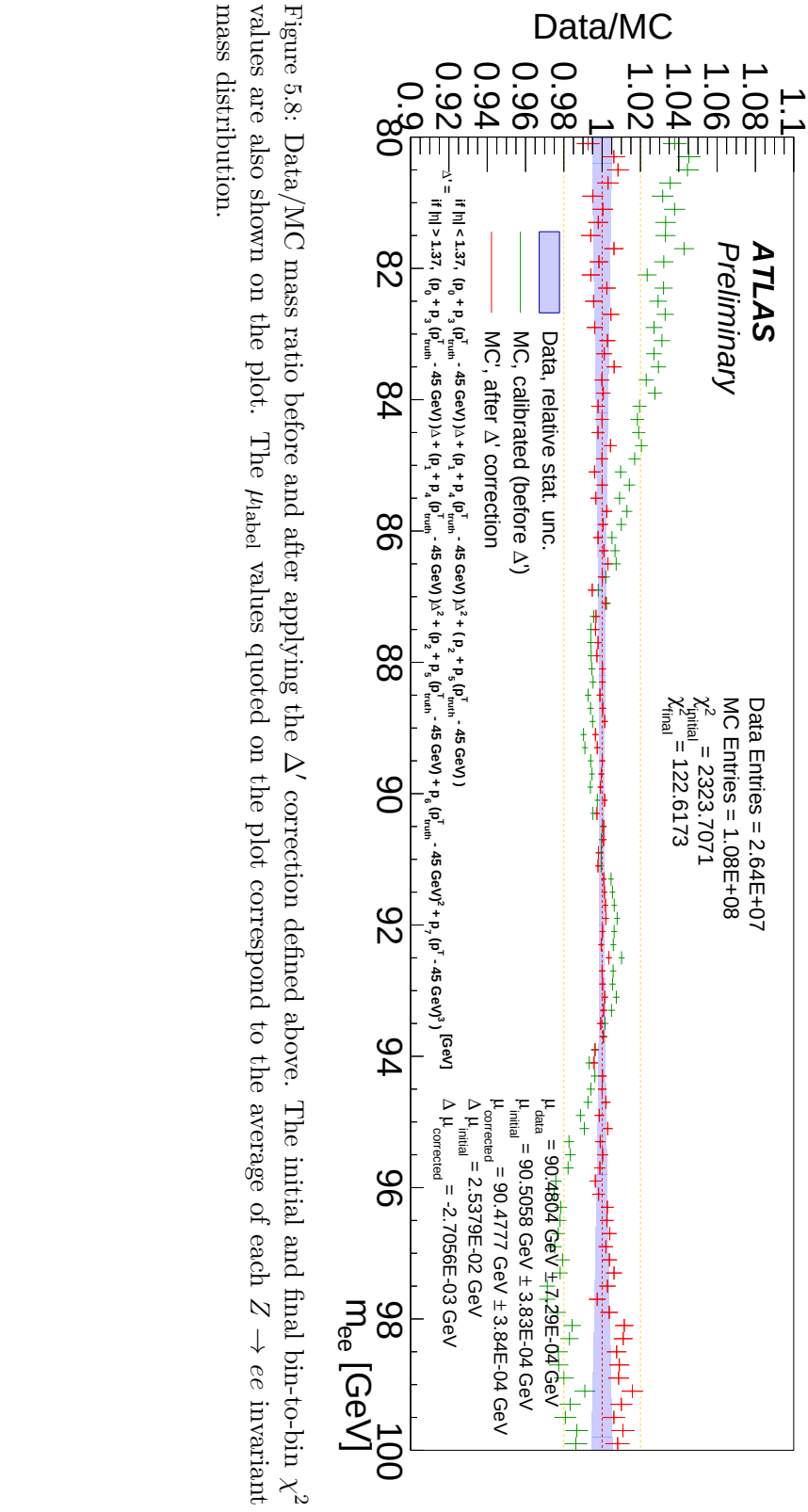

Figure 5.8: Data/MC mass ratio before and after applying the Δ' correction defined above. The initial and final bin-to-bin χ^2 values are also shown on the plot. The μ_{label} values quoted on the plot correspond to the average of each $Z \to ee$ invariant mass distribution.

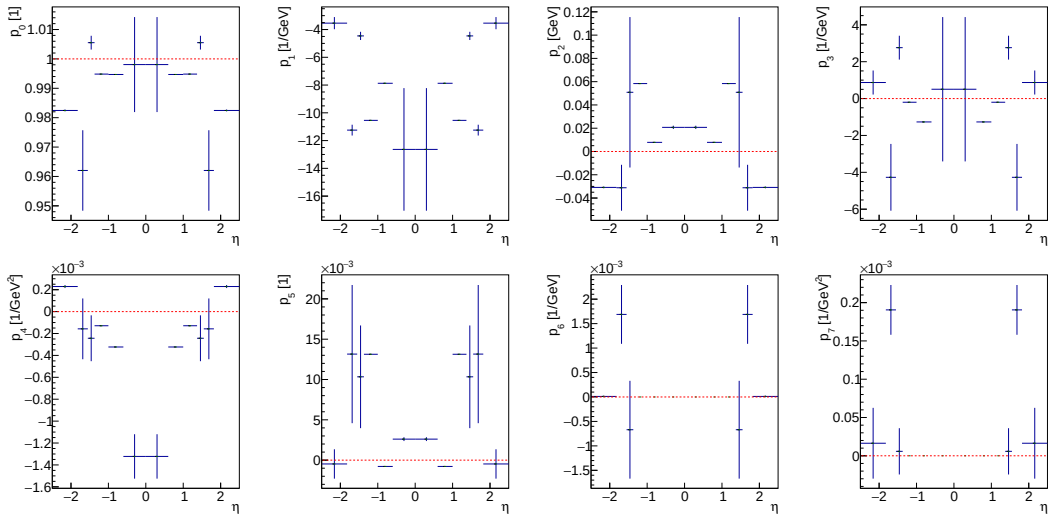

Figure 5.9: Fitted parameter values corresponding to the calibration shown in Fig. 5.8.

encouraged before proceeding to the following section.

5.7 Impact on samples of other years

As it has been described, the characterisation and fit of the chosen Δ' correction was performed using only the 2018 data and MC samples. In order to explore whether the chosen functional form and fitted parameters were generalisable (and thus, to better understand the underlying causes of the disagreement between data and its simulation), it became of interest to see their effect on the simulation of data corresponding to different years.

While physics remains exactly the same regardless of the time data was collected (at a given centre-of-mass energy), differences in collision conditions may have an important effect on the accuracy of the detector simulation. Looking back at Fig. 3.6, it quickly becomes clear that one of such differences is the distribution of collision pile-up that is induced each year, which is reflected as changes in pile-up noise. Despite keeping a constant topo-cluster threshold through all of these runs, pile-up difference could propagate to the definition of the topo-cluster used in the electron reconstruction process (see Section 3.3.2, particularly Eq. (3.9)), ultimately yielding a different measurement of the energy: a smaller pile-up noise contribution means larger cell energy significance (Eq. (3.9)), capable of measuring larger numerical values of the reconstructed energies. Moreover, additional physics differences, such as the bunch-filling scheme of the LHC, could prove to have an effect on the reconstruction.

The comparative study was undertaken by Edison Carrera Unaucho as part of an internship project [127], followed up with work by Niklas Bjorklund [128] and Aicha Kenani [129]. It consisted of the blind application of the parameters shown in Fig. 5.9 on the MC simulation of years 2015, 2016 and 2017, without re-fitting anything. Figure 5.10 summarises the results of such exercises by displaying the data/MC mass lineshape ratios, showing the bin-to-bin global χ^2 value, and the corresponding average pile-up $\langle\mu\rangle$ measured in each of the years.

The blind use of the parameters fitted on 2018 samples, shown in Fig. 5.10, seems to suggest that their implementation is generalisable, accounting for compatible energy resolution mismodelling effects across different years. Without additional tuning, the same parameter values can improve the agreement between data and MC through all of the tested years, leading to χ^2 values that are very close to the best possible permitted by such estimator. The biggest outlier of this behaviour is the year 2016, where the χ^2 improved from 1464.55 to the relatively large value of 267.23. Table 5.2 summarises the bin-to-bin χ^2 values, computed by comparing the entirety of the samples in the $m_{ee} \in [80, 100]$ GeV range with 100 uniform bins (thus, the best attainable χ^2 value should be $100 \pm \sqrt{2 \times 100} = 100 \pm 14.14$).

Figure 5.10 (as well as Fig. 5.8) also shows a better agreement between data and MC around 90 GeV after applying the parameters fitted to 2018 samples, which is in fact the

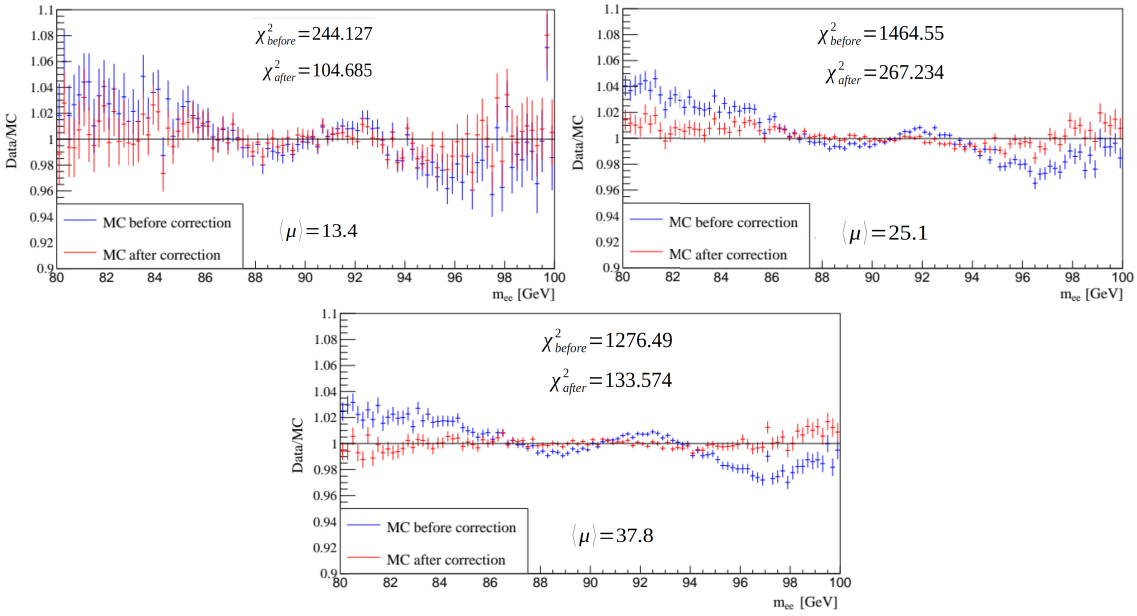

Figure 5.10: Effects of the Δ' parameters, fitted using 2018 samples, applied to 2015 (top-left), 2016 (top-right) and 2017 (bottom) samples without any intermediate treatment. The data/MC mass lineshape ratio is shown for histograms with 100 bins between 80 GeV and 100 GeV, as well as the bin-to-bin χ^2 value before (in blue) and after (in red) implementing the energy resolution corrections, and the average pile-up value $\langle\mu\rangle$ through each of the years. This particular study was developed by Edison Carrera Unaucho [127].

Sample year	$\langle\mu\rangle$	χ^2_{initial}	χ^2_{final}
2015	13.4	244.12	104.68
2016	25.1	1464.55	267.23
2017	37.4	1276.49	133.57
2018	36.1	2323.71	122.62

Table 5.2: Agreement between data and MC $Z \to ee$ samples corresponding to different years, quantified by the bin-to-bin χ^2 value between the histogrammed distributions, using 100 equal-sized bins. The mean pile-up value $\langle\mu\rangle$ for each year is also shown. The χ^2 values are labelled as "initial" and "final", corresponding respectively to the nominal samples (i.e. fully calibrated as per the calibration chain of Fig. 5.4), and the MC samples onto which the Δ' correction has been applied using the parameters fitted to the 2018 samples. These values correspond to the quantities shown in Fig. 5.10, which are a product of the work done by Edison Carrera Unaucho [127].

most sensitive region to the mass of the Z-boson. Furthermore, one sees in Fig. 5.10 that the relative improvement on the lineshape agreement of 2015, 2016 and 2017 samples is not as good as the one obtained on 2018 samples (Fig. 5.8), despite the fact the data collected in all of these runs use the same topo-cluster threshold. The difference may be a consequence of the topo-cluster construction (see Section 3.3.2), as their definition

(and consequently, their size) is slightly μ-dependent through the noise contribution shown in Eq. (3.9), making it is sensitive as well to pile-up mismodelling, which leads to a μ-dependent reconstructed energy. This pile-up dependency is illustrated for the invariant mass of Z-boson decays in Fig. 5.11, which implies that the fitted Δ' parameters cannot be pile-up independent.

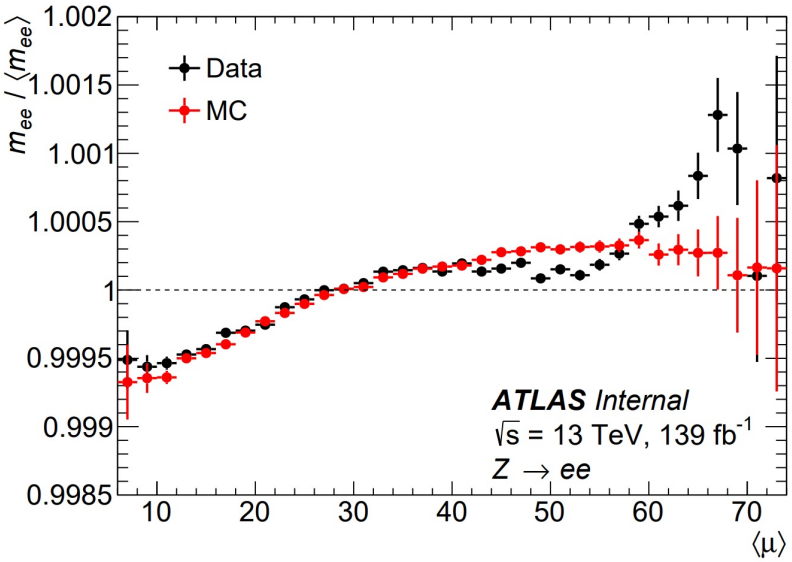

Figure 5.11: Relative variation of the peak position of the reconstructed dilepton mass distribution in $Z \rightarrow ee$ events as a function of the actual number of pile-up interaction $\langle \mu \rangle$ [113].

5.8 Impact on low pile-up samples

Seeking to test further the generalisability of the parameters fitted to 2018, Edison Carrera Unaucho [127] repeated the same exercises described in Section 5.7 on special low pile-up samples. These samples, depicted in the bottom-left corner of Fig. 3.6 at $\langle \mu \rangle \approx 2$, account for a minuscule portion of the total, and are of particular interest due to the potentially large sensitivity that these can shed on precision measurements (see, for instance, the measurement of the transverse momentum of the W-boson [130]). Low pile-up runs are especially interesting for W-boson studies, as the decreased pile-up noise allows to reliably estimate properties of the non-measurable neutrinos (such as its transverse momentum) via the missing transverse energy (see Section 3.3.5). Consequently, a natural interest is to study the impact of the Δ' correction on e.g. the measurement of the W-boson mass m_W.

Low pile-up runs use the same topo-cluster definition described in Section 3.3.2 in order to reconstruct the energies of electrons and photons. However, as the purpose of

these runs is to permit high precision measurements and to take advantage of the low pile-up induced background, the energy threshold used in the topo-cluster construction is lowered [118, 131]. This means that the measurement of an electron during a low pile-up run will include more cells than the standard high pile-up scenario, leading to overall larger reconstructed energies and slightly differently behaving energy resolutions when compared to the high pile-up equivalence.

Seeking to ultimately study the effect on the W-boson low pile-up samples, the effect of the Δ' correction was inspected on $Z \to ee$ samples at 5 TeV (2017) and 13 TeV (2017 and 2018), which comes along the samples of inclusive $W^{\pm} \to \ell\ \nu_l$ used in W-boson mass fits and cross-section determination. Due to the much smaller size of the low pile-up samples, 40 equal-sized bin histograms are used in the $m_{ee} \in [80, 100]$ GeV range. Figure 5.12 shows the effect of the parameters fitted on the high pile-up data when being applied to the low pile-up samples without additional tuning.

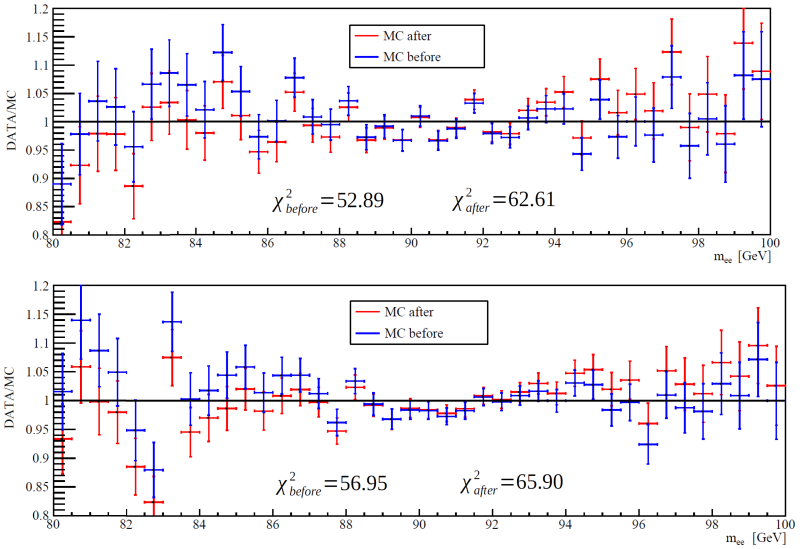

Figure 5.12: Effects of the Δ' parameters fitted using 2018 high pile-up samples ($\langle\mu\rangle \approx 36.1$) on the 2017 5 TeV (top) and 2017 13 TeV (bottom) low pile-up samples ($\langle\mu\rangle \approx 2$). The data/MC mass lineshape ratio is shown for histograms with 40 equal-sized bins between 80 GeV and 100 GeV, as well as the bin-to-bin χ^2 value before (in blue) and after (in red) implementing the energy resolution corrections, and the average pile-up value $\langle\mu\rangle$ through each of the years. This particular study was developed by Edison Carrera Unaucho [127].

Looking at the mass lineshape before and after the implementation of the Δ' correction and the χ^2 values shown in Fig. 5.12, it becomes clear that the blind application of the parameters fitted with the 2018 (high pile-up) samples is not compatible with these low pile-up runs: the χ^2 values degrade by $15 - 20\%$, leading to a significant increase in disagreement around the tails of the m_{ee} peak (i.e., towards 80 and 100 GeV). Generally speaking, this suggests that the correction inferred from the high pile-up sample does not

apply to the low pile-up ones.

As briefly described above, the main difference between high and low pile-up samples is that the latter has a lowered topo-cluster energy threshold, which has an effect on the total reconstructed energy. Let us think of a hypothetical case where an electron is measured using both thresholds, which will be labelled high-μ and low-μ. The yielded reconstructed energy would then be $E_{\text{reco}}^{\text{high-}\mu}$ and $E_{\text{reco}}^{\text{low-}\mu}$, where

$$E_{\text{reco}}^{\text{low-}\mu} = E_{\text{reco}}^{\text{high-}\mu} + \delta^{\text{diff. threshold}} \qquad \text{for} \qquad \delta^{\text{diff. threshold}} > 0.$$

For a simulated electron, the choice of threshold has no effect on the "truth" energy value, leaving it unchanged. By computing the event resolution Δ, one gets

$$\Delta^{\text{high-}\mu} = E_{\text{reco}}^{\text{high-}\mu} - E_{\text{truth}}$$

and

$$\begin{aligned}\Delta^{\text{low-}\mu} &= E_{\text{reco}}^{\text{low-}\mu} - E_{\text{truth}} = E_{\text{reco}}^{\text{high-}\mu} + \delta^{\text{diff. threshold}} - E_{\text{truth}} \\ &= \Delta^{\text{high-}\mu} + \delta^{\text{diff. threshold}}.\end{aligned}$$

This means that all the measured Δ values using a lower threshold will be larger than the larger threshold counterparts. Consequently, this implies that the resolution distribution (which is the accumulation in a histogram of Δ values around a single reference E_{truth}) in the low pile-up case will be shifted and show different features. As the MC Δ distributions are different at low and high pile-up, their correction to match data cannot be the same, even if the data/MC ratio shows similar features in the tails (as Fig. 5.14 could suggest). These effects, propagated to the dilepton mass distribution, are shown in Fig. 5.13. Overall, this implies that if one wishes to verify the impact of the Δ' method on low pile-up samples (and its propagation to derived studies, such as measurements of the W-boson mass), it is imperative to repeat the fit process on the corresponding low pile-up $Z \to ee$ samples.

While it is clear that there are intrinsic differences between high and low pile-up samples, one must not be misled to believe that the disagreement between data and the corresponding MC is caused due to completely unrelated effects. Figure 5.14, which shows the mass lineshape ratio of different pile-up runs, tries to motivate this, as one can notice the presence of very similar features across the ratio of both samples. Consequently, this simply means that the same resolution correction method may be applicable for both cases, although the best-fitted coefficients will, most likely, be different.

The impact of the Δ' method is hard to estimate, as the best possible attainable in a 40 bin histogram is $40 \pm \sqrt{2 \times 40} = 40 \pm 8.9$. Looking at the χ^2 values between data and MC (Fig. 5.12), which shows an average initial χ^2 agreement of about 54, it is hard to predict how much more improvement (if any) over the lineshape agreement can be obtained. At the very least, it would not be as drastic as the change seen in high pile-up samples (see Table 5.2).

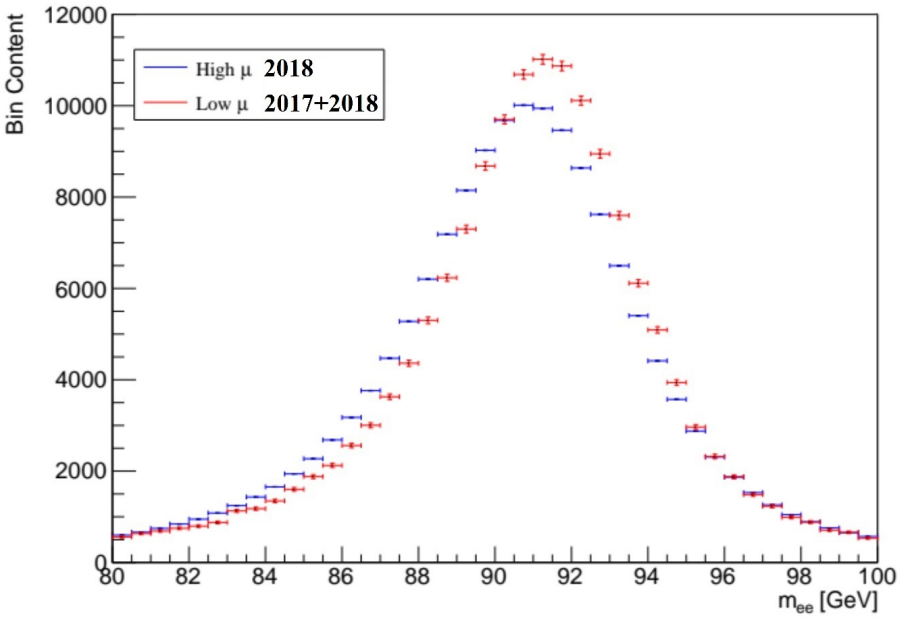

Figure 5.13: $Z \to ee$ dilepton mass distribution, corresponding to high (2018) and low (2017+2018) pile-up runs. The effect of the choice of topo-cluster threshold manifests as a shift of the peak of the distribution, while the different pile-up noise contributions provide differently shaped tails [127].

Repeating the Δ' study in low pile-up samples allows for additional considerations:

- Due to the reduced statistical sample, instead of using 6 η-regions as shown in Table 5.1, one may opt to use wider boundaries, pooling few regions into a single one, and potentially neglecting the crack region ($1.37 < \eta < 1.55$).
- As the initial data to MC agreement is relatively good, it is encouraged to try different Δ' functional forms in an attempt to optimise the parameter fit process and facilitate the posterior parameter error estimation.

A study focused on the re-implementation of the Δ' method on the 13 TeV low pile-up samples and the inspection of its impact in the measurement of the W-boson mass was undertaken by Aicha Kenani [129]. The study consisted in the repetition of the parameter fit for several Δ' functional forms using the low pile-up $Z \to ee$ samples, the eventual application of the minimised correction factors on the corresponding $W\pm \to e^{\pm}\nu$, and the fit of m_W using the template method.

Aicha found out that the parametrisation described by Eq. (5.18) can be applied to the low pile-up samples by using 40-bin m_{ee} histograms (i.e., each bin has a width of 0.5 GeV), using the $|\eta_{\text{calo}}|$ binning defined by the edges

$$\{0.00, 0.60, 1.37, 1.55, 1.82, 2.47\}$$

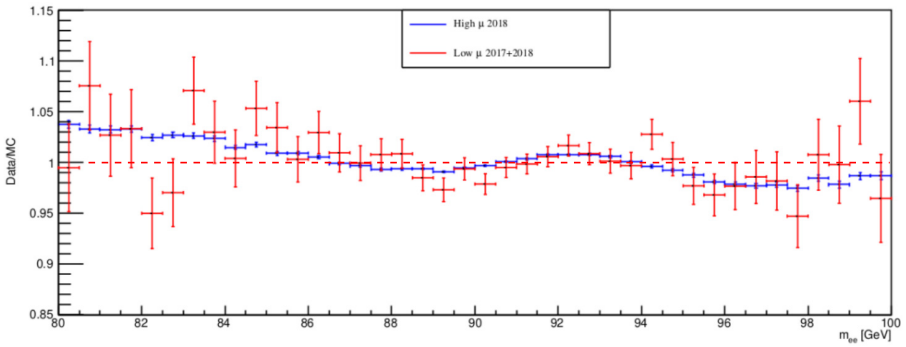

Figure 5.14: Comparison of nominal mass lineshape ratios (data/MC) using high and low pile-up samples [127].

and excluding the crack ($1.37 < |\eta_{\text{calo}}| < 1.55$). The improvement in the agreement between data and MC invariant mass lineshapes is shown in Fig. 5.15, leading to an improvement in χ^2 from 83.88 to 63.70 when the crack is excluded.

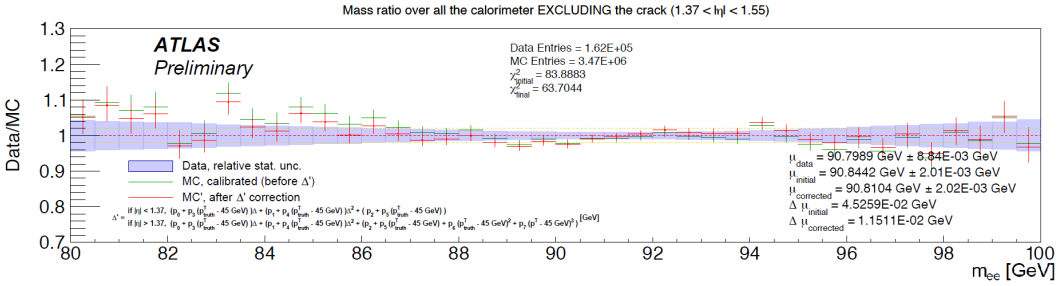

Figure 5.15: Agreement between the 13 TeV low pile-up $Z \to ee$ data and MC samples after the Δ' method has been applied, as found by Aicha Kenani [129].

The application of the parameters fitted on the low pile-up samples on the $W^{\pm} \to e^{\pm}\nu$ samples (generated at $m_W = 80.4$ GeV) leads to new calibrated m_{T} distributions (which shall be named "Nominal_Custom") that are different from the pre-Δ' nominal distributions. Figure 5.16 shows the relative changes of m_{T} for W^- and W^+, using as reference the pre-fit nominal distribution (labelled "Nominal_Default"). For comparison purposes, the relative change of ± 100 MeV mass shifts around the pre-fit distributions are also shown.

Performing a basic W-boson mass fit via the standard template method around the "Nominal_Custom" distribution leads to mass shifts of $\Delta m_{W^-} = (-17 \pm 19)$ MeV and $\Delta m_{W^+} = (-17 \pm 20)$ MeV with respect to the "Nominal_Defaut" distributions (N.B. $m_W^{\text{nom}} = 80.4$ GeV), where the quoted errors correspond to the statistical uncertainty of the fit.

Due to time constraints, further studies on low pile-up samples are not studied as part of this thesis work, but its development is encouraged in order to explore the potential

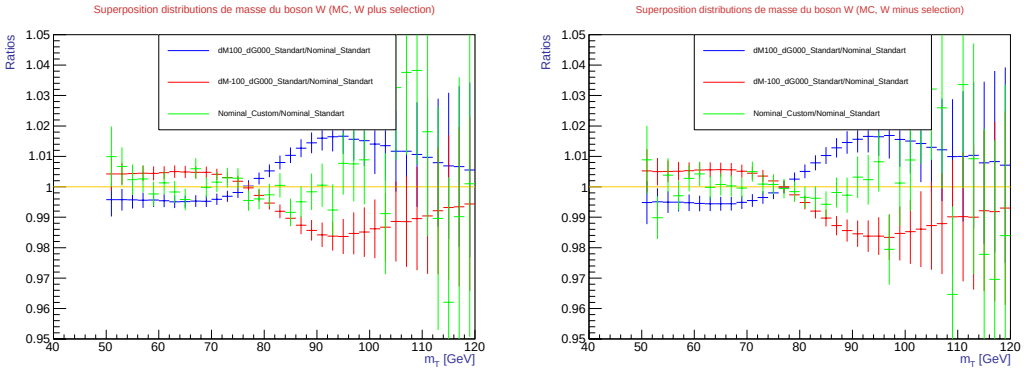

Figure 5.16: Relative m_{T} distribution changes, relative to the nominal pre-fit distribution ($m_W = 80.4$ GeV). The change induced by the Δ' calibration, as determined by Aicha Kenani [129], is shown in green under the label "Nominal_Custom/Nominal_Default". The relative change of ± 100 MeV around "Nominal_Default" are shown in blue and red.

effect of energy resolution correction in other studies. Particularly, it is of interest to understand the physicality and further implications of the observed mass shift.

5.9 ATLAS Internal Note [1]: Electron energy resolution corrections

The following pages contain the entirety of the technical report [1], which describes in detail the work done by the author of this thesis for the new calibration method. The note is provided as available on the CERN Document Server (CDS).

Similarly to Section 5.3, the note begins with a general description of the starting point of the study on the 2018 $Z \to ee$ data and MC, the motivation and conceptual methodology behind the new calibration technique. It is followed by a description of the `MINUIT` software, focusing on the libraries which resulted relevant to this study. Subsequently, various parameter estimators are discussed in the context of the fit of the Δ', highlighting the discontinuity problem arising from a direct bin-to-bin χ^2, and contrasting with the improved "bin-to-fittedPDF" estimator [2] built with the methodology described in Section 5.10. Very specific details on the implementation of the improved estimator are provided, showing the modified Crystal-Ball and Breit-Wigner-like parametrisations and the treatment of correlations during the estimation of the χ^2. The note is then followed by a description of the searches for the best definition of the Δ' functional form, exploring the effect of various functional dependencies (such as explicit dependency on Δ, Δ^2, E^{T}, etc), the binning (12 regions in η, compared to 6 regions in $|\eta|$), and exploring kinematic properties of the the various regions that compose the entirety of the relevant phase-space. The results of several fits are shown for a variety of situations, covering variations motivated by arguments derived from the above properties. The note concludes by providing the best definition of Δ' found during this study for this particular dataset, which improves the total data to MC χ^2 almost to the best possible value.

The appendix of the note shows the effect on the χ^2 curve generated by performing bootstrap resampling on the data sample, which illustrates the statistical uncertainty around any χ^2 measurement. Finally, a compendium of figures summarising relevant results and characteristics for several of the fits performed on the sample is provided on the last pages of the note.

1st October 2021

Electron energy resolution corrections

Juan Salvador Tafoya Vargas[1], Louis Fayard[1], Zhiqing Zhang[1]

Summary

The calibration of the Liquid Argon Electromagnetic Calorimeter at the ATLAS experiment is done with $Z \to ee$ Data and MC. While the continuous efforts of the collaboration have improved the agreement between both samples, there is a remaining non-negligible discrepancy between the Data and MC dilepton invariant mass lineshape that has not been accounted for by existent corrections. As measurements coming from the tracker (and their simulation) are highly precise, the energy measurement at the calorimeter seems to be the most likely culprit.

This study aims to better understand the mass lineshape discrepancy by performing energy resolution corrections on MC. These are performed on an event-by-event basis with scalings of $\Delta = E_{\text{reco}} - E_{\text{truth}}$ via some parametrization $\Delta' = f_\eta(\Delta, E^{\text{T}}_{\text{truth}})$, where the explicit dependence on $E^{\text{T}}_{\text{truth}}$ seeks to account for the changing kinematics of the electron-pair across different regions of the calorimeter. As the Δ' correction translates into a shape deformation of the energy resolution distribution, it allows to account for specific effects, such as tails and negative smearing corrections, which have an important effect on the lineshape agreement.

[1] *IJCLab, Université Paris-Saclay, CNRS/IN2P3, 91405, Orsay; France*

Contents

1 Introduction

In the ATLAS experiment, the energy of electrons and photons is completely determined by the Liquid Argon (LAr) electromagnetic calorimeter. Since these measurements are of fundamental importance for any other study, such as precision electroweak studies, the proper calibration of the detector is imperative, which motivates for continuous efforts to improve higher order effects.

Seeking to properly simulate the response of the detector and to best extract the observations from the measured Data, a well defined chain of calibration is followed as shows schematically in Figure 1. Each step is designed to correct for particular phenomena on either of the samples, systematically improving the agreement between both. Such agreement can be evaluated by looking at the difference between distributions of e.g. momentum or invariant mass.

In ATLAS, the calibration is done by concentrating on "easily" measurable phenomena, such as $Z \to ee$, where all the sub-products can be detected within the calorimeter and the parent particle is completely reconstructed.

The particular study described through this note is proposed to take effect at a late stage of the calibration sequence (shown in a red circle in Figure 1), right before the data-driven scale validation.

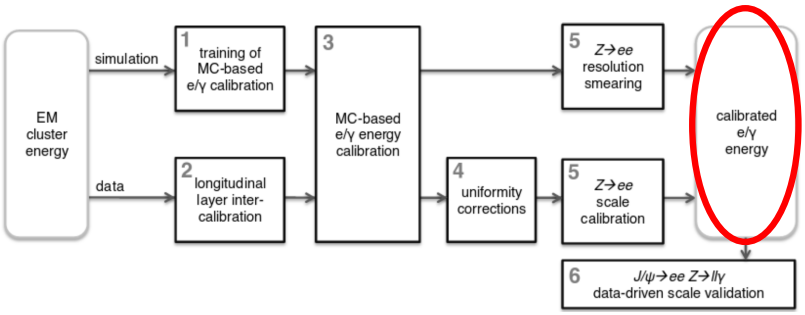

Figure 1: Schematic representation of the calibration chain for e/γ. The study described in this report is applied on MC (i.e. simulation) after step 5 i.e. on top of the resolution smearing and scale calibration (red circle). Diagram obtained from Ref. [1].

2 Motivation

While many studies before this one have improved considerably the agreement between the Data and MC mass lineshape, it is still not perfect (see, for instance, Figure 2). It is suspected that this disagreement may be caused primarily by a miscalibration of the simulated calorimeter, and thus many efforts have been done aiming to improve the corresponding MC sample.

This particular work aims to calibrate the MC energy resolution via scalings in order to better account for specific effects, such as tails and small/negative smearing corrections.

An initial study on this technique has already been done by the USTC group [2], which was focused towards the forward part of the calorimeter. This same study serves as the initial reference for the following work.

2.1 Nominal Data and MC samples

The calibration study presented here is done on 2018 Data, using only the $Z \to ee$ process (luminosity of 58.45 fb^{-1}). The corresponding MC sample is weighted (for pileup, cross section, etc.), and normalized to the luminosity of Data. The exact samples used for the study are:

> mc18_13TeV.361106.PowhegPythia8EvtGen_AZNLOCTEQ6L1_Zee.deriv.DAOD_EGAM1.e3601_s3126_r10724_p4089
> data18_13TeV.periodAllYear.physics_Main.PhysCont.DAOD_EGAM1.grp18_v01_p4088

Both Data and MC have a E^{T} cut at 27 GeV, which is preserved through the calibration procedure. Further details on the selection criteria and cuts is provided in Ref. [3].

The current study is done on top of the energy scale calibration described in Ref. [3], which treats both samples for resolution smearing and energy scale correction via the so called template method (step 5 in Figure 1). Figure 2 shows the nominal dilepton mass lineshape after all the selection criteria have been applied, displaying Data in blue, and in green the normalized MC. The shape comparison between both (bin-to-bin χ^2) is also shown.

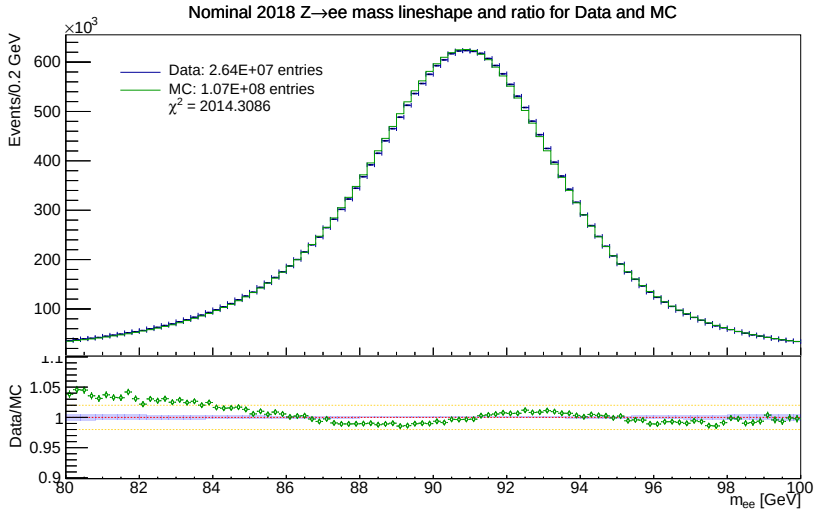

Figure 2: $Z \to ee$ invariant mass lineshape, including all the available sample after the energy scale correction described in Ref. [3]. The bin-to-bin χ^2 value between Data and MC is shown, along with the size of each sample.

2.2 Glossary of terms

Many variables are used along this study, so it is useful to provide a brief description and summary of these.

On the MC side, there are primarily two types of variable: measured at generation (also called "truth") and at reconstruction (called "reco"):

- **Truth** correspond to the physical quantities measured at Dressed level (after Final State Radiation [FSR] and including collinear photons, see Figure 3), before any detector simulation. These are the quantities one would measure if there were no resolution and systematical effects in the detector. Ergo, these quantities are independent of any calibration, and their values remain fixed.
- **Reco** quantities are measured after the detector has been simulated (i.e. post GEANT4 + other corrections). Reconstructed quantities should (normally) be very close to their corresponding truth value, up to the resolution of the (simulated) detector.

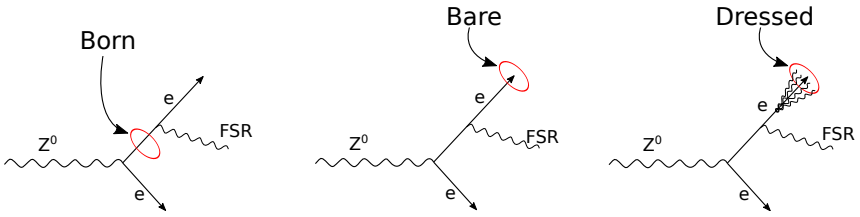

Figure 3: Definitions of "truth" level. Born: before FSR. Bare: after FSR, electron alone. Dressed: after FSR, electron + collinear photons

Furthermore, for both Data and MC, different parts of the calorimeter can give a measurement for the same quantity. Selecting which measurement to use depends greatly on the purpose. For this study, the following are used:

- E_{reco}: energy, measured by the calorimeter.
- $E^{\text{T}}_{\text{reco}}$: transverse energy, measured by the calorimeter ($E^{\text{T}} \approx E/\cosh\eta$).
- $\eta_{\text{tracker}} = \eta$: pseudo-rapidity, measured by the tracker.
- $\phi_{\text{tracker}} = \phi$: azimuthal angle, measured by the tracker.
- η_{calo}: pseudo-rapidity, measured by the calorimeter.

where the first 4 are used for the invariant mass computation, and the last one only for classification purposes (i.e. to determine the corresponding η-region of the calorimeter). It is worth mentioning that, unless specified otherwise, the quantities used correspond to the *reco* level.

3 Energy resolution corrections

Along this study, Data will be considered as a perfect sample, and thus all corrections are done on the MC side. We define the MC resolution Δ as the difference between the Reconstructed energies E_{reco} (GEANT4 + Energy Scale Correction [3]) and their corresponding values at generation E_{truth} (Truth = Dressed level), i.e.

$$\Delta = E_{\text{reco}} - E_{\text{truth}}. \tag{1}$$

We define then a corrected resolution value Δ' as

$$\Delta' = f(\Delta), \tag{2}$$

such that the corrected energy E'_{reco} looks like

$$E'_{\text{reco}} = E_{\text{truth}} + \Delta' \tag{3}$$

One of the most simple parametrizations Δ' looks like

$$\Delta' = p_0\Delta + p_1\Delta^2 + p_2, \tag{4}$$

and this will in fact be the base for the more complex forms explored ahead.

3.1 η dependency

In order to account for different effects as a function of the region of the calorimeter, this calibration study is performed in regions of pseudo-rapidity η. These are defined following the physical sections of the calorimeter, and making a distinction between the positive and negative regions. For simplicity, we use an integer number (running from 1 to 12) to identify each of the regions, defined by the following convention:

η_{calo}	-2.47	-1.82	-1.55	-1.37	-1.00	-0.60	0.00	0.60	1.00	1.37	1.55	1.82	2.47
region	-	1	2	3	4	5	6	7	8	9	10	11	12	-
name	endcap			crack	barrel						crack	endcap		

where e.g. 1 corresponds to the left-most region (negative end-cap, $-2.47 < \eta < -1.82$), 6 to the center-most negative one (negative barrel, $-0.6 < \eta < 0.0$), and 12 to the right-most one (positive end-cap, $1.82 < \eta < 2.47$).

All the previous means that there is total of 12 sets of parameters $\vec{p}_\eta = (p_0, p_1, p_2, ..)$ that must be determined in order to calibrate all the calorimeter (not to be confused with the momentum $\vec{p}$, which lacks the "η" sub-index).

3.2 Particularities of the study

Since this study looks at $Z \to ee$ samples, there is a total of two electrons per event, both of which are affected by the resolution correction. In this study, we only differentiate

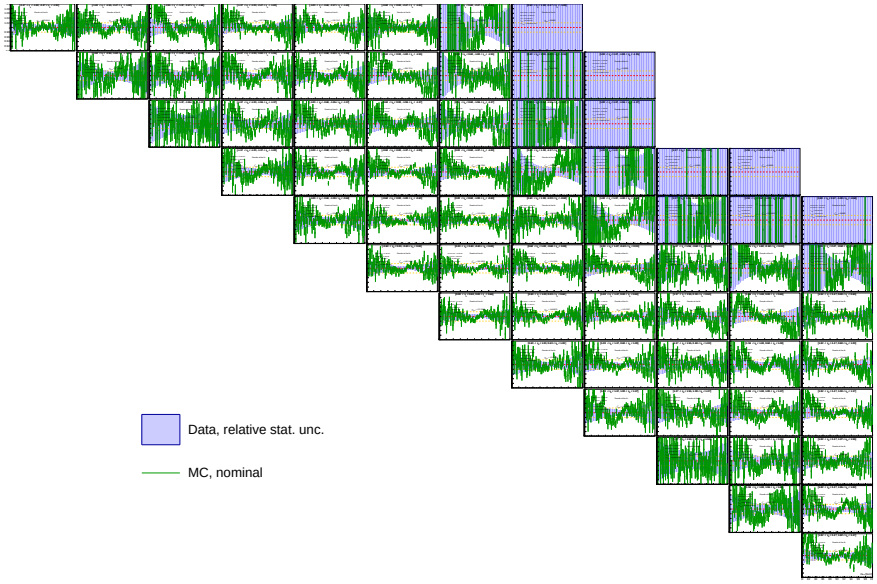

Figure 4: Nominal Data/MC mass line ratios, in the [η-1,η-2] grid seen by the calibration process. All ratio plots go from 0.9 to 1.1 (vertical axis), in the 80 to 100 GeV range.

electrons by their pseudo-rapidity η_1 and η_2, so the calibration runs on a grid of, at most, 78 [η-1,η-2] bins. Figure 4 shows the mass line ratio in this grid, for the nominal Data and MC.

Following the naming convention from earlier, each of the regions in the grid will be identified by a pair of integers, e.g.:

- Region 1-1 requires that both electrons have $-2.47 < \eta_{\text{calo}} < -1.82$
- Region 6-2 = 2-6 requires one electron with $-1.82 < \eta_{\text{calo}} < -1.55$ and the other with $-0.6 < \eta_{\text{calo}} < 0.0$.

Also in reference to Figure 4, the terms "diagonal" and "off-diagonal" bins are commonly used. The former makes reference to any case where both electrons fall in the same region (e.g. region 1-1), while the latter includes all scenarios where each electron falls in a different section of the calorimeter (e.g. regions 6-2 and 6-5).

Inspecting Figure 4, one can notice that some regions (such as 12-1, where the electrons are back-to-back [$\eta_1 \approx -\eta_2$] and going to the far endcap on opposite sides) are effectively empty. To understand this, one just has to remember that (at first order) $E_Z^{\text{T}} \approx 0$, and that close to back-to-back case $p_Z^{\text{L}} \approx 0$. Due to 4-momentum conservation, both electrons would have almost the same momentum $\vec{p}$ ($|p| \approx m_Z/2$), with E^{T} decreasing as η increases. This means that after large enough pseudo-rapidity value ($|\eta| \gtrsim 1.1$ in the back-to-back case), the E^{T} of the events is bellow the 27 GeV cut, and are not seen anymore. Taking this in consideration, the total number of useful regions gets reduced to about 60.

4 Minimization and parameter determination

Since the purpose of this study is to improve the agreement between Data and MC invariant mass lineshapes, the best parameters $\hat{\vec{p}}_\eta$ are determined by comparing the shape of both distributions, and minimizing their difference. Various (almost equivalent) techniques can be used to measure and reduce this difference, such as χ^2 minimization or likelihood $\mathcal{L}$ maximization, each with their advantages and limitations. The possibilities explored for this particular study are briefly summarized in Subsection 4.3.

4.1 MINUIT

Due to the nature of this study, a large amount of parameters must be determined in order to calibrate the whole calorimeter. For instance, looking at the most basic definition of Δ' (with 3 free parameters, Eq. (4)) and the binning of Figure 4, 36 separate (and correlated) parameters are needed. Consequently, traditional approaches (such as parabolic fits on a χ^2 curve) are not feasible, and more general multidimensional-friendly methods must be used.

Originally written in Fortran by Frederic James, MINUIT [4] is a multidimensional customizable numerical minimizer. It is widely used in statistical analyses, and extensively used in ROOT (for instance, every time one does `h→Fit()`). In a basic level, MINUIT just needs to be provided with a function FCN whose value depends on a set of free parameters $\vec{\theta} = (\theta_1, .., \theta_n)$ such that FNC : $\mathbb{R}^n \to \mathbb{R}$. By performing variations of these parameters through either of the available algorithms (see bellow), MINUIT is capable of learning information from FCN, such as gradients, correlations, position of the minimum and parameter errors.

For the particular study described in this document, the function FCN is built with a χ^2 or likelihood

$$\text{FCN} = \text{FCN}(\vec{\theta}) = \begin{cases} \chi^2 \\ -2\log\mathcal{L} \end{cases}$$

where $\vec{\theta} = \vec{p}_\eta$.

From among all the available algorithms within MINUIT, each focused on learning different aspects of FCN, the following 3 are the most pertinent for this study:

- `MIGRAD`: Main (and most reliable) minimization algorithm. Relies completely on knowledge of the gradient, whether this is provided analytically or estimated numerically on the fly, which is used to do steps towards the expected position of the minimum by assuming that the function FCN is quadratic-like. In consequence, it works best when the curve corresponding to FCN is smooth, so "bumpy" curves can prove to be problematic.

- `HESSE`: Faster way to estimate symmetric errors of the fitted parameters. The corresponding covariance matrix V_{ij} is obtained by inverting the Fisher information matrix $I_{ij}(\vec{\theta})$, so that

$$\left(V^{-1}\right)_{ij} = -I_{ij}(\hat{\vec{\theta}}) = -E\left[H_{ij}(\vec{\theta})\right] = -E\left[\frac{\partial^2 \ln \text{FCN}}{\partial\theta_i \partial\theta_j}\right],$$

where E is the expectation value and H_{ij} the hessian matrix of FCN($\vec{\theta}$). This algorithm provides a good (and quick) estimation of the parameter errors, provided there are no non-linearities and the gradient can be trusted.

- `MINOS`: Algorithm to estimate asymmetric errors. It does so by numerically looking at positive and negative variations $\delta^{\pm}$ around the minimum s.t. for parameter i, FCN($\hat{\vec{\theta}}\pm\delta_i^{\pm}$) = FCN($\hat{\vec{\theta}}$)+1 where $\delta^{\pm}$ corresponds to a 1-σ error (68%) for ΔFCN = 1. It is considerably slower than the Hesse method, but the results are more reliable, and less dependent on the accuracy of the gradient.

Regardless of the algorithm, there are few technical aspects of MINUIT which are worth mentioning, such as the when-to-stop criteria. The following are the most relevant for the presented study:

- `EDM = Estimated vertical distance to the minimum`: Since in reality the FCN curve will not be perfectly parabolic and numerical precision is not infinite, one can only aim to get close enough to the actual minimum of FCN when using numerical methods. Assuming a parabolic behaviour, the EDM judges the vertical distance towards the analytical minimum (i.e. EDM($\vec{\theta}$) $\approx$ FCN($\vec{\theta}$)$-$FCN$^{\text{min}}$). In practice, for a covariance matrix V and gradient GS, it is estimated via $EDM = GS^T * V * GS$. Any algorithm stops (and converges) when the EDM goes bellow a given threshold.

- `Tolerance`: Defines the threshold for the EDM, bellow which a minimization can stop. For MIGRAD, for instance, one says that a minimization converges when EDM $< 0.1 \times$ tolerance.

- `Precision`: Relative floating point arithmetic precision, particularly useful when the curve FCN is not prefectly smooth as to "smoothen" small bumps.

□ N.B. if FCN is not smooth and the bumps are not adequately ignored with the precision, the gradient may not be well estimated, and the EDM could get artificially enlarged. This means that even if the best parameters $\hat{\vec{\theta}}$ are found, local fluctuations could inflate the EDM above the threshold and wrongly consider the minimization as "failed" despite an improvement in FCN.

For this particular study, Minuit2 (the implementation of MINUIT written in C++) is used with ROOT 6.08/02 [5] as an interface, through the `ROOT::Fit::Fitter` class.

4.2 Minimization sequence

As mentioned above, the current study aims to minimize the shape difference between the Data and corrected MC mass lines. This means that, for each proposed set of parameters $\vec{p}_\eta$ (provided by MINUIT), the dilepton mass distribution must be obtained using e.g. a histogram. Nevertheless, the Δ' correction acts on the individual energy of each of the electrons E_{reco} (and their original resolution Δ), and there are 2 electrons per Z-boson event. Figure 5 shows a simplified schematic representation of this process.

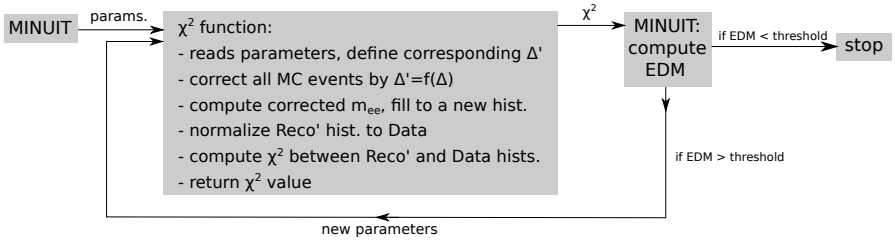

Figure 5: Schematic representation of the minimization process used to estimate the best Δ' parameters, for FCN $= \chi^2$.

Entering in more detail, the minimization obeys the following algorithm:

1. At each step, MINUIT will propose a set of parameters $\vec{p}_\eta^{\,\text{step}}$.
2. All the individual electrons (one pair per event) are corrected with $\Delta'(\Delta; \vec{p}_\eta^{\,\text{step}})$.
3. Seeking to preserve electron invariant mass and since we are in the ultra-relativistic case, the corrected $E^{\text{T}}_{\text{reco}}$ is computed via

$$E^{\text{T}}_{\text{reco,corr}} = E'_{\text{reco}} / \cosh \eta. \tag{5}$$

4. The dilepton invariant mass is computed for each event, using e.g.

$$m'_{ee} = 2E'_{\text{reco},1} E'_{\text{reco},2} (1 - \cos\theta_{12}) = 2E^{\text{T}}_{\text{corr},1} E^{\text{T}}_{\text{corr},2} \left[\cosh(\eta_1 - \eta_2) - \cos(\phi_1 - \phi_2)\right]. \tag{6}$$

5. Each corrected dilepton mass is stored in a 100 bin histogram `hrecoP`$(\vec{p}_\eta^{\,\text{step}})$, with range from 80 to 100 GeV.
6. `hrecoP`$(\vec{p}_\eta^{\,\text{step}})$ is then normalized to the Data dilepton mass histogram `hdata`.
7. FCN$(\vec{p}_\eta^{\,\text{step}})$ is computed between `hrecoP`$(\vec{p}_\eta^{\,\text{step}})$ and `hdata`.
8. The numerical value of FCN$(\vec{p}_\eta^{\,\text{step}})$ is returned to MINUIT.
9. The cycle repeats until MINUIT estimates the gradient at a given point and computes the EDM.
10. The minimization converges when the EDM for a given set of parameters $\hat{\vec{p}}_\eta$ is bellow the tolerance threshold.
11. At FCN$(\hat{\vec{p}}_\eta)$, further variations are done to compute the corresponding Hessian matrix, and to estimate the covariance matrix.

4.3 FCN definition

The initial approach consisted in a direct bin-to-bin χ^2 comparison. This means that, for a couple of normalized histograms, built with the same number of bins in identical mass ranges (80 to 100 GeV), FCN could be defined as

$$\mathrm{FCN}(\vec{p}_\eta) = \chi^2 = \sum_{i=1}^{n\ \mathrm{bins}} \frac{[\mathrm{bin}_{\mathrm{Data},i} - \mathrm{bin}_{\mathrm{MC},i}(\vec{p}_\eta)]^2}{\sigma^2_{\mathrm{Data},i} + \sigma^2_{\mathrm{MC},i}(\vec{p}_\eta)} \tag{7}$$

where, for the histogram hist = {Data, MC}, $\mathrm{bin}_{\mathrm{hist},i}$ is the content of the i-th bin, and $\sigma_{\mathrm{hist},i}$ its statistical uncertainty. Equation (7) is attractive because of its simplicity, providing a straight-forward shape comparison, and it is in fact used in many other studies (such as Ref. [3]).

Before providing Eq. (7) to MINUIT, it is of interest to know the shape of the χ^2 curve and perform a closure test. This was done by scanning over one of the parameters (i.e. by manually changing its value) while the rest remain fixed. Furthermore, in order to see a meaningful χ^2 curve, the scan was performed with PseudoData, i.e.

- Half of the MC sample (even-numbered events) is used as MC.
- The rest of the MC sample (odd-numbered events) is used as PseudoData, built with known $\vec{p}_\eta^{\,\mathrm{pseudo}}$ parameters.

The scan, shown with blue dots in Figure 6, revealed huge fluctuations, sometimes larger than $\Delta\chi^2 = 5$, with multiple nonphysical local minima. Since most of the studies that use on bin-to-bin χ^2 simply rely on a parabolic fit (as that shown also in Figure 6 with a faint continuous blue line), only large parameter steps (along e.g. p_2) are done and the fluctuations are normally not relevant (if seen at all). Unfortunately, as already discussed, parabolic fits are not an option for the current study, and an unhealthy (untreated) χ^2 curve could not be minimized by MINUIT.

Trying to get rid of such problem with re-sampling techniques (such as Bootstrap [6] [7]) is not a viable technique, as the χ^2 fluctuations do not have a statistical origin. This is briefly discussed in Appendix A.

Overcoming this issues was, in fact, the most time-consuming part of this whole study. Since other analyses overlook the fluctuations, this issue had not been formally addressed somewhere else before, and thus there was not a treatment or clear understating of it. In consequence, it led to developing a technique to overcome the issues, and to write a whole separate note [8] describing it.

Briefly summarizing the content of Ref. [8]: Let us think of a couple of MC histograms $\texttt{hMC}(\vec{p}_\eta)$ and $\texttt{hMC}(\vec{p}_\eta + \mathrm{d}\vec{p})$. By modifying the parameters with $\vec{p}_\eta + \mathrm{d}\vec{p}$, the mass m_{ee} of each event will be modified (even if slightly). This means that, compared to $\texttt{hMC}(\vec{p}_\eta)$, the majority of events will fall in the same bin, but some others will **migrate** to a neighbouring one. Such migration of events creates a non-continuous change in the sample size contained by each bin, which propagates as a non-continuously changing histogram. Since the Data histogram `hData` remains constant, all the previous translates into a non-smooth χ^2 curve. Thus, the fluctuations are a direct consequence of comparing histogram v. histogram.

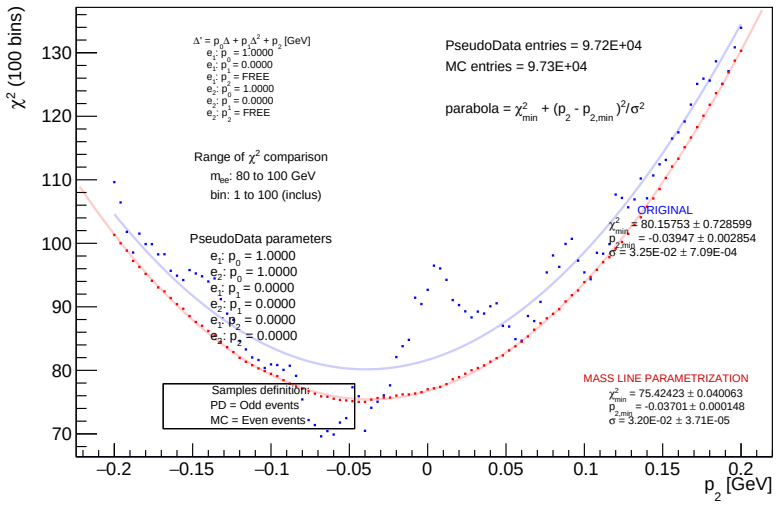

Figure 6: χ^2 scan on PseudoData in η-bin 10-10, for $\Delta' = p_0\Delta + p_1\Delta^2 + p_2$ along $p_2^{\eta\text{-}10}$. The blue dots show the original bin-to-bin χ^2 curve, while the red one corresponds to the treated bin-to-profiledPDF χ^2 curve (as described in Ref. [8]).The faint continuous blue and red lines correspond to a parabolic fit on each curve, whose parameters are shown also within the plot.

A solution to this is to approximate $\texttt{hMC}(\vec{p}_\eta)$ by a continuous PDF, which is equivalent to predicting the case of infinitely large sample size (withing statistical uncertainties). The easiest way is to fit a functional form $f(m_{ee};\vec{\theta})$ on the MC histogram, and then to use this profiled PDF to "predict" the content of each MC bin. Provided a large enough MC sample, $f(m_{ee};\vec{\theta})$ is capable of changing (almost) continuously as a function of $\vec{p}_\eta$, where one has the indirect dependence $\vec{\theta} = \vec{\theta}(\vec{p}_\eta)$.

Looking back at Figure 6, an example of the aforementioned technique is shown with red dots. Not only this technique gets rid of the fluctuations, but it gives a curve very closely followed by its parabolic fit. Furthermore, as a closure test, the PseudoData parameter is correctly recovered within uncertainty.

The aforementioned method is not a perfect solution due to technical limitations, but the small imperfections are (somewhat) easily avoided by tweaking MINUIT parameters, such as the precision.

Two functional forms of $f(m_{ee};\vec{\theta})$ are used in this study, depending on the region (and sample size):

$1.37 < |\eta| < 1.55$ | $|\eta| < 1.37$ or $1.55 < |\eta|$

CrystalBall with exponential tails:

$$f(x) = \begin{cases} 80 < x < c_1: & e^{D(x-P)} + R \\ c_1 < x < c_2: & \frac{C}{B\sqrt{2\pi}} e^{-\frac{1}{2}\left(\frac{x-A}{B}\right)^2} \\ c_2 < x < 100: & e^{E(x-Q)} + S \end{cases}$$

Breit-Wigner-like

$$f(x) = \begin{cases} 80 < x < c_1: & e^{F(x-P)} + R \\ c_1 < x < c_2: & \frac{C}{(x-A)^2 + B} + E(x-D)^2 \\ c_2 < x < 100: & e^{G(x-Q)} + S \end{cases}$$

where $x = m_{ee}$. Here, R, S are used to ensure function continuity, and P, Q continuity of the derivative. It is worth mentioning that the best cuts c_1 and c_2 are also fitted along the rest of the parameters i.e. the position of the nodes is not fixed.

Figure 7 shows an example of the MC mass lineshape for η-bin 9-9 and the fitted PDF f^{MC} (for this region, a Breit-Wigner-like function is used), as well as their ratio, showing a very good description of the shape and non-noticeable bias.

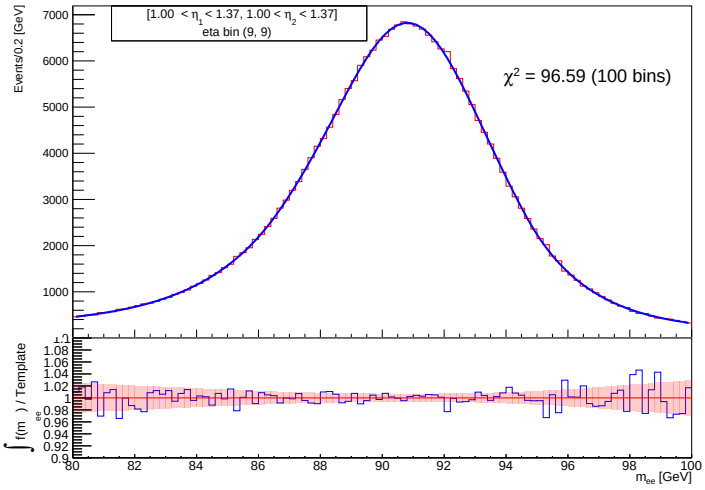

Figure 7: MC mass lineshape η-bin 9-9 (red), and its corresponding profiled PDF (Breit-Wigner-like, in blue).

Once the PDF $f^{\mathrm{MC}}(x;\vec{\theta}(\vec{p}_\eta))$ for a particular histogram $\texttt{hMC}(\vec{p}_\eta)$ has been estimated and normalized to `hData`, one can choose from a couple of FCN definitions. The following were found to be the most reliable and quick ones.

4.3.1 Bin-to-profiledPDF χ^2

Now that a functional description of the MC is available, one can define a χ^2 between a Data histogram `hData` and the corresponding MC PDF $f^{\mathrm{MC}}(x;\vec{\theta})$. However, since f^{MC}

was obtained through a fit, the parameters $\vec{\theta}$ have an uncertainty that must be taken into consideration.

In the asymptotic limit, the content of the k-th MC bin (with center at x_k) is predicted with

$$\text{bin}_k^{\text{MC,pred}} = \overline{f(x)}\Big|_{x_k} = \left(\int_{x_k-0.5\text{binwidth}}^{x_k+0.5\text{binwidth}} f(x)\mathrm{d}x\right) /\text{binwidth}$$

i.e. the average value of f^{MC}. Nonetheless, due to the uncertainties and correlations of $\vec{\theta}$, one cannot use a simplified χ^2 definition as in Eq. (7). Instead, the more generalized definition that includes the covariance matrix is required.

By noticing that

$$\mathrm{d}f\Big|_{x_k} = \sum_i \overline{\frac{\partial f}{\partial \theta_i}}\Big|_{x_k} \mathrm{d}\theta_i,$$

(where $f = f^{\text{MC}}$), the covariance between two predicted MC bins k and l looks as

$$\begin{aligned}
\text{cov}^{\text{MC}}(x_k, x_l) = V_{k,l}^{\text{MC}} &= \langle \mathrm{d}f\Big|_{x_k}, \mathrm{d}f\Big|_{x_l} \rangle \\
&= \langle \sum_i \overline{\frac{\partial f}{\partial \theta_i}}\Big|_{x_k} \mathrm{d}\theta_i, \sum_j \overline{\frac{\partial f}{\partial \theta_j}}\Big|_{x_l} \mathrm{d}\theta_j \rangle \\
&= \sum_{i,j} \overline{\frac{\partial f}{\partial \theta_i}}\Big|_{x_k} \overline{\frac{\partial f}{\partial \theta_j}}\Big|_{x_l} \sigma_i \sigma_j \rho_{ij}
\end{aligned}$$

where σ_i and σ_j are the fit errors for the parameters of f, ρ_{ij} their respective correlation, and $\overline{\frac{\partial f}{\partial \theta_i}}\Big|_{x_k}$ the average value of the gradient in the bin k. Figure 8 shows an example of the corresponding correlation matrix for the predicted MC histogram.

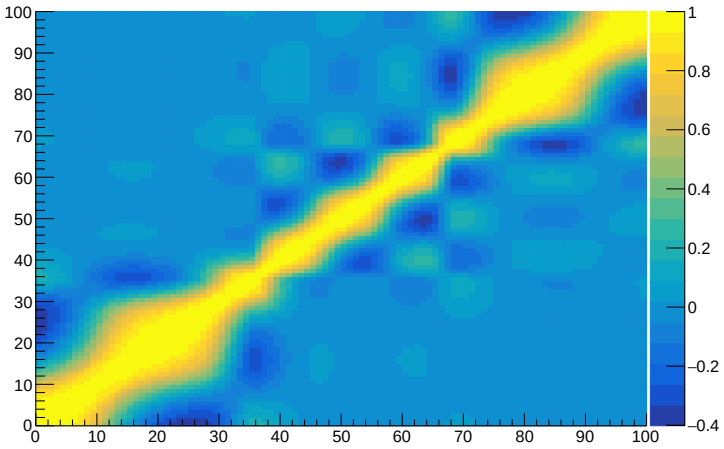

Figure 8: Example of the MC correlation predicted from the profiled PDF f^{MC}.

Since `hData` has not been modified, its corresponding covariance matrix V^{Data} remains diagonal. By defining the vector of distances $\vec{d} = (d_1, .., d_{100})$ between Data - MC bins as

$$d_k = \text{bin}_k^{\text{Data}} - \text{bin}_k^{\text{MC,pred}},$$

the χ^2 can be written in its most general form

$$\text{FCN} = \chi^2(\vec{p}_\eta) = \vec{d}^{\,\text{T}} * V^{-1} * \vec{d}, \tag{8}$$

where $V = V^{\text{Data}} + V^{\text{MC}}$ is the total covariance matrix, and $\vec{d}^{\,\text{T}}$ is the transpose of the distance vector $\vec{d}$. The red dots in Figure 6 correspond to this χ^2 definition, visually showing the improvement gained with this technique.

4.3.2 Negative Logarithm Unbinned Likelihood Ratio

A way to go away from possible binning bias (or systematics) is to use the individual Data events in an unbinned likelihood. For a particular region η-i-j, this likelihood can be written as

$$\mathcal{L} = \prod_k^{n \text{ events Data}} f^{\text{MC}}(x_k^{\text{Data}}; \vec{\theta}(\vec{p}_\eta)) \tag{9}$$

where f^{MC} must be normalized so that its integral is equals to 1. Maximizing Eq. (9) allows to find the parameters $\hat{\vec{p}}_\eta$ that best describe the data distribution.

Nevertheless, a likelihood as in Eq. (9) is not invariant under space transformations and does not provide a goodness-of-fit measurement. An easy solution is to go to an unbinned likelihood ratio, which overcomes both of these problems while keeping a small numerical value at its minimum (close to 0, which is ideal to prevent floating point precision issues). This is possible because, similarly to MC, a PDF f^{Data} can be fitted on `hData` (only once, at the beginning), and thus define

$$\mathcal{L}_R = \prod_k^{n \text{ events Data}} \frac{f^{\text{MC}}(x_k^{\text{Data}}; \vec{\theta}(\vec{p}_\eta))}{f^{\text{Data}}(x_k^{\text{Data}})}. \tag{10}$$

It is worth noticing that the denominator $\prod_k f^{\text{Data}}(x_k^{\text{Data}})$ has a constant value, so the numerical maximum of Eq. (10) should be at the same position as for Eq. (9), up to a vertical shift.

In practice, instead of maximizing Eq. (10) we will focus on minimizing $-2\log\mathcal{L}_R$, i.e. looking for the best parameters $\hat{\vec{p}}_\eta$ where

$$\text{FCN} = -2\log\mathcal{L}_R = -2 \sum_k^{n \text{ events Data}} \log\left[\frac{f^{\text{MC}}(x_k^{\text{Data}}; \vec{\theta}(\vec{p}_\eta))}{f^{\text{Data}}(x_k^{\text{Data}})}\right], \tag{11}$$

is minimum.

N.B. the uncertainty of the fit is neglected in this scenario, which in consequence allows for a quicker computation compared to the χ^2 of Eq. (8). Nonetheless, this seemed to have no noticeable effect on the position of the minima (again, compared with the χ^2 scenario), although the size of the errors of $\vec{p}_\eta$ could be miss-estimated if no further inspection is done.

4.3.3 Mixing multiple channels

Looking back at Figure 4, it is clear that a single set of parameters can be measured through multiple channels e.g. $\vec{p}_{\eta\text{-}1}$ can be estimated with regions 1-1, 2-1, 3-1, etc. If all of this channels are combined to obtain a single, global set of parameters, a global χ^2 (or likelihood) must be defined.

For χ^2, a global χ^2_{global} is defined trivially through

$$\chi^2_{\text{global}} = \chi^2_{\eta\text{-}1\text{-}1} + \chi^2_{\eta\text{-}2\text{-}1} + \chi^2_{\eta\text{-}3\text{-}1} + ... \tag{12}$$

which is possible since all the η-regions are completely uncorrelated, and the χ^2 computation at each regions imposes a sense of mutual normalization (since $\chi^2_{\text{min}} \approx \text{n.d.f.} \approx 100$).

For the unbinned likelihood, the procedure is less trivial. Since different regions remain completely independent, one could naively define

$$\mathcal{L}_{\text{vglobal}} = \mathcal{L}_{\eta\text{-}1\text{-}1} \cdot \mathcal{L}_{\eta\text{-}2\text{-}1} \cdot \mathcal{L}_{\eta\text{-}3\text{-}1} ...$$

But given that each region has a different sample size, one must manually include a normalization (or scaling) factor $\kappa_{i,j}$ to each individual $\mathcal{L}_{\eta\text{-}i\text{-}j}$, which would give

$$\mathcal{L}_{\text{global}} = (\mathcal{L}_{\eta\text{-}1\text{-}1})^{\kappa_{1,1}} \cdot (\mathcal{L}_{\eta\text{-}2\text{-}1})^{\kappa_{2,1}} \cdot (\mathcal{L}_{\eta\text{-}3\text{-}1})^{\kappa_{3,1}} ... \tag{13}$$

That being said, the estimation of $\kappa_{i,j}$ is not trivial, and investigating it is beyond the scope of this study.

Based on the previous, the χ^2 of Eq. (8) (along Eq. (12)) will be the preferred definition of FCN. Moreover, seeking to optimally use the bin-to-profiledPDF technique described in Subsection 4.3, only η-bins with more than 40,000 Data events are included in the global χ^2 computation.

5 First fits and additional kinematics checks

Starting with the most basic Δ' definition, that is $\Delta' = p_0\Delta + p_1\Delta^2 + p_2$, the initial approach to the calibration consists of the most simple case scenario: provided no additional dependencies and no inter-region correlations, the sets of parameters $\vec{p}_{\eta\text{-}i}$ can be fitted individually using only the diagonal η-regions i-i. This means that 12 independent fits should be enough to correct the whole calorimeter. Figure 9 shows how these initial fits propagate to the rest of the calorimeter, where several remarks can be done:

- The agreement of all the diagonal bins (1-1, 2-2, etc.) improves. This is expected, as the parameters were fitted using these alone.
- Some off-diagonal bins (such as 2-1, 3-1, 2-1, etc.) also improve. This, however, happens only for bins very close to the diagonal.
- Some other off-diagonal bins, specially those where $|\eta_1 - \eta_2|$ is large, are considerably degraded. Such is the case of e.g. 6-2 and 7-2.

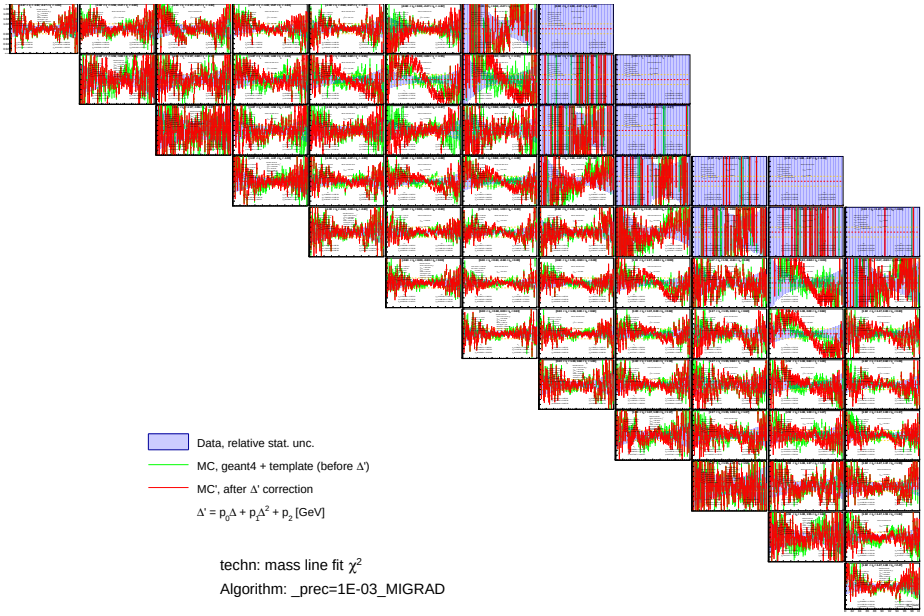

Figure 9: Data/MC mass lineshape ratios, before (green) and after (red) energy resolution correction via $\Delta' = p_0\Delta + p_1\Delta^2 + p_2$. The sets of best parameters $\hat{\vec{p}}_\eta$ were fitted individually, using only the diagonal bins.

The uneven improvement and great degradation of many bins initially led to believe that Δ' as defined in Eq. (4) is too simple, and that the inclusion of additional parameters was necessary. Several definitions were attempted using the same fitting methodology, such as

- $\Delta' = p_0\Delta + p_1\Delta^2 + p_2$
- $\Delta' = p_0\Delta + p_1\Delta^2 + p_2 + p_3\Delta^3$
- $\Delta' = p_0\Delta + p_1\Delta^2 + p_2 + p_3 \cdot E^{\mathrm{T}}_{\mathrm{truth}}$
- $\Delta' = p_0\Delta + p_1\Delta^2 + p_2 + p_3 \cdot E^{\mathrm{T}}_{\mathrm{reco}}$
- $\Delta' = p_0\Delta + p_1\Delta^2 + p_2 + p_3 \cdot E_{\mathrm{reco}}$
- $\Delta' = (p_0\Delta + p_1\Delta^2 + p_2)\,(1+p_3) + p_3 \cdot E_{\mathrm{truth}}$ (here, p_3 = energy scale α from Ref. [3])
- $\Delta' = \begin{cases} p_0\Delta + p_1\Delta^2 + p_2 & \text{if } \Delta > 0 \\ p_3\Delta + p_4\Delta^2 + p_2 & \text{if } \Delta < 0 \end{cases}$

but none of these were enough to account for off-diagonal effects.

By noticing that the disagreement grows as $|\eta_1 - \eta_2|$ increases and keeping Eq. (6) in mind, a couple of possible explanations quickly arise: either there is a problem with the

calibration of the tracker, or the diagonal and off-diagonal bins have different kinematics; both of which deserve further investigation (shown bellow).

The following checks were done for 3 regions in particular: an off-diagonal bin were the lineshape agreement greatly degrades (6-2, i.e. $[-0.60 < \eta < 0.00] \times [-1.82 < \eta < -1.52]$), and the corresponding diagonal ones (2-2 and 6-6).

5.1 Kinematics

In order to not do blind tests, let us remember Eq. (6), which gives a clear insight of the relationship between the dilepton mass and individual electron kinematics:

$$m_{ee}^2 = 2E_1E_2(1-\cos\theta_{12}) = 2E_1^{\mathrm{T}}E_2^{\mathrm{T}}\left[\cosh(\eta_1-\eta_2)-\cos(\phi_1-\phi_2)\right].$$

Since the azimuthal distribution ϕ should be homogeneous (up to local non-uniformities of the calorimeter, already corrected by this stage of the global calibration procedure, Figure 1), it is of interest to see mainly the behaviour of m_{ee}, energy, E^{T} and η. The corresponding distributions are shown in Figure 10.

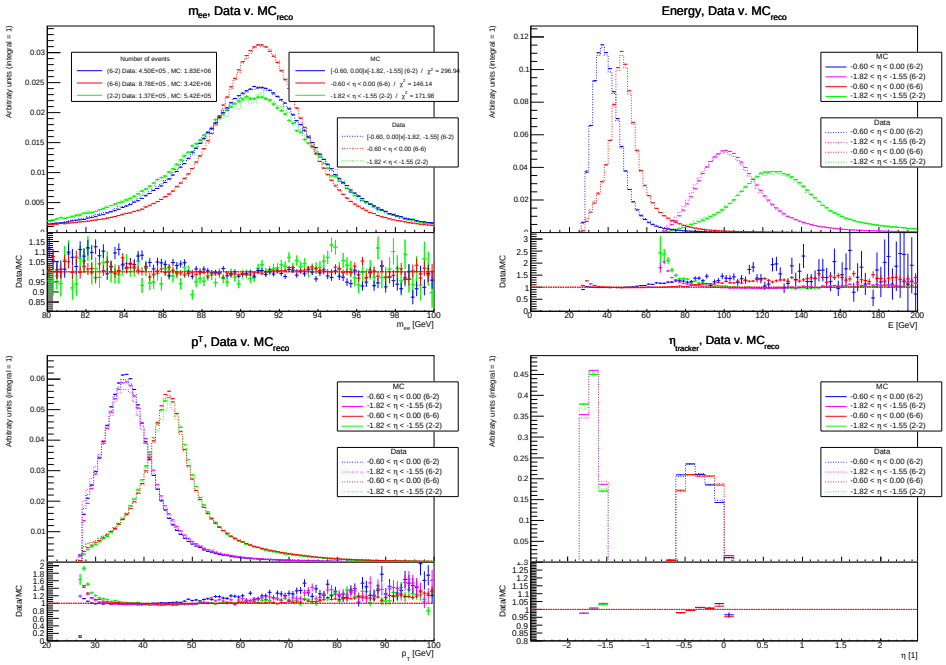

Figure 10: Comparison of kinematics between Data and nominal Reco MC for regions 6-6, 2-2, and 6-2. The integral of all the distributions has been normalized to 1.

5.1.1 Di-lepton mass m_{ee}

The least impressive check is the mass lineshape (Figure 10, top-left) ,as the changing shape of the distributions can be easily understood. Since the energy resolution degrades at larger η values due to geometrical (the endcaps point $\pm$ 4 cm away from the center of the calorimeter), structural (the electrons travel through more matter, specially at the cracks) and granularity reasons, one expects the original Breit-Wigner curve to be widened more for events measured in the endcap (e.g. at 2-2) than in the barrel (e.g. at 6-6). Furthermore, Bremsstrahlung at larger η contributes with additional tails at lower mass. The most relevant remark from this plot is that the Data/MC agreement is better at the barrel (red) than at the endcap (green and blue).

5.1.2 Energy E

As one would intuitively expect, events measured in the barrel are less energetic than those reaching the endcap (Figure 10, top-right). The agreement between Data and MC at the core of each distribution (that is, where most events are located) is reasonably good, degrading mainly towards the tails of each. That being said, there is a remaining non-negligible discrepancy, possibly created by the simulated resolution of the MC, which one would hope to reduce via the present study.

5.1.3 Transverse energy E^{T}

To first order, let us consider that the Z-boson has zero transverse energy i.e. $E_{\mathrm{Z}}^{\mathrm{T}} \approx 0$. For simplicity, let us assume also that the $Z \to ee$ reaction occurs immediately, at the geometrical center of the calorimeter, and that it has a width $\Gamma_Z = 0$. As 4-momentum conservation implies that $\vec{p}_1 + \vec{p}_2 = \vec{p}_{\mathrm{Z}}$,

$$E_1^{\mathrm{T}} \approx E_2^{\mathrm{T}}.$$

In the case where $p_{\mathrm{Z}}^{\mathrm{L}} \approx 0$, the total energy of the boson is $E_{\mathrm{Z}} = m_{\mathrm{Z}}$, so 4-momentum conservation implies that the electrons are emitted (almost) back-to-back with

$$|p_1| \approx |p_2| \approx m_{\mathrm{Z}}/2.$$

If both electrons fall in the same region by the center of the barrel (e.g. in 6-6), then $p_1^{\mathrm{L}} \approx p_2^{\mathrm{L}} \gtrsim 0$ while

$$E_1^{\mathrm{T}} \approx E_2^{\mathrm{T}} \approx 45 \text{ GeV}.$$

Furthermore, applying a boost along the longitudinal direction would increase the total energy of the boson (and of the electrons), all while E_i^{T} remains unchanged, forcing both electrons to be in the same region at larger η. This means that the E^{T} distribution in diagonal bins should be roughly the same, despite the region. The bottom-left plot of Figure 10 shows exactly this (red and green curves).

By extension, off-diagonal regions can be reached with non-longitudinal boosts, which would simply reduce the transverse energy of both electrons by a factor $\cos\theta^*$. This is also seen in Figure 10 (blue and purple, corresponding to each of the individual regions of 6-2).

Having understood these distributions, the main takeaway is that diagonal and off-diagonal bins correspond to different "points" in the E^{T} spectrum. Other studies, such as the one described in Ref. [3], treat this effect with (η, E^{T}) binning. However, this would greatly increase the number of parameters and regions that must be fitted. An alternative is to include the explicit dependence on E^{T} in the definition of Δ'. Since the resolution correction acts only on MC, a candidate for such dependence is

$$\begin{aligned}\Delta' = &\left[p_0 + p_3(E^{\mathrm{T}}_{\mathrm{truth}} - 45\ \mathrm{GeV})\right]\Delta + \left[p_1 + p_4(E^{\mathrm{T}}_{\mathrm{truth}} - 45\ \mathrm{GeV})\right]\Delta^2 \\ &+ \left[p_2 + p_5(E^{\mathrm{T}}_{\mathrm{truth}} - 45\ \mathrm{GeV})\right]\end{aligned} \tag{14}$$

5.1.4 Pseudo-rapitidy η

Looking back at Figure 9 and noticing that the bigger degradation occurs at large $|\eta_1 - \eta_2|$, along with the dependence in Eq. (6), it is of interest to check whether the tracker plays a role in the mass lineshape disagreement. The distributions of pseudo-rapidity measured with the tracker are shown at the bottom-right of Figure 10. While the disagreement between Data and MC is relatively small, it is not perfect and cannot be explained by the statistical uncertainty alone. Since the dilepton mass depends greatly on η (and ϕ, Equations (5) and (6)), the tracker deserve additional checks, which are presented in Subsection 5.2.

5.2 Influence of the tracker in the mass discrepancy

A quick way to check whether the discrepancy in the η distributions shown in Figure 10 has an impact on the invariant mass distribution is by reweighting the MC sample, so that the agreement with Data becomes perfect. Figure 11 shows the effect of such reweighting on the distributions of pseudo-rapidity η (also shown within each mass lineshape plot), which is of interest due to its contribution to the computation of E^{T} and $\eta_1 - \eta_2$. The reweighting was done for η-regions 2-2, 6-6, and 6-2.

Comparing the before and after mass ratios (and χ^2 to data), it is clear that the exactness of the MC reconstruction of η does not play a major role in the observed mass discrepancy. This is specially clear when looking at the bottom plot of Figure 11, which shows the relative change of MC mass lineshape after the reweighting.

As shown by Eq. (6), the invariant mass computation depends explicitly on the difference of angles $\eta_1 - \eta_2$ and $\phi_1 - \phi_2$, so having an insight of these distributions is also of interest. These are presented in Figure 12, by comparing Data to Reco MC (top), and Reco MC to Truth MC (bottom).

Similarly to the distributions of η (Figure 11, top-left), there is a small discrepancy of a few per-cent between Data and MC which proved to have a negligible impact on the mass lineshape. Furthermore, the two plots at the bottom of Figure 12 show an almost perfect reconstruction of these angle differences, meaning that the resolution of the MC tracker has no noticeable impact on these angle differences.

Finally, the MC resolution of the tracker (Figure 13, bottom-right) is briefly inspected. Seeking to discard a possible bias from the tracker reconstruction, the nominal reconstructed mass $m_{ee,\mathrm{reco}}$ is compared to the cases where either η_{truth} or ϕ_{truth} replace

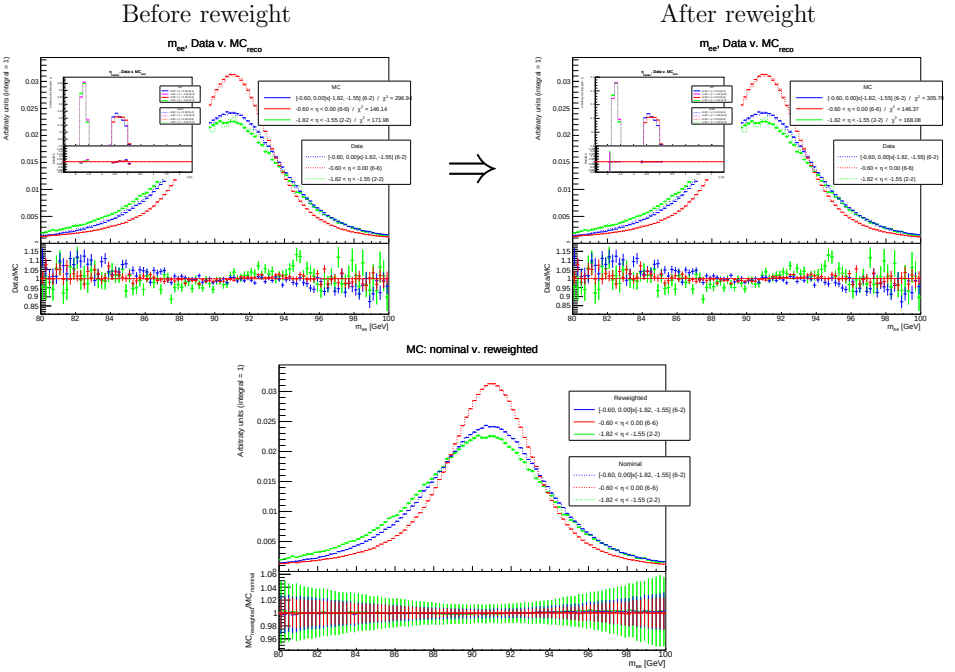

Figure 11: Top: mass lineshape comparison for bins 6-6, 2-2 and 6-2 before and after reweighting the MC distributions of η to perfectly match those of Data. The η distributions (before and after) are shown within the margins of the corresponding lineshape plot. Bottom: comparison of nominal and reweighted MC mass lineshapes, showing the isolated effect of the reweighting on the mass distribution.

the analogous Reco quantity, effectively getting rid of resolution effects. Figure 13 shows this in 3 different ways:

- $\eta_{\text{reco}} \to \eta_{\text{truth}}$: corresponding to the mass $m_{ee,\text{reco}}(\eta_{\text{truth}})$
  (in consequence, $E^{\text{T}}_{\text{reco}}$ also changes, Eq. (5))
- $\phi_{\text{reco}} \to \phi_{\text{truth}}$: corresponding to the mass $m_{ee,\text{reco}}(\phi_{\text{truth}})$
- $\eta_{\text{reco}}, \phi_{\text{reco}} \to \eta_{\text{truth}}, \eta_{\text{truth}}$: corresponding to the mass $m_{ee,\text{reco}}(\eta_{\text{truth}}, \phi_{\text{truth}})$
  (i.e. no tracker resolution whatsoever $\to E^{\text{T}}_{\text{reco}}$ also changes).

A quick comparison between these plots reveals that the resolution of η_{tracker} plays a larger role than that of ϕ_{tracker}, as the induced discrepancy in the mass ratio is larger. Nevertheless, it is well within statistical uncertainty, and shows no bias in any of the 3 studied cases.

Putting all the previous inspections together, one can safely discard the tracker as the source of the mass discrepancy. Of course, more rigorous checks can always be done in

order to completely trust the tracker calibration and take it as perfect, but this is beyond the scope of the study presented here.

Furthermore, while angular measurements seem to play no role, different regions show different kinematics, which are well described by their E^{T} distributions. Thus, following energy resolution calibration studies are done keeping this dependence in mind, using Δ' definitions as that shown in Eq. (14).

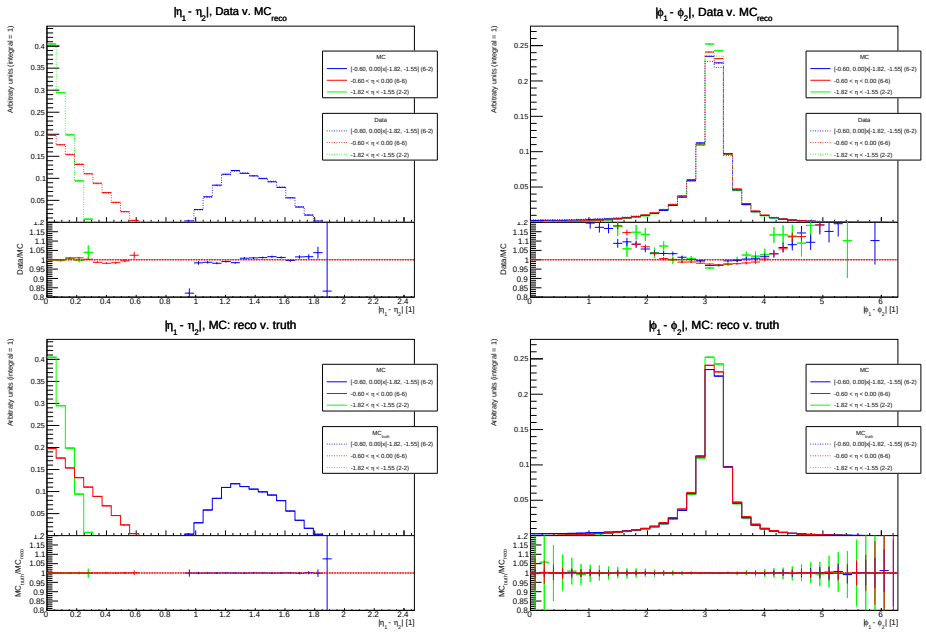

Figure 12: Distributions of $|\eta_1 - \eta_2|$ and $|\phi_1 - \phi 2|$ for regions 2-2, 6-6, and 6-2. Top: comparison of Data to Reco MC Bottom: comparison of Reco MC to Truth MC.

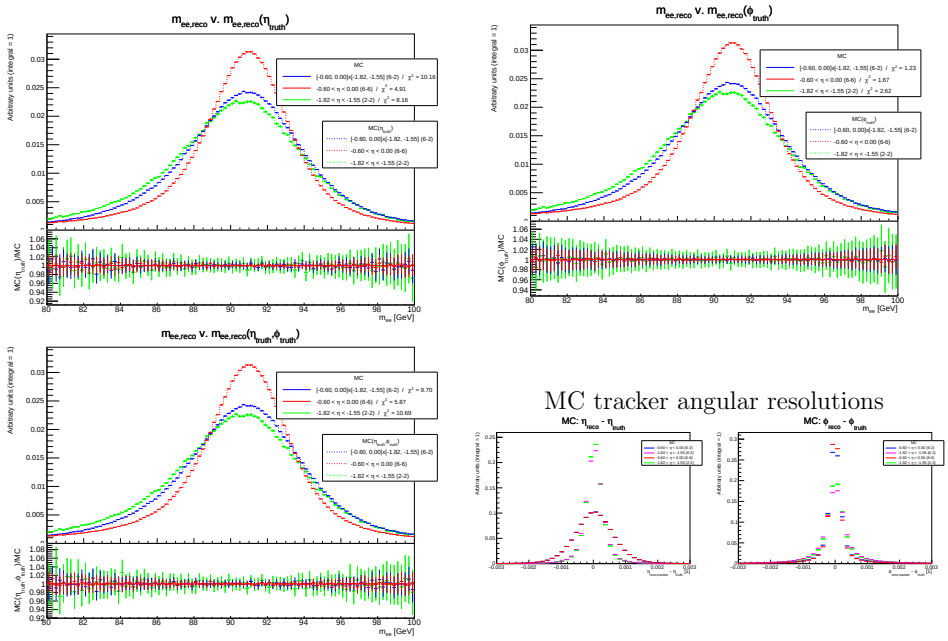

Figure 13: Effect of the MC tracker resolution on the mass discrepancy. The plots show the effect of completely removing the simulated resolution (using Truth instead of Reco) for η (top-left), ϕ (top-right) and η, ϕ simultaneously (bottom-left). The MC tracker resolutions (i.e. Reco $-$ Truth) for both angular quantities are shown at the bottom-right.

6 Calibration

Having in mind the checks done in Section 5, the search for a "good" definition of Δ' that works on all the calorimeter is not a completely blind task anymore. We have learned that:

- Bin-to-profiledPDF χ^2 should be used to find the best parameters $\hat{\vec{p}}_\eta$
- Increasing the complexity of Δ' is not a guaranty of improving the mass lineshape agreement
  - More parameters = more difficult problem for MINUIT
- No noticeable tracker effects $\rightarrow$ no explicit angular dependence required
- Kinematics change for different η-regions $\rightarrow$ specially different E^{T} distributions
  - Explicit parameter $E^{\mathrm{T}}_{\mathrm{truth}}$ dependence is promising

so, as it has already been suggested with Eq. (14), a good candidate is

$$\Delta' = \left[p_0 + p_3(E^{\mathrm{T}} - 45\ \mathrm{GeV})\right]\Delta + \left[p_1 + p_4(E^{\mathrm{T}} - 45\ \mathrm{GeV})\right]\Delta^2 + \left[p_2 + p_5(E^{\mathrm{T}} - 45\ \mathrm{GeV})\right].$$

There is a subtlety here: as explained in Subsection 5.1, each η-region corresponds (roughly) to a single E^{T} point. This means that simply fitting on the diagonal bins and propagating to the rest of the calorimeter is not enough anymore.

Since different momentum regions must be sampled in order to estimate the E^{T} dependence for a particular set $\vec{p}_\eta$ (in Eq. (14), these are p_3, p_4, p_5), the χ^2_{global} used in the minimization must include few regions at different E^{T}. So, in order to estimate e.g. $\vec{p}_{\eta\text{-}2}$ and looking at Figure 10 (bottom-left), one could include regions 2-2 and 6-2. This hints a few minimization methodologies, which are discussed in Subsection 6.1.

6.1 Minimization methodologies

6.1.1 3-bin fits

The most simple approach consists of using as few bins as possible, while sampling different kinematic regions. If we are interested in determining $\vec{p}_{\eta\text{-}i}$, a sensible choice would be to include the corresponding diagonal bin and one off-diagonal, i.e. i-i and i-j (for $i \neq j$). But since i-j is also sensitive to the parameters $\vec{p}_{\eta\text{-}j}$, one could include the corresponding diagonal bin, j-j, and minimize both sets of parameters simultaneously. Going back to Figure 10, this means that $\vec{p}_{\eta\text{-}2}$ and $\vec{p}_{\eta\text{-}6}$ can be simultaneously determined by minimizing

$$\chi^2_{\mathrm{global}} = \chi^2_{2\text{-}2} + \chi^2_{6\text{-}2} + \chi^2_{6\text{-}6},$$

which allows to account for inter-region correlations while sampling at two different E^{T} sectors for each set of parameters.

The main disadvantage of this method is that many combinations could give multiple measurements of the same set, e.g. by determining $\vec{p}_{\eta\text{-}2}$ and $\vec{p}_{\eta\text{-}6}$, $\vec{p}_{\eta\text{-}2}$ and $\vec{p}_{\eta\text{-}5}$, $\vec{p}_{\eta\text{-}2}$ and $\vec{p}_{\eta\text{-}4}$, etc. Each measurement would probe E^{T} with different sensitivities and changing correlations, so combining them into a single value becomes non-trivial.

6.1.2 Global fits

On the other extreme, there is the global fit. This means that all 12 sets of parameters could be determined simultaneously by looking at the whole calorimeter i.e. minimizing $12 \times 6 = 72$ parameters over ~ 60 different regions. A Global Fit is the ideal way to go, as it samples all the available phase-space and follows the inter-region correlations for all parameters, but it comes at a price.

By including more free parameters and increasing the complexity of the FCN $= \chi^2_{\text{global}}$ function, the time needed by MINUIT to minimize it scales exponentially, and the small χ^2 fluctuations mentioned earlier contribute to a poor estimation of the gradient. This translates into an excessively long waiting time before MINUIT finishes a single iteration, which can take over a day to estimate the gradient at a single $[\vec{p}_1, .., \vec{p}_{12}]$ point, without a guarantee of obtaining an improvement at the end.

6.1.3 SemiGlobal fits

It is clear that fits must include as many η-regions as possible (if not all), and that the parameters of different regions $\vec{p}_\eta$ must talk among themselves. A good approach for this is a compromise between 3-bin fits and Global studies, which will be called iterative SemiGlobal fits.

A single SemiGlobal fit will consist of minimizing a single set of parameters $\vec{p}_{\eta\text{-}k}$ at a time, using the whole calorimeter (equivalent to using all the regions k-j $\forall j$), while leaving the rest of the parameters fixed. This give 12 independent estimations for each of the parameter sets, as exemplified in Figure 14. However, there is no inter-region communication, and since off-diagonal regions are affected by two sets of parameters at a time (2 different electrons), a single fit like this is not enough. Thus, iterations must be done.

The procedure is as follows:

1. Set the initial value of all sets of parameters to their default value i.e. $p_0 = 1.0$ and $p_1 = p_2 = ... = 0.0$.
2. Do a first SemiGlobal fit for each set of parameters i.e. 12 independent fits.
3. Set the latest fitted parameters as new initial values for all regions.
   - Which is equivalent to "correct" the calorimeter with these.
   - This gives an improvement in the diagonal, but can degrade the other regions (until enough iterations are done).
4. Re-do the 12 independent SemiGlobal fits.
5. Repeat from step 3 until all parameters stabilize (about 20 iterations required).

In an attempt to not contaminate the fits with poor statistics regions, far off-diagonal bins (e.g. 7-1 and beyond) are excluded from the χ^2 computation. As the number of events contained in such regions is extremely small (relative to those closer to the diagonal), and the E^{T} distributions get truncated close to their core due to the 27 GeV cut, excluding such bins should not have a major impact in the minimization process.

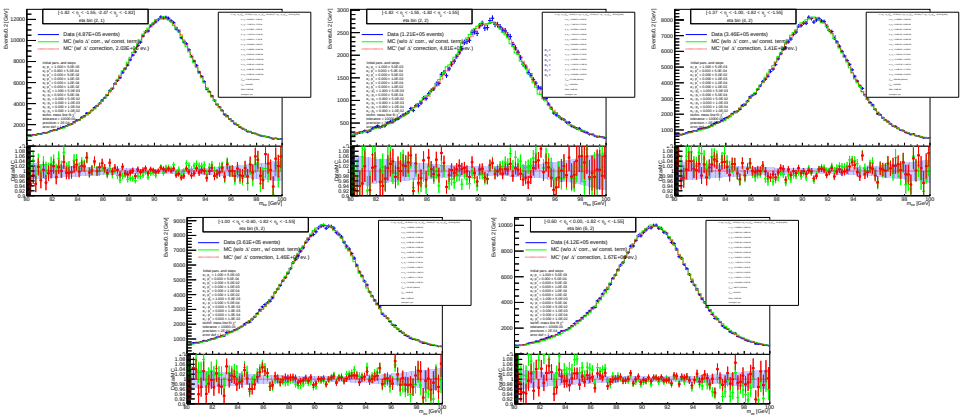

Figure 14: Initial SemiGlobal fit for parameters $\vec{p}_{\eta\text{-}2}$ using Δ' as defined in Eq. (14), determined using regions 2-1, 2-2, 4-2, 5-2 and 6-2. The values of $\vec{p}_{\eta\text{-}1}, \vec{p}_{\eta\text{-}4}, \vec{p}_{\eta\text{-}5}, \vec{p}_{\eta\text{-}6}$ are kept at their initial value. N.B. a standalone iterative fit improves the mass agreement in all regions (as shown above), but combining it with the fitted parameters from other regions will lead to degradation in the off-diagonal region due to over-correction. Thus, iterations are necessary.

6.2 Interpretation of results

Since the minimizations are done in an $[\eta_1, \eta_2]$-bin basis, looking at a grid as in Figure 4 can give a very good insight of the impact in small regions (which should improve almost by definition), as well as possible asymmetric effects in the calorimeter. Nonetheless, a better way to visualize it is by looking at the effect of the calibration in larger regions, such as barrel/endcap regions or the whole calorimeter.

The following few sections show the fitted results summarized in very few plots. A more comprehensive selection of plots can be found in Appendix B for each of the Δ' definitions of interest.

6.2.1 Energy resolution

Seeking to track down the impact of this study into the detector resolution, it is useful to remind that

$$\frac{\sigma_E}{E} = \frac{a}{\sqrt{E}} \oplus \frac{b}{E} \oplus c \tag{15}$$

where a is the stochastic term (i.e. associated to the signal), b accounts for noise, and c is the constant term of the calorimeter. The resolution curves (before and after calibration) can be found in Appendix B.

While the description of the relative resolution given in Eq. (15) is typically enough, it best works for symmetric, normally-distributed resolution curves. The reason for that being that the quantity σ_E is a measurement of the resolution distribution width, and

does not take into consideration its actual shape. Moreover, the energy of the detected particles is affected by Bremsstrahlung, which increases the lower energy tails.

This simply means that, while it is interesting to look at the values of a, b, c before and after the calibration, their comparison must be done with care, as these are not capable of accounting for asymmetries and tail effects (which can be strongly modified by the Δ' correction).

6.3 First order $E^{\mathrm{T}}_{\mathrm{truth}}$ dependence, for positive and negative η

$$\Delta' = \left[p_0 + p_3(E^{\mathrm{T}}_{\mathrm{truth}} - 45\ \mathrm{GeV})\right]\Delta + \left[p_1 + p_4(E^{\mathrm{T}}_{\mathrm{truth}} - 45\ \mathrm{GeV})\right]\Delta^2 + \left[p_2 + p_5(E^{\mathrm{T}}_{\mathrm{truth}} - 45\ \mathrm{GeV})\right] \tag{16}$$

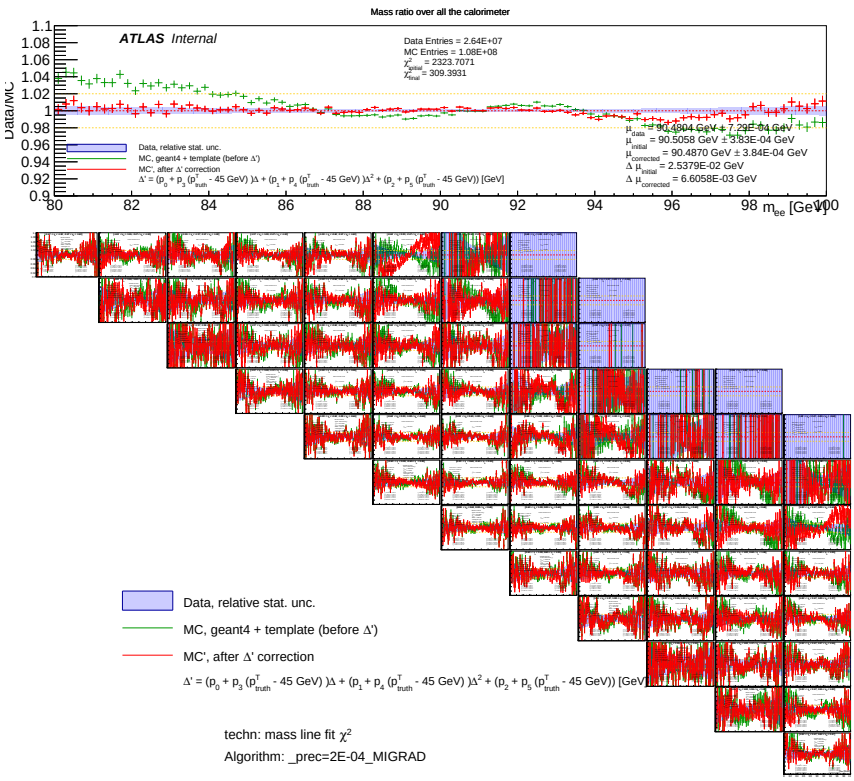

Figure 15: Data/MC mass lineshape ratios, for Δ' defined as in Eq. (16). The sets of best parameters $\hat{\vec{p}}_\eta$ were estimated iteratively with SemiGlobal fits.

A more detailed set of plots for the same parametrization can be found in Appendix B.1.

Quickly inspecting the mass ratios at high $\Delta\eta$ in Figure 15 for conceptually symmetric bins (such as 6-1 and 12-7), one can observe non-negligible differences after the Δ' correction, even if the initial ratios are very similar. Moreover, large geometrical asymmetries are not expected a priori. Since this study seeks to concentrate on the effects of the Δ' correction rather than on more specialized detector inhomogeneities, in the following fits are performed in bins of $|\eta|$ i.e. only 6 sets of parameters are to be found, although the results are still shown in the 12 by 12 grid to spot such inhomogeneities (if present).

6.4 First order $E^{\mathrm{T}}_{\mathrm{truth}}$ dependence, for $|\eta|$

$$\Delta' = \left[p_0 + p_3(E^{\mathrm{T}}_{\mathrm{truth}} - 45\ \mathrm{GeV})\right]\Delta + \left[p_1 + p_4(E^{\mathrm{T}}_{\mathrm{truth}} - 45\ \mathrm{GeV})\right]\Delta^2 + \left[p_2 + p_5(E^{\mathrm{T}}_{\mathrm{truth}} - 45\ \mathrm{GeV})\right] \tag{17}$$

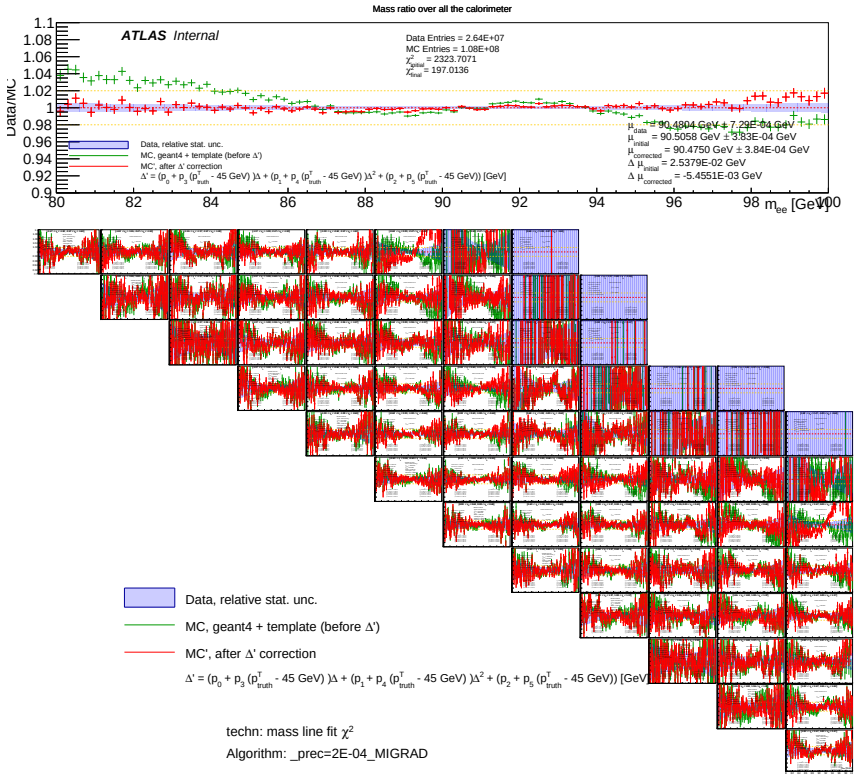

Figure 16: Data/MC mass lineshape ratios, for Δ' defined as in Eq. (17). The sets of best parameters $\hat{\vec{p}}_\eta$ were estimated iteratively with SemiGlobal fits.

When looking at the effect over all the calorimeter (Figure 16, top), there is an evident improvement compared to Subsection 6.3, likely due to the reduced number number of

free parameters, which in turn allows for simpler correlations. Nonetheless, η-bins with large $\Delta\eta$ (far from the diagonal, see the bottom plot of Figure 16) get degraded, showing that linear E^{T} dependence is not enough. A more detailed set of plots for the same parametrization can be found in Appendix B.2.

6.5 Second order $E^{\mathbf{T}}_{\mathbf{truth}}$ dependence, for $|\eta|$

$$\begin{aligned}\Delta' = &\left[p_0 + p_3(E^{\mathrm{T}}_{\mathrm{truth}} - 45\ \mathrm{GeV})\right]\Delta + \left[p_1 + p_4(E^{\mathrm{T}}_{\mathrm{truth}} - 45\ \mathrm{GeV})\right]\Delta^2 \\ &+ \left[p_2 + p_5(E^{\mathrm{T}}_{\mathrm{truth}} - 45\ \mathrm{GeV}) + p_6(E^{\mathrm{T}}_{\mathrm{truth}} - 45\ \mathrm{GeV})^2\right]\end{aligned} \tag{18}$$

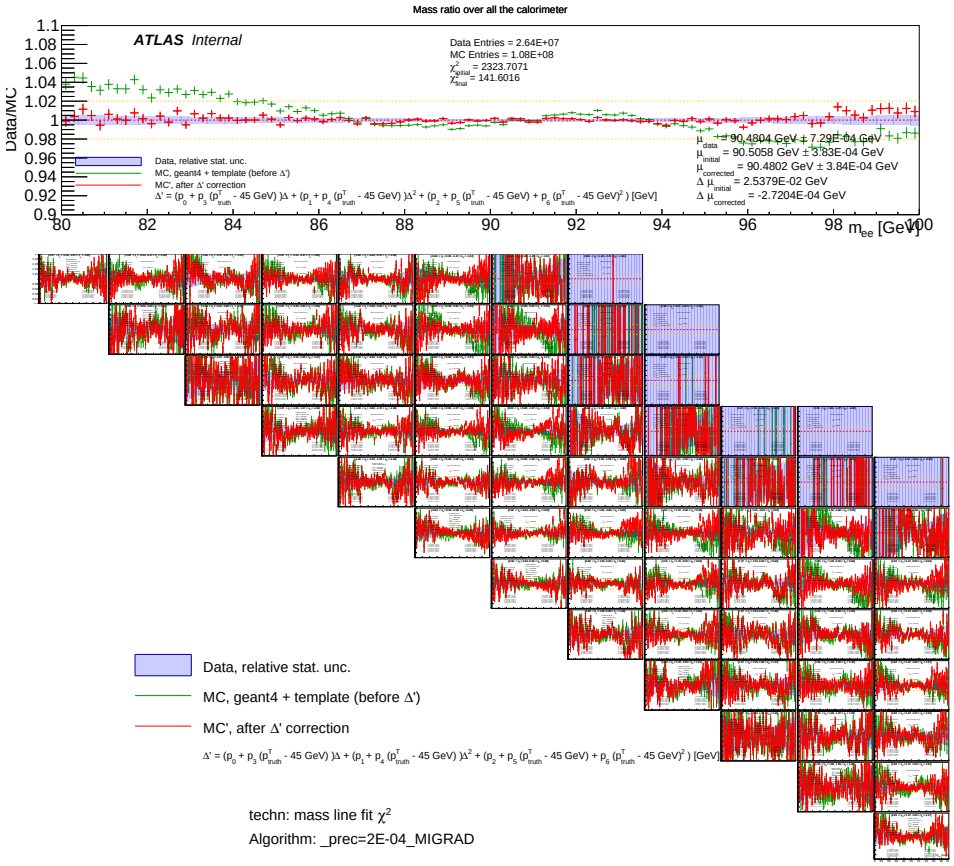

Figure 17: Data/MC mass lineshape ratios, for Δ' defined as in Eq. (18). The sets of best parameters $\hat{\vec{p}}_\eta$ were estimated iteratively with SemiGlobal fits.

A more detailed set of plots for the same parametrization can be found in Appendix B.3.

6.6 Third order $E^{\mathrm{T}}_{\mathrm{truth}}$ dependence, for $|\eta|$

$$\Delta' = \left[p_0 + p_3(E^{\mathrm{T}}_{\mathrm{truth}} - 45\ \mathrm{GeV})\right]\Delta + \left[p_1 + p_4(E^{\mathrm{T}}_{\mathrm{truth}} - 45\ \mathrm{GeV})\right]\Delta^2 + \left[p_2 + p_5(E^{\mathrm{T}}_{\mathrm{truth}} - 45\ \mathrm{GeV}) + p_6(E^{\mathrm{T}}_{\mathrm{truth}} - 45\ \mathrm{GeV})^2 + p_7(E^{\mathrm{T}}_{\mathrm{truth}} - 45\ \mathrm{GeV})^3\right] \quad (19)$$

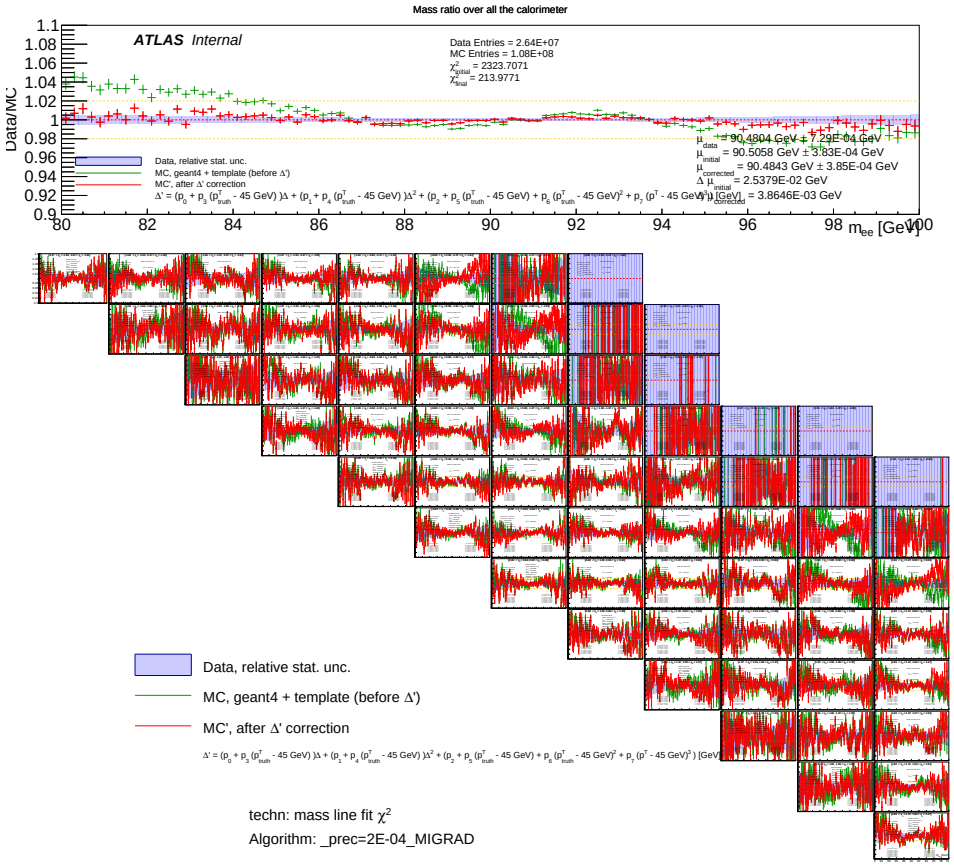

Figure 18: Data/MC mass lineshape ratios, for Δ' defined as in Eq. (19). The sets of best parameters $\hat{\vec{p}}_\eta$ were estimated iteratively with SemiGlobal fits.

A more detailed set of plots for the same parametrization can be found in Appendix B.4.

6.7 Problem with resolution distributions

While there is a clear improvement of the mass lineshape agreement, the story is not perfect for other physical quantities. Let us look for instance at the behaviour of the energy resolution (Figure 19) obtained for Δ' as defined by Eq. (19).

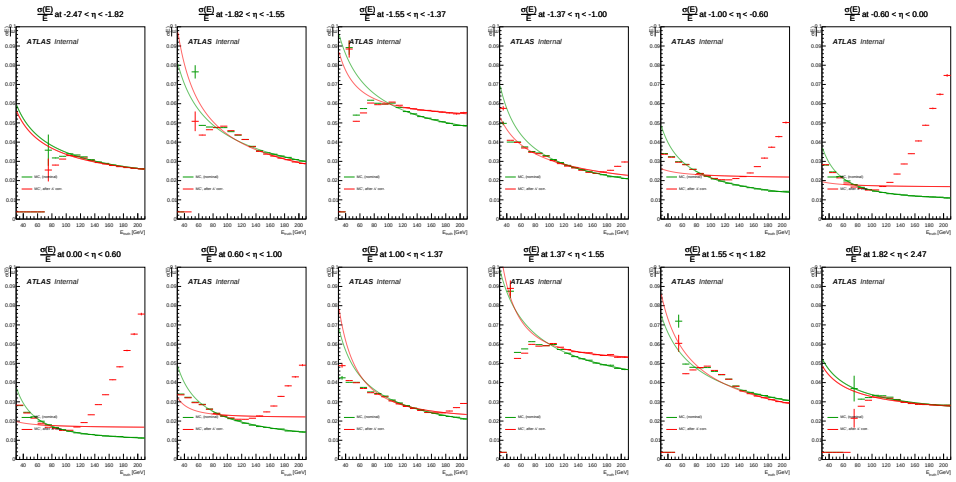

Figure 19: Resolution curves, obtained for each η region before and after the Δ' correction. The curves are fitted with Eq. (15), using only the range $E_{\text{truth}} > \cosh\eta_{\text{max}} \times 50$ GeV in order to stay away from the 27 GeV $E^{\text{T}}_{\text{truth}}$ cut (and the corresponding truncation of the resolution distribution).

While the resolution is well behaved in the endcaps ($|\eta| > 1.37$), there is a non-physical behaviour in the barrel ($|\eta| < 1.37$) at energies above 100 GeV. In order to understand this, one must look at the corresponding resolution distributions. Figure 20 shows examples of these distributions, for a couple of energies in the $0.0 < \eta < 0.6$ region, which are consequently used to obtain some of the values plotted in Figure 19.

Focusing on the resolution distributions after the Δ' correction (Figure 20, in red), an unhealthy deformation of the distribution is visible by eye. The strange shape is in fact artifact of having different parameter values $\vec{p}_\eta$ for each region: since each of the shown distributions collect events from different η-bins (such as 7-1,7-2,7-3,etc.) and there is a strong correlation with the sibling-electron (and the corresponding correction parameters), a small mis-estimation of the parameters can generate a splitting of the original resolution distribution into the number of parameter sets. In this particular case, since the fit was done in regions of $|\eta|$, the splitting generates up to 6 sub-distributions.

Moreover, keeping in mind the energy distribution shown in Figure 10 along Eq. (6), and baring in mind that the minimization of the parameters of Δ' is done in the 80 to 100 GeV range, it is easy to realize that (in the barrel) large energies give masses outside the fit range, and thus their correction is being extrapolated.

If the best parameters obtained through the fit are not at the exact minimum (which could happen in this scenario due to the remnant χ^2 micro-fluctuations and large number of free parameters), consistency across η-regions could be lost. Furthermore, the E^{T} dependence (equivalent to energy, up to a $\cosh\eta$ factor) of the Δ' function can greatly amplify the effect of the parameter mis-estimation, specially for higher order E^{T} dependence.

From a technical point of view, the previous remarks simply mean that high order E^{T} dependencies should not be abused. Moreover, looking at Figure 19, this problem can be localized to only the barrel, which arises a natural alternative: to use linear E^{T} dependence for $|\eta| < 1.37$, and third order one for the rest of the calorimeter. This combined definition of Δ' is briefly studied in Subsection 6.8.

While beyond the scope of this initial study, a possible (more generalized) treatment to such problems with the extrapolation is to investigate the influence of different fitting ranges in the post-fit mass agreement and the corresponding resolution distributions.

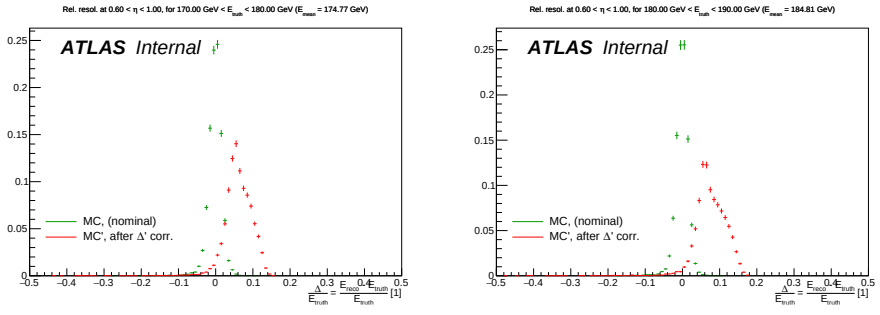

Figure 20: Resolution distributions for Δ' as in Eq. (19), in $0.0 < \eta < 0.6$, for energies $170 < E_{\mathrm{truth}} < 180$ GeV (left) and $180 < E_{\mathrm{truth}} < 190$ GeV (right). The nominal distribution (in green) follows the typical quasi-gaussian behaviour, but the corrected one can get over-deformed and split into several sub-distributions (up to one per set of $\vec{p}_\eta$).

6.8 Combined First and Third order $E^{\mathrm{T}}_{\mathrm{truth}}$ dependence, for $|\eta|$

$$\Delta' = \left[p_0 + p_3(E^{\mathrm{T}}_{\mathrm{truth}} - 45\ \mathrm{GeV})\right]\Delta + \left[p_1 + p_4(E^{\mathrm{T}}_{\mathrm{truth}} - 45\ \mathrm{GeV})\right]\Delta^2 + \begin{cases} \left[p_2 + p_5(E^{\mathrm{T}}_{\mathrm{truth}} - 45\ \mathrm{GeV})\right] & \text{if } |\eta| < 1.37 \\ \left[p_2 + p_5(E^{\mathrm{T}}_{\mathrm{truth}} - 45\ \mathrm{GeV}) + p_6(E^{\mathrm{T}}_{\mathrm{truth}} - 45\ \mathrm{GeV})^2 + p_7(E^{\mathrm{T}}_{\mathrm{truth}} - 45\ \mathrm{GeV})^3\right] & \text{if } |\eta| > 1.37 \end{cases} \quad (20)$$

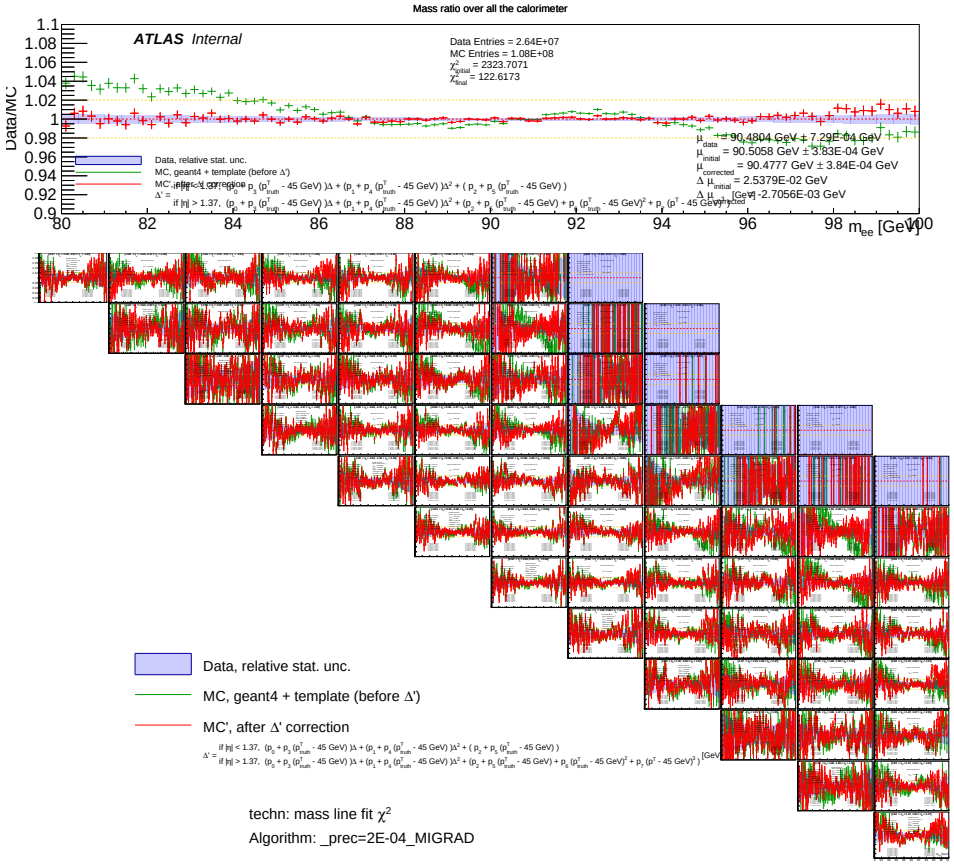

Figure 21: Data/MC mass lineshape ratios, for Δ' defined as in Eq. (20). The sets of best parameters $\hat{\vec{p}}_\eta$ were estimated iteratively with SemiGlobal fits.

Compared to the First (Subsection 6.4), Second (Subsection 6.5) and Third (Subsection 6.6) order E^{T} dependences, the combined Δ' definition of Eq. (20) shows the best and most stable improvement in all regions of the calorimeter. Moreover, it extrapolates well to energy regions outside of the phase-space of the fit. This is specially easy to notice by inspecting the plots for larger regions shown in Appendix B.5.

7 Conclusions

Seeking to better understand the mass lineshape discrepancy between the Data and MC of $Z \to ee$ events, the effects of the tracker and the calorimeter have been inspected. The former was shown to have a negligible impact in the mass distribution, being incapable of explaining (to first order) the lineshape disagreement. Thus, the study shown here is focused on the latter, particularly on the energy resolution distributions, and on a newly proposed correction methodology based on resolution scalings.

By looking at the event-by-event MC energy resolution $\Delta = E_{\text{reco}} - E_{\text{truth}}$, a proposed event-wise resolution correction is applied through scalings via some parametrization $\Delta' = f(\Delta)$ (typically a polynomial form), capable of finely tuning the shape of the energy resolution distribution by accounting for specific effects, such as tails and negative smearing corrections.

As shown through this study, performed in regions of η, the shape of the energy resolution distribution is of key importance to understand the mass lineshape discrepancy between Data and MC. Namely, the lineshape agreement can be substantially improved via deformation of the resolution distribution shape alone.

Furthermore, purely Δ-dependent scalings were found to not be enough to properly correct the energy resolution through all the calorimeter. As the kinematics of the electron-pair change across different regions of the calorimeter, E^{T}-dependent scalings were required in order to properly account for them. This just means that the studied corrections took the general form $\Delta' = f(\Delta, E^{\text{T}}_{\text{truth}})$.

As Δ scalings deform the resolution distributions in non-symmetric ways, the typical description of the resolution via $\sigma_E/E = a/\sqrt{E} \oplus b/E \oplus c$ (which only looks at the width of the distribution) is not enough to account for such fine changes. This means that one cannot expect a reduction of the relative resolution σ_E/E even when the lineshape agreement has improved greatly.

Moreover, one must be conservative with the inclusion of higher order dependencies in the definition of Δ', specially for energy (and equivalently, E^{T}) related ones. The reason being that a small mis-estimation of the minimum could greatly propagate as a non-physical deformation of the resolution distribution when extrapolating the resolution correction to electrons with energies outside of the fit range.

Overall, energy resolution corrections via scalings show very promising improvements in the Data/MC mass lineshape agreement. It shows that possible mis-modeling of the response of the detector could be the cause of (some of) the remaining observed discrepancies, which are well counteracted by using Eq. (20).

Further investigation is encouraged, both to find a definition of Δ' that works better than that shown in Eq. (20), and to properly estimate the fitted parameter errors via resampling techniques (such as toy replicas or bootstrap). Now that a stable framework has been designed, the previous tasks are considerably easier to be performed although time consuming. That being said, one can also aim to find ways of enhancing the code, as by using alternative techniques (or improving the current ones) one could optimise the minimisation time and precision of the fitted parameter values. Moreover, such improvements could eventually allow to perform a global minimization where the parameters for all the η-regions are simultaneously determined, fully taking into account their correlations.

Acknowledgements

We would also like to thank Guillaume Unal and Maarten Boonekamp for their continuous feedback and suggestions along the development of this study. We also thank Linghua Guo for quickly making available the latest Data and MC samples, and further discussions which allowed to better understand the nominal samples.

References

[1] Hicham Atmani; et al. *Electron energy calibration using in-situ energy and resolution scale factors from* Z → *ee events*. *ATLAS Internal Note*, ATL-COM-PHYS-2017-757, 2017.

[2] Siqi Yang; Cheng Wang. https://indico.cern.ch/event/857807/contributions/3615377/attachments/1932510/3201225/ElectronCalibration.pdf. (Online; accessed 12.08.2021).

[3] Linghua Guo. *Electron energy in-situ calibration and linearity measurements from* Z → *ee events*. *ATL-COM-PHYS-2020-757*, Oct 2020.

[4] Frederick James. *MINUIT Function Minimization and Error Analysis: Reference Manual Version 94.1*. *CERN-D-506*, 1994.

[5] Rene Brun and Fons Rademakers. *ROOT: An object oriented data analysis framework*. *Nucl. Instrum. Meth. A*, 389:81–86, 1997.

[6] Glen Cowan. Statistical Data Analysis. Oxford science publications. Clarendon Press, 1998.

[7] Bradley Efron. The Jackknife, the Bootstrap and Other Resampling Plans. Society for Industrial and Applied Mathematics, 1982.

[8] Juan Salvador Tafoya Vargas. *Treatment of* χ^2 *fluctuations due to bin-to-bin event migration in inter-sample distribution shape comparisons*. *ATL-COM-SOFT-2021-082*, Oct 2021.

A Bootstrap

One of the first attempts to understand and treat the χ^2 fluctuations was through re-sampling techniques. In particular, by doing bootstrap when creating the MC histogram, and inspecting the variance of the χ^2 curve at each value of $\vec{p}$.

A simple check was done on a manual χ^2 scan for $\Delta' = p_0\Delta + p_1\Delta^2 + p_2$, where p_0 and p_1 are left as fixed to their initial values (1 and 0, respectively), and only p_2 changes. The χ^2 is computed bin-to-bin between PseudoData (computed using half of the MC for $\vec{p}_{\text{pseudo}} = (1, 0, 0)$) and MC (using only the remaining half, so that it is uncorrelated to PseudoData).

For each value of p_2, 100 bootstrap replicas of the MC histogram where obtained, and the corresponding bin-to-bin χ^2 value against PseudoData was computed. Naturally, this means that for each p_2 there is an (almost gaussian) distribution of χ^2 values, whose standard deviation corresponds to the variance of the χ^2. Figure 22 shows the central value of the curve (before bootstrap was done), as well as the envelope generated by standard deviation obtained after bootstrap at each point.

The initial hope was that, if the fluctuations of the central curve were simply due to statistical effects, the distribution generated by the bootstrap would yield a parabolic smooth envelope around the nominal curve. Nevertheless, as it can be seen in Figure 22, this is not the case, and the envelope fluctuates in the same fashion as the original curve.

As it is described in Ref. [8], the fluctuations are consequence of event migration between bins in a histogram, which generate a discontinuous change in the sample size of each bin. Thus, this cannot be captured (and compensated) through typical re-sampling.

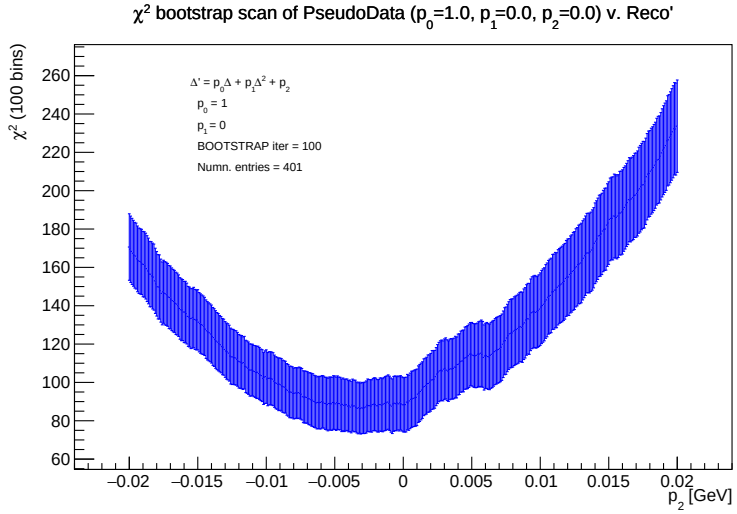

Figure 22: Manual bin-to-bin χ^2 scan done for PseudoData, showing the χ^2 envelope (size = 1 RMS) obtained via performing bootstrap on MC for each value p_2. As it is known, the variance of the χ^2 is roughly $\sqrt{2 \times \text{d.o.f.}}$.

B Fit results

Bellow are shown several plots useful to inspect the results for the parametrizations shown in Subsection 6.4, 6.5 and 6.6. These consist primarily of Data/MC mass lineshape ratios, before (green) and after (red) the resolution correction via Δ', as well as its effect on the resolution curve.

For each of the Δ' definitions of interest, the following plots are shown (in order):

- Grid of $[\eta_1, \eta_2]$ mass ratios, showing the impact of the fitted parameters in the regions seen by MINUIT.
- The value of the fitted parameters $\hat{\vec{p}}$, in order of increasing index value (p_0,p_1,p_2...) from left to right, and top to bottom.
- Mass ratio in larger regions, excluding the crack ($1.37 < |\eta| < 1.55$)
  - Barrel-Barrel: both electrons s.t. $0 < |\eta_i| < 1.37$
  - Endcap-Endcap: both electrons s.t. $1.55 < |\eta_i| < 2.47$
  - Barrel-Endcap: $0 < |\eta_1| < 1.37$ and $1.55 < |\eta_2| < 2.47$ (or vice-versa).
- Analogous to the previous point, but in the regions defined in the W-boson analyses (crack at $1.2 < |\eta| < 1.8$)
  - Barrel-Barrel: both electrons s.t. $0 < |\eta_i| < 1.2$
  - Endcap-Endcap: both electrons s.t. $1.8 < |\eta_i| < 2.37$
  - Barrel-Endcap: $0 < |\eta_1| < 1.2$ and $1.8 < |\eta_2| < 2.37$ (or vice-versa).
- Global mass ratios including all the calorimeter, as well as
  - Excluding the typical crack ($1.37 < |\eta| < 1.55$)
  - Excluding the W-boson analysis crack ($1.2 < |\eta| < 1.8$).
- Relative resolution $\sigma(E)/E$ plots, per η-region, as a function of the energy E.

B.1 First order $E^{\mathrm{T}}_{\mathrm{truth}}$ dependence, for positive and negative η

$$\Delta' = \left[p_0 + p_3(E^{\mathrm{T}}_{\mathrm{truth}} - 45\ \mathrm{GeV})\right]\Delta + \left[p_1 + p_4(E^{\mathrm{T}}_{\mathrm{truth}} - 45\ \mathrm{GeV})\right]\Delta^2 + \left[p_2 + p_5(E^{\mathrm{T}}_{\mathrm{truth}} - 45\ \mathrm{GeV})\right]$$

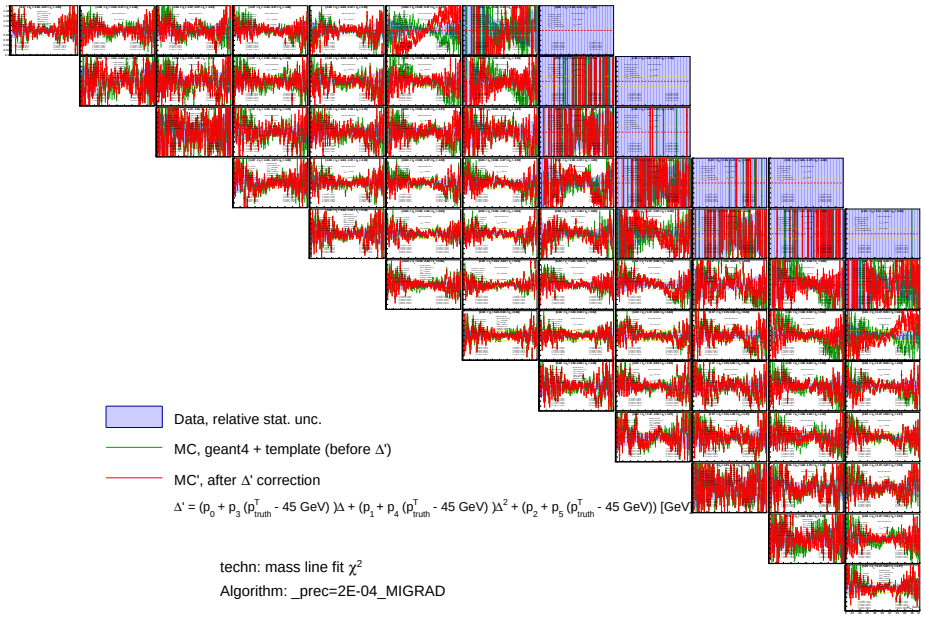

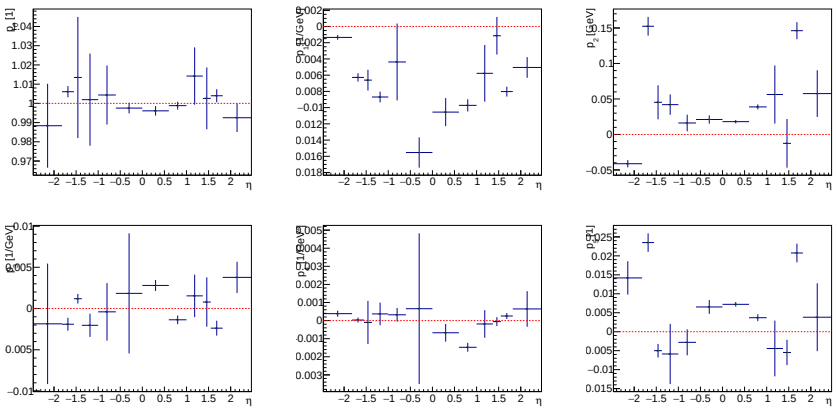

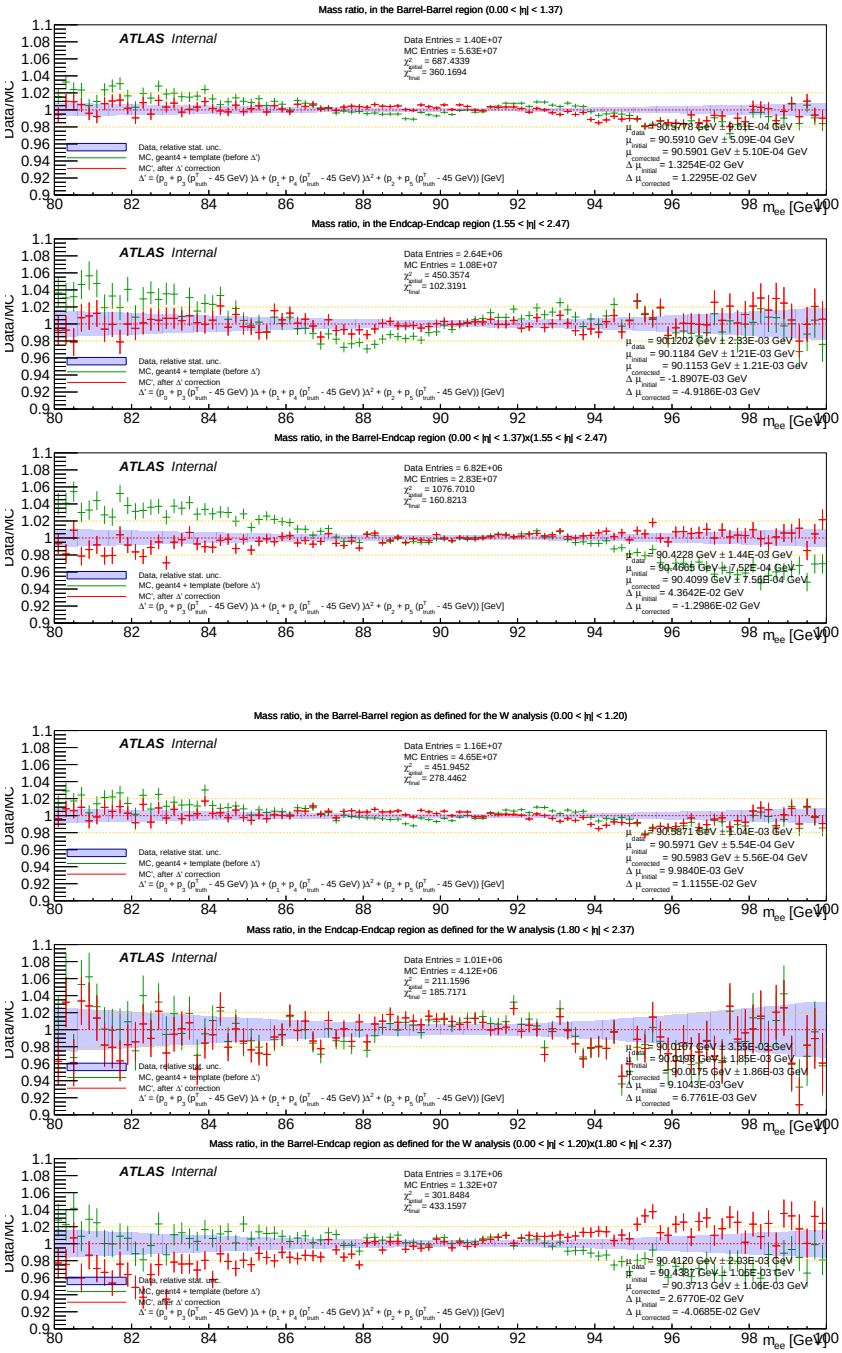
Mass ratio, in the Barrel-Barrel region (0.00 < |η| < 1.37)
ATLAS Internal
Data Entries = 1.40E+07
MC Entries = 5.63E+07
χ²initial = 687.4339
χ²final = 360.1694
Data, relative stat. unc.
MC, geant4 + template (before Δ')
MC', after Δ' correction
Δ' = (p0 + p3 (pTtruth - 45 GeV)) Δ + (p1 + p4 (pTtruth - 45 GeV)) Δ² + (p2 + p5 (pTtruth - 45 GeV)) [GeV]
μdata = 90.5910 GeV ± 5.09E-04 GeV
μinitial = 90.5901 GeV ± 5.10E-04 GeV
Δ μinitial = 1.3254E-02 GeV
Δ μcorrected = 1.2295E-02 GeV
Data/MC
mee [GeV]
Mass ratio, in the Endcap-Endcap region (1.55 < |η| < 2.47)
ATLAS Internal
Data Entries = 2.64E+06
MC Entries = 1.08E+07
χ²initial = 450.3574
χ²final = 102.3191
μdata = 90.1184 GeV ± 1.21E-03 GeV
μinitial = 90.1153 GeV ± 1.21E-03 GeV
Δ μinitial = -1.8907E-03 GeV
Δ μcorrected = -4.9186E-03 GeV
Mass ratio, in the Barrel-Endcap region (0.00 < |η| < 1.37)x(1.55 < |η| < 2.47)
ATLAS Internal
Data Entries = 6.82E+06
MC Entries = 2.83E+07
χ²initial = 1076.7010
χ²final = 160.8213
μdata = 90.4228 GeV ± 1.44E-03 GeV
μinitial = 90.4099 GeV ± 7.52E-04 GeV
Δ μinitial = 4.3642E-02 GeV
Δ μcorrected = -1.2986E-02 GeV
Mass ratio, in the Barrel-Barrel region as defined for the W analysis (0.00 < |η| < 1.20)
ATLAS Internal
Data Entries = 1.16E+07
MC Entries = 4.65E+07
χ²initial = 451.9452
χ²final = 278.4462
μdata = 90.5971 GeV ± 5.54E-04 GeV
μinitial = 90.5983 GeV ± 5.56E-04 GeV
Δ μinitial = 9.9840E-03 GeV
Δ μcorrected = 1.1155E-02 GeV
Mass ratio, in the Endcap-Endcap region as defined for the W analysis (1.80 < |η| < 2.37)
ATLAS Internal
Data Entries = 1.01E+06
MC Entries = 4.12E+06
χ²initial = 211.1596
χ²final = 185.7171
μdata = 90.0175 GeV ± 1.86E-03 GeV
Δ μinitial = 9.1043E-03 GeV
Δ μcorrected = 6.7761E-03 GeV
Mass ratio, in the Barrel-Endcap region as defined for the W analysis (0.00 < |η| < 1.20)x(1.80 < |η| < 2.37)
ATLAS Internal
Data Entries = 3.17E+06
MC Entries = 1.32E+07
χ²initial = 301.8484
χ²final = 433.1597
μdata = 90.4331 GeV ± 1.06E-03 GeV
μinitial = 90.3713 GeV ± 1.06E-03 GeV
Δ μinitial = 2.6770E-02 GeV
Δ μcorrected = -4.0685E-02 GeV

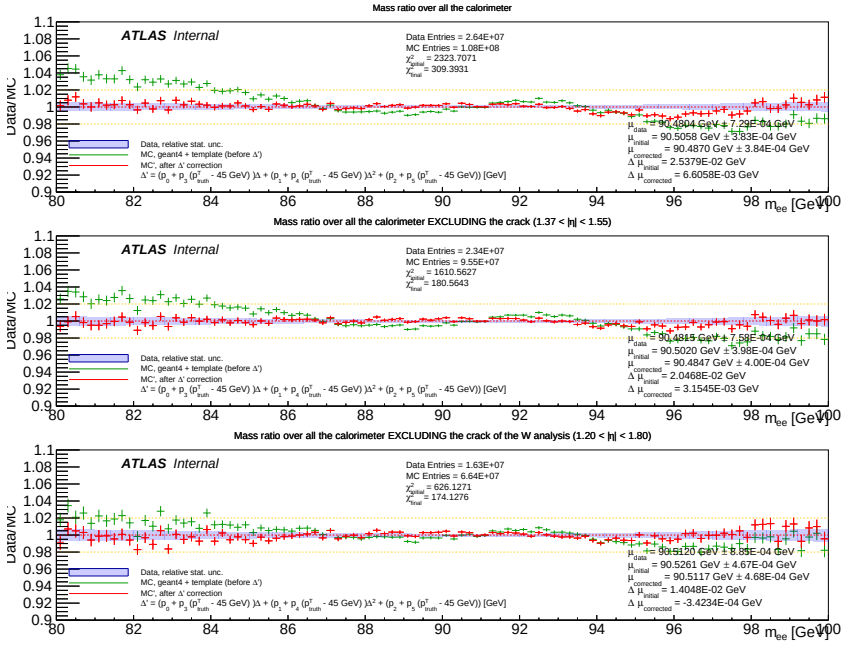
Mass ratio over all the calorimeter
ATLAS Internal
Data Entries = 2.64E+07
MC Entries = 1.08E+08
χ²initial = 2323.7071
χ²final = 309.3931
Data/MC
mee [GeV]
Data, relative stat. unc.
MC, geant4 + template (before Δ')
MC', after Δ' correction
μdata = 90.4904 GeV ± 7.29E-04 GeV
μinitial = 90.5058 GeV ± 3.83E-04 GeV
μcorrected = 90.4870 GeV ± 3.84E-04 GeV
Δ μinitial = 2.5379E-02 GeV
Δ μcorrected = 6.6058E-03 GeV
Mass ratio over all the calorimeter EXCLUDING the crack (1.37 < |η| < 1.55)
ATLAS Internal
Data Entries = 2.34E+07
MC Entries = 9.55E+07
χ²initial = 1610.5627
χ²final = 180.5643
Data/MC
mee [GeV]
Data, relative stat. unc.
MC, geant4 + template (before Δ')
MC', after Δ' correction
μdata = 90.4885 GeV ± 7.59E-04 GeV
μinitial = 90.5020 GeV ± 3.98E-04 GeV
μcorrected = 90.4847 GeV ± 4.00E-04 GeV
Δ μinitial = 2.0468E-02 GeV
Δ μcorrected = 3.1545E-03 GeV
Mass ratio over all the calorimeter EXCLUDING the crack of the W analysis (1.20 < |η| < 1.80)
ATLAS Internal
Data Entries = 1.63E+07
MC Entries = 6.64E+07
χ²initial = 626.1271
χ²final = 174.1276
Data/MC
mee [GeV]
Data, relative stat. unc.
MC, geant4 + template (before Δ')
MC', after Δ' correction
μdata = 90.5120 GeV ± 8.85E-04 GeV
μinitial = 90.5261 GeV ± 4.67E-04 GeV
μcorrected = 90.5117 GeV ± 4.68E-04 GeV
Δ μinitial = 1.4048E-02 GeV
Δ μcorrected = -3.4234E-04 GeV

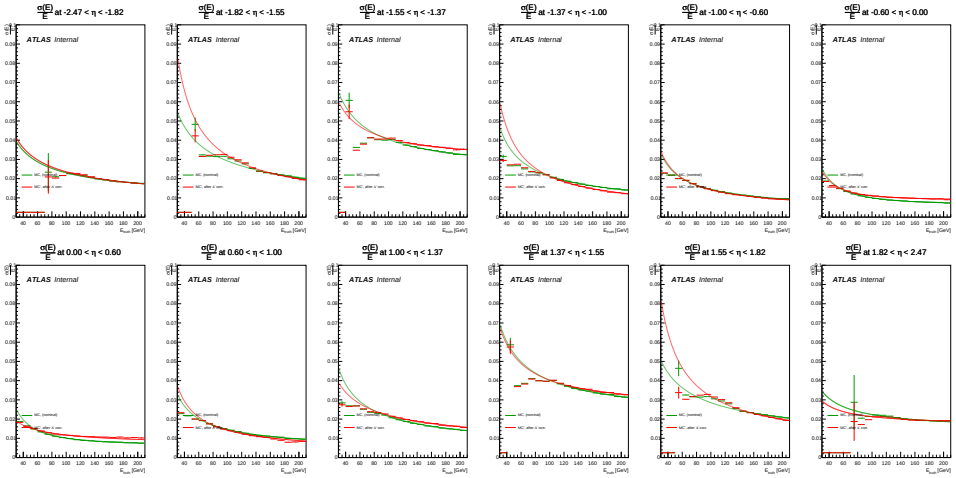
σ(E)/E at -2.47 < η < -1.82
σ(E)/E at -1.82 < η < -1.55
σ(E)/E at -1.55 < η < -1.37
σ(E)/E at -1.37 < η < -1.00
σ(E)/E at -1.00 < η < -0.60
σ(E)/E at -0.60 < η < 0.00
σ(E)/E at 0.00 < η < 0.60
σ(E)/E at 0.60 < η < 1.00
σ(E)/E at 1.00 < η < 1.37
σ(E)/E at 1.37 < η < 1.55
σ(E)/E at 1.55 < η < 1.82
σ(E)/E at 1.82 < η < 2.47
ATLAS Internal

B.2 First order $E^{\mathrm{T}}_{\mathrm{truth}}$ dependence, for $|\eta|$

$$\Delta' = \left[p_0 + p_3(E^{\mathrm{T}}_{\mathrm{truth}} - 45\ \mathrm{GeV})\right]\Delta + \left[p_1 + p_4(E^{\mathrm{T}}_{\mathrm{truth}} - 45\ \mathrm{GeV})\right]\Delta^2 + \left[p_2 + p_5(E^{\mathrm{T}}_{\mathrm{truth}} - 45\ \mathrm{GeV})\right]$$

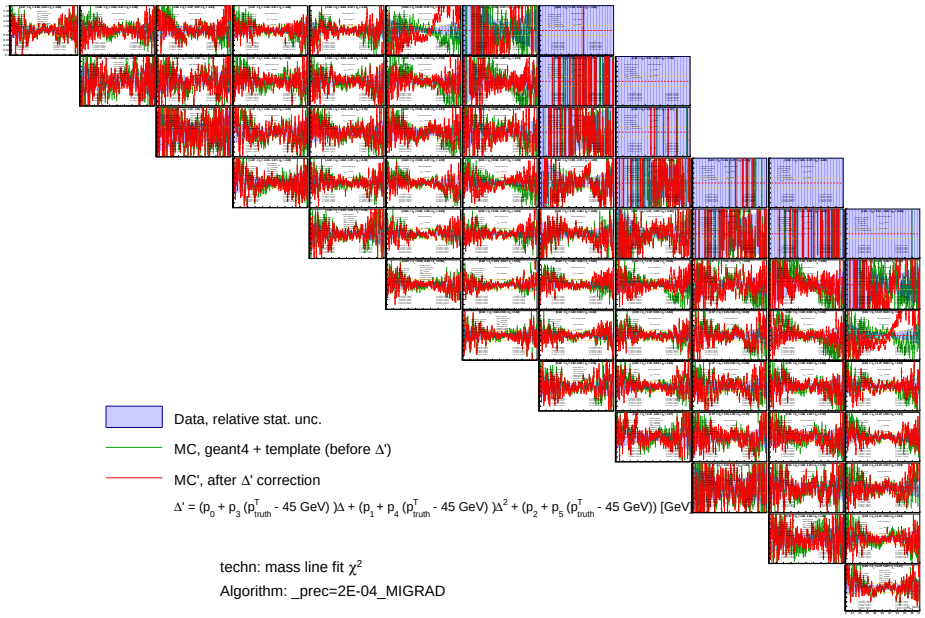

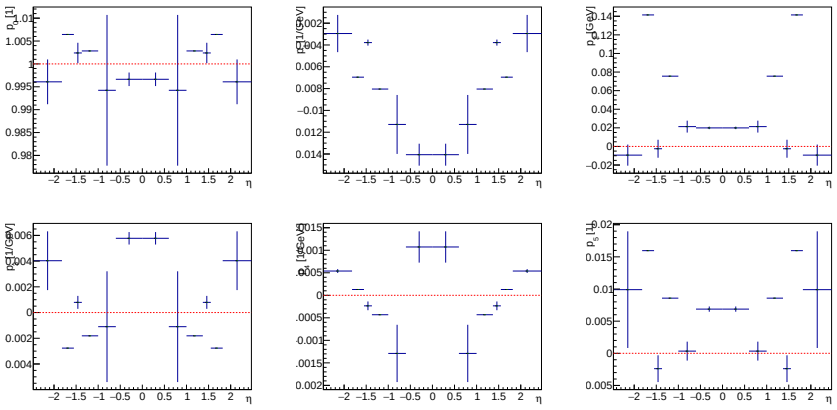

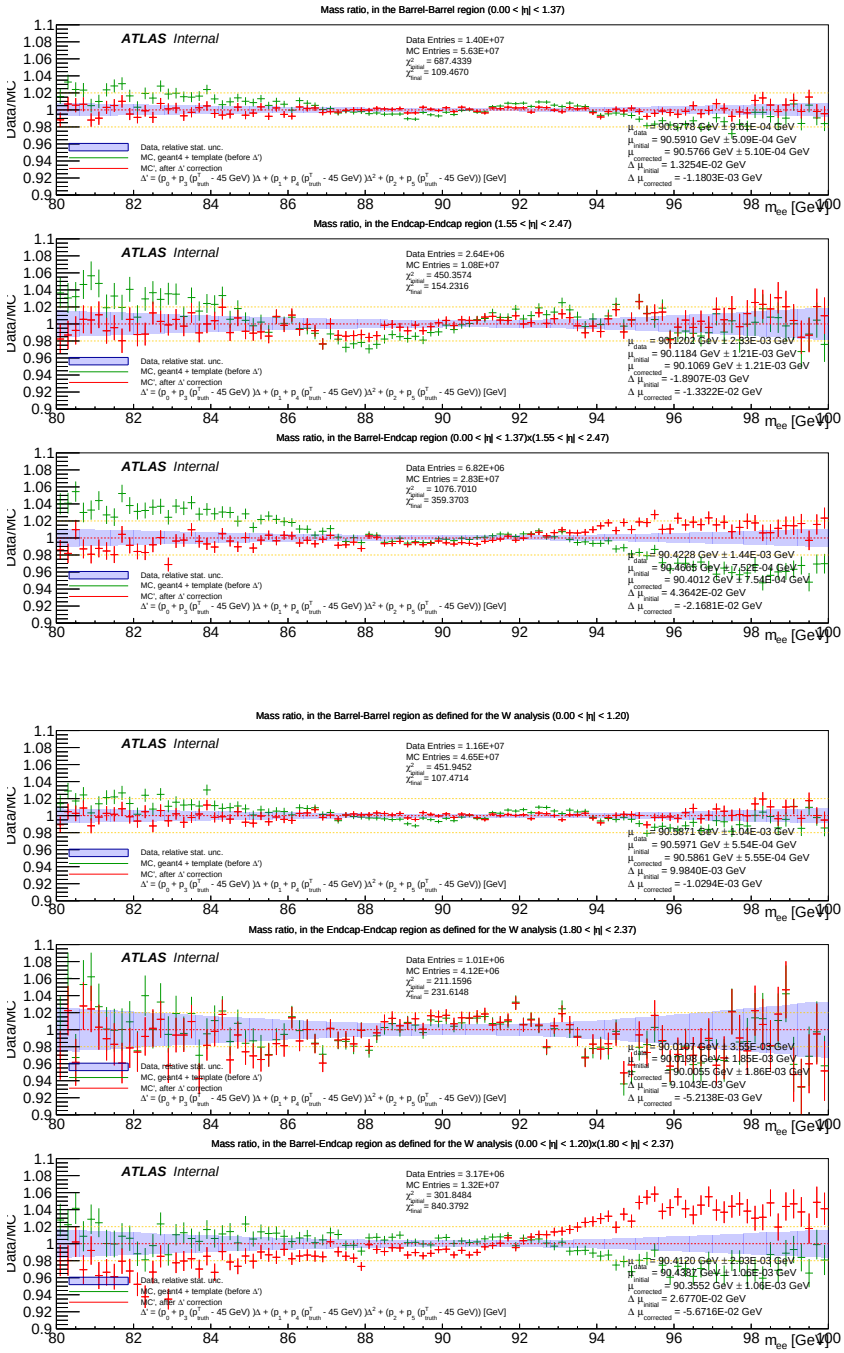
Mass ratio, in the Barrel-Barrel region (0.00 < |η| < 1.37)
ATLAS Internal
Data Entries = 1.40E+07
MC Entries = 5.63E+07
Mass ratio, in the Endcap-Endcap region (1.55 < |η| < 2.47)
ATLAS Internal
Data Entries = 2.64E+06
MC Entries = 1.08E+07
Mass ratio, in the Barrel-Endcap region (0.00 < |η| < 1.37)x(1.55 < |η| < 2.47)
ATLAS Internal
Data Entries = 6.82E+06
MC Entries = 2.83E+07
Mass ratio, in the Barrel-Barrel region as defined for the W analysis (0.00 < |η| < 1.20)
ATLAS Internal
Data Entries = 1.16E+07
MC Entries = 4.65E+07
Mass ratio, in the Endcap-Endcap region as defined for the W analysis (1.80 < |η| < 2.37)
ATLAS Internal
Data Entries = 1.01E+06
MC Entries = 4.12E+06
Mass ratio, in the Barrel-Endcap region as defined for the W analysis (0.00 < |η| < 1.20)x(1.80 < |η| < 2.37)
ATLAS Internal
Data Entries = 3.17E+06
MC Entries = 1.32E+07
Data/MC
m_ee [GeV]

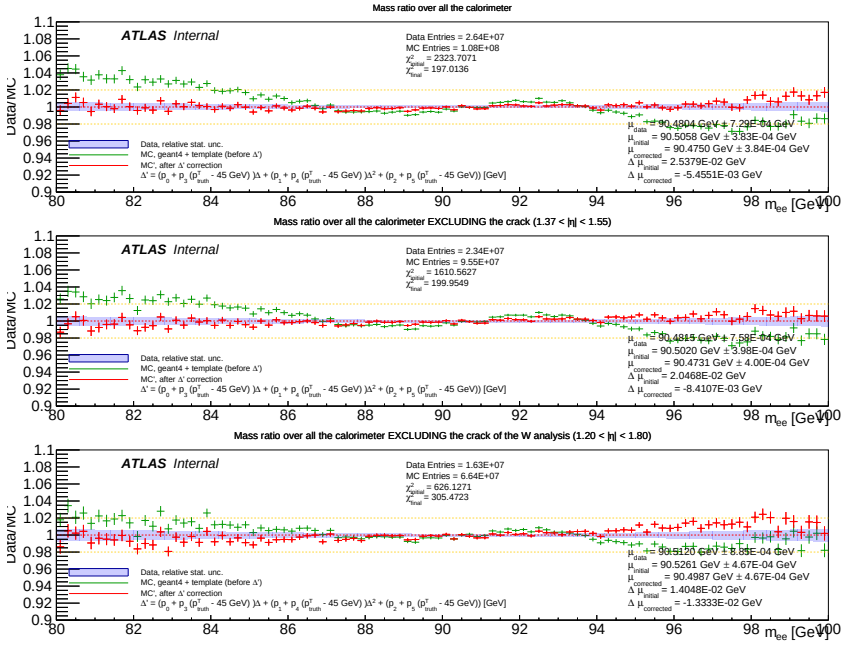
Mass ratio over all the calorimeter
ATLAS Internal
Data Entries = 2.64E+07
MC Entries = 1.08E+08
Data/MC
Data, relative stat. unc.
MC, geant4 + template (before Δ')
MC', after Δ' correction
m_ee [GeV]
Mass ratio over all the calorimeter EXCLUDING the crack (1.37 < |η| < 1.55)
ATLAS Internal
Data Entries = 2.34E+07
MC Entries = 9.55E+07
Data/MC
Data, relative stat. unc.
MC, geant4 + template (before Δ')
MC', after Δ' correction
m_ee [GeV]
Mass ratio over all the calorimeter EXCLUDING the crack of the W analysis (1.20 < |η| < 1.80)
ATLAS Internal
Data Entries = 1.63E+07
MC Entries = 6.64E+07
Data/MC
Data, relative stat. unc.
MC, geant4 + template (before Δ')
MC', after Δ' correction
m_ee [GeV]

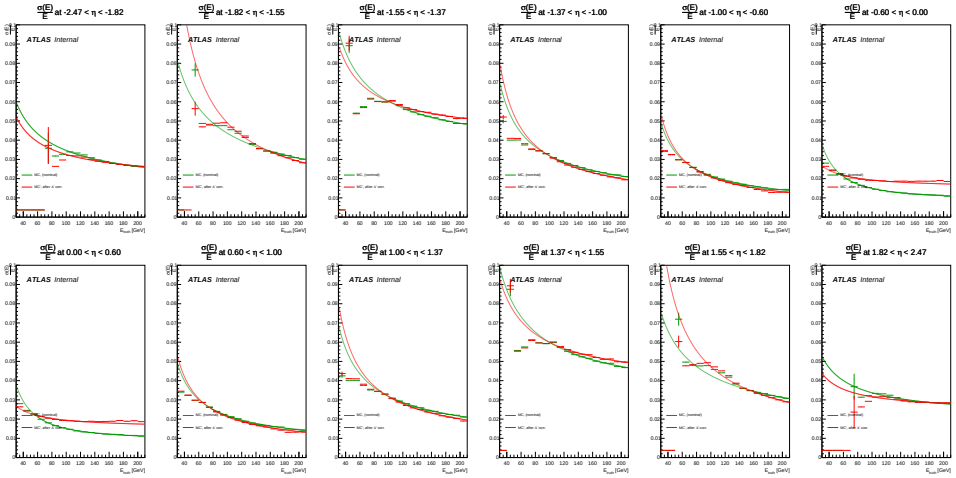
σ(E)/E at -2.47 < η < -1.82
σ(E)/E at -1.82 < η < -1.55
σ(E)/E at -1.55 < η < -1.37
σ(E)/E at -1.37 < η < -1.00
σ(E)/E at -1.00 < η < -0.60
σ(E)/E at -0.60 < η < 0.00
σ(E)/E at 0.00 < η < 0.60
σ(E)/E at 0.60 < η < 1.00
σ(E)/E at 1.00 < η < 1.37
σ(E)/E at 1.37 < η < 1.55
σ(E)/E at 1.55 < η < 1.82
σ(E)/E at 1.82 < η < 2.47
ATLAS Internal

B.3 Second order $E_{\text{truth}}^{\text{T}}$ dependence, for $|\eta|$

$$\Delta' = \left[p_0 + p_3(E_{\text{truth}}^{\text{T}} - 45\ \text{GeV})\right]\Delta + \left[p_1 + p_4(E_{\text{truth}}^{\text{T}} - 45\ \text{GeV})\right]\Delta^2 + \left[p_2 + p_5(E_{\text{truth}}^{\text{T}} - 45\ \text{GeV}) + p_6(E_{\text{truth}}^{\text{T}} - 45\ \text{GeV})^2\right]$$

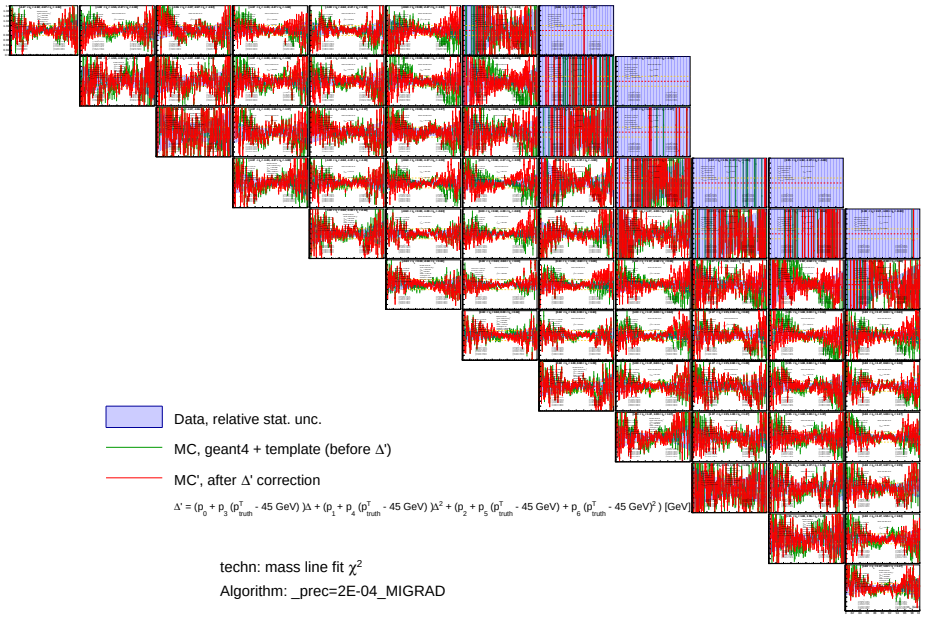

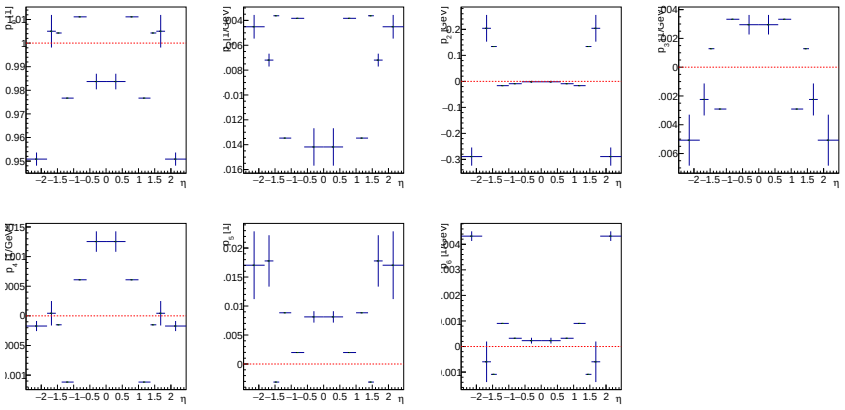

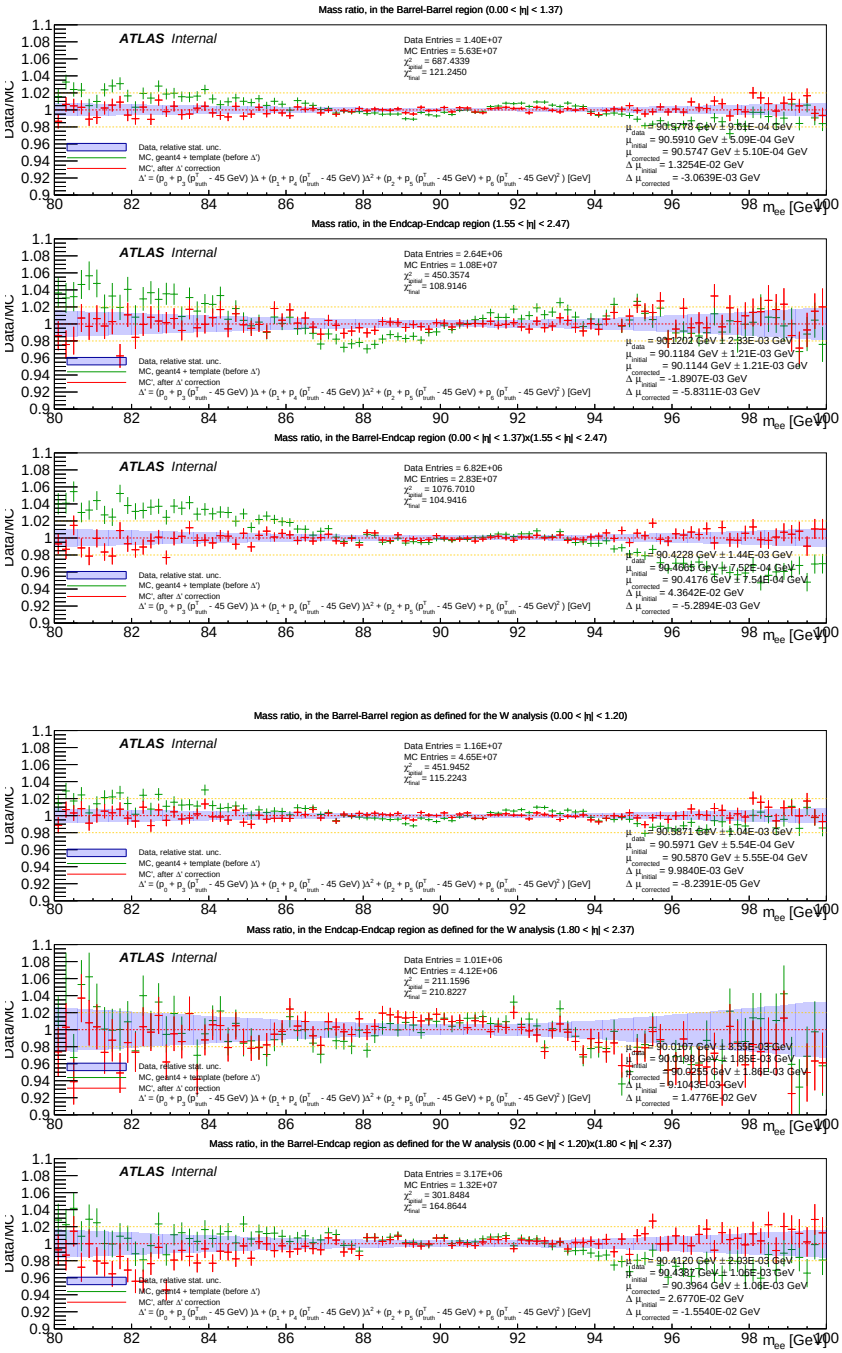
Mass ratio, in the Barrel-Barrel region (0.00 < |η| < 1.37)
ATLAS Internal
Data Entries = 1.40E+07
MC Entries = 5.63E+07
χ²initial = 687.4339
χ²final = 121.2450
Data, relative stat. unc.
MC, geant4 + template (before Δ')
MC', after Δ' correction
Δ' = (p0 + p1 (pTtruth - 45 GeV)) Δ + (p2 + p3 (pTtruth - 45 GeV)) Δ² + (p4 + p5 (pTtruth - 45 GeV) + p6 (pTtruth - 45 GeV)²) [GeV]
μdata = 90.5778 GeV ± 9.01E-04 GeV
μinitial = 90.5910 GeV ± 5.09E-04 GeV
μcorrected = 90.5747 GeV ± 5.10E-04 GeV
Δ μinitial = 1.3254E-02 GeV
Δ μcorrected = -3.0639E-03 GeV
Data/MC
mee [GeV]
Mass ratio, in the Endcap-Endcap region (1.55 < |η| < 2.47)
ATLAS Internal
Data Entries = 2.64E+06
MC Entries = 1.08E+07
χ²initial = 450.3574
χ²final = 108.9146
μdata = 90.1203 GeV ± 2.33E-03 GeV
μinitial = 90.1184 GeV ± 1.21E-03 GeV
μcorrected = 90.1144 GeV ± 1.21E-03 GeV
Δ μinitial = -1.8907E-03 GeV
Δ μcorrected = -5.8311E-03 GeV
Mass ratio, in the Barrel-Endcap region (0.00 < |η| < 1.37)x(1.55 < |η| < 2.47)
ATLAS Internal
Data Entries = 6.82E+06
MC Entries = 2.83E+07
χ²initial = 1076.7010
χ²final = 104.9416
μdata = 90.4228 GeV ± 1.44E-03 GeV
μinitial = 90.4665 GeV ± 7.52E-04 GeV
μcorrected = 90.4176 GeV ± 7.54E-04 GeV
Δ μinitial = 4.3642E-02 GeV
Δ μcorrected = -5.2894E-03 GeV
Mass ratio, in the Barrel-Barrel region as defined for the W analysis (0.00 < |η| < 1.20)
ATLAS Internal
Data Entries = 1.16E+07
MC Entries = 4.65E+07
χ²initial = 451.9452
χ²final = 115.2243
μdata = 90.5871 GeV ± 1.04E-03 GeV
μinitial = 90.5971 GeV ± 5.54E-04 GeV
μcorrected = 90.5870 GeV ± 5.55E-04 GeV
Δ μinitial = 9.9840E-03 GeV
Δ μcorrected = -8.2391E-05 GeV
Mass ratio, in the Endcap-Endcap region as defined for the W analysis (1.80 < |η| < 2.37)
ATLAS Internal
Data Entries = 1.01E+06
MC Entries = 4.12E+06
χ²initial = 211.1596
χ²final = 210.8227
μdata = 90.0107 GeV ± 3.55E-03 GeV
μinitial = 90.0188 GeV ± 1.85E-03 GeV
μcorrected = 90.0255 GeV ± 1.84E-03 GeV
Δ μinitial = 8.1043E-03 GeV
Δ μcorrected = 1.4776E-02 GeV
Mass ratio, in the Barrel-Endcap region as defined for the W analysis (0.00 < |η| < 1.20)x(1.80 < |η| < 2.37)
ATLAS Internal
Data Entries = 3.17E+06
MC Entries = 1.32E+07
χ²initial = 301.8484
χ²final = 164.8644
μdata = 90.4120 GeV ± 2.93E-03 GeV
μinitial = 90.4311 GeV ± 1.08E-03 GeV
μcorrected = 90.3964 GeV ± 1.06E-03 GeV
Δ μinitial = 2.6770E-02 GeV
Δ μcorrected = -1.5540E-02 GeV

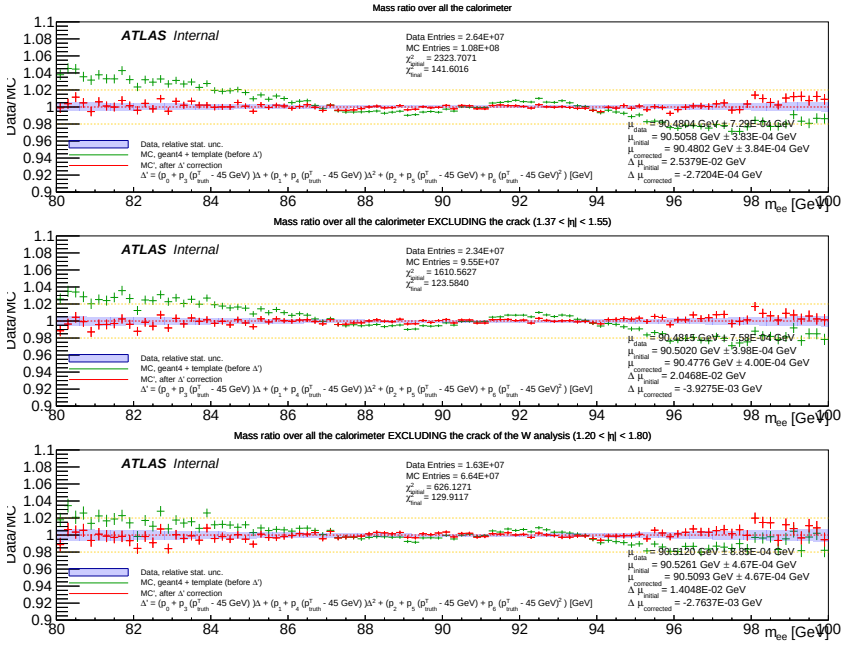
Mass ratio over all the calorimeter
ATLAS Internal
Data Entries = 2.64E+07
MC Entries = 1.08E+08
Data/MC
Data, relative stat. unc.
MC, geant4 + template (before Δ')
MC', after Δ' correction
m_ee [GeV]
Mass ratio over all the calorimeter EXCLUDING the crack (1.37 < |η| < 1.55)
ATLAS Internal
Data Entries = 2.34E+07
MC Entries = 9.55E+07
Data/MC
Data, relative stat. unc.
MC, geant4 + template (before Δ')
MC', after Δ' correction
m_ee [GeV]
Mass ratio over all the calorimeter EXCLUDING the crack of the W analysis (1.20 < |η| < 1.80)
ATLAS Internal
Data Entries = 1.63E+07
MC Entries = 6.64E+07
Data/MC
Data, relative stat. unc.
MC, geant4 + template (before Δ')
MC', after Δ' correction
m_ee [GeV]

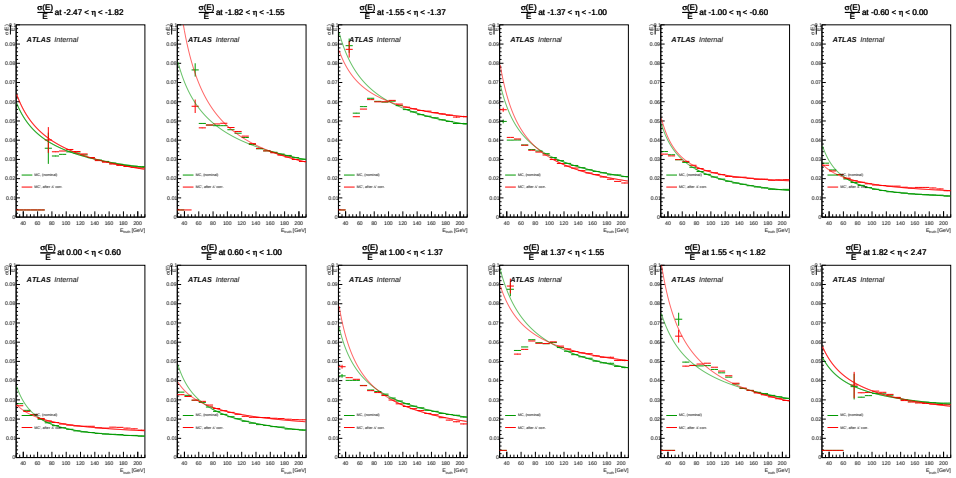
σ(E)/E at -2.47 < η < -1.82
σ(E)/E at -1.82 < η < -1.55
σ(E)/E at -1.55 < η < -1.37
σ(E)/E at -1.37 < η < -1.00
σ(E)/E at -1.00 < η < -0.60
σ(E)/E at -0.60 < η < 0.00
σ(E)/E at 0.00 < η < 0.60
σ(E)/E at 0.60 < η < 1.00
σ(E)/E at 1.00 < η < 1.37
σ(E)/E at 1.37 < η < 1.55
σ(E)/E at 1.55 < η < 1.82
σ(E)/E at 1.82 < η < 2.47
ATLAS Internal

B.4 Third order $E^{\mathrm{T}}_{\mathrm{truth}}$ dependence, for $|\eta|$

$$\Delta' = \left[p_0 + p_3(E^{\mathrm{T}}_{\mathrm{truth}} - 45\ \mathrm{GeV})\right]\Delta + \left[p_1 + p_4(E^{\mathrm{T}}_{\mathrm{truth}} - 45\ \mathrm{GeV})\right]\Delta^2 + \left[p_2 + p_5(E^{\mathrm{T}}_{\mathrm{truth}} - 45\ \mathrm{GeV}) + p_6(E^{\mathrm{T}}_{\mathrm{truth}} - 45\ \mathrm{GeV})^2 + p_7(E^{\mathrm{T}}_{\mathrm{truth}} - 45\ \mathrm{GeV})^3\right]$$

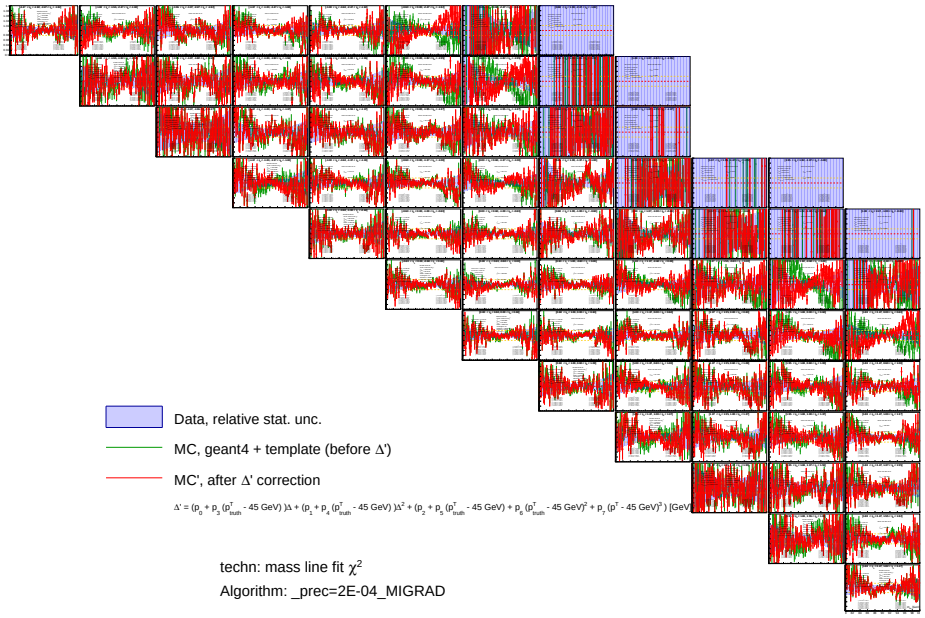

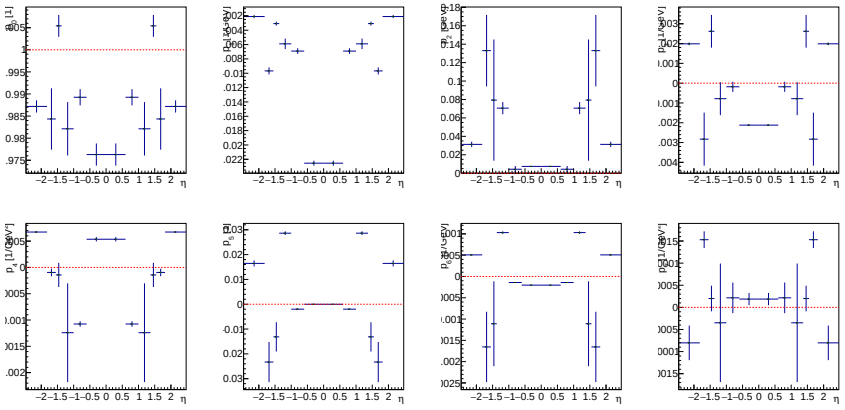

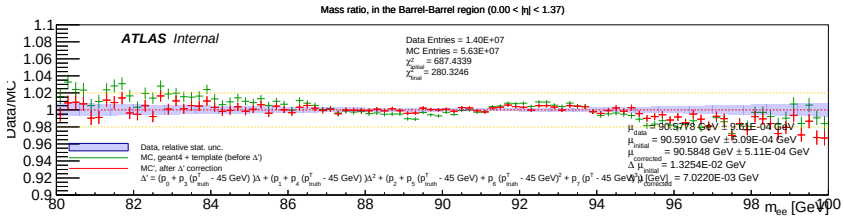
Mass ratio, in the Barrel-Barrel region (0.00 < |η| < 1.37)
ATLAS Internal
Data Entries = 1.40E+07
MC Entries = 5.63E+07
χ²initial = 687.4339
χ²final = 280.3246
Data, relative stat. unc.
MC, geant4 + template (before Δ')
MC', after Δ' correction
Δ' = (p0 + p3 (pTtruth - 45 GeV)) Δ + (p1 + p4 (pTtruth - 45 GeV)) Δ² + (p2 + p5 (pTtruth - 45 GeV)) + p6 (pTtruth - 45 GeV)² + p7 (pT - 45 GeV)
μdata = 90.5778 GeV ± 9.11E-04 GeV
μinitial = 90.5910 GeV ± 5.09E-04 GeV
μcorrected = 90.5848 GeV ± 5.11E-04 GeV
Δ μinitial = 1.3254E-02 GeV
Δ μcorrected = 7.0220E-03 GeV
Data/MC
mee [GeV]

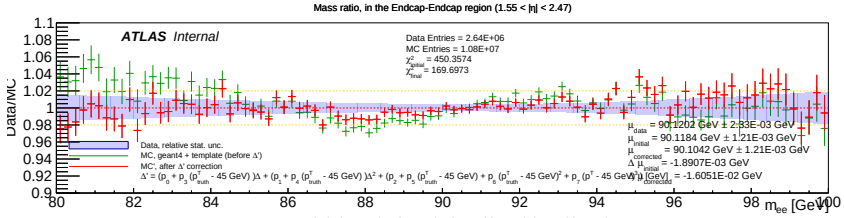
Mass ratio, in the Endcap-Endcap region (1.55 < |η| < 2.47)
ATLAS Internal
Data Entries = 2.64E+06
MC Entries = 1.08E+07
χ²initial = 450.3574
χ²final = 169.6973
Data, relative stat. unc.
MC, geant4 + template (before Δ')
MC', after Δ' correction
Δ' = (p0 + p3 (pTtruth - 45 GeV)) Δ + (p1 + p4 (pTtruth - 45 GeV)) Δ² + (p2 + p5 (pTtruth - 45 GeV)) + p6 (pTtruth - 45 GeV)² + p7 (pT - 45 GeV)
μdata = 90.1202 GeV ± 2.33E-03 GeV
μinitial = 90.1184 GeV ± 1.21E-03 GeV
μcorrected = 90.1042 GeV ± 1.21E-03 GeV
Δ μinitial = -1.8907E-03 GeV
Δ μcorrected = -1.6051E-02 GeV
Data/MC
mee [GeV]

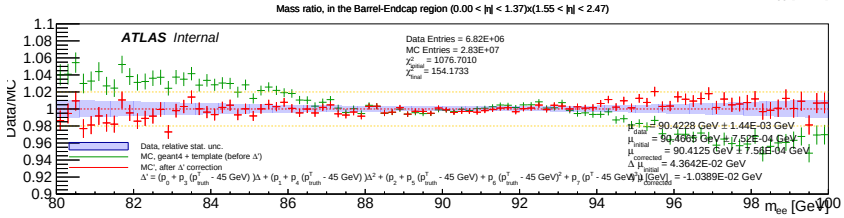
Mass ratio, in the Barrel-Endcap region (0.00 < |η| < 1.37)x(1.55 < |η| < 2.47)
ATLAS Internal
Data Entries = 6.82E+06
MC Entries = 2.83E+07
χ²initial = 1076.7010
χ²final = 154.1733
Data, relative stat. unc.
MC, geant4 + template (before Δ')
MC', after Δ' correction
Δ' = (p0 + p3 (pTtruth - 45 GeV)) Δ + (p1 + p4 (pTtruth - 45 GeV)) Δ² + (p2 + p5 (pTtruth - 45 GeV)) + p6 (pTtruth - 45 GeV)² + p7 (pT - 45 GeV)
μdata = 90.4228 GeV ± 1.44E-03 GeV
μinitial = 90.4065 GeV ± 7.52E-04 GeV
μcorrected = 90.4125 GeV ± 7.56E-04 GeV
Δ μinitial = 4.3642E-02 GeV
Δ μcorrected = -1.0389E-02 GeV
Data/MC
mee [GeV]

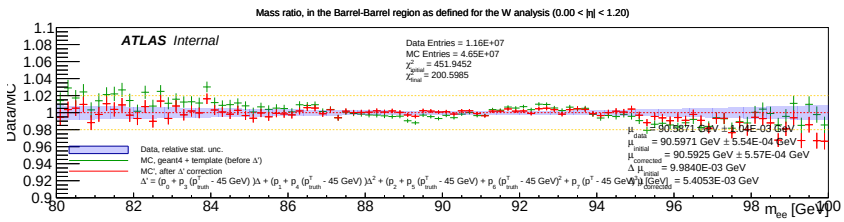
Mass ratio, in the Barrel-Barrel region as defined for the W analysis (0.00 < |η| < 1.20)
ATLAS Internal
Data Entries = 1.16E+07
MC Entries = 4.65E+07
χ²initial = 451.9452
χ²final = 200.5985
Data, relative stat. unc.
MC, geant4 + template (before Δ')
MC', after Δ' correction
Δ' = (p0 + p3 (pTtruth - 45 GeV)) Δ + (p1 + p4 (pTtruth - 45 GeV)) Δ² + (p2 + p5 (pTtruth - 45 GeV)) + p6 (pTtruth - 45 GeV)² + p7 (pT - 45 GeV)
μdata = 90.5871 GeV ± 1.04E-03 GeV
μinitial = 90.5971 GeV ± 5.54E-04 GeV
μcorrected = 90.5925 GeV ± 5.57E-04 GeV
Δ μinitial = 9.9840E-03 GeV
Δ μcorrected = 5.4053E-03 GeV
Data/MC
mee [GeV]

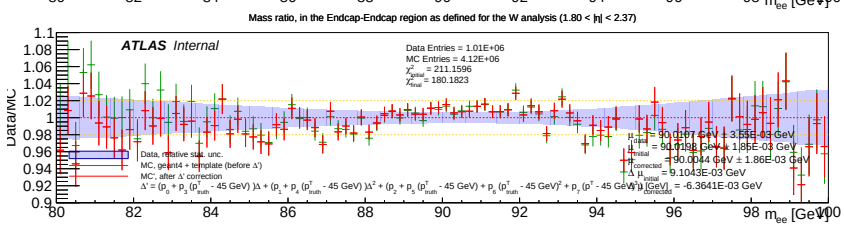
Mass ratio, in the Endcap-Endcap region as defined for the W analysis (1.80 < |η| < 2.37)
ATLAS Internal
Data Entries = 1.01E+06
MC Entries = 4.12E+06
χ²initial = 211.1596
χ²final = 180.1823
Data, relative stat. unc.
MC, geant4 + template (before Δ')
MC', after Δ' correction
Δ' = (p0 + p3 (pTtruth - 45 GeV)) Δ + (p1 + p4 (pTtruth - 45 GeV)) Δ² + (p2 + p5 (pTtruth - 45 GeV)) + p6 (pTtruth - 45 GeV)² + p7 (pT - 45 GeV)
μdata = 90.0107 GeV ± 3.55E-03 GeV
μinitial = 90.0188 GeV ± 1.85E-03 GeV
μcorrected = 90.0044 GeV ± 1.86E-03 GeV
Δ μinitial = 9.1043E-03 GeV
Δ μcorrected = -6.3641E-03 GeV
Data/MC
mee [GeV]

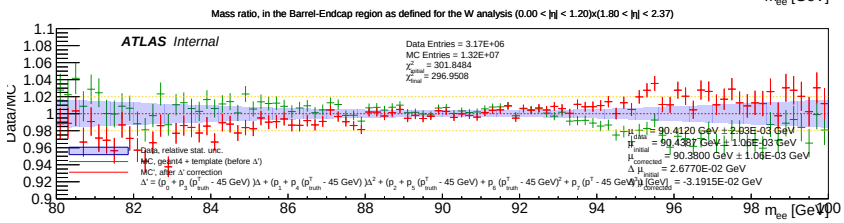
Mass ratio, in the Barrel-Endcap region as defined for the W analysis (0.00 < |η| < 1.20)x(1.80 < |η| < 2.37)
ATLAS Internal
Data Entries = 3.17E+06
MC Entries = 1.32E+07
χ²initial = 301.8484
χ²final = 296.9508
Data, relative stat. unc.
MC, geant4 + template (before Δ')
MC', after Δ' correction
Δ' = (p0 + p3 (pTtruth - 45 GeV)) Δ + (p1 + p4 (pTtruth - 45 GeV)) Δ² + (p2 + p5 (pTtruth - 45 GeV)) + p6 (pTtruth - 45 GeV)² + p7 (pT - 45 GeV)
μdata = 90.4120 GeV ± 2.93E-03 GeV
μinitial = 90.4381 GeV ± 1.06E-03 GeV
μcorrected = 90.3800 GeV ± 1.06E-03 GeV
Δ μinitial = 2.6770E-02 GeV
Δ μcorrected = -3.1915E-02 GeV
Data/MC
mee [GeV]

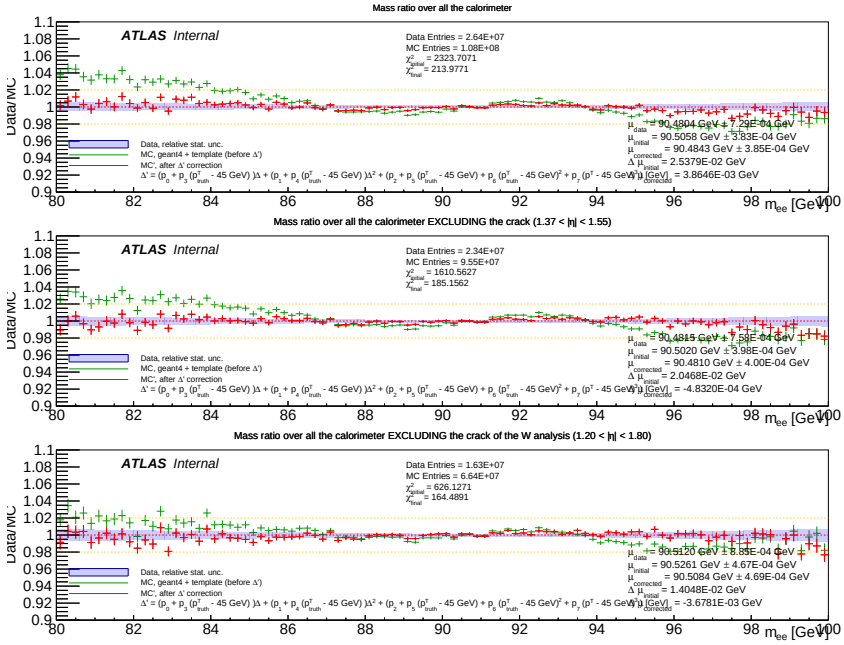
Mass ratio over all the calorimeter
ATLAS Internal
Data Entries = 2.64E+07
MC Entries = 1.08E+08
Data/MC
Mass ratio over all the calorimeter EXCLUDING the crack (1.37 < |η| < 1.55)
ATLAS Internal
Data Entries = 2.34E+07
MC Entries = 9.55E+07
Data/MC
Mass ratio over all the calorimeter EXCLUDING the crack of the W analysis (1.20 < |η| < 1.80)
ATLAS Internal
Data Entries = 1.63E+07
MC Entries = 6.64E+07
Data/MC

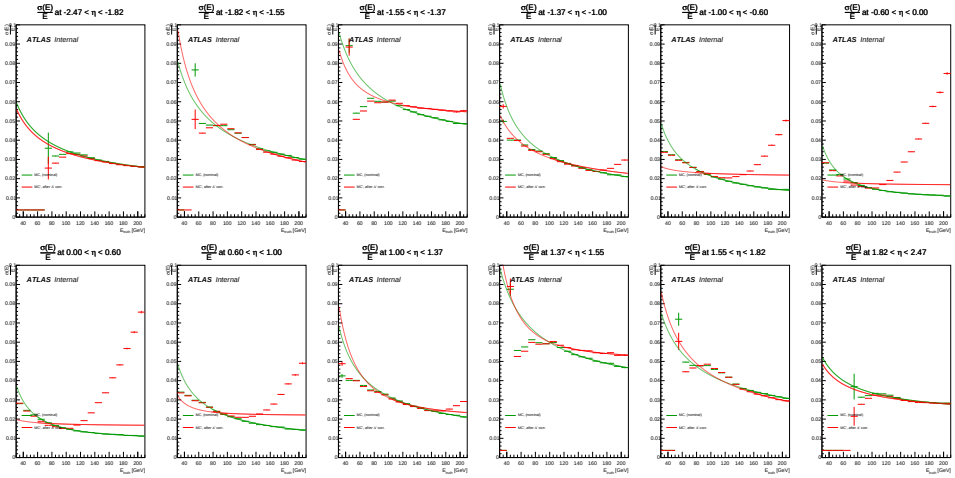
ATLAS Internal

B.5 Combined First and Third order $E^{\mathrm{T}}_{\mathrm{truth}}$ dependence, for $|\eta|$

$$\Delta' = \left[p_0 + p_3(E^{\mathrm{T}}_{\mathrm{truth}} - 45\ \mathrm{GeV})\right]\Delta + \left[p_1 + p_4(E^{\mathrm{T}}_{\mathrm{truth}} - 45\ \mathrm{GeV})\right]\Delta^2 + \begin{cases} \left[p_2 + p_5(E^{\mathrm{T}}_{\mathrm{truth}} - 45\ \mathrm{GeV})\right] & \text{if } |\eta| < 1.37 \\ \left[p_2 + p_5(E^{\mathrm{T}}_{\mathrm{truth}} - 45\ \mathrm{GeV}) + p_6(E^{\mathrm{T}}_{\mathrm{truth}} - 45\ \mathrm{GeV})^2 + p_7(E^{\mathrm{T}}_{\mathrm{truth}} - 45\ \mathrm{GeV})^3\right] & \text{if } |\eta| > 1.37 \end{cases}$$

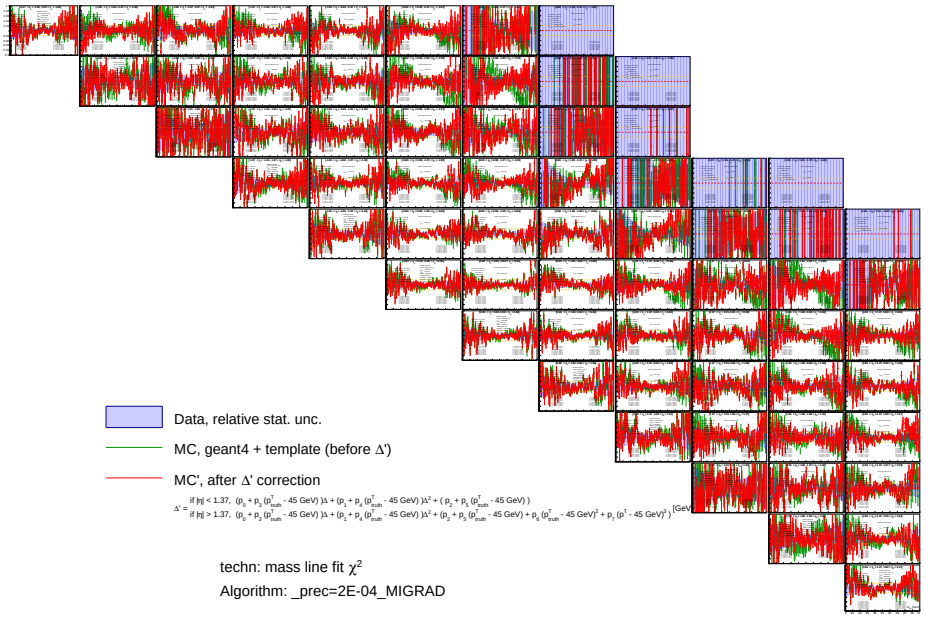

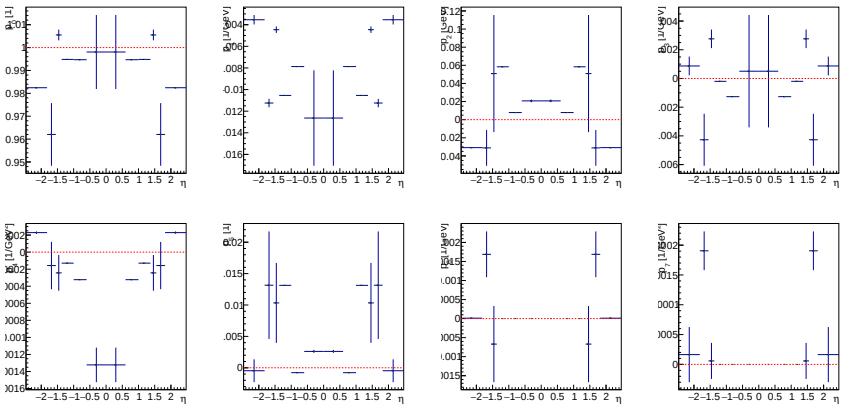

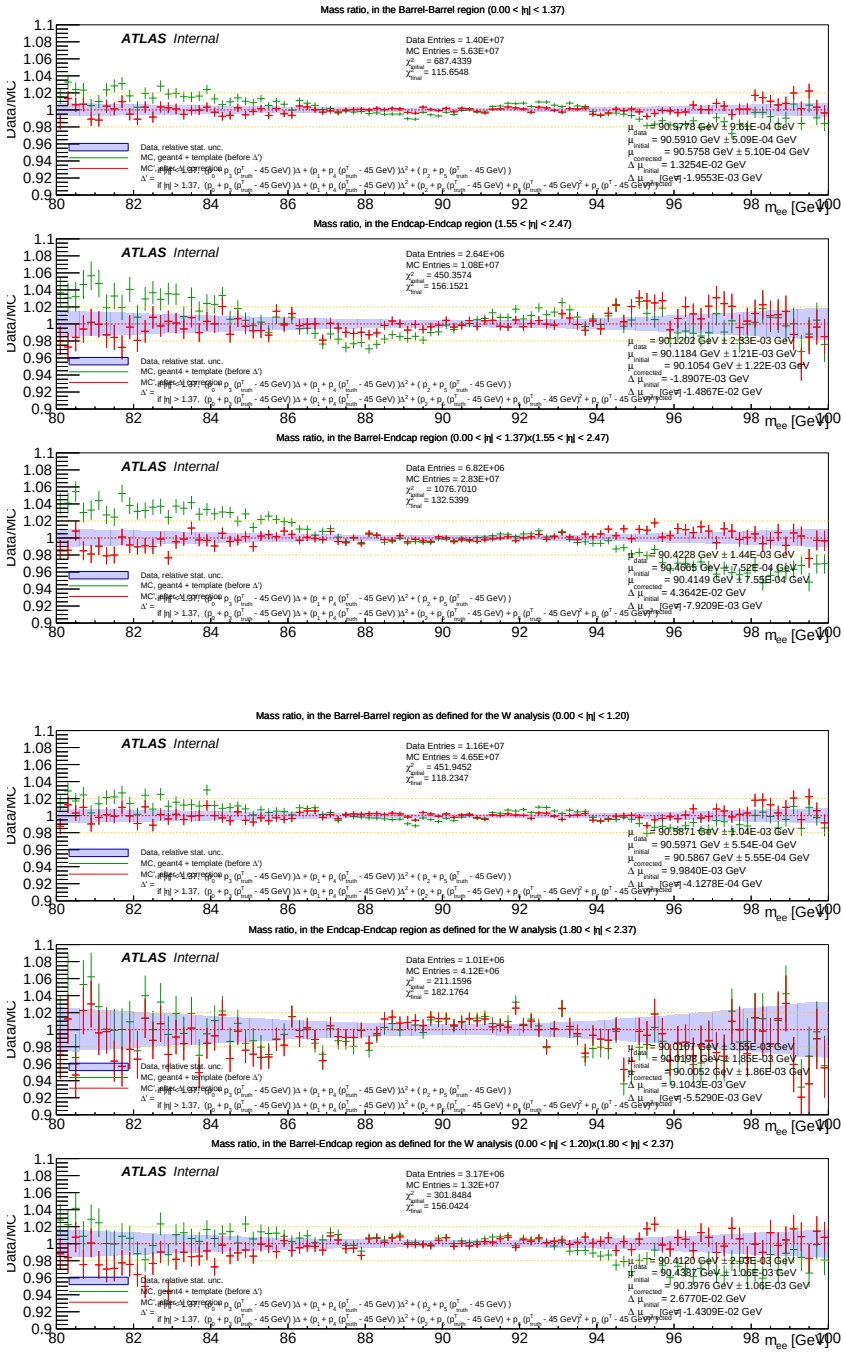
Mass ratio, in the Barrel-Barrel region (0.00 < |η| < 1.37)
ATLAS Internal
Data Entries = 1.40E+07
MC Entries = 5.63E+07
Mass ratio, in the Endcap-Endcap region (1.55 < |η| < 2.47)
ATLAS Internal
Data Entries = 2.64E+06
MC Entries = 1.08E+07
Mass ratio, in the Barrel-Endcap region (0.00 < |η| < 1.37)x(1.55 < |η| < 2.47)
ATLAS Internal
Data Entries = 6.82E+06
MC Entries = 2.83E+07
Mass ratio, in the Barrel-Barrel region as defined for the W analysis (0.00 < |η| < 1.20)
ATLAS Internal
Data Entries = 1.16E+07
MC Entries = 4.65E+07
Mass ratio, in the Endcap-Endcap region as defined for the W analysis (1.80 < |η| < 2.37)
ATLAS Internal
Data Entries = 1.01E+06
MC Entries = 4.12E+06
Mass ratio, in the Barrel-Endcap region as defined for the W analysis (0.00 < |η| < 1.20)x(1.80 < |η| < 2.37)
ATLAS Internal
Data Entries = 3.17E+06
MC Entries = 1.32E+07
Data/MC
m_ee [GeV]

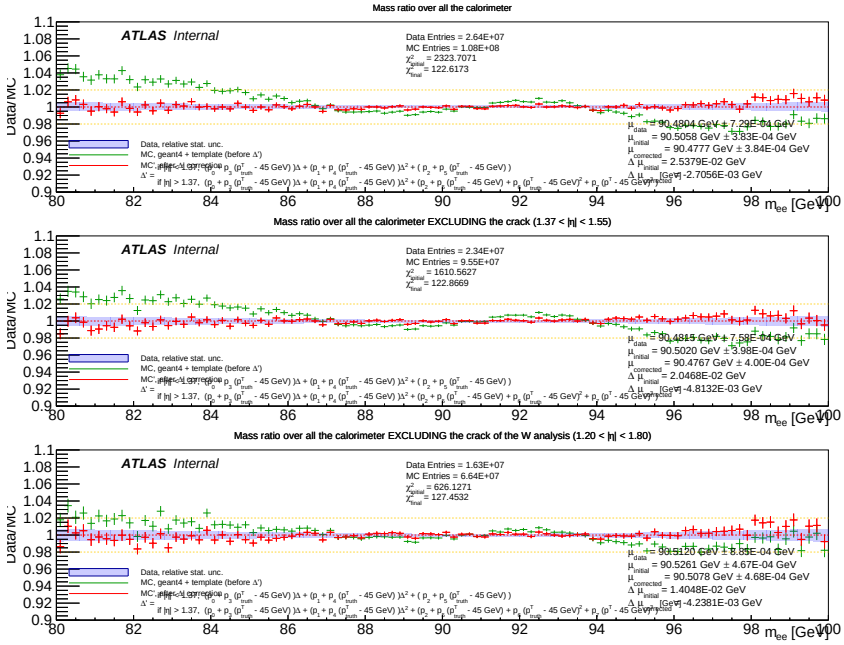
Mass ratio over all the calorimeter
ATLAS Internal
Data Entries = 2.64E+07
MC Entries = 1.08E+08
Data/MC
Mass ratio over all the calorimeter EXCLUDING the crack (1.37 < |η| < 1.55)
Data Entries = 2.34E+07
MC Entries = 9.55E+07
Mass ratio over all the calorimeter EXCLUDING the crack of the W analysis (1.20 < |η| < 1.80)
Data Entries = 1.63E+07
MC Entries = 6.64E+07
Data, relative stat. unc.
MC, geant4 + template (before Δ')
MC, after Δ' correction
m_ee [GeV]

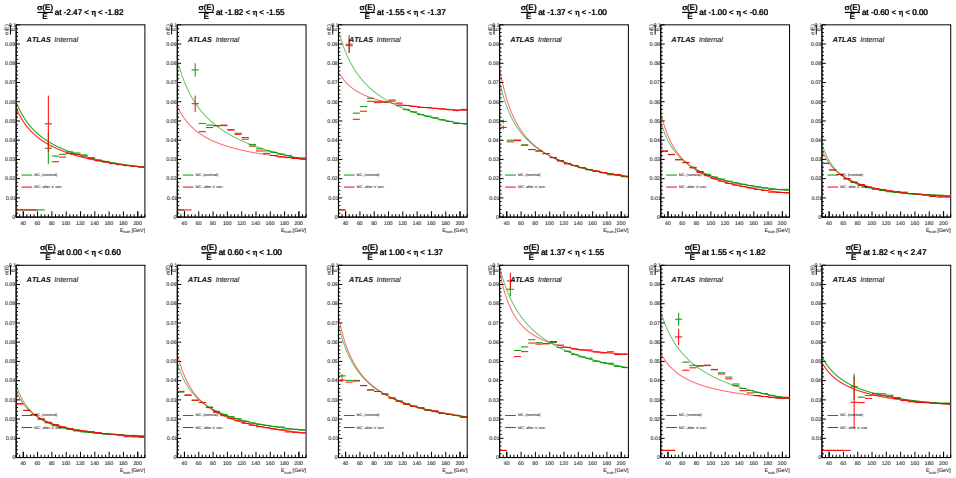
σ(E)/E at -2.47 < η < -1.82
σ(E)/E at -1.82 < η < -1.55
σ(E)/E at -1.55 < η < -1.37
σ(E)/E at -1.37 < η < -1.00
σ(E)/E at -1.00 < η < -0.60
σ(E)/E at -0.60 < η < 0.00
σ(E)/E at 0.00 < η < 0.60
σ(E)/E at 0.60 < η < 1.00
σ(E)/E at 1.00 < η < 1.37
σ(E)/E at 1.37 < η < 1.55
σ(E)/E at 1.55 < η < 1.82
σ(E)/E at 1.82 < η < 2.47
ATLAS Internal

5.10 ATLAS PubNote [2]: Methods for χ^2 parameter estimation using histograms

Similarly to Section 5.9, the following pages provide the complete note describing the bin-to-fittedPDF estimator technique [2] proposed as part of this thesis work. The proposal and implementation of this method are fundamental for the effective application of the Δ' technique, as it retrieves a continuous multidimensional unbiased estimator.

The method is destined to treat cases where the χ^2 curve is discontinuous due to the migration of events between bins. In a nutshell, the method consists of the definition of a χ^2 estimator that compares the bin content of one histogram and the continuous approximation of another one given by the fit of a case-specific functional form. In the case of the Δ' study, said functional form would be described by either a Crystal-Ball function with exponential tails or a Breit-Wigner-like function. The correct implementation of this estimator leads back to a continuous χ^2 curve, which enables simultaneous multidimensional parameter fits to be performed with numerical frameworks such as `MINUIT`.

ATLAS PUB Note
ATL-PHYS-PUB-2022-046
3rd November 2022

Methods for χ^2 parameter estimation using histograms

The ATLAS Collaboration

A common procedure in high energy physics data analysis is to derive correction factors to simulated events that make them better agree with data. This is often done using histograms created from data, and a Monte Carlo sample that is modified by some correction parameters. However, as the simulated events are modified, events will migrate between bins. This introduces discontinuities in the prediction: an infinitesimal perturbation of the correction factor can result in an event migrating across a bin boundary. As a result, a standard χ^2 minimization will not work. This note discusses this problem and proposes a solution.

1 Introduction

The optimization of parameters via shape comparison (with e.g. χ^2 minimization) is a very common practice in particle physics. Most commonly, it is encountered when fitting a user-defined function to a distribution (observed in a histogram). Nonetheless, it is also common to compare the shapes of two independent distributions, and to modify one of them so that their shapes are as similar as possible (as is the case for calibration of simulated to real data, or W boson mass fits via the template method [1]).

The main focus of the study presented in this document is around the later scenario, when two samples are compared to each other. It is of interest because such studies typically lead to discontinuous χ^2 curves (with many non-physical minima), which are generally left untreated and worked around with approximate methods, but the lack of treatment sets a limit on the accuracy (and implementability) of such a calibration and can provide misleading results.

By deepening into the available bibliography, one can find studies where such discontinuities are treated. However, these typically depend on a solution that is custom-made for a specific scenario. Such is the case of top-quark measurement studies [2], where functional forms that depend indirectly on physics parameters are fitted to data distributions. Consequently, extracting and generalizing the procedure may be difficult for the average reader.

Our goal is to provide in this note a general description of a method to treat χ^2 discontinuities, as well as a practical example, aiming to make such a method accessible to a general public.

2 The migration problem

2.1 Traditional χ^2 minimization: histogram vs. PDF

Let us think of a simple example, where a sample comprised of 10^5 entries is generated with a Gaussian of known standard deviation $\sigma = 1$, but unknown mean μ. The corresponding distribution, histogrammed with n bins between -3 and 3, is shown in Figure 1 (top-left). If we are interested in fitting a Gaussian PDF, such as

$$f(x;\sigma=1,\mu,K) = \frac{K}{\sqrt{2\pi\sigma^2}} e^{-\frac{(x-\mu)^2}{2\sigma^2}} = \frac{1}{\sqrt{2\pi}} e^{-\frac{(x-\mu)^2}{2}} \tag{1}$$

(Figure 1, bottom-left), where the normalization constant K takes into account the size of the sample (roughly, $K \approx$ number of events), one can define a χ^2 as the difference between the bin content N_i of the histogram and the function $f(x;\mu,K)$ evaluated at the center of each bin x_i (with bin width h_i) for some μ, weighted by the bin error δ_i. In other words,

$$\chi^2(\mu,K) = \sum_i^n \frac{[N_i - h_i \times f(x_i;\mu,K)]^2}{[\delta_i]^2}, \tag{2}$$

where N_i and δ_i remain constant. In the literature [3], Eq. (2) is known as the *modified least-squares method (MLS)*.

Please note that, for this particular example, the sample size is sufficiently large compared to the bin width. That is, the number of events N_i in each of the bins i is large enough as to approximate the corresponding

Poisson distribution by a Gaussian (for instance, there are at least 70 events per bin in the far tails of Figure 1, whose histogram is comprised of $n = 40$ bins), thus enabling the use of the χ^2 defined in Eq. (4). Should the sample be considerably smaller and bins in the tails contain just a few events, a more appropriate way to study the shape of the distribution would be achieved via the binned likelihood approach [3], which takes into account the Poissonian nature of the bin contents.

Such a χ^2 definition results in a (typically parabolic) continuous curve as a function of μ, as shown in Figure 1 (right hand side). Following traditional statistics, the best estimator of μ, called $\hat{\mu}$, is the value at the minimum of the χ^2 curve, i.e. $\chi^2(\hat{\mu}) = \chi^2_{\text{min}}$. Similarly, one can estimate the corresponding parameter uncertainty $\sigma(\mu)$ by looking for

$$\Delta\chi^2 = \chi^2(\hat{\mu} \pm \sigma(\mu)) - \chi^2(\hat{\mu}) = 1. \tag{3}$$

This is illustrated in Figure 1, where a parabolic fit to the χ^2 curve indicates a minimum at $\hat{\mu} = -0.0040$ with error $\sigma_{\Delta\chi^2=1} = 0.0032$, which is consistent with the distribution of the nominal sample (see the statistics box in the top-left graph of Figure 1).

In most parameter optimization studies, this method can be used to estimate the value of unknown parameters, with a big caveat: the analytical form of the PDF must be known a priori. The case considered here, where there is no direct access to an analytical PDF and two samples are compared directly to each other, can prove to be challenging as described below.

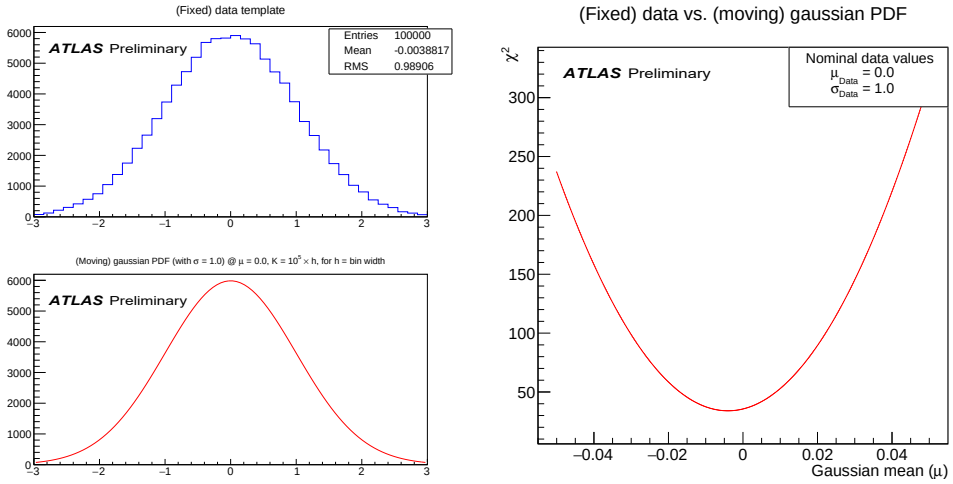

Figure 1: Traditional χ^2 minimization scenario. A fixed data template (known to be Gaussian with $\sigma = 1$, top-left) is being fitted by a Gaussian PDF (also with $\sigma = 1$ but variable μ, bottom-left). The right plot shows the χ^2 between the fixed template and the PDF as a function of μ [$\chi^2(\mu)$], fixing the normalization constant to $K = 10^5 \times h$, where h is the bin width.

2.2 Histogram vs. histogram χ^2 minimization

Following the previous section, let us consider now the case where we have two independent samples, which shall be called data and MC, and we want to match the shape of their corresponding distributions by

doing an event-by-event correction to the MC sample. Trying to keep things simple for the moment, let us define such samples as follows:

- Data remains the same distribution as in the previous example (top-left of Figure 1, also top-left of Figure 2), i.e., $N_{\text{data}} = 10^5$ events that have been generated with a Gaussian of $\sigma_{\text{data}} = 1$ and $\mu_{\text{data}} = 0$ (although μ_{data} is considered as unknown a priori). This sample remains constant through the study.
- MC is also generated (only once) with a Gaussian of $\sigma_{\text{MC}} = 1$ for $\mu_{\text{MC}} = 0$, containing a total of N_{MC} events. We do not have access anymore to the analytical PDF, but the list of individual events is available (and in fact, filling them into a histogram gives their distribution, bottom-left of Figure 2).

Let us realize first that a change in the mean value $\mu_{\text{MC}} \rightarrow \mu'_{\text{MC}} = \mu_{\text{MC}} + \Delta\mu$ is equivalent to shift all the events i by $\Delta\mu$ (i.e. $x_i \rightarrow x'_i = x_i + \Delta\mu$). As we are trying to match the shape of the MC distribution to that of data, and we know that (once normalized to the number of events) they only differ by their mean value, one could look for the value of $\Delta\mu$ such that the distribution of data and MC' (this is, after the shift) are as similar as possible. In other words, the MC distribution is being fitted to data.

First, let us notice that for each value of $\Delta\mu$ there is a distribution of events (in a histogram). As we are purely interested in matching the shape of the MC distribution to that of the data, and the samples may have different sizes (in general, $N_{\text{data}} \neq N_{\text{MC}}$), one must normalize the MC to the data. For this particular case, we choose to multiply the MC histogram by some factor $C^{\text{norm.}}$ such that the integral of data and MC histograms have the same value. One could then naively define a χ^2 by looking at the difference between normalized histograms i.e.

$$\chi^2(\Delta\mu) = \sum_i^n \frac{\left[N_i^{\text{data}} - N_i^{\text{MC}'}(\Delta\mu)\right]^2}{[\delta_i^{\text{data}}]^2 + [\delta_i^{\text{MC}'}(\Delta\mu)]^2}, \tag{4}$$

(where the MC uncertainty has been included, as it may not be negligible) and minimizing it with respect to $\Delta\mu$. Nonetheless, if one were to provide this function to a minimization algorithm (such as MINUIT [4]), it would completely fail. The reason is simple, but only noticeable when the plot is available: the χ^2 curve in the histogram vs. histogram case **is not continuous**.

In order to understand the reason behind the discontinuity, it is useful to notice that a χ^2 defined as in Eq. (4) is nothing more than the sum of n individual χ_i^2 values, one per bin, with

$$\chi_i^2 = \chi_i^2(\Delta\mu) = \frac{\left[N_i^{\text{data}} - N_i^{\text{MC}'}(\Delta\mu)\right]^2}{[\delta_i^{\text{data}}]^2 + [\delta_i^{\text{MC}'}(\Delta\mu)]^2}. \tag{5}$$

By shifting the individual events by $\Delta\mu$, there is a partial migration of events from one bin to a neighbouring one (or even further), i.e., after the shift, some events will remain in the same i-th bin, while others will migrate to a different one. Since this migration is discrete, an infinitesimal change of $\chi_i^2(\Delta\mu)$ is followed by a non-continuous change of the bin content $N_i^{\text{MC}'}(\Delta\mu)$ (as well as its error $\delta_i^{\text{MC}'}$), which leads to a discontinuous change of $\chi_i^2(\Delta\mu)$, and eventually of $\chi^2(\Delta\mu)$.

Figure 2 (right hand side, blue curve) shows the effect of the event migration, where the χ^2 values were computed using Eq. (4), all while using the same data distribution as in Figure 1. The MC sample was generated only once with $\sigma_{\text{MC}} = 1$ and $\mu_{\text{MC}} = 0$ (the nominal distribution is shown in the bottom-left of Figure 2), and shifted in steps of $\Delta\mu$. For comparison, the red curves showing the analogous analytical scenario histogram vs. PDF (previously discussed, shown in Figure 1) are superimposed. Note that the blue χ^2 curve is wider than the red one due to the non-negligible effect of the MC statistical uncertainty. In the case of an infinitely large MC sample, the blue curve would tend towards the red one.

The huge χ^2 discontinuities generate multiple local minima a few χ^2-units deep, and not even the global minimum is obvious anymore. In this particular example, there seems to be a global minimum at 0.0065, which is completely wrong when comparing to the analytical estimate. Furthermore, the estimation of parameter errors (following from Eq. (3)) is not reliable anymore, as looking for

$$\Delta\chi^2 = 1$$

becomes completely obscured by the size of the discontinuities. This is particularly noticeable in Figure 3, at e.g. $\Delta\mu = 0.001$ and $\Delta\mu = 0.0065$.

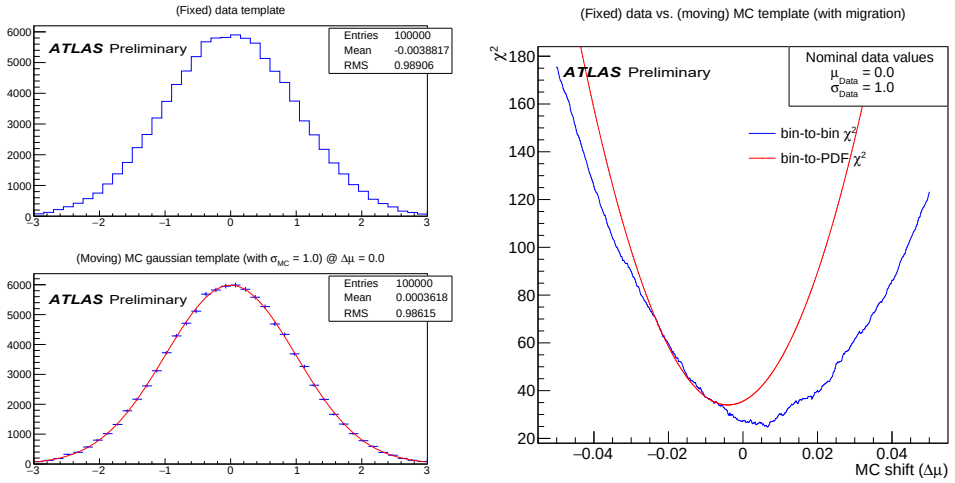

Figure 2: Discontinuous χ^2 curve between two samples (histogram vs. histogram) due to event migration (shown in blue on the right hand side). The analogous analytical scenario (identical to Figure 1) is shown in red.

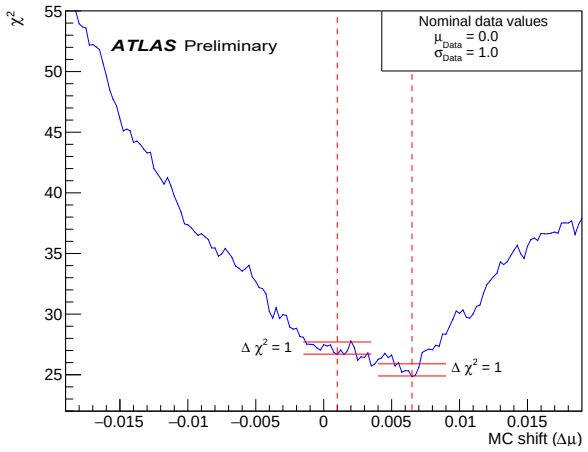

Figure 3: Amplified view of the bin-to-bin χ^2 curve shown in Figure 2 (right hand side).

2.3 The typical workaround

In relatively simple studies with only one or two free parameters, one can use an (approximate) approach to work around the discontinuities with the so-called template method. To first order, this consists of doing a manual χ^2 scan for different parameter values, and simply fitting a parabola to estimate the position of the minimum.

The caveat here is that, in order to increase the reliability of this technique, one must do the parabolic fit to a sufficiently large region such that the discontinuities are relatively small. However, by going far enough from the minimum one risks leaving the Gaussian regime, and entering in asymmetric cases that cannot be described with a parabola anymore.

Moreover, there is an additional complication with such an approach. Looking at Figure 2 (right hand side, blue curve), let us consider the MC histograms for two different shifts, that is, MC($\Delta\mu_1$) and MC($\Delta\mu_2$). As the data and MC samples do not have correlations, the corresponding values χ^2_1 and χ^2_2 can be computed with Eq. (4). However, one must notice that the individual base events that make up the MC sample (before the $\Delta\mu$ shift) do not change, so the histograms MC($\Delta\mu_1$) and MC($\Delta\mu_2$) are correlated due to the event migration between bins. This means that while the computation of χ^2_1 and χ^2_2 do not need additional considerations, their values share a relation due to indirect correlation, so comparing χ^2_1 to χ^2_2 (i.e. putting them in the same plot) must be done with care. Potentially, one could aim to get rid of the χ^2 discontinuities if the migration can be perfectly quantified and taken into account, but such an approach is not trivial to implement. Furthermore, if the previous considerations are not taken into account, the parabolic fit approach would not directly provide a reliable estimate of the real position of the minimum, and additional treatment may be required.

As a final note, while parabolic fits are a quick workaround to the χ^2 discontinuities for a single parameter, such a technique is not feasible for a large number of free parameters, which very quickly increases the complexity of the implementation.

2.4 Resampling techniques

While one may be tempted to use resampling techniques (such as studies with bootstrap or data replicas fluctuated by its statistical uncertainty) in order to return to the continuous χ^2 scenario, these are unfortunately unable to explain/correct the discontinuities. There are primarily two reasons for this:

- By definition, resampling techniques must conserve the size of the sample, i.e., no new events are generated. This means that even if 10^6 replicas of the sample are created and averaged, the effective sample size will remain the same, and in fact the average χ^2 values would remain constant due to the Central Limit Theorem [3].
- The discontinuities in the χ^2 curve are artifacts of the finite MC sample size, rather than straightforward statistical effects. One could suppress the discontinuities if the bin-to-bin migration becomes infinitesimal (relative to the total MC sample, normalized to data), which is achievable only if the sample becomes infinitely large (extremely impractical).

While resampling remains useful for error propagation estimation, a different technique must be used to treat the discontinuities.

3 Getting rid of the migration-induced discontinuities: histogram vs. fitted PDF minimization

The treatment for χ^2 discontinuities due to event migration may be obvious by now: one should avoid directly comparing the histogrammed shapes of two samples, and prefer histogram vs. PDF comparisons. That being said, this is not a luxury we always have, as many samples (such as fully calibrated MC samples) have been through several complex correction steps, and cannot be described exactly with an analytical PDF.

In order to go back to the case described in Subsection 2.1, one must estimate the PDF corresponding to the MC sample. In other words, for a set of free parameters $\vec{p}$ acting event-by-event on the MC sample (giving a corresponding distribution in a histogram $\texttt{histMC}(\vec{p})$), we wish to estimate the corresponding analytical description $f^{\text{MC}}(x;\vec{p})$ in a non-parametric way (i.e. when the dependence on $\vec{p}$ is not explicit), and use a χ^2 as defined in Eq. (2).

A possibility is to use Kernel Density Estimation (KDE) [5] to approximate the PDF of the MC sample using e.g. a Gaussian kernel. This allows infinitesimal changes in $\vec{p}$ to be well accounted for while giving a function $f^{\text{MC}}_{\text{KDE}}(x;\vec{p})$ that is continuous by definition, and can be used directly in Eq. (2). A downside, however, is that the estimation of a kernel density becomes time-consuming for large samples.

An alternative to this, not limited by the size of the sample, is to identify a case-tailored functional form capable of describing well enough the shape of the distribution, i.e., to fit a function $f_{\text{fit}}(x;\vec{\theta})$ (built for the specific study) to the distribution $\texttt{histMC}(\vec{p})$ such that $\chi^2_{\text{fit-on-histMC}}/n_{\text{dof}} \approx 1$ (where n_{dof} is the number of degrees of freedom of the fit) and the bias induced in the shape is minimal (see Subsection 4.3 for a practical example).

As a general rule, the procedure involves replacing the χ^2 function (Eq. (2)) used by the minimization algorithm (e.g. Minuit) such that the algorithm evaluates a new quantity at each point in the parameter space. The quantity is calculated as follows:

1. Correct all the events in the MC sample for a given value of $\vec{p}$
2. Build/draw the corresponding distribution in a histogram $\texttt{histMC}(\vec{p})$
3. Fit the already defined functional form $f_{\text{fit}}(x;\vec{\theta})$ to $\texttt{histMC}(\vec{p})$
   $\rightarrow$ this gives $f^{\text{MC}}_{\text{fit}}(x;\hat{\vec{\theta}}(\vec{p}))$
4. Use $f^{\text{MC}}_{\text{fit}}(x;\hat{\vec{\theta}}(\vec{p}))$ to evaluate a modified χ^2 quantity, as described in Subsection 3.1, that takes account of bin-to-bin correlations

Note that the fitted values $\hat{\vec{\theta}}$ depend indirectly on $\vec{p}$, and thus $f^{\text{MC}}_{\text{fit}}$ depends implicitly on the parameters $\vec{p}$.

A well chosen functional form of $f_{\text{fit}}(x;\vec{\theta})$ must fulfill certain criteria:

- It must be able to describe well enough the shape of the distribution $\texttt{histMC}(\vec{p})$.
  - this also translates in including enough free parameters $\vec{\theta}$.
- There should not be any obvious bias of the shape of the distribution, neither for the initial histogrammed distributions, nor for the MC distribution after applying some $\vec{p}$ within parameter limits (e.g. the fitted function should remain within the statistical uncertainty of $\texttt{histMC}(\vec{p})$).

- It must be capable of accounting for small changes in the parameter values i.e. to correctly see the effect of a small change $\vec{\Delta p}$.
  $\rightarrow$ in practice, it is desired that an (almost[1]) infinitesimal change of the free parameters of the correction
  $$\vec{p} \rightarrow \vec{p} + \mathrm{d}\vec{p}$$
  corresponds to an (almost) infinitesimal change of the fitted parameters
  $$\hat{\vec{\theta}}(\vec{p}) \rightarrow \hat{\vec{\theta}}(\vec{p}) + \mathrm{d}\vec{\theta}$$
  for some $\mathrm{d}\vec{\theta}$.

An example of a poorly chosen $f_{\text{fit}}(x;\vec{\theta})$ is the use of a simple Gaussian (Eq. (1)) to describe a Breit-Wigner distribution (unknown a priori):

$$f^{\text{BW}}(x) = \frac{k}{(x^2 - m^2) + m^2\Gamma^2}. \tag{6}$$

While both are symmetric and have a well defined mean (respectively μ and m, which in fact would yield similar values in both cases due to symmetry), the standard deviation σ of the Gaussian function is not compatible with the width Γ of the BW, and thus, the final estimation of $\vec{p}$ would be biased by this forced change of shape. A better description could be attained by including additional free parameters to f_{fit} (e.g. polynomials as in

$$f_{\text{fit}}(x;\mu,\sigma,A,B) = \frac{1}{\sqrt{2\pi\sigma^2}} e^{-\frac{(x-\mu)^2}{2\sigma^2}} + A(x-\mu) + B(x-\mu)^2,$$

which could follow more closely the shape of the distribution), but again, this has to be tailored for the particular study.

It is worth mentioning that, while the addition of free parameters allows more complex distribution shapes to be described, strongly correlated ones can lead to multiple sets of solutions $\hat{\vec{\theta}}$ describing well enough the distribution (i.e. multiple local minima exist). As any of the minima can be randomly found by the fit, this does not satisfy the third criterion above, as $\hat{\vec{\theta}}$ is no longer a continuous function of $\vec{p}$. In practice, these multiple local minima can lead to equally correct data vs. MC($\vec{p}$) χ^2 curves, equivalent up to a small vertical shift. Numerically this is problematic, because if the same minimum is not followed as $\vec{p}$ changes and the fit finds different ones randomly, the observed χ^2 curve values can alternate between the corresponding curves, appearing as a branching of the observed χ^2 surface (see for instance the example in Figure 4). There are multiple "tricks" that allow the "good" set of solutions to be selected consistently, which are good practices for any fit, such as:

- Providing an ansatz of the starting parameters $\vec{\theta}_{\text{initial}}$ for the fit of f_{fit}. One can look at e.g. the mean, RMS or position of the maximum of `histMC(`$\vec{p}$`)`.
- Dynamically defining tight enough limits for the free parameters $\vec{\theta}$ to exclude undesired minima, yet loose enough to not interfere with the fit.

[1] We say "almost" because, in reality, the MC sample has a finite size, so one could find a small enough $\vec{\Delta p}^{\,\text{min}}$ that generates no migration. This means that the corresponding histograms would be exactly the same `histMC(`$\vec{p}$`) = histMC(`$\vec{p} + \vec{\Delta p}^{\,\text{min}}$`)`, and thus $f_{\text{fit}}^{\text{MC}}(x;\hat{\vec{\theta}}(\vec{p})) = f_{\text{fit}}^{\text{MC}}(x;\hat{\vec{\theta}}(\vec{p} + \vec{\Delta p}^{\,\text{min}}))$. That being said, MC samples are typically large enough for this to not be an issue, so doing steps as small as $\vec{\Delta p}^{\,\text{min}}$ would not make sense from a computational point of view.

Note that in general, these are not enough. Additional considerations may be required for more complex problems.

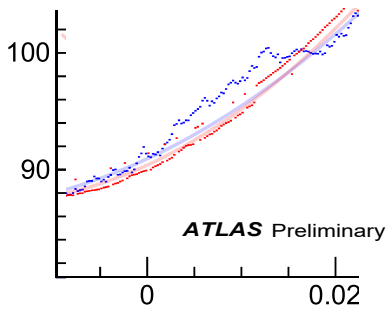

Figure 4: Example of χ^2 branching caused by the unsupervised addition of free parameters. The blue dots show the bin-to-bin discontinuities χ^2, while the red is computed using the bin-to-fittedPDF technique described in this study.

3.1 Bin-to-fitted PDF χ^2 minimization

Intrinsic to the fit of $f_{\text{fit}}^{\text{MC}}(x;\hat{\vec{\theta}}(\vec{p}))$, there are uncertainties and correlations among all the fitted parameters, which must be propagated to the uncertainty in $f_{\text{fit}}^{\text{MC}}$ itself (and correlation between predicted MC bin contents). Consequently, it is not possible to directly use the χ^2 definition shown in Eq. (2), but rather the more generalized form is necessary:

$$\chi^2 = \vec{d}^{\,\text{T}} V^{-1} \vec{d}, \tag{7}$$

where $\vec{d}$ is the vector of differences between data and MC such that $d_i = N_i^{\text{data}} - N_i^{\text{MC,pred}}$ and V the total covariance matrix.

There are two options to compute $N_i^{\text{MC,pred}}$: either to take the value of $f_{\text{fit}}^{\text{MC}}(x;\hat{\vec{\theta}}(\vec{p}))$ at the middle of each bin, or to take the average of the function along each bin. As the former option yields a bias if the function has a sizeable curvature inside a given bin, in the following we choose to use the later, which also happens to be consistent with the definition of a PDF. That is, for $f(x) = f_{\text{fit}}^{\text{MC}}(x;\hat{\vec{\theta}}(\vec{p}))$ and equally-sized bins of width h, we define

$$d_i = N_i^{\text{data}} - \overline{f(x)}\big|_{x_k} = N_i^{\text{data}} - \left[\int_{x_i-\frac{h}{2}}^{x_i+\frac{h}{2}} f(x)\mathrm{d}x\right]\frac{1}{h}. \tag{8}$$

In the most general case, the total covariance matrix is defined as

$$V = V^{\text{data}} + V^{\text{MC}}, \tag{9}$$

where

$$\left(V^{\text{data}}\right)_{ij} = \delta_{i,j}\cdot(\sigma_i^{\text{data}})^2,$$

and where δ_{ij} is the Kronecker delta, and σ_i^{data} the statistical bin uncertainty of data. This means that, as expected, the covariance matrix for data remains diagonal, and there are no inter-bin correlations.

Different from the data case, V^{MC} is not a diagonal matrix. Since its content propagates from the error of the fitted $\hat{\vec{\theta}}$ and the correlations between parameters $\rho_{k,l}$, the entries of V^{MC} are to be estimated on the fly via

$$V_{i,j}^{\text{MC}} = V^{\text{MC}}(x_i, x_j) = \langle \mathrm{d}f\big|_{x_i}, \mathrm{d}f\big|_{x_j} \rangle = \langle \sum_k \overline{\frac{\partial f}{\partial \theta_k}}\Big|_{x_i} \mathrm{d}\theta_k, \sum_l \overline{\frac{\partial f}{\partial \theta_l}}\Big|_{x_j} \mathrm{d}\theta_l \rangle \tag{10}$$

$$\Rightarrow V_{i,j}^{\text{MC}} = \sum_{k,l} \overline{\frac{\partial f}{\partial \theta_k}}\Big|_{x_i} \overline{\frac{\partial f}{\partial \theta_l}}\Big|_{x_j} \sigma_k \sigma_l \rho_{kl}, \tag{11}$$

where σ_k and σ_l are the fit errors for the parameters of f, ρ_{kl} their respective correlation, and $\overline{\frac{\partial f}{\partial \theta_k}}\Big|_{x_i}$ the average value of the gradient in the bin i.

Putting all the previous into practice for the (trivial) Gaussian example of Subsection 2.2, one can very easily obtain the migration-treated χ^2 curve as displayed in Figure 5 (in red). It follows closely the behaviour of the migration-affected χ^2, but conserving the parabolic behaviour and being free of multiple minima.

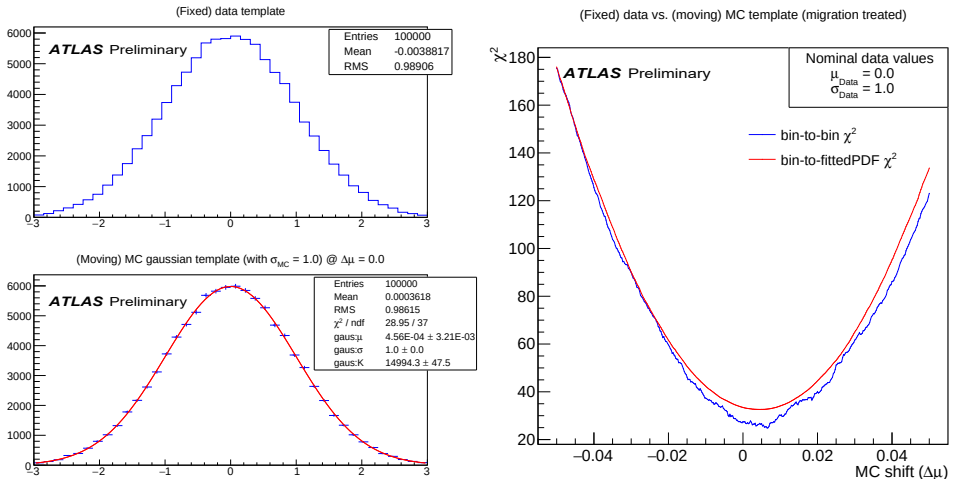

Figure 5: χ^2 treated due to event migration-induced discontinuities, corresponding to the simplified case described in the beginning of Subsection 2.2. It shows in blue the original untreated curve, and in red the result of the method described in Subsection 3.1. Note that the blue curve is the same as in Figure 1, while the red one is obtained with a different method.

4 A practical example

While the case described in the previous section is rather pedagogical and demonstrative, it may seem redundant and unnecessary (we are, in the end, generating a sample with a Gaussian distribution, and then fitting it with a Gaussian). In this section we study a more realistic example.

Let us think of a hypothetical calibration procedure using $Z \to ee$ events, after simulating the detector effects of the ATLAS experiment, looking only at the region around the Z resonance, i.e. 80 GeV $< m_{ee} <$ 100 GeV. We define first our pseudodata as a subset of the whole simulated sample (e.g. half of it), and MC as the rest of the sample (i.e. the other half). The objective of this calibration method is to minimize the shape difference between the pseudodata and (normalized) MC binned distributions by uniformly changing the reconstructed MC energy scale event by event as

$$E^{\mathrm{MC}}_{\mathrm{corr}} = E^{\mathrm{MC}} + p_0,$$

such that the calibrated reconstructed dilepton mass would roughly look as

$$m^{\mathrm{corr}}_{ee} \approx 2E^{\mathrm{corr}}_1 E^{\mathrm{corr}}_2 (1 - \cos(\Delta\theta)).$$

In other words, we want to find the best value of p_0 such that the χ^2 between pseudodata and MC histograms is minimized.

While the corresponding "truth" distribution of the MC m_{ee} is expected to be a Breit-Wigner function, the smearing of energies due to the simulation of detector effects generates a sample with no analytical PDF. This means that a bin-to-PDF minimization is not possible. However, by using the method described in Subsection 3.1, one can get rid of χ^2 discontinuities due to event migration (as exemplified in Figure 8), thus allowing a binned study to be performed.

4.1 Functional forms

Two functional forms have been seen to best describe the mass lineshape, although there may be others that do a just-as-well (or perhaps even better) job at describing the lineshape. These two forms shall be called *Breit-Wigner-like* (BW) and *Crystal Ball with exponential tails* (CB). These are defined respectively as:

$$f^{\mathrm{BW}}(x) = \begin{cases} 80 < x < c_1: & e^{F(x-P)} + R \\ c_1 < x < c_2: & \dfrac{C}{(x-A)^2 + B} + E(x-D)^2 \\ c_2 < x < 100: & e^{G(x-Q)} + S \end{cases} \tag{12}$$

and

$$f^{\mathrm{CB}}(x) = \begin{cases} 80 < x < c_1: & e^{D(x-P)} + R \\ c_1 < x < c_2: & \dfrac{C}{B\sqrt{2\pi}} e^{-\frac{1}{2}\left(\frac{x-A}{B}\right)^2} \\ c_2 < x < 100: & e^{E(x-Q)} + S, \end{cases} \tag{13}$$

where the parameters P, Q, R and S are used to assure continuity of $f(x)$ and $\mathrm{d}f(x)/\mathrm{d}x$ (see Subsection 4.2). Variables A through G are the free parameters of the fit, as well as the nodes c_1 and c_2 (i.e. the transition points between the exponential tails and the core-function).

It is important to mention that, while some of these parameters can have a physical interpretation, a priori these do not have to be connected to a physical quantity. For this particular application, the only purpose of the functional forms is to describe the shape of the template as well as possible.

4.2 Continuity of the function and its derivative

As there is no reason to expect a non-smooth template in the infinite-statistics scenario, the functional forms should follow the same hypothesis. This means that both $f(x)$ and $\mathrm{d}f(x)/\mathrm{d}x$ should be continuous along the whole range (and particularly at the nodes c_1 and c_2).

The procedure to assure continuity is analogous for either functional form. Let us focus particularly at $x = c_1$ for the Breit-Wigner-like function (Eq. (12)):

$$f^{\mathrm{BW}}(x) = \begin{cases} 80 < x < c_1: & f^{\mathrm{BW}}_{\mathrm{left-tail}}(x) = e^{F(x-P)} + R \\ c_1 < x < c_2: & f^{\mathrm{BW}}_{\mathrm{core}}(x) \\ c_2 < x < 100: & f^{\mathrm{BW}}_{\mathrm{right-tail}} = e^{G(x-Q)} + S. \end{cases}$$

4.2.1 Derivative continuity

Since we are interested in a smooth function at the nodes, we can simply establish derivative continuity via

$$\left.\frac{\mathrm{d}\, f^{\mathrm{BW}}_{\mathrm{core}}(x)}{\mathrm{d}x}\right|_{x=c_1} = \left.\frac{\mathrm{d}\, f^{\mathrm{BW}}_{\mathrm{left-tail}}(x)}{\mathrm{d}x}\right|_{x=c_1} = F e^{F(x-P)}|_{x=c_1}$$

$$\Rightarrow P = \frac{-1}{F} \ln\left(\left.\frac{\mathrm{d}\, f^{\mathrm{BW}}_{\mathrm{core}}(x)}{\mathrm{d}x}\right|_{x=c_1} \times \frac{1}{F} \right) + c_1 \,.$$

The determination of Q for derivative continuity at c_2 is analogous.

4.2.2 Function continuity

Similarly, we want

$$f^{\mathrm{BW}}_{\mathrm{core}}(x)\big|_{x=c_1} = f^{\mathrm{BW}}_{\mathrm{left-tail}}(x)\big|_{x=c_1} = e^{F(c_1-P)} + R,$$

which implies

$$R = f^{\mathrm{BW}}_{\mathrm{core}}(x)\big|_{x=c_1} - e^{F(c_1-P)},$$

where P has already been determined, and the rest are free parameters. The parameter S, which provides function continuity at c_2, is determined in the same fashion.

4.3 Bias induced by the functional form

Before proceeding with the study, it must be decided whether the functional forms describe well enough the data and MC distributions. In order to judge this, one can look at the induced bias and χ^2 of the fit.

We define the bias, in a bin by bin manner, as the ratio between the average of the fitted function and the histogram (Figure 6, bottom plot). A good enough functional form should be able to describe the shape of the distribution along the whole range, i.e., the ratio should be close to 1 (within statistical uncertainty). A badly chosen function would show systematic deformations of this ratio (consider for instance, the ratio of a Gaussian and a Breit-Weigner curve).

In a more quantitative approach, it is also good to continuously monitor the χ^2_{fit} value of the fit, and assure it remains in an acceptable range. This is a good indicator of the quality of the fit and whether the functional form remains capable of describing the shape of the distribution. In general, for n_{dof} degrees of freedom, it is desired to have $\chi^2_{\text{fit}} \in [n_{\text{dof}} - \sqrt{2 \times n_{\text{dof}}}\ ,\ n_{\text{dof}} + \sqrt{2 \times n_{\text{dof}}}]$. Such a range, though, should also be tuned for each study.

Note that, for a set of parameters $\vec{p} = \{p_0, p_1, ...\}$ being optimized, if $\chi^2_{\text{fit}}(\vec{p}_{\text{initial}})$ is acceptable but $\chi^2_{\text{fit}}(\vec{p}_1)$ gets very degraded for some $\vec{p}_1$, it can mean either that the functional form is not capable of properly catching the effects of changing the parameters $\vec{p}$, or that the possible values of the parameter should be limited to a narrower range. Failing to do so could further bias the optimization of the parameters $\vec{p}$.

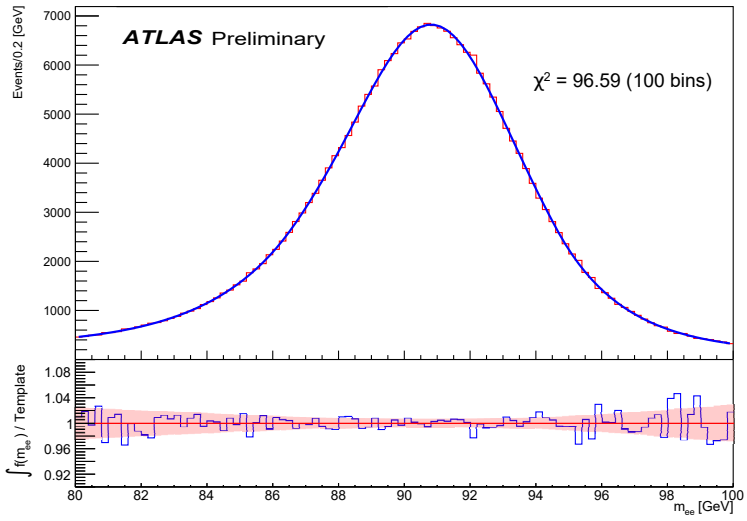

Figure 6: Bias inspection of the Crystal Ball function (Eq. (13), 7 free parameters) fitted to the MC distribution. The ratio shows the average of the fitted function, per bin, to the histogram, and the band shows the relative bin statistical uncertainty.

4.4 Propagation of correlation

The covariance matrix for the predicted MC template is computed using Eq. (11). An example of the bin-to-bin MC correlation is shown in Figure 7 for a 100 bin histogram (in the 80 to 100 GeV range), where the transition nodes (c_1 and c_2) can be noticed by eye, and a strong correlation between neighbouring bins is evident. Nonetheless, the correlation between far apart bins is weak.

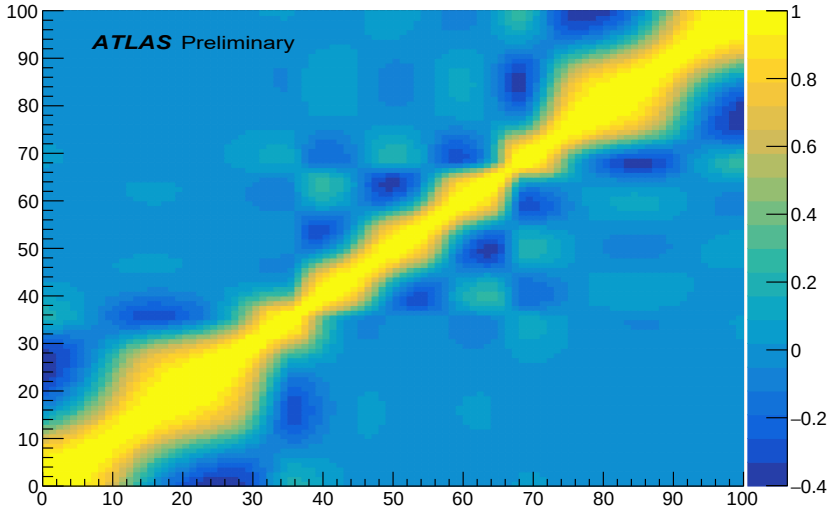

Figure 7: Example of correlation matrix for the Breit-Wigner-like functional form.

4.5 Migration treated χ^2 curve

Putting all the previous quantities together using Eq. (7), we can build the corresponding χ^2 value for a particular shift in p_0. Repeating the same procedure for many different values of p_0, we can build the corresponding migration-less χ^2 curve as shown in red in Figure 8. A parabolic fit is also shown in Figure 8 for both of the χ^2 curves (in the same colour as the corresponding curve, but fainter).

The first remark one can make is that the χ^2 discontinuities nearly disappear with the bin-to-fitted PDF method, and the minimum of the curve becomes well defined. Furthermore, the red curve follows almost perfectly the corresponding parabolic fit, which is expected in the completely analytical case.

As briefly mentioned before, an approximate quick treatment to the migration problem is to simply fit a parabola to the discontinuous curve. As shown with the blue curve in Figure 8, such a fit can approximate well enough the position of the minimum and size of the error, and the only way to improve it is by doing the scan in a larger region, e.g., $-0.5 < p_0 < 0.5$, with the latent risk of including points outside the region where the χ^2 is parabolic. Furthermore, this is only viable in the few free parameter scenario, strongly motivating the use of the bin-to-fittedPDF method.

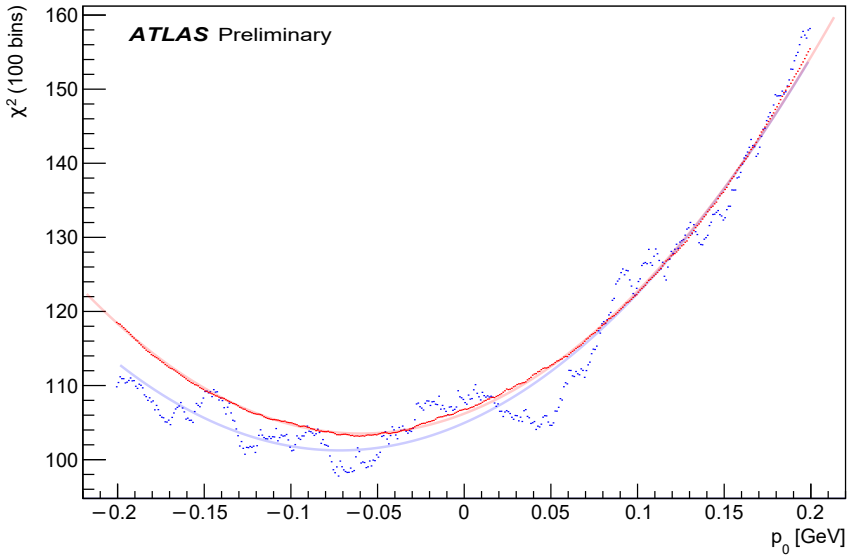

Figure 8: Practical example of the bin-to-fitted PDF method proposed in Subsection 3.1 (shown with red dots). The corresponding bin-to-bin discontinuous χ^2 is displayed with blue dots. For comparison, the parabolic fits on each of the χ^2 curves are plotted as faint continuous lines (in the same colour as the corresponding dotted curves).

5 Unbinned likelihood approach

Since the method described here explicitly provides an analytical approximation to the PDF of the distribution, one could even ditch completely the χ^2 method and use an unbinned likelihood. Furthermore, the same functional form can be fitted to the data distribution, enabling as well the use of a Likelihood ratio[2] such as

$$-2\log\mathcal{L}_R(\vec{p}) = -2\sum_i^{N_{\text{data}}}\log\frac{f(x_i;\hat{\vec{\theta}}_{\text{MC}}(\vec{p}))}{f(x_i;\hat{\vec{\theta}}_{\text{data}})}, \tag{14}$$

where the sum $\sum_i^{N_{\text{data}}}$ runs over all the individual data events (in the previous example, each of these corresponds to a single $Z \to ee$ event), $f(x_i;\hat{\vec{\theta}}_{\text{data}})$ has been fitted (only once) to the data histogram distribution, and $f(x_i;\hat{\vec{\theta}}_{\text{MC}}(\vec{p}))$ is fitted to MC for each $\vec{p}$ during the minimization procedure. Note that the functional form fitted to data and MC must be the same (e.g. both should be Breit-Wigner-like), and that the values of the fitted parameters $\hat{\vec{\theta}}_{\text{data}}$ and $\hat{\vec{\theta}}_{\text{MC}}$ will be, in general, different.

[2] N.B. as the denominator is completely independent of $\vec{p}$ (and in fact, it can be separated as a constant $+2\sum_i^{N_{\text{data}}}\log f(x_i;\hat{\vec{\theta}}_{\text{data}})$), it will not modify the position of the minimum of $-2\sum_i^{N_{\text{data}}}\log f(x_i;\hat{\vec{\theta}}_{\text{MC}}(\vec{p}))$. Moreover, the denominator normalizes the negative log-likelihood, allowing to work with very small numbers by bringing the minimum along the y-axis to ~ 0 instead of being at arbitrarily large numbers. This is also preferred by the minimizer, because the likelihood values are used to compute gradients using very small variations along the $\vec{p}$-space.

Minimizing Eq. (14) yields the same results as the method described in Subsection 3.1, up to a trade-off:

- It is faster (computationally speaking) to compute $-2\log\mathcal{L}_R(\vec{p})$ than the treated χ^2 for the same values of $\vec{p}$, because no covariance matrix must be estimated (i.e., the likelihood relies completely on the central value of $\hat{\vec{\theta}}_{\text{MC}}$ and $\hat{\vec{\theta}}_{\text{data}}$, and does not include information on their errors and correlations),

BUT

- The uncertainties on the fit of $f(x_i;\hat{\vec{\theta}}_{\text{data}})$ and $f(x_i;\hat{\vec{\theta}}_{\text{MC}}(\vec{p}))$ are neglected, which could lead to an undersetimation of the uncertainties on $\vec{p}$ if one uses the $\Delta\chi^2 = 1$ approach.

The choice of method is study-dependent, with the biggest impact being in the time that e.g. MINUIT [4] would need to find the best parameters $\hat{\vec{p}}$.

6 Parameter errors in the hist. vs. fitted PDF case

First, there is a remark worth making: if the minimization methods are unbiased, one should be able to find exactly the same central values of the parameters $\hat{\vec{p}}$ by minimizng either a χ^2 or $-2\log\mathcal{L}_R$. That being said, the estimation of the errors on $\hat{\vec{p}}$ typically depends on the shape of the curve (which is indeed method-dependent), so some considerations should be taken into account.

If one were to drastically zoom in on the red curves of Figures 5 (right hand side) and 8, which show results of the hist. vs. fitted PDF procedure, tiny imperfections around a parabolic curve (consequence of the MC statistical uncertainty) would be seen. Normally this is not problematic, as it is possible to set a value of sensitivity with which the minimizer "sees" the χ^2. In MINUIT, for instance, this is done through the `precision` variable. That being said, such micro-discontinuities and sensitivity have an effect on the estimation of the gradient of the χ^2 surface, which can be problematic for methods that completely rely on knowledge of the derivative, such as the estimation of errors via inversion of the Fisher's information matrix (also called Hessian method) [3].

Alternatively, one may consider the use of algorithms that estimate parameter errors $\sigma(\mu)$ by numerically looking for e.g. $\Delta\chi^2 = \chi^2(\hat{\mu}\pm\sigma(\mu)) - \chi^2(\hat{\mu}) = 1$ (as illustrated in Eq. (3)), such as MINUIT's MINOS [4]. However, as MINOS still relies on the knowledge of the gradient to provide an ansatz for the size of $\sigma(\mu)$, error estimations are perturbed by the remaining micro-discontinuities, even if the effect is milder than in the case of the Hessian method. We observed that this leads to non-reliable error values in 10-20% of the cases. Moreover, using the MINOS algorithm can dramatically extend the computing time required by MINUIT, which in general is not worth it.

It is important to note that the unbinned likelihood approach described in Section 5 does not directly include information of the correlations due to the fit of the PDFs $f(x_i;\hat{\vec{\theta}}_{\text{MC}}(\vec{p}))$ and $f(x_i;\hat{\vec{\theta}}_{\text{data}})$, thus mis-estimating the errors of the parameters $\hat{\vec{p}}$. Should one wish to include the corresponding correlations, a more generalized form of Eq (14) is required, with the drawback of extended computing time at each iteration of the minimization. Moreover, just as in the bin-to-fittedPDF χ^2 technique, it is vulnerable to the same micro-discontinuities, so the corresponding Hessian errors are not reliable.

With all the previous in mind, we suggest to use the errors estimated with any of these methods only as indicative. For precise error determination, it is encouraged to use numerical approaches, such as

resampling studies via pseudodata replicas obtained around the original data distribution [6] (for χ^2) or bootstrap [7] (for unbinned likelihoods).

7 Conclusions

We have described a technique capable of treating and suppressing χ^2 discontinuities generated due to bin-to-bin event migration, allowing to go from a completely unminimizable curve to an almost-parabolic scenario that can be easily optimized by a minimization framework such as MINUIT. Such a technique allows the long-standing histogram vs. histogram minimization problems, which are typically worked around via other approximate methods, to be treated, and enables the posibility for higher-dimensional minimizations. By showing a real-life example, the power of the technique is demonstrated, as well as the relative improvement when compared to the untreated scenario.

References

[1] ATLAS Collaboration,
Measurement of the W-boson mass in pp collisions at $\sqrt{s} = 7$ TeV with the ATLAS detector,
The European Physical Journal C **78** (2018),
URL: https://doi.org/10.1140/epjc/s10052-017-5475-4 (cit. on p. 2).

[2] ATLAS Collaboration, *Top-quark mass measurement in the all-hadronic $t\bar{t}$ decay channel at $\sqrt{s} = 8$ TeV with the ATLAS detector*, JHEP **09** (2017) 118, arXiv: 1702.07546 [hep-ex]
(cit. on p. 2).

[3] G. Cowan, *Statistical Data Analysis*, Oxford science publications, Clarendon Press, 1998,
ISBN: 9780198501558, URL: https://books.google.fr/books?id=ff8ZyW0nlJAC
(cit. on pp. 2, 3, 6, 16).

[4] F. James, *MINUIT Function Minimization and Error Analysis: Reference Manual Version 94.1*,
CERN-D-506 (1994) (cit. on pp. 4, 16).

[5] M. Rosenblatt, *Remarks on Some Nonparametric Estimates of a Density Function*,
The Annals of Mathematical Statistics **27** (1956) 832,
URL: https://doi.org/10.1214/aoms/1177728190 (cit. on p. 7).

[6] G. J. Feldman and R. D. Cousins,
Unified approach to the classical statistical analysis of small signals, Phys. Rev. D **57** (7 1998) 3873,
URL: https://link.aps.org/doi/10.1103/PhysRevD.57.3873 (cit. on p. 17).

[7] ATLAS Collaboration,
Evaluating statistical uncertainties and correlations using the bootstrap method,
ATL-PHYS-PUB-2021-011 (2021), URL: https://cds.cern.ch/record/2759945
(cit. on p. 17).

6 Combined EW+PDF fits

The precise determination of proton parton distribution functions can be considered as one of the main challenges of current particle physics. As Section 1.6 suggests, the main crux of PDF determination studies is the lack of a formal QCD-based prediction for the dynamics of each parton. Consequently, this means that PDFs must be determined using sensitive cross-section data, typically done after proposing a functional form for the parametrisation of the functions $xf_i(x)$. The complexity of PDF studies is such that it requires dedicated techniques and various theoretical assumptions, leading to non-trivial scenarios with a plethora of nuances. One of these approximations relies on the assumed decorrelation between the EW and QCD sectors, leading to PDFs that are fitted for a set of fixed EW parameters, or precision EW measurements that assume the description predicted by a given PDF. As Section 6.1 briefly documents, late ATLAS studies take advantage of the large statistical samples available and use sophisticated analysis methodologies to improve the final uncertainty on precision measurements, whose reduction develops into leading uncertainty contributions from the PDF. Hence, the potential uncertainty misestimation, a consequence of the neglected interplay between the PDF and EW measurements, motivates the development of dedicated studies where both sectors are simultaneously constrained in order to understand their correlation better; the latter sections of this Chapter document a first study of this kind within the ATLAS collaboration.

This Chapter starts with a brief quantitative description of the interest in doing simultaneous EW and PDF studies, focusing specifically towards the mass of the W-boson (m_W). Afterwards, a general overview of the measurement and prediction of cross sections is provided, showing their relationship with the PDF and highlighting relevant technical details; this is complemented with a description of the practical side of the PDF fitting process, providing details of the minimisation framework. It is followed by a series of studies of the cross-section sensitivity to changes of m_W as a function of various observables, eventually leading to the implementation of combined (i.e. simultaneous) EW+PDF fits.

6.1 Motivation

The continuous collection of high-quality data by the ATLAS experiment is constantly increasing the size of the samples available for analysis by the collaboration. Recent precision studies take advantage of these large sample sizes in order to perform measurements with an enhanced statistical uncertainty, leading to total uncertainties where the statistical part contributes minimally. Consequently, most of the uncertainty on a given measurement is given by systematic sources of error, where the contribution of the PDF is a dominant one.

Typical LHC studies assume the EW and PDF parts to be completely uncorrelated. Standard PDF fits use a set of fixed EW parameters (boson masses and widths, coupling factors, etc.) that are considered as perfectly known quantities, in such a way that the only free parameters are related to QCD. Conversely, EW precision measurements assume the PDF description (up to considering PDF parametrisation uncertainties), leading to studies where the base PDF is immutable (up to profiling techniques [132], which gives estimates of the impact of new data on existent PDFs under the assumption of perfectly Gaussian [thus, linearly-behaving] variables, which is not guaranteed to be true even in the classical case). Since PDFs are the dominant source of uncertainties in precision measurements, neglecting possible correlations between the EW and QCD sectors leads to misestimation of the total uncertainty on a given measurement, tarnishing our interpretation of data by unknown amounts.

The ATLAS collaboration has provided a couple of the most precise W-boson mass measurements up to date. In the 2017 study [23], this measurement yielded (after combination) a value of

$$\begin{aligned} m_W &= 80370 \pm 7(\text{stat.}) \pm 11(\text{exp. syst.}) \pm 14(\text{mod. syst.}) \text{ MeV} \\ &= 80370 \pm 19 \text{ MeV}, \end{aligned}$$

with an uncertainty breakdown as shown in Tab. A.1 (Appendix A). The dominant uncertainty contribution comes from the PDF, accounting (in quadrature) with 9.3 MeV out of a total of 18.5 MeV. As this measurement assumes nil correlation with the PDF, the potential misestimation of the final uncertainty may lead to values above or below those where the correlation is properly taken into account. Moreover, the re-analysis study [25] yields an improved handling of the systematics, leading to a smaller final uncertainty:

$$\begin{aligned} m_W &= 80360 \pm 5(\text{stat.}) \pm 15(\text{syst.}) \text{ MeV} \\ &= 80360 \pm 16 \text{ MeV}, \end{aligned}$$

Similarly to the case of m_W, the preliminary measurement of the effective leptonic weak mixing angle ($\sin^2 \theta^{\ell}_{\text{eff}}$) by the ATLAS collaboration [133] gets a major uncertainty

contribution from the PDF modelling. The combined measurement yields a value of

$$\begin{aligned}\sin^2\theta^{\ell}_{\text{eff}} &= 0.23140 \pm 0.00021(\text{stat.}) \pm 0.00024(\text{PDF}) \pm 0.00016(\text{syst.}) \\ &= 0.23140 \pm 0.00036,\end{aligned}$$

which further supports the aforementioned point. The full uncertainty breakdown is given in Tab. A.3 (Appendix A), where the contribution of the PDF uncertainty can be tracked for different measurement combinations.

As the examples above motivate, it is of interest to perform combined studies where both EW parameters and the PDF are simultaneously constrained, as this can provide a measurement of the correlation across both sectors. The non-triviality and complexity of such combined studies mean that these fall out of the scope of typical SM studies, which implies that only a handful of combined studies have been developed under very specific setups. An example of such analysis is the study carried out by the H1 [134] and ZEUS [135] collaborations, where boson masses, weak neutral-current couplings, and EW form factors are determined using HERA data.

The final goal of the study presented through this Chapter is to implement a combined m_W+PDF fit using ATLAS data, focusing primarily on measuring their correlation and estimating the total uncertainty around the mass of the W-boson.

6.2 Cross-section measurements and predictions

The interplay between the EW and QCD sectors in a final pp cross section is discussed through Chapter 1, where Section 1.6 focuses in particular on the prescription of the content of the proton. The primary result on which many LHC theoretical predictions are based is the factorisation theorem (given in Eq. (1.48)), which reads

$$\sigma_{pp\to X} = \sum_{i,j} \int \mathrm{d}x_1 \mathrm{d}x_2 \underbrace{f_i^p(x_1, Q^2)}_{PDF} \underbrace{f_j^p(x_2, Q^2)}_{PDF} \times \hat{\sigma}_{ij}(x_1 x_2 s, \alpha_s(Q^2)). \tag{6.1}$$

In brief, the factorisation theorem separates the mathematical objects responsible for the PDF and hard-scattering (EW) contributions onto the final theoretical estimation, which enables the generation of predictions where each part is computed separately. That said, as both sectors directly contribute to the shape of any differential cross-section prediction, one should expect the appearance of correlations when both sectors are simultaneously free. Before diving into combined studies, let us discuss the standard process used to measure the differential cross section of a given process.

6.2.1 Measurement from data

After identification and reconstruction, each LHC collision (or, for that matter, any kind of particle collision) yields a collection of objects and their 4-momenta, which accounts for all the sub-products generated at the interaction point. On its own, this conglomeration of particles and jets (and missing transverse momentum) is not associated with any specific process. Selection rules are applied in order to efficiently recover the signal generated by a process of interest while excluding as well as possible background processes which may yield a similar signature on the detector. Such selections may be qualitative, such as looking for pairs of oppositely charged electrons with a common vertex, or kinematic, such as looking at specific invariant mass windows and defining transverse momentum cuts. The specific choice of selection rules is study-dependent and boils down to a trade-off between the size of the post-selection sample (which should be as large as possible) and the associated background rejection capabilities.

The classification of the post-selection sample according to some observable (e.g., by filling $Z \to ee$ events into a histogram as a function of the total invariant mass m_{ee}) retrieves a detector-level differential cross section. This provides a first insight into the underlying physics but comes with 2 problems that must be addressed before extracting any meaningful physical result. The first one is that the selection rules are incapable of fully removing every single background event, and consequently, a detector-level cross section will mis-estimate the number of real events generated by a specific process due to overcounting "signal" or inefficient extraction of the relevant events. The second problem arises because any measurement done by the detector is affected by the resolution of each subsystem, which appears as a random smearing around the "real" value of a measured observable, ultimately leading to a differential cross-section distribution whose shape is deformed and whose values are highly dependent on the experimental setup.

Undesired background contributions may be accounted for individually, relying on Monte Carlo simulations or data-driven methods. This is achieved by identifying the exact physical process that may pass the selection rules defined for a study, simulating the corresponding samples such that these are normalized to the luminosity of the data (i.e. amount of collected events), and subtracting their contribution on a given differential cross section from that determined with data alone. See Section 6.6 for a concrete example of backgrounds in the case of a $W \to l\nu_l$ study.

Once background contributions have been removed, it is of interest to remove the detector effects which are deforming the measured cross section. Such effects propagate to the measurements as a (mainly Gaussian) smearing around the "truth" values, which can be modelled as a convolution [46] on top of such quantity by a quasi-Gaussian function. The resolution effect may further propagate and become non-trivial due to the handling of such measurements, such as the estimation of invariant masses. From a mathematical point of view, the removal of detector effects from a measurement corresponds to undoing the aforementioned convolution, which can be achieved via unfolding techniques [46, 136].

Unfolding

Unfolding techniques do not work on an event-by-event basis; instead, these rely on the collective manifestation of the applied convolution. A common approach used in particle physics is via Bayesian unfolding [137, 138], which is an iterative method based on the assumption of the Bayes's theorem. While the details of such techniques are not relevant for the subsequent discussion, the general steps of the unfolding process are briefly described below for the sake of completeness.

Let us consider a post-selection sample of measurements used to generate a differential cross section in 1-dimension according to some variable X, which is built on a histogram $h^{\text{data}}_{\text{reco}}$ such that background contributions have been removed. Let us consider the corresponding MC sample, where both the "truth" and simulated "measured" (labelled as "reco") values for each event are available. We build the 2-dimensional histogram $h^{\text{MC}}_{\text{reco\&truth},ij}$ of a sample by classifying each event (which passes simultaneously truth and reco selection rules) into bins according to the coordinate $(X_{\text{reco}}, X_{\text{truth}})$ (see Fig. 6.1 for an example using p^{ℓ}_{T}), which has the purpose of tracking the collective migration induced by the resolution on the "truth" distribution. The events of this MC sample may present one of two complications: an event can be generated at "truth" level (in the range of the measurement) but not reconstructed (also in the relevant range), or the converse situation can appear, where an electron is reconstructed but the corresponding truth is outside of the range; this leads to the definition of the corresponding efficiency ϵ_j and purity p_i [139] via

$$\epsilon_j = \frac{\sum_i h^{\text{MC}}_{\text{reco\&truth},ij}}{h^{\text{MC}}_{\text{truth},j}} \tag{6.2}$$

and

$$p_i = \frac{\sum_j h^{\text{MC}}_{\text{reco\&truth},ij}}{h^{\text{MC}}_{\text{reco},i}}. \tag{6.3}$$

Moreover, the "migration matrix" M_{ij} is defined as a representation of $h^{\text{MC}}_{\text{reco\&truth},ij}$ that has been normalised to unit in each truth bin j,

$$M_{ij} = \frac{h^{\text{MC}}_{\text{reco\&truth},ij}}{\sum_k h^{\text{MC}}_{\text{reco\&truth},kj}}. \tag{6.4}$$

By comparing the migration matrix with the truth $h^{\text{MC}}_{\text{truth}}$ and reconstructed $h^{\text{MC}}_{\text{reco}}$ cross-section distributions (taking into account the corresponding efficiency and purity), the Bayesian unfolding method allows an unfolding matrix $\mathbf{M}_X$ to be iteratively estimated such that at the k-th iteration,

$$h^{[k+1]}_{\text{unf}} = \mathbf{M}^{[k]}_X h_{\text{reco}} \quad \text{where} \quad h^{[k+1]}_{\text{unf}} \approx h_{\text{truth}}. \tag{6.5}$$

Once an unfolding matrix $\mathbf{M}_X$ has been determined, this can be applied on $h^{\text{data}}_{\text{reco}}$ in order to recover the corresponding detector-effects-free distribution $h^{\text{data}}_{\text{unf}}$.

The quality of an unfolded distribution is strongly tied to the statistical richness of the MC sample, as well as the number of iterations and the nature of the resolution effects. In the ideal scenario where the sample is infinitely large, and the effect seen on the migration is entirely Gaussian, Bayesian unfolding should be capable of fully reverting the convolution. However, in reality, unfolding techniques are just approximate methods which must be treated with care. In general, the complex nature of measurements (and the chosen observable) often leads to imperfect unfolded distributions, equivalent to a $h_{\text{unf}}^{[k+1]}$ that is very different from the corresponding h_{truth}. Such effect should be studied with care, as this could later be used to estimate the shape bias induced by the unfolding.

As the statistical size of the MC sample is finite, each bin of a post-unfolding distribution will have an associated statistical uncertainty, as well as an inter-bin correlation matrix. Moreover, one must propagate additional sources of uncertainty (such as systematics due to luminosity, triggering, identification, etc.) through the unfolding process, which (often) translates as fully correlated uncertainties on the unfolded differential cross section. Section 6.6 provides examples of the relevant systematic uncertainties in the low pile-up W-boson study.

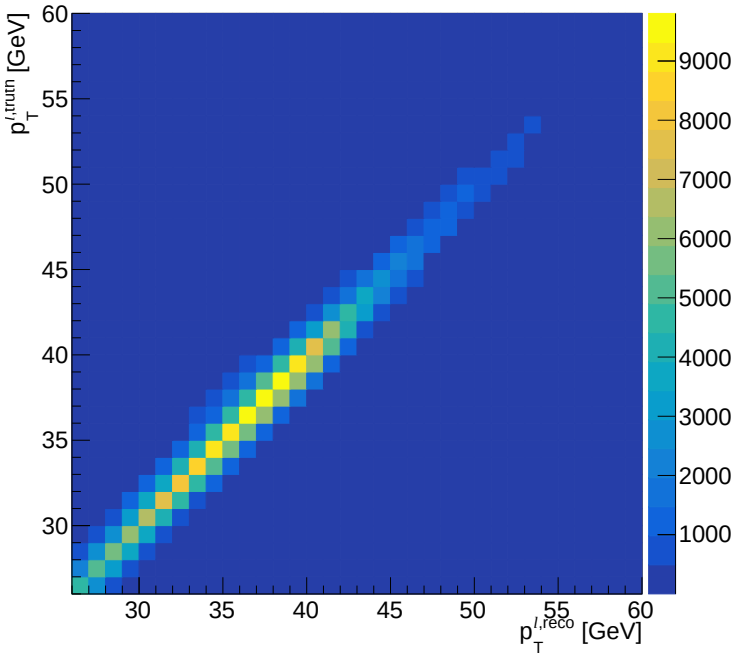

Figure 6.1: Matrix $h_{\text{reco\&truth},ij}^{\text{MC}}$ of the MC simulation of low pile-up $W^+ \to e^+\nu$ events at 5 TeV, given in 1 GeV wide bins of p_{T}^{ℓ}. The colour scheme accounts for the number of events according to the scale shown on the right-hand side. N.B. in the perfect case with no resolution effects, one has $p_{\text{T}}^{\ell,\text{reco}} = p_{\text{T}}^{\ell,\text{truth}}$, and a migration matrix that is exactly diagonal.

6.2.2 Theoretical prediction

As was briefly described in Section 6.2.1, a safe way to estimate cross-section predictions is via the analysis of simulated samples, such as those generated with POWHEG+PYTHIA prescriptions. These predictions are tied to specific PDFs chosen during the generation procedure, which uses previously defined PDF sets; however, once a sample has been generated, it is impossible to include additional weights for additional PDF sets without producing the whole sample again. Given that the generation of simulated events may take weeks before yielding reasonable statistics, and the fit of PDFs requires active (and quick) updates of the PDF parameters, these two approaches are incompatible.

Generally speaking, a set of configuration features must be chosen before generating any kind of prediction. These are related to the precision and intended rigour of the theoretical model, managing a trade-off between predictions that are simple but reliable and more precise but riddled with subtleties. Such choices can be of several sorts:

- Precision of the PDF, denoted via NLO, NNLO, N^{3}LO, etc. This should be consistent with the perturbative QCD order of the physics model, which translates as the number of possible loops in a single diagram (see Section 6.6 for an example at NLO).
- Inclusion (or lack) of resummation corrections by adding missing NNLL corrections, using
  - Partonic showering of a sample (e.g. with PYTHIA [95]);
  - Via direct resummation of a prediction (see Section 1.5);
  - Using cross-section K-factors (see Section 6.6 for an example).
- Inclusion (or lack) of electroweak corrections (see Section 6.6 for an example).

Aiming towards their use in PDF fits, the prediction of differential cross sections should prefer methods which rely on numerical or analytical prescriptions at the highest possible perturbative order and contain NNLL resummation corrections in some way. The specific choice is tightly linked to the type of phenomena one intends to predict, as the initial and final conditions dictate in great measure the required theoretical prescription. The main challenge associated with the theoretical prediction of a cross section is the computation of QCD processes at high enough order (including possible resummation corrections) and the modelling of their evolution. The following paragraphs briefly describe a few processes of interest and the standard methodology used for their simulation.

DIS data and the analytical approach

The prediction of deep inelastic scattering cross sections at truth level (see Section 6.3.3) is the least problematic to simulate. Since these processes are of the sort $e^{\pm}p \to e^{\pm}p$ (see Fig. 6.2), all the matrix elements involve a single PDF, which allows for fast analytical estimation via theory frameworks such as `QCDNUM` [140]. Generally speaking, such DIS theoretical predictions take just a couple of seconds, which is compatible with the active update of the PDF required during a fit.

In the context of PDF fits, DIS data is used as the main constraint of the PDF. For the study presented in this work, all of the HERA DIS cross-section data [32] will work as the base of any fit, on top of which additional data will be added in order to improve specific features of the PDFs. Further details on the exact HERA DIS data used for the PDF fit are provided in Section 6.3.4.

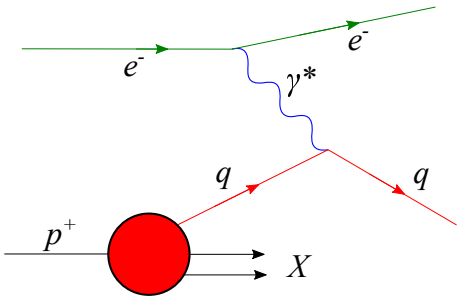

Figure 6.2: Schematic representation of a generic $e^{-}p$ DIS process.

Proton-proton data and fast interpolation grids

Contrary to the DIS cross sections, proton-proton data cannot be modelled via analytical methods. Since any pp collision is affected by a PDF through the parent particles (see Eq. (1.48)), the theoretical modelling of any interaction results in non-trivial matrix elements that must be integrated separately over the phase-space of both families of partons. The computation time depends strongly on the exact process and chosen perturbative order, but even in the most simple scenarios (such as Drell-Yan cross sections with `DYTURBO` [141], see Section 6.3.3), the estimation of a single resummed NNLO cross-section prediction with a reasonable statistical uncertainty may take up to 100 times longer than the corresponding fixed order NLO estimation.

Instead of computing a pp cross section from scratch, an alternative approach is to take advantage of the factorization theorem (described in Section 1.5 and depicted by Eq. (1.48)). In a nutshell, this consists in noticing that one can decompose a total pp cross section $\sigma_{pp\to X}$ as a function of the PDF $f_i^p(x, Q^2)$ for each parton i coming from each proton, and the hard scattering cross section of each parton-pair combination $\sigma_{ij}(\hat{s}, \alpha_s(Q^2))$.

By noticing that $\sigma_{ij}(\hat{s}, \alpha_s(Q^2))$ depends on the kinematic of each parton but does not explicitly depend on the PDF, one may attempt to pre-compute the values of σ_{ij} for a specific process, at several $\hat{s} = x_1 x_2 s$ and $\alpha_s(Q^2)$ values, which l to interpolate to the required ones and perform the integral over x (i.e. to implement the convolution with the PDFs). In other words, this technique can generate a prediction by simply doing

$$\frac{\mathrm{d}\sigma}{\mathrm{d}X} = \text{grid} * \text{PDF}. \tag{6.6}$$

While the production of cross-section grids is a time-consuming process that may take several days, this must be done only once, after which a single grid (estimated for a specific process and observable) can be used with any PDF. The actual convolution can be performed in the order of milliseconds, which makes it a perfect candidate for its use in PDF fits.

6.2.3 Fast interpolation cross-section grids and caveats

Cross-section grids (or simple grids) are a very powerful tool which makes possible PDF fits using *pp* data. However, the non-triviality of such predictions comes with approximations and theoretical caveats that must be kept in mind. Furthermore, since a grid cannot be modified after it has been generated, a few additional restrictions are placed on the precision that can be achieved from a statistical and physical point of view, as well as the information that can be retrieved from it. The following paragraphs briefly discuss some of these caveats, emphasising those related to the study documented in this Chapter.

Statistical precision and QCD perturbative order

The determination of the hard scattering cross sections used by the interpolation grid is done by performing variations of each flavour component in the PDF at different values of x and Q^2. This means that several predictions will be generated and used to factor out the effect of the PDF, leading to a table of factors that is fully PDF-independent. Once the grid has been generated, these factors remain fixed and no additional modifications can be applied without repeating the process from scratch. Consequently, the final cross-section grid is very sensitive to the modelling setup used for the initial predictions, and special care should be given to these conditions.

The generation of the initial predictions comes along with a choice of relative statistical precision, which propagates as an overall precision value to any prediction obtained with the final grid. This means that the statistical reliability offered by a cross-section grid must be selected before its generation. Generally speaking, the choice of better or worse statistical precision comes as a trade-off with the computation time needed to generate a grid.

Following from the previous point, one must notice that the initial predictions are fully

dependent on the perturbative order of the theoretical model. Consequently, the choice between a purely LO QCD prediction (e.g. the tree diagram in a $W \to e\nu$ process, see Section 6.6) and the inclusion of NLO contributions (such as the emission of ISR and FSR, or loops contributions; also depicted in Section 6.6) will define which Feynman diagrams are taken into account, which can induce large changes in the final grid factors, affecting the quality of the physics being described. One must also note that the PDF evolution equations used together with a grid must be done at the corresponding QCD order, which then limits the order of any PDF fitted using such a grid. Hence, one must choose the appropriate perturbative order, both as a function of the process being described and of the QCD precision desired for the to-be-fitted PDF.

Finally, it is natural (and important) to notice that the hard scattering cross sections contained in the grid are estimated for a given observable, using a specific set of selection rules and binning. This simply means a given grid can only be used to generate a specific cross-section prediction, with the only possible change that can be induced is the choice of PDF (and scale).

Fixed order QCD predictions

Factorisation of the contribution from the PDF on a cross section takes advantage of the explicit appearance of structure functions in the matrix element of a specific process (see Section 1.5). In broad terms, this completely separates the impact of a PDF from any sum of Feynman diagrams, which enables the estimation of the corresponding hard scattering cross sections at any desired QCD order. The direct sum of diagrams from all the possible contributing processes leads to a Fixed Order (F.O.) prediction.

As it has been described in Section 1.5, the inclusion of higher-order QCD processes and their inherent gluon radiation generates large logarithms that must be cancelled via resummation corrections. Such corrections, typically labelled as "NLL" or "NNLL" according to the order, are dependent on particle kinematics, which makes it incompatible with the principle described in the previous paragraph in order to factor out the effect of the PDF. Such corrections are not trivial to estimate: `DYTURBO` [141] may need 30 minutes to generate a fixed order prediction, while the estimation and application of resummation corrections can take several days. Consequently, all interpolation-grid-based predictions are limited to fixed order, so particular care should be given when choosing an observable of interest.

K-factors

The determination of cross-section predictions at NNLO via interpolation grids has only been made possible recently using state-of-the-art techniques. Since this is a recent technology, for the time being, NNLO-level grids can only be produced for specific processes, such as $t\bar{t}$ cross sections with `fastNLO` and jet-production `APPLfast` grids with `NNLOjet` [142]. However, for most other processes, cross-section grids can only be estimated at F.O. LO and F.O. NLO QCD due to computational challenges. On its own, and as a function of the fitted data, this implies limitations on the maximum precision (QCD-wise) attainable by a PDF fitted using this prediction. In general, one wishes to have as high as possible precision, which typically means NNLO or N^{3}LO QCD perturbative order. Seeking to increase the physics qualities in a prediction, fixed order predictions are used along what is known as "K-factors", which work as a simple multiplicative correction on top of the F.O. NLO cross-section shape.

In a nutshell, K-factors work under the assumption that, while a differential cross section at NLO and at NNLO (according to some binning) is fully dependent on the PDF, their bin-to-bin ratio is PDF-independent. This means that one can choose a reference PDF, estimate a resummed NNLO prediction (e.g. using `DYTURBO` [141]) and a F.O. NLO cross section (using interpolation grids), and obtain the ratio of cross sections for each bin i. Ultimately, this leads to a list of numbers $K_i^{\text{F.O. NLO}\to\text{NNLO QCD}}$ (1 per bin of the differential cross section) defined by

$$K_i^{\text{F.O. NLO}\to\text{NNLO QCD}} = \left(\frac{\mathrm{d}\sigma_{\text{DYTURBO}}^{\text{resummed NNLO QCD}}}{\mathrm{d}X}\right)_i \Bigg/ \left(\frac{\mathrm{d}\sigma_{\text{grid}}^{\text{F.O. NLO QCD}}}{\mathrm{d}X}\right)_i , \tag{6.7}$$

which provides corrections to

- go from NLO QCD to NNLO QCD;
- and apply (in rough terms) NNLL resummation corrections.

Seeking to improve the quality of the prediction further, one may want to increase the EW precision of the prediction using a similar approach, i.e., estimating bin-to-bin EW correction factors. Generally speaking, this leads to a total combined K-factor of the sort

$$K^{\text{NLO}\to\text{NNLO QCD}}.$$

In the case where the QCD and EW factors can be treated as multiplicative, one may define $K_i^{\text{LO}\to\text{NLO EW}}$ by obtaining the ratio of NLO EW and LO EW cross sections (both at the same QCD perturbative order), and combine it along the QCD K-factor such as

$$\left(K^{\text{NLO}\to\text{NNLO QCD}}_{\text{LO}\to\text{NLO EW}}\right)_i = K_i^{\text{F.O. NLO}\to\text{NNLO QCD}} \times K_i^{\text{LO}\to\text{NLO EW}}. \tag{6.8}$$

Putting everything together, it becomes possible to efficiently estimate a high-precision cross section whose PDF can be updated in a continuous manner. For the i-th bin, this

looks like

$$\left(\frac{\mathrm{d}\sigma^{\text{NNLO QCD}}_{\text{NLO EW}}}{\mathrm{d}X}\right)_i = \left(\frac{\mathrm{d}\sigma^{\text{F.O. NLO QCD}}_{\text{grid}}}{\mathrm{d}X}\right)_i \times \left(K^{\text{NLO}\to\text{NNLO QCD}}_{\text{LO}\to\text{NLO EW}}\right)_i = (\text{grid} * \text{PDF})_i \times \left(K^{\text{NLO}\to\text{NNLO QCD}}_{\text{LO}\to\text{NLO EW}}\right)_i, \tag{6.9}$$

which is the quantity that will be used in the PDF fitting process.

6.3 Fundamentals of PDF fitting

The determination and quality of a PDF are given by the choice of parameterisation, the minimisation method used to constrain the relevant parameters, and the selection of data used to probe the parton kinematics. Both of these qualities are described in the following pages.

6.3.1 The minimisation framework: `xFitter`

Previously known as `HERAFitter` [37], `xFitter` [38] is a QCD fit framework based on the minimisation of a χ^2 estimator. It is built on top of the minimisation tool `MINUIT` [47], and interfaced to many cross-section prediction codes (`QCDNUM` [140], `APPLgrid` [143], `APFELgrid` [144], `fastNLO` [145], and more) used to get real-time theoretical estimates as a function of the PDF.

The χ^2 estimator within `xFitter` is represented in a few different ways, which makes it capable of accounting for correlations (both between bins of a specific measurement and across different data files) and of taking into account the effect of nuisance parameters (see the reference article [37] for further details). For a data point μ_i with a corresponding theory prediction m_i, the χ^2 can be written in the covariance representation as

$$\chi^2(\boldsymbol{m}) = \sum_{i,j}(m_i - \mu_i)C^{-1}_{ij}(m_j - \mu_j), \tag{6.10}$$

where $C_{ij} = C^{\text{stat}}_{ij} + C^{\text{uncor}}_{ij} + C^{\text{syst}}_{ij}$ is the combined total covariance matrix for bins i and j. Moreover, in the nuisance parameter representation, the χ^2 is given by

$$\chi^2(\boldsymbol{m}, \boldsymbol{b}) = \sum_i \frac{\left[\mu_i - m_i\left(1 - \sum_j \gamma^i_j b_j\right)\right]^2}{\delta^2_{i,\text{unc}} m_i^2 + \delta^2_{i,\text{stat}}\mu_i m_i\left(1 - \sum_j \gamma^i_j b_j\right)} + \sum_j b_j^2, \tag{6.11}$$

where $\delta_{i,\text{stat}}$ and $\delta_{i,\text{unc}}$ are the relative statistical and uncorrelated systematic uncertainties of measurement i, while γ^i_j accounts for the sensitivity of the same measurement to the correlated systematic source j. The quantities b_j account for the nuisance parameters, the value of which must be determined at the same time as the PDF fit is been performed.

Combinations of these estimators can be implemented as a function of the qualities of each data-prediction pair, leading to a single total χ^2_{total} estimator that results from the sum over all the datasets $\boldsymbol{m}$; in other words,

$$\chi^2_{\text{total}} = \sum_{\boldsymbol{m}\in\text{datasets}} \chi^2(\boldsymbol{m}). \tag{6.12}$$

By default, `xFitter` parametrises the PDF using the HERAPDF style functional form (already given in Eq. (1.44)):

$$xq_i(x) = A_i x^{B_i}(1-x)^{C_i}(1+D_i x+E_i x^2) \underbrace{-A'_g x^{B'_g}(1-x)^{C'_g}}_{\text{term used exclusively for the gluon}} . \tag{6.13}$$

Within `xFitter`, each of the parameters associated to a specific parton is identified by an index, such that the $xu_v(x)$ and $x\bar{u}(x)$ PDFs are defined by the parameters `Auv,Buv,...` and `Aubar,Bubar,...`, while the gluon is described by `Ag,Bg,...,Agp,Bgp,Cgp` (the suffix "`p`" corresponds to the primed variables which describe the negative term of the gluon). The code is optimised to implement the sum rules during the fit process, allowing adequate normalisation to be kept at all times.

An exception to the rule described above is the PDF of the s-quark, namely $xs(x)$, whose parameters typically are given as a function of the u and d PDF parameters. The exact definition of $xs(x)$ depends on the constraining power of the available data, and it may look as

$$xs(x) = A_{\bar{d}} \times r_s \times x^{B_s}(1-x)^{C_s}, \tag{6.14}$$

where the strangeness ratio r_s is fitted along B_s and C_s, while $A_{\bar{d}}$ is reused from the $x\bar{d}(x)$ parametrisation (N.B. $A_s = A_{\bar{d}} \times r_s$. Specific $xs(x)$ examples are provided in Section 6.3.4.

Overall, `xFitter` directly constrains $xg(x)$, $xu_v(x)$, $x\bar{u}(x)$, $xd_v(x)$, $x\bar{d}(x)$ and $xs(x)$, whose parameters must be fitted simultaneously in order to account for correlations. The final set of parameters depends on the qualities of the data included during the fit, and it gets defined via the χ^2 saturation scheme: if adding further parameters induces a minimal change of χ^2, then such additional parameters can be neglected. This led to 14 free parameters in the HERAPDF 2.0 fit [36] and 21 in the case of ATLASpdf21 [44].

As mentioned at the beginning of the current Section, the fit of the PDF parameters relies on a standard `MINUIT`-based framework, where variations of the parameter values are performed in order to probe and minimise the shape difference between data and the corresponding prediction. Each time a numerical set of parameters is proposed by one of the subroutines of `MINUIT`, a theoretical estimation of all the included datasets is generated, which is then used to compute a total χ^2 value using a combination of the expressions given in Eqs. (6.10), (6.11) and (6.12). Such χ^2 values are used to determine the EDM (see Section 2.2) and judge the status of the minimisation procedure. Figure 6.3 shows a schematic representation of the minimisation algorithm implemented within `xFitter` by the `MIGRAD` subroutine.

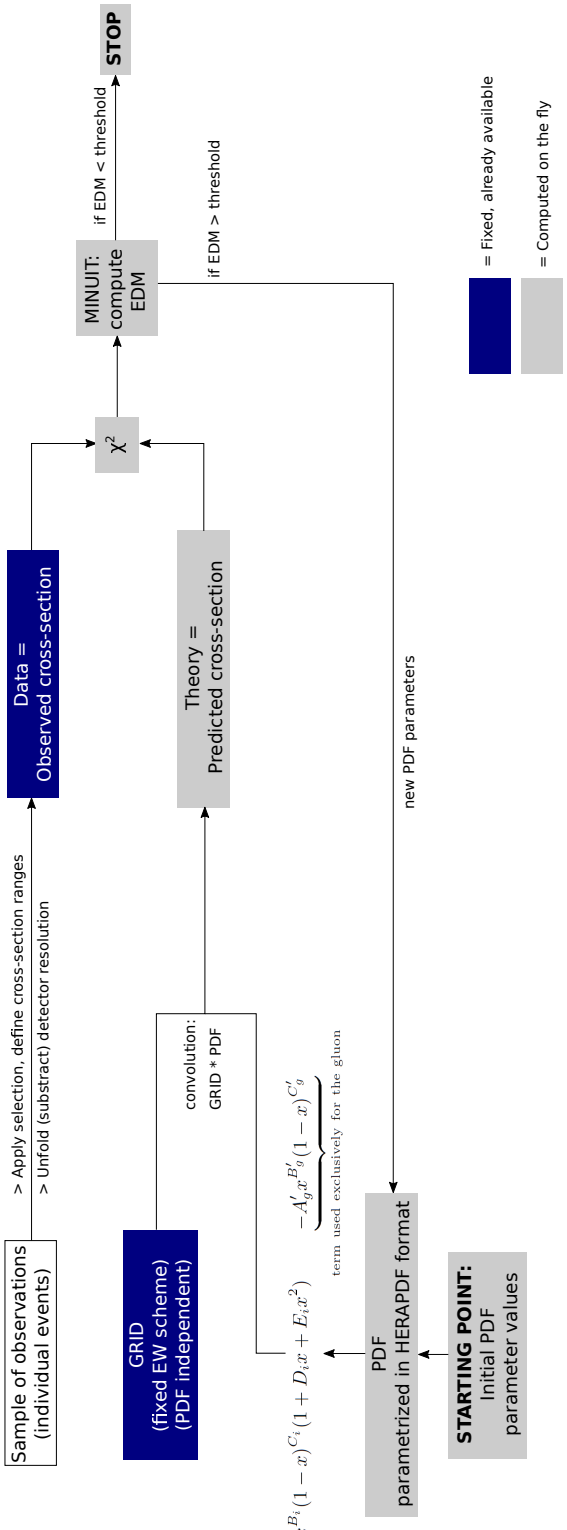

Figure 6.3: Schematic representation of the minimisation algorithm implemented by `xFitter`.

6.3.2 The `xFitter`-format datasets

The datasets read by `xFitter` are defined via text files (with extension `.dat`) which follow a particular format [146] in order to provide characteristics of the original measurement, along with instructions to generate a theoretical simulation of the data. While specific details of the format are not relevant to the studies described ahead, it is useful to understand the information associated with each data file and how it comes together to compare measurements with their corresponding predictions.

Firstly, each data file contains the numerical values of measured differential cross-sections. These values are given in a plain text table, where each row corresponds to a bin, and each column defines relevant quantities of the corresponding bin. Primarily, this includes the cross-section values μ_i, statistical uncertainty $\delta_{i,\text{stat}}$, and the uncorrelated $\delta_{i,\text{unc}}$ and correlated γ_j^i systematic uncertainty sources. Unfolding correlations between bins can be provided via an additional external `.dat` file that contains the numerical values of a matrix C_{ij} and nothing more.

Instructions to generate theoretical predictions are based on what internally receives the name of "`reactions`", which allows several physics-simulation codes to be interfaced and simple arithmetic operations on each bin to be performed. Typically, these `reactions` depend on a series of external files, such as `APPLgrid` format F.O. NLO cross-section grids, NLO $\to$ NNLO K-factor tables, scaling factors, etc. Consequently, the theory prediction m_i of a measurement μ_i given a set of parameters describing a PDF may look as

$$m_i = (\text{APPLgrid}_i * \text{PDF}) \times K_i^{\text{NLO}\to\text{NNLO}}$$

(see Section 6.2.3 for further details).

6.3.3 Constraining specific PDF features

The description of any process involving protons in the initial state relies heavily on good knowledge of the corresponding PDFs, which motivates the determination of the best possible description of partonic physics when fitting the PDF. One of the main challenges derived from the lack of a theoretical prediction of PDFs is the ambiguity regarding the existence of specific physics-motivated features in the shape of the distribution. While this motivates a generalised choice of parametrisation (such as the HERAPDF style functional form), the actual constraint of the parameters (and the quality of the predictions) is tightly tied to the data used during the fit. The main reason is that signals produced through a particular process provide additional sensitivity to specific features of a PDF, thus improving the physical meaningfulness of the fit by thoroughly selecting the data. While there is a plethora of relevant processes, the following paragraphs are intended to illustrate the impact of the choice of data on a PDF fit by briefly going over DIS data, Drell-Yan scattering, and $t\bar{t}$ production.

Data obtained from $e^{\pm}p$ DIS, such as that measured at HERA, is the main constraint

of any PDF fit. Since the content of a single proton interacts with an electron (which, as far as we know, has no internal structure), DIS data provides a very clean way to directly probe the base behaviour of all of the partons across all the x range and at different energy scales. Moreover, since $e^{\pm}p$ interactions are relatively easy to simulate (compared to pp collisions), DIS data provides a good way to test changes in the PDF induced by other datasets being fitted. Figure 6.2 provides a schematic representation of a neutral $e^{-}p$ DIS process at leading order, where the electron interacts with a quark q via the exchange of a virtual photon (N.B. no interactions between $e^{\pm}$ and gluons are possible at leading order).

The Drell-Yan (DY) scattering is a process found in pp collisions. It consists of the direct interaction of a pair of quarks, one from each proton, which propagates through a vector boson and results in the generation of a lepton-lepton or lepton-neutrino pair. Depending on the quark-pair combination, the interaction may be mediated by a $W^{\pm}$-boson or by Z/γ^{*}, which gets labelled respectively as "neutral" and "charged" DY currents, schematically depicted in Fig. 6.4. Neutral currents appear for quark-antiquark pairs of the same flavour and lead to the creation of a lepton-antilepton pair (which can be e, μ or τ). Charged currents need a u-type quark and a d-type antiquark (or vice-versa), one from each proton, leading to the generation of a lepton-antineutrino pair (or vice-versa, according to the sign of the W-boson). As a particular example, neutral DY data is interesting for PDF fits because it is a direct probe of the structure function of the u and d quarks using high-quality measurements. Moreover, by looking at different energy scales, one may probe high- or low-x regions of the PDF. By fitting DY data along with DIS measurements, one can aim to improve the description of the quarks PDF further.

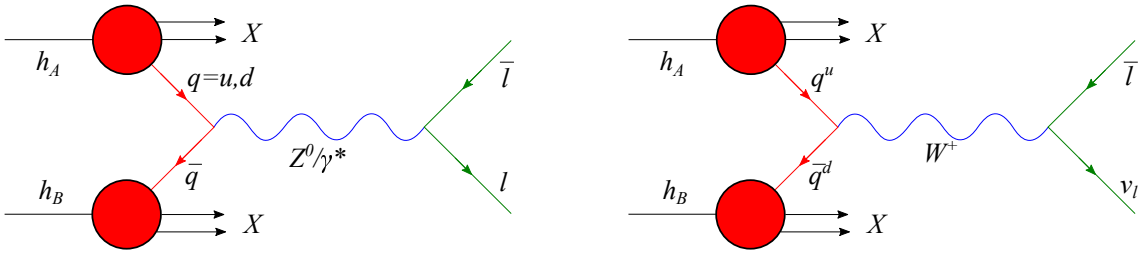

Figure 6.4: Schematic representation of pp neutral (left) and charged (right, illustrated for the positive-charge case) Drell-Yan scattering.

In order to further improve the gluon PDF, one may be interested in using $t\bar{t}$ production cross section. As one of the dominant production channels of $t\bar{t}$ at the LHC is via gluon fusion (see Fig. 6.5), it allows to probe the gluon kinematics at different x-ranges and provide valuable information to constrain both the positive and negative parts of the corresponding PDF.

The inclusion of different processes allows for further improvement of the reliability of the final PDF either by probing specific regions of the distribution functions, by allowing for more free parameters in the parametrisation of a specific parton, or by solving ambiguities caused by multiple similar local minima. Generally speaking, adding more

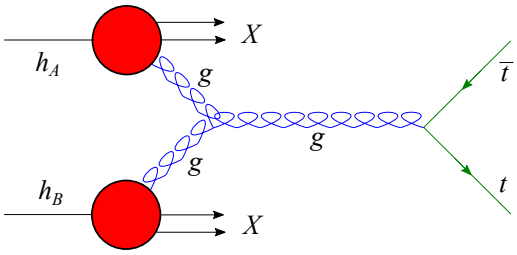

Figure 6.5: Schematic representation of $pp \to t\bar{t}$ production via gluon-gluon fusion.

data is always better, but one must be careful whenever inconsistent/correlated datasets are included. Checks of the impact of each dataset on the results of the fit (such as adding/removing datasets one by one) and parameterisation scans are used to find a good trade-off between fit complexity and returning sensitivity.

6.3.4 The ATLASpdf21 fit

In the context of PDF fits within the ATLAS collaboration, one of the most relevant results is presented in the ATLASpdf21 [44] study. This proton PDF fit was conceived seeking to extract a comprehensive description of several physics processes while using an extensive selection of ATLAS-only measurements on top of HERA I+II DIS data. Seeking to further iterate on the analysis done in ATLASpdf21, one of the final targets of the study described across the current Chapter is to implement an extension of the aforementioned PDF in order to inspect possible correlations with parameters of the EW sector while providing a competitive constrain of partonic physics. Consequently, a few details of the ATLASpdf21 study will be discussed.

The original ATLASpdf21 fit was obtained via the implementation of sequential cumulative fits. These fits start with HERA DIS and ATLAS W/Z production cross sections. After obtaining a successful fit, additional data ($t\bar{t}$ production) are included and the PDF is re-fitted. The process is repeated until the list of datasets (presented in Table 6.1) has been exhausted.

The complexity of the PDF parametrisation used in the ATLASpdf21 study changes according to the amount (and qualities) of the data included in the fit. While each parton distribution is parametrised by Eq. (6.13) (and Eq. (6.14)-like in the case of the s-quark), the selection of free parameters has been optimised seeking to improve the final data-to-prediction agreement and to get rid of ambiguities in the χ^2 phase-space (such as the existence of double minima). The number (and name) of free parameters at each stage of the iterative fit is shown in Table 6.2.

The official result documented for the fit of ATLASpdf21 [44] was obtained using a `Fortran`-based `xFitter` version, labelled `master_before_PionCeres_merge`. As the studies described further ahead are intended as an optional extension of the standard PDF

Table 6.1: List of datasets used in the fit of ATLASpdf21 [44]. The datasets are given in the order in which they were added to the fit. For instance, "+ ttbar8TeV" includes the HERA I+II DIS data, along the ATLAS W/Z production at $\sqrt{s} = 7$ TeV and $t\bar{t}$ production at $\sqrt{s} = 8$ TeV.

Label	Cross-section description
HERA	HERA I+II $e^{\pm}p$ DIS [32]
+ epWZ16	ATLAS inclusive W/Z Drell-Yan production at $\sqrt{s} = 7$ TeV [147]
+ ttbar8TeV	ATLAS $t\bar{t}$ production at $\sqrt{s} = 8$ TeV [148]
+ Vjets	ATLAS $W +$ jets [149] and $Z +$ jets [150] at $\sqrt{s} = 8$ TeV
+ z3d	ATLAS Drell-Yan triple differential Z cross sections at $\sqrt{s} = 8$ TeV [151]
+ Wxs8TeV	ATLAS W-boson production at $\sqrt{s} = 8$ TeV [152]
+ photon	ATLAS isolated-photon production at $\sqrt{s} = 13$ and 8 TeV [153]
+ top13TeV	ATLAS $t\bar{t}$ production at $\sqrt{s} = 13$ TeV [154]
+ jets	ATLAS inclusive jet production at $\sqrt{s} = 8$ TeV [155]

Table 6.2: Number of free parameters (and their name) used in the final recommendation of the ATLASpdf21 fit [44]. The parameters `Ag`, `Auv` and `Adv` are defined by the sum rules; the row "other parameters" shows numerical constraints on certain parameters; any parameter not explicitly listed is fixed to 0.

N. of datafiles:	46
N. free parameters:	21

Free parameters:	`Bg`
	`Cg`
	`Dg`
	`Agp`
	`Bgp`
	`Buv`
	`Cuv`
	`Duv`
	`Euv`
	`Bdv`
	`Cdv`
	`Ddv`
	`Aubar`
	`Bubar`
	`Cubar`
	`Adbar`
	`Bdbar`
	`Cdbar`
	`Bstr`
	`Cstr`
	`rs`

Other parameters:	`Cgp=25`

determination procedure, the corresponding fits and code modifications were implemented on the latest version of `xFitter`, which is written in `C++`. For the sake of consistency and in order to improve compatibility between results, the final fit of the ATLASpdf21 PDF

was re-done using the latest version of `xFitter`[1].

6.3.5 About the PDF fits

All the PDF fits determined as part of the work reported in this section take the final results of the ATLASpdf21 study as their departing points. This means that no dedicated parametrisation scan was performed. Instead, fits begin under the assumption that the set of parameters summarised in the last column of Table 6.2 are the optimal selection of parameters. Consequently, the comparison between the nominal ATLASpdf21 fit and future combined fits becomes more straightforward.

The uncertainty around the fitted PDF parameters is determined numerically using the Hessian method (see Section 2.2), which estimates the parameters' covariance matrix via the inversion of their Hessian matrix. Moreover, the propagation of the parameter errors into PDF error bands around the central curves was estimated in an asymmetric fashion using the Pumplin [156] method.

6.4 EW dependence in PDF fits

As described in the previous Section, PDF fits rely on the comparison of data differential cross sections to their predictions. As the factorisation theorem explicitly indicates (Eq. (6.1)), the shape of a prediction is influenced both by the PDF and the hard-scattering cross sections via $f_{i,j}^{p}(x_{1,2}, Q^2)$ and $\hat{\sigma}_{ij}(x_1 x_2 s, \alpha_s(Q^2))$, respectively. This means that while the factorisation theorem isolates these contributions within different terms, both of them have an influence on the final shape of the distribution, potentially competing when trying to best describe the corresponding data, which may lead to a correlation between terms.

The fast interpolation cross-section grids described in Section 6.2.3 offer an efficient way to quickly compute reliable pp cross-section predictions for any chosen PDF. These grids rely heavily on the precise description of proton-proton hard scattering cross sections as described by the factorisation theorem, which links their prediction capabilities to the prior knowledge of the electroweak sector. Since cross-section grids are shortcuts designed exclusively to enable PDF fits under the approximation that the QCD description is completely uncorrelated from the other sectors, EW parameters (such as masses, widths and coupling factors) take fixed values that cannot be changed once the grid file has been generated in the current approach. Consequently, by construction, standard grid-based

[1] One should notice that, for the moment, there are minor compatibility issues between the `Fortran` and `C++` versions of `xFitter`. This makes it non-trivial to reproduce the exact numerical values reported in the official ATLASpdf21 study with the latest version of `xFitter`. However, by using our own fit of this PDF (using the same data and parametrisation) obtained with the `C++` version, we can ensure a compatible comparison of results with those of the new fits described further ahead in this Chapter.

predictions cannot reflect changes in the value of any given EW parameter after the grid has been generated. Taking the previous into consideration, it is worth mentioning that the dependency on specific parameters can be factorised during the creation of a grid; such is the case of α_s (which is already routinely changed). In principle, such prior factorisation could also be done for a given EW parameter, but this is not yet implemented in `xFitter` and would require additional dedicated studies in order to check its viability.

Visualising the dependency of a differential cross-section distribution ($\mathrm{d}\sigma/\mathrm{d}X$) with respect to the change of an EW parameter requires dedicated sensitivity studies that must be performed prior to any PDF fit. For a given EW parameter, such studies consist in the choice of a reference previously-determined PDF (e.g. CT18NNLO [40] or MSHT20NNLO [41]), and generation of multiple predictions (using e.g. `DYTURBO`, `POWHEG+PYTHIA`, `MadGraph`) at different EW values. The comparison of such predictions (with respect to a chosen nominal value of reference) allows a bin-by-bin interpolation function $f_X(\text{EW variation})$ to determine, such that there is an individual (but continuous) function f_X for each bin-value X. In other words, a sensitivity study is vital in order to re-write a differential cross section as

$$\frac{\mathrm{d}\sigma}{\mathrm{d}X}(\text{EW variation}) = \left(\frac{\mathrm{d}\sigma}{\mathrm{d}X}\right)^{\text{nominal}} \times f_X(\text{EW variation}). \tag{6.15}$$

Section 6.5 provides details on a sensitivity study implemented for W-boson differential cross sections as a function of lepton p_{T}, seeking to study the dependency to changes of m_W.

In order to study the collective contributions of the PDF and EW parameters in a cross-section prediction and their effects in a PDF fit, it is necessary to implement a modification of the minimisation algorithm shown in Fig. 6.3. For a given cross-section channel predicted with an interpolation grid and its corresponding sensitivity dependency to a (set of) parameter(s) $\mathrm{EW}_{\mathrm{fit}}$, it is possible to apply the reweighting function $f_X(\text{EW variation})$ to the post-convolution predictions, accounting for changes in $\mathrm{EW}_{\mathrm{fit}}$ while allowing to change the PDF on the fly. From a technical point of view, and in the context of `xFitter`, this is equivalent to the definition of additional free parameters in such a way that a subset is used to define the fitted PDF while the rest are used for the $\mathrm{EW}_{\mathrm{fit}}$-dependent reweighting (this is schematically represented in Fig. 6.6). Ultimately, this approach is what enables the PDF and EW values to be fitted, giving an insight into the effect of their correlation.

In general terms, one should notice that there is a tight link between the EW parameter of interest and the dataset on which sensitivity studies are done, which leads to specific process channels capable of providing enhanced (or nil) sensitivity to a given parameter. For instance, the explicit generation of a W-boson in charged Drell-Yan scattering makes it a perfect candidate to study the sensitivity to m_W (see Fig. 6.4, right), while neutral Drell-Yan is only sensitive indirectly (through the relationship with the $\sin^2\theta_W$ and m_Z. Conversely, one may wish to study the quark-Z coupling factors with neutral Drell-Yan

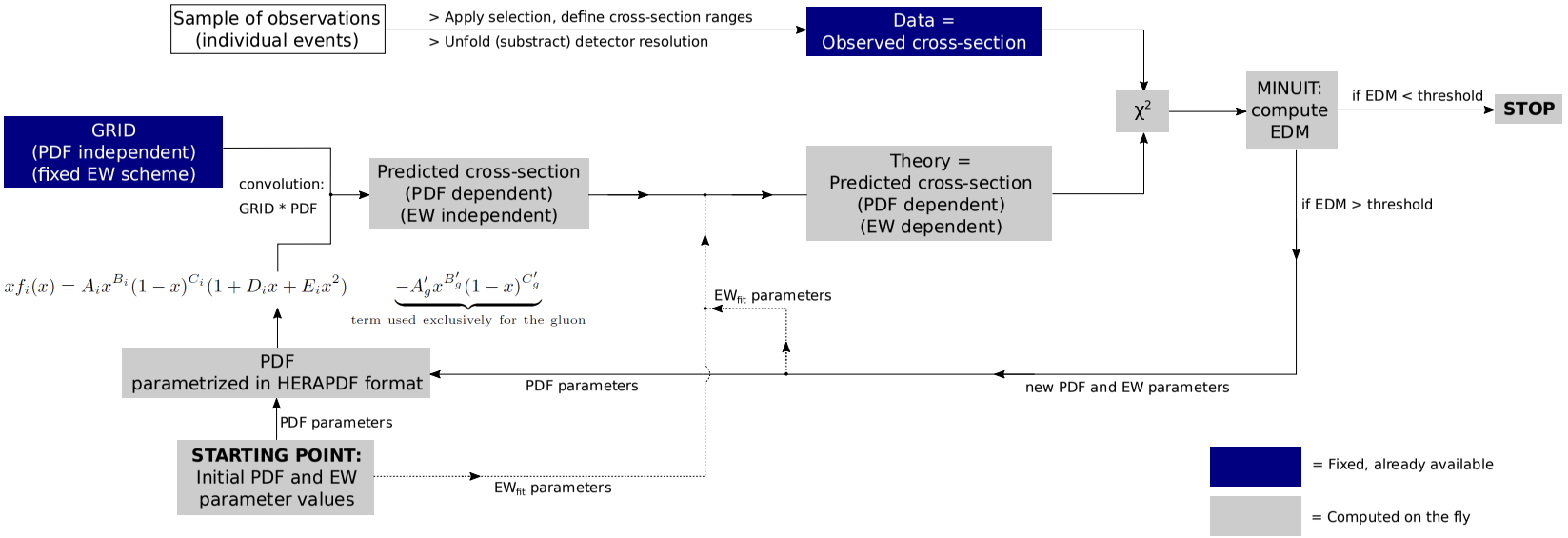

Figure 6.6: Schematic representation of the modified minimisation algorithm implemented in `xFitter`. It introduces cross-section dependency on a chosen EW parameter (or several of them) according to the behaviour determined via prior sensitivity studies.

scattering (Fig. 6.4, left), but not using the charged current counterpart.

The final target of the studies described in this Chapter is to perform a combined fit where m_W and a proton PDF are determined. Section 6.5 discusses the effect of changes in m_W propagated to the shape of differential cross sections measured through various channels.

6.5 Dataset sensitivity studies and m_W

Before proceeding to a combined m_W and PDF study, it is interesting to study the sensitivity of various observables to changes in m_W. These sensitivity studies are done entirely on theoretical predictions, as it is possible to control every physical aspect of the physics involved. The particular choice of theoretical simulation generator is given primarily by the kind of physics one wishes to reproduce, which allows (with some caveats) a user to select whichever simulation framework is more convenient.

For a given EW parameter, the specific choice of channel described by a cross-section study is given by the role played by the EW parameter in the underlying physics. Since the mathematical propagator describing a W-boson depends explicitly on m_W, natural candidates are charged Drell-Yan currents, as well as W+jets and inclusive W cross sections. Moreover, the selected measured observable dictates the degree of sensitivity that can be achieved; for m_W it is often linked through kinematics. Figure 6.7 illustrates the previous point with a schematic representation of the influence of m_W in a charged Drell-Yan scattering.

As PDF fits are done using measured data, one must always remember that the measurement for a process-observable combination must exist. Ergo, while one can perform sensitivity studies for any imaginable observable and extract valuable information on the relationship between an EW parameter and a cross section, this is useful only when the corresponding measurements exist.

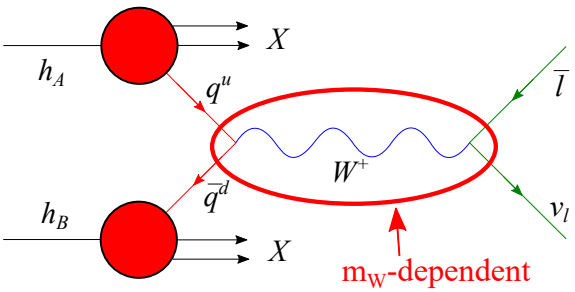

Figure 6.7: Interaction diagram of charged Drell-Yan scattering at LO in a pp collision. The dependency of the final state on m_W, given by the mathematical propagator, is indicated.

Later in the current Section, sensitivity studies are described for inclusive W cross sections with respect to lepton pseudorapidity (η_l), lepton transverse momentum (p_{T}^{ℓ}), and boson transverse momentum (p_{T}^{W}). Predictions for different values of m_W were obtained as a function of the available resources.

Samples (i.e. collections of simulated events) created with `POWHEG+PYTHIA` allow generating events at different mass values by taking advantage of the mathematical description of the W-boson cross section [23] given by

$$\frac{\mathrm{d}\sigma}{\mathrm{d}p_1\mathrm{d}p_2} = \left[\frac{\mathrm{d}\sigma(m;m_W)}{\mathrm{d}m}\right]\left[\frac{\mathrm{d}\sigma(y)}{\mathrm{d}y}\right]\left[\frac{\mathrm{d}\sigma(p^{\mathrm{T}},y)}{\mathrm{d}p^{\mathrm{T}}\mathrm{d}y}\left(\frac{\mathrm{d}\sigma(y)}{\mathrm{d}y}\right)^{-1}\right]\left[(1+\cos^2\theta)+\sum_{i=0}^{7}A_i(p^{\mathrm{T}},y)P_i(\cos\theta,\phi)\right], \quad (6.16)$$

where $p_{1,2}$ are the (anti)lepton four-momentum; m, p_{T}, and y are the invariant mass, transverse momentum, and rapidity of the dilepton system; θ and ϕ are the polar angle and azimuth of the lepton (given in the rest frame of the dilepton system); A_i are numerical angular coefficients, and P_i are spherical harmonics of order zero, one and two. Since the cross section depends directly on the Breit-Wigner mass distribution (around some value of m_W)

$$\frac{\mathrm{d}\sigma(m;m_W)}{\mathrm{d}m},$$

it is possible to assign a mass-dependent factor that can be used to reweight each event into specific m_W values, which leads to cross section predictions that are totally correlated across different mass values (thus, less affected by statistical fluctuations when comparing the behaviour across multiple m_W variations). Still referring to Eq. (6.16), it is of use to mention that the term

$$\frac{\mathrm{d}\sigma(p^{\mathrm{T}},y)}{\mathrm{d}p^{\mathrm{T}}\mathrm{d}y}\left(\frac{\mathrm{d}\sigma(y)}{\mathrm{d}y}\right)^{-1}$$

is defined by parton showers (i.e., carries resummation information), while higher-order perturbative QCD describes the rest of the terms. Although the `POWHEG+PYTHIA` approach offers a good physical description of the underlying physics that works simultaneously for several values of m_W (and in fact, this technique is used for the official measurement of the mass of the W-boson in the ATLAS experiment [23]), one should bear in mind that the generation of reweighted samples is not a trivial task to implement. Consequently, if such samples are not readily available, opting for one of the other approaches described below may be preferable.

A second alternative to generate predictions is via `DYTURBO` [141], which is capable of directly providing a differential cross-section estimation at QCD NNLO with resummation corrections already implemented. This method is very useful to generate K-factors for PDF fits, but the implementation of resummation corrections implies some level of decorrelation between bins, which requires high statistical precision before any comparison can be done.

Finally, a last approach, which follows from the grid generation procedure described in Section 6.2.3, is to inspect the changes using fixed order NLO predictions generated

with `MadGraph`. Due to the lack of resummation corrections, one should only rely on this method for observables that are weakly affected by parton showering. For instance, a good candidate for this is η_l cross sections, while p_{T}^{W} ones in inclusive processes cannot be described without NNLL resummation corrections.

In the case of other EW variables, such as the quark-Z coupling factors or mixing angles, one should bear in mind that their values may be hardcoded in the simulation framework. Such a scenario renders their modification impossible unless the code is modified and recompiled. Overall, this implies that stand-alone versions of the codes may have to be adapted on a case-scenario basis, forcing to work outside of official releases (such as those available within the ATLAS Athena framework [157]).

6.5.1 Boson transverse momentum (p_{T}^{W})

A natural candidate of the observable to study the sensitivity to m_W is p_{T}^{W} (such as the ATLAS measurement done using 5 and 13 TeV low pile-up data [130]), as kinematics during the generation of the W-boson may be affected by its mass due to 4-momentum conservation.

Predictions at different values of m_W around the nominal value of $m_W^{\mathrm{nom}} = 80.4$ GeV (up to $\Delta m_W = \pm 200$ MeV) were obtained via reweighted `POWHEG+PYTHIA` samples, plotted with the histogramming tool `HistMaker` [158], at $\sqrt{s} = 5$ TeV and using CT10NLO [159] as reference. Distributions for the $W^- \to e^-\bar{\nu}$ and $W^+ \to e^+\nu$ channels at each mass value are depicted at the bottom of Fig. 6.8, while the ratios with respect to m_W^{nom} are shown at the top of the same Figure.

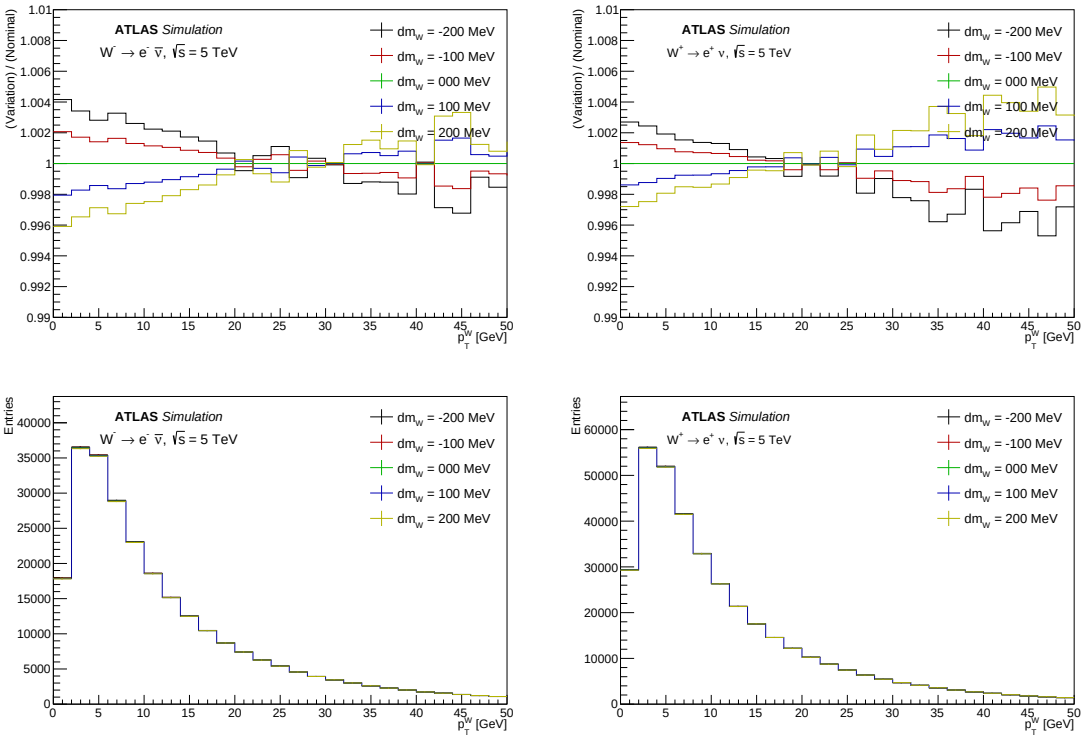

Figure 6.8: Inclusive $W \to e\nu$ truth-level distributions at $\sqrt{s} = 5$ TeV as a function of p_{T}^{W}, generated for variations of m_W around the nominal value of 80.4 GeV via `POWHEG+PYTHIA` reweighted samples, using CT10NLO as reference. The distributions were generated with `HistMaker` using the truth-level information of the official ATLAS low pile-up MC samples. The top plots show the ratios with respect to the nominal value for $W^- \to e^-\bar{\nu}$ and $W^+ \to e^+\nu$, while the bottom ones depict the distributions.

Increasing the value of m_W leads to higher $\sqrt{\hat{s}}$, which corresponds to a larger phase space and a harder p_{T}^{W} spectrum. As Fig. 6.8 indicates, this manifests as a shift of the

p_{T}^{W} distributions, leading to a small but clear bin-by-bin shape dependency that could not be explained by systematic errors alone. Given that PDF fits rely on shape comparison, at first order, p_{T}^{W} offers a viable way to probe the competition between the parameters of the PDFs and m_W.

Following from Section 6.3, the theoretical predictions used in a PDF fit are obtained via interpolation grids, which describe physical processes at fixed order NLO (N.B. state-of-the-art advancements are enabling the generation of NNLO grids for specific processes). One must note that the lack of NNLL corrections at NLO leads to a divergent p_{T}^{W} distribution that goes to infinity when $p_{\mathrm{T}}^{W} \to 0$ (see Fig. 4.3), requiring resummation corrections in order to absorb the divergence and adequately describe physics. As the computation of cross-section grids requires factorisation of the PDF contributions, the corresponding hard scattering cross sections at low p_{T}^{W} tend to be incorrectly determined due to the divergence of the distribution, leading to unreliable grids. Moreover, applying resummation corrections to the measured p_{T}^{W} spectrum leads to uncertainties that may potentially occlud the effect of changes in m_W. Consequently, inclusive W-boson cross sections as a function of p_{T}^{W} cannot be used in PDF fits without implementing dedicated NNLL corrections. Alternatively, one may be interested in exploring such behaviour using W+jets samples, which is not discussed in this study.

6.5.2 Lepton pseudorapidity (η_l)

The ATLASpdf21 fit uses inclusive W-boson cross sections as a function of the absolute value of η_l. As the measurements and grids are already available to be included in a PDF fit, it is interesting to check its sensitivity to m_W. Taking advantage of the good predictive power provided by the fixed order prediction given by cross-section grids (i.e. no inherent divergence problems due to the lack of NNLL corrections), the corresponding sensitivity study was performed using `MadGraph` [160]+`aMCfast` [161] grids. These were generated at different variations of m_W around the same nominal value than the aforementioned p_{T}^W distributions. The $W^{\pm}$ cross-section distribution variations and ratios with respect to m_W^{nom} are shown in Fig. 6.9, using CT18NNLO as reference PDF.

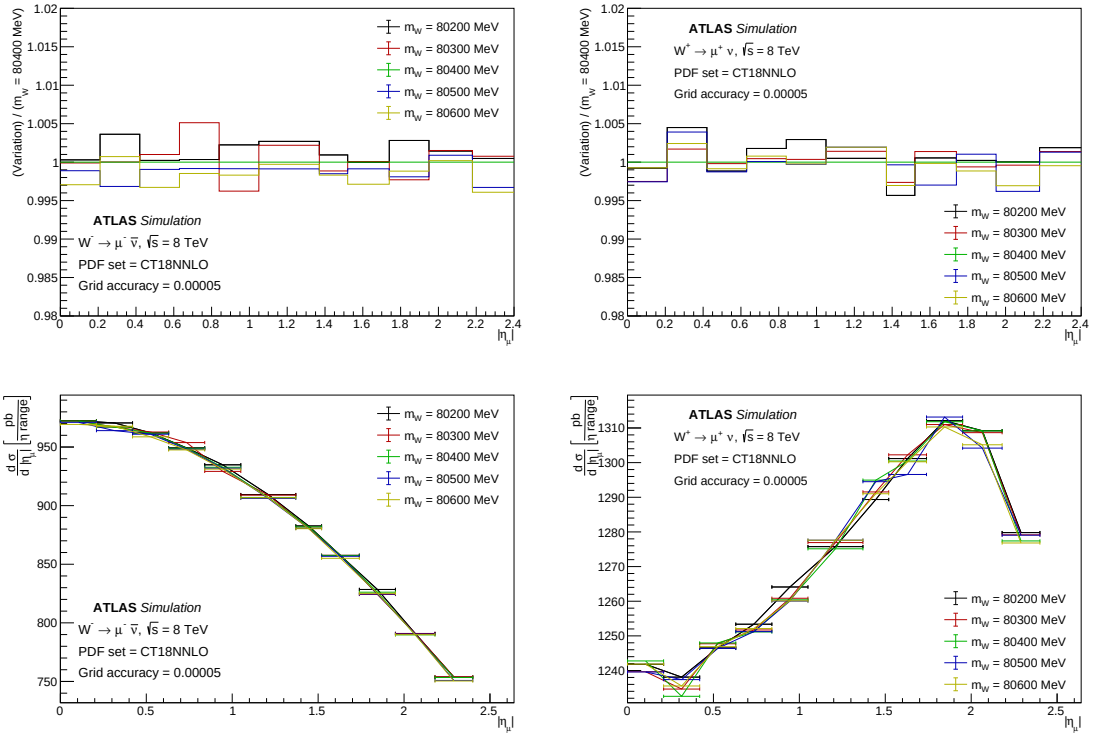

Figure 6.9: Inclusive $W \to \mu\nu$ F.O. NLO cross sections at $\sqrt{s} = 8$ TeV as a function of $|\eta^{\mu}|$, generated for variations of m_W around the nominal value of 80.4 GeV via `APPLgrids` convoluted with CT18NNLO. The distributions were generated with `MadGraph`+`aMCfast`. The top plots show the ratios with respect to the nominal value for $W^- \to \mu^-\bar{\nu}$ and $W^+ \to \mu^+\nu$, while the bottom ones depict the cross-section distributions.

As the ratio plots suggest, there is not a clear shape dependence induced by changes of m_W, leading to minimal fluctuations that the statistical uncertainty of each bin can easily explain. Hence, inclusive W-boson cross sections as a function of η_l will not be pursued as a constraint of m_W in the following studies.

6.5.3 Lepton transverse momentum (p_{T}^{ℓ})

While the ATLAS measurement of inclusive W-boson cross sections as a function of p_{T}^{ℓ} are not yet available, it is worth recognising the ongoing effort for its measurement using special low pile-up runs at $\sqrt{s} = 5$ and 13 TeV. These runs are expected to provide enhanced measurement of W processes, leading to high-precision cross-section and mass determinations. Since one could expect such measurements to become available in the near future, it is of interest to study their sensitivity to changes of m_W.

In a similar way to the p_{T}^{W} case, the study on p_{T}^{ℓ} was performed with reweighted `POWHEG+PYTHIA`, histogrammed with `HistMaker`. The cross-section distributions and ratio with respect to m_W^{nom} are shown in Fig. 6.10 for the $\sqrt{s} = 5$ TeV samples.

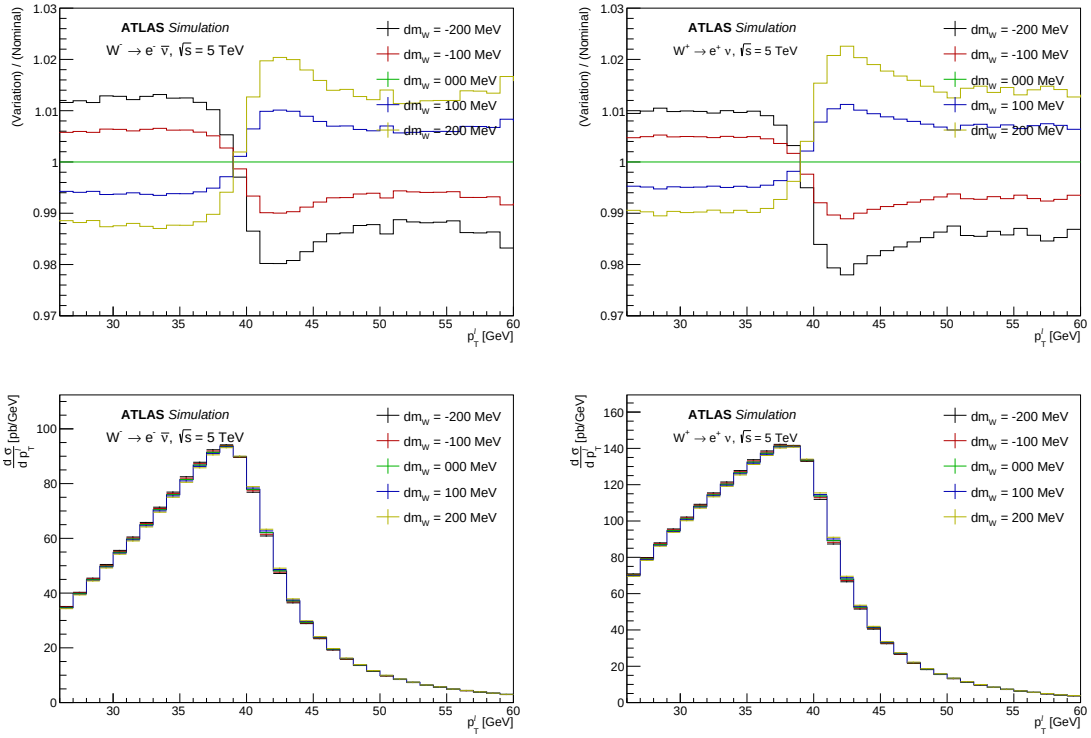

Figure 6.10: Inclusive $W \to e\nu$ NLO+NNLL differential cross sections at $\sqrt{s} = 5$ TeV as a function of p_{T}^{ℓ}, generated for variations of m_W around the nominal value of 80.4 GeV via `POWHEG+PYTHIA` reweighted samples, using CT10NLO as reference. The distributions were generated with `HistMaker` using the official ATLAS low pile-up MC samples. The top plots show the ratios with respect to the nominal value for $W^- \to e^-\bar{\nu}$ and $W^+ \to e^+\nu$, while the bottom ones depict the cross-section distributions.

Changes in m_W induce (primarily) horizontal shifts of the p_{T}^{ℓ} distribution, which is easily understandable by noticing that $p_{\mathrm{T}}^{\ell} \approx \frac{m_{\mathrm{boson}}}{2}$ (where m_{boson} is the mass value given to the parent W boson by the corresponding Breit-Wigner). Similarly to p_{T}^{W}, the bin-

by-bin shape dependency of p_{T}^{ℓ} to m_W makes it a good candidate for combined studies where the influence of m_W can compete with that propagated from the PDF. However, p_{T}^{ℓ} offers the added advantage of being less dependent on NNLL corrections as it is not affected directly by divergences, and the grid-based prediction is capable of providing a good description of the underlying physics at fixed order. Section 6.6 provides further details on the selection rules and properties of the cross-section grid.

Because of the aforementioned reasons, the combined m_W and PDF studies described ahead will be performed around inclusive W-boson cross sections as a function of p_{T}^{ℓ}. This aims, in the long term, to use the results of the ongoing low pile-up cross-section measurement, whose properties are also described in Section 6.6.

6.6 The low pile-up W-boson p_{T}^{ℓ} differential cross section

Precision measurements and differential cross-section studies of the W-boson must overcome a set of crucial challenges. The efficient rejection and simulation of background processes (i.e., those which may yield a similar detector signature), and the precise reconstruction of the momentum of the neutrino (which can only be estimated via $E_{\mathrm{T}}^{\mathrm{miss}}$) are just a couple of these, which motivates the use of special techniques and dedicated experimental setups.

In the ATLAS collaboration, the latest W-boson studies use data collected in dedicated low pile-up runs ($\langle\mu\rangle \approx 2$, see Fig. 6.11) at $\sqrt{s} = 5$ and 13 TeV, as these offer a set of measurements with enhanced sensitivity to the underlying physical processes involved in the interaction while allowing for better event reconstruction with respect to higher pile-up runs with richer particle output. The enhanced sensitivity of low pile-up runs has already proved to be of interest since it already led to the most precise measurement of the (inclusive) p_{T}^{W} distributions [130]. Therewithal, there is an ongoing effort to measure the mass of the W-boson and p_{T}^{ℓ} distribution using the same low pile-up data.

Following from the sensitivity study shown in Section 6.5 and foreseeing the results of the ongoing low pile-up p_{T}^{ℓ} measurements, it is of interest to study the effect of inclusive W-boson cross sections at $\sqrt{s} = 5$ TeV (the $\sqrt{s} = 13$ TeV data would give analogous results) in a combined m_W+PDF fit. Primary aspects (used up to this moment) of the low pile-up analysis are described through the rest of this section, followed by specific details of its theoretical modelling relevant to the PDF fit.

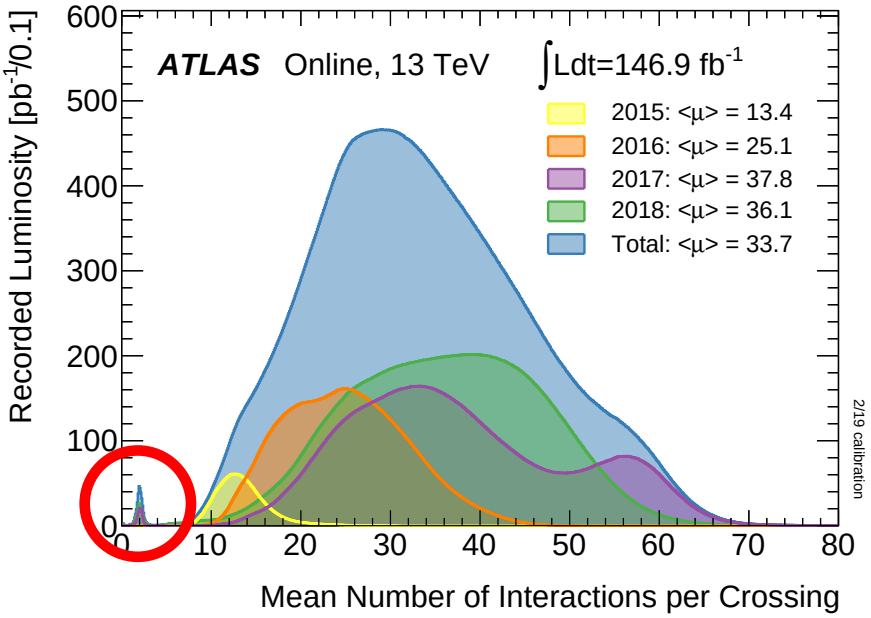

Figure 6.11: Luminosity-weighted distribution of the mean pile-up at ATLAS [55]. The special low pile-up runs ($\langle\mu\rangle \approx 2$) taken in 2017 (at 5 and 13 TeV) and 2018 (at 13 TeV) are highlighted with a red circle.

6.6.1 Measurement

The analysis of the 5 and 13 TeV low pile-up samples rely on the same selection rules and unfolding procedures. Thus, the following description is applicable to either.

The measurement of $W \to l\nu$ ($l = e^{\pm}, \mu^{\pm}$) is affected primarily by a handful of non-negligible sources of background, which must be taken into account at reco level. These correspond to backgrounds from electroweak (single-boson and diboson) and top-quark production (single-top and top-quark pair), both of which are simulated with MC, and QCD multijet production, which is estimated from data. Some of the dominant background processes are $W \to \tau\nu$ events, along $\tau \to l\nu\nu$ at low u_{T} and $t\bar{t}$ at higher u_{T} (see Section 3.3.5).

In order to discriminate as many of the background processes as possible and extract as much of the relevant sample as possible, several selection criteria are implemented on data, MC and background samples. In broad terms, this selection requires lepton candidates to be isolated, with the correct charge (to match W^+ or W^-) and type (e or μ), fulfilling lepton trigger matched and isolation conditions to discard fakes and secure high-quality measurements. The leptons of these events must be in a pseudorapidity range ($|\eta| < 2.47$ and $1.37 < |\eta| < 1.52$ for electrons; $|\eta| < 2.4$ for muons) with $p_{\mathrm{T}}^{\ell} > 25$ GeV, while the missing energy must fulfil $E_{\mathrm{T}}^{\mathrm{miss}} > 25$ GeV. Moreover, events are also required to have a

large enough W-boson transverse mass, with $m^{\mathrm{T}} = \sqrt{2p_{\mathrm{T}}^{\ell}E_{\mathrm{T}}^{\mathrm{miss}}(1-\cos\Delta\phi_{l\nu})} > 50$ GeV, where $\Delta\phi_{l\nu}$ is the azimuthal angle between the charged lepton and missing transverse momentum direction.

Resolution effects are removed with Bayesian Unfolding (Section 6.2.1). This is done with a migration matrix that uses selection rules on the truth variables ($p_{\mathrm{T}}^{\ell} > 25$ GeV, $|\eta_l| < 2.5$, $p_{\mathrm{T}}^{\nu} > 25$ GeV, $m_{\mathrm{T}}^{W} > 50$ GeV), which has the purpose of excluding kinematic regions with sub-optimal theoretical modelling.

The final bin uncertainty of the unfolded cross section is dictated by the corresponding statistical uncertainty and by a series of fully correlated systematic sources. One of the main systematics is a 1.6% uncertainty (uniform through all the bins) induced by the uncertainty in the luminosity measurement, which is followed by non-uniform (but fully correlated within themselves) reconstruction systematics due to lepton identification and isolation, reconstruction, and triggering.

The particular cross section distribution used for combined m_W and PDF studies is defined for 4 different channels ($W^{\pm} \to l^{\pm}\nu$, with $l = e, \mu$), using 1 GeV wide p_{T}^{ℓ} bins, in the 25 GeV $< p_{\mathrm{T}}^{\ell} <$ 60 GeV range.

6.6.2 Pseudodata

Rather than directly using unfolded data for any initial combined m_W and PDF study, it is more convenient to use pseudodata constructed as an "Asimov"-like dataset. Not only this generates reproducible results (as the real data analysis is still ongoing and changes are to be expected), but also permits for changes in the fitted value of m_W to be quantified. All of the pseudodata sets described in this chapter were obtained for $m_W^{\mathrm{nom}} = 80.4$ GeV.

The central values of the differential cross-section distributions are obtained with `DYTURBO`, generated at resummed NNLO level. The predictions for the 4 leptonic channels are generated using the member 0 (i.e. central PDF eigenvector) of either of 4 different reference PDFs:

- CT18NNLO [40],
- MSHT20NNLO [41] (full name: MSHT20nnlo_as118),
- NNPDF31NNLO [43] (full name: NNPDF31_nnlo_as_0118, although member 0 corresponds to a random eigenvector),
- ATLASpdf21_T3 [44];

leading, a priori, to 4 completely independent datasets.

`DYTURBO` predictions are generated using the same selection rules described earlier in this Section. The statistical and systematic errors propagated through the unfolding of real data are scaled to match the central values of the pseudodata. All of the previous

implies that the influence of the future low pile-up p_{T}^{ℓ} measurements can be tested in a realistic manner while knowing the injected value of m_W^{nom}. Figure 6.12 shows the W^+ and W^- cross-section predictions generated with `DYTURBO` using the aforementioned selection criteria for all of the reference PDFs.

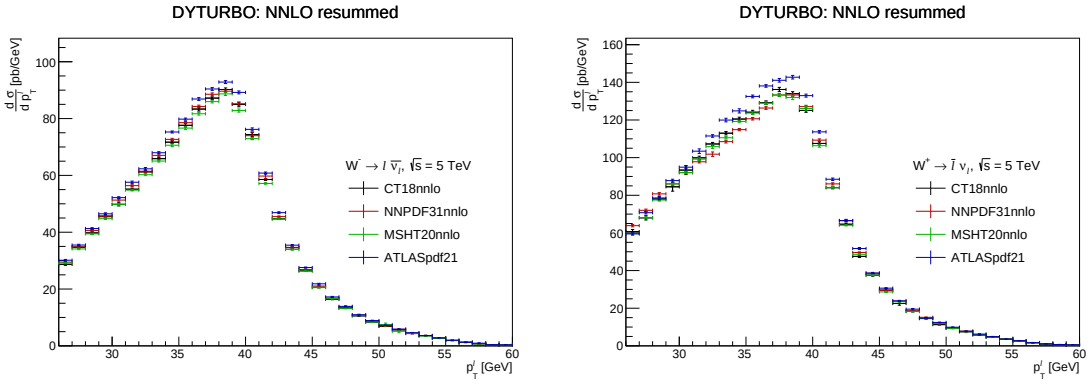

Figure 6.12: $W^- \to l^-\bar{\nu}$ (left) and $W^+ \to l^+\nu$ (right) resummed NNLO differential cross-section predictions at $\sqrt{s} = 5$ TeV, generated with `DYTURBO` using 4 PDFs.

The relative influence of the PDF on the final `DYTURBO` resummed NNLO predictions is provided in Fig. 6.13. The $W^- \to \ell^-\bar{\nu}$ channel shows PDF-induced changes that remain within the statistical uncertainty of the prediction. However, the $W^+ \to \ell^+\nu$ channel suggest a strong PDF dependency which leads to important differences between the pseudodata generated with ATLASpdf21 and the pseudodata produced with NNPDF31nnlo or MSHT20nnlo. Comparison of these changes with the relative m_W dependency shown in Fig. 6.10 suggest that a shifts in m_W could be expected as a way of improving the agreement between pseudodata and the corresponding theory prediction.

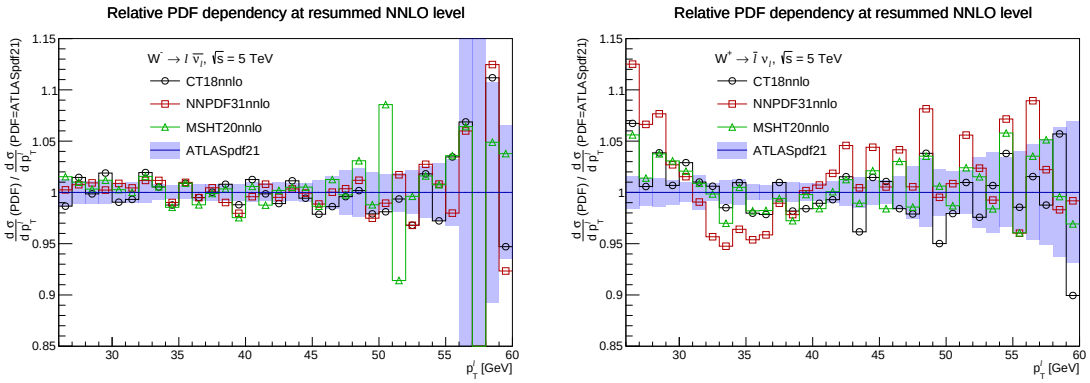

Figure 6.13: Relative shape dependency of the resummed NNLO predictions shown in Fig. 6.12. It shows the ratio of distributions with respect to the ATLASpdf21 prediction (normalised to have the same area among themselves). The blue transparent bands correspond to the relative uncertainty of the ATLASpdf21 prediction.

6.6.3 Theory prediction

The nominal cross-section predictions are estimated using fixed order NLO grids at $m_W^{\mathrm{nom}} = 80.4$ GeV. These are produced in `APPLgrid` format (version `1.6.27`) using `MadGraph5_aMC@NLO 2.9.12` (providing the theoretical prescription of the relevant physics) interfaced with `LHAPDF 6.4.0` (in order to use publicly available PDFs) and `aMCfast 1.3.0` (responsible for the PDF factorisation and grid file generation). Within `MadGraph5`, all of the grids were obtained using 4 quark flavours in the non-diagonal CKM matrix model. Code-wise, for a $W^+ \to e^+\nu$ cross section, the base configuration looks like

```
import model loop_sm-ckm
define p = 21 2 4 1 3 -2 -4 -1 -3
define j = p
set group_subprocesses False
generate p p > e+ ve [QCD]
```

with an accuracy of

```
0.00005 = req_acc_fo,
```

where the physics model `loop_sm-ckm` enables a non-diagonal CKM matrix, allowing to explicitly account for contributions of the $u+c$ and $d+s$ channels (see Section 6.6.5). The fixed order cross-section predictions, generated from the convolution of these `APPLgrids` with the 4 reference PDFs, are shown in Fig. 6.14 for the $W^- \to e^-\bar{\nu}$ and $W^+ \to e^+\nu$ channels. The peculiar shape of these fixed order predictions is discussed in Section 6.6.4.

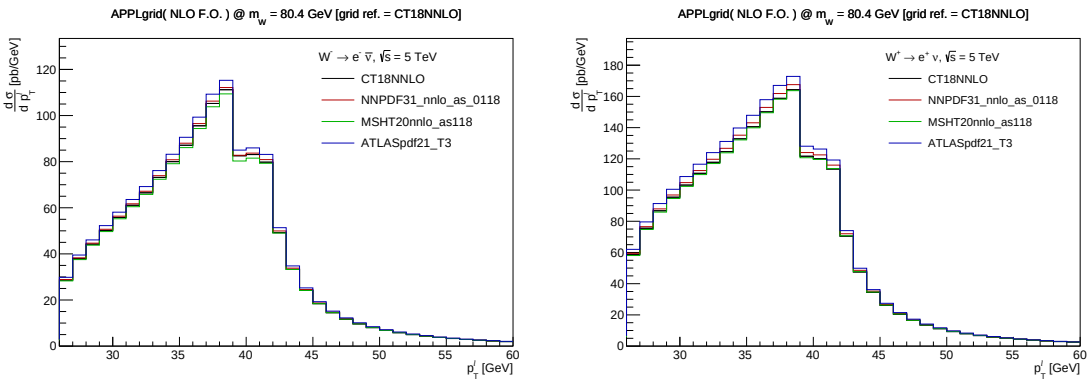

Figure 6.14: Differential cross-section predictions for $W^- \to e^-\bar{\nu}$ (left) and $W^+ \to e^+\nu$ (right) at $\sqrt{s} = 5$ TeV, generated at fixed order NLO level from `MadGraph5_aMC@NLO`+`aMCfast` `APPLgrids` convoluted with the 4 reference PDFs.

The above obtained fixed order NLO predictions are reweighted, on a bin-by-bin basis, to resummed NNLO order via multiplicative K-factors. These are defined using resummed NNLO QCD predictions computed with `DYTURBO 1.2.2` (see Fig. 6.12), via Eq. (6.7), by obtaining the ratio of predicted distributions generated with the same reference PDF.

Figure 6.15 summarises the K-factors for the $W^- \to e^-\bar{\nu}$ and $W^+ \to e^+\nu$ channels with respect to each of the reference PDFs.

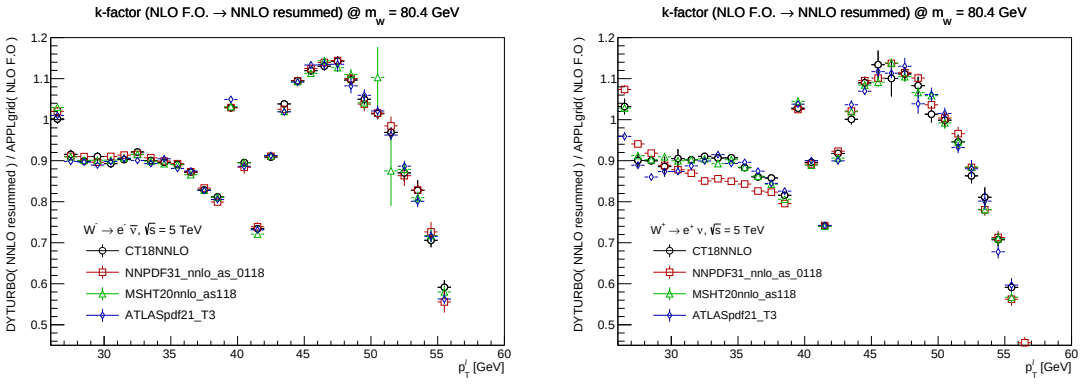

Figure 6.15: Fixed order NLO to resummed NNLO QCD K-factors of the $W^- \to e^-\bar{\nu}$ (left) and $W^+ \to e^+\nu$ (right) channels at $\sqrt{s} = 5$ TeV, defined as the ratio of `DYTURBO` and `APPLgrid` predictions (namely, it corresponds to the ratio of Fig. 6.12 and Fig. 6.14).

Effect of the PDF

Focusing on the fixed order NLO predictions shown in Fig. 6.14, one may notice slight differences in shape and normalisation of the cross-section distributions induced by the change of PDF. Analogous effects can be seen in the resummed NNLO order predictions of Fig. 6.12. These differences are entirely due to subtleties in the determination of each PDF, such as flavour treatment and parametrisation, which slightly modify the kinematics of each parton and propagate through the matrix element into specific features in a given prediction.

As cross-section normalisation affects the fixed order NLO and resummed NNLO corrections in similar ways, the ratio of these distributions (i.e. the K-factors) can be considered to be independent of such effect. However, looking at the K-factors plotted in Fig. 6.15 and comparing the values obtained with various reference PDFs, one can notice considerable differences across each set of values. Specifically, the NNPDF31NNLO K-factors seem to be away from the other PDFs, particularly in the case of $W^+ \to e^+\nu$. While typically K-factors are thought to be PDF-independent, it is worth keeping in mind that the p_{T}^{ℓ} fixed order predictions are very affected by the lack of resummation corrections (which appears as a jump in Fig. 6.7 around $p_{\mathrm{T}}^{\ell} = 40$ GeV). This leads to K-factors values that are very different from 1.0, potentially pushing the K-factor approximation into a less precise regime. While the simple exclusion of the region around $p_{\mathrm{T}}^{\ell} = 40$ GeV may arise as a natural approach to stay away from potential resummation-induced problems, one should notice that this region offers the most sensitivity to m_W [23]; hence, it is highly recommended to use this part of the spectrum in subsequent m_W+PDF fits.

In the following studies, each pseudodata (defined with a reference PDF) dataset will be coupled with the corresponding K-factors, in an attempt to reduce the shape bias induced by each of these PDFs. However, one should bear in mind that the remaining PDF-dependent cross-section shape may bias the fit result unless properly accounted for via dedicated QCD systematics, so care must be taken during the interpretation of results.

6.6.4 The fixed order effect on p_{T}^{ℓ}

Quick inspection of the fixed order NLO predictions provided in Fig. 6.14, contrary to the corresponding parton showered (Fig. 6.10) and resummed (Fig. 6.12) predictions, shows a (seemingly) discontinuous feature around $p_{\mathrm{T}}^{\ell} \approx m_W/2$. This is a direct consequence of the lack of resummation, which propagates from the gluon/quark sub-channels to the total cross-section estimation.

Let us consider the oversimplified Feynman diagrams shown in Fig. 6.16, which illustrate the different channels of charged-current quark scattering at fixed order NLO, as well as their contribution to the shape of the total prediction. The following is a very rough discussion of the actual physics behind fixed order predictions, which can be consulted in detail from dedicated sources [162]. The base diagram corresponds to "born" level (LO), whose contribution is accounted for via σ_1. At NLO, an additional contribution appears by allowing the emission of an initial state gluon, but also carrying a positively divergent term (represented by $\frac{1}{\epsilon}$), which is denoted by σ_3. Furthermore, the NLO prescription also spawns a diagram (exchange of gluons between the initial particles) that interferes negatively with the born diagram via the term σ_2, which is also linked to a negatively divergent term $-\frac{1}{\epsilon}$. In rough terms, one may write the final cross section as

$$\sigma_{\text{total}} = \sigma_1 + \left(-\frac{1}{\epsilon} + \sigma_2\right) + \left(\frac{1}{\epsilon} + \sigma_3\right) = \sigma_1 + \sigma_2 + \sigma_3.$$

From a computational point of view, the negative term σ_2 has the same shape as σ_1, but its integral is roughly the same (in absolute value) as that of σ_3. This means that the total cross section (i.e., the integral) at LO and NLO remains roughly unchanged, but the shape of the NLO distribution is modified by the interplay between σ_2 and σ_3. In broad terms, it is this competition between σ_2 and σ_3 which generates the bump at $p_{\mathrm{T}}^{\ell} \approx 40$ GeV seen in Fig. 6.14.

While the bump at $p_{\mathrm{T}}^{\ell} \approx 40$ GeV at fixed order is perfectly predictable, one should be aware of the large non-homogeneous difference with respect to a resummed prediction. The ratio of `DYTURBO` resummed predictions over the corresponding `MadGraph` fixed order ones (which are exactly the K-factors of Fig. 6.15) reveal relative factors around 1 (which is expected from a K-factor), but with large fluctuations around the bump region. While this does not induce a problem a priori due to the ad hoc resummation correction applied through the K-factor (for a given reference PDF), one must be careful so that residual resummation effects do not propagate as nonphysical features to the final shape of the prediction during a PDF fit, which could appear as a bias.

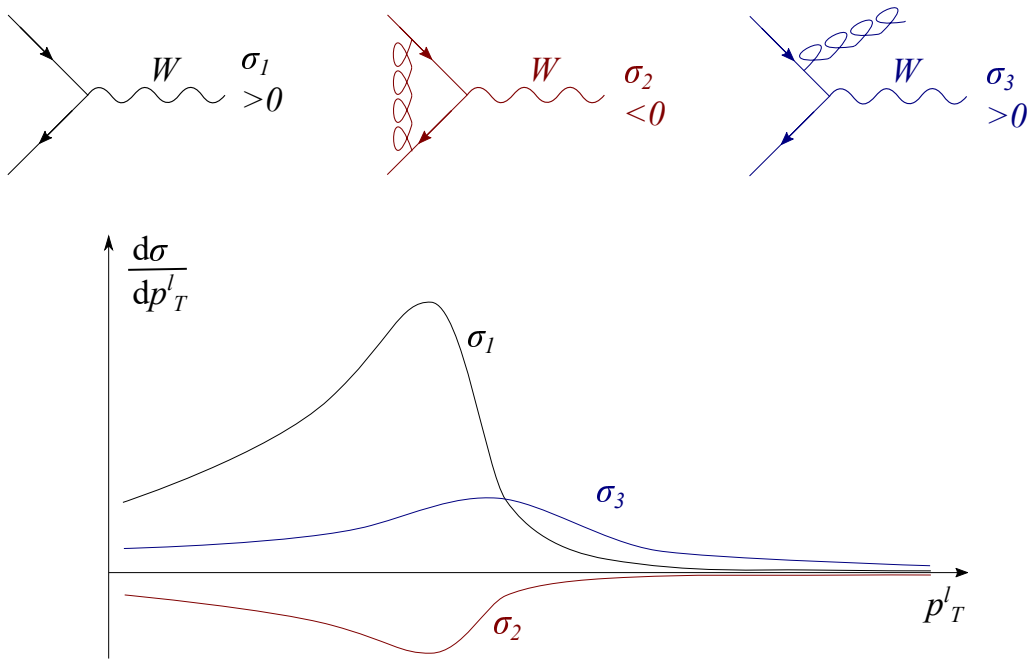

Figure 6.16: Feynman diagrams contributing to charged current fixed order NLO quark scattering. The born diagram (top-left, denoted by σ_1 interferes negatively with the NNLO diagram in the middle (top-centre, σ_2); the NLO diagram on the right (top-right, σ_3) contributes positively towards the total prediction. Schematic diagrams at the bottom represent the contribution of each

6.6.5 Quark/gluon cross-section decomposition

Following the notation used in the factorisation theorem (Eq. (6.1)), let us label the parton coming from each proton with the sub-index 1 or 2. Within `MadGraph5`, each non-ordered $q\bar{q}g_{1,2}$ parton combination (e.g. $\bar{u}dg$) is described by 14 Feynman diagrams (in fact, it is just 7 different ones, plus symmetric reflections with respect to proton-1 and proton-2, such as $\bar{u}_1 d_2$ and $d_1 \bar{u}_2$) that are explicitly added to build the fixed order NLO prediction. This is extended by adding analogous diagrams where quarks get replaced for others of the same family (e.g. $\bar{u}d \to \bar{u}c$). Looking at the initial particles (and focusing on the $\bar{u}$, d and g partons), this corresponds to 2 diagrams at born level (Fig. 6.17), 4 diagrams in the NLO $\bar{u}d$ sub-channel with a g in the final state, 4 for $\bar{u}g$ with a $\bar{d}$-quark in the final state, and 4 for dg with a u-quark in the final state. Appendix B shows all of the corresponding Feynman diagrams for processes with $\bar{u}$-quark, d-quark and/or g in the initial and final states via Fig. B.1 (same as Fig. 6.17), Fig. B.2, Fig. B.3 and Fig. B.4.

Fixed order NLO predictions generated with grids from `MadGraph5_aMC@NLO 2.9.12` groups together the diagrams for σ_1 and σ_3 under the process with the same $q_1 q_2$ initial state, which leads to a well-behaved curve; this is illustrated in Fig. 6.18, which shows a bump-less contribution from e.g. the ud sub-channel. However, the negative contribution

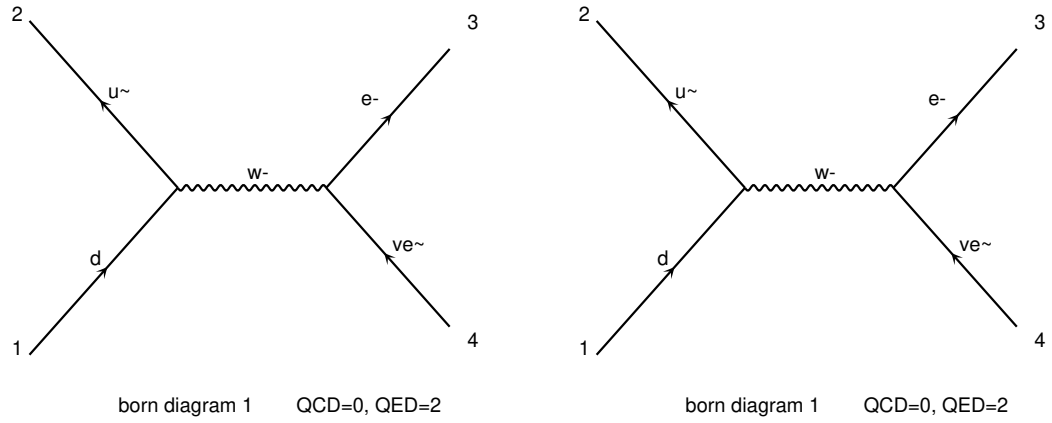

Figure 6.17: Feynman diagrams contributing at fixed order NLO to $pp \to W^- \to e^-\bar{\nu}$ at Born level (i.e. same as at LO), in the $\bar{u}d$ sub-channel. Diagrams generated by `MadGraph`.

of σ_2 is associated (i.e. added up) to channels with gluons in the initial state, such as ug or dg, which generates contributions with positive and negative parts (see Fig. 6.18).

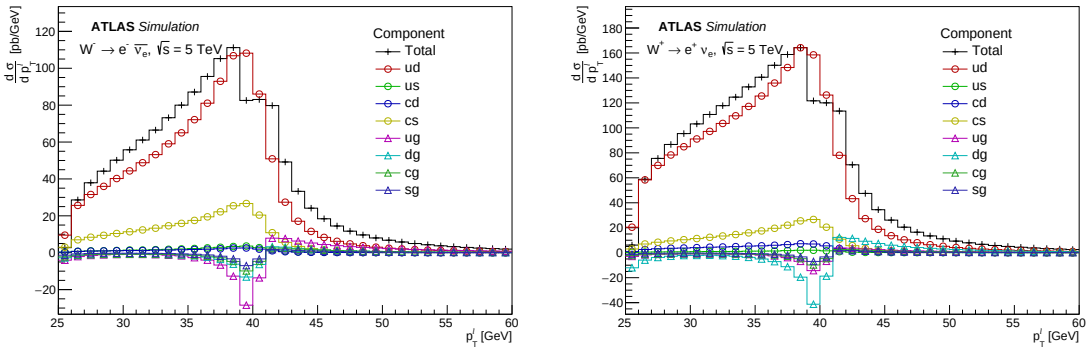

Figure 6.18: Parton sub-channel cross-section decomposition for the $W^- \to e^-\bar{\nu}$ (left) and $W^+ \to e^+\nu$ (right) channels at $\sqrt{s} = 5$ TeV channels. The sub-plots of a single channel are extracted from the global prediction of an `APPLgrid` file, achieved by convoluting with only the relevant PDF components.

6.6.6 Dependency to changes of m_W

The dependency on m_W of the predicted cross-section shape at a given p_{T}^{ℓ} bin can be taken into account through a bin-by-bin parametrisation according to Eq. (6.15). Following the sensitivity study done in Section 6.5 and inspecting the relative cross-section behaviour at different p_{T}^{ℓ} values shown in Fig. 6.10, one may define a parametric functional form $f_{p_{\mathrm{T}}^{\ell}}(m_W)$ capable of reliably describing these changes. Examples of such bin-by-bin studies are shown in Fig. 6.19, which gathers the relative cross-section dependency, for a few selected p_{T}^{ℓ} bins, as a function of m_W variations around $m_W^{\mathrm{nom}} = 80.4$ GeV.

For the particular case of these p_{T}^{ℓ} cross sections, the dependency on the value of m_W can be parametrised by a linear function of the form

$$f_{p_{\mathrm{T}}^{\ell}}(m_W) = 1 + F_{p_{\mathrm{T}}^{\ell}}(m_{\mathrm{W}} - 80.4\ \mathrm{GeV}), \tag{6.17}$$

where $F_{p_{\mathrm{T}}^{\ell}}$ is the only parameter whose value must be determined with a fit at each p_{T}^{ℓ} value. Such a fit is done using plots analogous to those of Fig. 6.19 prior to any combined PDF study.

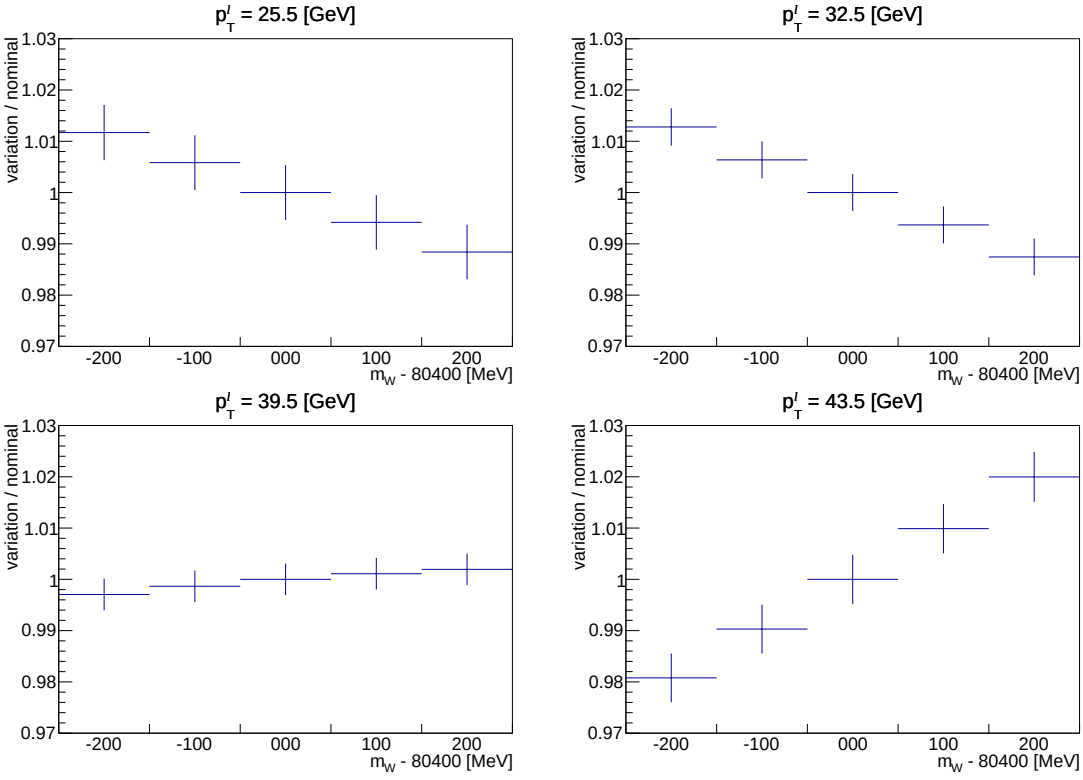

Figure 6.19: Relative dependency on m_W of the $W^- \to e^-\bar{\nu}$ NLO+NNLL differential cross sections at $\sqrt{s} = 5$ TeV. Each plot corresponds to a single p_{T}^{ℓ} bin, extracted from the ratios shown in Fig. 6.10. Analogous behaviour was found for all the p_{T}^{ℓ} bins in all the $W \to l\nu$ channels.

6.6.7 The final PDF and m_W dependent cross section

The final cross-section prediction as a function of the PDF and m_W can be written by combining all of the above together. Consequently, the combination of Eqs. (6.9), (6.15) and (6.17) leads to a final theoretical prediction, for each $W \to l\nu$ channel, described by

$$\frac{\mathrm{d}\sigma}{\mathrm{d}p_{\mathrm{T}}^{\ell}}(\mathrm{PDF}, m_W) = [\mathrm{GRID}_{\mathrm{NLO}} * \mathrm{PDF}] \times K_{\mathrm{EW,LO\to NLO}}^{\mathrm{QCD,NLO\to NNLO}} \times f_{p_{\mathrm{T}}^{\ell}}(m_W). \tag{6.18}$$

From a technical point of view, the parametrisation $f_{p_{\mathrm{T}}^{\ell}}(m_W)$ is encoded into `xFitter` via the definition of a new `Reaction` [163]. The parameters $f_{p_{\mathrm{T}}^{\ell}}$ are read from a single-column text file in a similar way to the factors read by the `KFactor Reaction`.

6.7 Closure and bias study for a combined m_W+PDF fit

Before performing a meaningful combined fit, it is of general interest to study closure and bias tests on this new technique in order to inspect its reliability and trace down the possible effects that could be seen on real data. Such tests take advantage of the use of the pseudodata described in Section 6.6.2 at $\sqrt{s} = 5$ TeV, where the injected PDF and value of m_W are known quantities that can be compared to the fitted ones. All the studies shown below were done in 4 different and independent instances, using each of the pseudodatasets (which were generated at $m_W^{\mathrm{nom}} = 80.4$ GeV for different reference PDFs [identified with the labels CT18NNLO, MSHT20NNLO, NNPDF31NNLO, ATLASpdf21]; see Section 6.6.2) and neglecting all of the corresponding systematics (i.e. only statistical uncertainty is being considered).

Closure tests consist of performing a minimally working fit, aiming to recover the injected modelling characteristics perfectly. In particular, we are interested in recovering the value of m_W^{nom}. The test is done in 2 steps:

1. The value of m_W^{fit} is fixed to 80.4 GeV. A classical PDF-only fit is done using the 4 channels of a given pseudodataset. This allows the reference PDF to be mimicked in this specific phase-space. N.B. the fitted PDF lacks physical generalisability and DOES NOT extrapolate to other processes (such as neutral Drell-Yan scattering or $t\bar{t}$ production).

2. The PDF parameters are fixed to the fitted values, m_W^{fit} is released with an initial step of 0.1 GeV, and the fit is repeated to determine m_W^{fit} on its own.

If there is closure, the retrieved value of m_W^{fit} should be compatible with m_W^{nom} within uncertainty.

Table 6.3 shows the value of the parameters fitted at each step of the closure test (labelled "PDFonly" or "mWonly") for the 4 sets of pseudodata. The header of each column identifies the pseudodataset, as well as the corresponding stage of the closure test. The value of m_W^{fit} is intuitively labelled as "Mw_fit". Parameters shown in blue are treated as fixed during the corresponding fit (thus the lack of uncertainties). The χ^2 values for these tests, as well as for any subsequent fit, are shown in Appendix C.

Table 6.3: Results of the closure tests, implemented completely within `xFitter` using the 4 pseudodatasets. The table shows the fitted parameter values, highlighting in blue any parameter that remained fixed. The fit χ^2 values are shown in Table C.1.

Parameter	ATLASpdf21 PDFonly	ATLASpdf21 mWonly	CT18NNLO PDFonly	CT18NNLO mWonly	NNPDF31NNLO PDFonly	NNPDF31NNLO mWonly	MSHT20NNLO PDFonly	MSHT20NNLO mWonly
'Adbar'	0.0879 ± 0.0022	0.08785	0.1933 ± 0.0047	0.1933	0.1284 ± 0.0034	0.1284	0.0973 ± 0.0027	0.09727
'Adv'	1.0000	1.0000	1.0000	1.0000	1.0000	1.0000	1.0000	1.0000
'Ag'	1.0000	1.0000	1.0000	1.0000	1.0000	1.0000	1.0000	1.0000
'Agp'	0.398 ± 0.041	0.3975	1.17 ± 0.22	1.166	0.440 ± 0.062	0.4398	0.431 ± 0.052	0.4306
'Auv'	1.0000	1.0000	1.0000	1.0000	1.0000	1.0000	1.0000	1.0000
'Bdbar'	-0.2345 ± 0.0054	−0.2345	-0.0570 ± 0.0055	−0.05697	-0.1370 ± 0.0058	−0.1370	-0.1779 ± 0.0060	−0.1779
'Bdv'	0.699 ± 0.029	0.6994	0.792 ± 0.037	0.7916	0.674 ± 0.029	0.6735	0.614 ± 0.026	0.6136
'Bg'	-0.506 ± 0.023	−0.5058	-0.304 ± 0.033	−0.3040	-0.511 ± 0.024	−0.5114	-0.540 ± 0.020	−0.5401
'Bgp'	-0.6192 ± 0.0089	−0.6192	-0.174 ± 0.045	−0.1738	-0.574 ± 0.013	−0.5740	-0.595 ± 0.011	−0.5951
'Buv'	0.735 ± 0.022	0.7354	0.755 ± 0.023	0.7546	0.725 ± 0.022	0.7246	0.704 ± 0.022	0.7040
'Cdbar'	2.65 ± 0.74	2.648	4.4 ± 1.2	4.391	3.20 ± 0.78	3.198	2.37 ± 0.54	2.369
'Cdv'	3.18 ± 0.19	3.178	4.63 ± 0.29	4.629	3.46 ± 0.22	3.460	3.12 ± 0.21	3.115
'Cg'	3.85 ± 0.29	3.849	3.51 ± 0.21	3.510	3.72 ± 0.28	3.717	3.56 ± 0.28	3.562
'Cgp'	25.00	25.00	25.00	25.00	25.00	25.00	25.00	25.00
'Cstr'	6.2 ± 3.2	6.159	10.7 ± 8.5	10.72	6.1 ± 2.5	6.055	5.5 ± 1.7	5.481
'Cubar'	7.1 ± 1.2	7.072	10.3 ± 1.2	10.27	9.2 ± 1.3	9.175	9.6 ± 1.2	9.622
'Cuv'	5.16 ± 0.11	5.162	5.23 ± 0.11	5.230	4.96 ± 0.11	4.964	4.90 ± 0.11	4.896
'Dubar'	4.5 ± 2.0	4.513	5.9 ± 1.9	5.926	6.1 ± 2.1	6.054	10.2 ± 2.4	10.24
'Euv'	15.7 ± 1.4	15.66	13.9 ± 1.3	13.87	12.6 ± 1.2	12.59	12.6 ± 1.1	12.57
'Mw_fit'	80.40	80.400 ± 0.018	80.40	80.400 ± 0.018	80.40	80.401 ± 0.018	80.40	80.401 ± 0.018
'rs'	0.94 ± 0.28	0.9429	0.78 ± 0.27	0.7811	0.94 ± 0.28	0.9363	1.30 ± 0.30	1.303

The "mWonly" step of each closure test has managed to reliably recover the injected value of m_W^{fit} within 1 MeV, while the statistical uncertainty of each pseudodataset (neglecting systematic uncertainties and correlation with the PDF) shows a constant value of 18 MeV. The results summarised in Table 6.3 (along Table C.1) allow the stability of the modifications done to `xFitter` to be verified, and the reliability of the methodology.

Now that the technical methodology has been validated, it is of interest to study the impact that a PDF has on the final shape of a prediction, which may propagate as a bias towards the mass measurement. This is motivated primarily due to the shape differences seen across Section 6.6 when changing the reference PDF, such as the `DYTURBO` resummed NNLO prediction from Fig. 6.12, the `APPLgrid` fixed order NLO prediction from Fig. 6.14, and the K-factors plotted in Fig. 6.15. We define a full bias test as a series of steps:

1. Select a reference set of pseudodata, e.g. ATLASpdf21
2. Do a PDF-only fit on the selected set, such that m_W^{fit} is fixed to 80.4 GeV. This will retrieve a set of parameters that mimic the behaviour of ATLASpdf21 in the corresponding phase-space.
3. Fix the parameters retrieved from the PDF-only fit and release m_W^{fit}. Perform an m_W-only fit to the 4 pseudodatasets using the very same PDF parameters in each case. By definition, the m_W-only fit on the ATLASpdf21 pseudodata is identical to

the closure test; the rest of the m_W^{fit} values will indicate the mass bias induced by the shape of the pseudodata due to the choice of PDF.

The results of the bias test using ATLASpdf21 as reference are summarised in Table 6.4. The column "Fitting ATLASpdf21" corresponds to a PDF-only fit on the homonymous pseudodataset, while the rest of the columns show m_W-only fits according to the other pseudodatasets. First, one should note that the m_W-only fit on the ATLASpdf21 pseudodata retrieves exactly the value of m_W^{nom} (again, this is identical to the corresponding closure test). By changing across columns, the value of m_W^{fit} starts to drift away from m_W^{nom}, reaching up to +79 MeV in the MSHT20NNLO pseudodata. In practical terms, this means that MSHT20NNLO induces a cross-section shape difference, with respect to ATLASpdf21, which can be partially compensated for with a shift of m_W of +79 MeV. This shape difference (similar to the one measured on CT18NNLO and NNPDF31NNLO) is generated, among other reasons, due to the parametrisation treatment used in each study, different heavy quark treatments, the selection of datasets included during the corresponding fits, and the theoretical predictions used during the fit.

An analogous bias test, with CT18NNLO as reference, is shown in Appendix C in Table C.3. The relative difference of m_W^{fit} across pseudodatasets are compatible with those shown in Table 6.4, which hints towards a "relative" (yet stable) bias propagated from intrinsic differences of the reference PDFs.

Table 6.4: Results of the bias tests implemented on the 4 pseudodatasets, using ATLASpdf21 as reference. N.B. the PDF parameters are exactly the same in all the fits. The fit χ^2 values are shown in Table C.2.

Parameter	Fitting ATLASpdf21	mW on ATLASpdf21	mW on CT18NNLO	mW on NNPDF31NNLO	mW on MSHT20NNLO
'Adbar'	0.0879 ± 0.0022	0.08785	0.08785	0.08785	0.08785
'Adv'	1.0000	1.0000	1.0000	1.0000	1.0000
'Ag'	1.0000	1.0000	1.0000	1.0000	1.0000
'Agp'	0.398 ± 0.041	0.3975	0.3975	0.3975	0.3975
'Auv'	1.0000	1.0000	1.0000	1.0000	1.0000
'Bdbar'	-0.2345 ± 0.0054	−0.2345	−0.2345	−0.2345	−0.2345
'Bdv'	0.699 ± 0.029	0.6994	0.6994	0.6994	0.6994
'Bg'	-0.506 ± 0.023	−0.5058	−0.5058	−0.5058	−0.5058
'Bgp'	-0.6192 ± 0.0089	−0.6192	−0.6192	−0.6192	−0.6192
'Buv'	0.735 ± 0.022	0.7354	0.7354	0.7354	0.7354
'Cdbar'	2.65 ± 0.74	2.648	2.648	2.648	2.648
'Cdv'	3.18 ± 0.19	3.178	3.178	3.178	3.178
'Cg'	3.85 ± 0.29	3.849	3.849	3.849	3.849
'Cgp'	25.00	25.00	25.00	25.00	25.00
'Cstr'	6.2 ± 3.2	6.159	6.159	6.159	6.159
'Cubar'	7.1 ± 1.2	7.072	7.072	7.072	7.072
'Cuv'	5.16 ± 0.11	5.162	5.162	5.162	5.162
'Dubar'	4.5 ± 2.0	4.513	4.513	4.513	4.513
'Euv'	15.7 ± 1.4	15.66	15.66	15.66	15.66
'Mw_fit'	80.40	80.400 ± 0.018	80.409 ± 0.018	80.442 ± 0.018	80.479 ± 0.018
'rs'	0.94 ± 0.28	0.9429	0.9429	0.9429	0.9429

Overall, these bias tests suggest a large sensitivity to PDF-related shape features

of the data, propagated as a way of compensating the PDF-specific features shown in Fig. 6.13 vie changes of m_W as shown in Fig. 6.10. While the main purpose of the study is to measure the correlation between m_W and the PDF, and not so much to extract a competitive measurement of m_W, it is of interest to quantify such bias as a function of PDF uncertainties. One should notice that the bias test is done using the prediction generated with the central replica (also called "replica" or "member") of each PDF set, but in reality, each of these contains tens of linearly independent replicas that contribute towards the envelope of uncertainty. In order to study the total spread of m_W^{fit} values, it is of interest to repeat the bias test (namely, the m_W-fit part) on pseudodata generated using every single PDF eigenvector, all while keeping the parameters fitted to ATLASpdf21 shown in Table 6.4. Overall, including the tests already performed, the total number of bias tests per PDF set is

- 53 for ATLASpdf21,
- 59 for CT18NNLO,
- 101 for NNPDF31NNLO,
- and 65 for MSHT20NNLO.

These tests retrieve a total of 278 measurements of m_W^{fit} with respect to the very same PDF parameters, such that the fit only accounts for cross-section shape differences via changes of m_W.

Figure 6.20 shows the histogrammed distribution of all values of m_W^{fit} retrieved from the bias tests where the PDF parameters remain fixed according to the PDF-only fit on ATLASpdf21. Each set of PDF eigenvectors yields a cluster of measurements arranged in an approximately normal distribution with their own mean value and standard deviation. The mean of each cluster is consistent with the values measured in Table 6.4, and their standard deviation alone (manifestation of the PDF uncertainty) is not enough to explain the relative mass shifts, discarding statistical effects as a possible explanation. This implies that the relative effect of a PDF in the shape of a prediction, and by extension in the value of m_W^{fit}, is unique to that PDF. An analogous study using CT18NNLO as reference PDF is shown in Fig. C.2 (Appendix C), which recovers consistent relative shift and standard deviation of each cluster with respect to the values observed in Fig. 6.20.

The relative mass shifts (with respect to the injected value $m_W^{\text{nom}} = 80.4$ GeV) are induced entirely by the effect of the PDF on the shape of the cross section. Consequently, it becomes natural to expect similar shifts in the value of m_W^{fit} according to the relative difference between the reference PDF (used to generate the pseudodata) and the PDF being fitted. Nonetheless, the shift is reduced when the reference and fitted PDF are similar between themselves (look at $\langle m_W^{\text{fit}} \rangle$ according to ATLASpdf21 in Fig. 6.20, and according to CT18NNLO in Fig. C.2), which enables the desired correlation studies between m_W and the PDF while the results are minimally affected by biases in the value of m_W^{fit}.

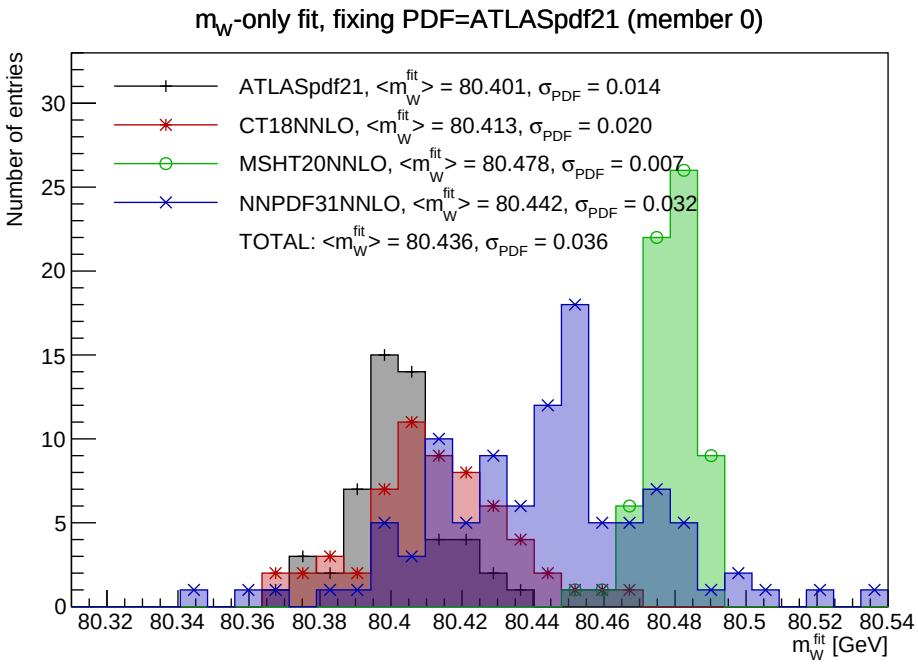

Figure 6.20: Distribution of m_W^{fit} determined from bias tests on pseudodata using all the PDF eigenvectors, keeping the ATLASpdf21 PDF-only parameters in each case (see Table 6.4). The mean value ($\langle m_W^{\text{fit}} \rangle$) and standard deviation (σ_{PDF}) are shown for each pseudodataset cluster, as well as for the total distribution (equivalent to the sum of all the others, explicitly shown in Fig. C.1). In all cases, the statistical uncertainty around the fitted value of m_W^{fit} is $\sigma_{\text{stat}} \approx 18$ MeV.

6.8 Combined m_W+PDF fits

One of the goals of this study is to perform an extension of the ATLASpdf21 fit [44] (fitted with 46 datafiles, see Table 6.1) by adding on top the low pile-up inclusive W cross sections at $\sqrt{s} = 5$ TeV (4 datafiles, one per leptonic channel), seeking to obtain a competitive description of the proton content while simultaneously constraining the mass of the W-boson; this will ultimately result in a PDF fit at NNLO QCD + NLO EW. While all of the 50 datafiles will be used to constrain an NNLO level PDF, only the low pile-up (pseudo)data is enabled to be sensitive[2] to changes of m_W via the implementation of Eq. (6.18). One should notice that the `xFitter` DIS predictions are implemented only with electroweak corrections at LO, which results in neglecting correlations between light-quark PDFs, the Weinberg angle and m_W. Thus, other processes relevant to the PDF fit, such as charged current DIS scattering, constrain m_W in a much weaker (or null) way

[2] Other datasets are much less sensitive to m_W (either directly or indirectly), so their constraining power is expected to be negligible in comparison to the p_{T}^{ℓ} spectrum. Hence, their dependency on m_W is not explicitly accounted for.

than any ATLAS W production process; ergo, these will not be considered as additional constraints of m_W.

The correlation of m_W^{fit} with the rest of the PDF parameters is quantified via the corresponding global correlation factor ρ_{m_W}, estimated with Eq. (2.13) using the correlation matrix C_{ij} approximated within `MINUIT`. The value of ρ_{m_W} will be shown below the corresponding tables of fitted parameters.

For each set of fits performed over the pseudodata generated with all the eigenvectors of a reference PDF, the uncertainty on m_W^{fit} quotes a partial uncertainty of the form $\sigma_{\text{stat}} \oplus \sigma_{\text{PDF}}$, where σ_{stat} is estimated during the fit by `MINUIT` (quoted from the fit result tables), and σ_{PDF} is defined as the standard deviation of the cluster of measurements (i.e. the value measured from e.g. Fig. 6.20).

Following from the closure and bias studies shown in Section 6.7, it is clear that one must choose carefully the reference PDF used to generate the pseudodata. From a standard PDF fit point of view, the addition of the low pile-up (pseudo)datasets provides similar constraints as the "epWZ16" dataset [147], resulting in no meaningful impact on the ATLASpdf21 PDF. This means that the cross-section shape according to the fit on the 50 datasets and to the official ATLASpdf21 PDF would yield compatible predictions, resulting in a minimal bias in the shift of m_W^{fit} (following from Fig. 6.20). Consequently, the recommendation for an ATLASpdf21 data + low pile-up combined m_W+PDF fit is to generate the pseudodata using the official ATLASpdf21 PDF. Moreover, when transitioning to real data, it is recommended to use ATLASpdf21 Monte Carlo in order to perform the unfolding and to use the unfolding bias in order to estimate an expected bias-induced shift of m_W. Keeping the previous arguments in mind, it remains interesting to explore how the global correlation ρ_{m_W} behaves when m_W changes, hence motivating analogous studies where the pseudodata is generated with CT18NNLO, NNPDF31NNLO and MSHT20NNLO; the corresponding results are shown in Appendix D.

6.8.1 Only statistical uncertainty

Similarly to the closure tests, pseudodata affected only by their statistical uncertainty will be considered, neglecting all other systematics for the time being. As a starting point for a combined m_W+PDF study, let us first check the behaviour of m_W^{fit} as a function of the reference PDF (and its eigenvectors) used to generate the pseudodata. As the PDF is allowed to change simultaneously to m_W, and in contrast to Fig. 6.20, the explicit effect of the correlation should motivate the expectation of slightly different behaviour of m_W^{fit}, both in the central values and distributions.

The combined m_W+PDF fit on the 50 datasets (where m_W is constrained simultaneously by the $W^- \to e^-\bar{\nu}$, $W^+ \to e^+\nu$, $W^- \to \mu^-\bar{\nu}$ and $W^+ \to \mu^+\nu$ channels) using pseudodata generated with the ATLASpdf21 PDF yields a mean value of $\langle m_W^{\text{fit}} \rangle = 80.387$ GeV with a statistical uncertainty of $\sigma_{\text{stat}} = 20$ MeV and PDF-propagated uncertainty of

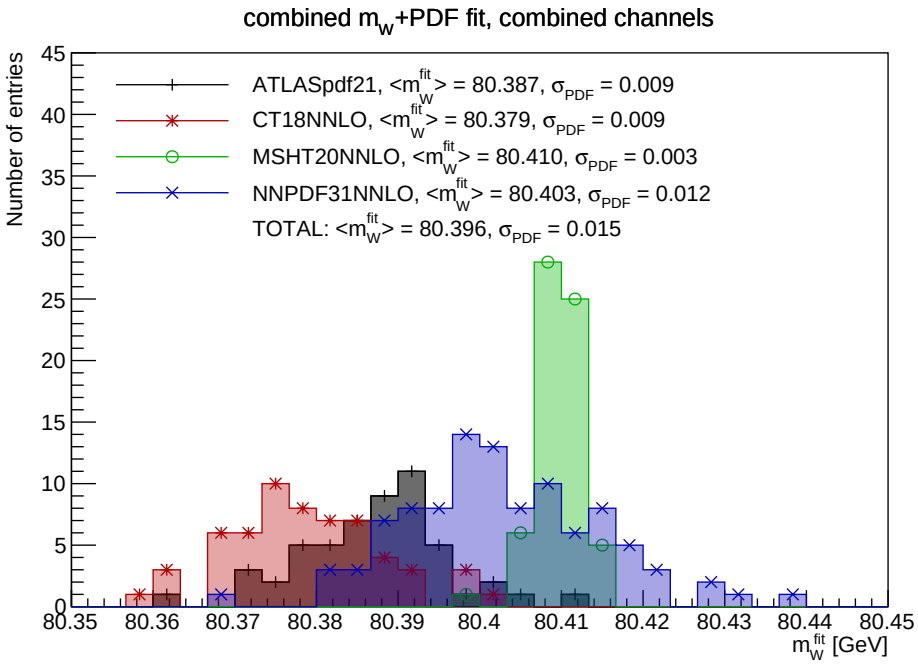

Figure 6.21: Distribution of m_W^{fit} determined via combined m_W+PDF fits, constrained with the low pile-up pseudodata (generated with all the eigenvectors of the 4 reference PDFs, only statistical uncertainty) added on top of the ATLASpdf21 data (listed in Table 6.1). The values of $\langle m_W^{\text{fit}} \rangle$ and σ_{PDF} are shown for each pseudodataset cluster, as well as for the total distribution (corresponding to the merging of all the others, explicitly shown in Fig. D.1). In all cases, the statistical uncertainty around the fitted value of m_W^{fit} is $\sigma_{\text{stat}} \approx 20$ MeV, while the global correlation is $\rho_{m_W} \approx 0.5$.

$\sigma_{\text{PDF}} = 9$ MeV (smaller than the 14 MeV found in Fig. 6.20), which is well within compatibility with m_W^{nom}. Moreover, these fits retrieve a global correlation value of $\rho_{m_W} \approx 0.45$, whose effect can be seen in the values of σ_{stat} and σ_{PDF}. The other reference PDFs also recover results compatible with m_W^{nom}, although it is worth noticing that CT18NNLO yields the largest m_W shift. Figure 6.21 summarises the fit results described earlier in this paragraph for all of the reference PDFs.

Henceforth, let us focus on pseudodata generated with the ATLASpdf21 PDF (analogous results for the other reference PDFs are shown in Section D.1). In order to better understand the shift of m_W^{fit}, it is interesting to inspect the separate contribution of each leptonic decay channel. This is motivated primarily by the production mechanism, based on pp collisions, which induces an inherent asymmetry between contributions of the u- and d-quarks. For such a study, the same combined m_W+PDF fit was repeated using only 47 data files: the 46 of the ATLASpdf21 study, plus the data file of a single $W^{\pm} \to (e/\mu)^{\pm}\,\nu$ channel.

The results of the individually fitted W decay channels are summarised in Fig. 6.22, which also shows the result for the fit on the combination of the 4 channels (same as the result shown in Fig. 6.21). Complementarily, Table 6.5 shows the parameter values fitted for the central replica of the reference pseudodata PDF, as well as the relative mass shifts $\Delta m_W = m_W^{\text{fit}} - m_W^{\text{nom}}$, the value of ρ_{m_W}, and the total post-fit χ^2 divided by the number of degrees of freedom (dof).

While the W^- decay channels retrieves $\langle m_W^{\text{fit}} \rangle \approx 40.397$ GeV $\pm$ (40 $\oplus$ 13) MeV, the W^+ channels gives $\langle m_W^{\text{fit}} \rangle \approx 40.366$ GeV $\pm$ (37 $\oplus$ 13) MeV. Repeating the same exercise using the other pseudodatasets yields different relative shifts across channels (this is illustrated in Section D.1 by Figs. D.2, D.3 and D.4), although the values remain compatible with m_W^{nom} within uncertainty. Such difference between W^- and W^+ is likely related to the specific treatment and constraining power on the u- and d-quark by the reference PDFs. It is worth noticing that regardless of the total shift of m_W^{fit}, the global correlation ρ_{m_W} remains relatively stable, taking values around 0.41 for channels fitted individually, and 0.53 when all the channels are fitted together (see the values summarised in Table 6.5).

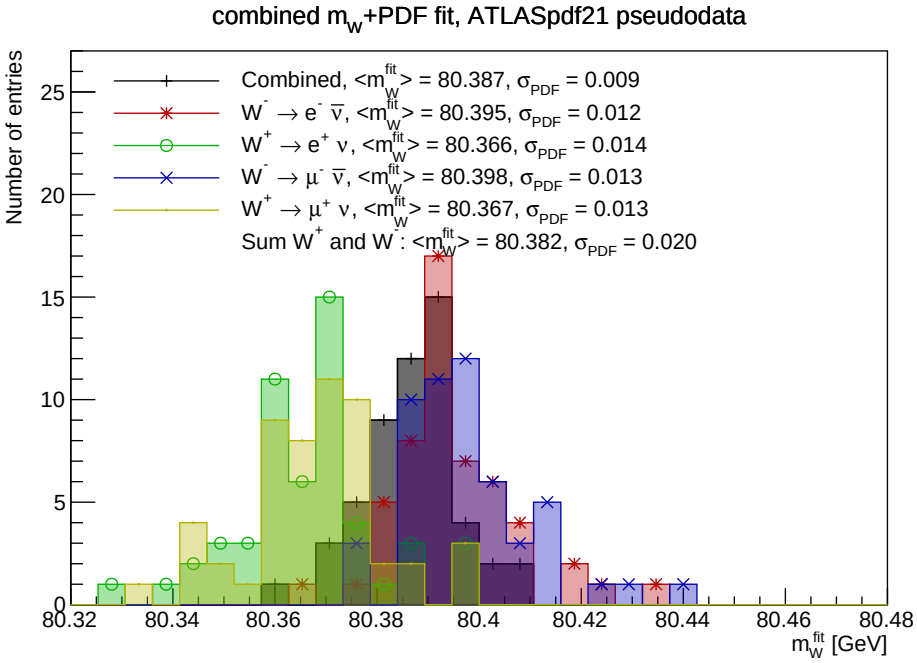

Figure 6.22: Distribution of m_W^{fit} determined via combined m_W+PDF fits, constrained with the low pile-up pseudodata (generated with the ATLASpdf21 PDF, only statistical uncertainty) added on top of the ATLASpdf21 data (listed in Table 6.1). The values of $\langle m_W^{\text{fit}} \rangle$ and σ_{PDF} are shown separately for the m_W+PDF fit on each W leptonic decay channel, as well as for the fit done simultaneously on the 4 channels (labelled as "combined"). The fitted parameter values and the corresponding ρ_{m_W} for the central replica of the reference PDF are shown in Table 6.5.

Table 6.5: Results of the combined m_W+PDF fits performed using pseudodata (only statistical uncertainty) generated with the ATLASpdf21 PDF, performed over individual W leptonic decay channels and on their combination. The global correlation ρ_{m_W} of each fit and the final χ^2/dof are shown at the bottom of the corresponding column. The complete correlation matrix of "AllChannels" fit is given in Table D.1.

Parameter	AllChannels	Wminusenu	Wplusenu	Wminusmunu	Wplusmunu
'Adbar'	0.153 ± 0.017	0.162 ± 0.020	0.141 ± 0.021	0.164 ± 0.018	0.154 ± 0.021
'Adv'	1.0000	1.0000	1.0000	1.0000	1.0000
'Ag'	1.0000	1.0000	1.0000	1.0000	1.0000
'Agp'	0.080 ± 0.017	0.078 ± 0.023	0.075 ± 0.023	0.078 ± 0.023	0.080 ± 0.022
'Aubar'	0.1323 ± 0.0028	0.1224 ± 0.0033	0.1261 ± 0.0032	0.1226 ± 0.0035	0.1289 ± 0.0032
'Auv'	1.0000	1.0000	1.0000	1.0000	1.0000
'Bdbar'	-0.125 ± 0.021	-0.113 ± 0.029	-0.139 ± 0.027	-0.111 ± 0.030	-0.122 ± 0.027
'Bdv'	0.714 ± 0.021	0.681 ± 0.026	0.699 ± 0.027	0.681 ± 0.026	0.702 ± 0.026
'Bg'	-0.754 ± 0.033	-0.773 ± 0.037	-0.754 ± 0.038	-0.769 ± 0.037	-0.765 ± 0.036
'Bgp'	-0.818 ± 0.012	-0.830 ± 0.013	-0.822 ± 0.014	-0.828 ± 0.013	-0.824 ± 0.015
'Bstr'	-0.081 ± 0.042	-0.055 ± 0.048	-0.063 ± 0.047	-0.054 ± 0.052	-0.086 ± 0.048
'Bubar'	-0.151 ± 0.010	-0.167 ± 0.016	-0.159 ± 0.016	-0.1669 ± 0.0058	-0.155 ± 0.018
'Buv'	0.699 ± 0.020	0.708 ± 0.021	0.702 ± 0.021	0.708 ± 0.021	0.702 ± 0.021
'Cdbar'	3.87 ± 0.61	3.70 ± 0.27	3.35 ± 0.19	3.72 ± 0.27	3.79 ± 0.28
'Cdv'	2.53 ± 0.38	2.41 ± 0.14	2.66 ± 0.35	2.40 ± 0.15	2.50 ± 0.14
'Cg'	4.81 ± 0.26	4.770 ± 0.083	4.87 ± 0.29	4.787 ± 0.090	4.773 ± 0.079
'Cgp'	25.00	25.00	25.00	25.00	25.00
'Cstr'	14.7 ± 2.1	15.5 ± 1.2	15.5 ± 2.4	15.6 ± 1.2	14.5 ± 2.4
'Cubar'	5.70 ± 0.34	5.49 ± 0.34	5.44 ± 0.45	5.51 ± 0.28	5.60 ± 0.40
'Cuv'	4.724 ± 0.096	4.77 ± 0.14	4.76 ± 0.15	4.77 ± 0.14	4.75 ± 0.15
'Ddv'	-0.80 ± 0.27	-0.82 ± 0.21	-0.69 ± 0.35	-0.82 ± 0.22	-0.79 ± 0.31
'Dg'	24.4 ± 5.0	26.0 ± 1.8	26.1 ± 2.1	26.0 ± 1.6	24.6 ± 1.8
'Duv'	1.51 ± 0.47	1.30 ± 0.41	1.28 ± 0.41	1.31 ± 0.40	1.40 ± 0.47
'Euv'	10.1 ± 1.1	10.3 ± 1.3	10.34 ± 0.99	10.3 ± 1.3	10.3 ± 1.1
'Mw_fit'	80.388 ± 0.021	80.394 ± 0.042	80.371 ± 0.036	80.395 ± 0.039	80.371 ± 0.037
'rs'	1.08 ± 0.25	1.10 ± 0.22	1.30 ± 0.31	1.09 ± 0.21	1.04 ± 0.30
Fit status	converged	converged	converged	converged	converged
Uncertainties	migrad-hesse	migrad-hesse	migrad-hesse	migrad-hesse	migrad-hesse
Δm_W	−12 MeV	−6 MeV	−29 MeV	−5 MeV	−29 MeV
ρ_{m_W}	0.555	0.400	0.418	0.395	0.421
χ^2/dof	2265/1755	2263/1653	2265/1653	2263/1653	2264/1653

6.8.2 Statistical uncertainty and luminosity systematic

Moving towards a realistic representation of the low pile-up cross sections, it is relevant to add the sources of systematic uncertainty expected to affect the final cross-section measurement. Particularly, it is important to inspect the effect of the luminosity systematic uncertainty, which affects the global normalisation of the relevant differential cross sections. This corresponds to an uncertainty of 1.6% that is totally correlated over all the p_{T}^{ℓ} bins and across all the W leptonic decay channels.

The fits discussed in this Section are analogous to those of Section 6.8.1. The only difference resides in the pseudodata, which now accounts for its statistical uncertainty and the contribution from the luminosity systematic. Equivalent studies using the other pseudodatasets are provided in Section D.2.

Figure 6.23 summarises the values of $\langle m_W^{\text{fit}} \rangle$ determined using the pseudodatasets generated with each reference PDF (all the leptonic decay channels of a given set are fitted simultaneously). Figure 6.24 shows the breakdown of the fit performed on the pseudodata generated with the ATLASpdf21 PDF in each of the leptonic decay channels, and Table 6.6 provides the fitted parameters of each fit.

Let us focus on the fit of all the leptonic decay channels. In comparison to the fits where only the statistical uncertainty of the low pile-up pseudodata is included, minimal differences are obtained due to the addition of the luminosity systematic (which does nothing more than regulate the normalisation of the predictions). Both cases yield a mass shift value of $\Delta m_W \approx -11$ MeV, with a fit uncertainty of 21 MeV and a global correlation of $\rho_{m_W} \approx 0.56$. The same remark is true for all the individual decay channels. This suggests that the normalisation of the prediction (alone) does not play an important role compared to the effect of the PDF. That said, the comparison of Figs. 6.22 and 6.24 shows a reduction in the values of σ_{PDF} that is caused by the inclusion of the luminosity systematic alone; since the totally correlated systematic accounts for normalisation of the p_{T}^{ℓ} distributions, the resulting fit becomes less sensitive to the changes induced in the pseudodata by the change of reference PDF eigenvector.

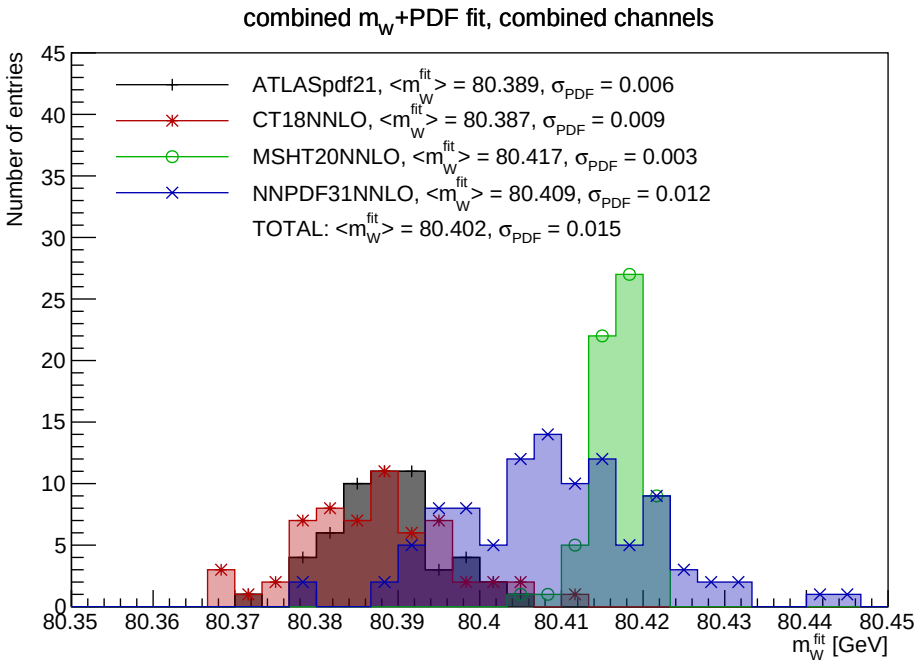

Figure 6.23: Distribution of m_W^{fit} determined via combined m_W+PDF fits, constrained with the low pile-up pseudodata (generated with all the eigenvectors of the 4 reference PDFs, only statistical and luminosity systematic uncertainties) added on top of the ATLASpdf21 data. The values of $\langle m_W^{\text{fit}} \rangle$ and σ_{PDF} are shown for each pseudodataset cluster, as well as for the total distribution (explicitly shown in Fig. D.5). In all cases, the statistical uncertainty around the fitted value of m_W^{fit} is $\sigma_{\text{stat}} \approx 20$ MeV, while the global correlation is $\rho_{m_W} \approx 0.5$.

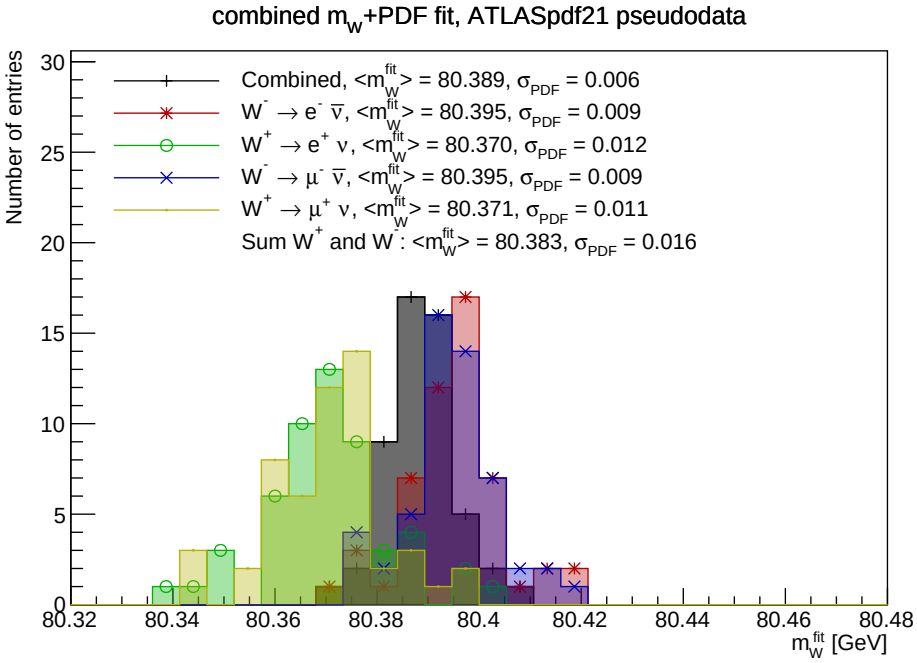

Figure 6.24: Distribution of m_W^{fit} determined via combined m_W+PDF fits, constrained with the low pile-up pseudodata (generated with the ATLASpdf21 PDF, only statistical and luminosity systematic uncertainties) added on top of the ATLASpdf21 data (listed in Table 6.1). The values of $\langle m_W^{\text{fit}} \rangle$ and σ_{PDF} are shown separately for the m_W+PDF fit on each W leptonic decay channel, as well as for the fit done simultaneously on the 4 channels (labelled as "combined"). The fitted parameter values and the corresponding ρ_{m_W} for the central replica of the reference PDF are shown in Table 6.6.

Table 6.6: Results of the combined m_W+PDF fits performed using pseudodata (only statistical and luminosity systematic uncertainties) generated with the ATLASpdf21 PDF, performed over individual W leptonic decay channels and on their combination. The global correlation ρ_{m_W} of each fit and the final χ^2/dof are shown at the bottom of the corresponding column. The complete correlation matrix of "AllChannels" fit is given in Table D.5.

Parameter	AllChannels	Wminusenu	Wplusenu	Wminusmunu	Wplusmunu
'Adbar'	0.158 ± 0.018	0.166 ± 0.024	0.160 ± 0.024	0.167 ± 0.025	0.160 ± 0.024
'Adv'	1.0000	1.0000	1.0000	1.0000	1.0000
'Ag'	1.0000	1.0000	1.0000	1.0000	1.0000
'Agp'	0.075 ± 0.015	0.073 ± 0.030	0.075 ± 0.023	0.073 ± 0.077	0.074 ± 0.017
'Aubar'	0.1342 ± 0.0039	0.1273 ± 0.0033	0.1275 ± 0.0034	0.1273 ± 0.0044	0.1291 ± 0.0079
'Auv'	1.0000	1.0000	1.0000	1.0000	1.0000
'Bdbar'	-0.120 ± 0.021	-0.109 ± 0.028	-0.118 ± 0.028	-0.108 ± 0.029	-0.117 ± 0.028
'Bdv'	0.719 ± 0.021	0.692 ± 0.027	0.699 ± 0.026	0.692 ± 0.030	0.703 ± 0.029
'Bg'	-0.758 ± 0.037	-0.775 ± 0.041	-0.775 ± 0.039	-0.774 ± 0.051	-0.772 ± 0.036
'Bgp'	-0.823 ± 0.017	-0.834 ± 0.019	-0.833 ± 0.019	-0.833 ± 0.033	-0.832 ± 0.018
'Bstr'	-0.090 ± 0.045	-0.073 ± 0.055	-0.080 ± 0.050	-0.072 ± 0.074	-0.086 ± 0.064
'Bubar'	-0.149 ± 0.016	-0.159 ± 0.018	-0.158275 ± 0.018	-0.160 ± 0.017	-0.156 ± 0.013
'Buv'	0.700 ± 0.021	0.708 ± 0.022	0.703 ± 0.021	0.708 ± 0.022	0.703 ± 0.021
'Cdbar'	3.98 ± 0.59	3.82 ± 0.65	3.84 ± 0.66	3.83 ± 0.78	3.86 ± 0.67
'Cdv'	2.57 ± 0.42	2.47 ± 0.52	2.49 ± 0.47	2.46 ± 0.65	2.51 ± 0.50
'Cg'	4.82 ± 0.24	4.79 ± 0.38	4.77 ± 0.31	4.79 ± 0.83	4.79 ± 0.26
'Cgp'	25.00	25.00	25.00	25.00	25.00
'Cstr'	14.7 ± 2.1	15.4 ± 3.0	14.9 ± 2.6	15.5 ± 5.4	14.8 ± 2.5
'Cubar'	5.79 ± 0.34	5.65 ± 0.41	5.57 ± 0.40	5.65 ± 0.60	5.62 ± 0.46
'Cuv'	4.727 ± 0.096	4.76 ± 0.10	4.746 ± 0.099	4.76 ± 0.12	4.75 ± 0.10
'Ddv'	-0.78 ± 0.32	-0.79 ± 0.17	-0.80 ± 0.33	-0.79 ± 0.48	-0.78 ± 0.36
'Dg'	25.9 ± 6.3	27.3 ± 7.6	26.8 ± 8.4	27.3 ± 7.2	27.0 ± 6.4
'Duv'	1.54 ± 0.48	1.36 ± 0.48	1.41 ± 0.48	1.36 ± 0.22	1.43 ± 0.49
'Euv'	10.1 ± 1.1	10.3 ± 1.1	10.2 ± 1.1	10.3 ± 1.3	10.3 ± 1.1
'Mw_fit'	80.389 ± 0.021	80.395 ± 0.043	80.370 ± 0.039	80.395 ± 0.047	80.372 ± 0.037
'rs'	1.00 ± 0.26	0.99 ± 0.27	1.01 ± 0.30	0.99 ± 0.48	0.99 ± 0.32
Fit status	converged	converged	converged	converged	converged
Uncertainties	migrad-hesse	migrad-hesse	migrad-hesse	migrad-hesse	migrad-hesse
Δm_W	-11 MeV	-5 MeV	-30 MeV	-5 MeV	-28 MeV
ρ_{m_W}	0.573	0.404	0.417	0.393	0.421
χ^2/dof	2265/1755	2263/1653	2264/1653	2263/1653	2264/1653

6.8.3 The full set of uncertainties

In order to study the full effect of the full low pile-up cross sections, the rest of the systematics (as expected from the unfolding of real data, scaled proportionally to the pseudodata) are added onto the pseudodata. Consequently, each (pseudo)measurement is affected by its statistical uncertainty and the sources of fully correlated systematics due to luminosity and lepton identification, isolation, reconstruction, energy scale uncertainty, and triggering; all the uncertainties are scaled proportionally to the pseudodata. Studies analogous to those documented in Section 6.8.1 and Section 6.8.2 are shown in this Section, emphasising around the pseudodata computed with the ATLASpdf21 reference PDF. Analogous results obtained with the other pseudodatasets are provided in Section D.3.

Figure 6.25 summarises the values of $\langle m_W^{\text{fit}} \rangle$ determined using the pseudodatasets generated with each reference PDF (all the leptonic decay channels of a given set are fitted simultaneously). Figure 6.26 shows the breakdown of the fit performed on the pseudodata generated with the ATLASpdf21 PDF in all the leptonic decay channels, and Table 6.7 provides the fitted parameters of each fit.

Again, let us focus on the fit of all the leptonic decay channels. The value of m_W^{fit} relative to its uncertainty indicates an improvement with respect to the ones found in sections 6.8.1 and 6.8.2, as the shift of the fitted mass gets decreased to $\Delta m_W \approx -7$ MeV with an uncertainty of 23 MeV. Moreover, the most relevant change appears in the value of the global correlation, which now wanders around $\rho_{m_W} = 0.39$. Such drastic changes are a consequence of the availability of the different sources of systematic uncertainty, which are capable of accounting for additional shape inaccuracies of the low pile-up (pseudo)measurements and decrease the impact of the PDF on the shape of a prediction (with respect to the scenario with only statistical uncertainties), ultimately reducing the correlation between the PDF and the parameter m_W.

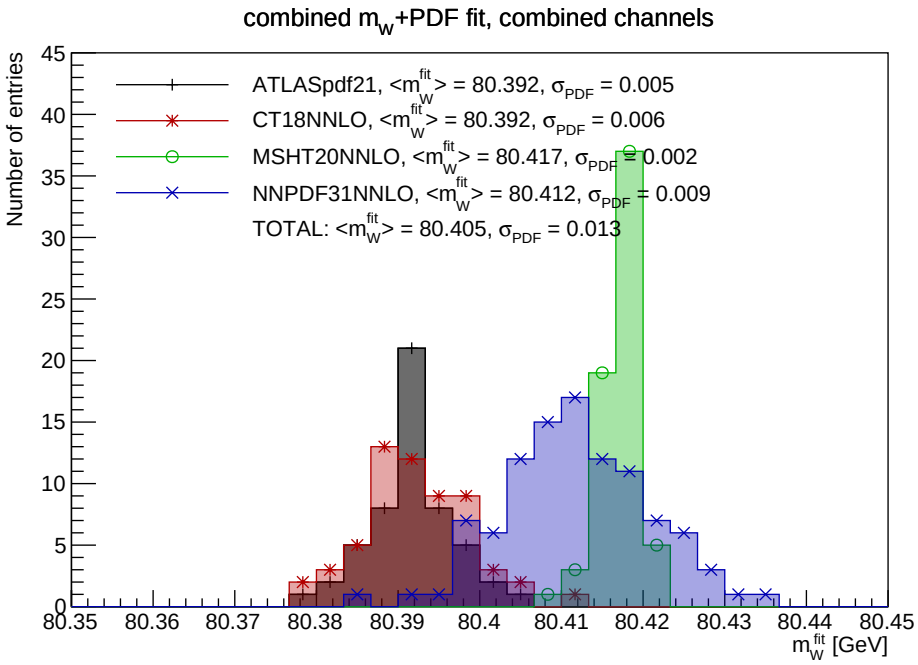

Figure 6.25: Distribution of m_W^{fit} determined via combined m_W+PDF fits, constrained with the low pile-up pseudodata (generated with all the eigenvectors of the 4 reference PDFs, with statistical uncertainty and all sources of systematics) added on top of the ATLASpdf21 data. The values of $\langle m_W^{\text{fit}} \rangle$ and σ_{PDF} are shown for each pseudodataset cluster, as well as for the total distribution (explicitly shown in Fig. D.9). In all cases, the statistical uncertainty around the fitted value of m_W^{fit} is $\sigma_{\text{stat}} \approx 20$ MeV, while the global correlation is $\rho_{m_W} \approx 0.4$.

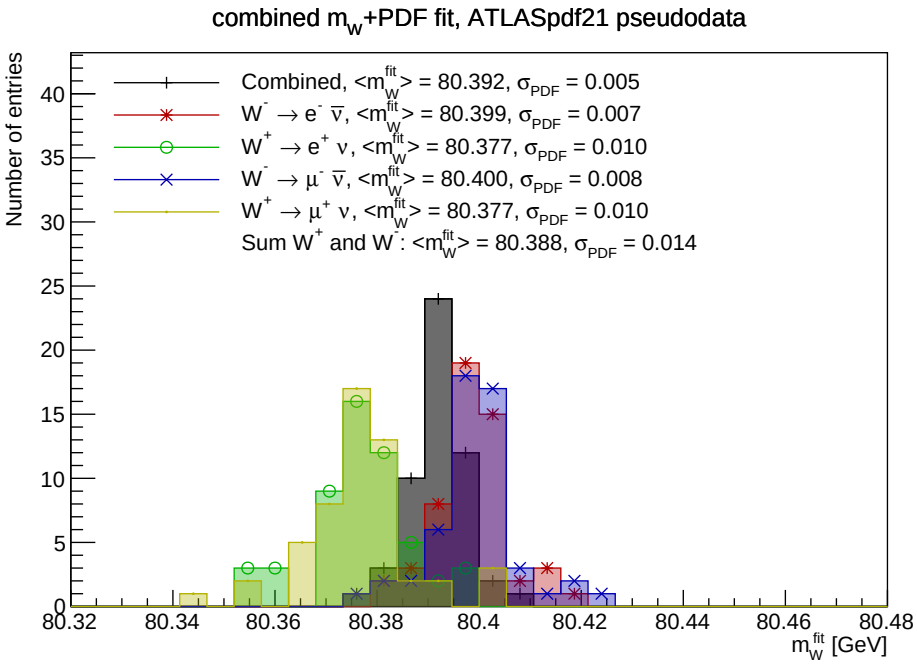

Figure 6.26: Distribution of m_W^{fit} determined via combined m_W+PDF fits, constrained with the low pile-up pseudodata (generated with the ATLASpdf21 PDF, with statistical uncertainty and all sources of systematics) added on top of the ATLASpdf21 data (listed in Table 6.1). The values of $\langle m_W^{\text{fit}} \rangle$ and σ_{PDF} are shown separately for the m_W+PDF fit on each W leptonic decay channel, as well as for the fit done simultaneously on the 4 channels (labelled as "combined"). The "Sum W^+ and W^-" label corresponds to the average of the individually fitted channels. The fitted parameter values and the corresponding ρ_{m_W} for the central replica of the reference PDF are shown in Table 6.7.

Table 6.7: Results of the combined m_W+PDF fits performed using pseudodata (with statistical uncertainty and all sources of systematics) generated with the ATLASpdf21 PDF, performed over individual W leptonic decay channels and on their combination. The global correlation ρ_{m_W} of each fit and the final χ^2/dof are shown at the bottom of the corresponding column. The complete correlation matrix of "AllChannels" fit is given in Table D.9.

Parameter	AllChannels	Wminusenu	Wplusenu	Wminusmunu	Wplusmunu
'Adbar'	0.152 ± 0.018	0.165 ± 0.025	0.161 ± 0.017	0.165 ± 0.022	0.160 ± 0.011
'Adv'	1.0000	1.0000	1.0000	1.0000	1.0000
'Ag'	1.0000	1.0000	1.0000	1.0000	1.0000
'Agp'	0.077 ± 0.020	0.073 ± 0.024	0.0727 ± 0.0087	0.073 ± 0.016	0.073 ± 0.011
'Aubar'	0.1301 ± 0.0030	0.1271 ± 0.0030	0.1303 ± 0.0033	0.1272 ± 0.0029	0.1280 ± 0.0026
'Auv'	1.0000	1.0000	1.0000	1.0000	1.0000
'Bdbar'	-0.127 ± 0.022	-0.110 ± 0.028	-0.115 ± 0.022	-0.110 ± 0.026	-0.117 ± 0.019
'Bdv'	0.711 ± 0.022	0.693 ± 0.027	0.704 ± 0.024	0.693 ± 0.026	0.700 ± 0.054
'Bg'	-0.757 ± 0.038	-0.776 ± 0.040	-0.774 ± 0.037	-0.776 ± 0.039	-0.775 ± 0.041
'Bgp'	-0.822 ± 0.018	-0.835 ± 0.019	-0.834 ± 0.017	-0.835 ± 0.018	-0.834 ± 0.020
'Bstr'	-0.072 ± 0.046	-0.075 ± 0.057	-0.096 ± 0.037	-0.075 ± 0.051	-0.084 ± 0.038
'Bubar'	-0.155 ± 0.017	-0.159 ± 0.017	-0.153 ± 0.017	-0.159 ± 0.018	-0.157 ± 0.019
'Buv'	0.701 ± 0.020	0.708 ± 0.022	0.704 ± 0.021	0.708 ± 0.023	0.705 ± 0.021
'Cdbar'	3.78 ± 0.67	3.81 ± 0.63	3.85 ± 0.62	3.81 ± 0.80	3.81 ± 0.18
'Cdv'	2.54 ± 0.40	2.47 ± 0.54	2.51 ± 0.38	2.47 ± 0.51	2.50 ± 0.49
'Cg'	4.82 ± 0.29	4.79 ± 0.32	4.79 ± 0.22	4.79 ± 0.21	4.79 ± 0.24
'Cgp'	25.00	25.00	25.00	25.00	25.00
'Cstr'	15.1 ± 2.3	15.3 ± 2.8	14.7 ± 1.8	15.3 ± 2.5	14.9 ± 1.7
'Cubar'	5.61 ± 0.35	5.63 ± 0.40	5.70 ± 0.36	5.64 ± 0.37	5.61 ± 0.35
'Cuv'	4.736 ± 0.097	4.76 ± 0.10	4.751 ± 0.097	4.762 ± 0.099	4.75 ± 0.11
'Ddv'	-0.79 ± 0.29	-0.79 ± 0.37	-0.78 ± 0.28	-0.79 ± 0.48	-0.8 ± 1.9
'Dg'	25.5 ± 6.9	27.6 ± 9.9	27.5 ± 3.4	27.6 ± 3.1	27.4 ± 3.1
'Duv'	1.44 ± 0.48	1.35 ± 0.50	1.41 ± 0.46	1.35 ± 0.53	1.39 ± 0.44
'Euv'	10.2 ± 1.1	10.3 ± 1.1	10.3 ± 1.1	10.3 ± 1.0	10.3 ± 1.0
'Mw_fit'	80.393 ± 0.023	80.398 ± 0.047	80.380 ± 0.042	80.399 ± 0.045	80.377 ± 0.039
'rs'	1.13 ± 0.28	0.99 ± 0.37	0.94 ± 0.19	0.99 ± 0.21	1.00 ± 0.32
Fit status	converged	converged	converged	converged	converged
Uncertainties	migrad-hesse	migrad-hesse	migrad-hesse	migrad-hesse	migrad-hesse
Δm_W	-7 MeV	-2 MeV	-20 MeV	-1 MeV	-23 MeV
ρ_{m_W}	0.394	0.272	0.346	0.274	0.362
χ^2/dof	2265/1755	2263/1653	2263/1653	2263/1653	2263/1653

6.8.4 Effect on the PDFs

In the context of PDF fits it is of interest to inspect the effect of the low pile-up (pseudo)data on the final distributions of each parton with respect to the case where such dataset is not included at all. A nominal PDF fit was performed with `xFitter` using the original 46 data files, and it is this fit which is used as a reference to gauge changes in the distributions. The impact of the combination of decay channels of the low pile-up (pseudo)data, in the context of combined m_W+PDF fits, is extracted from the studies shown in sections 6.8.1, 6.8.2 and 6.8.3. Figures 6.27, 6.28, 6.29 and 6.30 show a few examples of the aforementioned PDFs fits at $Q^2 = 6464$ GeV$^2 = (80.4$ GeV$)^2 = (m_W^{\text{nom}})^2$, as well as the ratio of these distributions with respect to the nominal fit of ATLASpdf21. The corresponding PDF parameters are summarised in Table 6.8. A comprehensive list of these PDF fits is shown at $Q^2 = 1.9$ GeV^2 and $Q^2 = (80.4$ GeV$)^2$ in Appendix E, which also displays the relative error band around the central value of the PDFs.

Table 6.8: Summary of the fitted parameters corresponding to the PDF distributions shown in this Section (as well as all the figures displayed in Appendix E.)

	Nominal PDF fit	Combined m_W+PDF fit		
Parameter	ATLASpdf21_fit (without LowPileup)	ATLASpdf21 +LowPileup_StatOnly	ATLASpdf21 +LowPileup_StatAndLumi	ATLASpdf21 +LowPileup_StatAllSyst
'Adbar'	0.165 ± 0.027	0.154 ± 0.017	0.158 ± 0.018	0.152 ± 0.018
'Adv'	1.0000	1.0000	1.0000	1.0000
'Ag'	1.0000	1.0000	1.0000	1.0000
'Agp'	0.070 ± 0.019	0.079 ± 0.017	0.075 ± 0.015	0.077 ± 0.020
'Aubar'	0.1253 ± 0.0038	0.1343 ± 0.0069	0.1342 ± 0.0039	0.1301 ± 0.0030
'Auv'	1.0000	1.0000	1.0000	1.0000
'Bdbar'	-0.110 ± 0.029	-0.124 ± 0.021	-0.120 ± 0.021	-0.127 ± 0.022
'Bdv'	0.697 ± 0.028	0.717 ± 0.022	0.719 ± 0.021	0.711 ± 0.022
'Bg'	-0.797 ± 0.037	-0.754 ± 0.033	-0.758 ± 0.037	-0.757 ± 0.038
'Bgp'	-0.848 ± 0.017	-0.818 ± 0.012	-0.823 ± 0.017	-0.822 ± 0.018
'Bstr'	-0.074 ± 0.046	-0.090 ± 0.053	-0.090 ± 0.045	-0.072 ± 0.046
'Bubar'	-0.162 ± 0.018	-0.149 ± 0.011	-0.149 ± 0.016	-0.155 ± 0.017
'Buv'	0.708 ± 0.022	0.699 ± 0.020	0.700 ± 0.021	0.701 ± 0.020
'Cdbar'	4.06 ± 0.71	3.88 ± 0.61	3.98 ± 0.59	3.78 ± 0.67
'Cdv'	2.50 ± 0.48	2.55 ± 0.38	2.57 ± 0.42	2.54 ± 0.40
'Cg'	4.62 ± 0.30	4.81 ± 0.26	4.82 ± 0.24	4.82 ± 0.29
'Cgp'	25.00	25.00	25.00	25.00
'Cstr'	14.7 ± 2.6	14.7 ± 2.1	14.7 ± 2.1	15.1 ± 2.3
'Cubar'	5.63 ± 0.42	5.77 ± 0.40	5.79 ± 0.34	5.61 ± 0.35
'Cuv'	4.76 ± 0.10	4.724 ± 0.096	4.727 ± 0.096	4.736 ± 0.097
'Ddv'	-0.75 ± 0.37	-0.79 ± 0.27	-0.78 ± 0.32	-0.79 ± 0.29
'Dg'	28.8 ± 8.1	24.4 ± 5.0	25.9 ± 6.3	25.5 ± 6.9
'Duv'	1.35 ± 0.50	1.52 ± 0.47	1.54 ± 0.48	1.44 ± 0.48
'Euv'	10.4 ± 1.1	10.0 ± 1.1	10.1 ± 1.1	10.2 ± 1.1
'Mw_fit'	80.40	80.387 ± 0.021	80.389 ± 0.021	80.393 ± 0.023
'rs'	0.97 ± 0.24	1.04 ± 0.29	1.00 ± 0.26	1.13 ± 0.28
Fit status	converged	converged	converged	converged
Uncertainties	migrad-hesse	migrad-hesse	migrad-hesse	migrad-hesse
Δm_W	0 MeV	-12 MeV	-11 MeV	-7 MeV
ρ_{m_W}	0.00	0.555	0.573	0.394
χ^2/dof	2256/1620	2265/1755	2265/1755	2265/1755

The parameter values summarised in Table 6.8 show compatible values (within uncer-

tainties) between the nominal PDF fit of the ATLASpdf21 data, as well as the combined fits that include the low pile-up pseudodata. This suggests that the addition of the low pile-up set does not provide further strong constraints of the PDF, which is expected given that the ATLASpdf21 fit already contains inclusive W-boson cross sections (see Table 6.1).

Figures 6.27 to 6.30 illustrate the effect of the parameters in Table 6.8 on the PDF shape at $Q^2 = (80.4\text{ GeV})^2$. Overall, and consistently to the parameter values, the PDFs fitted with the low pile-up (pseudo)data result in changes that remain within the uncertainty bands of the nominal ATLASpdf21 PDF. While the combined fits have a minor effect on the u_v and d_v distributions (of the order of a few per cent), the most relevant change can be seen in the gluon PDF (Figure 6.30). This change in the gluon PDF may be consequence of the NLO fixed order effects generated from the APPLgrid prediction of the p_{T}^{ℓ} (see Fig. 6.18) cross sections, which may not be completely absorbed by the k-factor, specially around the $p_{\mathrm{T}}^{\ell} \approx 40$ GeV bump.

Figure 6.31 compares the shape of the (pseudo)data and the corresponding prediction after a combined fit, and it shows the re-apparition of a feature at 40 GeV, which supports further the hypothesis of imperfect resummation corrections. Moreover, the large reduction of the PDF uncertainty band after the combined fit may also result from artificially enhanced constraining power caused by the p_{T}^{ℓ} fixed order APPLgrids. A quick check of the influence of the region around the bump is presented in Appendix F, where the region $37 < p_{\mathrm{T}}^{\ell} < 43$ GeV is excluded from the final combined fit in order to reduce the effects of this bump while sacrificing the region that is most sensitive to m_W. Further studies are encouraged in order to study the physicality of these mass shifts, such as replacing the APPLgrid approach with the generation of DYTURBO NNLO resummed predictions directly within xFitter (a feature that is currently under development but has not yet been released).

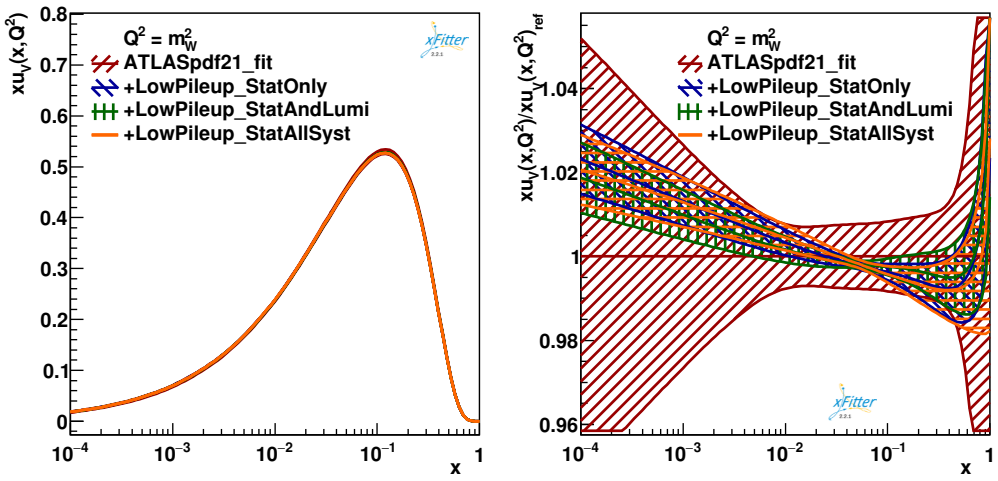

Figure 6.27: PDF of the u_v quark at $Q^2 = (80.4\ \text{GeV})^2$, fitted with `xFitter`. The distributions are shown for a nominal fit on the ATLASpdf21 data (46 data files) and combined m_W+PDF fits where the 4 decay channels of the low pile-up pseudodata are added (i.e. a total of 50 files). The pseudodataset first includes only its statistical uncertainty, then the luminosity systematic is added, and finally the rest of the systematics are integrated. The combined fits correspond to the results of the column "AllChannels" shown in Tables 6.5, 6.6 and 6.7. The ratio of each PDF with respect to the nominal fit of ATLASpdf21 is also provided, as well as the corresponding relative uncertainty bands.

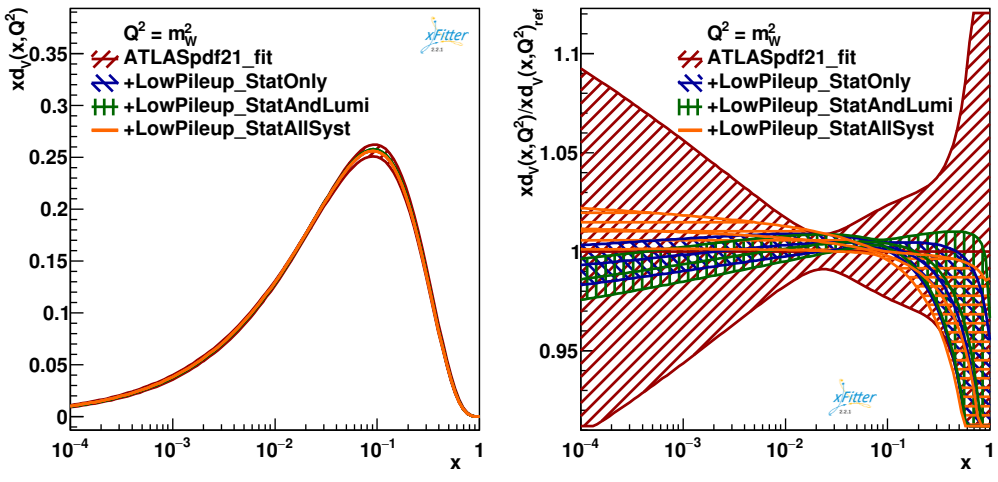

Figure 6.28: PDF of the d_v quark at $Q^2 = (80.4\ \text{GeV})^2$, fitted with `xFitter`. These fits are a continuation of the results shown in Fig. 6.27.

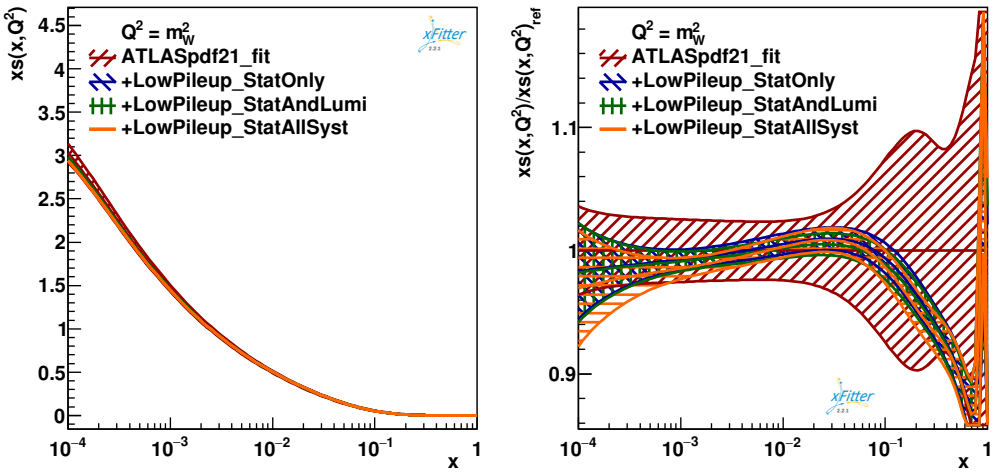

Figure 6.29: PDF of the s-quark at $Q^2 = (80.4\ \text{GeV})^2$, fitted with `xFitter`. These fits are a continuation of the results shown in Fig. 6.27.

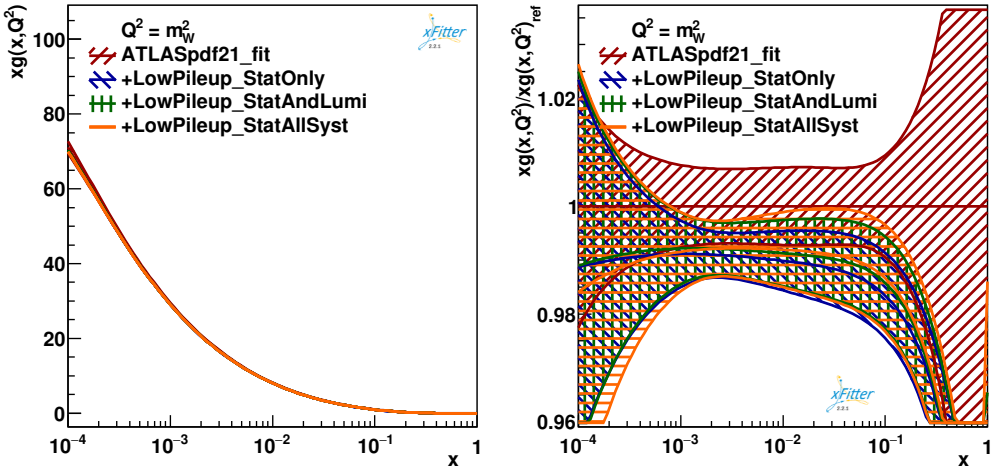

Figure 6.30: PDF of the gluon at $Q^2 = (80.4\ \text{GeV})^2$, fitted with `xFitter`. These fits are a continuation of the results shown in Fig. 6.27.

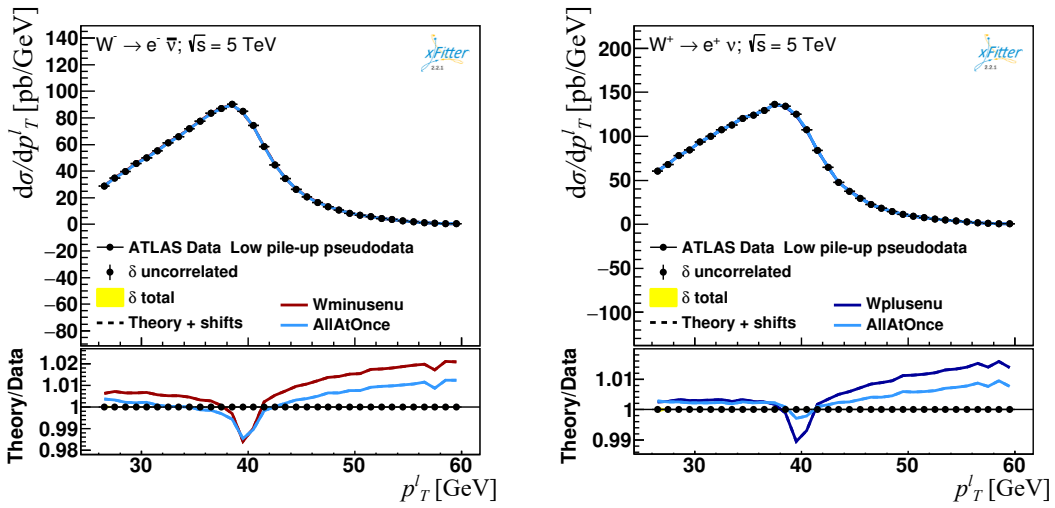

Figure 6.31: Standard agreement between the p_{T}^{ℓ} pseudodata and post-fit prediction of the low pile-up cross section in the $W^{\pm} \to e^{\pm}\nu$ channels. The "AllAtOnce" label corresponds to the result where the 4 channels are fitted simultaneously, while "Wminusenu" and "Wplusenu" account for a single decay channel. The statistical and experimental uncertainties have been removed from the plot in order to illustrate the shape agreement properly (hence, systematic shifts are not displayed despite the label "Theory + shifts"). N.B. the feature at $p_{\mathrm{T}}^{\ell} \approx 40$ GeV is compatible with that seen on the fixed order predictions.

6.8.5 Parametrisation uncertainty

Motivated by standard PDF studies, it is of interest to inspect the effect of the parametrisation uncertainty on the fitted value of m_W. This was done via the release of additional free PDF parameters, leading to combinations of $D_{\bar{d}}$, $D_{\bar{u}}$ and F_{u_v}. The results of these fits are summarised in Table 6.9, which shows the total post-fit χ^2 and m_W^{fit} for all the parametrisation uncertainty studies. Overall, the choice of parametrisation is responsible for a variance of $\sigma_{\text{param.}} = 3.45$ MeV on m_W^{fit}.

Table 6.9: Summarised results of the parametrisation uncertainty study on the combined m_W+PDF fit, showing the final χ^2/dof and the corresponding value of m_W^{fit}. The "Reference" PDF corresponds to the standard fit shown in Table. 6.5, on top of which the additional parameters are released. All the fitted values of m_W showed an uncertainty of ±23 MeV.

Fit	χ^2/dof	m_W^{fit} [GeV]
Reference	2265/1755	80.392
$D_{\bar{d}}$	2265/1754	80.392
$D_{\bar{u}}$	2269/1754	80.385
F_{u_v}	2264/1754	80.392
$D_{\bar{d}} + D_{\bar{u}}$	2269/1753	80.383
$D_{\bar{d}} + F_{u_v}$	2264/1753	80.392
$D_{\bar{u}} + F_{u_v}$	2268/1753	80.387
$D_{\bar{d}} + D_{\bar{u}} + F_{u_v}$	2263/1752	80.390

6.9 Summary of the study

A combined m_W+PDF fit was enabled within `xFitter` via the reweighting of differential cross-section predictions using a linear parametrisation function at each bin. Via sensitivity studies, it was determined that inclusive W cross sections as a function of p_{T}^{ℓ} are a good candidate to inspect the correlation between m_W and the PDF, which takes advantage of the ongoing effort to measure the analogous cross section using low pile-up samples. For the purpose of the study, and seeking to understand the capabilities of the proposed technique, the study was performed using pseudodata generated with $m_W^{\text{nom}} = 80.4$ GeV.

Closure tests verified the reliability of the fitting technique, while bias studies revealed a large interplay between the determined value of m_W^{fit} and the PDF used to generate a prediction. The same closure and bias tests retrieved an estimation of the uncertainty around the fitted mass of m_W due to the statistical uncertainty of the low pile-up (pseudo)data, giving a value of 18 MeV when the 4 leptonic decay channels are simultaneously fitted.

Seeking to obtain a realistic and competitive constraint of the proton PDF, all the data used for the ATLASpdf21 study [44] was added on top of the low pile-up pseudodata. Combined m_W+PDF fits were carried out using pseudodata generated with various

reference PDFs, seeking to inspect the global correlation of m_W with the rest of the PDF parameters as m_W changes. These fits also explored the effect of the uncertainties on the low pile-up pseudodata, verifying the impact of the statistical uncertainty alone, the effect on normalisation from the luminosity uncertainty, and the influence of all the other relevant systematics.

The addition of a totally correlated luminosity systematic over the statistical uncertainty had a minimal effect on the fit (in the absence of other systematics), showing compatible results within the pseudodatasets generated with different reference PDFs; focusing on the pseudodata generated with the ATLASpdf21 PDF, fits over the 4 leptonic decay channels yields consistently a shift of $\Delta m_W = (-11 \pm 21)$ MeV, while the global correlation remains around values of $\rho \approx 0.56$.

Combined m_W+PDF fits after the addition of the rest of the relevant systematics on the p_{T}^{ℓ} cross sections (propagated through the unfolding process and scaled to pseudodata) revealed a reduced shift of the fitted mass, yielding $\Delta m_W = (-7 \pm 23)$ MeV with a global correlation of $\rho_{m_W} \approx 0.39$. Fits on pseudodata generated with the other reference PDFs retrieved similar uncertainty and global correlation values, showing the stability of the correlation, while the shifts were specific to each pseudodataset (although compatible with m_W^{nom} within uncertainty).

Looking at the distributions of the fitted PDFs, one can notice that the addition of the low pile-up (pseudo)data has a small impact on the central value of the nominal ATLASpdf21 fit, yielding changes that remain well within uncertainty. The improved uncertainty bands after the inclusion of the low pile-up pseudodata may also be caused by said fixed order features, as such numerical effects could appear as artificially enhanced constraining power.

7 Summary of results

The work described in this document presents the development, implementation and results of new analysis approaches. The following paragraphs summarise the specific contributions of the author towards each of the studies, and the main results of each part.

– Full development of a minimisation framework to fit and implement the newly proposed calibration method based on electron energy resolution corrections of MC samples, labelled as Δ' technique, seeking to improve the remaining disagreement between the data and MC Z-boson invariant mass lineshapes.

– The Δ' technique was applied to the 2018 $Z \to ee$ samples, improving the total data to MC χ^2 from 2323 to 122 in a 100-bin histogram.

– Direct supervision of internship students allowed for the re-implementation of the Δ' calibration on low pile-up $Z \to ee$ and $W^{\pm} \to e^{\pm}\nu$ samples, which allowed the impact of the calibration technique in the measurement of the W-boson mass to be inspected. The study was performed on pseudodata and it measured a shift of m_W of (-17 ± 19) MeV in the 13 TeV samples due to the calibration method alone.

– A novel statistical method for the minimisation of discontinuous χ^2 was proposed by the author, which was later released as an ATLAS PubNote.

– Introduction of the method to permit combined m_W+PDF fits as an extension of the already-existing fitting framework `xFitter`.

– Study of the sensitivity of W-boson differential cross sections to variations of m_W with respect to resummed QCD NLO and NNLO predictions, and estimation of the PDF-independent hard scattering cross section factors for the quick generation of fixed order NLO predictions.

– Closure and bias studies of combined m_W+PDF fit technique using low pile-up W inclusive differential cross sections pseudodata (generated at $m_W^{\text{nom}} = 80.4$ GeV) as a function of p_{T}^{ℓ}.

– Implementation of combined m_W+PDF fits on the low pile-up pseudodata, added on top of a large amount of ATLAS and HERA data. The study explored the effect of

the statistical and systematic uncertainties on the low pile-up pseudodata, tracking the fitted values of m_W^{fit} and its global correlation ρ_{m_W} with all the other PDF parameters. Studies on the uncertainty eigenvectors of the PDF used to generate the pseudodata were observed to propagate as an uncertainty of $\sigma_{\text{PDF}} = 9$ MeV (which acts on top of the fit uncertainty determined by `MINUIT`).

– The addition of a totally correlated luminosity systematic over the statistical uncertainty showed (on its own) to have a minimal effect on the fit, yielding compatible results. Combined m_W+PDF fits which include the 4 leptonic decay channels yield consistently a shift of $\Delta m_W = (-11 \pm 21)$ MeV, with global correlations around values of $\rho \approx 0.56$.

– The addition of the rest of the relevant systematics on the p_{T}^{ℓ} cross sections propagates as a reduced shift of the fitted mass, which retrieves $\Delta m_W = (-7 \pm 23)$ MeV with a global correlation of $\rho_{m_W} \approx 0.39$.

– The inclusion of the p_{T}^{ℓ} cross sections induced changes of the PDF central distributions that, in general, remain well within uncertainty of the nominal ATLASpdf21 fit. The most noticeable change, which still remains within uncertainties, is the gluon PDF, which may be induced by the fixed order effects observed in quark/gluon decomposition of the shape of the p_{T}^{ℓ} distributions.

A PDF uncertainty in precision measurements

Table A.1: Uncertainty breakdown of all the combination channels used in the measurement of m_W by the ATLAS collaboration [23]. The total uncertainty and contribution by the PDF are highlighted with red rectangles.

Combined categories	Value [MeV]	Stat. Unc.	Muon Unc.	Elec. Unc.	Recoil Unc.	Bckg. Unc.	QCD Unc.	EW Unc.	PDF Unc.	Total Unc.	χ^2/dof of Comb.
m_{T}, W^+, e-μ	80370.0	12.3	8.3	6.7	14.5	9.7	9.4	3.4	16.9	30.9	2/6
m_{T}, W^-, e-μ	80381.1	13.9	8.8	6.6	11.8	10.2	9.7	3.4	16.2	30.5	7/6
m_{T}, $W^\pm$, e-μ	80375.7	9.6	7.8	5.5	13.0	8.3	9.6	3.4	10.2	25.1	11/13
p_{T}^ℓ, W^+, e-μ	80352.0	9.6	6.5	8.4	2.5	5.2	8.3	5.7	14.5	23.5	5/6
p_{T}^ℓ, W^-, e-μ	80383.4	10.8	7.0	8.1	2.5	6.1	8.1	5.7	13.5	23.6	10/6
p_{T}^ℓ, $W^\pm$, e-μ	80369.4	7.2	6.3	6.7	2.5	4.6	8.3	5.7	9.0	18.7	19/13
p_{T}^ℓ, $W^\pm$, e	80347.2	9.9	0.0	14.8	2.6	5.7	8.2	5.3	8.9	23.1	4/5
m_{T}, $W^\pm$, e	80364.6	13.5	0.0	14.4	13.2	12.8	9.5	3.4	10.2	30.8	8/5
m_{T}-p_{T}^ℓ, W^+, e	80345.4	11.7	0.0	16.0	3.8	7.4	8.3	5.0	13.7	27.4	1/5
m_{T}-p_{T}^ℓ, W^-, e	80359.4	12.9	0.0	15.1	3.9	8.5	8.4	4.9	13.4	27.6	8/5
m_{T}-p_{T}^ℓ, $W^\pm$, e	80349.8	9.0	0.0	14.7	3.3	6.1	8.3	5.1	9.0	22.9	12/11
p_{T}^ℓ, $W^\pm$, μ	80382.3	10.1	10.7	0.0	2.5	3.9	8.4	6.0	10.7	21.4	7/7
m_{T}, $W^\pm$, μ	80381.5	13.0	11.6	0.0	13.0	6.0	9.6	3.4	11.2	27.2	3/7
m_{T}-p_{T}^ℓ, W^+, μ	80364.1	11.4	12.4	0.0	4.0	4.7	8.8	5.4	17.6	27.2	5/7
m_{T}-p_{T}^ℓ, W^-, μ	80398.6	12.0	13.0	0.0	4.1	5.7	8.4	5.3	16.8	27.4	3/7
m_{T}-p_{T}^ℓ, $W^\pm$, μ	80382.0	8.6	10.7	0.0	3.7	4.3	8.6	5.4	10.9	21.0	10/15
m_{T}-p_{T}^ℓ, W^+, e-μ	80352.7	8.9	6.6	8.2	3.1	5.5	8.4	5.4	14.6	23.4	7/13
m_{T}-p_{T}^ℓ, W^-, e-μ	80383.6	9.7	7.2	7.8	3.3	6.6	8.3	5.3	13.6	23.4	15/13
m_{T}-p_{T}^ℓ, $W^\pm$, e-μ	80369.5	6.8	6.6	6.4	2.9	4.5	8.3	5.5	9.2	18.5	29/27

Table A.2: Uncertainty breakdown of the re-analysis measurement of m_W by the ATLAS collaboration [25]. The total uncertainty and contribution by the PDF are highlighted with red rectangles.

Obs.	Mean [MeV]	Elec. Unc.	PDF Unc.	Muon Unc.	EW Unc.	PS & A_i Unc.	Bkg. Unc.	Γ_W Unc.	MC stat. Unc.	Lumi Unc.	Recoil Unc.	Total sys.	Data stat.	Total Unc.
p_{T}^ℓ	80360.1	8.0	7.7	7.0	6.0	4.7	2.4	2.0	1.9	1.2	0.6	15.5	4.9	16.3
m_{T}	80382.2	9.2	14.6	9.8	5.9	10.3	6.0	7.0	2.4	1.8	11.7	24.4	6.7	25.3

Table A.3: Uncertainty breakdown of all the combination channels used in the preliminary measurement of $\sin^2\theta^{\ell}_{\text{eff}}$ by the ATLAS collaboration [133]. The total uncertainty and contribution by the PDF are highlighted with red rectangles.

Channel	ee_{CC}	$\mu\mu_{CC}$	ee_{CF}	$ee_{CC} + \mu\mu_{CC}$	$ee_{CC} + \mu\mu_{CC} + ee_{CF}$
Central value	0.23148	0.23123	0.23166	0.23119	0.23140
	Uncertainties				
Total	68	59	43	49	36
Stat.	48	40	29	31	21
Syst.	48	44	32	38	29
	Uncertainties in measurements				
PDF (meas.)	8	9	7	6	4
p_{T}^{Z} modelling	0	0	7	0	5
Lepton scale	4	4	4	4	3
Lepton resolution	6	1	2	2	1
Lepton efficiency	11	3	3	2	4
Electron charge misidentification	2	0	1	1	< 1
Muon sagitta bias	0	5	0	1	2
Background	1	2	1	1	2
MC. stat.	25	22	18	16	12
	Uncertainties in predictions				
PDF (predictions)	37	35	22	33	24
QCD scales	6	8	9	5	6
EW corrections	3	3	3	3	3

B Inclusive W production Feynman diagrams at NLO

Summary of Feynman diagrams, as generated by `MadGraph`, used for the computation of the fixed order NLO $pp \to W^- \to e^-\bar{\nu}$ inclusive cross-section `APPLgrid` file. The diagrams shown here exclusively describe processes with $\bar{u}$-quark, d-quark and/or gluon in the initial or final states.

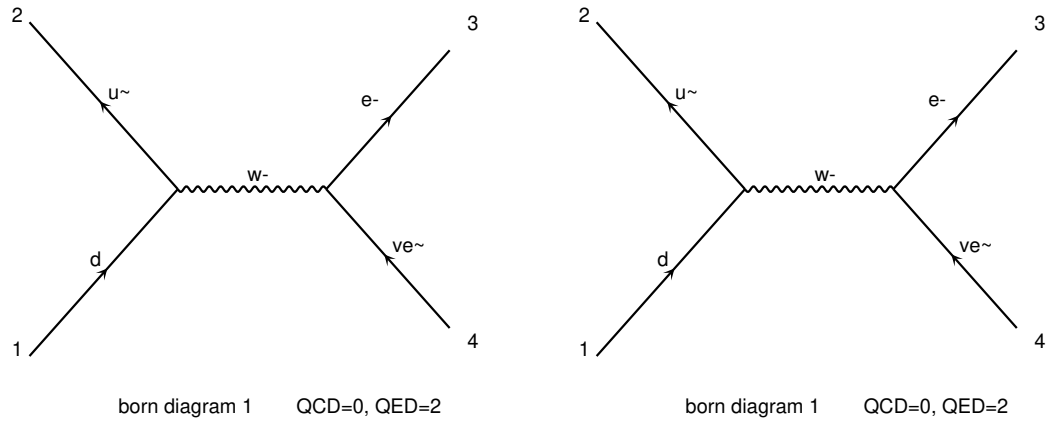

Figure B.1: Feynman diagrams contributing at fixed order NLO to $pp \to W^- \to e^-\bar{\nu}$ at Born level (i.e. same as at LO), in the $\bar{u}d$ sub-channel. Diagrams generated by `MadGraph`.

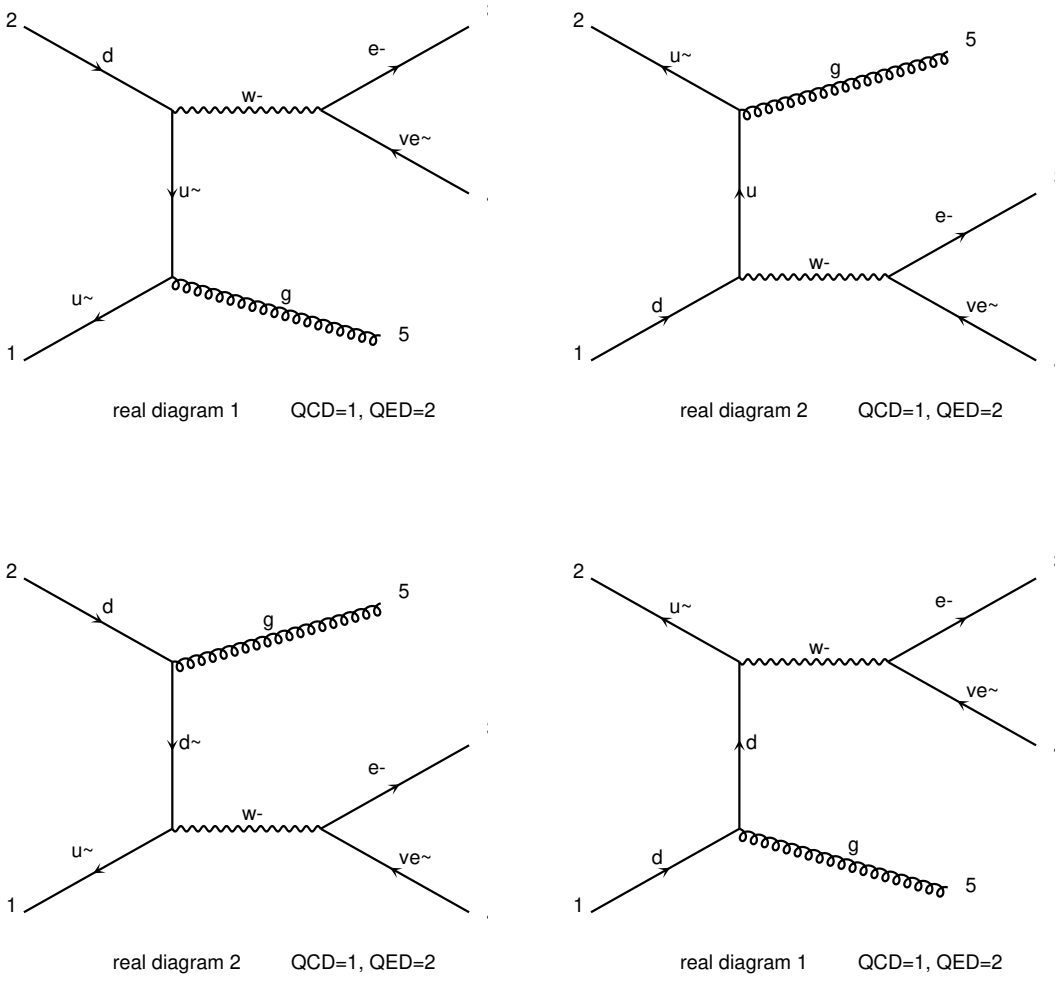

Figure B.2: Feynman diagrams contributing at fixed order NLO to $pp \to W^- \to e^-\bar{\nu}$, in the $\bar{u}d$ sub-channel with a g in the final state. Diagrams generated by `MadGraph`.

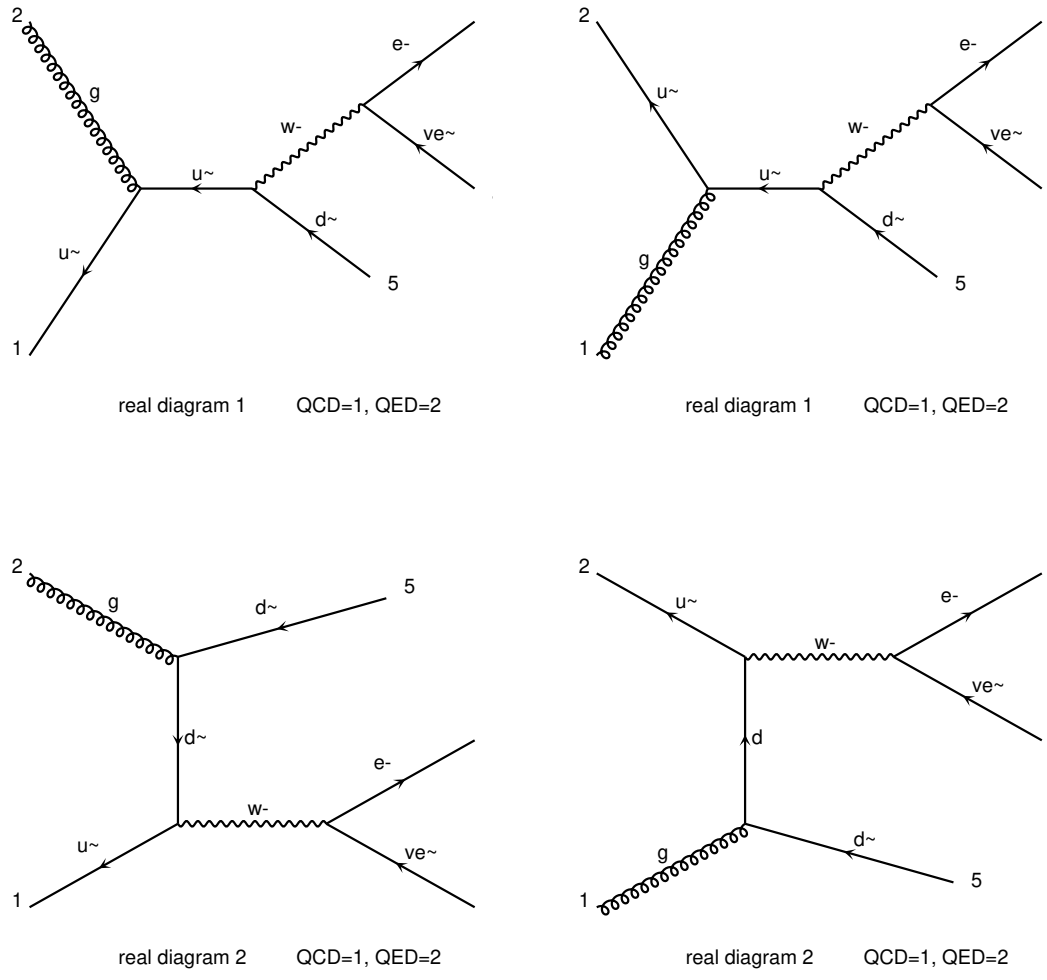

Figure B.3: Feynman diagrams contributing at fixed order NLO to $pp \to W^- \to e^-\bar{\nu}$, in the dg sub-channel with a d-quark in the final state. Diagrams generated by `MadGraph`.

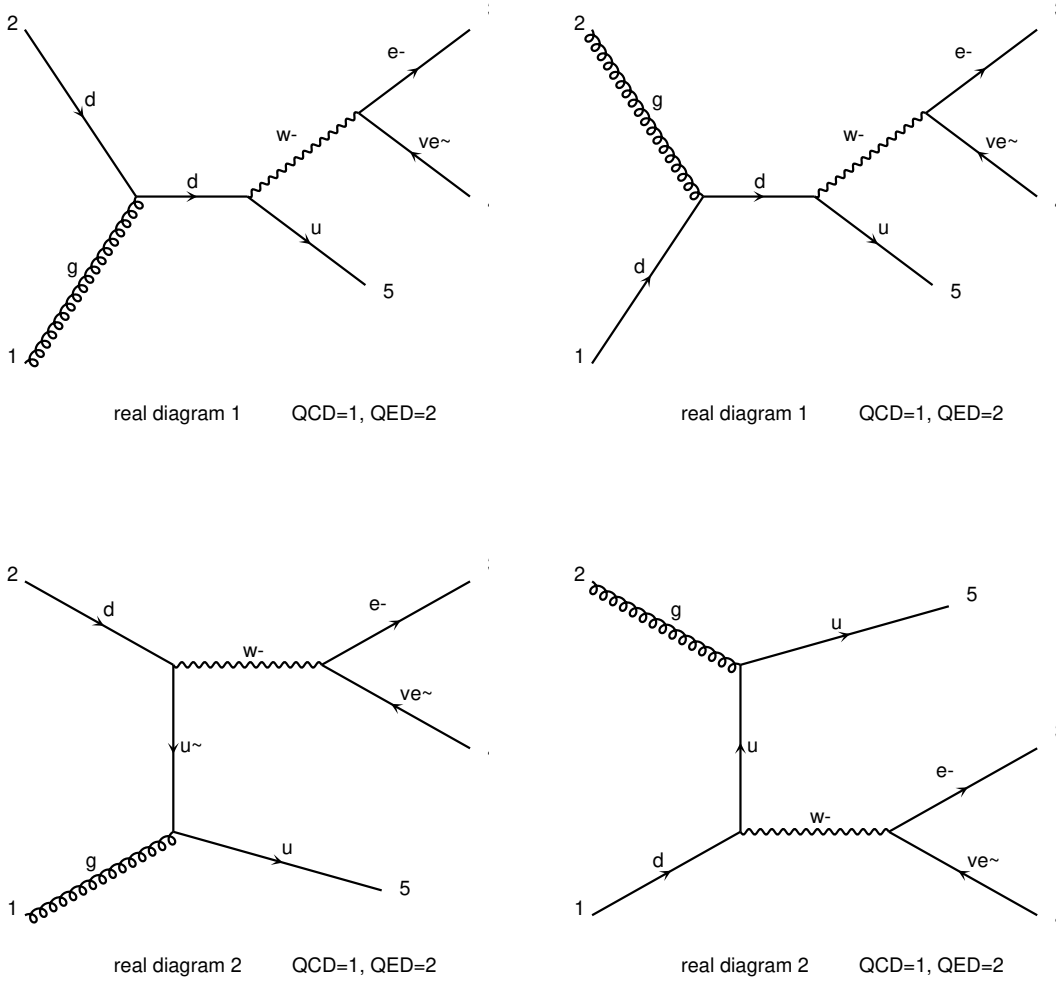

Figure B.4: Feynman diagrams contributing at fixed order NLO to $pp \to W^- \to e^-\bar{\nu}$, in the $\bar{u}g$ sub-channel with a $\bar{u}$-quark in the final state. Diagrams generated by `MadGraph`.

C Combined m_W+PDF fits: closure and bias tests

Table C.1: Results of the closure tests, implemented completely within `xFitter` using the 4 pseudodatasets. The table shows the final χ^2 value divided by the number of degrees of freedom. The corresponding fitted parameters are summarised in Table 6.3.

Dataset	ATLASpdf21 PDFonly	ATLASpdf21 mWonly	CT18NNLO PDFonly	CT18NNLO mWonly	NNPDF31NNLO PDFonly	NNPDF31NNLO mWonly	MSHT20NNLO PDFonly	MSHT20NNLO mWonly
MC XS low-mu Wplusenu pTl 5 TeV	0.0100 / 34	0.0100 / 34	0.0100 / 34	0.0100 / 34	0.020 / 34	0.020 / 34	0.030 / 34	0.030 / 34
MC XS low-mu Wminusenu pTl 5 TeV	0.0100 / 34	0.0100 / 34	0.0100 / 34	0.0100 / 34	0.0100 / 34	0.0100 / 34	0.020 / 34	0.020 / 34
MC XS low-mu Wminusmunu pTl 5 TeV	0.0100 / 34	0.0100 / 34	0.0100 / 34	0.0100 / 34	0.020 / 34	0.0100 / 34	0.020 / 34	0.020 / 34
MC XS low-mu Wplusmunu pTl 5 TeV	0.0100 / 34	0.0100 / 34	0.0100 / 34	0.0100 / 34	0.030 / 34	0.030 / 34	0.030 / 34	0.030 / 34
Correlated χ^2	0	0	0	0	0	0	0	0
Log penalty χ^2	-0.03	-0.03	-0.03	-0.03	-0.03	-0.02	-0.03	-0.02
Total χ^2 / dof	-0.0100 / 120	-0.0100 / 135	-0.0100 / 120	-0.0100 / 135	0.050 / 120	0.050 / 135	0.070 / 120	0.060 / 135
χ^2 p-value	1.00	1.00	1.00	1.00	1.00	1.00	1.00	1.00

Table C.2: Results of the bias tests implemented on the 4 pseudodatasets, using ATLASpdf21 as reference. The table shows the final χ^2 value divided by the number of degrees of freedom. The fit χ^2 values are shown in Table 6.4.

Dataset	Fitting ATLASpdf21	mW on ATLASpdf21	mW on CT18NNLO	mW on NNPDF31NNLO	mW on MSHT20NNLO
MC XS low-mu Wplusenu pTl 5 TeV	0.0100 / 34	0.0100 / 34	621 / 34	251 / 34	710 / 34
MC XS low-mu Wminusenu pTl 5 TeV	0.0100 / 34	0.0100 / 34	240 / 34	123 / 34	375 / 34
MC XS low-mu Wminusmunu pTl 5 TeV	0.0100 / 34	0.0100 / 34	264 / 34	136 / 34	413 / 34
MC XS low-mu Wplusmunu pTl 5 TeV	0.0100 / 34	0.0100 / 34	685 / 34	275 / 34	780 / 34
Correlated χ^2	0	0	0	0	0
Log penalty χ^2	-0.03	-0.03	+6.4	+4.2	+6.8
Total χ^2 / dof	-0.0100 / 120	-0.0100 / 135	1816 / 135	790 / 135	2284 / 135
χ^2 p-value	1.00	1.00	0.00	0.00	0.00

Table C.3: Results of the bias tests implemented on the 4 pseudodatasets, using CT18NNLO as reference. N.B. the PDF parameters are exactly the same in all the fits. The corresponding fitted parameters are summarised in Table C.4.

Parameter	Fitting CT18NNLO	mW on ATLASpdf21	mW on CT18NNLO	mW on NNPDF31NNLO	mW on MSHT20NNLO
'Adbar'	0.1933 ± 0.0047	0.1933	0.1933	0.1933	0.1933
'Adv'	1.0000	1.0000	1.0000	1.0000	1.0000
'Ag'	1.0000	1.0000	1.0000	1.0000	1.0000
'Agp'	1.17 ± 0.22	1.166	1.166	1.166	1.166
'Auv'	1.0000	1.0000	1.0000	1.0000	1.0000
'Bdbar'	-0.0570 ± 0.0055	−0.05697	−0.05697	−0.05697	−0.05697
'Bdv'	0.792 ± 0.037	0.7916	0.7916	0.7916	0.7916
'Bg'	-0.304 ± 0.033	−0.3040	−0.3040	−0.3040	−0.3040
'Bgp'	-0.174 ± 0.045	−0.1738	−0.1738	−0.1738	−0.1738
'Buv'	0.755 ± 0.023	0.7546	0.7546	0.7546	0.7546
'Cdbar'	4.4 ± 1.2	4.391	4.391	4.391	4.391
'Cdv'	4.63 ± 0.29	4.629	4.629	4.629	4.629
'Cg'	3.51 ± 0.21	3.510	3.510	3.510	3.510
'Cgp'	25.00	25.00	25.00	25.00	25.00
'Cstr'	10.7 ± 8.5	10.72	10.72	10.72	10.72
'Cubar'	10.3 ± 1.2	10.27	10.27	10.27	10.27
'Cuv'	5.23 ± 0.11	5.230	5.230	5.230	5.230
'Dubar'	5.9 ± 1.9	5.926	5.926	5.926	5.926
'Euv'	13.9 ± 1.3	13.87	13.87	13.87	13.87
'Mw_fit'	80.40	80.392 ± 0.017	80.400 ± 0.018	80.431 ± 0.017	80.466 ± 0.018
'rs'	0.78 ± 0.27	0.7811	0.7811	0.7811	0.7811

Table C.4: Results of the bias tests implemented on the 4 pseudodatasets, using CT18NNLO as reference. The table shows the final χ^2 value divided by the number of degrees of freedom. The corresponding fitted parameters are summarised in Table C.3.

Dataset	Fitting CT18NNLO	mW on ATLASpdf21	mW on CT18NNLO	mW on NNPDF31NNLO	mW on MSHT20NNLO
MC XS low-mu Wplusenu pTl 5 TeV	0.0100 / 34	624 / 34	0.0100 / 34	84 / 34	5.4 / 34
MC XS low-mu Wminusenu pTl 5 TeV	0.0100 / 34	242 / 34	0.0100 / 34	21 / 34	24 / 34
MC XS low-mu Wplusmunu pTl 5 TeV	0.0100 / 34	689 / 34	0.0100 / 34	94 / 34	5.8 / 34
MC XS low-mu Wminusmunu pTl 5 TeV	0.0100 / 34	268 / 34	0.0100 / 34	23 / 34	26 / 34
Correlated χ^2	0	0	0	0	0
Log penalty χ^2	-0.03	-6.50	-0.03	-2.23	+0.35
Total χ^2 / dof	-0.0100 / 120	1816 / 135	-0.0100 / 135	219 / 135	62 / 135
χ^2 p-value	1.00	0.00	1.00	0.00	1.00

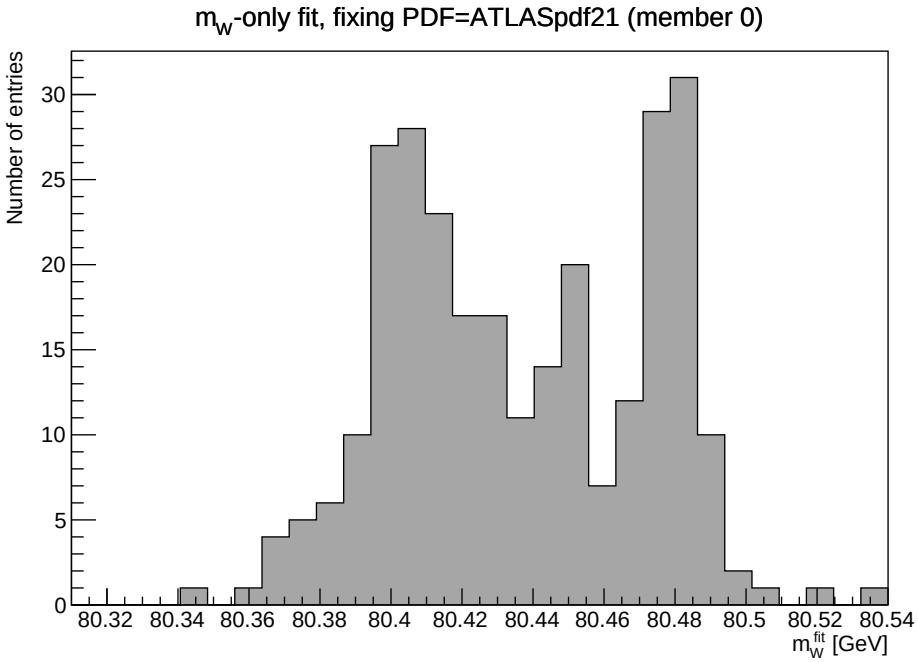

Figure C.1: Total distribution of m_W^{fit} determined from bias tests on pseudodata using all the PDF eigenvectors in all of the pseudodatasets, keeping the ATLASpdf21 PDF-only parameters in each case (see Table 6.4).

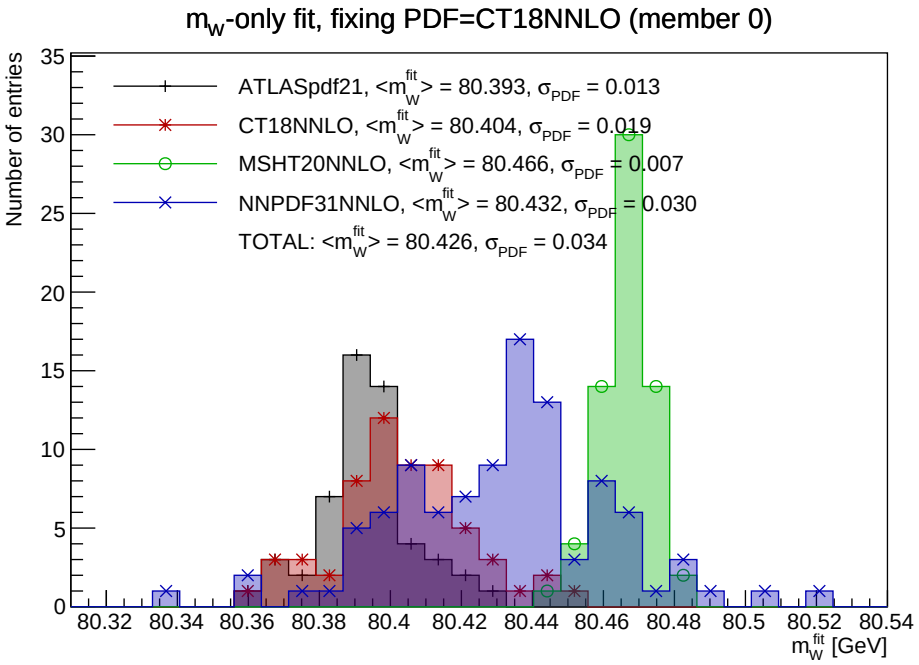

Figure C.2: Distribution of m_W^{fit} determined from bias tests on pseudodata using all the PDF eigenvectors, keeping the CT18NNLO PDF-only parameters in each case (see Table C.3). The values of $\langle m_W \rangle$ and σ_{PDF} of each pseudodataset is compatible with the mass measurements shown in Table C.3. The total distribution (combination of all the distributions given above) is shown in Fig. C.3. The results are analogue to those shown in Fig 6.20.

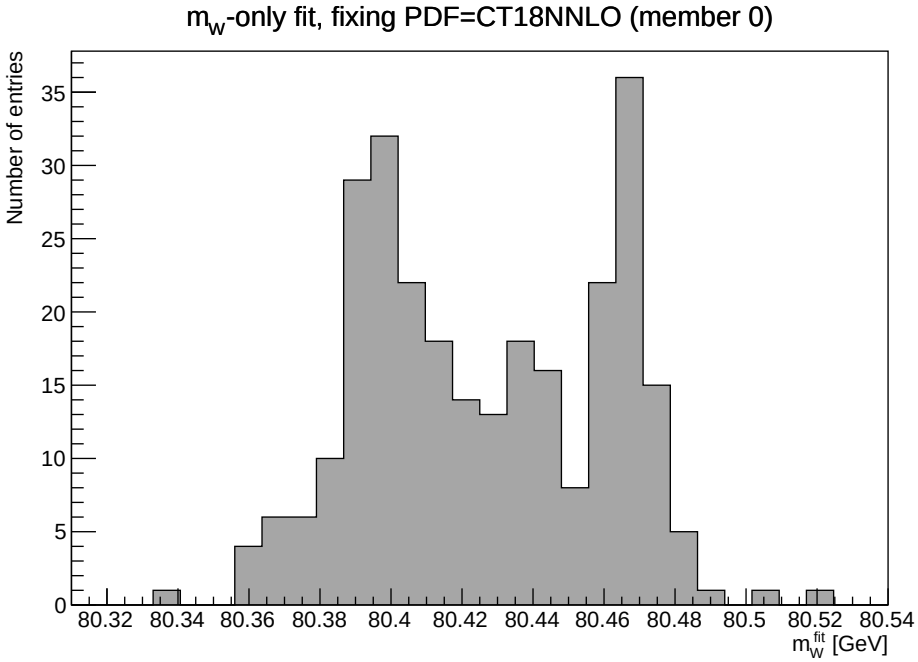

Figure C.3: Total distribution of $m_W^{\rm fit}$ determined from bias tests on pseudodata using all the PDF eigenvectors in all of the pseudodatasets, keeping the CT18NNLO PDF-only parameters in each case (see Table C.3).

D Combined m_W+PDF fits: results

D.1 Only statistical uncertainty

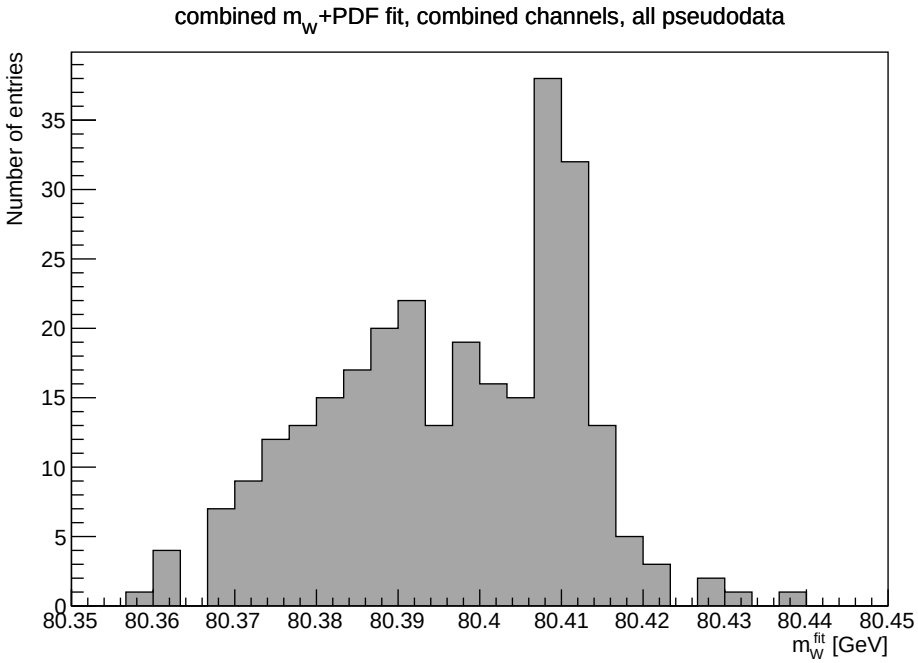

Figure D.1: Total distribution of m_W^{fit} determined via combined m_W+PDF fits, constrained with the low pile-up pseudodata (generated with all the eigenvectors of the 4 reference PDFs) added on top of the ATLASpdf21 data (listed in Table 6.1).

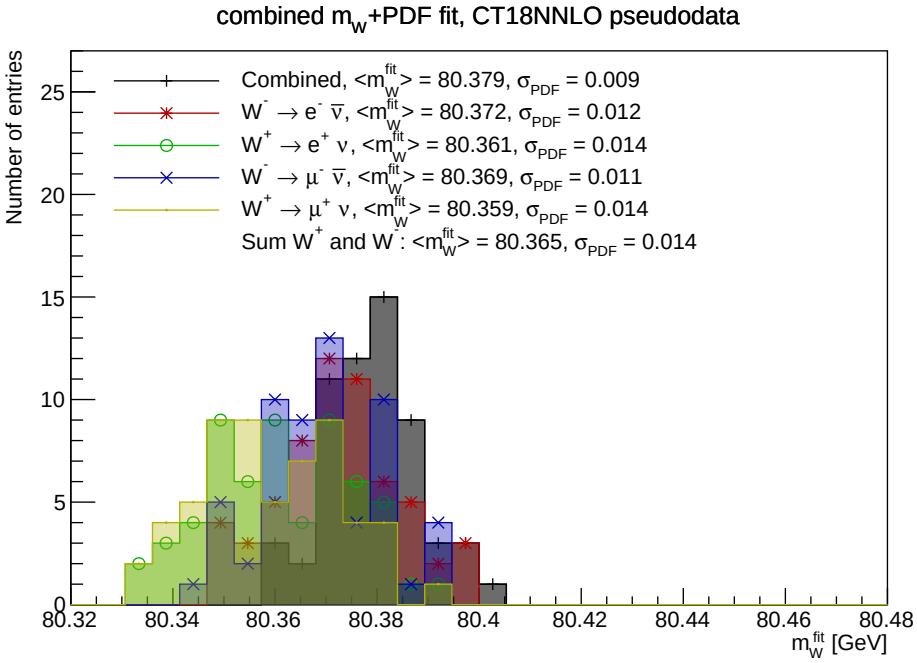

Figure D.2: Distribution of m_W^{fit} determined via combined m_W+PDF fits, constrained with the low pile-up pseudodata (generated with the CT18NNLO PDF, only statistical uncertainty) added on top of the ATLASpdf21 data (listed in Table 6.1). The values of $\langle m_W \rangle$ and σ_{PDF} are shown separately for the m_W+PDF fit to each W leptonic decay channel, as well as for the fit done simultaneously on the 4 channels (labelled as "combined"). The fitted parameter values and the corresponding ρ_{m_W} for the central replica of the reference PDF are shown in Table D.2.

Table D.1: Complete correlation C_{ij} matrix of the combined m_W+PDF fit performed using all the W decay channels, using pseudodata (only statistical uncertainty) generated with the reference PDF ATLASpdf21. The correlation values C_{ij} (and the global correlation ρ_i) are estimated by `xFitter` with `MINUIT`.

	ρ_i	Adbar	Agp	Aubar	Bdbar	Bdv	Bg	Bgp	Bstr	Bubar	Buv	Cdbar	Cdv	Cg	Cstr	Cubar	Cuv	Ddv	Dg	Duv	Edv	Mw_fit	rs
Adbar	0.99938	1.000	-0.035	0.428	0.983	-0.091	-0.002	-0.040	0.140	0.002	-0.121	0.751	-0.286	-0.162	0.028	0.418	-0.030	-0.150	-0.046	0.374	-0.018	-0.036	-0.514
Agp	0.99982	-0.035	1.000	-0.307	-0.028	-0.012	-0.613	0.060	-0.289	-0.001	0.051	0.182	0.115	-0.760	-0.542	-0.347	-0.170	0.074	-0.940	-0.063	-0.199	0.161	-0.285
Aubar	0.97745	0.428	-0.307	1.000	0.396	0.190	0.196	0.009	0.396	0.016	0.196	0.418	-0.172	0.054	0.150	0.780	0.116	-0.073	0.218	0.152	-0.029	0.059	0.063
Bdbar	0.99895	0.983	-0.028	0.396	1.000	-0.156	-0.024	-0.077	0.149	0.002	-0.002	0.691	-0.286	-0.146	0.060	0.400	0.039	-0.140	-0.050	0.268	-0.010	-0.097	-0.483
Bdv	0.98336	-0.091	-0.012	0.190	-0.156	1.000	-0.054	-0.031	0.012	0.003	0.136	0.316	0.392	-0.014	-0.133	0.330	-0.214	0.214	0.076	0.116	-0.253	0.160	0.056
Bg	0.99969	-0.002	-0.613	0.196	-0.024	-0.054	1.000	0.736	0.281	0.001	-0.069	-0.187	-0.073	0.727	0.539	0.083	0.165	-0.070	0.393	-0.007	0.224	0.056	0.315
Bgp	0.99930	-0.040	0.060	0.009	-0.077	-0.031	0.736	1.000	0.071	-0.000	-0.086	-0.100	0.019	0.337	0.204	-0.170	0.039	-0.035	-0.247	-0.011	0.097	0.232	0.125
Bstr	0.99727	0.140	-0.289	0.396	0.149	0.012	0.281	0.071	1.000	-0.005	0.012	0.058	-0.076	0.120	0.640	0.257	-0.020	-0.043	0.139	0.083	-0.068	0.030	0.759
Bubar	0.07084	0.002	-0.001	0.016	0.002	0.003	0.001	-0.000	-0.005	1.000	-0.000	0.001	0.001	0.001	-0.001	0.004	-0.000	0.000	0.001	0.001	-0.000	0.000	-0.004
Buv	0.99642	-0.121	0.051	0.196	-0.002	0.136	-0.069	-0.086	0.012	-0.000	1.000	-0.092	0.192	0.011	0.062	0.188	0.452	0.163	-0.045	-0.831	0.089	-0.108	0.148
Cdbar	0.99260	0.751	0.182	0.418	0.691	0.316	-0.187	-0.100	0.058	0.001	-0.092	1.000	-0.222	-0.410	-0.367	0.315	-0.069	-0.134	-0.238	0.359	-0.021	0.190	-0.485
Cdv	0.99820	-0.286	0.115	-0.172	-0.286	0.392	-0.073	0.019	-0.076	0.001	0.192	-0.222	1.000	-0.049	0.066	-0.042	0.077	0.946	-0.074	-0.233	0.036	0.026	0.129
Cg	0.99689	-0.162	-0.760	0.054	-0.146	-0.014	0.727	0.337	0.120	0.001	0.011	-0.410	-0.049	1.000	0.467	0.053	0.244	-0.071	0.763	-0.063	0.238	-0.095	0.270
Cstr	0.97302	0.028	-0.542	0.150	0.060	-0.133	0.539	0.204	0.640	-0.001	0.062	-0.367	0.066	0.467	1.000	0.086	-0.029	0.042	0.407	-0.083	-0.081	-0.090	0.609
Cubar	0.96965	0.418	-0.347	0.780	0.400	0.330	0.083	-0.170	0.257	0.004	0.188	0.315	-0.042	0.053	0.086	1.000	-0.007	-0.021	0.316	0.218	-0.169	-0.186	-0.030
Cuv	0.99432	-0.030	-0.170	0.116	0.039	-0.214	0.165	0.039	-0.020	-0.000	0.452	-0.069	0.077	0.244	-0.029	-0.007	1.000	0.213	0.151	-0.576	0.878	-0.062	0.016
Ddv	0.99758	-0.150	0.074	-0.073	-0.140	0.214	-0.070	-0.035	-0.043	0.000	0.163	-0.134	0.946	-0.071	0.042	-0.021	0.213	1.000	-0.064	-0.207	0.168	0.002	0.068
Dg	0.99962	-0.046	-0.940	0.218	-0.050	0.076	0.393	-0.247	0.139	0.001	-0.045	-0.238	-0.074	0.763	0.407	0.316	0.151	-0.064	1.000	0.070	0.162	-0.195	0.190
Duv	0.99449	0.374	-0.063	0.152	0.268	0.116	-0.007	-0.011	0.083	0.001	-0.831	0.359	-0.233	-0.063	-0.083	0.218	-0.576	-0.207	0.070	1.000	-0.395	0.049	-0.213
Edv	0.99498	-0.018	-0.199	-0.029	-0.010	-0.253	0.224	0.097	-0.068	-0.000	0.089	-0.021	0.036	0.238	-0.081	-0.169	0.878	0.168	0.162	-0.395	1.000	0.040	-0.066
Mw_fit	0.55501	-0.036	0.161	0.059	-0.097	0.160	0.056	0.232	0.030	0.000	-0.108	0.190	0.026	-0.095	-0.090	-0.186	-0.062	0.002	-0.195	0.049	0.040	1.000	0.017
rs	0.99847	-0.514	-0.285	0.063	-0.483	0.056	0.315	0.125	0.759	-0.004	0.148	-0.485	0.129	0.270	0.609	-0.030	0.016	0.068	0.190	-0.213	-0.066	0.017	1.000

Table D.2: Results of the combined m_W+PDF fits performed using pseudodata (only statistical uncertainty) generated with the CT18NNLO PDF, performed over individual W leptonic decay channels and on their combination. The global correlation ρ_{m_W} of each fit and the final χ^2/dof are shown at the bottom of the corresponding column.

Parameter	AllChannels	Wminusenu	Wplusenu	Wminusmunu	Wplusmunu
'Adbar'	0.0943 ± 0.0097	0.113 ± 0.013	0.0901 ± 0.0022	0.114 ± 0.013	0.0900 ± 0.0090
'Adv'	1.0000	1.0000	1.0000	1.0000	1.0000
'Ag'	1.0000	1.0000	1.0000	1.0000	1.0000
'Agp'	0.122 ± 0.036	0.117 ± 0.032	0.130 ± 0.025	0.119 ± 0.034	0.131 ± 0.032
'Aubar'	0.1250 ± 0.0073	0.1129 ± 0.0083	0.115 ± 0.073	0.1131 ± 0.0083	0.1159 ± 0.0083
'Auv'	1.0000	1.0000	1.0000	1.0000	1.0000
'Bdbar'	-0.197 ± 0.021	-0.164 ± 0.022	-0.203 ± 0.025	-0.162 ± 0.021	-0.204 ± 0.022
'Bdv'	0.523 ± 0.072	0.547 ± 0.071	0.560 ± 0.073	0.542 ± 0.071	0.563 ± 0.076
'Bg'	-0.491 ± 0.050	-0.634 ± 0.051	-0.622 ± 0.051	-0.624 ± 0.052	-0.615 ± 0.058
'Bgp'	-0.660 ± 0.021	-0.733 ± 0.027	-0.721 ± 0.029	-0.727 ± 0.027	-0.717 ± 0.024
'Bstr'	-0.042 ± 0.072	-0.048 ± 0.068	-0.093 ± 0.069	-0.044 ± 0.068	-0.096 ± 0.063
'Bubar'	-0.161 ± 0.014	-0.177 ± 0.016	-0.167 ± 0.016	-0.177 ± 0.016	-0.166 ± 0.019
'Buv'	0.693 ± 0.020	0.700 ± 0.021	0.6925 ± 0.0023	0.700 ± 0.021	0.692 ± 0.021
'Cdbar'	2.02 ± 0.18	2.09 ± 0.18	1.96 ± 0.18	2.10 ± 0.18	1.97 ± 0.16
'Cdv'	4.89 ± 0.34	4.60 ± 0.36	4.66 ± 0.36	4.61 ± 0.35	4.66 ± 0.35
'Cg'	5.48 ± 0.32	5.20 ± 0.31	5.13 ± 0.30	5.22 ± 0.32	5.14 ± 0.31
'Cgp'	25.00	25.00	25.00	25.00	25.00
'Cstr'	14.4 ± 1.3	14.5 ± 1.7	12.5 ± 1.4	14.7 ± 1.8	12.6 ± 1.6
'Cubar'	4.87 ± 0.55	4.86 ± 0.48	4.65 ± 0.42	4.86 ± 0.48	4.68 ± 0.48
'Cuv'	4.68 ± 0.13	4.72 ± 0.10	4.71 ± 0.19	4.71 ± 0.11	4.71 ± 0.12
'Ddv'	7.2 ± 3.1	4.4 ± 2.9	4.8 ± 2.8	4.5 ± 2.9	4.7 ± 2.7
'Dg'	10.6 ± 3.7	15.5 ± 4.0	13.8 ± 3.5	15.0 ± 4.0	13.4 ± 3.6
'Duv'	0.75 ± 0.43	0.80 ± 0.46	0.70 ± 0.57	0.81 ± 0.46	0.72 ± 0.43
'Euv'	10.1 ± 1.1	10.1 ± 1.1	10.33 ± 0.99	10.0 ± 1.1	10.32 ± 0.97
'Mw_fit'	80.379 ± 0.022	80.369 ± 0.044	80.362 ± 0.032	80.366 ± 0.041	80.360 ± 0.032
'rs'	2.45 ± 0.49	1.86 ± 0.58	1.99 ± 0.58	1.88 ± 0.59	1.97 ± 0.56
Fit status	converged	converged	converged	converged	converged
Uncertainties	migrad-hesse	migrad-hesse	migrad-hesse	migrad-hesse	migrad-hesse
Δm_W	-21 MeV	-31 MeV	-38 MeV	-34 MeV	-40 MeV
ρ_{m_W}	0.541	0.452	0.397	0.397	0.435
χ^2/dof	2319/1755	2293/1653	2294/1653	2293/1653	2296/1653

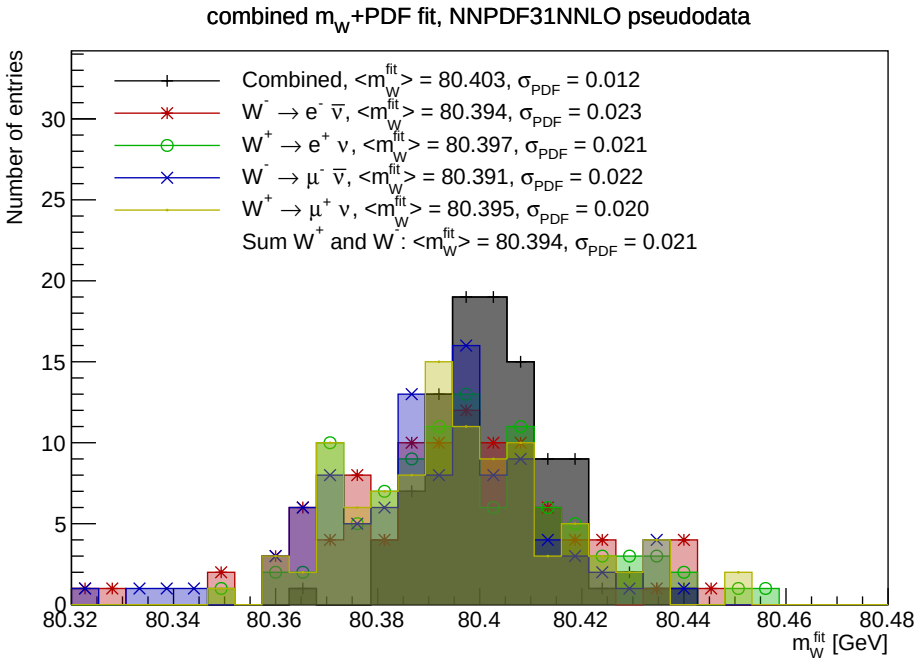

Figure D.3: Distribution of m_W^{fit} determined via combined m_W+PDF fits, constrained with the low pile-up pseudodata (generated with the NNPDF31NNLO PDF, only statistical uncertainty) added on top of the ATLASpdf21 data (listed in Table 6.1). The values of $\langle m_W \rangle$ and σ_{PDF} are shown separately for the m_W+PDF fit to each W leptonic decay channel, as well as for the fit done simultaneously on the 4 channels (labelled as "combined"). The fitted parameter values and the corresponding ρ_{m_W} for the central replica of the reference PDF are shown in Table D.3.

Table D.3: Results of the combined m_W+PDF fits performed using pseudodata (only statistical uncertainty) generated with the NNPDF31NNLO PDF, performed over individual W leptonic decay channels and on their combination. The global correlation ρ_{m_W} of each fit and the final χ^2/dof are shown at the bottom of the corresponding column.

Parameter	AllChannels	Wminusenu	Wplusenu	Wminusmunu	Wplusmunu
'Adbar'	0.1074 ± 0.0088	0.112 ± 0.010	0.100 ± 0.010	0.113 ± 0.010	0.100 ± 0.011
'Adv'	1.0000	1.0000	1.0000	1.0000	1.0000
'Ag'	1.0000	1.0000	1.0000	1.0000	1.0000
'Agp'	0.110 ± 0.032	0.101 ± 0.032	0.105 ± 0.036	0.102 ± 0.032	0.106 ± 0.036
'Aubar'	0.1200 ± 0.0083	0.113 ± 0.011	0.116 ± 0.011	0.113 ± 0.011	0.116 ± 0.010
'Auv'	1.0000	1.0000	1.0000	1.0000	1.0000
'Bdbar'	-0.179 ± 0.016	-0.169 ± 0.023	-0.190 ± 0.021	-0.168 ± 0.018	-0.190 ± 0.021
'Bdv'	0.583 ± 0.067	0.581 ± 0.072	0.597 ± 0.078	0.577 ± 0.074	0.599 ± 0.076
'Bg'	-0.629 ± 0.045	-0.689 ± 0.045	-0.687 ± 0.048	-0.685 ± 0.049	-0.683 ± 0.048
'Bgp'	-0.735 ± 0.021	-0.771 ± 0.024	-0.7678 ± 0.0025	-0.768 ± 0.028	-0.765 ± 0.024
'Bstr'	-0.061 ± 0.062	-0.061 ± 0.072	-0.088 ± 0.069	-0.058 ± 0.073	-0.090 ± 0.071
'Bubar'	-0.166 ± 0.015	-0.175 ± 0.021	-0.168 ± 0.021	-0.176 ± 0.020	-0.167 ± 0.019
'Buv'	0.694 ± 0.020	0.704 ± 0.019	0.696 ± 0.021	0.703 ± 0.016	0.696 ± 0.020
'Cdbar'	2.09 ± 0.18	2.09 ± 0.23	2.03 ± 0.16	2.09 ± 0.24	2.03 ± 0.17
'Cdv'	4.61 ± 0.35	4.50 ± 0.40	4.51 ± 0.40	4.51 ± 0.40	4.51 ± 0.41
'Cg'	5.27 ± 0.31	5.13 ± 0.39	5.10 ± 0.35	5.14 ± 0.38	5.10 ± 0.36
'Cgp'	25.00	25.00	25.00	25.00	25.00
'Cstr'	14.7 ± 1.6	14.6 ± 2.0	13.5 ± 1.7	14.7 ± 2.0	13.5 ± 1.8
'Cubar'	4.96 ± 0.45	4.87 ± 0.44	4.77 ± 0.56	4.86 ± 0.48	4.79 ± 0.56
'Cuv'	4.69 ± 0.10	4.73 ± 0.11	4.72 ± 0.11	4.73 ± 0.11	4.72 ± 0.11
'Ddv'	3.9 ± 2.5	3.4 ± 2.4	3.3 ± 2.7	3.5 ± 2.4	3.3 ± 2.5
'Dg'	16.3 ± 3.9	19.5 ± 5.6	18.7 ± 5.9	19.2 ± 5.6	18.5 ± 5.9
'Duv'	0.94 ± 0.45	0.79 ± 0.42	0.81 ± 0.43	0.79 ± 0.41	0.82 ± 0.45
'Euv'	9.9 ± 1.1	10.1 ± 1.1	10.2 ± 1.0	10.1 ± 1.0	10.2 ± 1.1
'Mw_fit'	80.402 ± 0.021	80.392 ± 0.044	80.397 ± 0.039	80.390 ± 0.044	80.396 ± 0.037
'rs'	1.90 ± 0.53	1.76 ± 0.51	1.79 ± 0.59	1.77 ± 0.50	1.78 ± 0.56
Fit status Uncertainties	converged migrad-hesse	converged migrad-hesse	converged migrad-hesse	converged migrad-hesse	converged migrad-hesse
Δm_W	+2 MeV	−8 MeV	−3 MeV	−10 MeV	−4 MeV
ρ_{m_W}	0.541	0.417	0.379	0.419	0.382
χ^2/dof	2287/1755	2279/1653	2280/1653	2279/1653	2280/1653

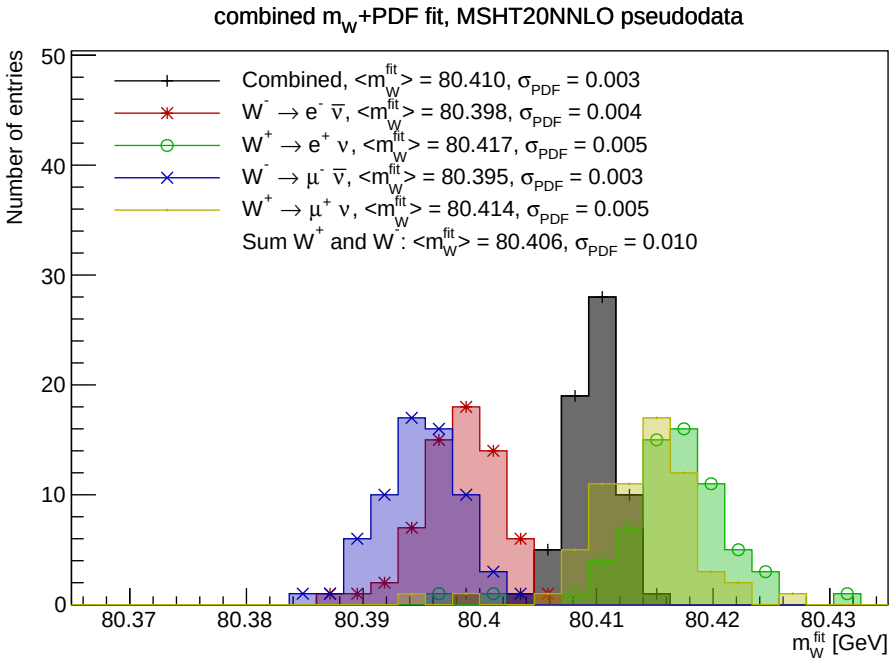

Figure D.4: Distribution of m_W^{fit} determined via combined m_W+PDF fits, constrained with the low pile-up pseudodata (generated with the MSHT20NNLO PDF, only statistical uncertainty) added on top of the ATLASpdf21 data (listed in Table 6.1). The values of $\langle m_W \rangle$ and σ_{PDF} are shown separately for the m_W+PDF fit to each W leptonic decay channel, as well as for the fit done simultaneously on the 4 channels (labelled as "combined"). The fitted parameter values and the corresponding ρ_{m_W} for the central replica of the reference PDF are shown in Table D.4.

Table D.4: Results of the combined m_W+PDF fits performed using pseudodata (only statistical uncertainty) generated with the MSHT20NNLO PDF, performed over individual W leptonic decay channels and on their combination. The global correlation ρ_{m_W} of each fit and the final χ^2/dof are shown at the bottom of the corresponding column.

Parameter	AllChannels	Wminusenu	Wplusenu	Wminusmunu	Wplusmunu
'Adbar'	0.0971 ± 0.0081	0.101 ± 0.012	0.0904 ± 0.0097	0.102 ± 0.012	0.0904 ± 0.0092
'Adv'	1.0000	1.0000	1.0000	1.0000	1.0000
'Ag'	1.0000	1.0000	1.0000	1.0000	1.0000
'Agp'	0.136 ± 0.038	0.126 ± 0.032	0.131 ± 0.034	0.127 ± 0.032	0.131 ± 0.032
'Aubar'	0.1139 ± 0.0069	0.1085 ± 0.0081	0.1116 ± 0.0084	0.1086 ± 0.0080	0.1120 ± 0.0080
'Auv'	1.0000	1.0000	1.0000	1.0000	1.0000
'Bdbar'	-0.186 ± 0.017	-0.177 ± 0.022	-0.198 ± 0.021	-0.177 ± 0.022	-0.199 ± 0.020
'Bdv'	0.517 ± 0.068	0.522 ± 0.075	0.529 ± 0.078	0.519 ± 0.074	0.531 ± 0.081
'Bg'	-0.576 ± 0.050	-0.644 ± 0.048	-0.628 ± 0.051	-0.640 ± 0.048	-0.624 ± 0.049
'Bgp'	-0.694 ± 0.026	-0.734 ± 0.026	-0.724 ± 0.028	-0.731 ± 0.026	-0.721 ± 0.026
'Bstr'	-0.061 ± 0.058	-0.062 ± 0.065	-0.077 ± 0.062	-0.060 ± 0.065	-0.079 ± 0.070
'Bubar'	-0.173 ± 0.013	-0.180 ± 0.016	-0.174 ± 0.016	-0.181 ± 0.016	-0.173 ± 0.015
'Buv'	0.690 ± 0.019	0.700 ± 0.020	0.693 ± 0.020	0.700 ± 0.020	0.693 ± 0.016
'Cdbar'	2.00 ± 0.16	2.01 ± 0.16	1.95 ± 0.16	2.01 ± 0.16	1.95 ± 0.16
'Cdv'	4.67 ± 0.26	4.62 ± 0.32	4.66 ± 0.29	4.63 ± 0.31	4.66 ± 0.31
'Cg'	5.21 ± 0.32	5.09 ± 0.30	5.10 ± 0.31	5.10 ± 0.30	5.11 ± 0.31
'Cgp'	25.00	25.00	25.00	25.00	25.00
'Cstr'	13.2 ± 1.5	13.1 ± 1.5	12.4 ± 1.5	13.1 ± 1.5	12.5 ± 1.5
'Cubar'	4.67 ± 0.39	4.63 ± 0.47	4.55 ± 0.48	4.63 ± 0.46	4.56 ± 0.46
'Cuv'	4.701 ± 0.100	4.73 ± 0.10	4.716 ± 0.099	4.73 ± 0.10	4.715 ± 0.096
'Ddv'	6.0 ± 3.2	5.3 ± 3.3	5.7 ± 3.4	5.4 ± 3.3	5.6 ± 3.4
'Dg'	12.0 ± 3.2	14.7 ± 3.8	13.8 ± 3.7	14.5 ± 3.8	13.6 ± 3.8
'Duv'	0.80 ± 0.42	0.65 ± 0.44	0.67 ± 0.43	0.66 ± 0.44	0.68 ± 0.49
'Euv'	10.2 ± 1.0	10.3 ± 1.0	10.4 ± 1.0	10.3 ± 1.0	10.4 ± 1.1
'Mw_fit'	80.410 ± 0.021	80.399 ± 0.044	80.417 ± 0.039	80.395 ± 0.041	80.414 ± 0.039
'rs'	2.10 ± 0.55	1.96 ± 0.59	2.11 ± 0.59	1.97 ± 0.60	2.09 ± 0.59
Fit status	converged	converged	converged	converged	converged
Uncertainties	migrad-hesse	migrad-hesse	migrad-hesse	migrad-hesse	migrad-hesse
Δm_W	+10 MeV	−1 MeV	+17 MeV	−5 MeV	+14 MeV
ρ_{m_W}	0.538	0.404	0.423	0.409	0.438
χ^2/dof	2299/1755	2292/1653	2295/1653	2292/1653	2295/1653

D.2 Statistical uncertainty and luminosity systematic

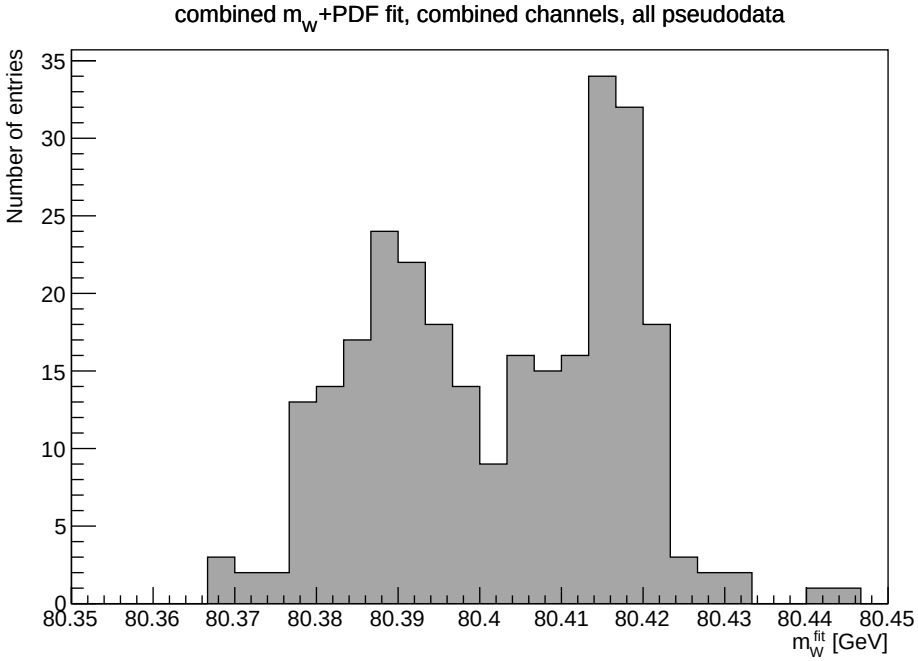

Figure D.5: Total distribution of m_W^{fit} determined via combined m_W+PDF fits, constrained with the low pile-up pseudodata (generated with all the eigenvectors of the 4 reference PDFs) added on top of the ATLASpdf21 data (listed in Table 6.1).

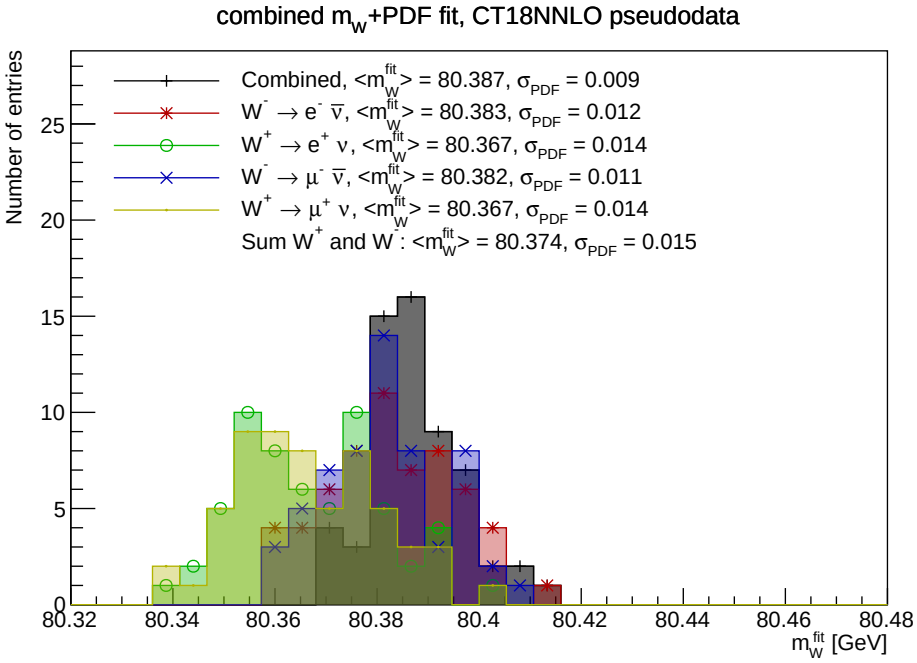

Figure D.6: Distribution of m_W^{fit} determined via combined m_W+PDF fits, constrained with the low pile-up pseudodata (generated with the CT18NNLO PDF, only statistical and luminosity systematic uncertainties) added on top of the ATLASpdf21 data (listed in Table 6.1). The values of $\langle m_W \rangle$ and σ_{PDF} are shown separately for the m_W+PDF fit to each W leptonic decay channel, as well as for the fit done simultaneously on the 4 channels (labelled as "combined"). The fitted parameter values and the corresponding ρ_{m_W} for the central replica of the reference PDF are shown in Table D.6.

Table D.5: Complete correlation C_{ij} matrix of the combined m_W+PDF fit performed using all the W decay channels, using pseudodata (only statistical and luminosity systematic uncertainties) generated with the reference PDF ATLASpdf21. The correlation values C_{ij} (and the global correlation ρ_i) are estimated by `xFitter` with `MINUIT`.

	ρ_i	Adbar	Agp	Aubar	Bdbar	Bdv	Bg	Bgp	Bstr	Bubar	Buv	Cdbar	Cdv	Cg	Cstr	Cubar	Cuv	Ddv	Dg	Duv	Euv	Mw_fit	rs
Adbar	0.99781	1.000	-0.118	0.464	0.978	-0.044	-0.104	-0.198	0.122	-0.011	-0.080	0.764	-0.252	-0.177	0.047	0.409	-0.007	-0.137	0.059	0.364	-0.006	-0.023	-0.551
Agp	0.99981	-0.118	1.000	-0.345	-0.071	-0.105	-0.276	0.395	-0.307	0.159	-0.018	0.108	0.068	-0.664	-0.520	-0.296	-0.147	0.044	-0.941	-0.055	-0.159	0.122	-0.213
Aubar	0.96387	0.464	-0.345	1.000	0.424	0.210	0.071	-0.159	0.403	0.080	0.237	0.439	-0.157	0.021	0.168	0.749	0.121	-0.076	0.260	0.138	-0.038	0.070	0.025
Bdbar	0.99694	0.978	-0.071	0.424	1.000	-0.132	-0.077	-0.144	0.121	0.084	0.022	0.708	-0.266	-0.162	0.064	0.409	0.059	-0.137	0.007	0.267	0.002	-0.094	-0.523
Bdv	0.98015	-0.044	-0.105	0.210	-0.132	1.000	-0.136	-0.176	0.041	-0.347	0.130	0.329	0.376	-0.011	-0.110	0.302	-0.224	0.213	0.178	0.140	-0.258	0.176	0.043
Bg	0.99961	-0.104	-0.276	0.071	-0.077	-0.136	1.000	0.759	0.188	0.462	-0.078	-0.205	-0.065	0.628	0.394	0.034	0.160	-0.056	0.023	-0.050	0.209	0.048	0.296
Bgp	0.99913	-0.198	0.395	-0.159	-0.144	-0.176	0.759	1.000	-0.064	0.509	-0.119	-0.145	-0.009	0.200	0.003	-0.135	0.037	-0.029	-0.567	-0.046	0.080	0.124	0.120
Bstr	0.99685	0.122	-0.307	0.403	0.121	0.041	0.188	-0.064	1.000	0.223	0.061	0.042	-0.054	0.103	0.654	0.222	-0.014	-0.033	0.162	0.043	-0.077	0.048	0.743
Bubar	0.82193	-0.011	0.159	0.080	0.084	-0.347	0.462	0.509	0.223	1.000	0.259	-0.140	-0.354	0.127	0.221	0.036	0.137	-0.334	-0.316	-0.287	0.009	-0.048	0.245
Buv	0.99609	-0.080	-0.018	0.237	0.022	0.130	-0.078	-0.119	0.061	0.259	1.000	-0.080	0.148	0.037	0.105	0.195	0.448	0.123	0.024	-0.821	0.080	-0.105	0.161
Cdbar	0.99313	0.764	0.108	0.439	0.708	0.329	-0.205	-0.145	0.042	-0.140	-0.080	1.000	-0.198	-0.412	-0.343	0.330	-0.051	-0.125	-0.142	0.370	-0.009	0.185	-0.516
Cdv	0.99710	-0.252	0.068	-0.157	-0.266	0.376	-0.065	-0.009	-0.054	-0.354	0.148	-0.198	1.000	-0.030	0.068	0.046	0.061	0.957	-0.025	-0.184	0.030	0.034	0.126
Cg	0.99639	-0.177	-0.664	0.021	-0.162	-0.011	0.628	0.200	0.103	0.127	0.037	-0.412	-0.030	1.000	0.429	0.007	0.246	-0.052	0.630	-0.093	0.233	-0.083	0.257
Cstr	0.96874	0.047	-0.520	0.168	0.064	-0.110	0.394	0.003	0.654	0.221	0.105	-0.343	0.068	0.429	1.000	0.045	-0.035	0.044	0.377	-0.109	-0.096	-0.064	0.581
Cubar	0.96534	0.409	-0.296	0.749	0.409	0.302	0.034	-0.135	0.222	0.036	0.195	0.330	-0.046	0.007	0.045	1.000	-0.005	-0.022	0.258	0.218	-0.181	-0.203	-0.069
Cuv	0.99127	-0.007	-0.147	0.121	0.059	-0.224	0.160	0.037	-0.014	0.137	0.448	-0.051	0.061	0.246	-0.035	-0.005	1.000	0.183	0.114	-0.570	0.876	-0.062	0.006
Ddv	0.99616	-0.137	0.044	-0.076	-0.137	0.213	-0.056	-0.029	-0.033	-0.334	0.123	-0.125	0.957	-0.052	0.044	-0.022	0.183	1.000	-0.028	-0.162	0.146	0.005	0.068
Dg	0.99971	0.059	-0.941	0.260	0.007	0.178	0.023	-0.567	0.162	-0.316	0.024	-0.142	-0.025	0.630	0.377	0.258	0.114	-0.028	1.000	0.069	0.112	-0.147	0.109
Duv	0.99429	0.364	-0.055	0.138	0.267	0.140	-0.050	-0.046	0.043	-0.287	-0.821	0.370	-0.184	-0.093	-0.109	0.218	-0.570	-0.162	0.069	1.000	-0.389	0.049	-0.248
Euv	0.99312	-0.006	-0.159	-0.038	0.002	-0.258	0.209	0.080	-0.077	0.009	0.080	-0.009	0.030	0.233	-0.096	-0.181	0.876	0.146	0.112	-0.389	1.000	0.044	-0.080
Mw_fit	0.57304	-0.023	0.122	0.070	-0.094	0.176	0.048	0.124	0.048	-0.048	-0.105	0.185	0.034	-0.083	-0.064	-0.203	-0.062	0.005	-0.147	0.049	0.044	1.000	0.025
rs	0.99833	-0.551	-0.213	0.025	-0.523	0.043	0.296	0.120	0.743	0.245	0.161	-0.516	0.126	0.257	0.581	-0.069	0.006	0.068	0.109	-0.248	-0.080	0.025	1.000

Table D.6: Results of the combined m_W+PDF fits performed using pseudodata (only statistical and luminosity systematic uncertainties) generated with the CT18NNLO PDF, performed over individual W leptonic decay channels and on their combination. The global correlation ρ_{m_W} of each fit and the final χ^2/dof are shown at the bottom of the corresponding column.

Parameter	AllChannels	Wminusenu	Wplusenu	Wminusmunu	Wplusmunu
'Adbar'	0.1022 ± 0.0085	0.174 ± 0.015	0.107 ± 0.012	0.121 ± 0.026	0.107 ± 0.012
'Adv'	1.0000	1.0000	1.0000	1.0000	1.0000
'Ag'	1.0000	1.0000	1.0000	1.0000	1.0000
'Agp'	0.092 ± 0.028	0.081 ± 0.032	0.085 ± 0.023	0.095 ± 0.024	0.085 ± 0.023
'Aubar'	0.1248 ± 0.0085	0.1300 ± 0.0028	0.1179 ± 0.0099	0.1156 ± 0.0031	0.1183 ± 0.0099
'Auv'	1.0000	1.0000	1.0000	1.0000	1.0000
'Bdbar'	-0.194 ± 0.016	-0.099 ± 0.023	-0.185 ± 0.021	-0.164 ± 0.028	-0.186 ± 0.021
'Bdv'	0.603 ± 0.076	0.685 ± 0.064	0.645 ± 0.080	0.622 ± 0.027	0.647 ± 0.080
'Bg'	-0.665 ± 0.052	-0.748 ± 0.051	-0.734 ± 0.044	-0.715 ± 0.041	-0.733 ± 0.044
'Bgp'	-0.765 ± 0.027	-0.814 ± 0.023	-0.805 ± 0.024	-0.788 ± 0.020	-0.804 ± 0.024
'Bstr'	-0.032 ± 0.066	-0.077 ± 0.047	-0.094 ± 0.068	-0.045 ± 0.054	-0.094 ± 0.068
'Bubar'	-0.162 ± 0.015	-0.157 ± 0.016	-0.165 ± 0.019	-0.174 ± 0.016	-0.164 ± 0.019
'Buv'	0.702 ± 0.021	0.706 ± 0.022	0.704 ± 0.021	0.704 ± 0.022	0.703 ± 0.021
'Cdbar'	2.08 ± 0.18	3.87 ± 0.22	2.08 ± 0.19	2.20 ± 0.61	2.09 ± 0.19
'Cdv'	4.78 ± 0.34	2.44 ± 0.66	4.31 ± 0.59	4.31 ± 0.45	4.31 ± 0.61
'Cg'	5.31 ± 0.30	4.82 ± 0.38	5.06 ± 0.28	5.09 ± 0.30	5.07 ± 0.28
'Cgp'	25.00	25.00	25.00	25.00	25.00
'Cstr'	15.8 ± 1.7	15.8 ± 2.2	14.5 ± 1.8	16.1 ± 2.7	14.5 ± 1.8
'Cubar'	4.89 ± 0.43	5.84 ± 0.40	4.8978 ± 0.0028	4.91 ± 0.38	4.90 ± 0.56
'Cuv'	4.68 ± 0.10	4.76 ± 0.11	4.74 ± 0.11	4.72 ± 0.10	4.74 ± 0.11
'Ddv'	4.2 ± 2.8	-0.80 ± 0.13	1.9 ± 2.5	2.02 ± 0.28	1.9 ± 1.5
'Dg'	20.3 ± 6.3	23.7 ± 7.0	24.4 ± 7.5	21.2 ± 6.9	24.3 ± 7.4
'Duv'	0.82 ± 0.45	1.42 ± 0.47	0.82 ± 0.45	0.93 ± 0.19	0.83 ± 0.45
'Euv'	9.9 ± 1.1	10.2 ± 1.1	10.2 ± 1.1	9.8 ± 1.1	10.2 ± 1.1
'Mw_fit'	80.387 ± 0.021	80.380 ± 0.044	80.366 ± 0.039	80.379 ± 0.042	80.366 ± 0.037
'rs'	2.30 ± 0.67	0.94 ± 0.42	1.62 ± 0.51	1.71 ± 0.32	1.62 ± 0.50
Fit status Uncertainties	converged migrad-hesse	converged migrad-hesse	converged migrad-hesse	converged migrad-hesse	converged migrad-hesse
Δm_W	-13 MeV	-20 MeV	-34 MeV	-21 MeV	-34 MeV
ρ_{m_W}	0.554	0.374	0.0.457	0.379	0.471
χ^2/dof	2303/1755	2274/1653	2277/1653	2281/1653	2277/1653

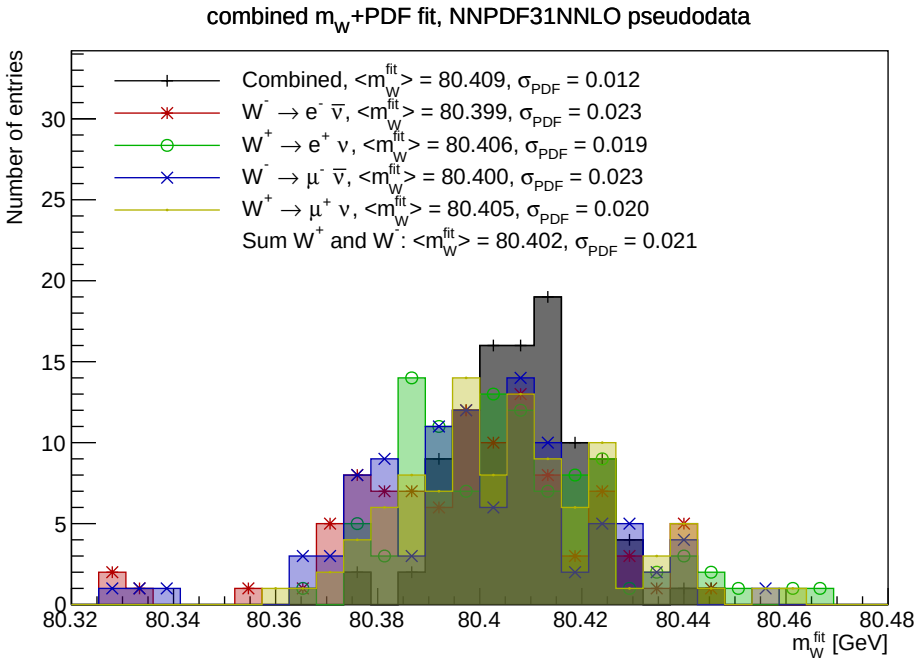

Figure D.7: Distribution of m_W^{fit} determined via combined m_W+PDF fits, constrained with the low pile-up pseudodata (generated with the NNPDF31NNLO PDF, only statistical and luminosity systematic uncertainties) added on top of the ATLASpdf21 data (listed in Table 6.1). The values of $\langle m_W \rangle$ and σ_{PDF} are shown separately for the m_W+PDF fit to each W leptonic decay channel, as well as for the fit done simultaneously on the 4 channels (labelled as "combined"). The fitted parameter values and the corresponding ρ_{m_W} for the central replica of the reference PDF are shown in Table D.7.

Table D.7: Results of the combined m_W+PDF fits performed using pseudo-data (only statistical and luminosity systematic uncertainties) generated with the NNPDF31NNLO PDF, performed over individual W leptonic decay channels and on their combination. The global correlation ρ_{m_W} of each fit and the final χ^2/dof are shown at the bottom of the corresponding column.

Parameter	AllChannels	Wminusenu	Wplusenu	Wminusmunu	Wplusmunu
'Adbar'	0.113 ± 0.018	0.117 ± 0.013	0.152 ± 0.012	0.130 ± 0.014	0.131 ± 0.022
'Adv'	1.0000	1.0000	1.0000	1.0000	1.0000
'Ag'	1.0000	1.0000	1.0000	1.0000	1.0000
'Agp'	0.091 ± 0.025	0.115 ± 0.021	0.083 ± 0.022	0.077 ± 0.020	0.072 ± 0.023
'Aubar'	0.1208 ± 0.0029	0.1107 ± 0.0095	0.1233 ± 0.0096	0.1223 ± 0.0068	0.1243 ± 0.0033
'Auv'	1.0000	1.0000	1.0000	1.0000	1.0000
'Bdbar'	-0.176 ± 0.023	-0.168 ± 0.022	-0.123 ± 0.021	-0.152 ± 0.022	-0.151 ± 0.028
'Bdv'	0.652 ± 0.021	0.594 ± 0.080	0.685 ± 0.077	0.679 ± 0.079	0.693 ± 0.025
'Bg'	-0.713 ± 0.038	-0.721 ± 0.042	-0.763 ± 0.044	-0.752 ± 0.044	-0.750 ± 0.038
'Bgp'	-0.790 ± 0.020	-0.783 ± 0.023	-0.821 ± 0.023	-0.819 ± 0.023	-0.822 ± 0.020
'Bstr'	-0.064 ± 0.044	-0.012 ± 0.070	-0.077 ± 0.069	-0.087 ± 0.061	-0.095 ± 0.046
'Bubar'	-0.165 ± 0.017	-0.182 ± 0.019	-0.163 ± 0.018	-0.161 ± 0.013	-0.158 ± 0.013
'Buv'	0.703 ± 0.020	0.708 ± 0.022	0.703 ± 0.021	0.709 ± 0.022	0.706 ± 0.020
'Cdbar'	2.16 ± 0.63	2.16 ± 0.20	3.59 ± 0.20	2.46 ± 0.22	2.74 ± 0.66
'Cdv'	4.23 ± 0.50	4.39 ± 0.62	2.42 ± 0.59	3.42 ± 0.80	2.99 ± 0.46
'Cg'	5.10 ± 0.31	4.88 ± 0.27	4.78 ± 0.28	5.00 ± 0.28	4.99 ± 0.30
'Cgp'	25.00	25.00	25.00	25.00	25.00
'Cstr'	15.7 ± 2.3	15.7 ± 1.9	14.7 ± 1.9	16.1 ± 2.0	15.5 ± 2.4
'Cubar'	5.03 ± 0.36	4.64 ± 0.55	5.47 ± 0.55	5.32 ± 0.47	5.37 ± 0.40
'Cuv'	4.725 ± 0.099	4.71 ± 0.11	4.76 ± 0.11	4.78 ± 0.12	4.781 ± 0.099
'Ddv'	1.59 ± 0.37	2.6 ± 1.6	-0.8 ± 2.5	0.0 ± 2.8	-0.46 ± 0.32
'Dg'	21.9 ± 6.2	17.0 ± 7.5	24.3 ± 6.4	26.7 ± 6.7	28.0 ± 7.4
'Duv'	0.96 ± 0.45	0.79 ± 0.46	1.33 ± 0.46	0.98 ± 0.48	1.07 ± 0.46
'Euv'	9.9 ± 1.1	9.7 ± 1.1	10.3 ± 1.1	10.3 ± 1.1	10.4 ± 1.1
'Mw_fit'	80.407 ± 0.022	80.406 ± 0.044	80.408 ± 0.039	80.396 ± 0.042	80.406 ± 0.037
'rs'	1.74 ± 0.27	2.04 ± 0.53	1.09 ± 0.51	1.33 ± 0.48	1.26 ± 0.29
Fit status	converged	converged	converged	converged	converged
Uncertainties	migrad-hesse	migrad-hesse	migrad-hesse	migrad-hesse	migrad-hesse
Δm_W	+7 MeV	+6 MeV	+8 MeV	−4 MeV	+6 MeV
ρ_{m_W}	0.581	0.415	0.482	0.413	0.451
χ^2/dof	2281/1755	22767/1653	2269/1653	2273/1653	2271/1653

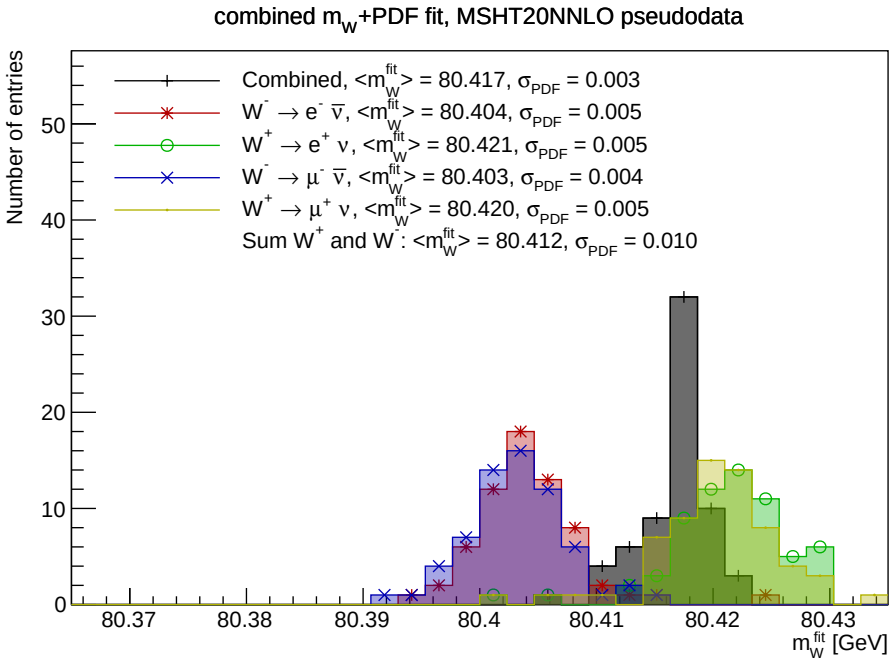

Figure D.8: Distribution of m_W^{fit} determined via combined m_W+PDF fits, constrained with the low pile-up pseudodata (generated with the MSHT20NNLO PDF, only statistical and luminosity systematic uncertainties) added on top of the ATLASpdf21 data (listed in Table 6.1). The values of $\langle m_W \rangle$ and σ_{PDF} are shown separately for the m_W+PDF fit to each W leptonic decay channel, as well as for the fit done simultaneously on the 4 channels (labelled as "combined"). The fitted parameter values and the corresponding ρ_{m_W} for the central replica of the reference PDF are shown in Table D.8.

Table D.8: Results of the combined m_W+PDF fits performed using pseudodata (only statistical and luminosity systematic uncertainties) generated with the MSHT20NNLO PDF, performed over individual W leptonic decay channels and on their combination. The global correlation ρ_{m_W} of each fit and the final χ^2/dof are shown at the bottom of the corresponding column.

Parameter	AllChannels	Wminusenu	Wplusenu	Wminusmunu	Wplusmunu
'Adbar'	0.1057 ± 0.0076	0.111 ± 0.013	0.107 ± 0.012	0.112 ± 0.013	0.107 ± 0.012
'Adv'	1.0000	1.0000	1.0000	1.0000	1.0000
'Ag'	1.0000	1.0000	1.0000	1.0000	1.0000
'Agp'	0.090 ± 0.017	0.084 ± 0.022	0.085 ± 0.021	0.084 ± 0.021	0.085 ± 0.022
'Aubar'	0.1148 ± 0.0023	0.1138 ± 0.0096	0.1140 ± 0.0093	0.1138 ± 0.0094	0.1142 ± 0.0093
'Auv'	1.0000	1.0000	1.0000	1.0000	1.0000
'Bdbar'	-0.182 ± 0.015	-0.175 ± 0.022	-0.181 ± 0.021	-0.175 ± 0.022	-0.181 ± 0.021
'Bdv'	0.593 ± 0.068	0.623 ± 0.080	0.621 ± 0.076	0.623 ± 0.079	0.621 ± 0.076
'Bg'	-0.716 ± 0.050	-0.741 ± 0.044	-0.740 ± 0.043	-0.740 ± 0.043	-0.739 ± 0.043
'Bgp'	-0.792 ± 0.020	-0.809 ± 0.024	-0.807 ± 0.023	-0.808 ± 0.023	-0.807 ± 0.023
'Bstr'	-0.056 ± 0.039	-0.077 ± 0.071	-0.080 ± 0.069	-0.076 ± 0.070	-0.081 ± 0.069
'Bubar'	-0.172 ± 0.016	-0.172 ± 0.018	-0.171 ± 0.018	-0.172 ± 0.018	-0.171 ± 0.018
'Buv'	0.702 ± 0.020	0.708 ± 0.022	0.705 ± 0.021	0.708 ± 0.022	0.705 ± 0.021
'Cdbar'	2.05 ± 0.15	2.09 ± 0.20	2.06 ± 0.19	2.09 ± 0.20	2.06 ± 0.19
'Cdv'	4.51 ± 0.40	4.32 ± 0.62	4.35 ± 0.54	4.32 ± 0.61	4.35 ± 0.54
'Cg'	5.11 ± 0.28	5.05 ± 0.28	5.04 ± 0.27	5.05 ± 0.27	5.05 ± 0.28
'Cgp'	25.00	25.00	25.00	25.00	25.00
'Cstr'	14.5 ± 1.6	14.7 ± 1.9	14.3 ± 1.8	14.7 ± 1.9	14.3 ± 1.8
'Cubar'	4.73 ± 0.32	4.87 ± 0.55	4.80 ± 0.54	4.86 ± 0.54	4.81 ± 0.54
'Cuv'	4.72 ± 0.10	4.75 ± 0.11	4.75 ± 0.11	4.75 ± 0.11	4.75 ± 0.11
'Ddv'	3.4 ± 2.5	2.2 ± 2.6	2.4 ± 2.4	2.2 ± 2.6	2.4 ± 2.5
'Dg'	22.5 ± 6.8	25.0 ± 6.7	24.6 ± 6.2	25.0 ± 6.3	24.6 ± 6.3
'Duv'	0.81 ± 0.41	0.76 ± 0.47	0.77 ± 0.45	0.76 ± 0.46	0.77 ± 0.45
'Euv'	10.07 ± 0.98	10.2 ± 1.1	10.2 ± 1.1	10.2 ± 1.1	10.2 ± 1.1
'Mw_fit'	80.416 ± 0.021	80.404 ± 0.045	80.422 ± 0.039	80.403 ± 0.042	80.421 ± 0.038
'rs'	1.92 ± 0.39	1.64 ± 0.53	1.69 ± 0.52	1.65 ± 0.53	1.68 ± 0.52
Fit status	converged	converged	converged	converged	converged
Uncertainties	migrad-hesse	migrad-hesse	migrad-hesse	migrad-hesse	migrad-hesse
Δm_W	+16 MeV	+4 MeV	+22 MeV	+3 MeV	+21 MeV
ρ_{m_W}	0.567	0.413	0.489	0.427	0.473
χ^2/dof	2283/1755	2275/1653	2277/1653	2275/1653	2277/1653

D.3 The full set of uncertainties

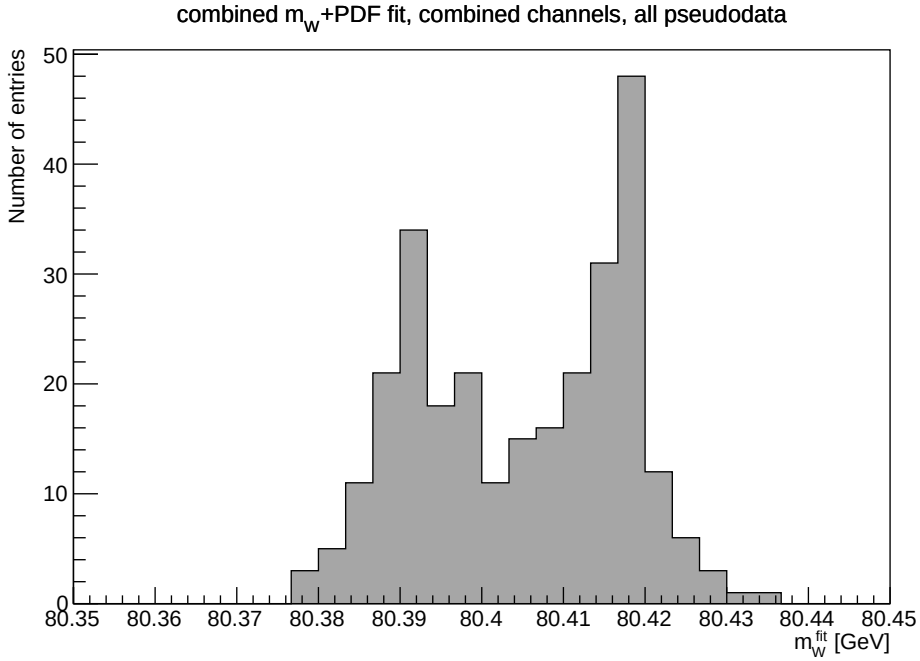

Figure D.9: Total distribution of m_W^{fit} determined via combined m_W+PDF fits, constrained with the low pile-up pseudodata (generated with all the eigenvectors of the 4 reference PDFs) added on top of the ATLASpdf21 data (listed in Table 6.1).

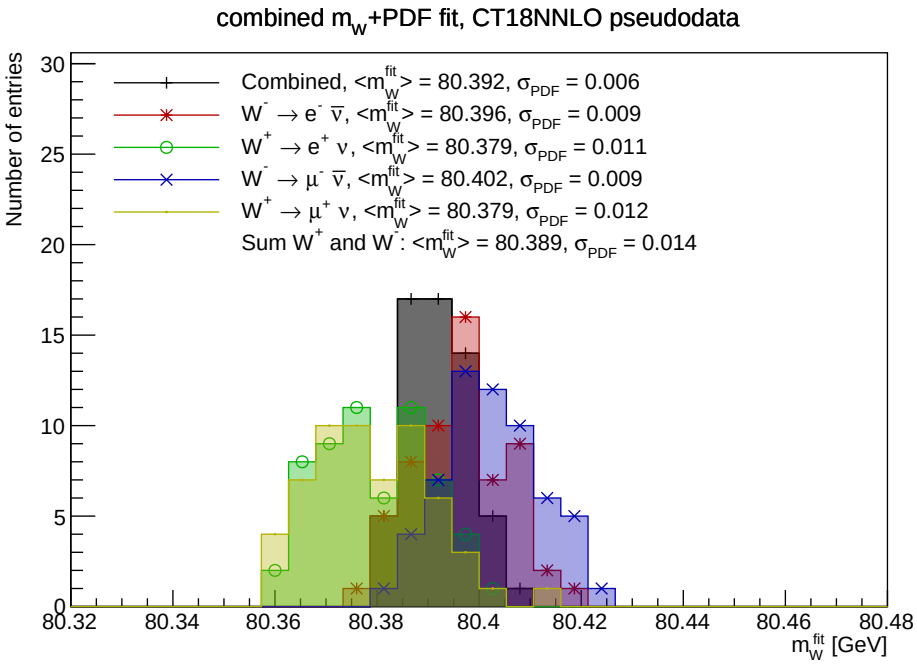

Figure D.10: Distribution of m_W^{fit} determined via combined m_W+PDF fits, constrained with the low pile-up pseudodata (generated with the CT18NNLO PDF, with statistical uncertainty and all sources of systematics) added on top of the ATLASpdf21 data (listed in Table 6.1). The values of $\langle m_W \rangle$ and σ_{PDF} are shown separately for the m_W+PDF fit to each W leptonic decay channel, as well as for the fit done simultaneously on the 4 channels (labelled as "combined"). The fitted parameter values and the corresponding ρ_{m_W} for the central replica of the reference PDF are shown in Table D.10.

Table D.9: Complete correlation C_{ij} matrix of the combined m_W+PDF fit performed using all the W decay channels, using pseudodata (with statistical uncertainty and all sources of systematics) generated with the reference PDF ATLASpdf21. The correlation values C_{ij} (and the global correlation ρ_i) are estimated by `xFitter` with `MINUIT`.

	ρ_i	Adbar	Agp	Aubar	Bdbar	Bdv	Bg	Bgp	Bstr	Bubar	Buv	Cdbar	Cdv	Cg	Cstr	Cubar	Cuv	Ddv	Dg	Duv	Euv	Mw_fit	rs
Adbar	0.99617	1.000	-0.528	0.428	0.960	0.042	0.280	-0.334	-0.031	0.345	-0.264	0.540	-0.283	0.460	0.493	0.506	-0.103	0.364	-0.006	-0.023	-0.551	-0.223	-0.339
Agp	0.99995	-0.528	1.000	-0.555	-0.483	0.126	-0.657	0.545	-0.094	-0.391	0.189	-0.078	0.064	-0.901	-0.665	-0.546	-0.234	-0.055	-0.159	0.122	-0.213	0.141	-0.014
Aubar	0.99689	0.428	-0.555	1.000	0.429	0.123	0.371	-0.273	-0.484	0.949	0.020	0.091	0.029	0.495	0.192	0.797	0.137	0.138	-0.038	0.070	0.025	-0.073	-0.492
Bdbar	0.99514	0.960	-0.483	0.429	1.000	-0.080	0.300	-0.258	-0.030	0.353	-0.176	0.494	-0.206	0.450	0.434	0.479	-0.065	0.267	0.002	-0.094	-0.523	-0.258	-0.317
Bdv	0.99845	0.042	0.126	0.123	-0.080	1.000	-0.338	-0.204	-0.430	0.254	0.240	-0.001	-0.653	-0.249	0.023	0.373	0.145	0.140	-0.258	0.176	0.043	0.011	-0.425
Bg	0.99986	0.280	-0.657	0.371	0.300	-0.338	1.000	0.267	0.167	0.219	-0.270	0.067	0.139	0.832	0.494	0.289	0.163	-0.050	0.209	0.048	0.296	-0.034	0.165
Bgp	0.99956	-0.334	0.545	-0.273	-0.258	-0.204	0.267	1.000	0.039	-0.236	-0.083	0.002	0.234	-0.212	-0.316	-0.342	-0.135	-0.046	0.080	0.124	0.120	0.134	0.128
Bstr	0.99898	-0.031	-0.094	-0.484	-0.030	-0.430	0.167	0.039	1.000	-0.660	-0.144	0.056	0.104	0.105	0.515	-0.344	-0.121	0.043	-0.077	0.048	0.743	0.000	0.936
Bubar	0.99675	0.345	-0.391	0.949	0.353	0.254	0.219	-0.236	-0.660	1.000	0.030	0.051	-0.008	0.331	0.031	0.707	0.131	-0.287	0.009	-0.048	0.245	-0.049	-0.643
Buv	0.99648	-0.264	0.189	0.020	-0.176	0.240	-0.270	-0.083	-0.144	0.030	1.000	-0.310	0.136	-0.220	-0.067	0.103	0.486	-0.821	0.080	-0.105	0.161	0.012	-0.016
Cdbar	0.96034	0.540	-0.078	0.091	0.494	-0.001	0.067	0.002	0.056	0.051	-0.310	1.000	-0.169	0.083	0.070	0.121	-0.537	0.370	-0.009	0.185	-0.516	-0.033	-0.163
Cdv	0.99211	-0.283	0.064	0.029	-0.206	-0.653	0.139	0.234	0.104	-0.008	0.136	-0.169	1.000	0.061	-0.151	-0.215	-0.084	-0.184	0.030	0.034	0.126	0.087	0.224
Cg	0.99874	0.460	-0.901	0.495	0.450	-0.249	0.832	-0.212	0.105	0.331	-0.220	0.083	0.061	1.000	0.569	0.435	0.247	-0.093	0.233	-0.083	0.257	-0.107	0.042
Cstr	0.97369	0.493	-0.665	0.192	0.434	0.023	0.494	-0.316	0.515	0.031	-0.067	0.070	-0.151	0.569	1.000	0.298	0.134	-0.109	-0.096	-0.064	0.581	-0.075	0.397
Cubar	0.98689	0.506	-0.546	0.797	0.479	0.373	0.289	-0.342	-0.344	0.707	0.103	0.121	-0.215	0.435	0.298	1.000	0.147	0.218	-0.181	-0.203	-0.069	-0.207	-0.406
Cuv	0.99255	-0.103	-0.234	0.137	-0.065	0.145	0.163	-0.135	-0.121	0.131	0.486	-0.537	-0.084	0.247	0.134	0.147	1.000	-0.570	0.876	-0.062	0.006	-0.022	-0.034
Ddv	0.99895	-0.092	-0.182	0.030	0.018	-0.948	0.365	0.168	0.329	-0.100	-0.143	-0.014	0.822	0.310	-0.026	-0.236	-0.139	1.000	0.112	-0.098	0.152	0.008	0.371
Dg	0.99987	0.524	-0.964	0.503	0.462	-0.049	0.463	-0.700	0.055	0.355	-0.154	0.082	-0.106	0.831	0.599	0.536	0.225	0.112	1.000	0.248	0.317	-0.157	-0.043
Duv	0.99517	0.450	-0.235	0.077	0.351	0.033	0.168	-0.075	0.118	0.026	-0.838	0.469	-0.352	0.226	0.168	0.198	-0.575	-0.098	0.248	1.000	-0.477	-0.111	-0.064
Euv	0.99435	-0.089	-0.364	0.170	-0.076	-0.137	0.357	-0.085	-0.059	0.150	0.170	-0.461	0.139	0.399	0.139	0.041	0.866	0.152	0.317	-0.477	1.000	0.031	0.021
Mw_fit	0.38756	-0.223	0.141	-0.073	-0.258	0.011	-0.034	0.134	0.000	-0.049	0.012	-0.033	0.087	-0.107	-0.075	-0.207	-0.022	0.008	-0.157	-0.111	0.031	1.000	0.069
rs	0.99913	-0.339	-0.014	-0.492	-0.317	-0.425	0.165	0.128	0.936	-0.643	-0.016	-0.163	0.224	0.042	0.397	-0.406	-0.034	0.371	-0.043	-0.064	0.021	0.069	1.000

Table D.10: Results of the combined m_W+PDF fits performed using pseudodata (with statistical uncertainty and all sources of systematics) generated with the CT18NNLO PDF, performed over individual W leptonic decay channels and on their combination. The global correlation ρ_{m_W} of each fit and the final χ^2/dof are shown at the bottom of the corresponding column.

Parameter	AllChannels	Wminusenu	Wplusenu	Wminusmunu	Wplusmunu
'Adbar'	0.1005 ± 0.0085	0.128 ± 0.013	0.106 ± 0.012	0.168 ± 0.011	0.107 ± 0.012
'Adv'	1.0000	1.0000	1.0000	1.0000	1.0000
'Ag'	1.0000	1.0000	1.0000	1.0000	1.0000
'Agp'	0.090 ± 0.027	0.076 ± 0.022	0.084 ± 0.022	0.080 ± 0.011	0.084 ± 0.022
'Aubar'	0.1236 ± 0.0086	0.1190 ± 0.0095	0.1163 ± 0.0099	0.1276 ± 0.0024	0.1163 ± 0.0098
'Auv'	1.0000	1.0000	1.0000	1.0000	1.0000
'Bdbar'	-0.196 ± 0.016	-0.155 ± 0.022	-0.185 ± 0.022	-0.105 ± 0.018	-0.184 ± 0.021
'Bdv'	0.600 ± 0.080	0.668 ± 0.079	0.637 ± 0.079	0.686 ± 0.080	0.637 ± 0.078
'Bg'	-0.675 ± 0.051	-0.745 ± 0.045	-0.739 ± 0.044	-0.756 ± 0.053	-0.739 ± 0.044
'Bgp'	-0.771 ± 0.027	-0.816 ± 0.024	-0.808 ± 0.023	-0.819 ± 0.026	-0.808 ± 0.023
'Bstr'	-0.033 ± 0.067	-0.074 ± 0.071	-0.089 ± 0.069	-0.076 ± 0.036	-0.089 ± 0.069
'Bubar'	-0.164 ± 0.015	-0.167 ± 0.018	-0.167 ± 0.019	-0.159 ± 0.017	-0.167 ± 0.019
'Buv'	0.702 ± 0.021	0.708 ± 0.022	0.705 ± 0.021	0.707 ± 0.022	0.705 ± 0.021
'Cdbar'	2.06 ± 0.17	2.36 ± 0.21	2.07 ± 0.19	3.79 ± 0.19	2.07 ± 0.19
'Cdv'	4.78 ± 0.34	3.60 ± 0.64	4.34 ± 0.60	2.44 ± 0.68	4.33 ± 0.60
'Cg'	5.28 ± 0.30	5.05 ± 0.28	5.05 ± 0.28	4.81 ± 0.28	5.05 ± 0.28
'Cgp'	25.00	25.00	25.00	25.00	25.00
'Cstr'	15.5 ± 1.7	16.3 ± 1.9	14.4 ± 1.9	15.4 ± 1.7	14.4 ± 1.9
'Cubar'	4.86 ± 0.45	5.23 ± 0.55	4.86 ± 0.56	5.75 ± 0.36	4.86 ± 0.56
'Cuv'	4.69 ± 0.10	4.78 ± 0.12	4.74 ± 0.11	4.76 ± 0.11	4.74 ± 0.11
'Ddv'	4.3 ± 3.0	0.3 ± 2.6	2.1 ± 2.5	-0.8 ± 3.0	2.1 ± 2.5
'Dg'	21.0 ± 5.6	27.1 ± 6.4	24.9 ± 6.5	24.5 ± 2.2	24.9 ± 6.6
'Duv'	0.80 ± 0.45	0.99 ± 0.47	0.78 ± 0.46	1.38 ± 0.47	0.79 ± 0.46
'Euv'	9.9 ± 1.0	10.3 ± 1.1	10.3 ± 1.1	10.2 ± 1.0	10.2 ± 1.1
'Mw_fit'	80.392 ± 0.023	80.393 ± 0.049	80.379 ± 0.043	80.395 ± 0.045	80.379 ± 0.040
'rs'	2.32 ± 0.68	1.42 ± 0.53	1.65 ± 0.51	0.98 ± 0.31	1.64 ± 0.50
Fit status Uncertainties	converged migrad-hesse	converged migrad-hesse	converged migrad-hesse	converged migrad-hesse	converged migrad-hesse
Δm_W	-8 MeV	-7 MeV	-21 MeV	-5 MeV	-21 MeV
ρ_{m_W}	0.388	0.278	0.329	0.286	0.389
χ^2/dof	2302/1755	2277/1653	2276/1653	2272/1653	2276/1653

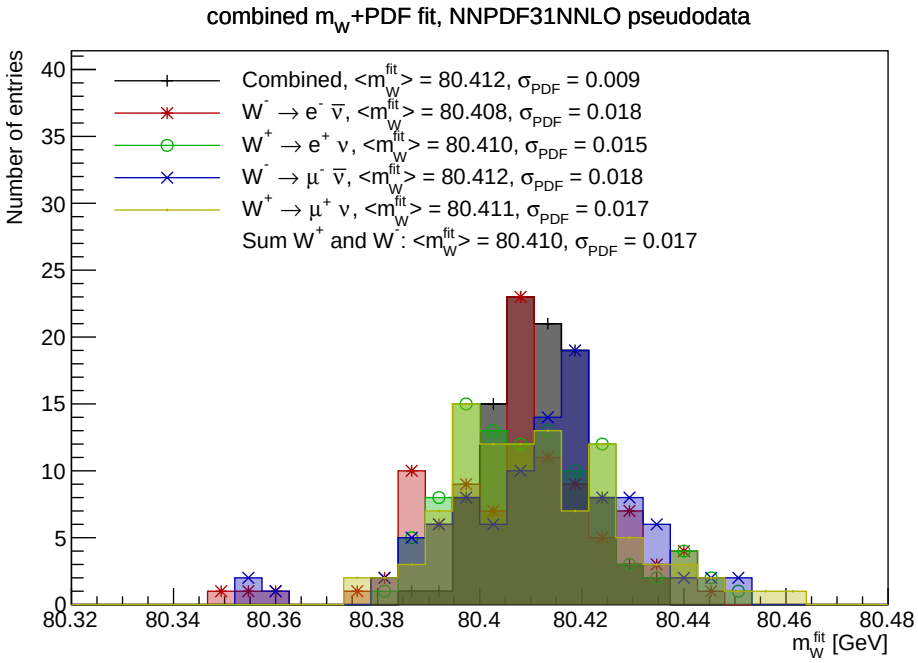

Figure D.11: Distribution of m_W^{fit} determined via combined m_W+PDF fits, constrained with the low pile-up pseudodata (generated with the NNPDF31NNLO PDF, with statistical uncertainty and all sources of systematics) added on top of the ATLASpdf21 data (listed in Table 6.1). The values of $\langle m_W \rangle$ and σ_{PDF} are shown separately for the m_W+PDF fit to each W leptonic decay channel, as well as for the fit done simultaneously on the 4 channels (labelled as "combined"). The fitted parameter values and the corresponding ρ_{m_W} for the central replica of the reference PDF are shown in Table D.11.

Table D.11: Results of the combined m_W+PDF fits performed using pseudodata (with statistical uncertainty and all sources of systematics) generated with the NNPDF31NNLO PDF, performed over individual W leptonic decay channels and on their combination. The global correlation ρ_{m_W} of each fit and the final χ^2/dof are shown at the bottom of the corresponding column.

Parameter	AllChannels	Wminusenu	Wplusenu	Wminusmunu	Wplusmunu
'Adbar'	0.111 ± 0.010	0.124 ± 0.013	0.120 ± 0.013	0.133 ± 0.013	0.121 ± 0.012
'Adv'	1.0000	1.0000	1.0000	1.0000	1.0000
'Ag'	1.0000	1.0000	1.0000	1.0000	1.0000
'Agp'	0.083 ± 0.025	0.076 ± 0.021	0.074 ± 0.021	0.073 ± 0.021	0.075 ± 0.020
'Aubar'	0.1195 ± 0.0094	0.1205 ± 0.0098	0.1199 ± 0.0097	0.1227 ± 0.0096	0.1206 ± 0.0096
'Auv'	1.0000	1.0000	1.0000	1.0000	1.0000
'Bdbar'	-0.179 ± 0.018	-0.161 ± 0.022	-0.166 ± 0.022	-0.147 ± 0.022	-0.164 ± 0.021
'Bdv'	0.623 ± 0.077	0.692 ± 0.080	0.685 ± 0.080	0.680 ± 0.081	0.685 ± 0.080
'Bg'	-0.714 ± 0.045	-0.756 ± 0.043	-0.760 ± 0.042	-0.747 ± 0.042	-0.757 ± 0.043
'Bgp'	-0.795 ± 0.024	-0.822 ± 0.023	-0.825 ± 0.022	-0.819 ± 0.023	-0.823 ± 0.022
'Bstr'	-0.055 ± 0.075	-0.087 ± 0.070	-0.098 ± 0.071	-0.093 ± 0.070	-0.101 ± 0.071
'Bubar'	-0.167 ± 0.018	-0.164 ± 0.019	-0.162 ± 0.019	-0.161 ± 0.019	-0.162 ± 0.019
'Buv'	0.702 ± 0.021	0.711 ± 0.022	0.708 ± 0.022	0.706 ± 0.022	0.708 ± 0.022
'Cdbar'	2.11 ± 0.19	2.48 ± 0.20	2.33 ± 0.20	2.64 ± 0.20	2.36 ± 0.20
'Cdv'	4.47 ± 0.59	3.23 ± 0.63	3.44 ± 0.65	3.28 ± 0.64	3.42 ± 0.65
'Cg'	5.17 ± 0.30	4.96 ± 0.28	4.99 ± 0.28	5.01 ± 0.27	4.99 ± 0.28
'Cgp'	25.00	25.00	25.00	25.00	25.00
'Cstr'	15.5 ± 1.9	15.5 ± 1.8	15.4 ± 1.9	15.8 ± 1.8	15.3 ± 1.9
'Cubar'	4.93 ± 0.54	5.34 ± 0.56	5.20 ± 0.57	5.35 ± 0.55	5.24 ± 0.57
'Cuv'	4.71 ± 0.11	4.79 ± 0.11	4.80 ± 0.12	4.77 ± 0.12	4.79 ± 0.12
'Ddv'	2.7 ± 2.6	-0.3 ± 2.6	0.0 ± 2.6	-0.1 ± 2.6	0.0 ± 2.6
'Dg'	24.1 ± 7.7	27.2 ± 6.9	28.5 ± 6.9	27.5 ± 6.7	27.9 ± 6.8
'Duv'	0.90 ± 0.45	0.96 ± 0.46	0.93 ± 0.45	1.04 ± 0.46	0.95 ± 0.45
'Euv'	9.9 ± 1.1	10.4 ± 1.1	10.5 ± 1.1	10.4 ± 1.1	10.5 ± 1.1
'Mw_fit'	80.411 ± 0.023	80.405 ± 0.048	80.407 ± 0.043	80.418 ± 0.046	80.409 ± 0.040
'rs'	1.85 ± 0.57	1.40 ± 0.52	1.39 ± 0.53	1.25 ± 0.52	1.35 ± 0.53
Fit status	converged	converged	converged	converged	converged
Uncertainties	migrad-hesse	migrad-hesse	migrad-hesse	migrad-hesse	migrad-hesse
Δm_W	+11 MeV	+5 MeV	+7 MeV	+18 MeV	+9 MeV
ρ_{m_W}	0.383	0.273	0.332	0.313	0.393
χ^2/dof	2279/1755	2271/1653	2271/1653	2271/1653	2271/1653

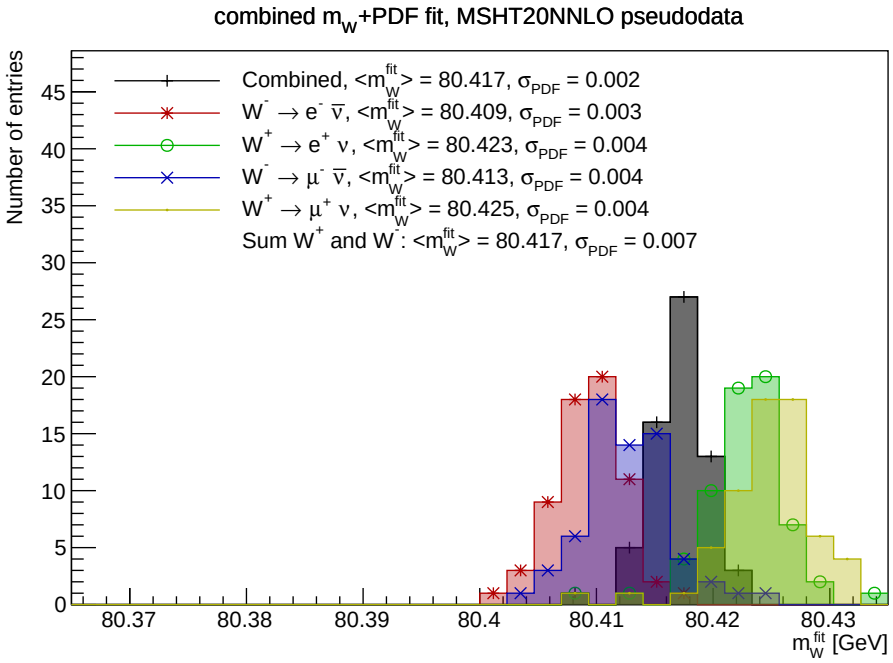

Figure D.12: Distribution of m_W^{fit} determined via combined m_W+PDF fits, constrained with the low pile-up pseudodata (generated with the MSHT20NNLO PDF, with statistical uncertainty and all sources of systematics) added on top of the ATLASpdf21 data (listed in Table 6.1). The values of $\langle m_W \rangle$ and σ_{PDF} are shown separately for the m_W+PDF fit to each W leptonic decay channel, as well as for the fit done simultaneously on the 4 channels (labelled as "combined"). The fitted parameter values and the corresponding ρ_{m_W} for the central replica of the reference PDF are shown in Table D.12.

Table D.12: Results of the combined m_W+PDF fits performed using pseudodata (with statistical uncertainty and all sources of systematics) generated with the MSHT20NNLO PDF, performed over individual W leptonic decay channels and on their combination. The global correlation ρ_{m_W} of each fit and the final χ^2/dof are shown at the bottom of the corresponding column.

Parameter	AllChannels	Wminusenu	Wplusenu	Wminusmunu	Wplusmunu
'Adbar'	0.111 ± 0.010	0.124 ± 0.013	0.120 ± 0.013	0.133 ± 0.013	0.121 ± 0.012
'Adv'	1.0000	1.0000	1.0000	1.0000	1.0000
'Ag'	1.0000	1.0000	1.0000	1.0000	1.0000
'Agp'	0.083 ± 0.025	0.076 ± 0.021	0.074 ± 0.021	0.073 ± 0.021	0.075 ± 0.020
'Aubar'	0.1195 ± 0.0094	0.1205 ± 0.0098	0.1199 ± 0.0097	0.1227 ± 0.0096	0.1206 ± 0.0096
'Auv'	1.0000	1.0000	1.0000	1.0000	1.0000
'Bdbar'	-0.179 ± 0.018	-0.161 ± 0.022	-0.166 ± 0.022	-0.147 ± 0.022	-0.164 ± 0.021
'Bdv'	0.623 ± 0.077	0.692 ± 0.080	0.685 ± 0.080	0.680 ± 0.081	0.685 ± 0.080
'Bg'	-0.714 ± 0.045	-0.756 ± 0.043	-0.760 ± 0.042	-0.747 ± 0.042	-0.757 ± 0.043
'Bgp'	-0.795 ± 0.024	-0.822 ± 0.023	-0.825 ± 0.022	-0.819 ± 0.023	-0.823 ± 0.022
'Bstr'	-0.055 ± 0.075	-0.087 ± 0.070	-0.098 ± 0.071	-0.093 ± 0.070	-0.101 ± 0.071
'Bubar'	-0.167 ± 0.018	-0.164 ± 0.019	-0.162 ± 0.019	-0.161 ± 0.019	-0.162 ± 0.019
'Buv'	0.702 ± 0.021	0.711 ± 0.022	0.708 ± 0.022	0.706 ± 0.022	0.708 ± 0.022
'Cdbar'	2.11 ± 0.19	2.48 ± 0.20	2.33 ± 0.20	2.64 ± 0.20	2.36 ± 0.20
'Cdv'	4.47 ± 0.59	3.23 ± 0.63	3.44 ± 0.65	3.28 ± 0.64	3.42 ± 0.65
'Cg'	5.17 ± 0.30	4.96 ± 0.28	4.99 ± 0.28	5.01 ± 0.27	4.99 ± 0.28
'Cgp'	25.00	25.00	25.00	25.00	25.00
'Cstr'	15.5 ± 1.9	15.5 ± 1.8	15.4 ± 1.9	15.8 ± 1.8	15.3 ± 1.9
'Cubar'	4.93 ± 0.54	5.34 ± 0.56	5.20 ± 0.57	5.35 ± 0.55	5.24 ± 0.57
'Cuv'	4.71 ± 0.11	4.79 ± 0.11	4.80 ± 0.12	4.77 ± 0.12	4.79 ± 0.12
'Ddv'	2.7 ± 2.6	-0.3 ± 2.6	0.0 ± 2.6	-0.1 ± 2.6	0.0 ± 2.6
'Dg'	24.1 ± 7.7	27.2 ± 6.9	28.5 ± 6.9	27.5 ± 6.7	27.9 ± 6.8
'Duv'	0.90 ± 0.45	0.96 ± 0.46	0.93 ± 0.45	1.04 ± 0.46	0.95 ± 0.45
'Euv'	9.9 ± 1.1	10.4 ± 1.1	10.5 ± 1.1	10.4 ± 1.1	10.5 ± 1.1
'Mw_fit'	80.411 ± 0.023	80.405 ± 0.048	80.407 ± 0.043	80.418 ± 0.046	80.409 ± 0.040
'rs'	1.85 ± 0.57	1.40 ± 0.52	1.39 ± 0.53	1.25 ± 0.52	1.35 ± 0.53
Fit status Uncertainties	converged migrad-hesse	converged migrad-hesse	converged migrad-hesse	converged migrad-hesse	converged migrad-hesse
Δm_W	+18 MeV	+9 MeV	+23 MeV	+12 MeV	+25 MeV
ρ_{m_W}	0.386	0.281	0.333	0.302	0.374
χ^2/dof	2283/1755	2274/1653	2276/1653	2274/1653	2276/1653

E

Fitted PDFs

This appendix shows the distributions of a few relevant PDFs reported in the main body of text, at $Q^2 = 1.9$ GeV^2 and $Q^2 = 6464$ GeV$^2 = (80.4$ GeV$)^2$, extending those already provided in Section 6.8.4. Each plot shows the result of a nominal PDF fit to the ATLASpdf21 data (46 data files) and the output of combined m_W+PDF fits (which adds the 4 decay channels of the low pile-up pseudodata generated with the ATLASpdf21 PDF, i.e. a total of 50 files). The combined fits are shown when only the statistical uncertainty is included ($\Delta m_W = (-12 \pm 21)$ MeV, $\rho_{m_W} = 0.555$), after adding the luminosity systematic ($\Delta m_W = (-11 \pm 21)$ MeV, $\rho_{m_W} = 0.573$), and when all systematics are available ($\Delta m_W = (-7 \pm 23)$ MeV, $\rho_{m_W} = 0.394$); these results correspond to the column "AllChannels" of Tables 6.5, 6.6 and 6.7. The uncertainty band corresponding to the nominal fit of ATLASpdf21 is displayed in all the plots. The ratio with respect to the nominal fit of ATLASpdf21, which illustrates the effect of the low pile-up pseudodata in the final PDF, is also provided; the ratio plots also show the uncertainty band around the combined fit "+LowPileup_StatAllSyst".

E.1 PDFs at $Q^2 = 1.9$ GeV^2

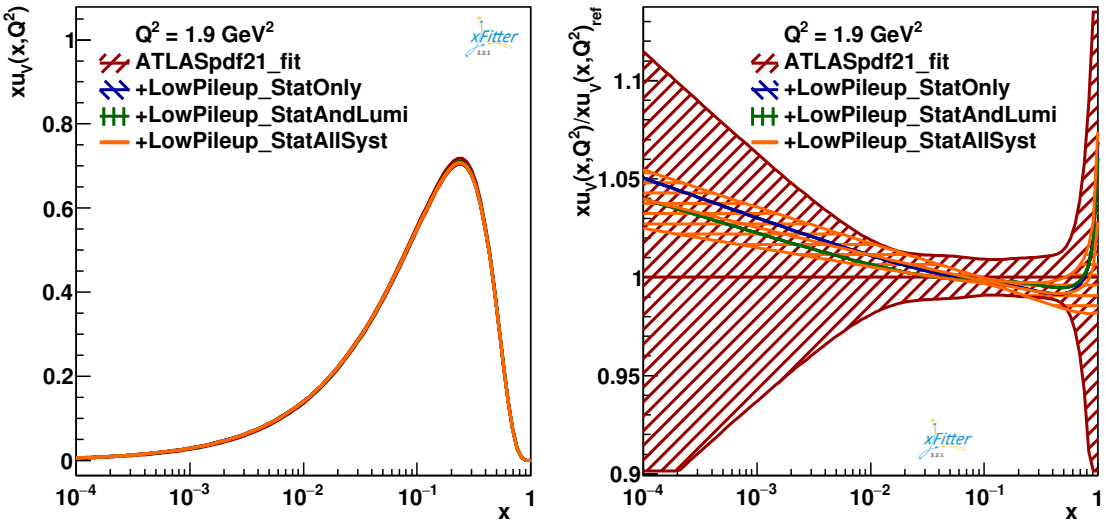

Figure E.1: PDF of the u_v quark at $Q^2 = 1.9$ GeV^2, fitted with `xFitter`.

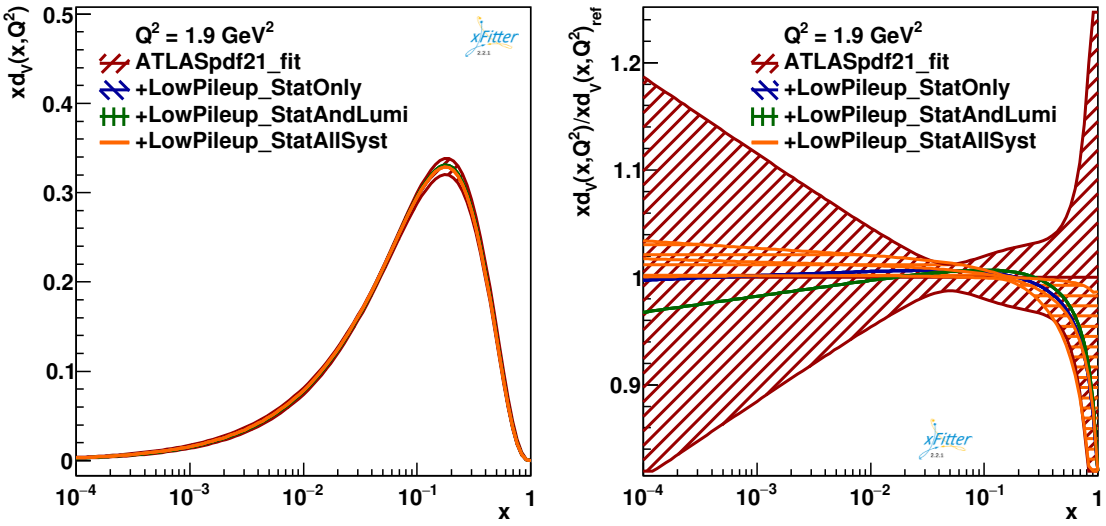

Figure E.2: PDF of the d_v quark at $Q^2 = 1.9$ GeV^2, fitted with `xFitter`.

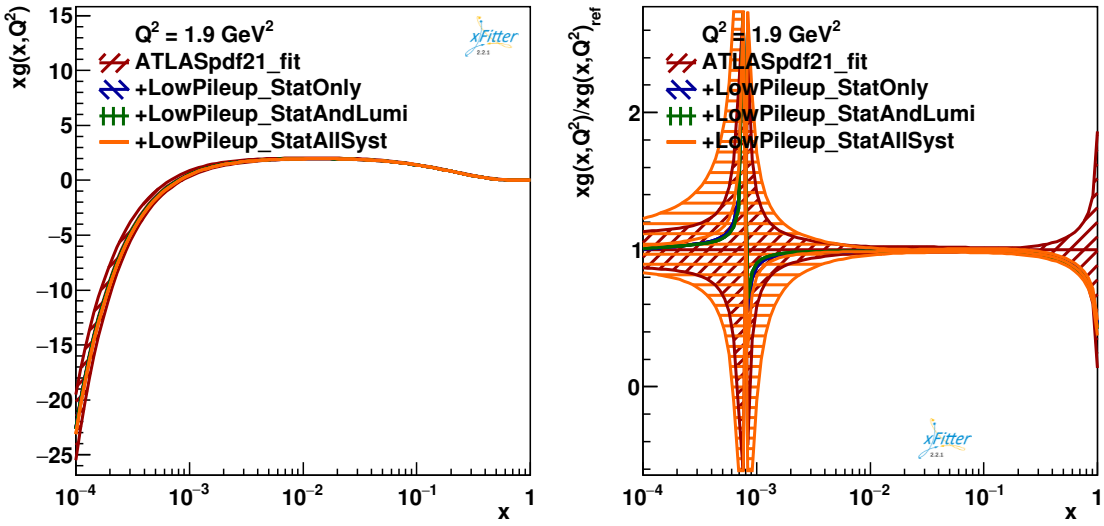

Figure E.3: PDF of the gluon at $Q^2 = 1.9$ GeV^2, fitted with `xFitter`.

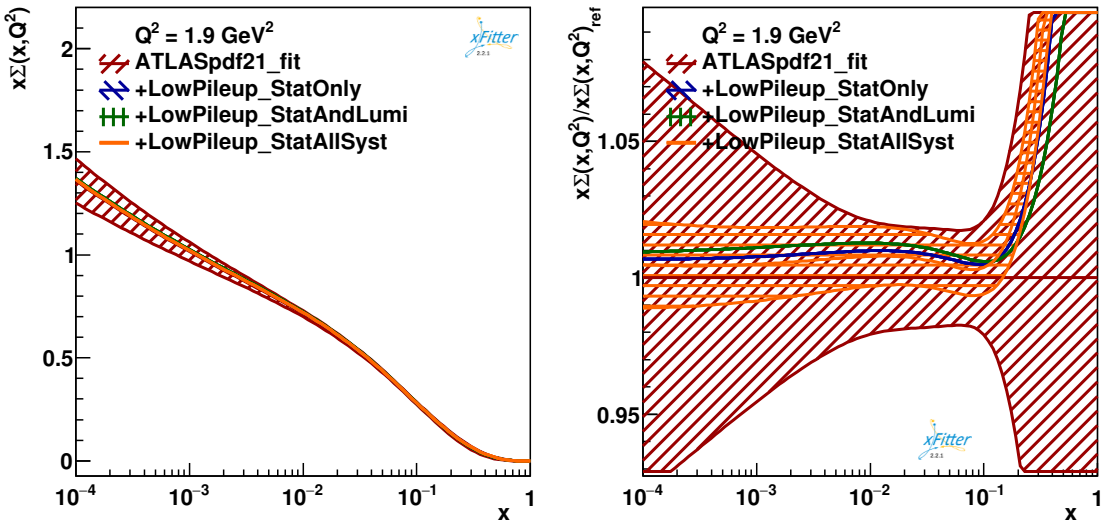

Figure E.4: PDF of the sea (Σ) at $Q^2 = 1.9$ GeV^2, fitted with `xFitter`.

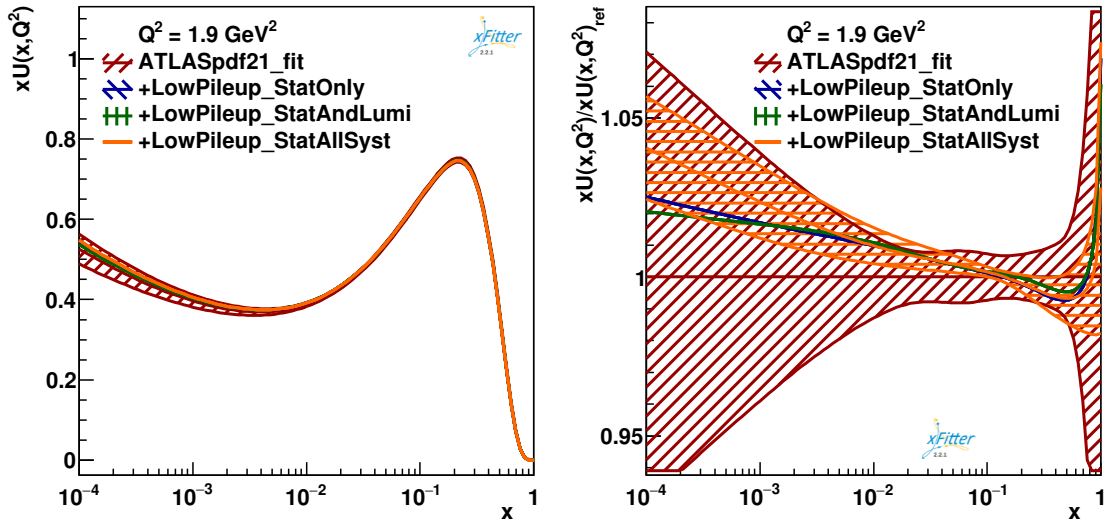

Figure E.5: PDF of the U sea at $Q^2 = 1.9$ GeV^2, fitted with `xFitter`.

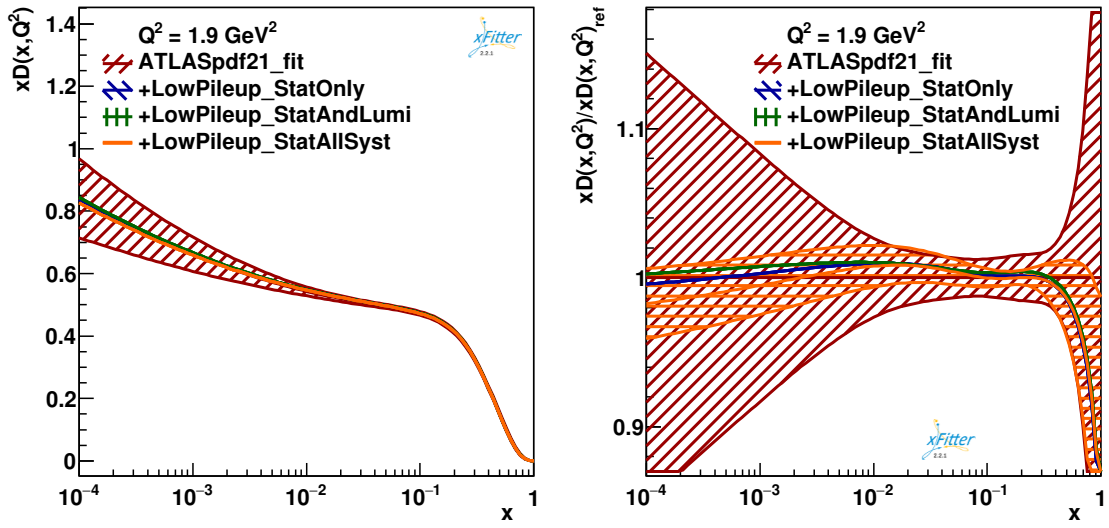

Figure E.6: PDF of the D sea at $Q^2 = 1.9$ GeV^2, fitted with `xFitter`.

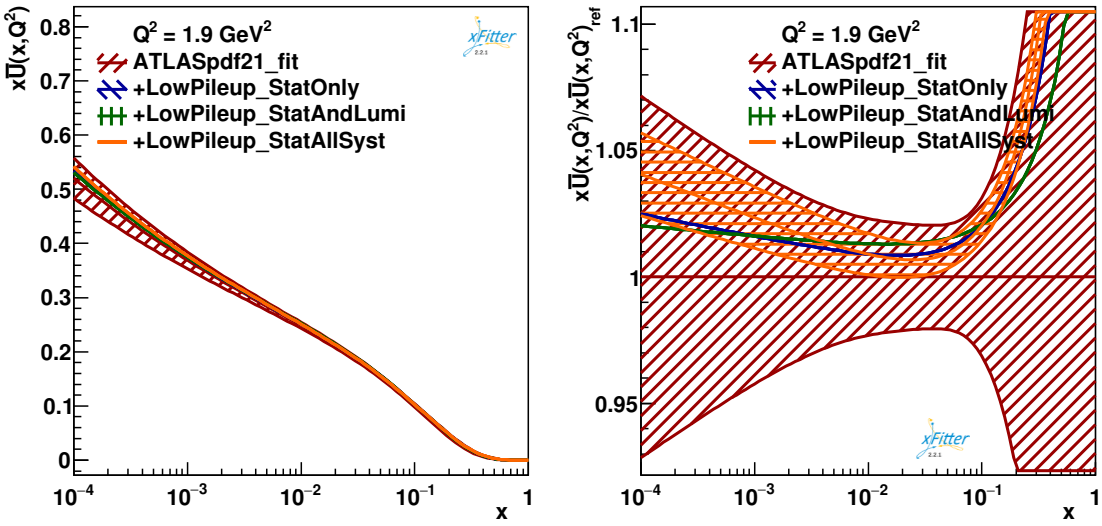

Figure E.7: PDF of the $\bar{U}$ sea at $Q^2 = 1.9$ GeV^2, fitted with `xFitter`.

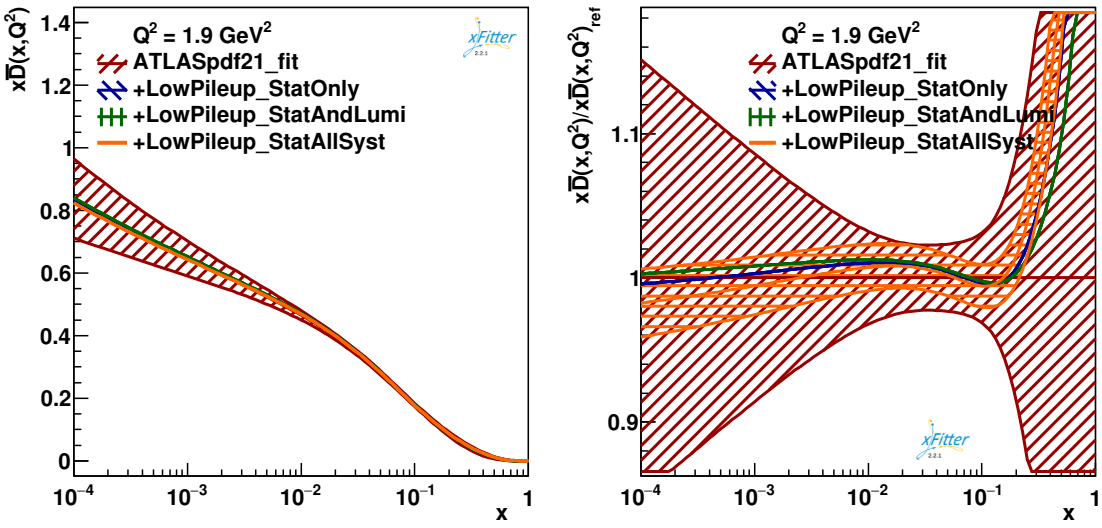

Figure E.8: PDF of the $\bar{D}$ sea at $Q^2 = 1.9$ GeV^2, fitted with `xFitter`.

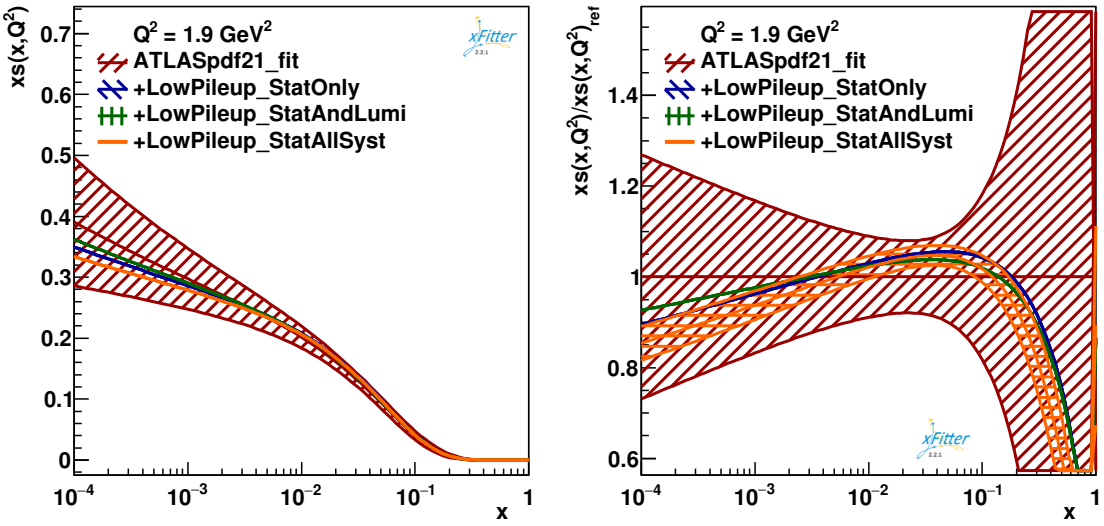

Figure E.9: PDF of the s-quark at $Q^2 = 1.9$ GeV^2, fitted with `xFitter`.

E.2 PDFs at $Q^2 = (80.4\ \text{GeV})^2$

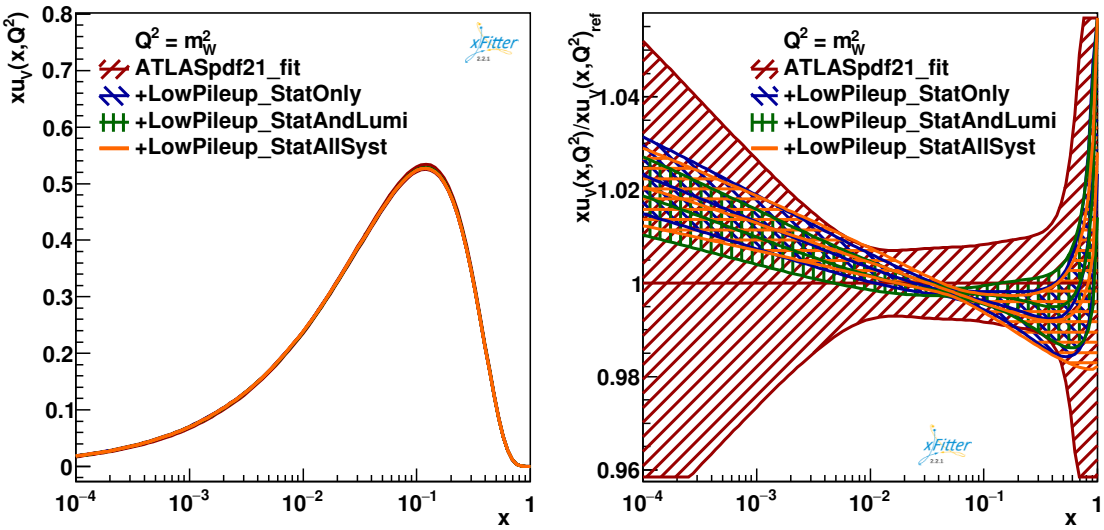

Figure E.10: PDF of the u_v quark at $Q^2 = (80.4\ \text{GeV})^2$, fitted with `xFitter`.

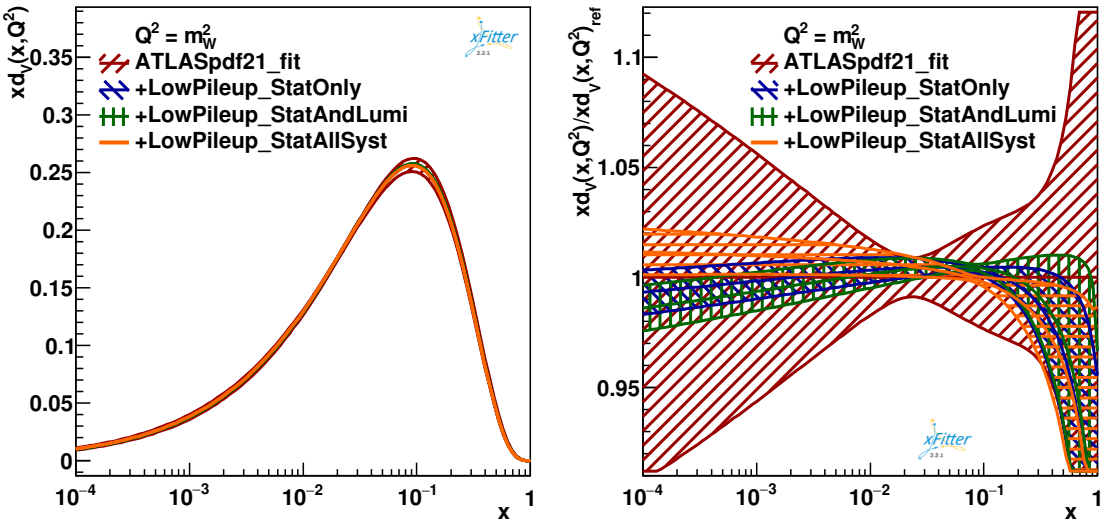

Figure E.11: PDF of the d_v quark at $Q^2 = (80.4\ \text{GeV})^2$, fitted with `xFitter`.

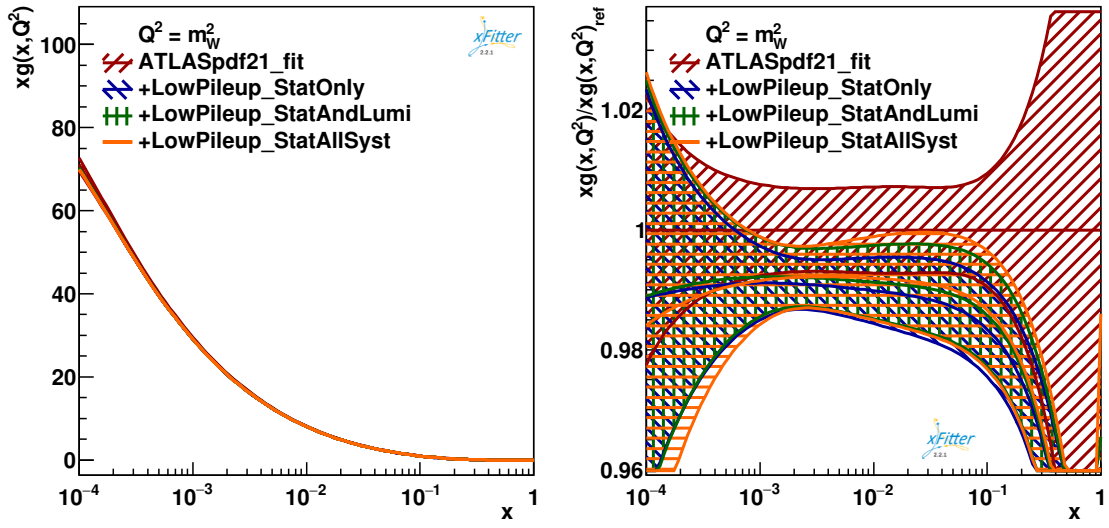

Figure E.12: PDF of the gluon at $Q^2 = (80.4\ \text{GeV})^2$, fitted with `xFitter`.

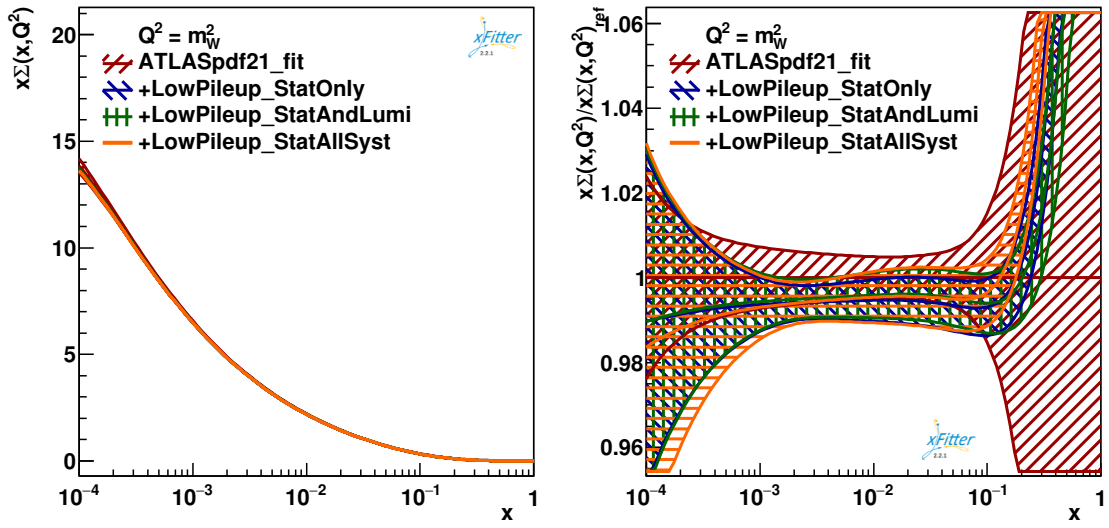

Figure E.13: PDF of the sea (Σ) at $Q^2 = (80.4\ \text{GeV})^2$, fitted with `xFitter`.

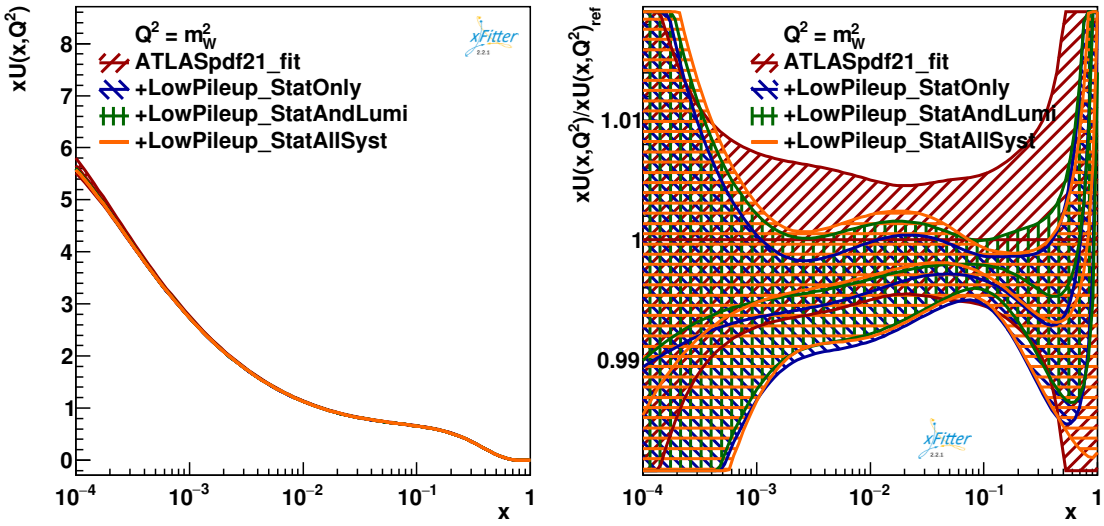

Figure E.14: PDF of the U sea at $Q^2 = (80.4\ \text{GeV})^2$, fitted with `xFitter`.

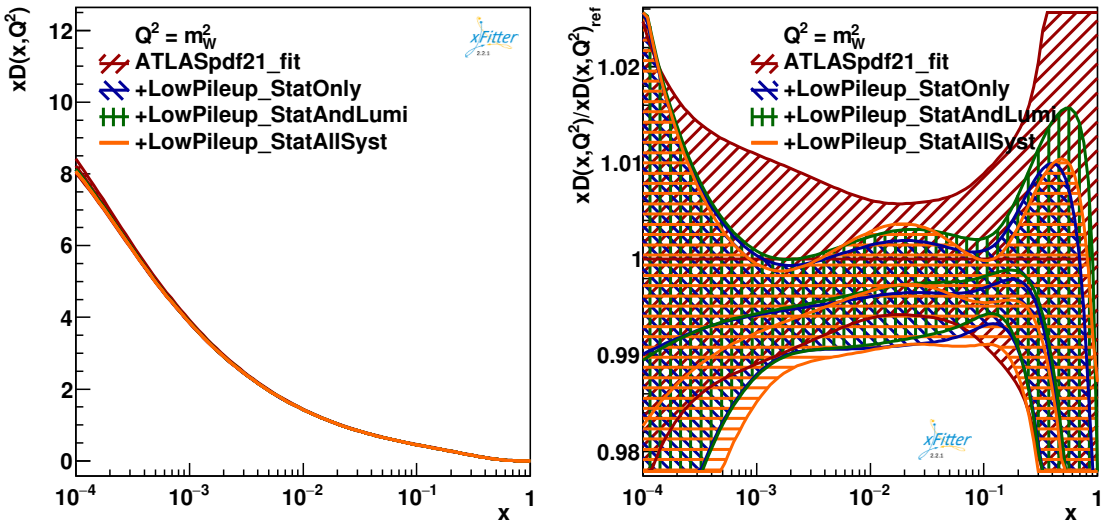

Figure E.15: PDF of the D sea at $Q^2 = (80.4\ \text{GeV})^2$, fitted with `xFitter`.

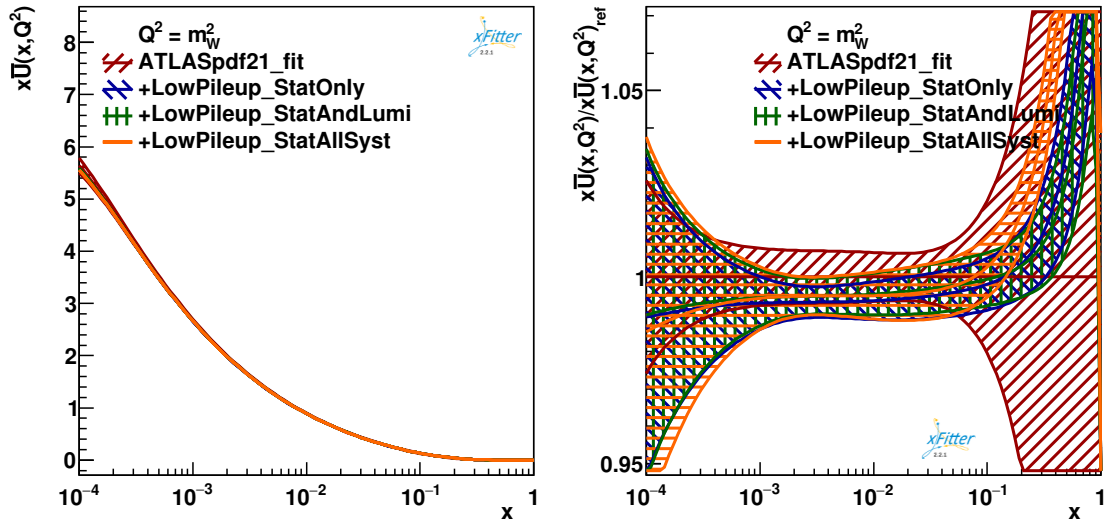

Figure E.16: PDF of the $\bar{U}$ sea at $Q^2 = (80.4\ \text{GeV})^2$, fitted with `xFitter`.

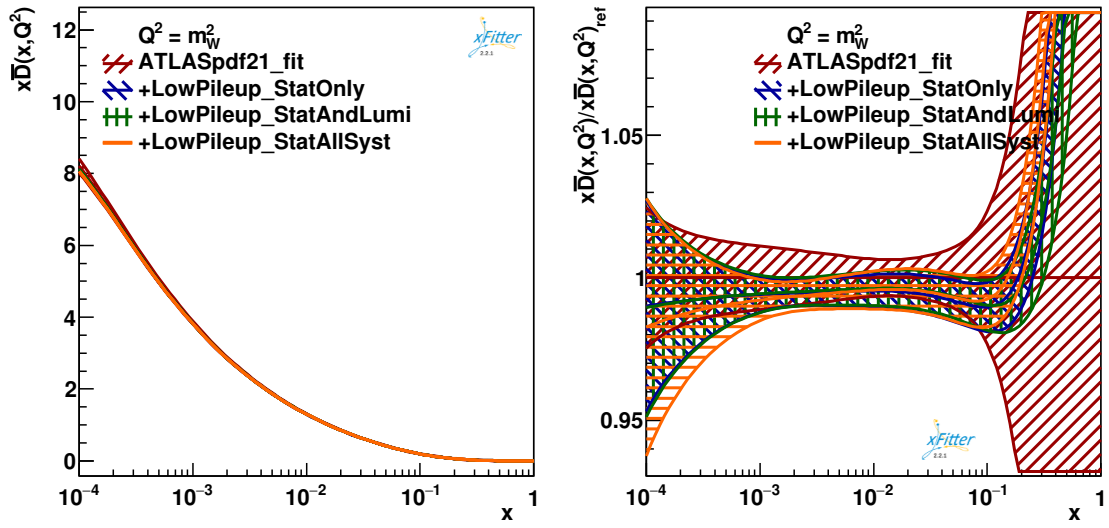

Figure E.17: PDF of the $\bar{D}$ sea at $Q^2 = (80.4\ \text{GeV})^2$, fitted with `xFitter`.

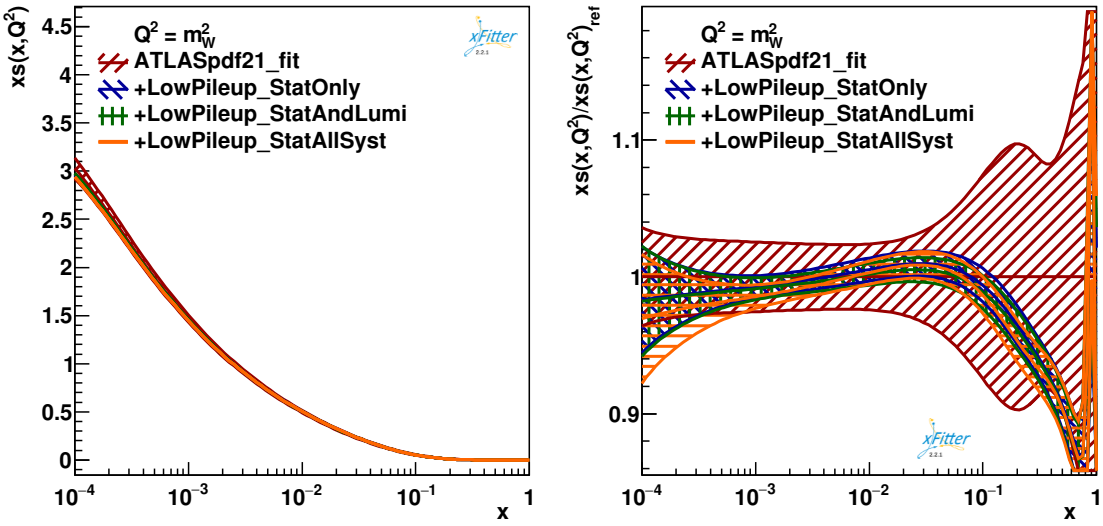

Figure E.18: PDF of the s-quark at $Q^2 = (80.4\ \text{GeV})^2$, fitted with `xFitter`.

F Excluding the core of the p_{T}^{ℓ} cross sections

Section 6.6.4 discusses the effect of fixed order theory in NLO predictions of the p_{T}^{ℓ} distribution, which appear as a distinctive bump at $p_{\mathrm{T}}^{\ell} \approx 40$ GeV in that particular binning choice. In order to better understand the effect of this feature in the final result of a fit, such as those presented at the end of Section 6.8, and aiming for fits on real p_{T}^{ℓ} data, dedicated studies should be performed. Examples of these studies are the use of different binnings (particularly, exploring larger bins with boundaries away from 80.4 GeV), excluding the region around the bump, and using different prediction generators (such as using DYTURBO directly within `xFitter`, a feature that should soon become available). This short Appendix focuses on the second of these proposals.

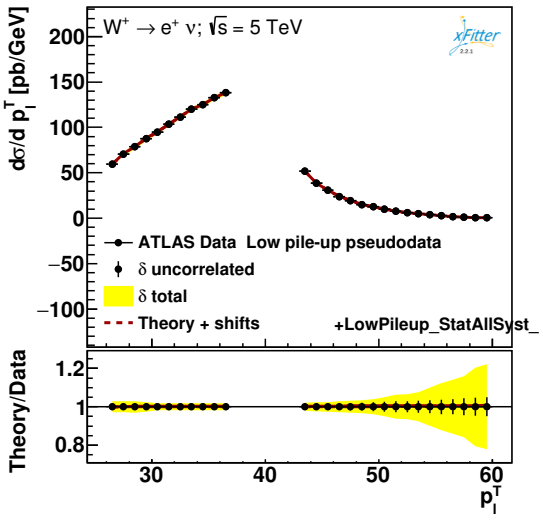

Figure F.1: Modified p_{T}^{ℓ} differential cross section in the $W^+ \to e^+\nu$ channel where the core of the distribution has been excluded. That is, the corresponding m_W+PDF does not include the region $37 < p_{\mathrm{T}}^{\ell} < 43$ GeV in the global χ^2 computation. The results of this fit and its comparison against standard fits are reported in Table F.1

The results summarised ahead use the same p_{T}^{ℓ} pseudodata distributions Section 6.6.2 and the same corresponding interpolation grids, including also the statistical and all of

the systematic uncertainties. The region $37 < p_{\mathrm{T}}^{\ell} < 43$ GeV was entirely excluded from the fit in order to stay away from the bump (which was achieved by directly switching the corresponding bin flags from 1 to 0 in the `.dat` file read by `xFitter`). An example of the resulting effective distributions seen at fit-time is shown in Fig. F.1. While this approach minimises the effect of the fixed order features at $p_{\mathrm{T}}^{\ell} \approx 40$ GeV, one should realise that most of the sensitivity to m_W is, in fact, located in the excluded region; hence, reduced sensitivity to m_W and enlarged fit uncertainty are to be expected.

The aforedescribed modified pseudodata was used in a combined m_W+PDF fit analogous to that shown in Section 6.8.3; the result of said combined fit is summarised in Table F.1. A grosso modo, the PDF parameters shown little dependence to whether the core of the p_{T}^{ℓ} distribution is included or not. However, the shift on m_W^{fit} grows to $-32\ \mathrm{MeV} \pm 40\ \mathrm{MeV}$ (compared to $-7\ \mathrm{MeV} \pm 23\ \mathrm{MeV}$ when the entirety of the distribution is used) and global correlation of 0.529, which one could justify under the loss of sensitivity due to the exclusion of the core.

Following the treatment shown in Section D.3, combined fits on pseudodata generated with all of the PDF eigenvector variations were obtained in a channel-by-channel and all-channels-at-once basis. The results are summarised in Fig. F.2. The main observation to extract from these distributions is that the exclusion of the core of the distribution degrades considerably the sensitivity to m_W regardless of the fit approach while keeping closure within the uncertainty of the fit.

Overall, the exclusion of the core in the context of the binning described in Section 6.6.2 does not show relevant effects on the constraining power of the fitted PDF parameter. Moreover, it leads to scenarios further away from perfect closure due to the reduced sensitivity to m_W. Therefore, one may want to avoid using this technique when performing fits to real data (although a similar check is encouraged whenever trying different p_{T}^{ℓ} binnings).

Table F.1: Comparison between the nominal and combined PDF fit results (summarised in Table 6.8) and the combined fit where the $37 < p_{\mathrm{T}}^{\ell} < 43$ GeV region is being excluded.

	Nominal PDF fit	Combined m_W+PDF fit	
Parameter	ATLASpdf21_fit (without LowPileup)	ATLASpdf21 +LowPileup_StatAllSyst	ATLASpdf21 +LowPileup_StatAllSyst_ExcludingCore
'Adbar'	0.164 ± 0.027	0.152 ± 0.018	0.154 ± 0.020
'Adv'	1.0000	1.0000	1.0000
'Ag'	1.0000	1.0000	1.0000
'Agp'	0.081 ± 0.018	0.077 ± 0.020	0.074 ± 0.014
'Aubar'	0.1298 ± 0.0086	0.1301 ± 0.0030	0.1334 ± 0.0036
'Auv'	1.0000	1.0000	1.0000
'Bdbar'	-0.110 ± 0.030	-0.127 ± 0.022	-0.121 ± 0.028
'Bdv'	0.694 ± 0.030	0.711 ± 0.022	0.716 ± 0.022
'Bg'	-0.763 ± 0.037	-0.757 ± 0.038	-0.773 ± 0.051
'Bgp'	-0.825 ± 0.019	-0.822 ± 0.018	-0.832 ± 0.021
'Bstr'	-0.093 ± 0.070	-0.072 ± 0.046	-0.1187
'Bubar'	-0.153 ± 0.014	-0.155 ± 0.017	-0.147 ± 0.017
'Buv'	0.702 ± 0.022	0.701 ± 0.020	0.705 ± 0.020
'Cdbar'	3.95 ± 0.70	3.78 ± 0.67	3.9 ± 1.0
'Cdv'	2.52 ± 0.69	2.54 ± 0.40	2.56 ± 0.30
'Cg'	4.67 ± 0.27	4.82 ± 0.29	4.78 ± 0.31
'Cgp'	25.00	25.00	25.00
'Cstr'	14.6 ± 2.7	15.1 ± 2.3	13.8 ± 2.6
'Cubar'	5.65 ± 0.47	5.61 ± 0.35	5.79 ± 0.36
'Cuv'	4.76 ± 0.10	4.736 ± 0.097	4.748 ± 0.099
'Ddv'	-0.74 ± 0.57	-0.79 ± 0.29	-0.76 ± 0.16
'Dg'	23.3 ± 5.3	25.5 ± 6.9	26.9 ± 4.6
'Duv'	1.39 ± 0.51	1.44 ± 0.48	1.39 ± 0.46
'Euv'	10.5 ± 1.1	10.2 ± 1.1	10.2 ± 1.1
'Mw_fit'	80.40	80.393 ± 0.023	80.368 ± 0.040
'rs'	0.93 ± 0.34	1.13 ± 0.28	0.91 ± 0.35
Fit status	converged	converged	converged
Uncertainties	migrad-hesse	migrad-hesse	migrad-hesse
Δm_W	0 MeV	-7 MeV	-32 MeV
ρ_{m_W}	0.00	0.394	0.529
χ^2/dof	2256/1620	2265/1755	2264/1731

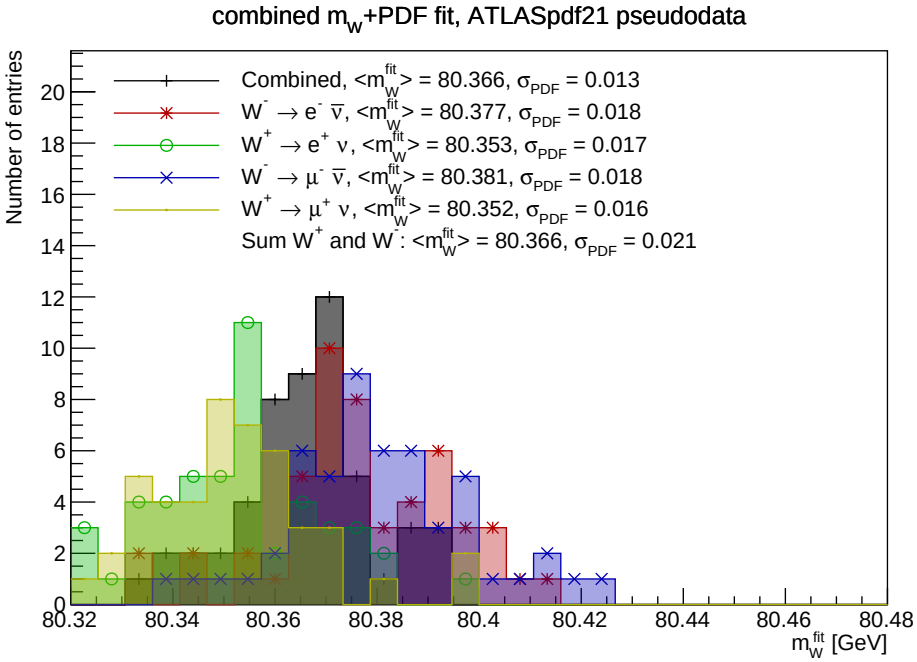

Figure F.2: Distribution of m_W^{fit} determined via combined m_W+PDF fits, constrained with the low pile-up pseudodata (generated with the ATLASpdf21 PDF, with statistical uncertainty and all sources of systematics, excluding the $37 < p_{\mathrm{T}}^{\ell} < 43$ GeV regions) added on top of the ATLASpdf21 data (listed in Table 6.1). The values of $\langle m_W \rangle$ and σ_{PDF} are shown separately for the m_W+PDF fit to each W leptonic decay channel, as well as for the fit done simultaneously on the 4 channels (labelled as "combined"). The fitted parameter value and the corresponding ρ_{m_W} for the central replica of the reference PDF is shown in the last column of Table F.1.

Bibliography

[1] Juan Salvador Tafoya Vargas, Zhiqing Philippe Zhang, and Louis Fayard, Electron energy resolution corrections, Technical report, CERN, ATL-COM-PHYS-2021-896, Geneva, 2021, https://cds.cern.ch/record/2784105. (Cited on pages xi, 4, 87, 96, 99, 101, 102, and 113.)

[2] ATLAS Collaboration, Methods for χ^2 parameter estimation using histograms, Technical report, CERN, ATL-PHYS-PUB-2022-046, Geneva, 2022, https://cds.cern.ch/record/2839912. (Cited on pages xi, 4, 87, 96, 99, 113, and 167.)

[3] Noether, E., Invariante Variationsprobleme, *Nachrichten von der Gesellschaft der Wissenschaften zu Göttingen, Mathematisch-Physikalische Klasse*, 1918:235–257, 1918, http://eudml.org/doc/59024. (Cited on page 11.)

[4] MissMJ, Cush, Standard Model of Elementary Particles, (Online; accessed 2023.06.13), https://en.wikipedia.org/wiki/Standard_Model. (Cited on page 13.)

[5] Michael E. Peskin and Daniel V. Schroeder, *An Introduction to quantum field theory*, Addison-Wesley, Reading, USA, 1995, http://home.ustc.edu.cn/~gengb/200923/Peskin,%20An%20Introduction%20to%20Quantum%20Field%20Theory.pdf. (Cited on page 12.)

[6] Matthew Robinson, *Symmetry and the Standard Model*, Springer New York, 2011, https://doi.org/10.1007/978-1-4419-8267-4. (Cited on page 12.)

[7] Ken J. Barnes, *Group Theory for the Standard Model of Particle Physics and Beyond*, Taylor & Francis, 2010, https://library.oapen.org/handle/20.500.12657/50881. (Cited on page 12.)

[8] S. Weinberg, The making of the Standard Model, *The European Physical Journal C*, 34(1):5–13, may 2004, https://doi.org/10.1140/epjc/s2004-01761-1. (Cited on page 12.)

[9] C. N. Yang and R. L. Mills, Conservation of Isotopic Spin and Isotopic Gauge Invariance, *Phys. Rev.*, 96:191–195, Oct 1954, https://link.aps.org/doi/10.1103/PhysRev.96.191. (Cited on page 13.)

[10] Murray Gell-Mann, Symmetries of Baryons and Mesons, *Phys. Rev.*, 125:1067–1084, Feb 1962, https://link.aps.org/doi/10.1103/PhysRev.125.1067. (Cited on pages 14 and 20.)

[11] R. P. Feynman, Space-Time Approach to Quantum Electrodynamics, *Phys. Rev.*, 76:769–789, Sep 1949, https://link.aps.org/doi/10.1103/PhysRev.76.769. (Cited on page 16.)

[12] Michelangelo L Mangano, Introduction to QCD, *1998 European School on High-Energy Physics*, 2000, https://cds.cern.ch/record/454171. (Cited on page 16.)

[13] UA1 Collaboration, Experimental observation of lepton pairs of invariant mass around 95 GeV/c^2 at the CERN SPS collider, *Physics Letters B*, 126(5):398–410, 1983, https://www.sciencedirect.com/science/article/pii/0370269383901880. (Cited on page 16.)

[14] UA2 Collaboration, Evidence for $Z^0 \to e^+e^-$ at the CERN $\bar{p}p$ Collider, *Phys. Lett. B*, 129:130–140, 1983, https://doi.org/10.1016/0370-2693(83)90744-X. (Cited on page 16.)

[15] UA1 Collaboration, Experimental Observation of Isolated Large Transverse Energy Electrons with Associated Missing Energy at $\sqrt{s} = 540$ GeV, *Phys. Lett. B*, 122:103–116, 1983, https://doi.org/10.1016/0370-2693(83)91177-2. (Cited on page 16.)

[16] UA2 Collaboration, Observation of Single Isolated Electrons of High Transverse Momentum in Events with Missing Transverse Energy at the CERN anti-p p Collider, *Phys. Lett. B*, 122:476–485, 1983, https://doi.org/10.1016/0370-2693(83)91605-2. (Cited on page 16.)

[17] Particle Data Group, Review of Particle Physics, *PTEP*, 2022:083C01, 2022, https://doi.org/10.1093/ptep/ptac097. (Cited on pages 17, 18, 19, 22, and 82.)

[18] Nicola Cabibbo, Unitary Symmetry and Leptonic Decays, *Phys. Rev. Lett.*, 10:531–533, Jun 1963, https://link.aps.org/doi/10.1103/PhysRevLett.10.531. (Cited on page 17.)

[19] Makoto Kobayashi and Toshihide Maskawa, CP-Violation in the Renormalizable Theory of Weak Interaction, *Progress of Theoretical Physics*, 49(2):652–657, 02 1973, https://doi.org/10.1143/PTP.49.652. (Cited on page 17.)

[20] UA2 Collaboration, An Improved determination of the ratio of W and Z masses at the CERN $\bar{p}p$ collider, *Phys. Lett. B*, 276:354–364, 1992, https://doi.org/10.1016/0370-2693(92)90332-X. (Cited on page 18.)

[21] CDF and D0 Collaboration, Combination of CDF and D0 W-Boson Mass Measurements, *Phys. Rev. D*, 88(5):052018, 2013, https://doi.org/10.1103/PhysRevD.88.052018. (Cited on page 18.)

[22] ALEPH, DELPHI, L3, OPAL, LEP Electroweak Collaboration, Electroweak Measurements in Electron-Positron Collisions at W-Boson-Pair Energies at LEP, *Phys. Rept.*, 532:119–244, 2013, https://doi.org/10.1016/j.physrep.2013.07.004. (Cited on page 18.)

[23] ATLAS Collaboration, Measurement of the W-boson mass in pp collisions at $\sqrt{s}$ = 7 TeV with the ATLAS detector, *The European Physical Journal C*, 78(110), 2018, https://doi.org/10.1140/epjc/s10052-017-5475-4. (Cited on pages 18, 186, 207, 218, and 249.)

[24] LHCb Collaboration, Measurement of the W boson mass, *Journal of High Energy Physics*, 2022(1), jan 2022, https://doi.org/10.1007/JHEP01(2022)036. (Cited on page 18.)

[25] ATLAS Collaboration, Improved W boson Mass Measurement using 7 TeV Proton-Proton Collisions with the ATLAS Detector, Technical report, CERN, ATLAS-CONF-2023-004, Geneva, 2023, https://cds.cern.ch/record/2853290. (Cited on pages 18, 186, and 249.)

[26] CDF Collaboration, High-precision measurement of the W boson mass with the CDF II detector, *Science*, 376(6589):170–176, 2022, https://doi.org/10.1126/science.abk1781. (Cited on page 18.)

[27] Simone Amoroso et al., Compatibility and combination of world W-boson mass measurements, *arXiv*, 8 2023, https://arxiv.org/abs/2308.09417. (Cited on page 18.)

[28] Robin Devenish and Amanda Cooper-Sarkar, *Deep Inelastic Scattering*, Oxford University Press, 11 2003, https://doi.org/10.1093/acprof:oso/9780198506713.001.0001. (Cited on pages 21, 23, and 26.)

[29] C. Anastasiou, L. Baudis, V. Chiochia, Chapter 9. Proton structure in QCD, 2011, https://edu.itp.phys.ethz.ch/fs11/ppp2/PPP2_9.pdf. (Cited on page 21.)

[30] Bjorken, J. D., Curren Algebra at Small Distances, *Conf. Proc. C*, 670717:55–81, 1967, https://inspirehep.net/literature/51092. (Cited on page 22.)

[31] Martin Griffiths, End of a HERA for particle accelerator, *Physics World*, 20(8):8, aug 2007, https://dx.doi.org/10.1088/2058-7058/20/8/13. (Cited on page 24.)

[32] H1 and ZEUS Collaborations, Combination of Measurements of Inclusive Deep Inelastic $e^{\pm}p$ Scattering Cross Sections and QCD Analysis of HERA Data, 2015, https://arxiv.org/abs/1506.06042. (Cited on pages 24, 25, 192, and 202.)

[33] Dokshitzer, Yuri L., Calculation of the Structure Functions for Deep Inelastic Scattering and e+ e- Annihilation by Perturbation Theory in Quantum Chromodynamics., *Sov. Phys. JETP*, 46:641–653, 1977, https://inspirehep.net/literature/126153. (Cited on page 26.)

[34] G. Altarelli and G. Parisi, Asymptotic freedom in parton language, *Nuclear Physics B*, 126(2):298–318, 1977, https://www.sciencedirect.com/science/article/pii/0550321377903844. (Cited on page 26.)

[35] V. N. Gribov and L. N. Lipatov, Deep inelastic e p scattering in perturbation theory, *Sov. J. Nucl. Phys.*, 15:438–450, 1972, https://inspirehep.net/literature/73449. (Cited on page 26.)

[36] H1 and ZEUS Collaborations, HERA Inclusive Neutral and Charged Current Cross Sections and a New PDF Fit, HERAPDF 2.0, 2015, https://arxiv.org/abs/1511.05402. (Cited on pages 29 and 197.)

[37] S. Alekhin et al, HERAFitter, Open Source QCD Fit Project, 2015, https://arxiv.org/abs/1410.4412. (Cited on pages 29 and 196.)

[38] The xFitter Developers' Team, xFitter: An Open Source QCD Analysis Framework. A resource and reference document for the Snowmass study, 2022, https://arxiv.org/abs/2206.12465. (Cited on pages 29, 30, and 196.)

[39] S. Alekhin, J. Bluemlein, S. Moch, and R. Placakyte, The new ABMP16 PDF, 2016, https://arxiv.org/abs/1609.03327. (Cited on page 29.)

[40] T.-J. Hou et al., Progress in the CTEQ-TEA NNLO global QCD analysis, 2019, https://arxiv.org/abs/1908.11394. (Cited on pages 29, 204, and 215.)

[41] S. Bailey, T. Cridge, L. A. Harland-Lang, A. D. Martin, and R. S. Thorne, Parton distributions from LHC, HERA, Tevatron and fixed target data: MSHT20 PDFs, *The European Physical Journal C*, 81(4), apr 2021, https://doi.org/10.1140/epjc/s10052-021-09057-0. (Cited on pages 29, 204, and 215.)

[42] J. McGowan, T. Cridge, L. A. Harland-Lang, and R. S. Thorne, Approximate N^{3}LO Parton Distribution Functions with theoretical uncertainties: MSHT20aN3LO PDFs, *The European Physical Journal C*, 83(3), mar 2023, https://doi.org/10.1140/epjc/s10052-023-11236-0. (Cited on page 29.)

[43] NNPDF Collaboration, Parton distributions from high-precision collider data, *The European Physical Journal C*, 77(10), oct 2017, https://doi.org/10.1140/epjc/s10052-017-5199-5. (Cited on pages 30 and 215.)

[44] ATLAS Collaboration, Determination of the parton distribution functions of the proton using diverse ATLAS data from pp collisions at $\sqrt{s} = 7$, 8 and 13 TeV., *Eur. Phys. J. C*, 82(5):438, 2022, https://cds.cern.ch/record/2798650. (Cited on pages 30, 197, 201, 202, 215, 227, and 245.)

[45] Butterworth J et al., PDF4LHC recommendations for LHC Run II, *Journal of Physics G: Nuclear and Particle Physics*, 43(2):023001, jan 2016, https://doi.org/10.1088/0954-3899/43/2/023001. (Cited on pages 30 and 78.)

[46] G. Cowan, *Statistical Data Analysis*, Oxford science publications. Clarendon Press, 1998, https://books.google.fr/books?id=ff8ZyW0nlJAC. (Cited on pages 31, 32, 33, 40, 41, and 188.)

[47] F. James, MINUIT Function Minimization and Error Analysis: Reference Manual Version 94.1, *CERN-D-506*, 1994, https://cds.cern.ch/record/2296388. (Cited on pages 33, 36, and 196.)

[48] Frederick E James, *Statistical Methods in Experimental Physics; 2nd ed.*, World Scientific, Singapore, 2006, https://cds.cern.ch/record/1019859. (Cited on page 34.)

[49] F. James and M. Roos, Minuit - a system for function minimization and analysis of the parameter errors and correlations, *Computer Physics Communications*, 10(6):343–367, 1975, https://www.sciencedirect.com/science/article/pii/0010465575900399. (Cited on pages 34, 36, and 38.)

[50] R. Fletcher, A new approach to variable metric algorithms, *The Computer Journal*, 13(3):317–322, 01 1970, https://doi.org/10.1093/comjnl/13.3.317. (Cited on page 37.)

[51] Bradley Efron, *The Jackknife, the Bootstrap and Other Resampling Plans*, Society for Industrial and Applied Mathematics, 1982, https://epubs.siam.org/doi/book/10.1137/1.9781611970319. (Cited on page 40.)

[52] Gary J. Feldman and Robert D. Cousins, Unified approach to the classical statistical analysis of small signals, *Phys. Rev. D*, 57:3873–3889, Apr 1998, https://link.aps.org/doi/10.1103/PhysRevD.57.3873. (Cited on page 40.)

[53] ATLAS Collaboration, Evaluating statistical uncertainties and correlations using the bootstrap method, *ATL-PHYS-PUB-2021-011*, Apr 2021, https://cds.cern.ch/record/2759945. (Cited on page 41.)

[54] Esma Mobs, The CERN accelerator complex in 2019. Complexe des accélérateurs du CERN en 2019, General Photo, 2019, https://cds.cern.ch/record/2684277. (Cited on page 45.)

[55] ATLAS Collaboration, ATLAS Luminosity Public Results Run2, https://twiki.cern.ch/twiki/bin/view/AtlasPublic/LuminosityPublicResultsRun2. (Cited on pages 48, 49, 50, and 214.)

[56] ATLAS Collaboration, ATLAS Stand-Alone Event Displays, https://twiki.cern.ch/twiki/bin/view/AtlasPublic/EventDisplayStandAlone. (Cited on page 50.)

[57] Joao Pequenao, Computer generated image of the whole ATLAS detector, CERN, 2008, https://cds.cern.ch/record/1095924. (Cited on page 51.)

[58] The ATLAS Collaboration, The ATLAS Experiment at the CERN Large Hadron Collider, *Journal of Instrumentation*, 3(08):S08003, aug 2008, https://dx.doi.org/10.1088/1748-0221/3/08/S08003. (Cited on page 52.)

[59] TikZ, coordinate system, https://tikz.net/axis3d_cms/. (Cited on page 53.)

[60] ATLAS Collaboration, *ATLAS inner detector: Technical Design Report, 1*, Technical design report. ATLAS. CERN, Geneva, 1997, https://cds.cern.ch/record/331063. (Cited on page 54.)

[61] ATLAS Collaboration, Experiment Briefing: Keeping the ATLAS Inner Detector in perfect alignment, General Photo, 2020, https://cds.cern.ch/record/2723878. (Cited on page 54.)

[62] ATLAS IBL Collaboration, Production and Integration of the ATLAS Insertable B-Layer, *JINST*, 13(05):T05008, 2018, https://dx.doi.org/10.1088/1748-0221/13/05/T05008. (Cited on page 55.)

[63] ATLAS Collaboration, ATLAS Insertable B-Layer Technical Design Report Addendum, Technical report, CERN, CERN-LHCC-2012-009, ATLAS-TDR-19-ADD-1, 5 2012, https://cds.cern.ch/record/1451888. (Cited on page 54.)

[64] Joao Pequenao, Computer generated image of the ATLAS Liquid Argon, CERN, 2008, https://cds.cern.ch/record/1095928. (Cited on page 56.)

[65] ATLAS Collaboration, *ATLAS liquid-argon calorimeter: Technical Design Report*, Technical design report. ATLAS. CERN, Geneva, 1996, https://cds.cern.ch/record/331061. (Cited on pages 55, 57, and 87.)

[66] D. Fournier, Liquid argon calorimetry, In *ECFA Large Hadron Collider (LHC) Workshop: Physics and Instrumentation*, pages 356–359, 10 1990, https://cds.cern.ch/record/215299. (Cited on pages 55 and 87.)

[67] Luís Hervás, The ATLAS liquid argon electromagnetic calorimeter: construction, commissioning and selected test beam results, *IEEE Trans. Instrum. Meas.*, 54(4):1505–1512, 2005, http://cds.cern.ch/record/912970. (Cited on page 58.)

[68] Pawel Klimek, Performance of the ATLAS Tile Calorimeter, Technical report, CERN, ATL-TILECAL-PROC-2020-002, Geneva, 2020, https://cds.cern.ch/record/2707947. (Cited on page 58.)

[69] Joao Pequenao, Computer Generated image of the ATLAS calorimeter, CERN, 2008, https://cds.cern.ch/record/1095927. (Cited on page 59.)

[70] ATLAS Collaboration, *ATLAS muon spectrometer: Technical Design Report*, Technical design report. ATLAS. CERN, Geneva, 1997, https://cds.cern.ch/record/331068. (Cited on page 60.)

[71] Joao Pequenao, Computer generated image of the ATLAS Muons subsystem, CERN, 2008, https://cds.cern.ch/record/1095929. (Cited on page 60.)

[72] ATLAS Collaboration, *ATLAS magnet system: Technical Design Report, 1*, Technical design report. ATLAS. CERN, Geneva, 1997, https://cds.cern.ch/record/338080. (Cited on page 61.)

[73] A. Yamamoto et al., The ATLAS central solenoid, *Nuclear Instruments and Methods in Physics Research Section A: Accelerators, Spectrometers, Detectors and Associated Equipment*, 584(1):53–74, 2008, https://www.sciencedirect.com/science/article/pii/S0168900207020414. (Cited on page 61.)

[74] Ana Maria Rodriguez Vera and Joao Antunes Pequenao, ATLAS Detector Magnet System, 2021, CERN, https://cds.cern.ch/record/2770604. (Cited on page 61.)

[75] R. Bartoldus et al., TDAQ Phase 1 Upgrade Technical Design Report, Technical report, CERN, ATL-COM-DAQ-2013-054, Geneva, 2013, https://cds.cern.ch/record/1559696. (Cited on page 62.)

[76] Joao Pequenao and Paul Schaffner, How ATLAS detects particles: diagram of particle paths in the detector, 2013, CERN, https://cds.cern.ch/record/1505342. (Cited on page 63.)

[77] ATLAS Collaboration, Performance of the ATLAS track reconstruction algorithms in dense environments in LHC Run 2, *The European Physical Journal C*, 77(10), oct 2017, https://doi.org/10.1140/epjc/s10052-017-5225-7. (Cited on page 65.)

[78] ATLAS Collaboration, Electron reconstruction and identification in the ATLAS experiment using the 2015 and 2016 LHC proton–proton collision data at $\sqrt{s} =$ 13 TeV, Technical report, CERN, CERN-EP-2018-273, arXiv:1902.04655, Geneva, 2019, https://doi.org/10.1140/epjc/s10052-019-7140-6. (Cited on pages 66 and 67.)

[79] ATLAS Collaboration, Topological cell clustering in the ATLAS calorimeters and its performance in LHC Run 1, *Eur. Phys. J. C*, 77:490, 2017, https://cds.cern.ch/record/2138166. (Cited on page 67.)

[80] Matteo Cacciari, Gavin P. Salam, and Gregory Soyez, The anti-kt jet clustering algorithm, *Journal of High Energy Physics*, 2008(04):063, apr 2008, https://dx.doi.org/10.1088/1126-6708/2008/04/063. (Cited on page 68.)

[81] ATLAS Collaboration, Jet Calibration and Systematic Uncertainties for Jets Reconstructed in the ATLAS Detector at $\sqrt{s} = 13$ TeV, Technical report, CERN, ATL-PHYS-PUB-2015-015, Geneva, 2015, https://cds.cern.ch/record/2037613. (Cited on page 68.)

[82] ATLAS Collaboration, Jet reconstruction and performance using particle flow with the ATLAS Detector, *The European Physical Journal C*, 77(7), jul 2017, https://doi.org/10.1140/epjc/s10052-017-5031-2. (Cited on page 69.)

[83] ATLAS Collaboration, The HL-LHC project, https://hilumilhc.web.cern.ch/content/hl-lhc-project. (Cited on page 72.)

[84] ATLAS Collaboration, Technical Design Report for the ATLAS Inner Tracker Strip Detector, Technical report, CERN, CERN-LHCC-2017-005, ATLAS-TDR-025, 4 2017, https://cds.cern.ch/record/2257755. (Cited on page 72.)

[85] ATLAS Collaboration, Technical Design Report for the ATLAS Inner Tracker Pixel Detector, Technical report, CERN, CERN-LHCC-2017-021, ATLAS-TDR-030, Geneva, 2017, https://cds.cern.ch/record/2285585. (Cited on page 72.)

[86] ATLAS Collaboration, Technical Proposal: A High-Granularity Timing Detector for the ATLAS Phase-II Upgrade, Technical report, CERN, CERN-LHCC-2018-023, LHCC-P-012, Geneva, 2018, https://cds.cern.ch/record/2623663. (Cited on page 73.)

[87] ATLAS Collaboration, ATLAS Liquid Argon Calorimeter Phase-I Upgrade: Technical Design Report, Technical report, CERN, CERN-LHCC-2013-017, ATLAS-TDR-022, 2013, Final version presented to December 2013 LHCC., https://cds.cern.ch/record/1602230. (Cited on page 73.)

[88] ATLAS Collaboration, ATLAS Liquid Argon Calorimeter Phase-II Upgrade: Technical Design Report, Technical report, CERN, CERN-LHCC-2017-018, ATLAS-TDR-027, Geneva, 2017, https://cds.cern.ch/record/2285582. (Cited on page 73.)

[89] ATLAS Collaboration, Technical Design Report for the Phase-II Upgrade of the ATLAS TDAQ System, Technical report, CERN, CERN-LHCC-2017-020, ATLAS-TDR-029, Geneva, 2017, https://cds.cern.ch/record/2285584. (Cited on page 73.)

[90] Peter Clifford, 5 - Monte Carlo Methods, In John L. Stanford and Stephen B. Vardeman, editors, *Statistical Methods for Physical Science*, volume 28 of *Methods in Experimental Physics*, pages 125–153. Academic Press, 1994, https://www.sciencedirect.com/science/article/pii/S0076695X08602550. (Cited on page 76.)

[91] Gionata Luisoni, An introduction to POWHEG, last accessed on 2023-04-06, https://indico.cern.ch/event/656211/contributions/2673382/attachments/1498653/2333153/luisoni_powheg.pdf. (Cited on pages 77 and 79.)

[92] Andy Buckley, James Ferrando, Stephen Lloyd, Karl Nordström, Ben Page, Martin Rüfenacht, Marek Schönherr, and Graeme Watt, LHAPDF6: parton density access in the LHC precision era, *The European Physical Journal C*, 75(3), mar 2015, https://doi.org/10.1140/epjc/s10052-015-3318-8. (Cited on page 78.)

[93] S. Alioli, P. Nason, C. Oleari, and E. Re, A general framework for implementing NLO calculations in shower Monte Carlo programs: the POWHEG BOX, *JHEP*, 06:043, 2010, https://doi.org/10.1007/JHEP06(2010)043. (Cited on page 80.)

[94] ATLAS Collaboration, Studies of theoretical uncertainties on the measurement of the mass of the W boson at the LHC, Technical report, CERN, ATL-PHYS-PUB-2014-015, Geneva, 2014, https://cds.cern.ch/record/1956455. (Cited on page 81.)

[95] C. Bierlich et al., A comprehensive guide to the physics and usage of PYTHIA 8.3, 2022, https://doi.org/10.48550/arXiv.2203.11601. (Cited on pages 80, 81, and 191.)

[96] M. Bähr et al., Herwig++ physics and manual, *The European Physical Journal C*, 58(4):639–707, nov 2008, https://doi.org/10.1140/epjc/s10052-008-0798-9. (Cited on page 80.)

[97] T. Gleisberg et al., Event generation with SHERPA 1.1, *Journal of High Energy Physics*, 2009(02):007, feb 2009, https://dx.doi.org/10.1088/1126-6708/2009/02/007. (Cited on page 80.)

[98] E. Boos et al., Generic User Process Interface for Event Generators, 2001, https://doi.org/10.48550/arXiv.hep-ph/0109068. (Cited on page 82.)

[99] A. Buckley et al., Implementation of the ATLAS Run 2 event data model, Technical Report 7, CERN, ATL-SOFT-PROC-2015-003, Geneva, 2015, https://cds.cern.ch/record/2014150. (Cited on page 82.)

[100] ATLAS Collaboration, Impact of ROOT file parameters on ATLAS Analysis Object Data, Technical report, CERN, ATL-SOFT-PUB-2020-002, Geneva, 2020, https://cds.cern.ch/record/2723199. (Cited on page 82.)

[101] S. Agostinelli, J. Allison, et al, Geant4—a simulation toolkit, *Nuclear Instruments and Methods in Physics Research Section A: Accelerators, Spectrometers, Detectors and Associated Equipment*, 506(3):250–303, 2003, https://www.sciencedirect.com/science/article/pii/S0168900203013688. (Cited on page 83.)

[102] G. Parrour, S. Simion, and K. Kordas, Geant4 for the ATLAS electromagnetic calorimeter, CALOR2000, https://lappweb.in2p3.fr/archives/Calor2000/Contributions/Simulation/Kosta_Kordas.pdf. (Cited on page 85.)

[103] Siqi Yang; Cheng Wang, (Online; accessed 2023.04.10), https://indico.cern.ch/event/857807/contributions/3615377/attachments/1932510/3201225/ElectronCalibration.pdf. (Cited on pages 87 and 97.)

[104] Janos Kirz, X-Ray Data Booklet: Section 3.1 SCATTERING of X-RAYS from ELECTRONS and ATOMS., http://xdb.lbl.gov/Section3/Sec_3-1.html. (Cited on page 89.)

[105] ATLAS Collaboration, Drift Time Measurement in the ATLAS Liquid Argon Electromagnetic Calorimeter using Cosmic Muons, *The European Physical Journal C*, 70(3):755–785, oct 2010, https://doi.org/10.1140/epjc/s10052-010-1403-6. (Cited on page 90.)

[106] Nansi Andari, *Observation of a BEH-like boson decaying into two photons with the ATLAS detector at the LHC*, PhD thesis, Orsay, LAL, 9 2012, https://cds.cern.ch/record/1485052. (Cited on page 90.)

[107] Estelle Scifo, *Measurement of the Brout-Englert-Higgs boson couplings in its diphoton decay channel with the ATLAS detector at the LHC*, PhD thesis, Orsay, LAL, 7 2014, https://cds.cern.ch/record/1756391. (Cited on page 90.)

[108] Cyril Pascal Becot, *Diphoton lineshape of the BEH boson using the ATLAS detector at the LHC: calibration, mass, width and interferences*, PhD thesis, Diderot U., Paris, 9 2015, https://cds.cern.ch/record/2065179. (Cited on page 90.)

[109] ATLAS Collaboration, Performance of the electronic readout of the ATLAS liquid argon calorimeters, *Journal of Instrumentation*, 5, 09 2010, http://dx.doi.org/10.1088/1748-0221/5/09/P09003. (Cited on page 91.)

[110] ATLAS Collaboration, Electron and photon energy calibration with the ATLAS detector using LHC Run 1 data, *The European Physical Journal C*, 74(10), oct 2014, https://doi.org/10.1140/epjc/s10052-014-3071-4. (Cited on page 92.)

[111] ATLAS Collaboration, Electron and photon energy calibration with the ATLAS detector using 2015–2016 LHC proton-proton collision data, *Journal of Instrumentation*, 14(03):P03017–P03017, mar 2019, https://doi.org/10.1088/1748-0221/14/03/p03017. (Cited on pages 92 and 96.)

[112] ATLAS Collaboration, Electron and photon performance measurements with the ATLAS detector using the 2015–2017 LHC proton-proton collision data, *JINST*, 14(12):P12006, 2019, https://dx.doi.org/10.1088/1748-0221/14/12/P12006. (Cited on page 92.)

[113] ATLAS Collaboration, Electron and photon energy calibration with the ATLAS detector using LHC Run 2 data, Technical report, CERN, ATL-COM-PHYS-2022-647, Geneva, 2022, https://cds.cern.ch/record/2816050. (Cited on pages 92, 94, and 107.)

[114] Linghua Guo, *Improvement on the $H \to \gamma\gamma$ mass measurement by constraining the photon energy scale uncertainty and search for Higgs boson pair production in the $b\bar{b}\gamma\gamma$ final state with the ATLAS experiment using the full Run 2 at $\sqrt{s}$=13 TeV pp collision of LHC*, PhD thesis, IJCLab, Orsay, 2022, https://cds.cern.ch/record/2836293. (Cited on pages 92 and 95.)

[115] A. Hoecker et al, TMVA - Toolkit for Multivariate Data Analysis, 2009, https://tmva.sourceforge.net/, https://arxiv.org/abs/physics/0703039. (Cited on page 94.)

[116] J-B Blanchard, J-B de Vivie, and P Mastrandrea, In situ scales and smearings from Z and J/Ψ events, Technical report, CERN, ATL-COM-PHYS-2013-1653, Geneva, 2013, https://cds.cern.ch/record/1637533. (Cited on page 95.)

[117] Christophe Goudet, *Etalonnage du calorimètre électromagnétique de l'expérience ATLAS et application à la mesure des couplages du boson de (Brout-Englert-)Higgs dans le canal diphoton dans le cadre du Run 2 du LHC.*, PhD thesis, CEA Saclay, 2017, https://inspirehep.net/literature/1765256. (Cited on page 95.)

[118] Hicham Atmani, *Calibration of the ATLAS Electromagnetic Calorimeter and Measurement of W Boson Properties at* $\sqrt{s}$ *= 5 and 13 TeV with the ATLAS Detector at the LHC.*, PhD thesis, Université Paris-Saclay, U. Paris-Saclay, 2020, https://theses.hal.science/tel-03224873/. (Cited on pages 95 and 108.)

[119] Linghua Guo, Electron energy in-situ calibration and linearity measurements from Z $\rightarrow$ *ee* events, *ATL-COM-PHYS-2020-757*, Oct 2020, https://cds.cern.ch/record/2742791. (Cited on pages 96, 101, and 102.)

[120] Louis Martin, In-situ calibration of the EM calorimeter, presented on 24th of July 2019 at the ATLAS e/gamma calibration meeting, (Online; accessed 2023.05.30), https://indico.cern.ch/event/827055/contributions/3506176/attachments/1885454/3110615/Slide_ES.pdf. (Cited on page 96.)

[121] David Delgove, In-situ calibration for high-μ dataset, presented on 25th of March 2019 at the ATLAS-LAL meeting, (Online; accessed 2023.05.30), https://indico.ijclab.in2p3.fr/event/5550/contributions/17993/attachments/14001/17145/LAL_DDelgove.pdf. (Cited on page 96.)

[122] David Delgove, Systematics, presented on 14th of March 2019 at the ATLAS e/gamma calibration meeting , (Online; accessed 2023.05.30), https://indico.cern.ch/event/804207/contributions/3353868/attachments/1811758/2960413/Systematics_v2.pdf. (Cited on page 96.)

[123] ATLAS Collaboration, Electron and photon energy calibration with the ATLAS detector using LHC Run 2 data, Technical report, CERN, CERN-EP-2023-128, Geneva, 2023, http://cds.cern.ch/record/2870086. (Cited on page 97.)

[124] S. Yang et al, SM W/Z-Physics group Meeting on Wednesday 2 Oct 2019, (Online; accessed 2023.05.09), https://indico.cern.ch/event/852318/contributions/3584332/attachments/1918965/3173735/stwRel21.pdf. (Cited on page 97.)

[125] ATLAS Collaboration, Measurement of the effective leptonic weak mixing angle using electron and muon pairs from Z-boson decay in the ATLAS experiment at

$\sqrt{s}$ = 8 TeV, Technical report, CERN, ATLAS-CONF-2018-037, Geneva, 2018, https://cds.cern.ch/record/2630340. (Cited on page 97.)

[126] Zihan Zhao, Energy resolution parametrization from data, presented on 16th of March 2023 at the e/gamma workshop, (Online; accessed 2023.05.09), https://indico.cern.ch/event/1245976/contributions/5284626/attachments/2609460/4514118/ElectronResolution_Zihan230316.pdf. (Cited on page 97.)

[127] Edison Carrera Unaucho, Studies related to the measurement of the W-boson mass with the ATLAS experiment, 2022, https://indico.ijclab.in2p3.fr/event/8014/contributions/26942/attachments/19402/26305/atlas2_final.pdf. (Cited on pages 105, 106, 107, 108, 110, and 111.)

[128] Niklas Bjoklund, Low pile-up $Z \to ee$ calibration, IJCLab ATLAS meeting, (Online; accessed 2023.05.09), https://indico.ijclab.in2p3.fr/event/8733/contributions/28418/attachments/20280/27952/Niklas-Low-Pileup.pdf. (Cited on page 105.)

[129] Aicha Kenani, Étude de la résolution en énergie des électrons avec la distribution de la masse du boson Z et son impact sur la mesure de la masse du boson W, https://gitlab.com/akenani/l3_internship/-/raw/report/Rapport_Stage_AichaKenani.pdf. (Cited on pages 105, 110, 111, and 112.)

[130] ATLAS Collaboration, Precise measurements of W and Z transverse momentum spectra with the ATLAS detector at $\sqrt{s} = 5.02$ TeV and 13 TeV, *11th Large Hadron Collider Physics Conference 2023*, 2023, https://cds.cern.ch/record/2861057. (Cited on pages 107, 209, and 213.)

[131] Tairan Xu, Hicham Atmani, Ludovica Aperio Bella, and Jan Kretzschmar, Electron corrections for low pile-up runs taken in 2017 and 2018, Technical report, CERN, ATL-COM-PHYS-2019-077, Geneva, 2019, https://cds.cern.ch/record/2657152. (Cited on page 108.)

[132] Hannu Paukkunen and Pia Zurita, PDF reweighting in the Hessian matrix approach, *Journal of High Energy Physics*, 2014(12), dec 2014, https://doi.org/10.1007/jhep12(2014)100. (Cited on page 186.)

[133] ATLAS Collaboration, Measurement of the effective leptonic weak mixing angle using electron and muon pairs from Z-boson decay in the ATLAS experiment at $\sqrt{s}$ = 8 TeV, Technical report, CERN, ATLAS-CONF-2018-037, Geneva, 2018, https://cds.cern.ch/record/2630340. (Cited on pages 186 and 250.)

[134] H1 Collaboration and H. Spiesberger, Determination of electroweak parameters in polarised deep-inelastic scattering at HERA, 2018, https://arxiv.org/abs/1402.6623. (Cited on page 187.)

[135] ZEUS Collaboration, An NLO and EW analysis of inclusive ep cross section data from the ZEUS experiment, *ICHEP06*, ZEUS-prel-06-003, 2006, https://www.desy.de/~phch/conf/ichep06/hiq2/10/ZEUS-prel-06-003.ps. (Cited on page 187.)

[136] Stefan Schmitt, Data Unfolding Methods in High Energy Physics, *EPJ Web of Conferences*, 137:11008, 2017, https://doi.org/10.1051/epjconf/201713711008. (Cited on page 188.)

[137] G. D'Agostini, A multidimensional unfolding method based on Bayes' theorem, *Nuclear Instruments and Methods in Physics Research Section A: Accelerators, Spectrometers, Detectors and Associated Equipment*, 362(2):487–498, 1995, https://doi.org/10.1016/0168-9002(95)00274-X. (Cited on page 189.)

[138] G. D'Agostini, Improved iterative Bayesian unfolding, 2010, https://arxiv.org/abs/1010.0632. (Cited on page 189.)

[139] ATLAS Collaboration, Measurment of the p_{T} spectrum of W- and Z-bosons produced in pp collisions at $\sqrt{s} = 5$ TeV and 13 TeV in low-pileup runs, Technical report, CERN, ATL-COM-PHYS-2018-1084, Geneva, 2018, https://cds.cern.ch/record/2632159. (Cited on page 189.)

[140] M. Botje, QCDNUM: Fast QCD evolution and convolution, *Computer Physics Communications*, 182(2):490–532, feb 2011, https://doi.org/10.1016/j.cpc.2010.10.020. (Cited on pages 192 and 196.)

[141] S. Camarda et al., DYTurbo: fast predictions for Drell–Yan processes, *The European Physical Journal C*, 80(3), mar 2020, https://doi.org/10.1140/epjc/s10052-020-7757-5. (Cited on pages 192, 194, 195, and 207.)

[142] D. Britzger, A. Gehrmann-De Ridder, T. Gehrmann, E. W. N. Glover, C. Gwenlan, A. Huss, J. Pires, K. Rabbertz, D. Savoiu, M. R. Sutton, and J. Stark, NNLO interpolation grids for jet production at the LHC, 2022, https://doi.org/10.48550/arXiv.2207.13735. (Cited on page 195.)

[143] T. Carli et al., A posteriori inclusion of parton density functions in NLO QCD final-state calculations at hadron colliders: the APPLGRID project, *The European Physical Journal C*, 66(3-4):503–524, feb 2010, https://doi.org/10.1140/epjc/s10052-010-1255-0. (Cited on page 196.)

[144] V. Bertone, S. Carrazza, and N. P. Hartland, APFELgrid : A high performance tool for parton density determinations, *Computer Physics Communications*, 212:205–209, mar 2017, https://doi.org/10.1016/j.cpc.2016.10.006. (Cited on page 196.)

[145] T. Kluge, K. Rabbertz, and M. Wobisch, FastNLO: Fast pQCD calculations for PDF fits, In *14th International Workshop on Deep Inelastic Scattering*, pages 483–486, 9 2006, https://doi.org/10.1142/9789812706706_0110. (Cited on page 196.)

[146] xFitter Collaboration, xFitter - A PDF fit program from HERA. Wiki, (Online; accessed 2023.06.28), https://gitlab.cern.ch/fitters/xfitter/-/wikis/home. (Cited on page 199.)

[147] ATLAS Collaboration, Precision measurement and interpretation of inclusive W^+, W^- and Z/γ^* production cross sections with the ATLAS detector, *The European Physical Journal C*, 77(6), jun 2017, https://doi.org/10.1140/epjc/s10052-017-4911-9. (Cited on pages 202 and 228.)

[148] ATLAS Collaboration, Measurements of top-quark pair differential cross-sections in the lepton+jets channel in pp collisions at $\sqrt{s} = 8$ TeV using the ATLAS detector, *The European Physical Journal C*, 76(10), oct 2016, https://doi.org/10.1140/epjc/s10052-016-4366-4. (Cited on page 202.)

[149] ATLAS Collaboration, Measurement of differential cross sections and W^+/W^- cross-section ratios for W boson production in association with jets at $\sqrt{s} = 8$ TeV with the ATLAS detector, *Journal of High Energy Physics*, 2018(5), may 2018, https://doi.org/10.1007/jhep05(2018)077. (Cited on page 202.)

[150] ATLAS Collaboration, Measurement of the inclusive cross-section for the production of jets in association with a Z boson in proton-proton collisions at 8 TeV using the ATLAS detector, *The European Physical Journal C*, 79(10), oct 2019, https://doi.org/10.1140/epjc/s10052-019-7321-3. (Cited on page 202.)

[151] ATLAS Collaboration, Measurement of the Drell-Yan triple-differential cross section in pp collisions at $\sqrt{s} = 8$ TeV, *Journal of High Energy Physics*, 2017(12), dec 2017, https://doi.org/10.1007/jhep12(2017)059. (Cited on page 202.)

[152] ATLAS Collaboration, Measurement of the cross-section and charge asymmetry of W bosons produced proton-proton collisions at $\sqrt{s} = 8$ TeV with the ATLAS detector, *The European Physical Journal C*, 79(9), sep 2019, https://doi.org/10.1140/epjc/s10052-019-7199-0. (Cited on page 202.)

[153] ATLAS Collaboration, Measurement of the ratio of cross sections for inclusive isolated-photon production in pp collisions at $\sqrt{s} = 13$ and 8 TeV with the ATLAS detector, *Journal of High Energy Physics*, 2019(4), apr 2019, https://doi.org/10.1007/jhep04(2019)093. (Cited on page 202.)

[154] ATLAS Collaboration, Measurements of top-quark pair differential and double-differential cross-sections in the l+jets channel with pp collisions at $\sqrt{s} = 13$ TeV using the ATLAS detector, *The European Physical Journal C*, 79(12), dec 2019, https://doi.org/10.1140/epjc/s10052-019-7525-6. (Cited on page 202.)

[155] ATLAS Collaboration, Measurement of the inclusive jet cross-sections in proton-proton collisions at $\sqrt{s} = 8$ TeV with the ATLAS detector, *Journal of High Energy Physics*, 2017(9), sep 2017, https://doi.org/10.1007/jhep09(2017)020. (Cited on page 202.)

[156] Jon Pumplin, Data set diagonalization in a global fit, *Phys. Rev. D*, 80:034002, Aug 2009, https://link.aps.org/doi/10.1103/PhysRevD.80.034002. (Cited on page 203.)

[157] ATLAS Collaboration, Athena, April 2019, https://doi.org/10.5281/zenodo.2641997. (Cited on page 208.)

[158] ATLAS Collaboration, Precise measurements of W and Z transverse momentum spectra with the ATLAS detector at $\sqrt{s} = 5.02$ TeV and 13 TeV, Technical report, CERN, ATLAS-CONF-2023-028, Geneva, 2023, https://cds.cern.ch/record/2861057. (Cited on page 209.)

[159] Hung-Liang Lai, Marco Guzzi, Joey Huston, Zhao Li, Pavel M. Nadolsky, Jon Pumplin, and C.-P. Yuan, New parton distributions for collider physics, *Physical Review D*, 82(7), oct 2010, https://doi.org/10.1103/physrevd.82.074024. (Cited on page 209.)

[160] J. Alwall et al., The automated computation of tree-level and next-to-leading order differential cross sections, and their matching to parton shower simulations, *Journal of High Energy Physics*, 2014(7), jul 2014, https://doi.org/10.1007/jhep07(2014)079. (Cited on page 211.)

[161] V. Bertone, R. Frederix, S. Frixione, J. Rojo, and M. Sutton, aMCfast: automation of fast NLO computations for PDF fits, *Journal of High Energy Physics*, 2014(8), aug 2014, https://doi.org/10.1007/jhep08(2014)166. (Cited on page 211.)

[162] John Campbell, Joey Huston, and Frank Krauss, *The Black Book of Quantum Chromodynamics : a Primer for the LHC Era*, Oxford University Press, 2018, https://doi.org/10.1093/oso/9780199652747.001.0001. (Cited on page 219.)

[163] xFitter Collaboration, xFitter - Reactions. Wiki, (Online; accessed 2023.07.14), https://gitlab.cern.ch/fitters/xfitter/-/wikis/ReactionInterface. (Cited on page 223.)